

Copyright

by

Hoon Lee

2012

**The Dissertation Committee for Hoon Lee Certifies that this is the
approved version of the following dissertation:**

**Visual Performance Maps for Expanded Human Choice based on Duty /
Demand Cycles in Hybrid Vehicle's Multi-Speed Hub Drive Wheels**

Committee:

Delbert Tesar, Supervisor

Eric P Fahrenthold

Dragan Djurdjanovic

Dongmei Chen

Alexis Kwasinski

Pradeepkumar Ashok

**Visual Performance Maps for Expanded Human Choice based on Duty /
Demand Cycles in Hybrid Vehicle's Multi-Speed Hub Drive Wheels**

by

Hoon Lee, B.S.; M.S.E.

Dissertation

Presented to the Faculty of the Graduate School of

The University of Texas at Austin

in Partial Fulfillment

of the Requirements

for the Degree of

Doctor of Philosophy

The University of Texas at Austin

August 2012

Dedication

I dedicated this work to my parents and my beautiful wife

Acknowledgements

I would like to express my sincere gratitude to my supervisor Dr. Delbert Tesar, Director of Robotics Research Group at the University of Texas at Austin and Dr. Pradeepkumar Ashok for their patient guidance of this research effort.

Visual Performance Maps for Expanded Human Choice based on Duty / Demand Cycles in Hybrid Vehicle's Multi-Speed Hub Drive Wheels

Hoon Lee, Ph.D.

The University of Texas at Austin, 2012

Supervisor: Delbert Tesar

The Multi-speed hub Drive Wheel (MDW) for four-independent drive wheels of future electric vehicles has recently been designed by the Robotics Research Group at the University of Texas at Austin. The MDW is equipped with four distinct speeds (two electrical and two mechanical) with the aim of improving efficiency and enhancing the drivability features of the vehicle, such as acceleration and braking on the driver's command. The MDW will have different unsprung weights in the wheels depending on a range of suggested rated power levels such as 16, 20, 24, 32, up to a maximum of 40 hp, which would then become basic choices for the customer.

The overall objective of the research is to analytically develop a framework for maximizing human vehicle choice by means of visualizing human performance needs/requirements so that customer demands can be met at the time of purchase for an open architecture hybrid electric vehicle which would then be assembled on demand. In addition, based on the customer's individual duty/demand cycle, a vehicle can then be tailored to meet the particular customer priorities such as cost and efficiency, or on the other end of the spectrum, one who is an aggressive driver. This leads to expanded

human choice for future electric vehicles. To meet human needs, the appropriate MDW will be software customized to suit the customer's demand cycle.

Satisfying human needs implies responding directly to human commands / objectives over the life history of the vehicle. The decision framework developed in this study is based on detailed human needs structured by performance maps to visually guide the customer in terms of purchase / operation / maintenance / refreshment decisions.

This framework augments the MDW design procedure to maximize operational efficiency and drivability for unique customer requirements. The customer-oriented duty cycle analysis based on an individual's measured demand cycle is proposed to structure the MDW specification in terms of ten purchase criteria. Also, a comparison of two speed regimes in the MDW and Protean's single speed in-wheel model is made and discussed in terms of efficiency. The analytical result shows that a remarkable efficiency improvement in terms of loss reduction of 1.9x for urban and 1.8x for highway duty cycles is feasible. In addition, another loss reduction of 1.2x is expected by using the reconfigurable power/electronic controllers.

The present study looked at the effect of the unsprung mass on acceleration, braking, and cornering maneuvers under various road conditions (i.e., dry asphalt, wet asphalt, snowy or icy road) which was evaluated and compared based on the implementation of a nonlinear 14 DOF full-vehicle model based on ride (7 DOF), handling (3 DOF), tire (4 DOF), slip ratio, slip angle, and the tire magic formula. Based on the 14 DOF full-vehicle model, visual performance maps are generated in terms of ten operational criteria to assist the customer to visualize the vehicle's expected performance.

Table of Contents

List of Tables	xvi
List of Figures	xx
Chapter 1. Introduction.....	1
1.1 Background	1
1.1.1 Electric Vehicles	1
1.1.2 Multi-Speed Hub Drive Wheel	2
1.1.3 Human Choice	4
1.1.4 Visual Performance Maps.....	6
1.1.5 Duty Cycles / Demand Cycles	7
1.2 Research Problem	8
1.3 Research Objectives.....	10
1.4 Research Outline.....	11
Chapter 2. Literature Review.....	14
2.1 The History of In Wheel Motors.....	14
2.2 Electric Vehicle Configurations.....	15
2.3 Comparison of a MDW and an In-Wheel Motor	19
2.4 Drivability	21
2.4.1 Handling (Safety).....	21
2.4.2 Ride Comfort	23
2.4.3 Acceleration	28
2.4.4 Braking.....	29
2.5 Efficiency	32
2.6 Durability	35
2.7 Cost	35
2.8 Bearing Degradation	36
2.9 Crossed Roller Bearings, Four-Point Bearings, and Tapered Roller Bearings	38
2.10 Chapter Summary	40

Chapter 3.	Vehicle Multi-Speed Hub Drive Wheels	41
3.1	Star Compound Gear Train.....	41
3.2	Clutch.....	44
3.2.1	MDW Clutch Version 1	45
3.2.1.1	Spline Design	50
3.2.1.2	Clutch Ball Design	52
3.2.1.3	Belleville Spring Washers.....	53
3.2.1.4	Ring Cage Design.....	58
3.2.1.5	Clutch Shift Operation	59
3.2.2	MDW Clutch Version 2	62
3.3	Switched Reluctance Motor.....	65
3.4	Reconfigurable Power Controller	66
Chapter 4.	Vehicle Modeling.....	69
4.1	Overview of Vehicle Modeling based on a Bayesian Causal Network.....	70
4.1.1	Longitudinal Vehicle Dynamics	71
4.1.2	Acceleration Resistance	73
4.1.3	Aerodynamic Drag Resistance.....	75
4.1.4	Rolling Resistance	76
4.1.5	Grade Resistance.....	77
4.1.6	Comparison of Acceleration, Aerodynamic, Rolling, and Grade Resistances.....	78
4.1.7	Bayesian Causal Network	88
4.2	Vehicle Ride Model.....	90
4.2.1	Quarter-Vehicle (2 DOF) Ride Model.....	90
4.2.1.1	Handling Performance Maps (Dynamic Contact Force).....	101
4.2.1.2	Suspension Stroke Performance Maps (Suspension Stroke).....	105
4.2.1.3	Ride Comfort Performance Maps (Sprung Mass Acceleration).....	109
4.2.2	Half-Vehicle (4 DOF) Ride Model	113
4.2.3	Full-Vehicle (7 DOF) Ride Model.....	116

4.3	Vehicle Handling Model	123
4.3.1	Bicycle (2 DOF) Model	123
4.3.1.1	Simulation Results of Bicycle Model.....	127
4.3.1.2	Four wheel steering	129
4.3.2	Horizontal Handling (3 DOF) Model	131
4.4	Tire Model	137
4.4.1	Tire Coordinate System	137
4.4.2	Tire (4 DOF) Model.....	139
4.4.3	Slip Angle	141
4.4.4	Longitudinal Slip / Skid Ratio	142
4.4.5	Magic Formula.....	146
4.4.6	Friction Circle	151
4.4.7	Force Margin.....	152
4.5	Nonlinear 14 Degree-Of-Freedom Full-Vehicle Model	153
4.5.1	Trajectory Kinematics.....	153
4.5.2	Anti-Roll Bar	155
4.5.3	Center of Gravity	158
4.5.4	Normal Forces of Each Wheel.....	160
4.5.4.1	Static Normal Force	162
4.5.4.2	Grade Load Transfer	163
4.5.4.3	Aerodynamic Load Transfer	163
4.5.4.4	Longitudinal Load Transfer	164
4.5.4.5	Lateral Load Transfer.....	165
4.5.5	Nonlinear 14 Degree-of-Freedom Full-Vehicle Model	169
4.5.6	Validation of a Nonlinear 14 Degree-of-Freedom Full-Vehicle Model	170
4.5.7	Transient and Steady State Response	175
4.6	Chapter Summary	177
Chapter 5.	Vehicle Simulation Results.....	179
5.1	Effects of Unsprung Mass on Performance Criteria	179

5.1.1	Acceleration	179
5.1.2	Braking.....	185
5.1.3	Cornering Maneuver	191
5.1.3.1	Step Steer.....	192
5.1.3.2	Single-Lane Change	199
5.2	Effects of Increased Unsprung Mass under Various Road Conditions	205
5.2.1	Dry Asphalt Road	205
5.2.1.1	Acceleration and Braking.....	205
5.2.1.2	Cornering Maneuver	219
5.2.2	Wet Asphalt Road.....	233
5.2.2.1	Acceleration and Braking.....	233
5.2.2.2	Cornering Maneuver	247
5.2.3	Snowy Road	258
5.2.3.1	Acceleration and Braking.....	258
5.2.3.2	Cornering Maneuver	273
5.3	Performance Maps For Different Vehicle Weight.....	285
5.3.1	Acceleration Performance Map	285
5.3.2	Braking Performance Map.....	288
5.3.3	Force Margin Performance Map during a Cornering Maneuver	291
5.4	Performance Maps For The Same Vehicle Weight	296
5.4.1	Acceleration Performance Map	296
5.4.2	Braking Performance Map.....	299
5.4.3	Force Margin Performance Map during a Cornering Maneuver	301
5.5	Chapter Summary	305
Chapter 6.	Duty / Demand Cycles	307
6.1	Duty Cycle Analysis Based on Existing Duty Cycles	308
6.1.1	Standard Duty Cycles	309
6.1.1.1	Urban Dynamometer Driving Schedule (UDDS)	310
6.1.1.2	Highway Fuel Economy Test (HWFET)	311
6.1.1.3	Aggressive Driver (US06).....	312

6.1.2	Total Wheel Torque and Power	313
6.1.2.1	Urban Dynamometer Driving Schedule (UDDS)	315
6.1.2.2	Highway Fuel Economy Test (HWFET)	317
6.1.2.3	Aggressive Driver (US06).....	318
6.1.3	Speed-Acceleration Frequency Distribution.....	319
6.1.3.1	Urban Dynamometer Driving Schedule (UDDS)	319
6.1.3.2	Highway Fuel Economy Test (HWFET)	321
6.1.3.3	Aggressive Driver (US06).....	322
6.1.4	Wheel Torque-Speed	324
6.1.4.1	Urban Dynamometer Driving Schedule (UDDS)	324
6.1.4.2	Highway Fuel Economy Test (HWFET)	326
6.1.4.3	Aggressive Driver (US06).....	327
6.1.5	Motor Output Torque and Power.....	328
6.1.5.1	Urban Dynamometer Driving Schedule (UDDS)	329
6.1.5.2	Highway Fuel Economy Test (HWFET)	331
6.1.5.3	Aggressive Driver (US06).....	332
6.1.6	Motor Power Demand.....	334
6.1.7	MDW Specification	335
6.1.7.1	UDDS – How to Maximize efficiency in terms of a MDW? 336	
6.1.7.2	Highway Fuel Economy Test (HWFET)	344
6.1.7.3	US06 - How to Maximize Drivability in terms of a MDW? 347	
6.2	Energy Consumption Analysis	353
6.2.1	Estimating Input Power Demands from Output Power	353
6.2.2	Traction and Braking Energy Dissipation at Motor Output Power	354
6.2.3	Traction and Braking Energy Dissipation at Motor Input Power	355
6.2.4	Efficiency Based on Input Energy and Heat Energy	356
6.3	Comparison of a MDW and Protean’s In-Wheel Motor.....	358
6.3.1	Comparison of Two Speed Regimes and One Speed Regime..	358
6.3.1.1	Urban Duty Cycle (UDDS)	358

6.3.1.2	Highway Duty Cycle (HWFET)	363
6.3.2	Comparison of a MDW with a Reconfigurable Controller.....	367
6.4	Individual Demand Cycles.....	370
6.4.1	Acceleration Time of 0-60 mph.....	373
6.4.2	Maintaining Cruising Speed	376
6.4.3	Maximum gradeability.....	378
6.4.4	Acceleration from 30 to 50 mph	380
6.4.5	Acceleration from 50 mph to 70 mph.....	382
6.5	Chapter Summary	383
Chapter 7.	Purchase / Operation / Maintenance / Refreshment Standpoints	385
7.1	Purchase Criteria.....	386
7.1.1	Cost	386
7.1.2	Weight.....	389
7.1.3	Power	394
7.1.4	Acceleration	395
7.1.5	Gradeability.....	399
7.1.6	Braking.....	400
7.1.6.1	Normal Braking (420 ft-lb)	400
7.1.6.2	Emergency Braking (840 ft-lb)	404
7.1.7	Handling.....	408
7.1.8	Ride Comfort	412
7.1.9	Efficiency.....	415
7.1.10	Durability	416
7.2	Operation Criteria	418
7.2.1	Cornering Force Margin	418
7.2.2	Roll Angle.....	420
7.2.3	Sideslip Angle.....	421
7.2.4	Lateral Acceleration.....	423
7.2.5	Slip Angle	424
7.2.6	Yaw Rate.....	425

7.2.7	Acceleration Force Margin	427
7.2.8	Braking Force Margin.....	428
7.2.9	Pitch Angle.....	429
7.2.10	Travel Range.....	430
7.3	Maintenance Criteria.....	434
7.3.1	Efficiency.....	434
7.3.2	Power Level	436
7.3.3	Responsiveness	436
7.3.4	Torque Margin	437
7.3.5	Temperature Margin	439
7.3.6	Noise Margin	440
7.3.7	Sensor Degradation.....	441
7.3.8	Bearing Degradation	442
7.3.9	Wire Insulation Degradation.....	444
7.3.10	Clutch Degradation.....	444
7.4	Refreshment Criteria.....	446
7.4.1	Power Level	446
7.4.2	Cost Benefit / Replacement Cost	447
7.4.3	Efficiency Benefit	447
7.4.4	Torque Level.....	448
7.4.5	Enhanced Handling and Ride Comfort.....	449
7.4.6	Enhanced Sensors	449
7.4.7	Enhanced Control Software	450
7.4.8	Enhanced Durability	450
7.4.9	Enhanced Temperature Tolerance	451
7.4.10	Enhanced Safety.....	451
7.5	Chapter Summary	451
Chapter 8.	Summary and Conclusions	459
8.1	Research Objectives.....	459
8.2	Literature Review.....	460

8.3	Research Results and Discussions	462
8.3.1	Vehicle Modeling.....	462
8.3.1.1	Full-Vehicle (7 DOF) Ride Model	462
8.3.1.2	Horizontal Handling (3 DOF) Model.....	463
8.3.1.3	Tire (4 DOF) Model	466
8.3.1.4	Nonlinear 14 Degree-Of-Freedom Full-Vehicle Model...	469
8.3.2	Vehicle Simulation Results.....	471
8.3.2.1	Effects of Unsprung Mass on Performance Criteria ..	471
8.3.2.2	Effects of Increased Unsprung Mass under Various Road Conditions	474
8.3.3	Duty / Demand Cycles	477
8.3.4	Comparison of Two Speed Regimes and One Speed Regime ..	480
8.3.5	Comparison of a MDW with a Reconfigurable Controller.....	482
8.3.6	Purchase / Operation / Maintenance / Refreshment Standpoints....	485
8.4	Contributions.....	499
8.5	Recommendations and Future Work	501
8.5.1	Effects of the Total/Partial Failure on Performance Criteria	501
8.5.2	Operational Decision Making Based on the Total/Partial Failure	502
Appendix A.	Road Roughness Classification.....	505
Appendix B.	Standard Driving Cycles	509
Appendix C.	MDW Clutch Version 2	518
References.....		522
Vita		532

List of Tables

Table 1-1: MDW weight and power	3
Table 2-1: Comparison of Centre drives and Wheel-hub drives	16
Table 2-2: List of References on Handling	22
Table 2-3: Levels of acceptability of ride comfort	26
Table 2-4: List of Ride Comfort	27
Table 2-5: Classification of bearing failure causes [SKF; Wilcoxon-Research; Wilcock and Booser,1957].....	37
Table 3-1: Spline analysis for input shaft	51
Table 3-2: Clutch ball analysis for 1 st input pinion.....	53
Table 3-3: Belleville spring washers analysis.....	56
Table 3-4: Ring cage analysis	58
Table 4-1: Vehicle Parameters.....	80
Table 4-2: Vehicle system parameters for the quarter-vehicle model	93
Table 4-3: Vehicle Parameters.....	127
Table 4-4: Average values of friction coefficient	144
Table 4-5: Coefficient values in the Magic Formula for a vehicle tire.....	147
Table 5-1: Vehicle parameters used in simulation.....	182
Table 5-2: Normal forces of each wheel during acceleration	184
Table 5-3: Normal forces of each wheel during braking	191
Table 5-4: Normal forces of each wheel during step steer	198
Table 5-5: Normal forces of each wheel during single-lane change	204
Table 5-6: Normal forces of each wheel.....	209
Table 5-7: Traction and braking forces of each wheel ($m_u = 10\%$).....	211

Table 5-8: Traction and braking forces of each wheel ($m_u = 22\%$).....	213
Table 5-9: Force margins of each wheel.....	216
Table 5-10: Normal forces of each wheel.....	223
Table 5-11: Traction and braking forces of each wheel ($m_u = 10\%$, $\mu = 0.9$)	225
Table 5-12: Traction and braking forces of each wheel ($m_u = 22\%$, $\mu = 0.9$)	227
Table 5-13: Force margins of each wheel.....	230
Table 5-14: Comparison of acceleration and braking.....	236
Table 5-15: Normal forces of each wheel.....	238
Table 5-16: Traction and braking forces of each wheel ($m_u = 10\%$, $\mu = 0.5$)	240
Table 5-17: Traction and braking forces of each wheel ($m_u = 22\%$, $\mu = 0.5$)	242
Table 5-18: Force margins of each wheel.....	244
Table 5-19: Normal forces of each wheel.....	249
Table 5-20: Traction and braking forces of each wheel ($m_u = 10\%$, $\mu = 0.5$)	251
Table 5-21: Traction and braking forces of each wheel ($m_u = 10\%$, $\mu = 0.5$)	253
Table 5-22: Force margins of each wheel.....	255
Table 5-23: Comparison of acceleration and braking.....	261
Table 5-24: Normal forces of each wheel.....	263
Table 5-25: Traction and braking forces of each wheel ($m_u = 10\%$, $\mu = 0.2$)	265
Table 5-26: Traction and braking forces of each wheel ($m_u = 22\%$, $\mu = 0.2$)	267
Table 5-27: Force margins of each wheel ($\mu = 0.2$).....	269
Table 5-28: Minimum force margins of each wheel ($\mu = 0.2$)	270
Table 5-29: Normal forces of each wheel.....	275
Table 5-30: Traction and braking forces of each wheel ($m_u = 10\%$, $\mu = 0.2$)	277
Table 5-31: Traction and braking forces of each wheel ($m_u = 22\%$, $\mu = 0.2$)	279
Table 5-32: Force margins of each wheel.....	282

Table 5-33: Minimum force margins of each wheel ($\mu = 0.2$)	283
Table 5-34: Vehicle parameters used in simulation.....	286
Table 5-35: Vehicle parameters used in simulation.....	297
Table 6-1: Vehicle Parameters.....	314
Table 6-2: Simulation results	357
Table 6-3: Simulation results	367
Table 6-4: Vehicle Parameters.....	372
Table 7-1: Assumed component cost list	387
Table 7-2: Vehicle weight parameters in terms of DW and MDW	391
Table 7-3: Vehicle weight parameters in terms of the Intelligent Corner	392
Table 7-4: Speed Related Performance Values	409
Table 7-5: Speed Related Vertical Body Acceleration Performance Values	413
Table 7-6: Summary of Purchase Criteria	453
Table 7-7: Summary of Operation Criteria.....	455
Table 7-8: Summary of Maintenance Criteria	456
Table 7-9: Summary of Refreshment Criteria	457
Table 8-1: Summary of Literature Review	461
Table 8-2: Comparison of acceleration and braking.....	472
Table 8-3: Simulation results	481
Table 8-4: Summary of Purchase Criteria	489
Table 8-5: Summary of Operation Criteria.....	494
Table 8-6: Summary of Maintenance Criteria	496
Table 8-7: Acceleration, total power ratings, and torque responding to customer's choice	497
Table 8-8: Summary of Refreshment Criteria	498

Table 8-9: Summary of Contribution.....	500
Table 8-10: Summary of future work	504

List of Figures

Figure 1-1: MDW Configuration	4
Figure 1-2: Performance maps in an electromechanical actuator [Ashok and Tesar,2007]	6
Figure 2-1: First electric vehicle driven by in-wheel motor	14
Figure 2-2: Electric vehicle configurations: M-Motor, GB-Gearbox, D-Differential, C-Clutch, FG-Fixed Gear [Chan,2002]	15
Figure 2-3: In-wheel motor configurations.....	17
Figure 2-4: Comparison of Protean's in-wheel motor and the MDW	19
Figure 2-5: Effect of unsprung-to-sprung mass ratio on transmissibility, suspension travel, and dynamic tire deflection ratio	25
Figure 2-6: Acceleration plot as a function of wheel torque and speed.....	28
Figure 2-7: Functions achieved by an IWM [Murata,2011]	30
Figure 2-8: Motor ABS [Murata,2011].....	31
Figure 2-9: Efficiency map with respect to torque and speed	33
Figure 2-10: Torque analysis by Finite Element Method Magnetics [Tesar and Ashok,May, 2011]	34
Figure 2-11: Cross section of three different bearings.....	39
Figure 3-1: MDW Configuratoin	41
Figure 3-2: MDW-wheel/suspension geometry and short force path [Tesar,2007].....	43
Figure 3-3: Two-speed clutch mechanism.....	46
Figure 3-4: Wheel demands / response for 3000 lb vehicle (16 hp).....	48
Figure 3-5: Free-body diagram for a clutch disk	52
Figure 3-6: Belleville spring washers [SchNorr]	54

Figure 3-7: Clutch disk equipped with belleville spring washers.....	57
Figure 3-8: Ring cage of a clutch disk.....	59
Figure 3-9: Clutch shift operation.....	60
Figure 3-10: Force, acceleration, velocity, and displacement during clutch operation	61
Figure 3-11: Exploded view of the synchro mesh clutch assembly.....	62
Figure 3-12: Cross-section of freewheeling front amplifier gear	63
Figure 3-13: Efficiency Map.....	65
Figure 3-14: Torque Analysis of SRM	66
Figure 3-15: Reconfigurable power controller [Tesar and Ashok,May, 2011]	67
Figure 4-1: Forces acting on a two-axle vehicle.....	72
Figure 4-2: Air flow recirculation in a wheel well	75
Figure 4-3: Rolling resistance in a free rolling tire.....	76
Figure 4-4: Comparison of resistances and duty cycles for the MDW ($a = 0.1g$) .	82
Figure 4-5: Comparison of resistances and duty cycles for the MDW ($a = 0.2g$) .	83
Figure 4-6: Comparison of resistances and duty cycles for the MDW ($a = 0.3g$) .	85
Figure 4-7: Comparison of four different resistances for the MDW ($a = 0.1g$).....	86
Figure 4-8: Comparison of three different resistances for the MDW with no grade during high speed driving condition ($a = 0.1g$, $v = 120$ mph)	87
Figure 4-9: Bayesian causal network.....	88
Figure 4-10: Quarter-vehicle model and Free-body diagram	91
Figure 4-11: Effect of an increased unsprung mass on tire deflection, suspension stroke, and sprung mass acceleration versus time	96

Figure 4-12: Frequency response of dynamic contact force, suspension stroke, and sprung mass acceleration with four different unsprung-to-sprung mass ratios under a random average (asphalt) road input and constant velocity 13.2 m/s.....	97
Figure 4-13: Frequency response of dynamic contact force, suspension stroke, and sprung mass acceleration with four different unsprung-to-sprung mass ratios under a random average (asphalt) road input and constant velocity 13.2 m/s.....	100
Figure 4-14: Dynamic contact force with six different unsprung-to-sprung mass ratios under a random average (asphalt) road input, as a speed increases from 4.4 m/s to 30.8 m/s.....	102
Figure 4-15: Handling performance map (dynamic contact force) with respect to six different unsprung-to-sprung mass ratios and velocity in terms of five classes of road surfaces.....	103
Figure 4-17: Suspension stroke performance map with respect to six different unsprung-to-sprung mass ratios and velocity in terms of five classes of road surfaces	107
Figure 4-18: Sprung mass acceleration with six different unsprung-to-sprung mass ratios under a random average (asphalt) road input, as speed increases from 4.4 m/s to 30.8 m/s	110
Figure 4-19: Ride comfort performance map (frequency weighted RMS sprung acceleration) with respect to six different unsprung-to-sprung mass ratios and velocity in terms of 5 classes of road surfaces	111
Figure 4-20: Half-vehicle model.....	113
Figure 4-21: Free body diagram	114

Figure 4-22: Full-vehicle model	116
Figure 4-23: Free body diagram	117
Figure 4-24: Bicycle Model	124
Figure 4-25: Simulation results based on the Bicycle Model	128
Figure 4-26: Four-wheel steering vehicle at low speeds	129
Figure 4-27: Four-wheel steering vehicle at high speeds	130
Figure 4-28: Horizontal Handling (3 DOF) Model.....	132
Figure 4-29: Pitch motion due to braking or traction	133
Figure 4-30: Roll motion due to a cornering maneuver.....	135
Figure 4-31: ISO coordinate system	137
Figure 4-32: Lateral force as a function of normal force at different camber angles	138
Figure 4-33: One-wheel rotational dynamics	139
Figure 4-34: Slip angle induced tire self-aligning torque	141
Figure 4-35: Longitudinal, lateral forces and velocity components	142
Figure 4-36: Variation of tractive effort with respect to longitudinal slip.....	144
Figure 4-37: Friction coefficient versus longitudinal slip / skid ratio	145
Figure 4-38: Tire characteristics of the Magic Formula for fitting tire test data .	146
Figure 4-39: Longitudinal force w.r.t. normal force and longitudinal slip/skid ..	148
Figure 4-40: Lateral force w.r.t. normal force and slip angle	149
Figure 4-41: Self-aligning Moment w.r.t. normal force and slip angle	150
Figure 4-42: Lateral force versus longitudinal force at a given slip angle	151
Figure 4-43: Rigid vehicle in a planar motion	153
Figure 4-44: Volvo 80 MacPherson front wheel suspension and full-vehicle Adams Model[Wirje and Carlsson,2011].....	155
Figure 4-45: Roll moment of a vehicle in left cornering maneuver	156

Figure 4-46: Shift of the CG in the x direction.....	158
Figure 4-47: Shift of the CG in the y direction.....	159
Figure 4-48: Forces acting on a vehicle.....	162
Figure 4-49: Longitudinal load transfer.....	164
Figure 4-50: Lateral load transfer	165
Figure 4-51: Schematic diagram of 14 DOF full-vehicle model consisting of block diagrams in MATLAB/SIMULINK	169
Figure 4-52: Validation of lateral acceleration response	172
Figure 4-53: Validation of roll angle response	173
Figure 4-54: Comparative responses to step steer (14 DOF and 8 DOF models) [Shim and Ghike,2007].....	175
Figure 4-55: Validation of lateral acceleration and roll angle response to a step steer	176
Figure 5-1: Simulation results for acceleration of 0-60 mph.....	181
Figure 5-2: Simulation results of vehicle response for acceleration of 0–60 mph.....	183
Figure 5-3: Simulation results for braking 60–0 mph	187
Figure 5-4: Simulation results of vehicle response for braking 60-0 mph	189
Figure 5-5: Simulation results for a cornering maneuver (step steer 10°)	193
Figure 5-6: Simulation results of vehicle response for a cornering maneuver (10°).....	197
Figure 5-7: Simulation results for single-lane change maneuver	200
Figure 5-8: Simulation results of vehicle response for single-lane change maneuver	203
Figure 5-9: Simulation results for acceleration and braking on dry asphalt ($\mu = 0.9$)	207

Figure 5-10: Normal forces during acceleration and braking on dry asphalt ($\mu = 0.9$)	208
Figure 5-11: Traction and braking forces on dry asphalt ($m_u = 10\%$, $\mu = 0.9$)	210
Figure 5-12: Traction and braking forces on dry asphalt ($m_u = 22\%$, $\mu = 0.9$)	212
Figure 5-13: Effect of unsprung mass on force margin on dry asphalt ($\mu = 0.9$)	214
Figure 5-14: Force margins of each wheel on dry asphalt ($m_u = 0.22$, $\mu = 0.9$)	217
Figure 5-15: Simulation results for a single-lane change on dry asphalt ($\mu = 0.9$)	220
Figure 5-16: Normal forces for a single-lane change on dry asphalt ($\mu = 0.9$)	222
Figure 5-17: Longitudinal and lateral forces on dry asphalt ($m_u = 10\%$, $\mu = 0.9$)	224
Figure 5-18: Longitudinal and lateral forces on dry asphalt ($m_u = 22\%$, $\mu = 0.9$)	226
Figure 5-19: Effect of unsprung mass on force margin on dry asphalt ($\mu = 0.9$)	229
Figure 5-20: Front and rear slip angle	231
Figure 5-21: Force margin of each wheel on dry asphalt ($\mu = 0.9$)	232
Figure 5-22: Simulation results for acceleration and braking on wet asphalt ($\mu = 0.5$)	235
Figure 5-23: Normal forces during acceleration and braking on wet asphalt ($\mu = 0.5$)	237
Figure 5-24: Traction and braking forces on wet asphalt ($m_u = 10\%$, $\mu = 0.5$)	239
Figure 5-25: Traction and braking forces on wet asphalt ($m_u = 22\%$, $\mu = 0.5$)	241
Figure 5-26: Effect of unsprung mass on force margin on wet asphalt ($\mu = 0.5$)	243
Figure 5-27: Minimum Force margins of each wheel on wet asphalt ($m_u = 0.22$, $\mu = 0.5$)	245
Figure 5-28: Friction circles of each wheel on wet asphalt ($\mu = 0.5$)	247
Figure 5-29: Normal forces for a single-lane change on wet asphalt ($\mu = 0.5$)	248
Figure 5-30: Longitudinal and lateral forces on wet asphalt ($m_u = 10\%$, $\mu = 0.5$)	250

Figure 5-31: Longitudinal and lateral forces on wet asphalt ($m_u = 22\%$, $\mu = 0.5$)	252
Figure 5-32: Effect of unsprung mass on force margin on wet asphalt ($\mu = 0.5$)	254
Figure 5-33: Front and rear slip angle.....	256
Figure 5-34: Force margins of each wheel on wet asphalt ($m_u = 22\%$, $\mu = 0.5$)	257
Figure 5-35: Simulation results for acceleration and braking on snowy road ($\mu = 0.2$)	260
Figure 5-36: Normal forces during acceleration and braking on a snowy road ($\mu = 0.2$)	262
Figure 5-37: Traction and braking forces on a snowy road ($m_u = 10\%$, $\mu = 0.2$)	264
Figure 5-38: Traction and braking forces on a snowy road ($m_u = 22\%$, $\mu = 0.2$)	266
Figure 5-39: Effect of unsprung mass on force margin on a snowy road ($\mu = 0.2$)	268
Figure 5-40: Force margins of each wheel on a snowy road ($m_u = 0.22$, $\mu = 0.2$)	271
Figure 5-41: Friction circles of each wheel on a snowy road ($\mu = 0.2$).....	273
Figure 5-42: Normal forces for a single-lane change on a snowy road ($\mu = 0.2$)	274
Figure 5-43: Longitudinal and lateral forces on a snowy road ($m_u = 10\%$, $\mu = 0.2$)	276
Figure 5-44: Longitudinal and lateral forces on a snowy road ($m_u = 22\%$, $\mu = 0.2$)	278
Figure 5-45: Effect of unsprung mass on force margin on a snowy road ($\mu = 0.2$)	281
Figure 5-46: Force margin of each wheel on snowy road ($m_u = 0.22$, $\mu = 0.2$)...	284
Figure 5-47: Acceleration performance map given constant torque (290 N-m (214 ft-lb)).....	287
Figure 5-48: Braking performance map given constant torque (570 N-m(420 ft-lb))	289
Figure 5-49: Force margin performance map (front-inside) for a single-lane change	292

Figure 5-50: Force margin performance map (front-outside) for a single-lane change	293
Figure 5-51: Force margin performance map of rear-inside and rear-outside wheels	294
Figure 5-52: Acceleration performance map given constant torque (290 N-m (214 ft-lb))	298
Figure 5-53: Braking performance map given constant torque (570 N-m(420 ft-lb))	300
Figure 5-54: Force margin performance map (front-inside) for a single-lane change	302
Figure 5-55: Force margin performance map (front-outside) for a single-lane change	303
Figure 5-56: Force margin performance map of rear-inside and rear-outside wheels	304
Figure 6-1: Driving cycle (UDDS)	310
Figure 6-2: Driving cycle (HWFET)	311
Figure 6-3: Driving cycle (US06)	312
Figure 6-4: Total wheel torque and power requirement derived from duty cycle (UDDS)	316
Figure 6-5: Total wheel torque and power requirement derived from duty cycle (HWFET)	317
Figure 6-6: Total wheel torque and power requirement derived from duty cycle (US06)	318
Figure 6-7: Speed-acceleration frequency distribution plot (UDDS)	320
Figure 6-8: Speed-acceleration frequency distribution plot (HWFET)	321

Figure 6-9: Speed-acceleration frequency distribution plot (US06).....	322
Figure 6-10: Total wheel torque-speed (UDDS)	325
Figure 6-11: Total wheel torque-speed (HWFET).....	326
Figure 6-12: Total wheel torque-speed (US06)	327
Figure 6-13: Motor output speed, acceleration, torque, and power (UDDS)	330
Figure 6-14: Motor output speed, acceleration, torque, and power (HWFET).....	331
Figure 6-15: Motor output speed, acceleration, torque, and power (US06)	332
Figure 6-16: Efficiency map of a motor	334
Figure 6-17: Mapping wheel torque into motor torque w.r.t first and second stages (UDDS)	336
Figure 6-18: Mapping wheel torque into motor torque w.r.t first and second stages (UDDS)	339
Figure 6-19: Overall efficiency map w.r.t wheel torque and wheel speed (UDDS)	342
Figure 6-20: Mapping wheel torque into motor torque w.r.t first and second stages (HWFET)	344
Figure 6-21: Overall efficiency map w.r.t wheel torque and wheel speed (HWFET)	346
Figure 6-22: Mapping wheel torque into motor torque w.r.t first and second stages (US06).....	347
Figure 6-23: Mapping wheel torque into motor torque w.r.t first and second stages (US06).....	349
Figure 6-24: Overall efficiency map w.r.t wheel torque and wheel speed (US06)	351
Figure 6-25: Mapping Output Requirement to Input Demand (UDDS).....	353
Figure 6-26: Traction and braking energy extracted from motor output power (UDDS)	355

Figure 6-27: Traction and braking energy extracted from motor input power (UDDS)	356
Figure 6-28: Heat energy lost due to inefficiencies (UDDS)	356
Figure 6-29: Combined efficiency map of Protean's in- wheel motor during urban driving	358
Figure 6-30: Efficiency map of Protean's in-wheel motor	359
Figure 6-31: Combined Efficiency map of a MDW	360
Figure 6-32: Efficiency map of a MDW	361
Figure 6-33: Combined efficiency of an in- wheel motor during highway driving	363
Figure 6-34: Efficiency map of Protean's in-wheel motor	364
Figure 6-35: Combined Efficiency map of an MDW	365
Figure 6-36: Efficiency map of an MDW	366
Figure 6-37: Efficiency maps of an MDW without & with a reconfigurable controller	368
Figure 6-38: Efficiency maps of an MDW without & with a reconfigurable controller	369
Figure 6-39: Power performance map w.r.t. unsprung mass ratio and time	374
Figure 6-40: Wheel torque performance map w.r.t. unsprung mass ratio and time	375
Figure 6-41: Tractive effort versus velocity (MDW, 16 hp)	376
Figure 6-42: Tractive effort versus velocity (a) 20 hp, (b) 24 hp, (c) 32 hp, (d) 40 hp	377
Figure 6-43: Tractive effort versus velocity (MDW, 16 hp)	378
Figure 6-44: Tractive effort versus velocity (a) 20 hp, (b) 24 hp, (c) 32 hp, (d) 40 hp	380
Figure 6-45: 30 – 50 mph acceleration time of the MDWs	381

Figure 6-46: 50 – 70 mph acceleration time of the MDWs	382
Figure 7-1: Cost estimate map with respect to 0-60 mph acceleration time and vehicle components considering four independent wheels	388
Figure 7-2: Weight map with respect to 0-60 mph acceleration time and vehicle components considering four independent wheels	393
Figure 7-3: Power/Response map with respect to 0-60 acceleration time and vehicle weight considering four independent drive wheels	394
Figure 7-4: Torque/response map with respect to 0-60 acceleration time and vehicle weight considering four independent wheels.....	396
Figure 7-5: Acceleration map with respect to vehicle weight and various road conditions given constant torque (290 N-m (214 ft-lb)).....	397
Figure 7-6: Gradeability map with respect to 0-60 mph acceleration time and vehicle weight considering four independent wheels.....	399
Figure 7-7: Braking map with respect to vehicle weight and various road conditions given constant braking torque (570 N-m(420 ft-lb))	401
Figure 7-8: Force margin of each wheel on dry asphalt ($\mu=0.9$) and snowy road ($\mu=0.2$)	402
Figure 7-9: Stopping distance map with respect to vehicle weight and various road conditions given constant braking torque (570 N-m(420 ft-lb)).....	403
Figure 7-10: Braking map with respect to vehicle weight and various road conditions given constant braking torque (1140 N-m (840 ft-lb))	404
Figure 7-11: Force margin of each wheel on dry asphalt ($\mu=0.9$) and snowy road ($\mu=0.2$)	405
Figure 7-12: Stopping distance map with respect to vehicle weight and various road conditions given constant braking torque (570 N-m(420 ft-lb)).....	406

Figure 7-13: Stopping distance map with respect to velocity and normalized deceleration	407
Figure 7-14: Dynamic contact force with six different vehicle weights under a random average (asphalt) road input, as speed increases from 10 mph to 70 mph	408
Figure 7-15: Handling performance map (dynamic contact force) with respect to six different vehicle weight and velocity in terms of five classes of road surfaces	410
Figure 7-16: Sprung mass acceleration with six different vehicle weights under a random average (asphalt) road input, as speed increases from 10 mph to 70 mph	412
Figure 7-17: Ride comfort map (frequency weighted RMS sprung acceleration) with respect to six different vehicle weights and velocity in terms of five classes of road surfaces	414
Figure 7-18: Efficiency maps of an MDW without & with a reconfigurable controller	415
Figure 7-19: Durability map with respect to equivalent dynamic load and velocity	417
Figure 7-20: Force margin map with respect to vehicle weight and various road conditions for a single-lane change.....	419
Figure 7-21: Roll angle map with respect to vehicle weight and various road conditions	420
Figure 7-22: Sideslip angle map with respect to vehicle weight and various road conditions	422
Figure 7-23: Lateral acceleration map with respect to vehicle weight and various road conditions	423

Figure 7-24: Slip angle map with respect to vehicle weight and various road conditons in terms of the front and rear wheels	424
Figure 7-25: Yaw rate map with respect to vehicle weight and various road conditons	426
Figure 7-26: Acceleration force margin map with respect to vehicle weight and various road conditons given constant torque (290 N-m (214 ft-lb))	427
Figure 7-27: Braking force margin map with respect to vehicle weight and various road conditons given constant braking torque (570 N-m (420 ft-lb))	428
Figure 7-28: Pitch Angle map with respect to vehicle weight and various road conditons	429
Figure 7-29: Travel range with respect to the battery capacity and velocity	431
Figure 7-30: Energy loss map with respect to the auxiliary power and velocity.	432
Figure 7-31: Condition-based maintenance using NPC, APC, and RPC	434
Figure 7-32: Torque margin map with respect to vehcile weight and various road conditons for a single-lane change.....	438
Figure 7-33: Durability map with respect to Equivalent dynamic load and velocity	443
Figure 7-34: Updated Power/Response map with respect to 0-60 acceleration time and vehicle weight considering four independent drive wheels	446
Figure 7-35: Updatd torque/response map with resepect to 0-60 acceleration time and vehicle weight considering four independent wheels	448
Figure 8-1: Full-vehicle (7 DOF) ride model	462
Figure 8-2: Horizontal handling (3 DOF) model.....	464
Figure 8-3: Pitch motion due to braking or traction	465
Figure 8-4: Roll motion due to a cornering maneuver.....	465
Figure 8-5: One-wheel rotational dynamics	466

Figure 8-6: Longitudinal, later forces and velocity components	468
Figure 8-7: Schematic diagram of 14 DOF full-vehicle model consisting of block diagrams in MATLAB/SIMULINK	470
Figure 8-8: Friction circles of each wheel during acceleration and braking.....	471
Figure 8-9: Friction circles of each wheel during cornering.....	473
Figure 8-10: Acceleration map with the force margin of each wheel on dry asphalt, wet asphalt, and snowy road, given constant torque (290 N-m (214 ft- lb)).....	474
Figure 8-11: Acceleration map with force margin of each wheel on dry asphalt, wet asphalt, and snowy road, given constant braking torque (570 N-m(420 ft-lb))	475
Figure 8-12: Force margin map during a cornering maneuver	476
Figure 8-13: Flowchart illustrating the visual approach to duty cycle analysis ..	478
Figure 8-14: Comparison of efficiency maps	480
Figure 8-15: Comparison of efficiency maps under urban duty cycle	480
Figure 8-16: Comparison of efficiency maps under highway duty cycle	481
Figure 8-17: Efficiency maps of an MDW without & with a reconfigurable controller	483
Figure 8-18: Efficiency maps of an MDW without & with a reconfigurable controller	484
Figure 8-19: Power/Response and Torque/Response maps with respect to 0-60 acceleration time and vehicle weight considering four independent drive wheels	485
Figure 8-20: Handling maps	486
Figure 8-21: Ride comfort maps.....	487

Figure 8-22: Lateral acceleration and yaw rate map with respect to vehicle weight and various road conditons	490
Figure 8-23: Acceleration force margin map with respect to vehicle weight and various road conditons given constant torque (290 N-m (214 ft-lb))	491
Figure A-1: Typical spectral densities of road elevation profiles [Gillespie,1992]	505
Figure A-2: PSD as a function of spatial frequency for various types of road and runway [Wong,2008]	506
Figure A-3: Classification of road surface roughness proposed by ISO [Wong,2008]	507
Figure A-4: Profile amplitude of B class and D class by ISO [Verros, Natsiavas et al.,2005]	508
Figure B-1: IM240 Driving Cycle	509
Figure B-2: UDDS Driving Cycle	510
Figure B-3: FTP Driving Cycle	510
Figure B-4: HWFET Driving Cycle	511
Figure B-5: NYCC Driving Cycle	511
Figure B-6: US06 Driving Cycle	512
Figure B-7: SC03 Driving Cycle	512
Figure B-8: HUDDS Driving Cycle	513
Figure B-9: LA92 Driving Cycle.....	513
Figure B-10: LA92Short Driving Cycle	514
Figure B-11: ECE Driving Cycle.....	514
Figure B-12: EUDC Driving Cycle	515
Figure B-13: EUDC_LP Driving Cycle.....	515
Figure B-14: NEDC Driving Cycle	516

Figure B-15: J10 Driving Cycle.....	516
Figure B-16: J15 Driving Cycle.....	517
Figure B-17: J1015 Driving Cycle.....	517
Figure C-1: Layout of Freewheeling Gear Rim.....	518
Figure C-2: Layout of Freewheeling Gear Rim.....	519
Figure C-3: Layout of Freewheeling Gear Rim.....	519
Figure C-4: Layout of Push Bar Assembly.....	520
Figure C-5: Layout of Front End Output Gear Body Design	520
Figure C-6: Gear Clutch Disk Holds Ball Sockets	521
Figure C-7: Synchro Friction Clutch Spider Disk	521

Chapter 1. Introduction

1.1 BACKGROUND

There is no doubt that a customer is the dominant force in the marketplace. From a historical perspective, only companies that respond to their customers' needs have survived. The question raised is how to satisfy a customer in terms of the Multi-speed hub Drive Wheel (MDW) for a hybrid electric vehicle [Tesar and Ashok, May, 2011]. First, it is essential to know what the customer needs in terms of the purchase, operation, maintenance, and refreshment standpoints. These are discussed in terms of list 3 or 4 main criteria in Chapter 7.

We will discuss an electric vehicle and MDW used for four-independent drive wheels of future electric vehicles in Sections 1.1.1 and 1.1.2. The human choice and visual performance maps are explained in Sections 1.1.3 and 1.1.4. Different customers have different needs, hence the concept of human choice. Using visual performance maps, we will analytically demonstrate how different human choices affect the selection of a MDW in Sections 6.1 and 6.4. In addition, due to the 2 mechanical speeds, the efficiency improvement in terms of loss reduction is 1.9x for urban and 1.8x for highway duty cycles over the Protean's single speed in-wheel motor. Another loss reduction of 1.2x is expected by using the reconfigurable power/electronic controllers. This is described in Section 6.3.1 and 6.3.2. Finally, the duty cycles/demand cycles that can be used for selecting the appropriate MDW are presented in Section 1.1.5.

1.1.1 Electric Vehicles

Electric Vehicles (EVs), which include a Plug-in Hybrid Electric Vehicle (PHEV), an Extended-Range Electric Vehicle (E-REV), and a Battery Electric Vehicle (BEV), have become increasingly important due to global warming caused by greenhouse

gas emissions (CO_2) and the depletion of fossil fuels. The Toyota Prius plug-in and Nissan Leaf are PHEV and BEV, respectively. The Chevrolet Volt belongs to E-REV because of its extended range where the Internal Combustion Engine (ICE) drives a generator to charge the battery to extend its travel range [Tate, Harpster et al.,2008; Wang, Chen et al.,2011]. A hybrid electric vehicle (HEV) can be a parallel hybrid, series hybrid, and series-parallel hybrid (i.e., power-split hybrids). The Hyundai Sonata Hybrid and Toyota Prius are the parallel hybrid and the series-parallel hybrid, respectively [Chan and Wong,2004; Chan,2007; Consumer-Reports,2012].

In this research, we consider a series hybrid electric vehicle equipped with four-independent electric drive wheels. In addition, based on an all-electric modular automobile (AE/MA) with an open (modular) architecture [Tesar,2009], the HEV will consist of eight modules: 1) engine, 2) generator, 3) batteries/super capacitor, 4) skateboard chassis, 5) car body, 6) suspension, 7) drive wheel, and 8) operational software. It should be noted that these components have their own intelligence to enable rapid integration during assembly and response to system commands during operation. Furthermore, these modules are plug-and-play interchangeable for not only module repair but also for system updating [Tesar,Dec 11, 2011].

1.1.2 Multi-Speed Hub Drive Wheel

The Multi-speed Hub Drive Wheel (MDW) for four-independent drive wheels of future electric vehicles has recently been designed by the Robotics Research Group at the University of Texas at Austin [Tesar and Ashok,May, 2011]. The MDW has four distinct (two electrical and two mechanical) in order to improve efficiency and enhance drivability such as acceleration and braking on the command of the operator. The MDW will have different unsprung weights of wheels depending on the rated power such as 16,

20, 24, 32, up to 40 hp which would become choices by customers. The preliminary MDW weight and power values are shown by the data in Table 1-1.

	Value	Units	Value	Units
MDW 16 hp (with clutch)	34	kg	75	lb
MDW 20 hp (with clutch)	37.4	kg	82.5	lb
MDW 24 hp (with clutch)	40.8	kg	90	lb
MDW 32 hp (with clutch)	45.9	kg	101.3	lb
MDW 40 hp (with clutch)	51.0	kg	112.5	lb

Table 1-1: MDW weight and power

As can be seen in Figure 3-1, the MDW integrates a switched reluctance motor (SRM), a star compound gear train (SCGT) with clutch, and a brake systems into the wheel hubs of future electric vehicles.

The star compound gear train has extraordinary attributes: low velocity small diameter bearings in a rugged stationary backbone/cage, very low inertia to enhance acceleration, low velocity gear meshes, exceptionally rugged, compactness (light weight), all bearings are in fixed structures, all high speed bearings are small in diameter to reduce friction losses, and a strong backbone structure to separate the front and back ends to create a shell which is unusually rigid [Tesar and Ashok,May, 2011].

Regarding the MDW, the star compound gear train consists of two gear ratios such as 3.5:1 (front end) and 14:1 (back end). This leads to the gear reduction values such as 49:1 and 14:1 with a clutch. The gear ratio of 49:1 can be used for high torque and low speed: for urban driving at 300 RPM (22 mph) to 500 RPM (36 mph).

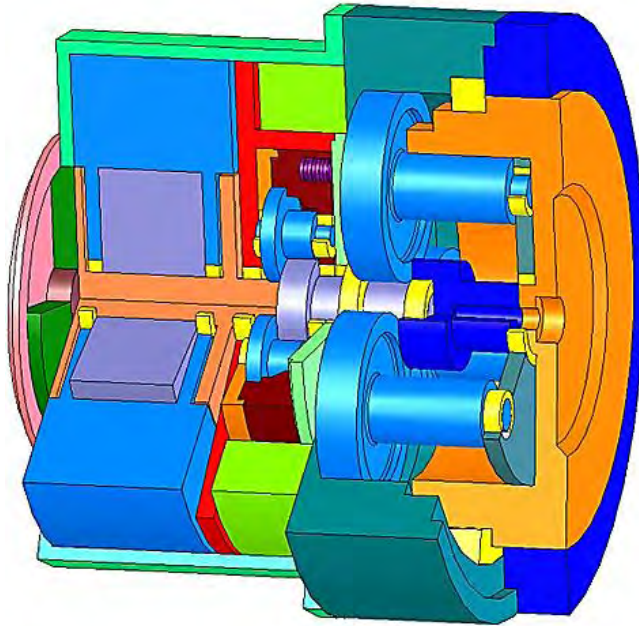


Figure 1-1: MDW Configuration

The gear ratio of 14:1 can be used for low torque and high speed: for highway driving at 840 RPM (60 mph) to 1000 RPM (70 mph). Assuming the clutch shift point of 280 RPM (20 mph), there are two speed ranges: first speed range is 0 RPM to 280 RPM, and second speed range is 281 RPM to 1000 RPM.

1.1.3 Human Choice

Satisfying human needs means to *respond directly to human commands / objectives at the time of purchase, in real time operation, and for maintenance / tech mods over the life history of the vehicle*. This leads to maximizing human choice. To meet human choice means to keep the human fully informed on a series of choices, instrument the human if necessary, maximize their self-awareness, and then marry these parametric descriptions, so that the human can best self-regulate the combination [Tesar, Dec 11, 2011].

The MDW designed to meet human needs is structured to offer a continuous expansion of human choice. The expanded choice for the customer can be characterized in terms of two basic operating regimes: drivability and efficiency. Drivability indicates acceleration, climbing a hill, and maneuverability to respond to emergencies, which demand wheel intelligence to respond to human command. Efficiency in terms of fuel consumption becomes completely dominant in the urban driving duty cycle [Tesar and Ashok,May, 2011].

Just as Dell computer does for personal computers, human choice is the dominant marketing priority for products to not only become competitive but also to stay ahead of competition. As discussed in Section 1.1.2, the MDW as a standard (i.e., 2 or 4 wheels) will have different unsprung weights of wheels depending on the rated power, which can be 16, 20, 24, 32, up to 40 hp (i.e., plug and play). Customers will have choices of changing from one module of a MDW to another in the same vehicle depending on their needs. These choices can be characterized by third-party apps, with the result of further enhancing customer choices.

In addition, these MDWs provide the original equipment manufacturer (OEM) with a potential after-market. The HEV could be assembled on demand based on a minimum set of highly certified, mass-produced, and cost-effective modules with a responsive supply chain. This leads to providing the OEM with more sales (i.e., Intel for computer chips – MDW hardware, Microsoft for operating systems – MDW software, Dell Computer for personal computers – automobile) [Tesar,2009; Tesar,2011, August; Tesar and Ashok,May, 2011].

1.1.4 Visual Performance Maps

Electro-mechanical systems have increasingly become more complex and inherently nonlinear. This nonlinearity is often neglected by simplified analytical models.

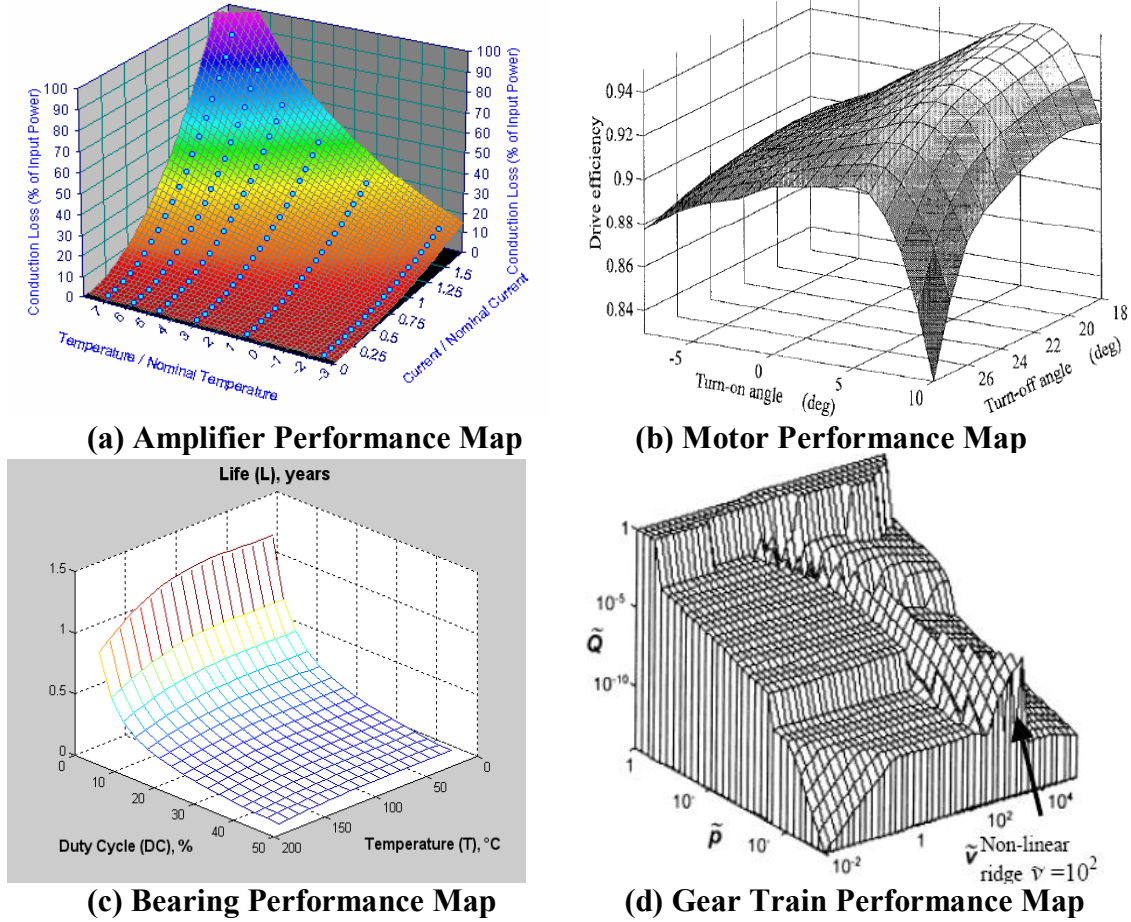


Figure 1-2: Performance maps in an electromechanical actuator [Ashok and Tesar,2007]

However, a performance map can capture the nonlinearity of the electro-mechanical system. A performance map can be defined as 2D or 3D plots from data through experimental measurement or analytical models. It shows how input parameters in a system affect an output parameter. Furthermore, combinations of performance maps,

an performance envelopes, become decision surfaces to offer visualization to support the human decision maker (HDM) [Ashok and Tesar,2008; Ashok and Tesar,2010].

Figure 1-2 (a) – (d) shows performance maps in terms of actuator amplifier, prime mover, bearing, and gear train. Figure 1-2 (a) shows conduction losses of the MOSFETs as a function of the current and the operating temperature [Tesar, Vaculik et al.,2005]. Figure 1-2 (b) shows the efficiency of a switched reluctance motor as a function of the phase turn off angle and turn on angle. This is a highly non-linear relationship [Reinert, Inderka et al.,2000]. The bearing life with respect to duty cycle and temperature is shown in Figure 1-2 (c). It can be seen that the bearing life is also highly dependent on the duty cycle [Tesar, Vaculik et al.,2005]. Figure 1-2 (d) shows gear teeth wear as a function of normalized sliding speed and the normalized pressure at their surface contact [Podra and Andersson,1999].

1.1.5 Duty Cycles / Demand Cycles

Optimal sizing of in-wheel drive, choice of battery and capacity, development of controllers, and realistic charging scenarios requires a discussion of vehicle duty cycles [Liaw and Dubarry,2007; Shahidinejad, Bibeau et al.,2010]. In this research, the demand cycle refers to the individual's driving history and can be described by a speed versus time curve. The duty cycle refers to a vehicle's history of power usage and the manufacturer can use it to design the drive wheel actuator. As a result, the components of the actuator will be sized to meet the duty cycle [Koran and Tesar,2008].

For instance, an aggressive driver might want 0-60 mph acceleration time in 5 s, but an efficiency-priority driver will want high efficiency instead of the quick 0-60 mph acceleration time. The demand cycle, depending on the customer, will be determined by the driver history's speed versus time curve. Consequently, manufacturers can configure

specific driving cycles for each particular customer. Based on their driving cycles, the actuator components will be tailored to that particular customer, which leads to expanded human choice. In addition, this leads to more optimized actuators so that the customer can be best satisfied with their purchase. We will discuss in detail how to evaluate, classify, and satisfy these individual customers in Section. 6.3. In addition, we will analytically demonstrate how the selection of the design components of MDWs differs for different types of customers such as an aggressive driver vs. an efficiency-priority driver, and describe design specifications.

1.2 RESEARCH PROBLEM

Recently, the Multi-speed Hub Drive Wheel (MDW) for four-independent drive wheels of future electric vehicles has been designed by the Robotics Research Group in the University of Texas at Austin.

- There is a lack of understanding with respect to human choice for the development of an in-wheel motor (IWM). The MDW is designed to improve human choice by achieving the desired drivability and efficiency so that customer requirements can be met at the time of purchase. However, Protean's IWM has only one speed regime as "the customer choice". In other words, there is a very limited set of choices for drivability and efficiency. This single-speed concept has one efficiency map and one drivability class [Tesar and Ashok, May, 2011].
- Visual performance maps are not available for humans to make decisions with regard to existing IWMs. Research has shown that the IWM will be a key technology for increasing the number of electric vehicles in the future [Watts, Vallance et al., 2010; Murata, 2011]. Various IWMs (i.e., different power ratings) are chosen depending on customer preferences. For instance, an aggressive driver

might want a 0-60 mph acceleration time in 5 s (say a 50 hp IWM), but a driver who prioritizes efficiency would rather have efficiency (say a 20 hp IWM). If drivers see visual performance maps, they can make a decision on what they want. Therefore, it is essential to develop visual performance maps to meet these IWM requirements, so that customers can make the right choice as to what they want.

- There has been little research in the literature describing the effect of increased unsprung mass on vehicle dynamic characteristics, despite extensive research literature on in-wheel drives. Research has shown the effect of the unsprung mass on ride comfort and handling [Rojas, Niederkofler et al.,2010; Anderson and Harty, 2010]. However, no results have been given on the effect of the unsprung mass on acceleration, braking, and cornering maneuvers that require a nonlinear 14 DOF full-vehicle model. In addition, we should evaluate how the unsprung mass affects performance criteria under various road conditions (i.e., dry, wet, snow, ice) and different road profiles (i.e., concrete, asphalt, gravel). As the road roughness and unsprung mass increase, the dynamic contact force might be increased, which will be discussed in Section 4.2.1. (i.e., given smooth highway / pasture (C class / E class) and velocity of 70 mph, 79 lb / 346 lb ($m_u/m_s = 0.1$) \rightarrow 104 lb / 454 lb ($m_u/m_s = 0.19$) \rightarrow 119 lb / 522 lb ($m_u/m_s = 0.26$))
- Significant information on duty/demand cycles is usually not considered in the selection of actuator components. Research has shown the consequence of sizing the electrical machine based on existing duty cycles [Kwon, Kim et al.,2008]. However, in this previous literature, individual demand cycles are not considered when sizing components. The individual demand cycle can be defined as the driving cycle associated with a particular customer. For instance, an aggressive

driver might want 0-60 mph acceleration time in 5 s. we will analytically demonstrate how to match the MDW to the customer need in Section 6.1 and 6.3.

1.3 RESEARCH OBJECTIVES

The overall objective of the research is to analytically develop a framework for maximizing human choice by means of visualizing human needs/requirements, so that customer demands can be met at the time of purchase of an open architecture HEV, which would be assembled on demand. In addition, based on the customer's individual duty/demand cycles, a vehicle will be tailored to meet the particular customer parameters such as an aggressive driver, an efficiency-priority driver, and a cost-priority driver, etc. This leads to expanded human choice for future electric vehicles. To meet human needs, the appropriate MDW will be customized to suit the customer's demand cycle.

Satisfying human needs implies responding directly to human commands / objectives at the time of purchase, in real time operation, and in maintenance / tech mods over the life history of the vehicle. This framework demonstrates detailed human needs structured by performance map-based decisions at the time of purchase / operation / maintenance / refreshment.

To achieve the overall objective of the research, the specific goals are as follows:

- Investigate previous research on IWMs.
- Implement a nonlinear 14 DOF full-vehicle model consisting of the ride model, handling model, tire model, slip ratio, slip angle, and magic formula; this model is implemented in a MATLAB/SIMULINK environment.
- Evaluate simulation results for a nonlinear 14 DOF full-vehicle model in terms of the effect of the unsprung mass on acceleration, braking, and cornering maneuvers under various road conditions (i.e., dry, wet, snow, ice)

- Evaluate simulation results for a quarter-vehicle model in terms of the effect of the unsprung mass on ride comfort and handling under different road profiles (i.e., concrete, asphalt, gravel).
- Implement algorithms to maximize the efficiency and drivability depending on customer choices.
- Describe MDW design specifications such as different acceleration levels, gear ratio, continuous torque, peak torque, power rating, and clutch shift point for a MDW.
- Develop visual performance maps that would be of interest to the customers in terms of purchase / operation / maintenance / refreshment standpoints.
- Demonstrate the achievability of the framework for separate decision scenarios for the different customer types which might be aggressive driver, efficiency-priority driver, and cost-priority driver.

1.4 RESEARCH OUTLINE

Chapter 1 introduces the background in terms of electric vehicles, Multi-Speed Hub Drive Wheel, human choice, visual performance map, and duty cycles / demand cycles. Research problem and objective of the current research are presented.

Chapter 2 provides a literature review that addresses the following key topics: comparison of center drives and wheel-hub drives, comparison of MDW and a single-speed in-wheel motor for drivability, efficiency and durability.

Chapter 3 presents the vehicle Multi-Speed Hub Drive Wheel consisting of the star compound gear train, clutch version 1 and 2, switched reluctance motor, and reconfigurable power controller.

Chapter 4 develops the handling and ride comfort performance map simulation based on a quarter vehicle model, and discusses a nonlinear 14 DOF full-vehicle model consisting of block diagrams which are the ride model, handling model, tire model, slip ratio, slip angle, and magic formula. Each block diagram in this research is implemented in a MATLAB/SIMULINK environment. The simulation results have been compared and validated based on previous research papers.

Chapter 5 evaluates simulation results performed through the nonlinear 14 DOF full vehicle model. The effects of unsprung mass on performance criteria such as acceleration, braking, and cornering maneuver (i.e., step steer and single-lane change) are quantified. The effects of increased unsprung mass under various road conditions such as dry asphalt, wet asphalt, and ice/snowy roads were evaluated. The vehicle behaviors are examined by simulation results in terms of acceleration, braking, and cornering maneuvers.

Chapter 6 develops a procedure for the analysis of the duty cycles in order to obtain not only how to maximize efficiency but also how to maximize drivability, based on the following duty cycles: Urban Dynamometer Driving Schedule (UDDS), Highway Fuel Economy Test (HWFET), and Aggressive Driver (US06). In addition, the comparison of a MDW and an in-wheel motor are analytically made in terms of the urban duty cycle (UDDS) and the highway duty cycle (HWFET). Lastly, five individual demand cycles are specified and evaluated in terms of five different electric vehicles.

Chapter 7 develops the performance maps regarding human choices in terms of purchase / operation / maintenance / refreshment standpoints. The cost and vehicle weight maps in terms of four different vehicle configurations are estimated, and if a modular all-electric automobile in an open architecture could be assembled on demand

based on the minimum set of highly certified, mass produced, and cost effective modules with a responsive supply chain, just as Dell computer does for personal computers.

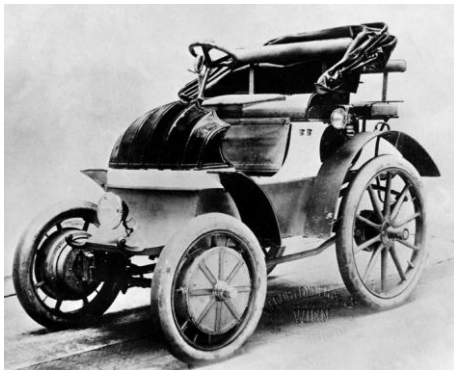
Chapter 8 summarizes the key results, conclusion, contribution of this research, and recommends future work. Even though this has been a groundbreaking and perhaps exhaustive effort, it still represents only a framework on how to satisfy customers and assist them in making decisions to meet their individual needs. As a consequence many numerical values may not necessarily be precise since the goal was to present an 80% solution to the human choice question and to develop perspective for those considering this core development for more electric vehicles of the future.

Chapter 2. Literature Review

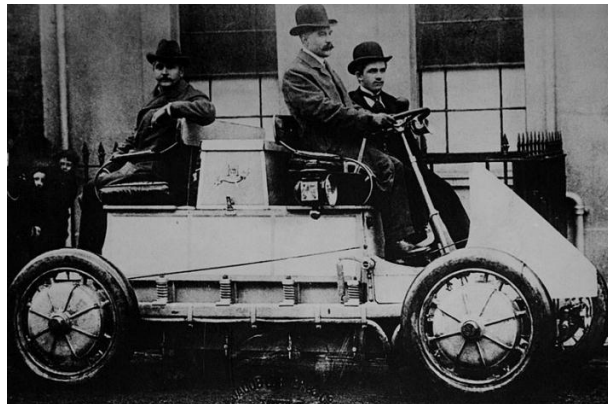
2.1 THE HISTORY OF IN WHEEL MOTORS

Equation Chapter 2 Section 1 In 1900, the first electric vehicle equipped with two in-wheel motors was designed by Ferdinand Porsche. This is referred to as ‘System Lohner-Porsche’ as shown in Figure 2-1 (a). This electric vehicle operates over 50 kph and set Austrian speed records. It was presented on 14th April 1900 at the automotive world exhibition in Paris. This vehicle is driven by 2 front in-wheel motors (i.e., power = 2.5 hp at 120 rpm, 44 cell battery with a capacity of 300 Ah, a nominal voltage of 80 V, vehicle weight of 1000 kg with the battery of 410 kg) [Wikipedia-1; Gruhler, Kranz et al.,2011]

In addition, Ferdinand Porsche developed the first series hybrid vehicle of ‘Lohner-Porsche Mixte Hybrid’ in 1901, as shown in Figure 2-1 (b). This hybrid vehicle is operated by 10-14 hp two/four hub-mounted electric motors, driven by electricity generated by internal combustion engine [Wikipedia-1; Watts, Vallance et al.,2010].



(a) System Lohner-Porsche



(b) Lohner-Porsche Mixte Hybrid

Figure 2-1: First electric vehicle driven by in-wheel motor

2.2 ELECTRIC VEHICLE CONFIGURATIONS

For EV configurations, there are six typical types due to the variations in electric propulsion systems. Figure 2-2 (a), (b), and (c) configurations are called centre drives based on a conventional ICE (Internal Combustion vehicle. Figure 2-2 (d) is a sprung geared motor front drive. Figure 2-2 (e) and (f) are called indirect-drive (geared) and direct-drive configurations, respectively. The configuration Figure 2-2 (f) is usually called in-wheel motor (Wheel-hub drives) which makes it possible to control drive torque and braking force independently.

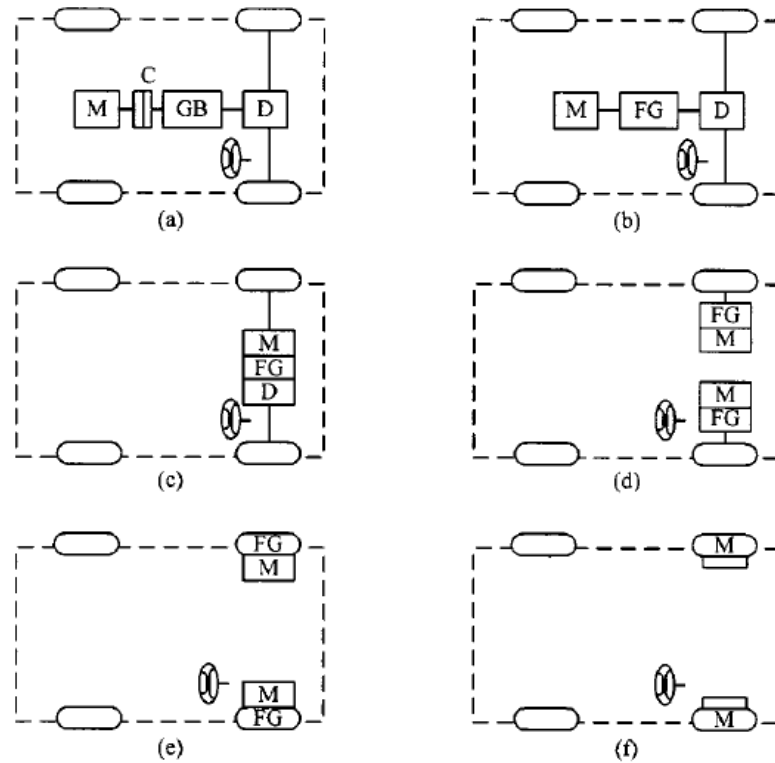


Figure 2-2: Electric vehicle configurations: M-Motor, GB-Gearbox, D-Differential, C-Clutch, FG-Fixed Gear [Chan,2002]

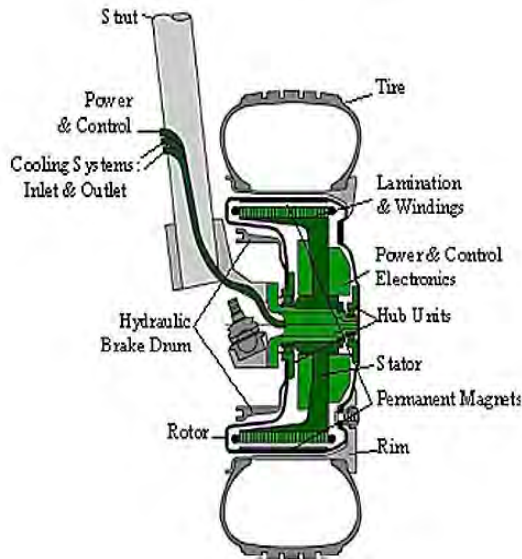
For the Figure 2-2 (e) and (f) configurations, the increased unsprung mass gives us the uncertainty of the effect on ride comfort and stability. The MDW belongs to Figure

2-2 (e) configuration with an internal clutch which is used for mechanical shifting from low speed to high speed [Darmstadt, Darmstadt et al.,2011].

Centre drives		
ex) Tesla Roadster Chevrolet Volt Nissan Leaf Toyota Prius Lexus RX400h Honda Civic IMA	Advantage	1) Use of existing ICE adopting longitudinal front-engine front-wheel drive
	Disadvantage	1) Inefficiency due to weight of mechanical drive-lines 2) Typical car drivelines can take up to 300 msec to respond to driver's commands
Wheel-hub drives		
1. Geared drive		
ex) Keio Ellici Sim Drive Toyota Fine x Magma E-car	Advantage	1) Fast response (a few milliseconds) 2) Precise and quick torque generation 3) Independent driving and braking the wheels 4) Large vertical component of driving force 5) No adverse effect on driveshaft stiffness 6) Use of Small motor 7) Low cost assuming that all components are standard / highly certified 8) More design freedom and interior space
	Disadvantage	1) Required coupling and gear box requires careful motor / gear design balance 2) More parts which may fail
2. Direct drive		
ex) TM4, Jestar, Volvo, PML Flightlink →Mini QED →Hi-Pa Electric Motor Fiat Downtown Siemens VDO eCorner Michelin Act. Wheel Mitsubi. Lancer MIEV Protean's IWM Mercedes-Benz Brabus	Advantage	1) Fast response (a few milliseconds) 2) Precise and quick torque generation 3) Independent driving and braking the wheels 4) Large vertical component of driving force 5) No adverse effect on driveshaft stiffness 6) More design freedom and interior space
	Disadvantage	1) High motor weight 2) High cost due to rare earth magnets 3) Low shock resistance: small diameter bearings

Table 2-1: Comparison of Centre drives and Wheel-hub drives

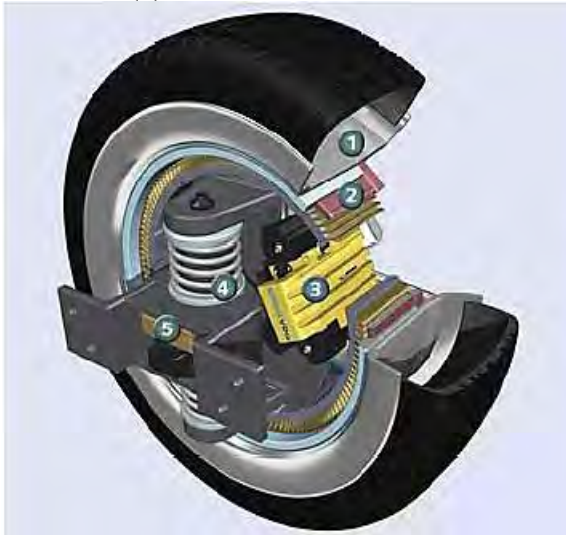
Table 2-1 shows advantages and disadvantages with regards to centre drives and wheel-hub drives (in-wheel drives) [Sim-Drive; Gerling, Dajaku et al.,2007; Murata,2011; Tesar,2011, August]. Especially, wheel-hub drives allow vehicles to remove transmission, propeller shaft, differential gear, and drive shaft for power transfer of engine from the centerline of the vehicle [Rinderknecht and Meier,2010]



(a) TM4 in-wheel motor



(b) Protean in-wheel motor



(c) Siemens VDO eCorner



(d) Michelin Active Wheel

Figure 2-3: In-wheel motor configurations

Figure 2-3 shows the configuration of in-wheel motor of each company. Figure 2-3 (a) shows an in-wheel motor of Canada Company TM4 [Zeraoulia, Benbouzid et al.,2006]. Figure 2-3 (b) shows that Protean Electric produces an in-wheel motor peak power of 110 hp, torque of 590 ft-lb, and weight of 68 lb, which directly powers the wheel [Protean-Electric; Watts, Vallance et al.,2012]. The comparison of the MDW and Protean's in-wheel motor is made in Section 2.3 in terms of efficiency, cost, ruggedness, cooling system, and choice.

Figure 2-3 (c) shows Siemens VDO (Vereinigte DEUTA (Deutsche Tachometerwerke GmbH), OTA (OTA Apparate GmbH)) eCorner combining drivetrain, steering, shock absorbers, and brake disk with electronic wedge brakes (EWB) which can decelerate each wheel separately to match the driving conditions. Figure 2-3 (d) shows Michelin Active Wheel (i.e. power of 40 hp, weight of 95 lb, 0-62 mph in 10 s) which can control ride height, pitch under motion braking, and roll motion during cornering [Michelin-Active-Wheel; Siemens-VDO].

2.3 COMPARISON OF A MDW AND AN IN-WHEEL MOTOR

Research [Tesar and Ashok, May, 2011] compares between Protean's in-wheel motor and the MDW. Based on this research, Figure 2-4 shows the summary of comparison of Protean's in-wheel motor (direct drive) and the MDW (geared drive).

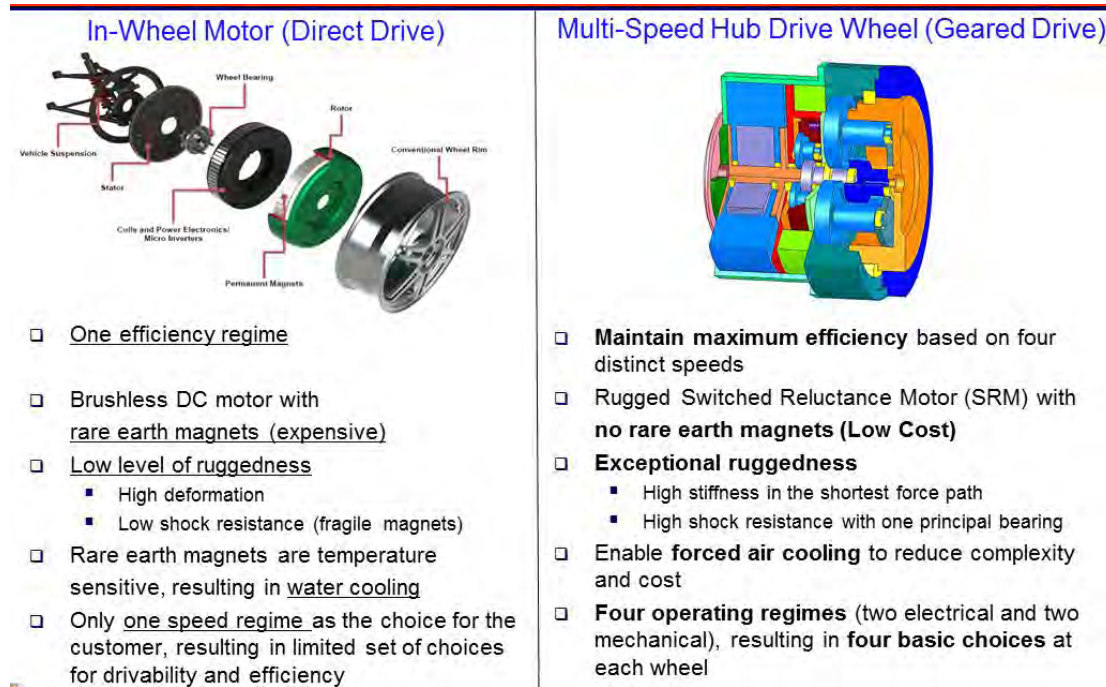


Figure 2-4: Comparison of Protean's in-wheel motor and the MDW

From an efficiency point of view, Protean's in-wheel motor has one efficiency regime. On the other hand, the MDW is designed to maintain maximum efficiency based on four distinct "speeds". Regarding a motor and its ruggedness, Protean's in-wheel motor uses brushless DC motor containing rare earth magnets which are fragile, and results in higher cost. Also, it has a large diameter of air gap (i.e., 16.5" diameter x 4.5" wide) which is difficult to protect against shock deformation due to small diameter bearings of hub shaft whose support is far removed from the air gap, which is kept small

(i.e., 0.1”) to generate higher torque. However, the MDW uses the SRM with no rare earth magnets, leading to lower cost [Tesar and Ashok, May, 2011]. In addition, it has exceptional ruggedness due to high stiffness in the shortest force path and high shock resistance with one principal bearing as part of the basic output gear train [Lee and Tesar, 2011].

In terms of cooling and operational choice, Protean’s in-wheel motor requires water cooling as a result of temperature-sensitive rare earth magnets. It has only one speed regime, leading to the limited performance choices. However, the MDW enables forced air cooling to reduce complexity and cost. This is because the MDW uses the SRM with no rare earth magnets. It is much more rugged and temperature tolerant. Furthermore, the MDW provides four distinct speeds (two electrical and two mechanical) to the customer with the aim of improving efficiency and enhancing drivability of the vehicle, such as acceleration, emergency maneuvers, and braking on the driver’s command [Tesar and Ashok, May, 2011].

2.4 DRIVABILITY

There are two essential operating regimes such as drivability (safety) and efficiency (durability). The driver's perception of the overall vehicle's response and behavior is termed drivability. Drivability covers many aspects of vehicle performance considering acceleration, engine noise, braking, automated shifting activity, and other behaviors [Opila, Wang et al.,2010]. In this research, drivability considers ride comfort, handling, acceleration, and braking in terms of the MDW.

2.4.1 Handling (Safety)

There is a tradeoff between ride comfort and handling. Good handling performance can be achieved by a stiff suspension, resulting in reducing ride comfort. On the other hand, good ride comfort performance can be obtained from a soft suspension. As a result, handling performance decreases [Kim, Joo et al.,2011]. Vehicle handling pertains to dynamic tire contact force (road holding), body response, tire-road adhesion, and issues of safety. Dynamic contact force performance of a vehicle can be characterized during cornering, braking and traction functions. In order to improve cornering, braking and traction, the variations in dynamic contact force must be minimized. This is attributed to the fact that the lateral and longitudinal forces generated by a tire depend directly on the dynamic contact force which is related to vertical tire deflection.

Table 2-2 shows the review list of the handling literature. Research has shown that the increased unsprung mass increases the dynamic contact force, thus leading to increased load variation at the tire contact patch. This results in deteriorated handling.

Reference	Description
[Kim, Joo et al.,2011]	<p>Significant ride comfort factors were compared on different road profiles, and then the effect of these factors on the handling performance under different driving maneuvers were analyzed. After that, the results were applied to the design of the chassis and seat structure of a compact SUV.</p> <p>This paper presents the best performance with a small slip angle against lateral acceleration, and roll angle / lateral acceleration around 2 Hz is decreased by damping for better roll response.</p>
[Anderson and Harty, 2010]	<p>Objective measurement results of steering behavior are consistent with the subjective results compiled by an expert driver. Steering torque versus yaw rate plot was consistent with the expert subjective results. Some differences are not beyond normal deviations.</p> <p>Analytically, the dynamic contact force is evaluated by key performance indicators (KPIs) based on a quarter vehicle model. KPIs are ranged from 0 to 10 (i.e., 10 indicate excellent performance).</p>
[Kajino, Buma et al.,2008]	<p>For handling performance, the criterion for roll rate is around $1.0 \text{ deg}/5\text{m/s}^2$ (roll angle / lateral acceleration) which was chosen from past research.</p> <p>They use feed forward plus feedback sky-hook control to achieve better handling performance.</p>
[Vos, Besselink et al.,2010]	<p>Increased unsprung mass has a negative effect on dynamic wheel load, resulting in increased load variation at the tire contact patch. Overall, the negative effects increase as road roughness is increased. They recommend an active suspension system to decrease the dynamic wheel load.</p>

Table 2-2: List of References on Handling

Regarding dynamic contact force (RMS), these papers give no results with respect to different road profiles (ISO 8608:1995)[Wong,2008]: A class (very good runway), B class (smooth runway), C class (smooth highway), D class (gravel highway), and E class (pasture). We will discuss the handling map (dynamic contact force) in Section 4.2.1.1.

2.4.2 Ride Comfort

Ride comfort is perceived as most comfortable when the natural frequency is about 1 Hz to 1.5 Hz related to the suspension of the average family sedan. The sports car will be around 2 Hz to 2.5 Hz. The frequencies between 0.5 Hz and 1 Hz result in motion sickness, and driver perceives as a harsh ride with a frequency over 3 Hz [Van Schalkwyk and Kamper,2006]. The ride comfort is associated with the extent to which a driver is affected by vehicle motion. If the vehicle rolls excessively right and left, or pitches during acceleration and braking, drivers will experience an uncomfortable ride [R.Q. Riley,2005]. Step response can be used for soft road simulation. Pulse response is used for pot hole simulation [Salem and Aly,2009; Johnston,2010; C. Alexandru,2011].

Wong describes the effect of unsprung mass to transmissibility ratio, suspension travel ratio, and dynamic tire deflection ratio based on a quarter vehicle model as shown in Figure 2-5 . The transmissibility ratio indicates the response of the sprung mass to the road excitation. It can be used for assessing ride comfort. The suspension travel ratio is the ratio of maximum relative displacement between sprung and unsprung mass to the road profile amplitude [Wong,2008].

The dynamic tire deflection ratio can be defined as the ratio of the maximum relative displacement between the unsprung mass and road surface to the road profile amplitude. This is related to dynamic contact force (road holding capability). Below the natural frequency of the sprung mass (1 Hz), there is little effect as the ratio of the sprung mass to the unsprung mass increases (0.05, 0.1, and 0.2) [Wong,2008].

However, between the natural frequencies of the sprung mass and the wheel hop frequency, the increased unsprung/sprung ratio increases transmissibility, suspension travel, and dynamic tire deflection ratio. Above the reference the wheel hop frequency,

transmissibility ratio and suspension stroke decreases slightly, while it has an insignificant effect on the dynamic tire deflection ratio [Wong,2008]. According to the international Standard ISO 2631-1:1997, the basic evaluation method for vibration uses the frequency-weighted RMS acceleration given by [ISO,1997]:

$$a_w = \left[\frac{1}{T} \int_0^T a_w^2(t) dt \right]^{1/2} \quad (2.1)$$

where T is the duration of the measurement and $a_w(t)$ is the weighted acceleration. In case the crest factor (= Peak/RMS) is greater than 9, the Maximum Transient Vibration Value (MTVV) and Vibration Dose Value (VDV) are used to account for the occasional shocks and transient vibration. MTVV is defined as the highest magnitude of $a_w(t_0)$ [Wong,2008]:

$$MTVV = \max [a_w(t_0)] \quad (2.2)$$

where $a_w(t_0)$ is the instantaneous frequency-weighted acceleration and t_0 instantaneous time. The running root mean square is as follows [ISO,1997]:

$$a_w(t_0) = \left\{ \frac{1}{\tau} \int_{t_0-\tau}^{t_0} [a_w(t)]^2 dt \right\}^{1/2} \quad (2.3)$$

The running RMS is calculated with 1-s integration time (τ) for a running average. The VDV is given by the fourth root of the integral regarding time of the fourth power of the acceleration which is weighted. This is the root-mean-quad approach. The use of the fourth power method makes VDV more sensitive to peaks, highlighting shocks. The VDV is given by [ISO,1997]:

$$VDV = \left\{ \int_0^T [a_w(t)]^4 dt \right\}^{1/4} \quad (2.4)$$

where $a_w(t)$ is the instantaneous frequency-weighted acceleration. Generally, the basic evaluation of ride comfort is characterized by the frequency-weighted RMS acceleration which is obtained by the power spectral density (PSD), which shows the power distribution of the acceleration with respect to frequencies (see Appendix A).

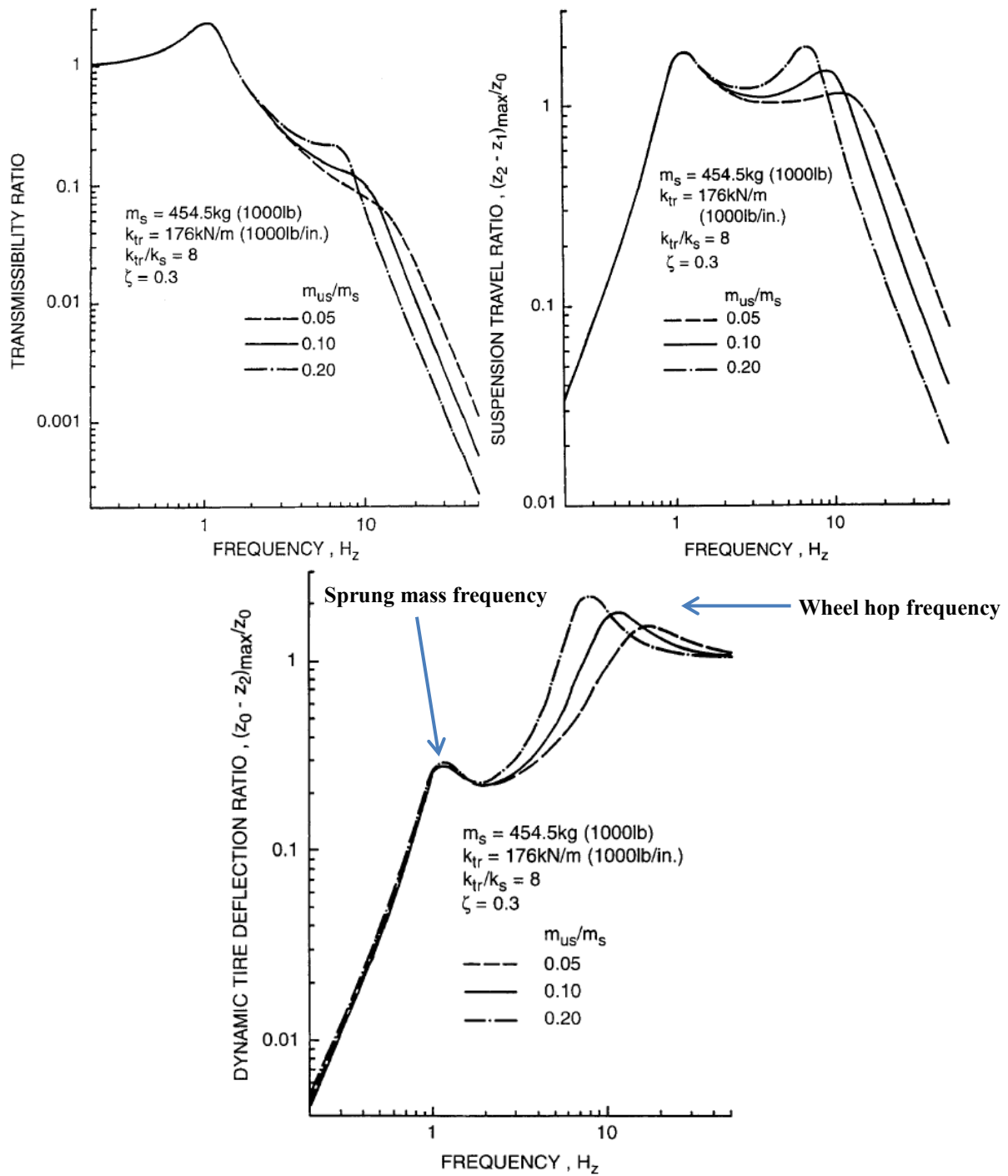


Figure 2-5: Effect of unsprung-to-sprung mass ratio on transmissibility, suspension travel, and dynamic tire deflection ratio

In order to determine the frequency-weighted RMS acceleration, the PSD is integrated over a one-third octave band which is the ratio of two frequencies ($w_2 / w_1 = 2^{(1/3)} = 1.26$). The RMS acceleration at each center frequency (f_c) can be 0.16 Hz, 0.2 Hz, 1 Hz, 1.25 Hz,, up to 16 Hz, which are given by [Wong,2008]:

$$a_i = \text{rms acceleration} = \left[\int_{0.89f_c}^{1.12f_c} S_v(f) df \right]^{1/2} \quad (2.5)$$

Above equation shows the center frequency of 1 Hz. For the conversion of one-third octave band data (i.e., from Equation (2.5), lower frequency bound = 0.89, upper frequency bound = 1.12), the overall frequency-weighted RMS acceleration will be determined as follows [Wong,2008]:

$$a_w = \left[\sum_i (W_i a_i)^2 \right]^{1/2} \quad (2.6)$$

where W_i is the weighting factor for the i th one-third octave band and a_i is the RMS acceleration for the i th one-third octave band from PSD. Based on the value of a_w , acceleration level will be determined, as shown in Table 2-3 [Wong,2008].

Acceleration Level	Description
$a_w < 0.315 \text{ m/s}^2$	Not Uncomfortable
$0.315 < a_w < 0.63 \text{ m/s}^2$	A Little Uncomfortable
$0.5 < a_w < 1 \text{ m/s}^2$	Fairly Uncomfortable
$0.8 < a_w < 1.6 \text{ m/s}^2$	Uncomfortable
$1.25 < a_w < 2.5 \text{ m/s}^2$	Very Uncomfortable
$a_w > 2 \text{ m/s}^2$	Extremely Uncomfortable

Table 2-3: Levels of acceptability of ride comfort

Table 2-4 gives a tabulation of ride comfort in terms of descriptions from the literature. Research has shown that the increased unsprung mass and road roughness reduce the ride comfort.

Reference	Description
[Rojas, Niederkofler et al.,2010]	This paper suggests new suspension systems to assure vehicle ride comfort (body acceleration) and safety (tire contact force) when using in-wheel motors. Given a deterministic signal, ride comfort and safety deteriorate due to the increased unsprung mass.
[Anderson and Harty, 2010]	<p>Subjective and objective measures of ride and handling are evaluated based on +30 kg unsprung mass with base vehicle weight. Numerical analysis is evaluated based on a quarter vehicle model with 50/80 kg unsprung mass. This paper describes the effect of hub motors on vehicle dynamics.</p> <p>Higher unsprung mass reduces the acceleration response of the vehicle body at frequencies above the wheel hop frequency, giving improved higher frequency noise and vibration attenuation. Wheel hop frequency is changed from 14 Hz to 10 Hz due to the increased unsprung mass.</p>
[Kajino, Buma et al.,2008]	Ride comfort control for a given road input is evaluated by sprung mass displacement/road displacement (0.8 or less) using sky-hook electric active suspension system.
[Vos, Besselink et al.,2010]	<p>In on-road experiments, the evaluation of ride comfort is performed with RMS acceleration and dynamic wheel load and suspension travel by adding 15 kg to each wheel, assuming continuous power of 30 kW (PMDC). They illustrate that the ride comfort and dynamic wheel load deteriorate as road roughness is increased.</p> <p>Also, an active suspension system is able to significantly decrease the dynamic wheel load.</p>
[Van Schalkwyk and Kamper,2006]	Frequency analysis and simulation of the system are done using a quarter vehicle model including practical experiments (adding 50 kg per wheel). The natural frequency for the hub driven vehicle falls within the acceptable frequency range of driver comfort and safety. It is shown that the added wheel mass has little effect on the stability of the vehicle.

Table 2-4: List of Ride Comfort

Regarding ride comfort, they give no results with respect to different road profiles (ISO 8608:1995)[Wong,2008]: A class (very good runway), B class (smooth runway), C class (smooth highway), D class (gravel highway), and E class (pasture). Frequency-weighted RMS sprung acceleration will be discussed in Section 4.2.1.3.

2.4.3 Acceleration

Vehicle acceleration depends primarily on torque generated by the motor. From the customer point of view, acceleration pertains to the time required to go from 0 to 60 miles per hour. According to [Wei and Rizzoni,2004; Consumer-Reports,2012], drivability metrics used in the automobile industry are described in terms of 0-60 mph, 30-50 mph, and 50-70 mph acceleration time.

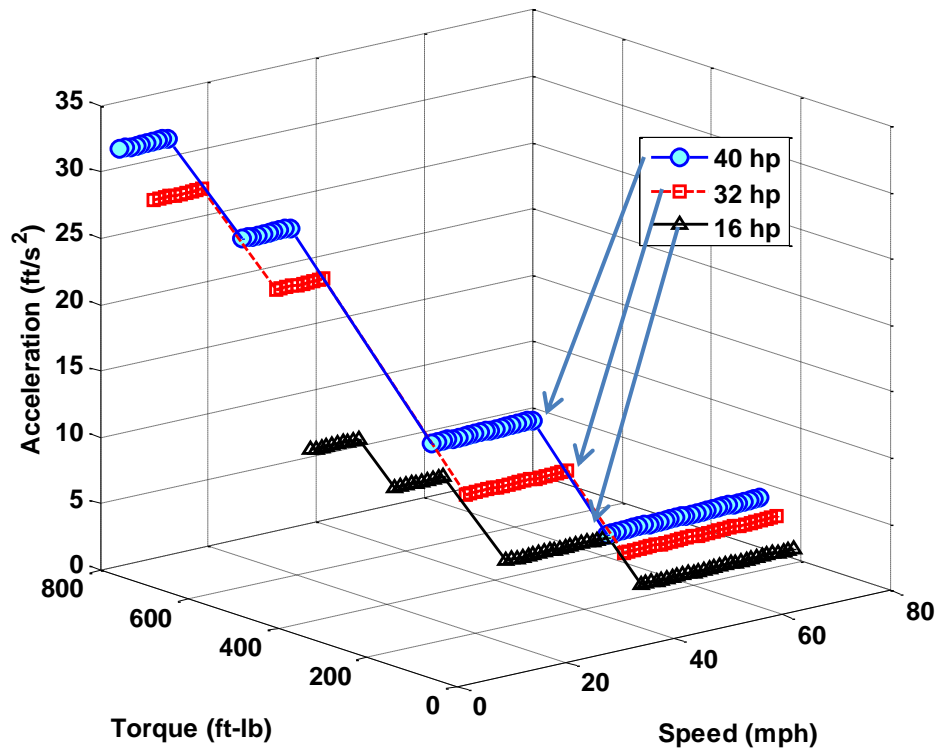


Figure 2-6: Acceleration plot as a function of wheel torque and speed

Figure 2-6 shows the acceleration levels with respect to wheel torque and speed in terms of the rated power of 16 hp, 32 hp, and 40 hp. The MDW have 4 choices on accelerations due to four distinct speeds (two electrical and two mechanical)[Tesar and Ashok,May, 2011]. The acceleration levels are chosen by the customer, thus resulting in required wheel torque versus speed (see Section 6.4). Wheel torque divided by the wheel radius in the traction force which depends on the tire-road friction coefficient which varies with the road condition. The traction force is the force exerted on the tire by the road [Milliken and Milliken,1995; Blundell and Harty,2004; Jazar,2008].

The acceleration map as a function of unsprung mass to sprung mass and various road conditions will be described in Section 5.3.1. The torque/response map as a function of vehicle weight and 0-60 mph acceleration time will be described in Section 7.1.4.

2.4.4 Braking

The braking performance is measured in stopping distance. According to [Wei and Rizzoni,2004], stopping distance consists of command reaction distance and braking distance. The former is the distance from the time a driver perceives a hazard to the time he/she steps on the brake. The latter is the distance a vehicle travels from the time that a driver applies the brake until the vehicle comes to a complete stop. With full braking on dry, level asphalt and an average perception-reaction time of 1.5 s, the stopping formula is given by:

$$\text{stopping distance} = 2.2V + 0.048V^2 \quad (2.7)$$

where stopping distance is in feet and velocity is in mph.

A simple distance formula is given by [Gillespie,1992]:

$$SD = \frac{v^2}{2a} \quad (2.8)$$

The stopping distance is proportional to the square of the velocity. This will be farther described in Section 5.1.2, 5.2.1.1, 5.2.2.1, and 5.2.3.1.

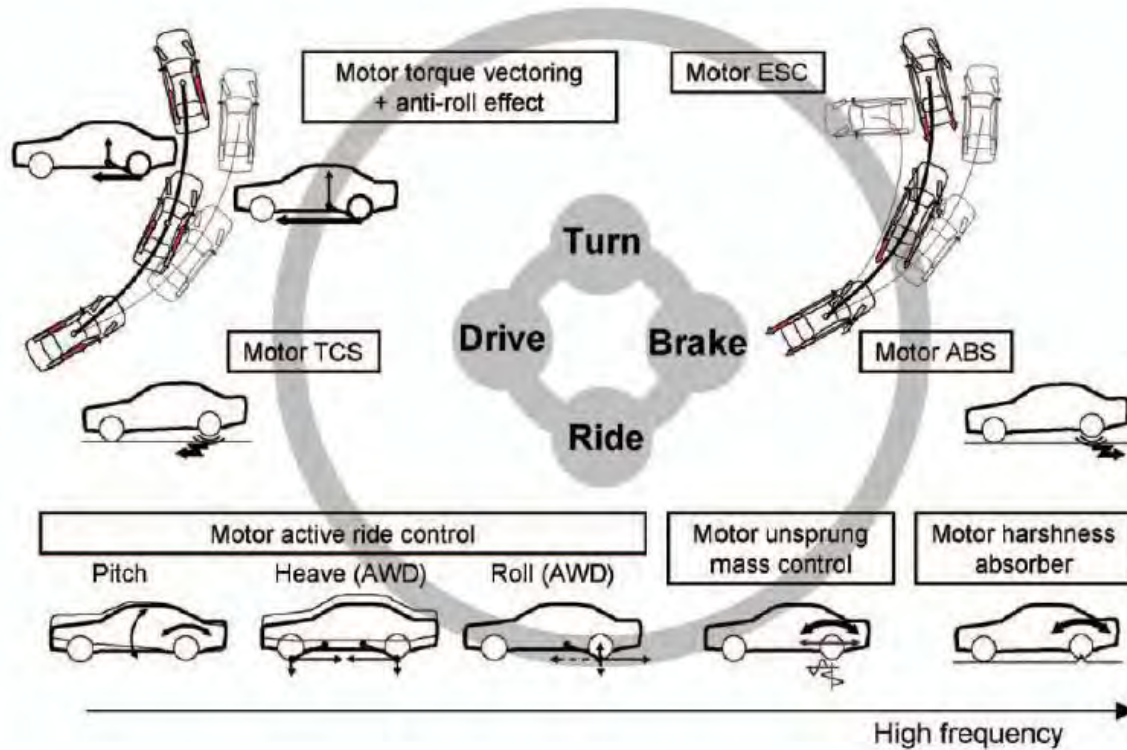
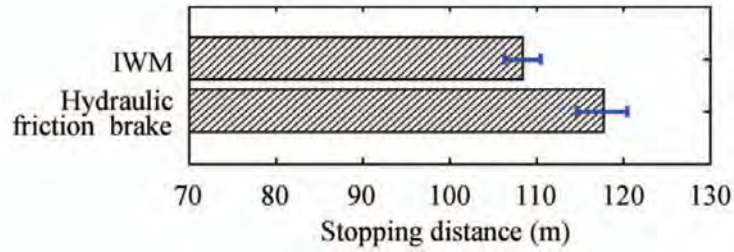
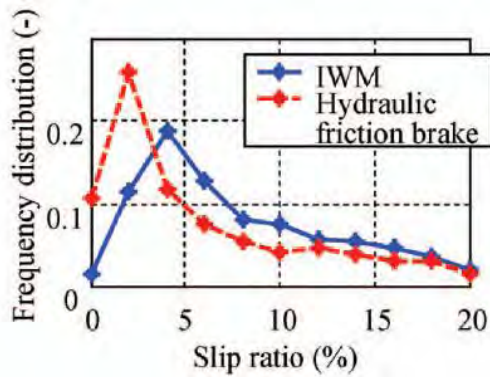


Figure 2-7: Functions achieved by an IWM [Murata,2011]

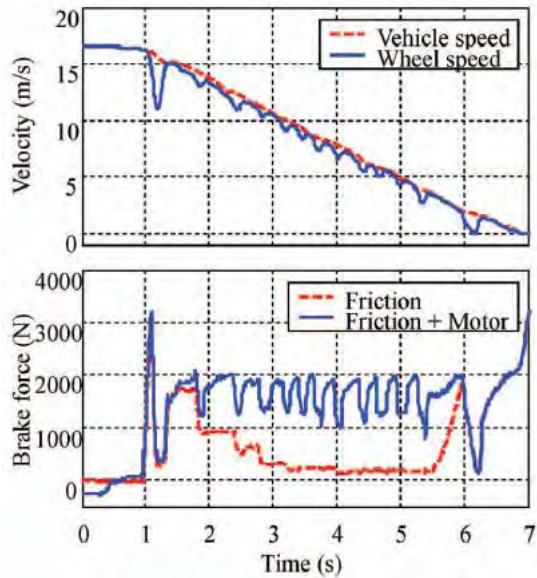
Figure 2-7 shows that an IWM can be used for improving driving, turning, stopping, and ride comfort under all driving conditions. The performance of anti-lock system (ABS), traction control system (TCS), and electronic stability control (ESC) are enhanced by an IWM. In addition, in order to optimize the distribution of driving force to each wheel, torque vectoring (TV) control can be achieved by an IWM, so that the yaw dynamic performance can be enhanced. Furthermore, the vertical motion of the sprung mass is controlled by an IWM based on an independently controlled driving force of the front and rear wheels [Murata,2011].



(a) 50 – 0 kph stopping distance on frozen road ($\mu = 0.1$)



(b) Slip ratio distribution ($\mu = 0.1$)



(c) Regenerative-friction ($\mu = 0.4$)

Figure 2-8: Motor ABS [Murata,2011]

Figure 2-8 (a) and (b) shows the comparison of an IWM and hydraulic friction brake in terms of the 50-0 kph stopping distance on frozen road ($\mu = 0.1$) and slip ratio distribution. The stopping distance is six meters shorter with an IWM, resulting in a reduction of 7%. As can be seen in Figure 2-8 (b), an IWM use the 4 – 10% slip ratio range for a longer time, leading to a large friction force. Figure 2-8 (c) shows the test results for regenerative-friction coordinated control on a low friction road ($\mu = 0.4$). It

can be seen that braking force fluctuation is controlled by an IWM which is highly responsive.

2.5 EFFICIENCY

Mecrow claims that increasing the efficiency of the electrical drive and integrating design of the drive and the driven load to maximize system efficiency become important until 2050 year and beyond [Mecrow and Jack,2008]. That is, the efficiency becomes dominant in the future. Mokhtari describes the efficiency map of SRM that has been used for different driving cycles to test the SRM performance as a vehicle propulsion motor [Mokhtari and Tara,2008]. The efficiency can be defined as the ratio given by [Larminie and Lowry,2003]:

$$\eta = \frac{\text{Torque} \times \omega}{\text{Torque} \times \omega + \text{Total_Losses} \left(k_c T^2 + k_i \omega + k_w \omega^3 + C \right)} \quad (2.9)$$

First, the copper losses are caused by electrical resistance of the wires of the motor, resulting in heating which is proportional to the square of the current ($I^2 R$). That is, the current is proportional to the torque ($k_c T^2$) where k_c is a constant depending on the resistance of the coil, and the magnetic flux. Hence, at the constant torque region, copper losses can be significant [Rahman, Butler et al.,2000]. Second, the iron losses are caused by magnetic effects in the iron of the motor. It is proportional to the frequency with which magnetic field changes related to the speed of the rotor ($k_i \omega$) where k_i is a constant [Ehsani, Rahman et al.,1997; Rahman, Ehsani et al.,2000]. The iron losses are more significant in the constant power region. It is attributed to the increased speed. Third, windage losses increase with the increased speed of the rotor ($k_w \omega^3$) where k_w is constant depending mainly on the size and shape of the rotor. Finally, constant losses (C) occur

even if the motor is totally stationary, and vary neither with speed or torque [Larminie and Lowry,2003].

The MDW is designed to increase efficiency based on 4 distinct speeds (2 electrical and 2 mechanical). The primary motor considered is the Switched Reluctance Motor (SRM) which performs better at high speeds, compared with BLDC motor. In addition, the SRM has high torque density and low cost due to no magnets [Tesar and Ashok,May, 2011].

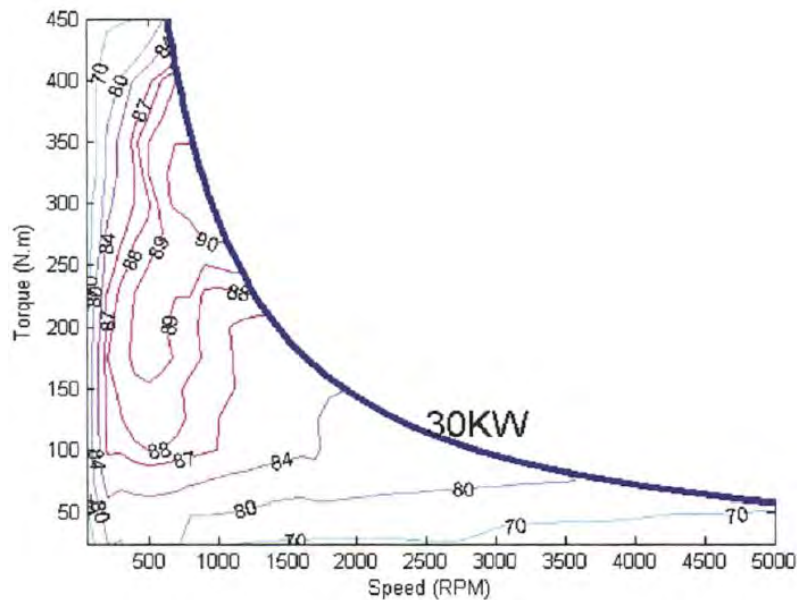


Figure 2-9: Efficiency map with respect to torque and speed

Figure 2-9 shows the efficiency plot in terms of torque and speed. The efficiency map shows the SRM efficiency at different operating points with 30 kW, showing that moderate speed and torque relative to high torque are efficient. However, the poor efficiency occurs at low and extremely high speeds. In addition, efficiency decreases at light load conditions.

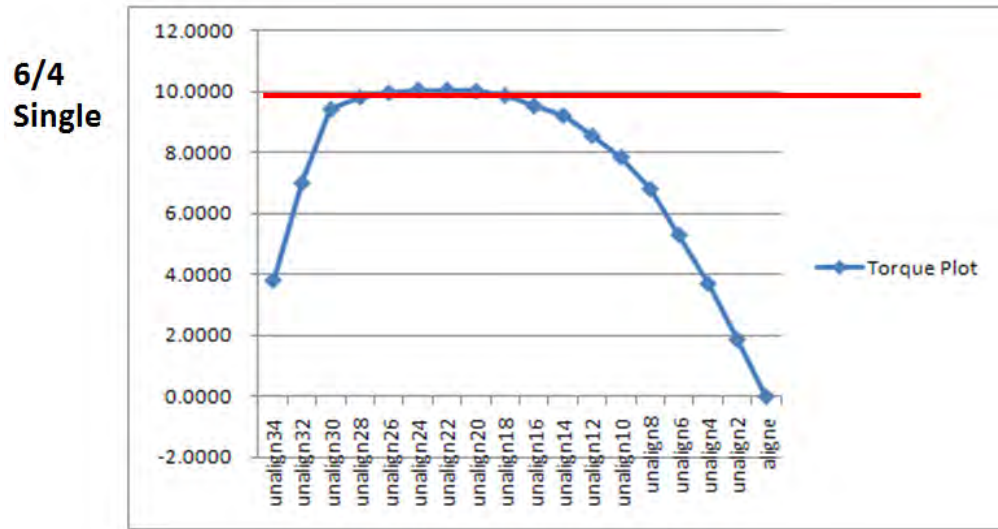
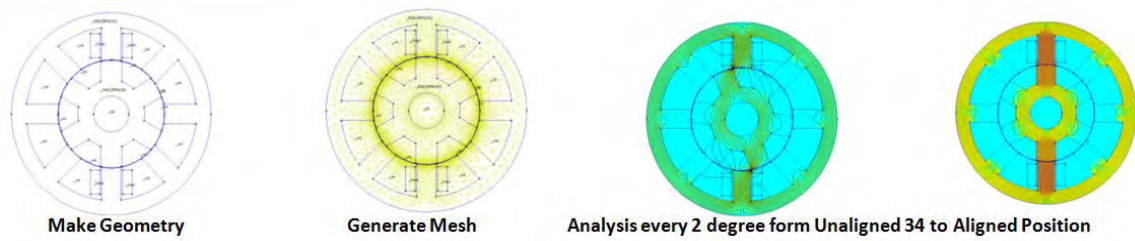


Figure 2-10: Torque analysis by Finite Element Method Magnetics [Tesar and Ashok, May, 2011]

To confirm the torque derived from an analytical method, the Finite Element Method Magnetics (FEMM) software was used as shown in Figure 2-10. This graph shows torque variation from unaligned 34° to aligned position. The maximum torque occurs from unaligned 28° to 18°.

2.6 DURABILITY

Durability is related to the remaining useful life (condition-based maintenance) which is influenced by duty cycles. The cube-root mean cube norm can be used for equivalent dynamic loads of a principal bearing of the MDW. The formula is as follows:

$$P = \sqrt[p]{P_1^p \left(\frac{n_1}{n_m}\right) \left(\frac{q_1}{100}\right) + P_2^p \left(\frac{n_2}{n_m}\right) \left(\frac{q_2}{100}\right) + \dots (N)} \quad (2.10)$$
$$n_m = n_1 \left(\frac{q_1}{100}\right) + n_2 \left(\frac{q_2}{100}\right) + \dots + (\min^{-1})$$

where $n_{1,2,\dots,n}$ is the speed approximation for each duration q , and the mean speed n_m . Also, p is 3 for ball bearings, and $p=10/3$ for roller bearing. However, the difference is negligible. The bearing fatigue life (millions of revolutions) can be expressed as:

$$L = \left(\frac{C}{P}\right)^p (10^6 \text{ revolutions}) \quad (2.11)$$

In this case, C is the dynamic load rating of the bearing associated with a purely radial load that 90 % of a group of the same bearings reach a life of 10^6 cycles before they fail as a result of fatigue [Brandlein,1999]. In this research, the customer wants to choose durability (5,000 up to 20,000 hour) versus cost [Tesar and Ashok,May, 2011]. In addition, the bearing fatigue life of crossed roller bearing will be evaluated based on duty cycles which will be discussed later.

2.7 COST

The cost is the most critical factor for customers in their purchase of an electric vehicle. Clearly, the MDW on an electric drive becomes a key whether it is expensive or not. Zeraoulia proposes the comparative study in terms of electric motors such as DC motors (DC), Induction Motor (IM), Brushless DC Motor (BLDC), and Switched Reluctance Motor (SRM) [Cuenca, Gaines et al.,2000; Zeraoulia, Benbouzid et al.,2006;

Hashemnia and Asaei,2008]. The SRM of the MDW uses various materials in place of rare earth materials which are very unstable in future cost estimates. In addition, the motor module can be considered as a plug-on module to two diameters (diameter 1-16, 20, 24 hp and diameter 2 – 32, 40 hp) to reduce cost by using the minimum set of laminate / wiring combination simply by using three lengths for the first diameter and two lengths for the second diameter. Finally, cost can continuously be lowered by mass production [Tesar and Ashok,May, 2011].

2.8 BEARING DEGRADATION

The life of a rolling-element bearing is given by the number of revolutions that the bearing can perform before incipient rolling element flaking occurs. However, it sometimes occurs that a bearing does not attain its calculated rating life. The reason of bearing failure may be caused by excessive loads, overheating, brinelling, fatigue failure, contamination, lubricant failure, corrosion, misalignment, loose/tight fits, and leakage current.

Table 2-5 shows the relationship between bearing symptom and bearing failure causes. For the bearing failure, under normal operating condition and good alignment, fatigue failure begins with a small flake, located below the surfaces of the raceway and rolling-element, which gradually propagates to the surface generating vibration and increasing noise levels [SKF; Wilcoxon-Research; Wilcock and Booser,1957]. Continuous stress causes material fragments to break loose where it produces localized fatigue phenomena. This leads to flaking or spalling. Once started, the affected area expands rapidly contaminating the lubrication and causing localized overloading over the entire circumference of the raceway. Consequently, the failure leads to rough running of the bearing [Brandlein,1999].




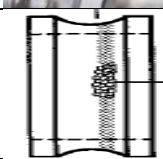
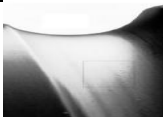
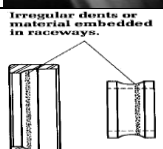

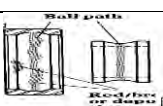
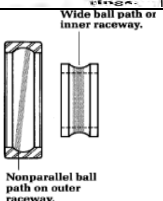

Pictures	Symptom	Main defect causes	May be relevant with
	-Heavily marked path pattern in raceways of both rings -Flaking usually in the most heavily loaded zone	1. Excessive loading -Localized flaking on raceway -Circumferential flaking on raceway -Excessive preloading	-Contamination -Overheating -Brinelling -Preloading -Tight fits -Preloading
	-Discoloration of the rings balls	2. Overheating -Causes the grease to break down which reduces its ability to lubricate the bearing	-Lubricant failure -Excessive loading
	-Indentation in the raceways which increase bearing vibration	3. Brinelling -Loads exceed the elastic limit of the ring material -A result of deformation caused by static overloading	-Excessive loading -Brinelling -Loose/Tight fits -Misalignment
	-Flaking and spalling on the inner ring, outer ring, or balls	4. Fatigue Failure -Spalling which is a fracture of the running surfaces -Begins with small flakes which gradually propagate to surface	-Excessive loading -Brinelling -Loose/Tight fits -Misalignment
	-Denting of bearing raceways, balls resulting in high vibration and wear	5. Contamination -Dirt and other foreign matter (perspiration) that is commonly present	-Overheating -Fatigue Failure -Excessive loading
	-Discolored which is blue/brown on the inner race and balls	6. Lubricant Failure -Rolling-elements are not allowed to rotate on the designed oil film causing increased levels of heating	-Overheating -Fatigue Failure -Excessive loading
	-Red/Brown areas on balls, race-way, and cages	7. corrosion -Produced by the presence of water, acids, and perspiration from careless handling during installation(deteriorated lub.)	-Contamination -Fatigue Failure
	-Ball wear path is not parallel to the raceways edges	8. Misalignment -Improper precision grade locknuts -Bending shaft	-Overheating -Fatigue Failure
	* Loose fits -Wide ball path inner raceway(wear, heat, noise, runout occurs) * Tight fits -A heavy ball wear path in the bottom of the raceway	9. Loose/Tight fits *Loose fits - Relative motion between mating parts causes fretting(oxidized small particles) *Tight fits - Results in high torque and rapid temperature rise which causes wear and fatigue	-Overheating -Fatigue Failure
	-Dark brown or greyish black fluting or craters in raceways and rollers	10. Leakage Current -Passage of electric current through rotating bearing	-Overheating

Table 2-5: Classification of bearing failure causes [SKF; Wilcoxon-Research; Wilcock and Booser,1957]

Contamination and corrosion frequently accelerate bearing failure because of the harsh environment present in most industrial settings. The abrasive nature of minute particles, whose hardness can vary from relatively soft to rough, cause pitting and sanding actions that give way to measurable wear of the balls and raceways. Improper lubrication includes both under- and over- lubrication. In either case, the rolling-elements are not allowed to rotate on the designed oil film causing increased levels of heating. Brinelling is the formation of indentations in the raceways as a result of deformation caused by static overloading[Wilcoxon-Research; Brandlein,1999]. We will discuss the bearing degradation as a function of equivalent dynamic load and velocity in Section 7.3.8.

2.9 CROSSED ROLLER BEARINGS, FOUR-POINT BEARINGS, AND TAPERED ROLLER BEARINGS

The crossed roller bearings, four-point bearings, and tapered roller bearings can be used for principal bearings because they can accommodate three different load types such as radial, axial, and moment loads. The crossed roller bearings consist of an inner ring, a two-part outer ring, and an X arrangement of the rolling elements. The cylindrical rollers, which are rolling elements, are arranged crosswise within an inner race having a 90° V-shaped groove. The crossed roller bearing can support radial, axial and moment loads with a single bearing position instead of double bearing position as shown in Figure 2-11 (a). For design purposes, it is very useful to save space as well as weight [THKBearing; Hara and Masuda,1995].

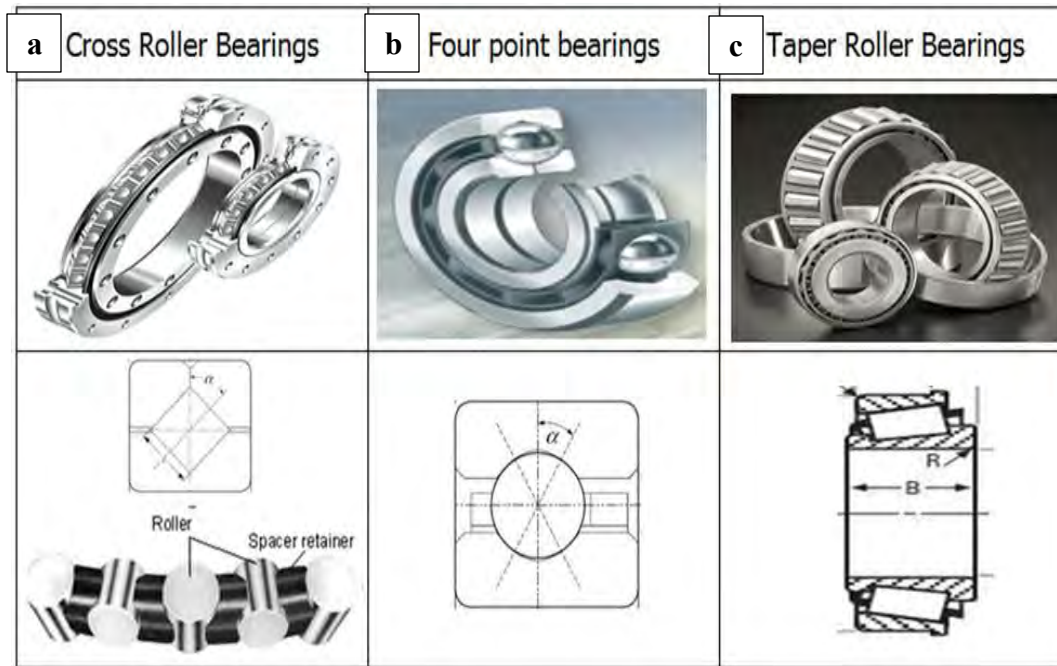


Figure 2-11: Cross section of three different bearings

On the other hand, four-point bearings comprise gothic arch-shaped inner / outer raceways as shown in Figure 2-11 (b). The reason they are called four-point bearings is that the balls, which are rolling elements, contact four points between the inner and outer races [Kaydon-Bearing; Rowntree,1985]. Both bearings are called thin section bearings due to a constant cross section within a dimensional series. Consequently, weight and space savings increase as bore diameter increases, in contrast to other light standard bearings [Gusovius,1992; Schmidt,1995]. Figure 2-11 (c) shows the tapered roller bearing. It is necessary to use paired tapered roller bearing such as double face and double back type to support three different types of loads. Due to the limitations of space and weight, it is preferable not to use tapered roller bearing for that reason [George,1983; Timken-Company,1983]. In this research, the crossed roller bearings are used in the MDW.

2.10 CHAPTER SUMMARY

In this section, we discussed the comparison of conventional drive train and wheel-hub drives (Section 2.2). The wheel-hub drives have numerous advantages: 1) fast response, 2) precise and quick torque generation, 3) independent driving and braking the wheels, 4) large vertical component of driving force, 5) no adverse effect on driveshaft stiffness, 6) more design freedom and interior space. Regarding the comparison of Protean's in-wheel motor (direct drive) and the MDW (geared drive), the MDW is designed to maintain maximum efficiency based on four distinct speeds, and has exceptional ruggedness due to high stiffness in the shortest force path and high shock resistance with one principal bearing (Section 2.3). In addition, the MDW enables forced air cooling to reduce complexity and cost. This is because the MDW uses the SRM with no rare earth magnets. Lastly, the MDW provides four distinct speeds (two electrical and two mechanical) to the customer with the aim of improving efficiency and enhancing drivability of the vehicle, such as acceleration, emergency maneuvers, and braking on the driver's command.

There are two essential operating regimes: drivability (safety) and efficiency (durability). Drivability in terms of handling, ride comfort, acceleration, and braking is described in Section 2.4. Efficiency and durability are explained in Section 2.5 and 2.6. Regarding bearing degradation, classification of bearing failure causes is discussed in Section 2.8. Lastly, the crossed roller bearings are explained in Section 2.9.

Chapter 3. Vehicle Multi-Speed Hub Drive Wheels

Equation Chapter 3 Section 1 The Multi-speed Hub Drive Wheel (MDW) for four-independent drive wheels of future electric vehicles has recently been designed by the Robotics Research Group at the University of Texas at Austin[Tesar and Ashok,May, 2011]. The MDW has four distinct speeds (two electrical and two mechanical) in order to improve efficiency and enhance drivability such as acceleration and braking on the command of the operator. The MDW will have different unsprung weights of wheels depending on the rated power such as 16, 20, 24, 32, up to 40 hp which would become choices by the customer. The MDW consists of gear trains, clutch, switched reluctance motor (SRM), and reconfigurable power controller. The gear trains and clutch will be presented in Sections 3.1 and 3.2. The SRM and the reconfigurable power controller will be described in Sections. 3.3 and 3.4.

3.1 STAR COMPOUND GEAR TRAIN

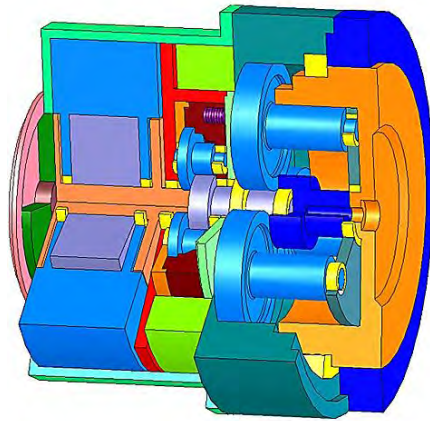


Figure 3-1: MDW Configuratioin

As can be seen in Figure 3-1, the MDW integrates several components: switched reluctance motor (SRM), star compound gear train (SCGT), and brake systems into the

wheels of future electric vehicles. The star compound gear train has extraordinary attributes: low velocity small diameter bearings in a rugged stationary backbone/cage, very low inertia to enhance acceleration, low velocity gear meshes, exceptionally rugged, compactness (light weight), all bearings are in fixed structures, all high speed bearings are small in diameter to reduce friction losses, and a strong backbone structure to separate the front and back ends to create a shell which is unusually rigid [Tesar and Ashok, May, 2011]. Regarding the MDW, the star compound gear train consists of two gear ratios such as 3.5:1 (front end) and 14:1 (back end). This leads to the gear reduction choice of 49:1 and 14:1 with a clutch. The gear ratio of 49:1 can be used for high torque and low speed: urban driving is 300 (22 mph) to 500 RPM (36 mph). The gear ratio of 14:1 can be used for low torque and high speed: highway driving is 840 RPM (60 mph) to 1000 RPM (70 mph). Assuming the clutch shift point of 280 RPM (20 mph), there are two speed ranges: first speed range is 0 to 280 RPM, and second speed range is 281 to 1000 RPM.

According to this research [Lee and Tesar, 2011; Tesar and Ashok, May, 2011], the shortest force path is necessary to reduce effects of deformation, temperature, tolerances, and to reduce weight, volume, and cost, as shown in . In addition, maximizing actuator stiffness is achieved by the short force pass through principal bearing from the shell to the output plate. As can be seen in Figure 3-2, the force path is labeled as A-B-C where it path passes through the principal bearing B (cross roller bearing) where A is shell structure, B is principal bearing, and C is the output-plate which is connected with wheel hub. The principal bearing can be used for acting as the joint bearing of a robot actuator as well as separating the sun gears and ring gears. Since the principal bearing connects the output-plate to actuator shell, all forces such as payload and weight of the robot structure are transferred as radial, axial, and moment loads to the suspension structure [Tesar, 2007].

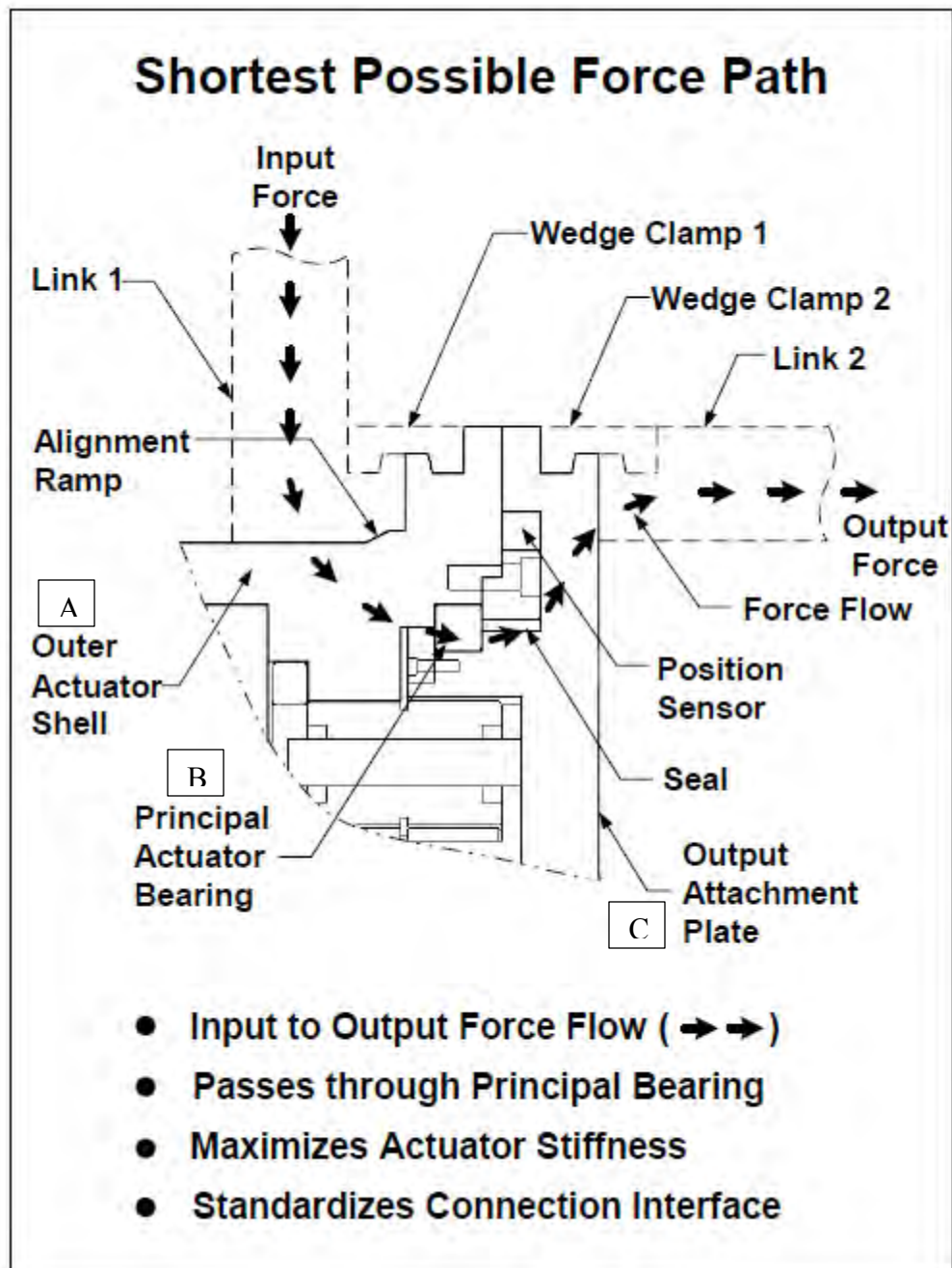


Figure 3-2: MDW-wheel/suspension geometry and short force path [Tesar,2007]

The MDW wheel / suspension geometry is shown in Figure 3-2: motor (SRM), first stage SCGT (3.5:1), clutch with neutral, second stage SCGT (14:1), and principal

cross roller bearing, etc. The short force path is directly related to the strong backbone of the actuator which prevents the circular structure (A and C and B (bearing)) from becoming oval under load. This leads to protecting all gear meshes (alignment) including bearings, clutch, etc. This means that they are protected from external shocks from the wheel or suspension. Furthermore, the switched reluctance motor is isolated from these shock effects to protect its air gap being mounted outside the critical force path [Tesar and Ashok, May, 2011].

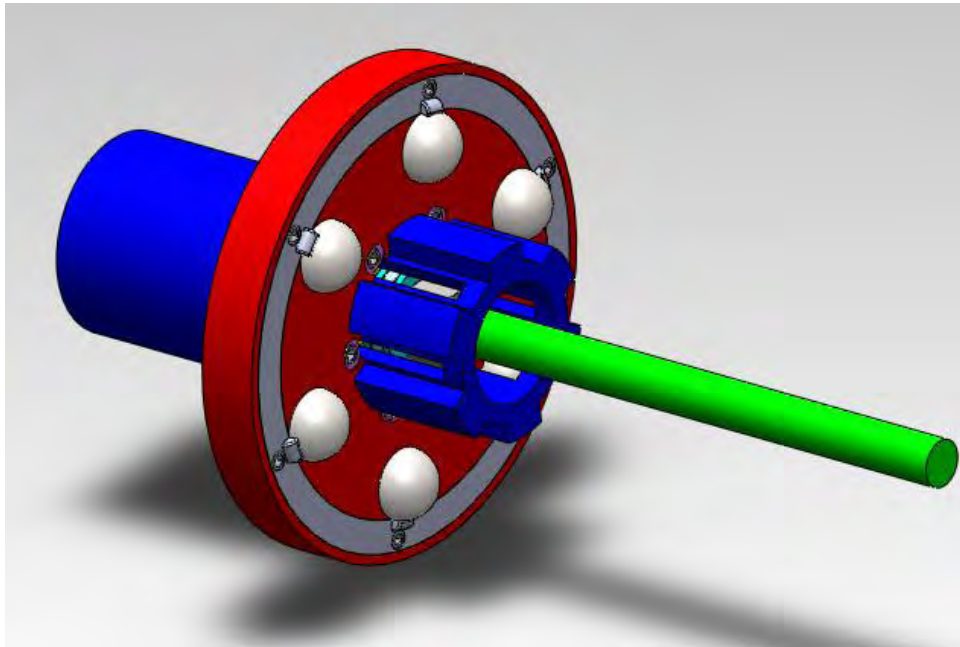
Regarding the star compound gear trains, [Bandaru and Tesar, 2011] developed a visual design process considering multiple stages of reduction: MDW is a two stage gear train. The design procedure allows a designer to manage more than 29 design parameters so that he / she can design for numerous gear train requirements (i.e., rated torque capacity, volume, weight, inertia, responsiveness, torque density, etc.), considering assembly constraints. Based on the design maps, a designer has the ability to obtain a preliminary design of a gear train to meet the design requirement.

3.2 CLUTCH

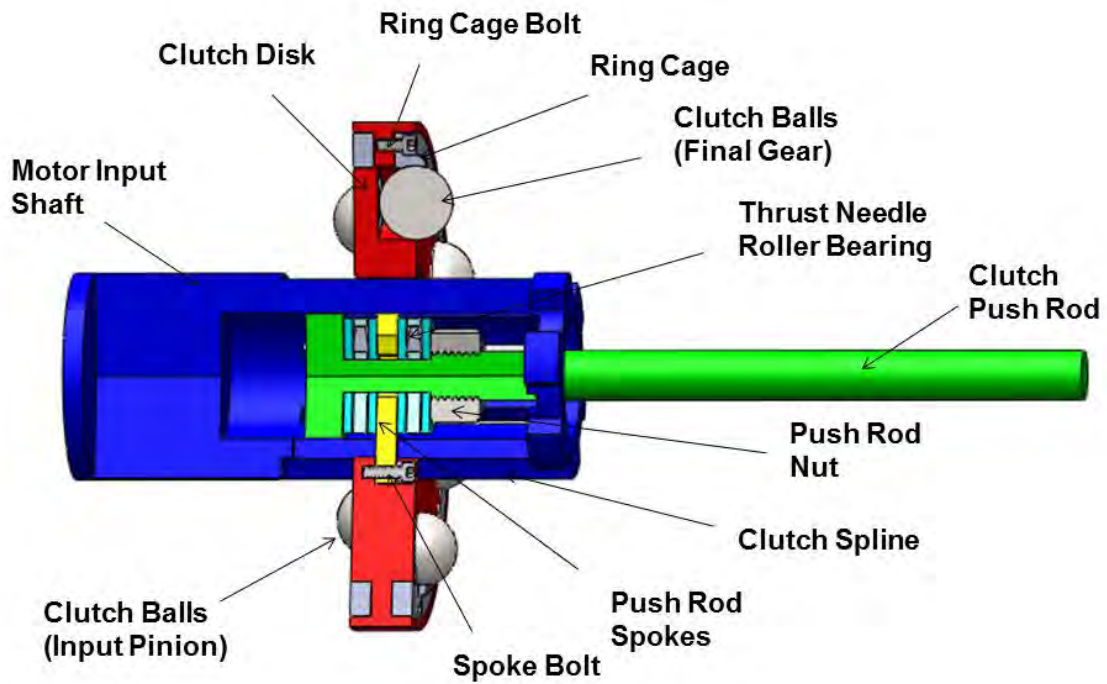
The University of Texas at Austin develops two types of clutch mechanism. The first clutch mechanism that UT developed is operated under the condition that all gears are always in mesh. The other one is operated by providing a synchro clutch in the output gear to make the amplifier gears of the front end star gears free wheel.

3.2.1 MDW Clutch Version 1

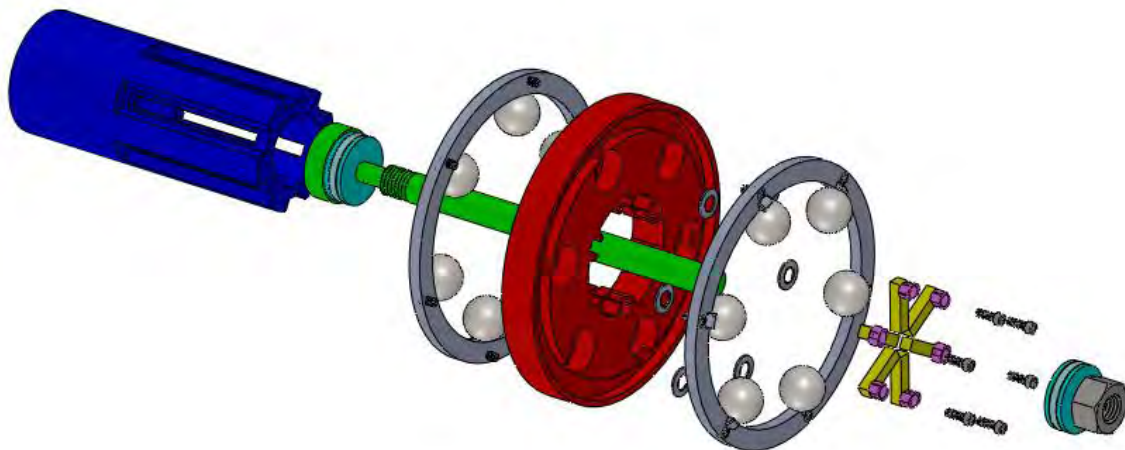
The requirements of drivability (acceleration, braking, climbing a hill, etc.) and that of efficiency cannot be met at one operating speed regime. Therefore, it is essential for the MDW to have two mechanical and two electrical speed regimes. Since the MDW has 4 distinct speeds (two electrical and two mechanical), the g (acceleration) level will have 4 different levels. Four distinct acceleration (g) levels associated with four distinct speed ranges will be g_1 (0 – 10 mph), g_2 (11 – 20 mph), g_3 (21 – 40 mph), and g_4 (41 mph – 70 mph). The clutch shift occurs at 20 mph from 49-to-1 (for low speed and high torque) to 14-to-1 (for high speed and low torque) for two mechanical speeds [Tesar and Ashok, May, 2011].



(a) Clutch configuration



(b) Cross-section of clutch configuration



(c) Clutch Exploded Assembly

Figure 3-3: Two-speed clutch mechanism

Figure 3-3 (a) and (b) show the picture of the clutch assembly and its cross-section, respectively. Figure 3-3 (c) shows the clutch unassembled. As can be seen in Figure 3-3 (b), the clutch disk is splined to the motor input shaft. This disk carries two sets of engaging balls to engage similar sized pockets: 1) drive the first amplifier gear (i.e., putting a 3.5-to-1 ratio into the system), 2) drive the pinion for the second stage of 14-to-1. Therefore, we have a clear choice of either 49-to-1 or 14-to-1 which are the MDW reduction gear ratio choices.

The clutch push rod with a set of drive spokes operates the shift disk to move it back and forth. This push rod is operated by a BDC motor driving a screw shaft. The push rod is held in its neutral position by a detent and in its engaged position. The push rod would ride in a fixed spline to prevent rotation while it pushes on the spokes riding in a groove at the end of the push rod [Tesar and Ashok, May, 2011].

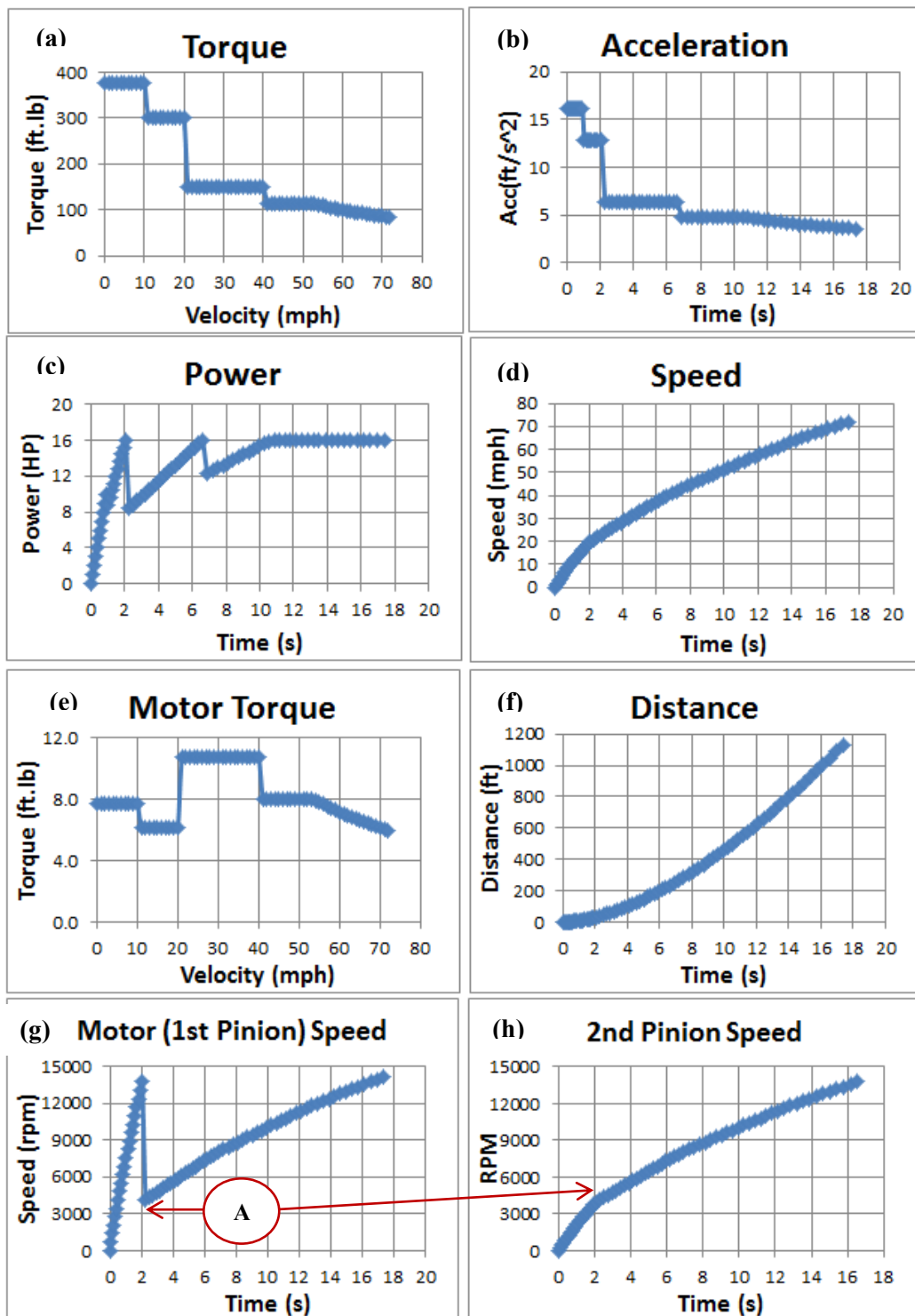


Figure 3-4: Wheel demands / response for 3000 lb vehicle (16 hp)

The key point of clutch operation is to match the clutch disk with the gears such as the first stage input pinion or the second stage input pinion. As can be seen in Figure 3-4 (g) and (h), the first stage input pinion or second stage input pinion correspond to the motor (1st pinion) speed and 2nd pinion speed. Figure 3-4 is simulated with different g (acceleration, 32.2 ft/s^2) levels: $g_1 = 0.5g$ (0 – 10 mph), $g_2 = 0.4g$ (11 – 20 mph), $g_3 = 0.2g$ (21 – 40 mph) and $g_4 = 0.15g$ (41 mph – 70 mph). The clutch shift occurs at 20 mph from 49-to-1 (for low speed and high torque) to 14-to-1 (for high speed and low torque) for two mechanical speeds, as shown by symbol ‘A’ in Figure 3-4 (g).

Consider a vehicle moving along a flat road, the motor speed operates from 0 to 13726 RPM (20mph) with a clutch. After a clutch shift, the motor speed is changed to match the second pinion speed (3922 RPM, 20 mph). Finally, after a clutch engages the second pinion, the vehicle operates up to 70 mph. At the same time, the second pinion speed increases up to 13726 RPM. Clearly, the motor speed increases also up to 13726 RPM. Conversely, consider a vehicle braking slowly along a flat road, disengagement is much less critical and can be achieved much more quickly. All of these choices can be embedded in the MDW electronic controller and prioritized based on the road conditions or the driver’s objectives. All of this maximizes individual wheel control which has been shown in commercial ABS braking systems to provide superior results. Furthermore, intelligent decision making in the MDW can be used for preserving traction and maneuverability, while accelerating the vehicle to enhance safety during all operating conditions of the vehicle [Tesar and Ashok, May, 2011].

3.2.1.1 Spline Design

The safety factor based on the shear stress due to input torque was evaluated. The rectangular spline teeth were analyzed for shear and compressive failure. The yield stress for shaft material (AISI 4140 steel) was 92,100 psi. In general, the allowable shear stress is taken as 50% of this value. In this design, the maximum allowable stress was taken as 35% of this value, which leads to a conservative design. The formulas for compressive and shear stresses are as follows[Shigley and Mischke; Norton,2006]:

$$\begin{aligned}\tau &= \frac{16Td_a}{\pi(d_a^4 - d_i^4)} \quad (\text{shear stress due to input torque}) \\ \tau &= \frac{2T}{d_a z l h} \quad (\text{compressive stress on a tooth}) \\ \tau &= \frac{2T}{d_a z l w} \quad (\text{shear stress on a tooth})\end{aligned} \quad (3.1)$$

	Parameters	Value	Units	Value	Units
Torque	T	11.8	N-m	8.7	ft-lb
Outer diameter	D	25.4	mm	1	in
Tooth width	w	6.4	mm	0.25	in
Tooth height	h	2.5	mm	0.1	in
Root diameter	d_r	20.3	mm	0.8	in
Average diameter	d_a	22.9	mm	0.9	in
Internal diameter of a hollow shaft	d_i	15.2	mm	0.6	in
Actual engaged length	l	25.4	mm	1	in
Number of spline teeth	z	6		6	

shear stress due to torque	$\tau = \frac{16Td_a}{\pi(d_a^4 - d_i^4)}$	6268.4	kPa	909	psi
AISI 4140 steel (Yield stress)	S_y	635191.3	kPa	62100	psi
AISI 4140 steel (allowable shear stress)	S_a	222317	kPa	32235	psi
Actual compressive stress on a tooth	$\frac{2T}{p_zlh}$	10667	kPa	1547	psi
Actual shear stress on a tooth	$\frac{2T}{p_zlw}$	4266.8	kPa	619	psi
Safety Factor	N	35		35	
Safety Factor (Compressive Failure)	N_c	21		21	
Safety Factor (Shear Failure)	N_s	52		52	

Table 3-1: Spline analysis for input shaft

Table 3-1 shows safety factors for compressive failure and shear failure due to torque. The safety factor associated with shear stress due to input torque is around 35. The safety factors associated with compressive stress and shear stress on a tooth are around 21 and 52, respectively. That is, the spline design is acceptable to be used in the MDW.

3.2.1.2 Clutch Ball Design

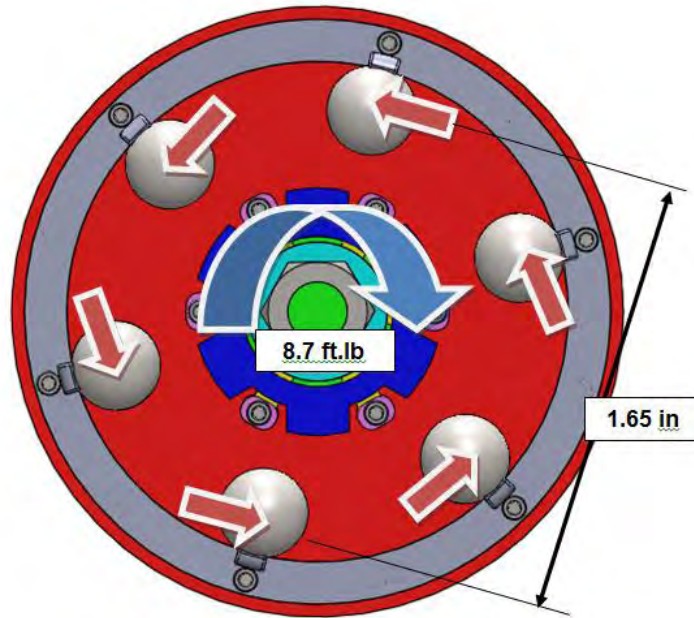


Figure 3-5: Free-body diagram for a clutch disk

The ball material is chosen as SAW 52100 (HRC 61) whose allowable shear stress is 123 ksi. Figure 3-5 shows the free-body diagram for a clutch disk. Based on the free-body diagram, the equation of equilibrium that can be used for obtaining force acting on each ball is as follows:

$$ccw + \sum M_o = 0 ; F = \frac{2T}{dn} = \frac{2 \times 8.7 \times 12}{1.65 \times 6} = 21lb \quad (3.2)$$

When engaged the input pinion or second stage pinion, a clutch ball can be modeled as a cantilever beam for obtaining safety factor. A clutch ball experiences maximum shear stress in the middle of ball. We chose clutch ball diameter of 0.355 in.

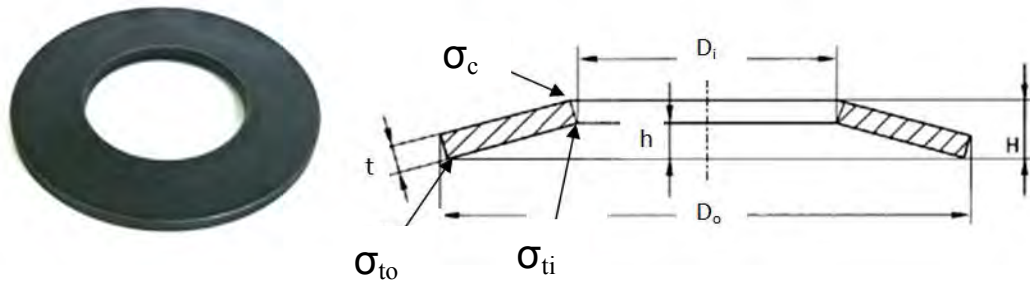
	Parameters	Value	Units	Value	Units
Torque	T	11.8	N-m	8.7	ft-lb
Diameter	D	42.0	mm	1.65	in
Ball Diameter	d_b	9.0	mm	0.355	in
Area	A	2.5	mm	0.099	in
Number of Balls	N_b	6		6	
Force	F	93.6	N	21	lb
Max Shear Stress	$\tau = \frac{4F}{3A}$	1955	kPa	284	psi
Allowable Shear Stress (SAE 52100 HRC61)	τ_a	850000	kPa	123224	psi
Safety Factor	S_f	435		435	

Table 3-2: Clutch ball analysis for 1st input pinion

Table 3-2 shows clutch ball analysis for 1st input pinion. The safety factor regarding the clutch ball is around 435. Therefore, the clutch ball that we chose is acceptable to be used in the MDW.

3.2.1.3 Belleville Spring Washers

The Belleville spring washers have a nonlinear force-deflection characteristic which can be used for certain applications. Their cross section is coned shape with thickness T and inside height h , as shown in Figure 3-6. They are extremely compact and are capable of large push forces. They should be operated only between about 15% and 85% of the deflection to flat.



Article No.	Ordering Dimensions						Weight/ 1000 pcs. [kg]	Stress σ_{OM} at $s = h_0$ [N/mm ²]
	D_e [mm]	D_i [mm]	t [mm]	l [mm]	H [mm]	h_0 [mm]		
000100	6	3.2	0.3	0.45	0.15	0.50	0.044	-1623

Figure 3-6: Belleville spring washers [SchNorr]

The load at the flat position ($y=h$) is given by:

$$F_{flat} = \frac{4Eht^3}{K_1 D_o^2 (1-\nu^2)} \quad (3.3)$$

$$\text{where } K_1 = \frac{6}{\pi \ln R_d} \left(\frac{(R_d - 1)^2}{R_d^2} \right) \text{ and } R_d = \frac{D_o}{D_i}$$

The stresses are concentrated at the edges of inside and outside diameters. The largest stress σ_c occurs at the inside radius on the convex side and is compressive. The expressions for stresses corresponding to each location as shown in Figure 3-6 are given by:

$$\begin{aligned}
\sigma_c &= -\frac{4Ey}{K_1 D_o^2 (1-\nu^2)} \left[K_2 \left(h - \frac{y}{2} \right) + K_3 t \right] \\
\sigma_{ti} &= \frac{4Ey}{K_1 D_o^2 (1-\nu^2)} \left[-K_2 \left(h - \frac{y}{2} \right) + K_3 t \right] \\
\sigma_{to} &= \frac{4Ey}{K_1 D_o^2 (1-\nu^2)} \left[K_4 \left(h - \frac{y}{2} \right) + K_5 t \right]
\end{aligned} \tag{3.4}$$

$$\begin{aligned}
\text{where } K_2 &= \frac{6}{\pi \ln R_d} \left(\frac{(R_d - 1)}{\ln R_d} - 1 \right) \text{ and } R_d = \frac{D_o}{D_i} \\
K_3 &= \frac{6}{\pi \ln R_d} \left(\frac{(R_d - 1)}{2} \right) \\
K_4 &= \left[\frac{R_d \ln R_d - (R_d - 1)}{\ln R_d} \right] \left[\frac{R_d}{(R_d - 1)^2} \right] \\
K_5 &= \frac{R_d}{2(R_d - 1)}
\end{aligned}$$

In this research, the outer and inner diameter are chosen as 6 mm (0.236 in) and 3.2 mm (0.126 in) respectively to support the clutch ball (diameter = 0.355 in). The Belleville washer's height (h) is 0.15 mm that 0.05 mm is preloaded and 0.1mm can be used for balancing the clutch ball during the clutch operation. The amount of the preload is around 23 lb corresponding to each ball and Belleville washer provide 70 lb at the flat position (h = 0.15 mm, maximum deflection)

	Parameters	Value	Units	Value	Units
Force	$F(flat)$	309	N	70	lb
Thickness	t	0.3	mm	0.012	in
Outer Diameter	D_o	6	mm	0.236	in
Inner Diameter	D_i	3.2	mm	0.126	in
Ratio	$R_d = \frac{D_o}{D_i}$	1.875		1.875	
Constant	K_1	0.66		0.66	
Ratio	h/t	0.500		0.5	
Height	h	0.15	mm	0.0059	in
Max Deflections	y_{max}	0.15	mm	0.0059	in
Free Length	H	0.45	mm	0.018	in
# of springs	N	1	EA	1	EA
Constant	K_2	1.19		1.19	
Constant	K_3	1.33		1.33	
Constant	K_4	1.18		1.18	
Constant	K_5	1.07		1.07	
Compressive stress	σ_c	-2795331	kPa	-405311	psi
Inner stress	σ_{ti}	1772282	kPa	256973	psi
Outer stress	σ_{to}	2348991	kPa	340594	psi
Unset carbon spring steel 50 HRC	S_y	1696602	kPa	246000	psi
Allowable Shear Stress					
Safety Factor(After Set Removed)	S_F	1.7		1.7	

Table 3-3: Belleville spring washers analysis

Table 3-3 shows the detailed calculation to obtain static safety factor considering compressive stress because compressive stress is larger than inner / outer stress. The maximum percent of ultimate tensile strength is 275 % due to after set removed. As a result of that, the safety factor will be 1.7 ($SF=2.75 * 246000 / 405311$).

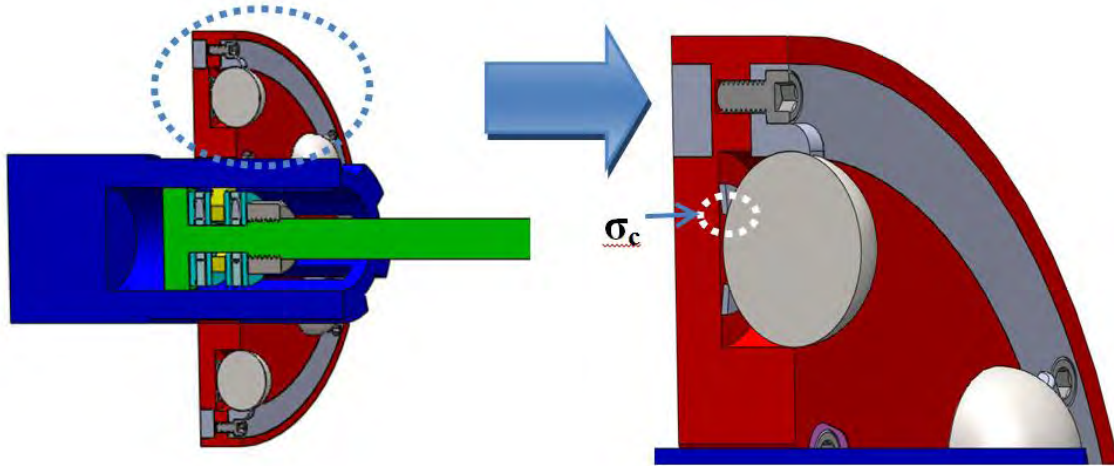


Figure 3-7: Clutch disk equipped with belleville spring washers

In practice, the safety factor will be larger than 1.7 by cutting out the amount of material for a ball to stably seat on a Belleville spring washer, as shown in Figure 3-7. The σ_c indicates the compressive stress shown in Figure 3-6. The detailed value can be seen in Table 3-3.

3.2.1.4 Ring Cage Design

	Parameters	Value	Units	Value	Units
Mass	$m=\rho v$	0.000246	kg	0.0000169	slug
Density	ρ	7750	kg/m ³	0.28	lb/in ³
Diameter	d	9	mm	0.3543	in
Distance	r	21.0	mm	0.825	in
Volume	v	382	mm ³	0.023292837	in ³
Angular Speed	w	15000	rpm	15000	rpm
Angular Speed	w	1571	rad/s	1571	rad/s
Number of balls	N	12		12	
Each centrifugal force	mrw^2	153	N	34	lb
Total centrifugal force	mrw^2	1834	N	412	lb

Table 3-4: Ring cage analysis

During the dynamic operation at the high speed, the clutch balls on the clutch disk create high centrifugal force. Table 3-4 shows the value of the centrifugal force in detail.

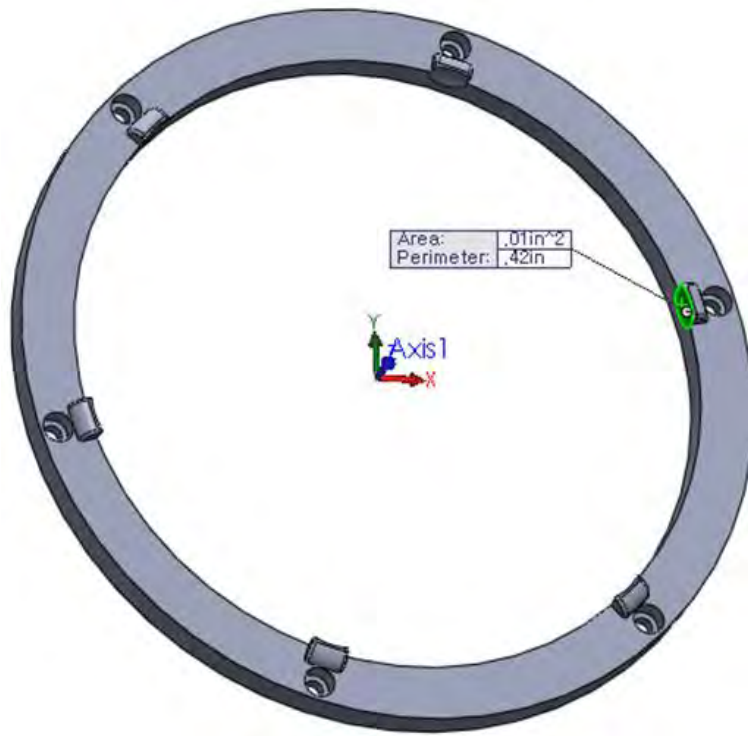


Figure 3-8: Ring cage of a clutch disk

To prevent each centrifugal force during the high speed operation, the ring cage was designed as one part, as shown in Figure 3-8. The contact area corresponding to a clutch ball is 0.01 in^2 , so that pressure can be 1700 psi ($P = F/A = 17/0.01$).

3.2.1.5 Clutch Shift Operation

The clutch disk is located at the neutral position at the beginning of stage as shown in Figure 3-9 (a). The shift length should be larger than 0.6 in due to the constraints ($0.18 \text{ (ball)} + 0.3 \text{ (clutch disk thickness)} + 0.18 \text{ (ball)}$). The actual engaged spline length between clutch disk and input shaft are selected 0.86 in, so that the space between ball end point and clutch disk can be 0.1 in. To engage the first and second

pinion, the travel length will be 0.28 in as shown in Figure 3-9 (b) and (c) corresponding to low speed and high torque (45:1) and high speed and low torque (14:1) respectively.

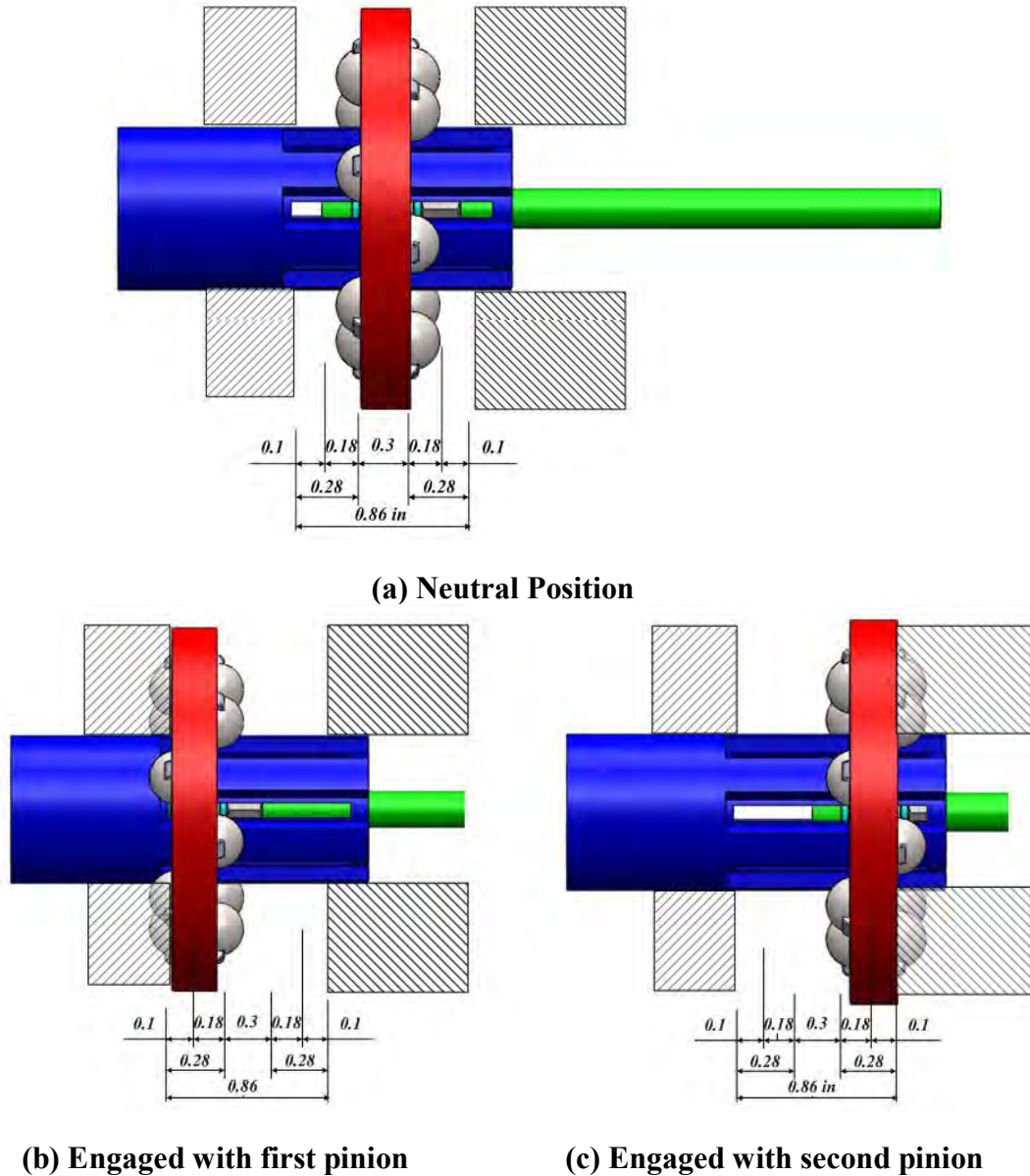


Figure 3-9: Clutch shift operation

The weight of the clutch including clutch disk, balls, push rod, thrust needle roller bearing, etc. is approximately 0.4 lb. Figure 3-9 shows the inertial force, acceleration,

velocity, and displacement during engagement with first pinion (travel length = 0.28 in). The engagement motion with second pinion is equivalent with engagement with first pinion. Assuming that time of clutch operation is 0.1 sec, the acceleration of clutch disk demands 9.2 ft/s^2 and the inertial force will be 0.114 lb, as shown in Figure 3-10.

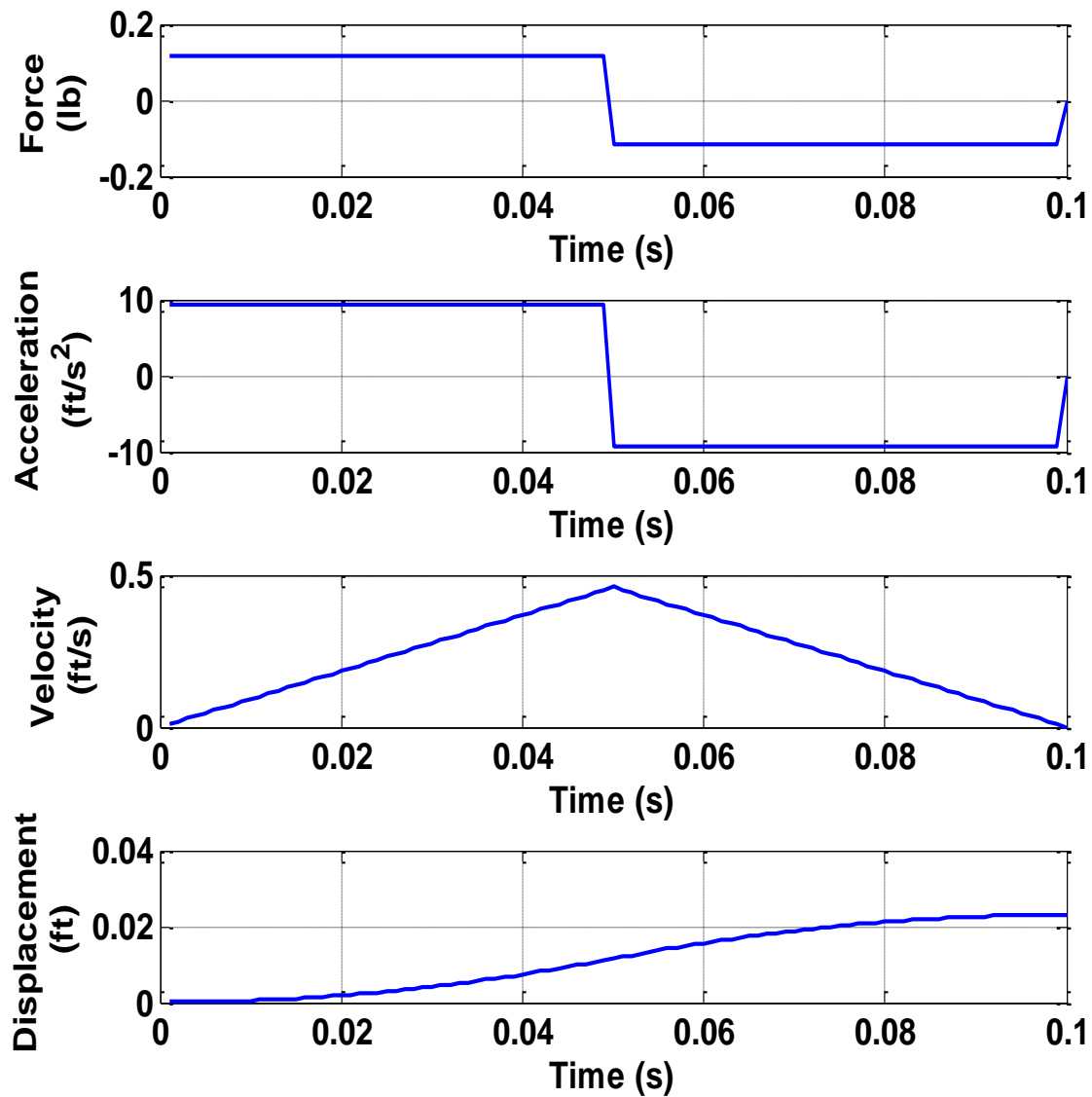


Figure 3-10: Force, acceleration, velocity, and displacement during clutch operation

Acceleration duration is from $t = 0$ s to $t = 0.05$ s, while deceleration duration is from $t = 0.05$ s to $t = 0.1$ s. The corresponding acceleration and force is positive, while the corresponding deceleration is negative. At that time, the maximum velocity reached a value of 0.45 ft/s, resulting in the distance of 0.0233 ft (0.28 in). The acceleration, velocity, and displacement equation based on singularity function are as follows:

$$\begin{aligned} y'' &= 9.2 \left[\langle t-0 \rangle^0 - \langle t-0.05 \rangle^0 \right] - 9.2 \left[\langle t-0.05 \rangle^0 - \langle t-0.1 \rangle^0 \right] \\ y' &= 9.2 \left[\langle t-0 \rangle^1 - \langle t-0.05 \rangle^1 \right] - 9.2 \left[\langle t-0.05 \rangle^1 - \langle t-0.1 \rangle^1 \right] \\ y &= \frac{1}{2} \left\{ 9.2 \left[\langle t-0 \rangle^2 - \langle t-0.05 \rangle^2 \right] - 9.2 \left[\langle t-0.05 \rangle^2 - \langle t-0.1 \rangle^2 \right] \right\} \end{aligned} \quad (3.5)$$

In summary, the inertia force due to acceleration is not significant for clutch operation as shown in Figure 3-10.

3.2.2 MDW Clutch Version 2

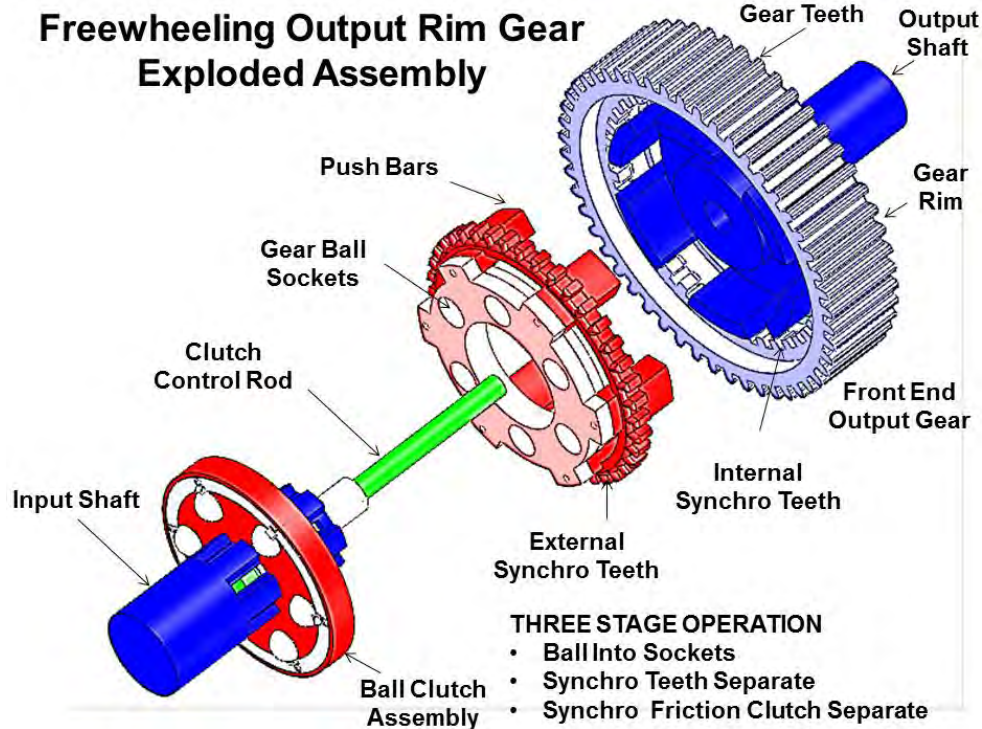


Figure 3-11: Exploded view of the synchro mesh clutch assembly

In order to decrease cost and unsprung weight, it is necessary for the SRM prime mover to operate up to 15000 RPM in the MDW. During high speed operation, the output gear of the front end gear train operates at 15000 RPM, resulting in the front end input pinion operating over 50000 RPM, which is undesirable. Therefore, to solve this issue, the amplifier gears of the front end star gears must freewheel by providing a synchro clutch in the output gear [Tesar,Jan, 2012].

Figure 3-11 shows the exploded view of the synchro mesh clutch assembly which enables the gear rim to freewheel. The ball clutch assembly is explained in the previous section. The output gear is composed of output shaft, output rim, internal synchro teeth, and external synchro teeth.

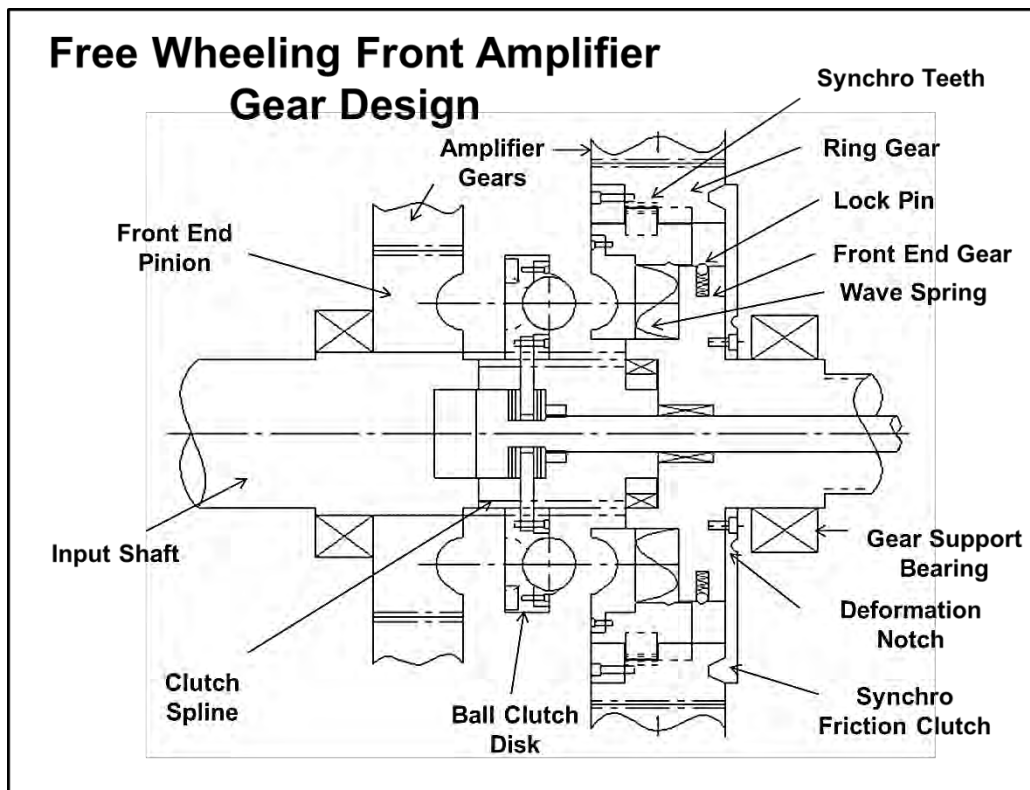


Figure 3-12: Cross-section of freewheeling front amplifier gear

Figure 3-12 shows the cross-section of front amplifier gear associated with Figure 3-11. The 3-stage sequence to disengage the amplifier gears is as follows:

- 1) Clutch disk driven by the clutch actuator place the balls to drive the output gear.
- 2) The clutch disk is further operated to move the socket external synchro teeth assembly, and at the same time compresses a wave spring. This leads to disengaging the internal synchro teeth in the output gear rim.
- 3) The clutch disk is operated a small additional distance. As a result, the push bars push out the synchro friction clutch, resulting in freewheeling the gear rim.

Therefore, the gear body drives the pinion of the MDW backend. Under the reverse conditions, step 3 becomes step 1 so that the friction clutch must drive the gear rim to match the velocity of the gear body. This enables the synchro teeth to be slid into engagement. The detail drawing is presented in Appendix C.

3.3 SWITCHED RELUCTANCE MOTOR

Some papers study and compare the advantage and disadvantages of different electric motors for an electric vehicle system[Zeraoulia, Benbouzid et al.,2006; Hashemnia and Asaei,2008].

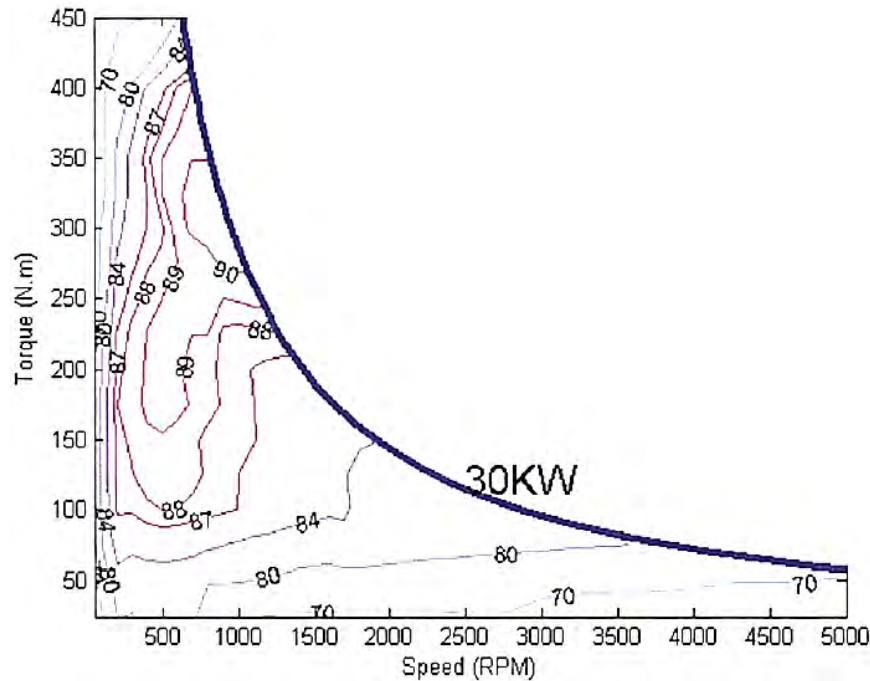


Figure 3-13: Efficiency Map

They show a comparative study in terms of DC motor, Induction Motor (IM), Permanent magnet synchronous motors (PMSM), and Switched reluctance motors (SRM). The primary motor considered is the Switched Reluctance Motor (SRM) which performs better at high speeds, compared with BLDC motor. In addition, the SRM has high torque density and low cost due to absence of magnets. Figure 3-13 shows the efficiency plot in terms of torque and speed. The efficiency map shows the SRM efficiency at different operating points for 30 kW, showing that moderate speed and torque relative to high torque are efficient. However, the poor efficiency occurs at low

and extremely high speeds. In addition, efficiency decreases under light loading conditions.

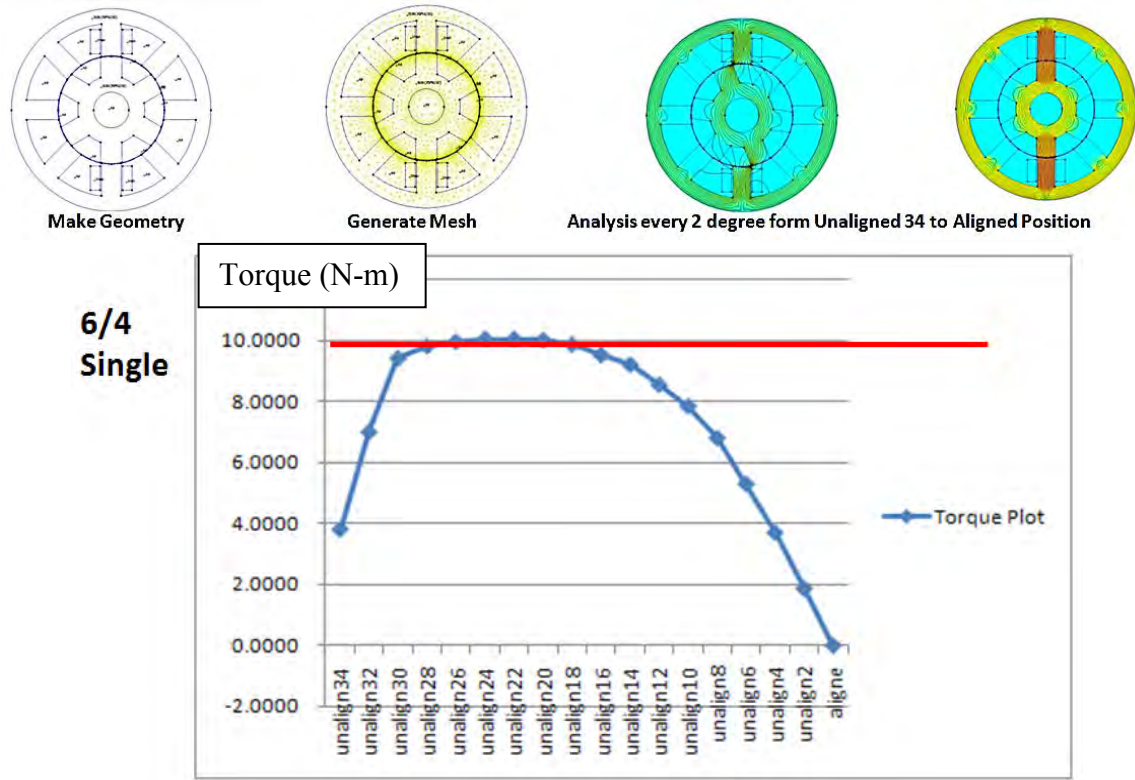


Figure 3-14: Torque Analysis of SRM

To confirm the torque derived from the analytical method, the Finite Element Method Magnetics (FEMM) software was used as shown in Figure 3-14. This graph shows the torque variation from unaligned 34° to aligned position. The maximum torque occurs from unaligned 28° to 18°.

3.4 RECONFIGURABLE POWER CONTROLLER

Industrial motors operate around a certain operating point and the efficiency is defined at that point. That is, they have one efficiency map which corresponds to only

one speed regime as the customer choice. For instance, the protean electric wheel motor belongs to this case[Protean Electric; Ifedi, Mecrow et al.,2011]. This leads to a limited set of choices in terms of drivability and efficiency. In order to enhance drivability and efficiency, it is essential to have multiple choices as a result of four different efficiency maps due to four distinct speeds (two electrical and two mechanical). Therefore, the electric vehicles with the MDW including a reconfigurable power controller can have a high efficiency over its entire torque-speed profile by raising and flattening the efficiency sweet spot [Tesar and Ashok,May, 2011].

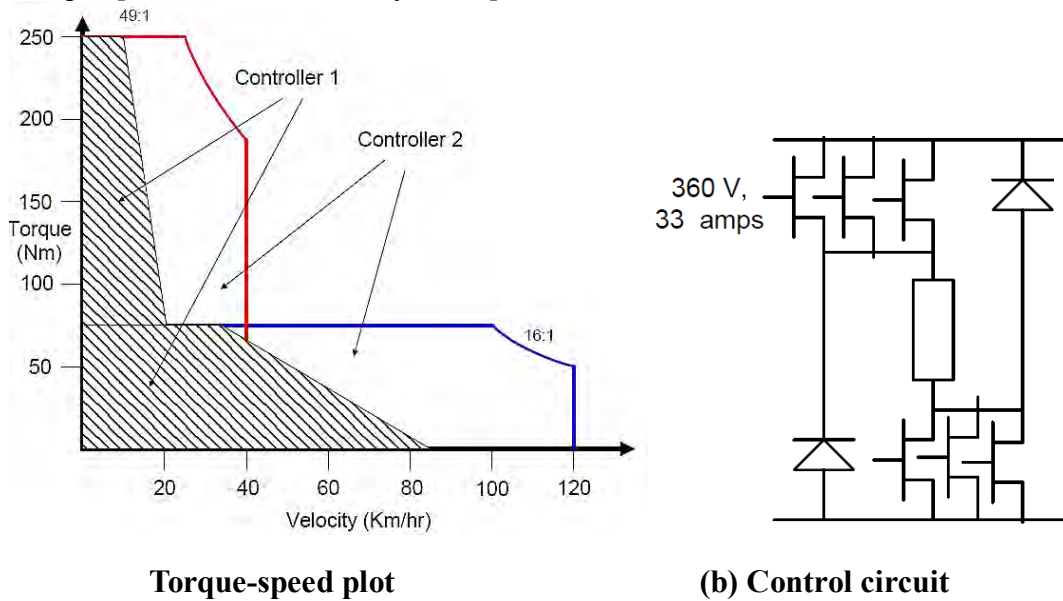


Figure 3-15: Reconfigurable power controller [Tesar and Ashok,May, 2011]

Figure 3-15 shows the basic torque speed profiles and reconfigurable power controller. The key idea is to choose different components (i.e., IGBT, MOSFET) within a controller depending on what the operating conditions are (i.e., high / low acceleration, efficiency driving, climbing a hill, etc.). By choosing appropriate components, the overall efficiency can be further improved to meet the customer requirements for different

purposes of the system in real time. The electric motor would be driven under two controller configurations, resulting in the equivalent of two additional speed regimes. This suggests that four distinct “speeds” are created with a mechanical clutch shift.

As can be seen in Figure 3-15 (a), there are a low power circuit (i.e., controller 1, IGBT rated for 110V, 50 amps) and high power circuit (i.e., controller 2, IGBT rated for 360 V, 100 amps) corresponding to low power operation and high power operation, respectively.

Consider a vehicle moving 0-60 mph acceleration, the MDW will operate with controller 1 and controller 2 before a clutch shift. After a clutch shift (i.e., 20 mph), the MDW will also operate with controller 1 and controller 2. Figure 3-15 (b) shows the control circuit in parallel considering the two controllers. The different power levels will be applied to configure two controllers such as low power operation and high power operation [Saini,;Ashok, P.; Tesar, D., 2012, in progress,"Design Process for a Reconfigurable Power Controller"].

Chapter 4. Vehicle Modeling

Equation Chapter 4 Section 1 A passenger vehicle can be analyzed as a system consisting of one vehicle body (sprung mass) and four wheels (unsprung mass), which are of the Multi-speed Hub Drive Wheel (MDW) in this case. The vehicle can be modeled as interactions among five bodies comprising sprung and unsprung masses. In other words, all of the five bodies can move freely with regards to each other in six degrees of freedom (DOF), resulting in thirty differential equations to account for the dynamics of the vehicle model. The six DOF represent longitudinal, lateral, heave, roll, pitch, and yaw motions. These motions are restricted by suspension geometries in electric vehicles, and are coupled to each other amongst the sprung and unsprung masses. However, using thirty differential equations is not efficient for control purposes [Macek, Thoma et al.,2007]. Therefore, a reduced order mathematical model is necessary to handle this problem by simplifying the vehicle model [Cao, Liu et al.,2008]. For instance, the models can be reduced to quarter-vehicle (2 DOF), half-vehicle (4 DOF), and full-vehicle (7 DOF) models. In addition, there are bicycle (2 DOF) models and 3 DOF handling models. Finally, the tire (4 DOF) models are associated with the angular velocities of the unsprung masses. These mathematical models enable us to obtain analytical results and an approximate mathematical description of the vehicle system.

This chapter begins with an overview of vehicle modeling based on a Bayesian causal network to establish the cause-effect relationships between design and customer needs which are performance criteria such as ride comfort, handling, acceleration, braking, efficiency, durability, and stiffness. Vehicle ride models and vehicle handling models will be presented in Secs. 4.2 and 4.3, respectively. A tire model including a “Magic Formula” that characterizes tire behavior from test data will be discussed in Sec.

4.4. The 14 DOF full-vehicle model will be explained in Sec. 4.5. Finally, the effect that different weight of wheels and road conditions have on performance with increased unsprung mass will be presented in Sec. 4.6 and Sec. 4.7. The summary will be presented in Sec. 4.8.

4.1 OVERVIEW OF VEHICLE MODELING BASED ON A BAYESIAN CAUSAL NETWORK

A Bayesian causal network is used to understand the cause-effect relationship among the variables of the system [Ashok and Tesar,2007]. An overview of vehicle modeling based on a Bayesian causal will be presented in Sec. 4.1.5, but first, we need to understand the cause-effect relationship based on dynamic equations of motion in a longitudinal direction, presented below in Sec. 4.1.1.

4.1.1 Longitudinal Vehicle Dynamics

The dynamic equation of motion along a vehicle's longitudinal direction is influenced by traction forces, aerodynamic drag resistance, rolling resistance, and grade resistance. These forces act on a vehicle moving on an inclined road as shown in Figure 4-1. The equation of motion can be expressed by the following:

$$\sum F_{longitudinal} = m_{eg} a_x; \quad F_t - \left(F_{aero} + F_{rolling} + F_{grade} \right) = m_{eg} a_x \quad (4.1)$$

$$F_t = F_{xR} + F_{xF}, \quad F_{aero} = \frac{1}{2} \rho_a A_f C_d (v_v + v_w)^2 \quad (4.2)$$

$$F_{rolling} = R_{xR} + R_{xF} = C_r mg \cos \theta, \quad F_{grade} = mg \sin \theta \quad (4.3)$$

where v_v = vehicle speed

v_w = wind velocity

m_{eq} = equivalent mass

ρ_a = air density (1.232 kg/m³)

A_f = vehicle frontal area

C_d = aerodynamic drag coefficient

C_r = rolling resistance coefficient

θ = grade angle

The sum of aerodynamic drag resistance (F_{aero}), rolling resistance ($F_{rolling}$), and grade resistance (F_{grade}) is referred to as “road load,” which is a minimal force on a vehicle moving on a road. For example, during cruising (i.e., acceleration (a_x)=0), traction force (F_t) given in terms of the slip between the tire and the road is equal to the road load, which consists of front traction force (F_{xF}) and rear traction force (F_{xR}). Similarly, rolling resistance ($F_{rolling}$) consists of front rolling resistance (R_{xF}) and rear

rolling resistance (R_{xR}). The difference between road loads and the traction force make it possible to accelerate or decelerate the vehicle [Ehsani, Rahman et al., 1997].

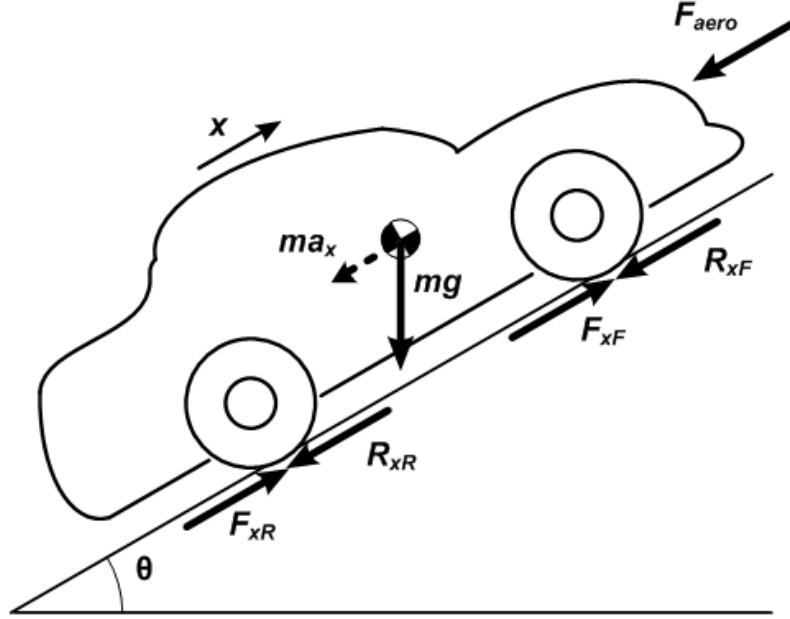


Figure 4-1: Forces acting on a two-axle vehicle

By introducing the inertial force, Equation (4.1) can be rewritten as:

$$F_t - \left(\begin{matrix} m_{eg} a_x + \\ F_{aero} + \\ F_{rolling} + \\ F_{grade} \end{matrix} \right) = 0 \quad (4.4)$$

Inertial force ($-m_{eg} a_x$) is called the D'Alembert force which is illustrated as a dotted line in Figure 4-1. In this example, inertial force ($-m_{eg} a_x$) is called the acceleration resistance and will be explained in the following section.

4.1.2 Acceleration Resistance

From Equation (4.1), equivalent mass (m_{eq}) is the sum of vehicle mass (m_v) and equivalent mass (m_r) of the rotating parts that contribute to the inertial effects of all the rotating components, such as the motor and wheels in electric vehicles [Guzzella and Sciarretta, 2005]. First, the total inertial torque of the wheels is given by:

$$\tau_{m,w} = I_w \dot{\omega}_w \quad (4.5)$$

where I_w is the moment of inertia of the wheel and ω_w is the wheel speed. The total inertial torque acts on the vehicle as an additional inertial force ($F_{m,w} = \tau_{m,w} / r_w$). Wheel slip (i.e., $v = \omega_w r_w$) is not usually considered. The additional inertial force of the wheel is:

$$F_{m,w} = \frac{I_w}{r_w^2} \dot{v} \quad (4.6)$$

The contribution of the wheels to the electric vehicle's overall inertia is given by:

$$m_{r,w} = \frac{I_w}{r_w^2} \quad (4.7)$$

Second, the inertial torque of the motor is given by:

$$\tau_{m,m} = I_m \dot{\omega}_m = I_m \frac{g_r \dot{v}}{r_w} \quad (4.8)$$

where I_m is the moment of inertia of the motor rotor, g_r is the gear ratio, and ω_m is the motor speed. This torque is transferred to the wheels as a force:

$$F_{m,m} = \frac{g_r}{r_w} \tau_{m,m} = \frac{g_r}{r_w} \left(I_m \frac{g_r \dot{v}}{r_w} \right) = g_r^2 \frac{I_m \dot{v}}{r_w^2} \quad (4.9)$$

Efficiency (η_g) of the gear train can be introduced to account for losses. The above equation is given by:

$$F_{m,m} = g_r^2 \frac{I_m \dot{v}}{\eta_g r_w^2} \quad (4.10)$$

The additional contribution of the motor to the electric vehicle's overall inertia is given by:

$$m_{r,m} = g_r^2 \frac{I_m}{\eta_g r_w^2} \quad (4.11)$$

Thus, the summation of equations (4.7) and (4.11) is equivalent mass (m_r) of the rotating parts:

$$m_r = m_{r,w} + m_{r,m} = \frac{I_w}{r_w^2} + g_r^2 \frac{I_m}{\eta_g r_w^2} \quad (4.12)$$

Consequently, the equivalent mass is given by [Guzzella and Sciarretta,2005]:

$$m_{eq} = m_v + N_w m_r = m_v + N_w (m_{r,w} + m_{r,m}) = m_v + N_w \left(\frac{I_w}{r_w^2} + g_r^2 \frac{I_m}{\eta_g r_w^2} \right) \quad (4.13)$$

where N_w is the number of drive wheels. The acceleration resistance is as follows:

$$m_{eg} a_x = (m_v + N_w m_r) a_x = \left\{ m_v + N_w \left(\frac{I_w}{r_w^2} + g_r^2 \frac{I_m}{\eta_g r_w^2} \right) \right\} a_x \quad (4.14)$$

For a conventional vehicle, the equivalent mass ($N_w m_r$) of the rotating parts (engine and flywheel) is around 0.065 when m_v is 1 [Miller,2004]. In contrast, the equivalent mass ($N_w m_r$) of the rotating parts of the MDW is 5 to 10 times lower than in a conventional vehicle [Tesar and Ashok,May, 2011].

4.1.3 Aerodynamic Drag Resistance

Aerodynamic drag resistance is the fluid drag force due to the friction created as the vehicle moves against the air. The aerodynamic drag resistance is given by:

$$F_{aero} = \frac{1}{2} \rho_a A_f C_d (v_v + v_w)^2 \quad (4.15)$$

It is a nonlinear function of the vehicle velocity. That is, it is proportional to the square of the velocity which is the sum of a vehicle and a wind velocity. The aerodynamic drag coefficients for a standard car and a truck are 0.3 and 1.5, respectively. In contrast, some electric vehicle designs have accomplished a value of 0.19 based on their streamlined shape. Electric vehicles have more flexibility in the placement of major components and less room is needed for cooling air ducts. In other words, the potential for reducing the value of the aerodynamic drag coefficient in electric vehicles is greater than in conventional vehicles, which need air to operate the internal combustion engine. Air intake affects the front shape of a vehicle, increasing the value of the drag coefficient [Gillespie,1992; Larminie and Lowry,2003].

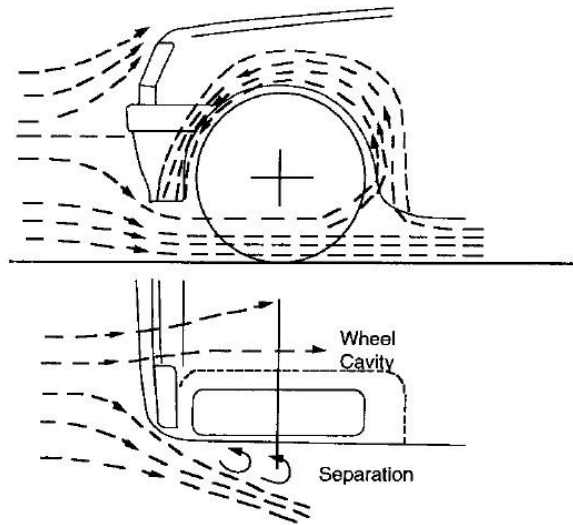


Figure 4-2: Air flow recirculation in a wheel well

As shown in Figure 4-2, complex airflow patterns occur around a wheel. Significant drag is created at the wheels due to the turbulent, recirculating airflow within the cavities. Experimental research shows that reducing the clearance between the underside of the vehicle and the ground, as well as minimizing the size of the wheel cavity, decreases the aerodynamic drag resistance [Gillespie,1992].

4.1.4 Rolling Resistance

Rolling resistance is caused by the friction of a vehicle's tires on the road. Total rolling resistance ($F_{rolling}$) is the sum of front resistance (R_{rf}) and rear resistance (R_{rr}) as shown in Figure 4-1. The rolling resistance is given by:

$$F_{rolling} = R_{xR} + R_{xF} = C_r mg \cos \theta \quad (4.16)$$

The rolling resistance of a pneumatic tire is affected by the structure of the tire (its construction and materials) and its operating conditions (surface conditions, inflation pressure, speed, temperature, etc.). Rolling resistance is usually increased by rough or dry surfaces, high inflation pressure, high speed, or low temperatures [Wong,2008].

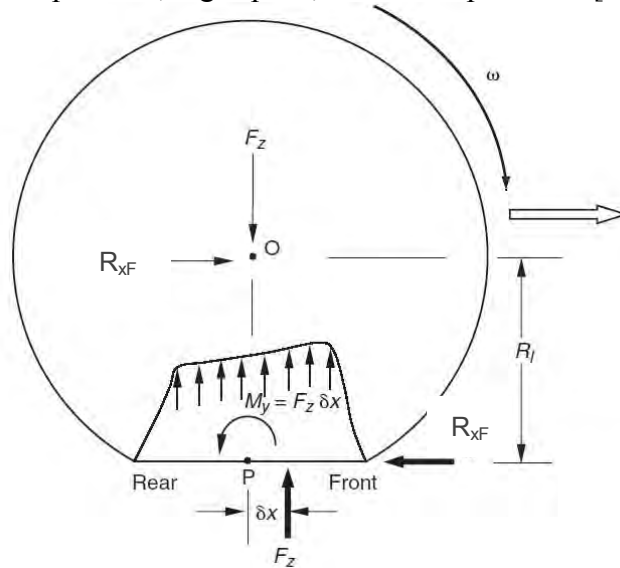


Figure 4-3: Rolling resistance in a free rolling tire

Figure 4-3 shows how rolling resistance is generated in a free rolling tire, in which case rolling resistance (R_{xF}) can be written as [Blundell and Harty,2004]:

$$R_{xF} = \frac{\delta x}{R_l} F_z \quad (4.17)$$

where F_z represents the vertical force acting on the tire and R_l is the rolling radius. The coefficient of the rolling resistance is represented by dividing the rolling resistance by the tire's vertical load and is given by $(C_r) = \frac{\delta x}{R_l}$. The rolling resistance moment is $M_y = F_z \delta x$. The value of the rolling resistance coefficient ranges from 0.01 to 0.04. For example, a conventional passenger car with radial tires has a value of 0.015 [Wong,2008].

4.1.5 Grade Resistance

Grade resistance (F_{grade}) is a function of the weight of a vehicle and the slope angle expressed in terms of percent grade ($\%Grade = 100\% \times \tan(\theta)$). Figure 4-1 shows the grade of a hill. The formula can be expressed by:

$$F_{grade} = mg \sin \theta \quad (4.18)$$

A 10% grade is around $\arctan(1/10)$ or 5.7° . Highway design places limits on road grades that depend on the local terrain, speed limit, and the expected usage of the road. For example, in Massachusetts, freeways designed for 65 mph speeds may have a maximum grade of 4% (2.3°), while a road in mountainous terrain designed for speeds of 25 mph may have a maximum 15% or 16% grade [Riner,2007]. According to this book [Miller,2008], typical grades are 3% and 7.2 % for normal driving and maximum 33% (18.26°) for vehicle launch.

Generally, acceleration and grade resistances can be significant considerations in MDW design, while aerodynamic and rolling resistances are relatively small. We will compare acceleration, aerodynamic, rolling, and grade resistances in the next section.

4.1.6 Comparison of Acceleration, Aerodynamic, Rolling, and Grade Resistances

To evaluate the demands on the MDW, it is necessary to compare the acceleration, aerodynamic, rolling, and grade resistances. First, we will derive the torque equation in terms of these four different resistances.

By introducing the concept of inertial (D'Alembert) force, the traction force from Equation (4.1) combined with Equation (4.14) can be expressed by:

$$F_t = \left[\left\{ m_c + N_w \left(\frac{I_w}{r_w^2} + g_r^2 \frac{I_m}{\eta_g r_w^2} \right) \right\} a_{car} + \left\{ \frac{1}{2} \rho_a A_f C_d (v_v + v_w)^2 + C_r m_c g \cos \theta + m_c g \sin \theta \right\} \right] \quad (4.19)$$

The total wheel torque is obtained by multiplying the radius of the wheel as follows:

$$\tau_{tw} = r_w F_t = r_w \left[\left\{ m_c + N_w \left(\frac{I_w}{r_w^2} + g_r^2 \frac{I_m}{\eta_g r_w^2} \right) \right\} a_{car} + \left\{ \frac{1}{2} \rho_a A_f C_d (v_v + v_w)^2 + C_r m_c g \cos \theta + m_c g \sin \theta \right\} \right] \quad (4.20)$$

If an electric vehicle uses four drive wheels, the required motor torque is inversely proportional to the gear ratio and is given by:

$$\tau_m = \frac{r_w F_t}{N_w g_r} = \frac{r_w}{N_w g_r} \left[\left\{ m_c + N_w \left(\frac{I_w}{r_w^2} + g_r^2 \frac{I_m}{\eta_g r_w^2} \right) \right\} a_{car} + \left\{ \frac{1}{2} \rho_a A_f C_d (v_v + v_w)^2 + C_r m_c g \cos \theta + m_c g \sin \theta \right\} \right] \quad (4.21)$$

If we consider the gear system efficiency, the required motor torque is given by:

$$\tau_m = \frac{r_w F_t}{N_w g_r \eta_g} = \frac{r_w}{N_w g_r \eta_g} \left[\left\{ m_c + N_w \left(\frac{I_w}{r_w^2} + g_r^2 \frac{I_m}{\eta_g r_w^2} \right) \right\} a_{car} + \left\{ \frac{1}{2} \rho_a A_f C_d (v_v + v_w)^2 + C_r m_c g \cos \theta + m_c g \sin \theta \right\} \right] \quad (4.22)$$

To simplify the analysis, we assume the following:

- 1) There is no gear loss ($\eta_g = 1$).
- 2) Neglect the moments of inertia of the motors and wheels.
- 3) The wind velocity is 0.
- 4) A weight of the vehicle is 3000 lb, and the wheel radius (r_w) is 12".
- 5) The first gear ratio (g_{r1}) is 49:1 from 0 to 20 mph, and the second gear ratio (g_{r2}) is 14:1 from 21 to 70 mph.

Equation (4.22) becomes as follows:

$$\tau_m = \frac{r_w F_t}{N_w g_r} = \frac{r_w}{N_w g_r} \left[m_c a_{car} + \left\{ \frac{1}{2} \rho_a A_f C_d (v_v + v_w)^2 + C_r m_c g \cos \theta + m_c g \sin \theta \right\} \right] \quad (4.23)$$

	Parameters	Value	Units	Value	Units
Number of wheels	N_w	4			
Vehicle mass	m_c	1360	kg	3000/g	slug
Wheel radius	r_w	0.305	m	12	in
Air density	ρ_a	1.23	kg/m ³	0.0024	slug/ft ³
Frontal area	A_f	1.3	m ²	14	ft ²
Drag coefficient	C_d	0.3			
Rolling coefficient	C_r	0.007			
Gear ratio	g_{r1}, g_{r2}	49,14			

Table 4-1: Vehicle Parameters

Table 4-1 shows the vehicle specifications for simple analysis. The power required to accelerate a vehicle is given by:

$$P = F_t v_c = \tau_t \omega_w \quad (4.24)$$

With respect to each drive wheel, mechanical power from the motor is transmitted through the gear train to the tire. Figure 4-4 plots eight variables and their response from 0 to 70 mph. The eight plots represent wheel power, wheel torque, total traction force and running resistance, velocity, distance, motor speed, motor torque with respect to time or velocity based on vehicle weight (3000 lb), and acceleration (0.1 g). Figure 4-5 and Figure 4-6 plot the same eight factors based on accelerations of 0.2 g and 0.3 g, respectively, under the same conditions.

At 0.1 g acceleration, as shown in Figure 4-4 (a) and (b), the required wheel torque ranges from 90 ft-lb to 160 ft-lb for 1°, 3°, and 5° grades, whereas the required wheel power ranges from 18 hp to 30 hp at 70 mph. Figure 4-4 (c) shows that the total

traction force of a vehicle is the sum of four different resistances. The running resistances such as acceleration, aerodynamic, rolling, and grade resistances are shown in Figure 4-4 (d). It is seen that acceleration and grade are significant factors in MDW design and operation. The comparison is made in Figure 4-7. Under the 0.1 g condition, vehicle acceleration from 0 to 60 mph in 28 seconds is shown in Figure 4-4 (e). In this case, the vehicle travels around 1300 ft. Figure 4-4 (g) and (h) show motor speed versus time and motor torque versus velocity, respectively. Since we have two gear ratios, the first speed ranges from 0 to 20 mph and the second speed ranges from 21 to 70 mph. In the first speed range, the MDW operates from 0 to 15000 rpm based on the first gear ratio of 49:1 (for low speed and high torque). After a gear changeover due to clutch shift at 20 mph, the MDW operates from 3922 to 13726 rpm from 21 to 70 mph. The motor torque delivers from 7 ft-lb to 11 ft-lb.

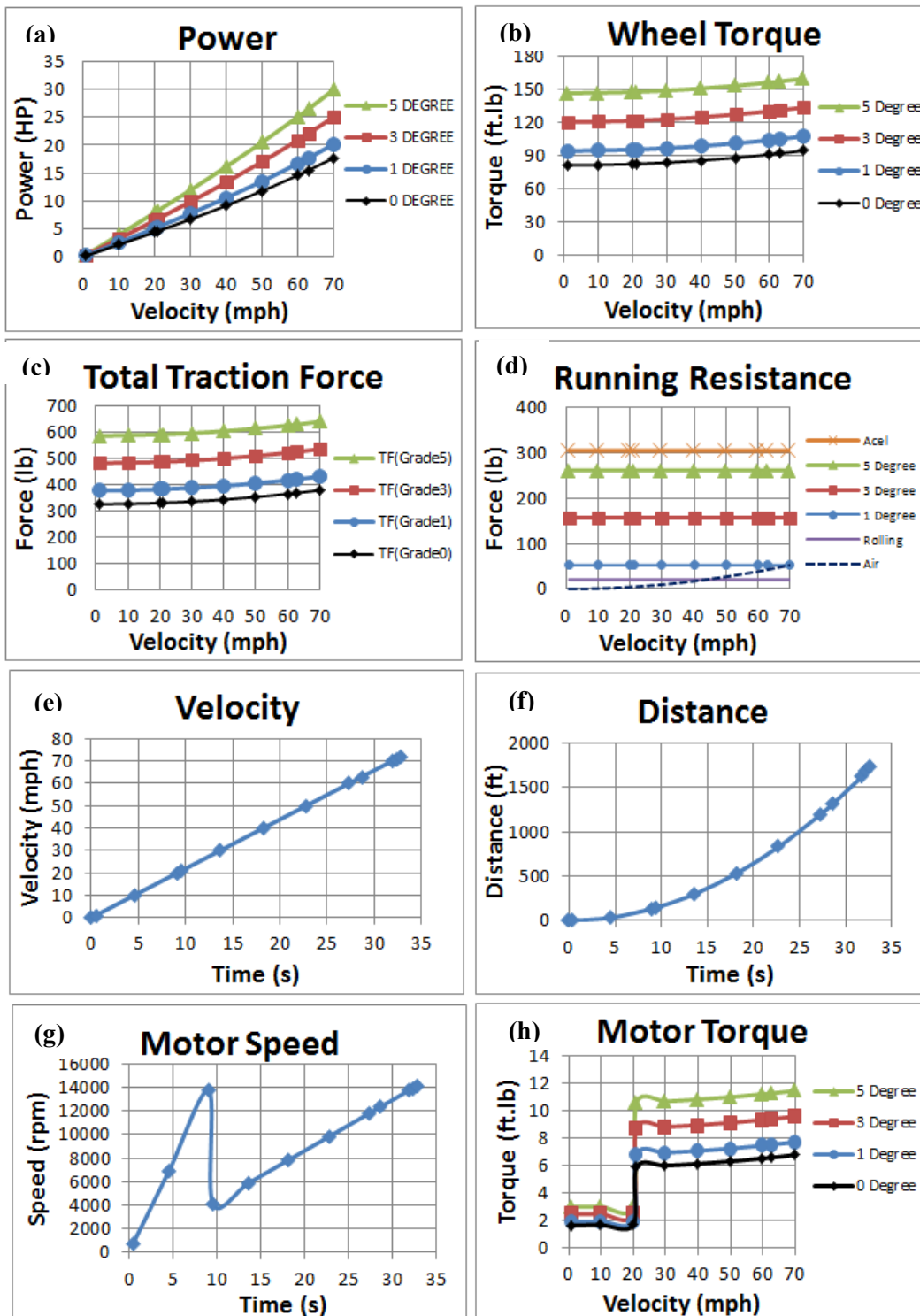


Figure 4-4: Comparison of resistances and duty cycles for the MDW (a = 0.1g)

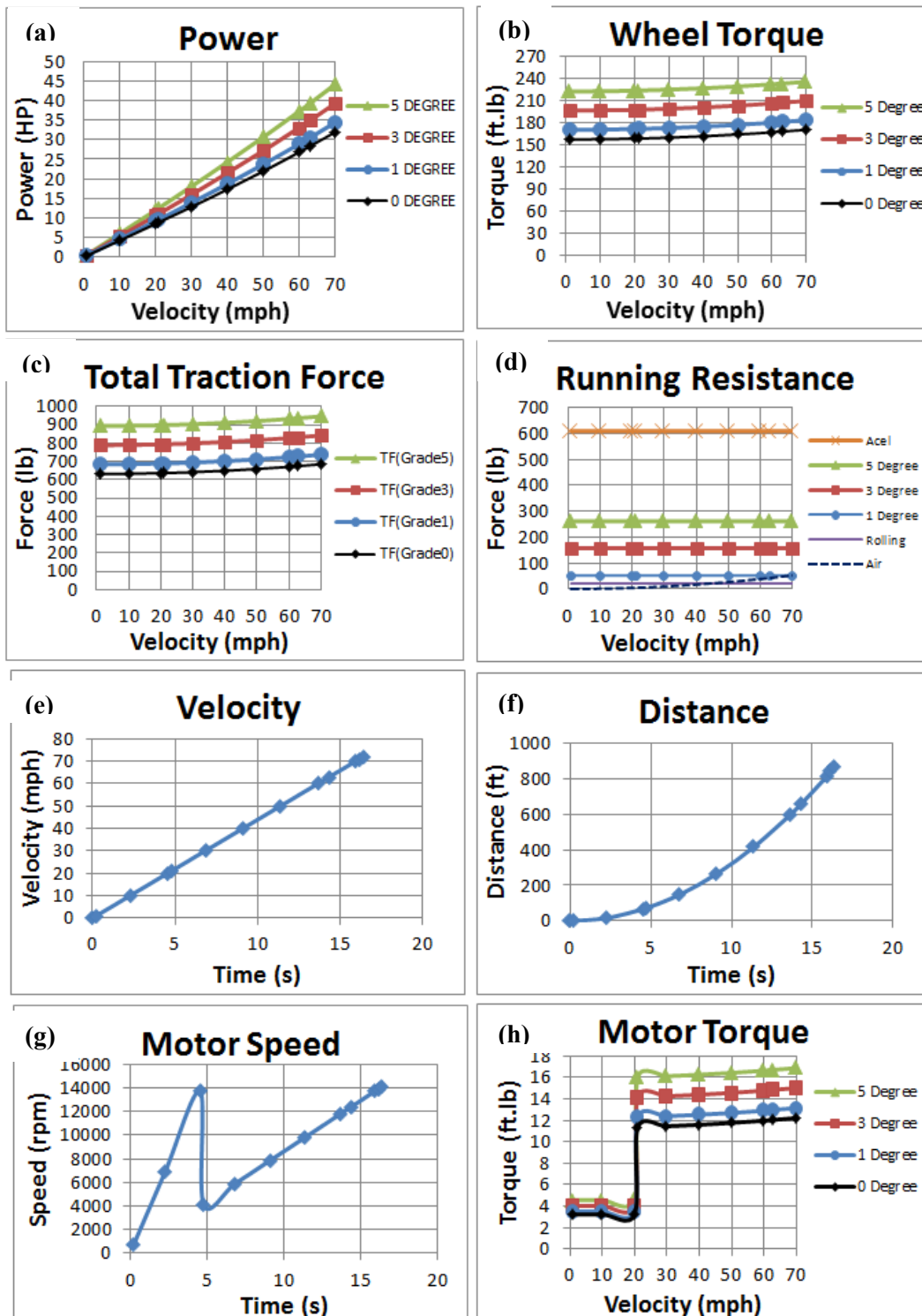


Figure 4-5: Comparison of resistances and duty cycles for the MDW ($a = 0.2g$)

Figure 4-5 shows that the power required to accelerate (0.2 g) a vehicle becomes 30 hp to 45 hp for 1°, 3°, and 5° grades, while the wheel torque required is 170 ft-lb to 240 ft-lb, which is approximately two times bigger than the torque in Figure 4-4 (0.1 g). The running resistances are the same except for the acceleration resistance. The grade resistance for a vehicle on 1° and 5° grades is 50 ft-lb and 250 ft-lb, respectively. The motor torque required is 12 ft-lb to 17 ft-lb. Figure 4-6 shows that the power required to accelerate (0.3 g) a vehicle becomes 45 hp to 60 hp, while the wheel torque is 240 ft-lb to 310 ft-lb for 1°, 3°, and 5° grades. The motor torque required is 18 ft-lb to 22 ft-lb.

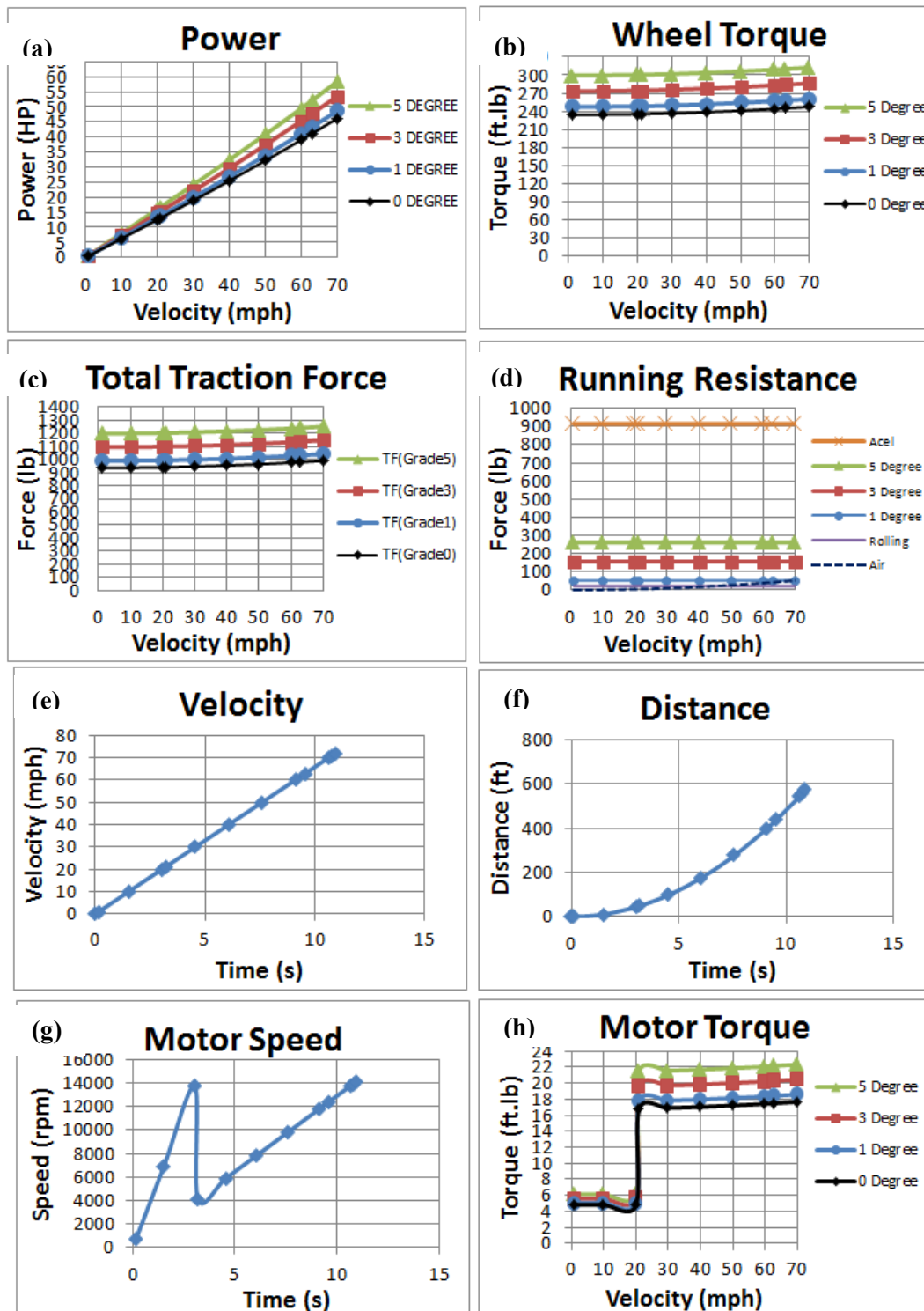


Figure 4-6: Comparison of resistances and duty cycles for the MDW ($a = 0.3g$)

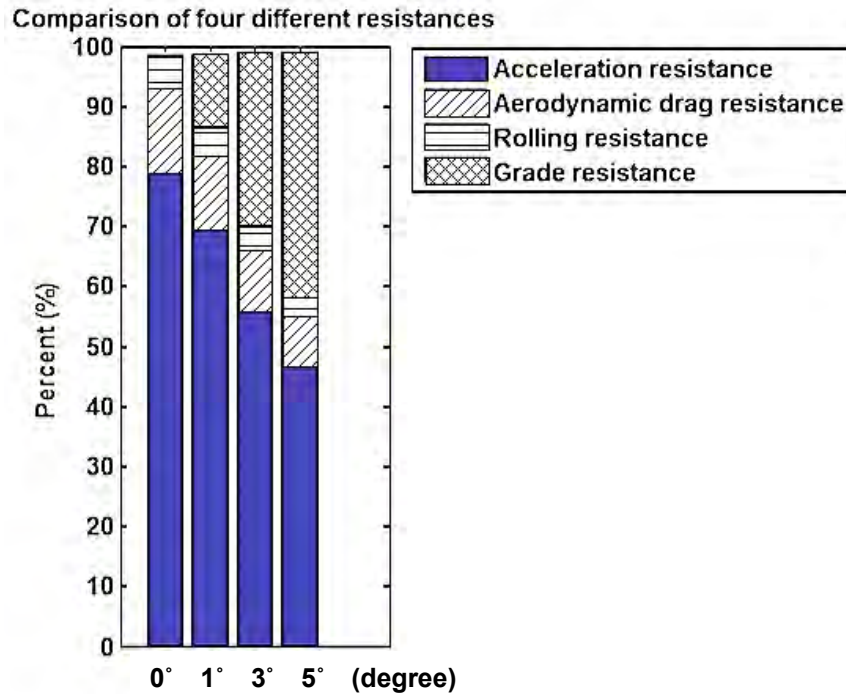


Figure 4-7: Comparison of four different resistances for the MDW ($a = 0.1g$)

We transform the data from Figure 4-4 (d) to Figure 4-7, which shows the percentages of the acceleration, aerodynamic, rolling, and grade resistances. At 0° , the percentage of acceleration resistance is 80%. The aerodynamic and rolling resistances are 14% and 6%, respectively. At 5° , the percentage of acceleration resistance is 47%. The aerodynamic and rolling resistances are 8% and 3%, while the grade resistance is 42%. In

other words, as the grade increases, the demands on the MDW increase rapidly. Generally, acceleration and grade resistances can be significant considerations for MDW design, while aerodynamic and rolling resistances are relatively small.

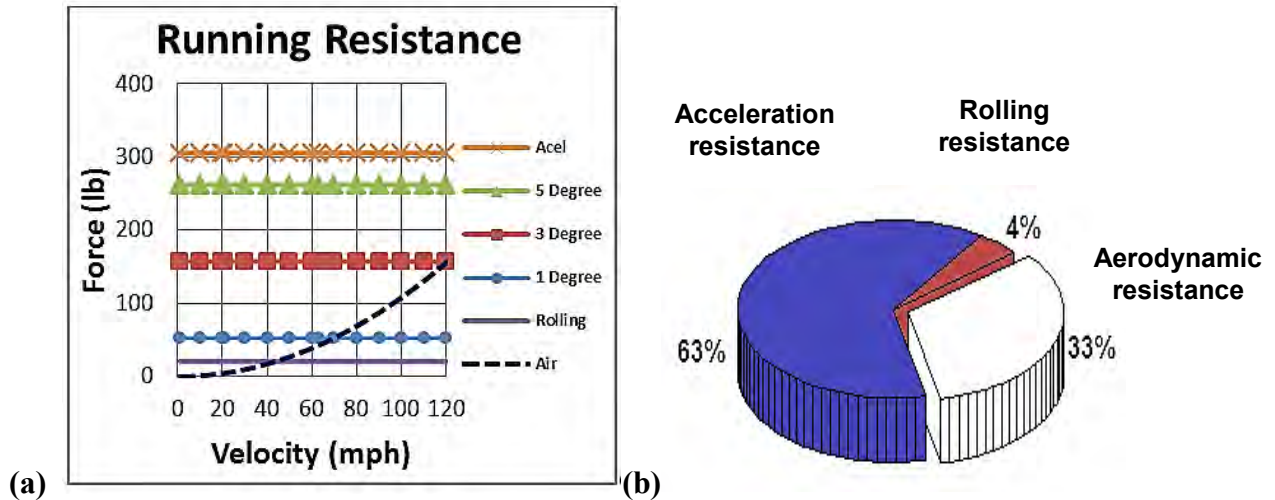


Figure 4-8: Comparison of three different resistances for the MDW with no grade during high speed driving condition ($a = 0.1g$, $v = 120$ mph)

Figure 4-8 (a) shows running resistance such as acceleration, grade, rolling, and aerodynamic resistance. It is plotted up to velocity 120 mph which might be sport car condition. At 120 mph, the aerodynamic resistance is increased by 160 lb as half of acceleration resistance (300lb). Figure 4-8 (b) shows the pie diagram in terms of acceleration, aerodynamic, and rolling resistance. It can be seen that aerodynamic resistance becomes an important factor, as a vehicle speed increases. At high speeds of 120 mph, 33 % of energy is spent on overcoming aerodynamic drag. Since the energy consumption due to acceleration and grade resistance can be partially restored through the regenerative braking of the electric vehicles, minimizing aerodynamic and rolling resistances will become important for future electric vehicles. According to [Chan and Chau,2001], the amount of energy through the regenerative braking is about 30-50% on

average. Assuming the efficiency of the gear train and power electronic is about 70%, this leads to 21-35% which is actually stored in the batteries.

4.1.7 Bayesian Causal Network

Longitudinal vehicle dynamics can be represented by a Bayesian causal network as shown in Figure 4-9. The net force, a dependent parameter, is affected by airflow resistance, rolling resistance, grade resistance, and traction force. The rolling resistance is caused by deformation of the tire and is roughly proportional to the normal force on the tire. These dependent parameters are controlled by speed, grade, and power with reference parameters (dashed circle) related to the frontal area, air density, drag coefficient, rolling coefficient, and vehicle weight. In this case, the grade and power are control parameters (heavy circle). In addition to the situational parameters, control and reference parameters could be human choices. The net force determines acceleration, which then provides speed, thus resulting in distance.

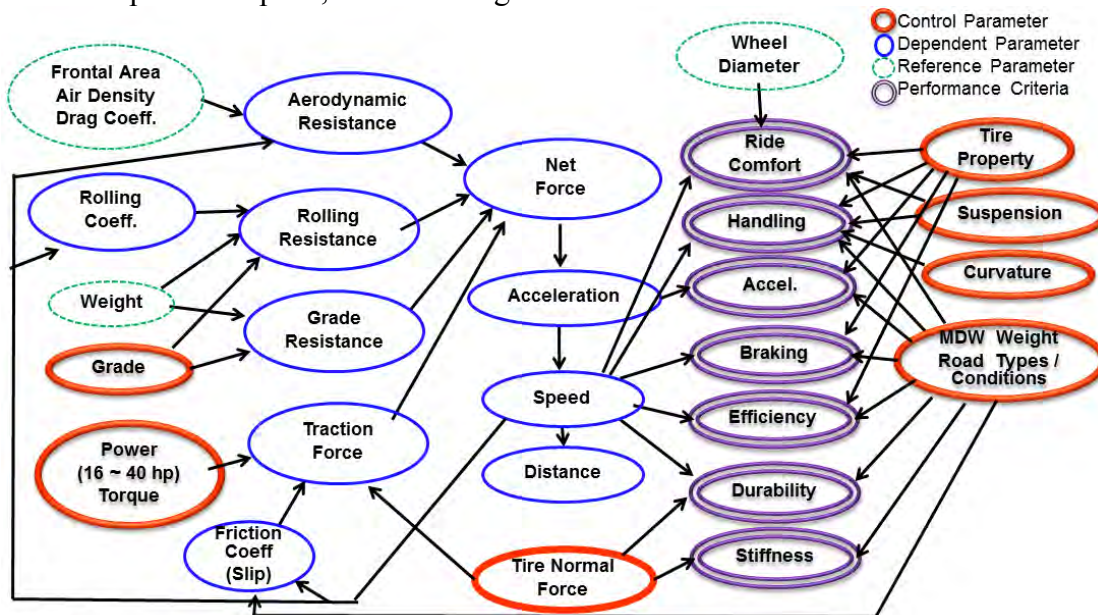


Figure 4-9: Bayesian causal network

From a performance criteria (double ellipse) point of view, ride comfort performance can be affected by tire properties, suspension, MDW weight, road type/condition, and speed. Wheel diameter is a reference parameter. The handling performance can be affected by tire properties, suspension, curvature, MDW weight, road type/condition, and speed. Braking can be affected by tire properties, MDW weight, road type and condition, and speed. In general, efficiency is governed primarily by torque and speed, but can vary with MDW weight, road type and condition, speed, and tire properties like temperature and pressure. Durability can be affected by speed and the normal force on the tires. Stiffness can also be affected by tire normal force as shown in Figure 4-9. One learns from this network which factors influence vehicle performance, in which way, and under what conditions.

4.2 VEHICLE RIDE MODEL

In order to investigate the effect of drive wheels on comfort, it is necessary to create vehicle ride models. There are three types of a vehicle ride models: quarter-vehicle (2 DOF), half-vehicle (4 DOF), and full-vehicle (7 DOF). First, we discuss the quarter-vehicle ride model.

4.2.1 Quarter-Vehicle (2 DOF) Ride Model

A quarter-vehicle model is often used to simulate vehicle ride dynamics based on suspension systems and takes into account vertical (heave) motion, but not pitch and roll motions. It is a system represented with two degrees of freedom (2 DOF) as shown in Figure 4-10; the number of degrees of freedom can be determined by the number of directions that a mass can move. A 2 DOF system indicates both the vehicle sprung mass (m_s) and the unsprung mass (m_u) including the wheel, tire, and axle assembly. Technically, a vehicle suspension system is excited harmonically by a road surface through springs and a shock absorber, which is modeled by a linear spring and viscous damper, respectively. The suspension stiffness (spring) and damper (shock absorber) are denoted by k_s and c_s . Tire stiffness and damping are represented by k_u and c_u . Note that tire damping (c_u) is negligible compared to suspension damping [Van Schalkwyk and Kamper,2006].

The mathematical model and equations of motion for the vehicle suspension system can be obtained from the free body diagram as shown in Figure 4-10 (b). By applying Newton's second law of motion in two coordinates (z_s, z_u) with origins at the static equilibrium positions, two equations associated with the sprung and unsprung mass can be expressed by [Sun,2003]:

$$\begin{aligned}
\sum F_{z_s} &= m_s \ddot{z}_s; & c_s (\dot{z}_u - \dot{z}_s) + k_s (z_u - z_s) - F_a &= m_s \ddot{z}_s \\
\sum F_{z_u} &= m_u \ddot{z}_u; & -c_s (\dot{z}_u - \dot{z}_s) - k_s (z_u - z_s) + c_u (\dot{z}_u - \dot{z}_0) + k_u (z_u - z_0) + F_a &= m_u \ddot{z}_u
\end{aligned}
\tag{4.25}$$

where F_a is the actuator force. The force from harmonic displacement by the road surface is transmitted to the sprung mass through the suspension system.

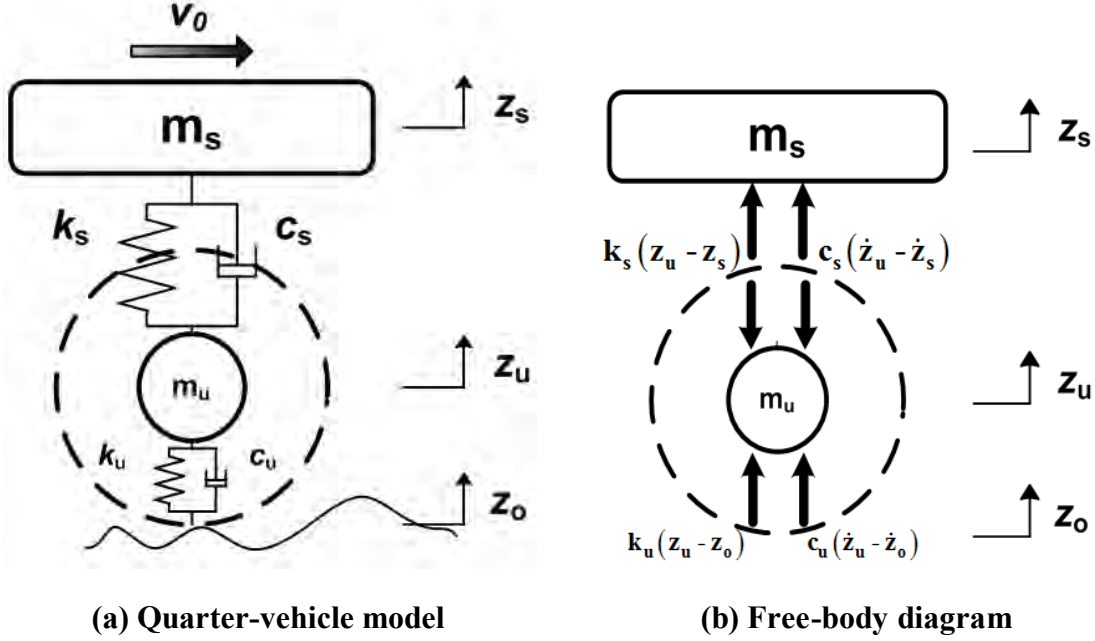


Figure 4-10: Quarter-vehicle model and Free-body diagram

Hence, the force acting on the sprung mass is the summation of the spring force $k_s(z_u - z_s)$ and damping force $c_s(\dot{z}_u - \dot{z}_s)$. The state space representation derived from the above equations is given by [ElMadany and Abduljabbar,1999; Chen and Guo,2001; Sun, Zhang et al.,2002; Chen and Guo,2005; Peng and Ulsoy,2006; Huang, Yu et al.,2010]:

$$\frac{d}{dt} \begin{bmatrix} z_u - z_0 \\ \dot{z}_u \\ z_s - z_u \\ \dot{z}_s \end{bmatrix} = \begin{bmatrix} 0 & 1 & 0 & 0 \\ -\frac{k_u}{m_u} & -\frac{(c_s + c_u)}{m_u} & \frac{k_s}{m_u} & \frac{c_s}{m_u} \\ 0 & -1 & 0 & 1 \\ 0 & \frac{c_s}{m_s} & -\frac{k_s}{m_s} & -\frac{c_s}{m_s} \end{bmatrix} \begin{bmatrix} z_u - z_0 \\ \dot{z}_u \\ z_s - z_u \\ \dot{z}_s \end{bmatrix} + \begin{bmatrix} 0 \\ \frac{m_s}{m_u} \\ 0 \\ -1 \end{bmatrix} \frac{F_a}{m_s} + \begin{bmatrix} -1 \\ \frac{c_u}{m_u} \\ 0 \\ 0 \end{bmatrix} \dot{z}_0 \quad (4.26)$$

$$\dot{\mathbf{x}} = \mathbf{Ax} + \mathbf{Bu} + \mathbf{Gw}$$

where $x_1 = z_u - z_0$ = tire deflection

$x_2 = \dot{z}_u$ = unsprung mass velocity

$x_3 = z_s - z_u$ = suspension stroke

$x_4 = \dot{z}_s$ = sprung mass velocity

Four state variables such as tire deflection, unsprung mass velocity, suspension stroke, and sprung mass velocity are defined as shown in Equation (4.26). In this calculation, since the active suspension control force is not considered, the equations represent the vertical motion with a passive suspension. In addition, tire damping is small relative to suspension damping and can be neglected. The ground velocity input ($w(t) = \dot{z}_0(t)$) is assumed to be zero-mean Gaussian with a variance of $2\pi n_0 \sqrt{Gv}$, where G is the roughness constant, v is the vehicle velocity, and n_0 is 0.15708 [Turkay and Akcay, 2005].

	Parameters	Value	Units	Value	Units
Sprung mass	m_s	340	kg	750/g	slug
Unsprung mass	m_u	34	kg	75/g	slug
Suspension damping	c_s	1.9	kN-s/m	10.6	lb-s/in
Suspension stiffness	k_s	22	kN/m	125	lb/in
Unsprung stiffness	k_u	176	kN/m	1000	lb/in
Sprung mass frequency	$w_s = \sqrt{\frac{k_s k_u}{m_s (k_s + k_u)}}$	7.6	rad/s	1.2	Hz
Wheel hop frequency	$w_u = \sqrt{\frac{k_s + k_u}{m_u}}$	76.3	rad/s	12.2	Hz
Damping ratio	$\zeta_s = \frac{c_s}{2m_s w_s}$	0.35			

Table 4-2: Vehicle system parameters for the quarter-vehicle model

Table 4-2 shows vehicle system parameters for simulation purpose. The natural frequency for most cars is on the order of 1 to 1.5 Hz range. For the sports car, handling is important than ride comfort of a vehicle. Therefore, natural frequency becomes up to 2 or 2.5 Hz as a result of a stiff suspension[Gillespie,1992].

The following three transfer functions such as tire deflection, suspension stroke, and sprung mass acceleration are of interest. In order to obtain these transfer functions, it is necessary to determine the output of state-space related to transfer functions:

$$\begin{aligned}
 \begin{bmatrix} y_1 \\ y_2 \\ y_3 \end{bmatrix} &= \begin{bmatrix} 1 & 0 & 0 & 0 \\ 0 & 0 & 1 & 0 \\ 0 & \frac{c_s}{m_s} & -\frac{k_s}{m_s} & -\frac{c_s}{m_s} \end{bmatrix} \begin{bmatrix} z_u - z_0 \\ \dot{z}_u \\ z_s - z_u \\ \dot{z}_s \end{bmatrix} + D\dot{z}_0 \\
 \mathbf{y} &= \mathbf{C} \mathbf{x} + D\mathbf{w}
 \end{aligned} \tag{4.27}$$

where D is 0, y_1 is the output of tire deflection, y_2 is the output of suspension stroke, and y_3 is the output of sprung mass acceleration, which is derived by [Sun, Zhang et al.,2002]:

$$y_3 = \ddot{z}_s = \dot{x}_4 = \frac{c_s}{m_s} x_2 - \frac{k_s}{m_s} x_3 - \frac{c_s}{m_s} x_4 \quad (4.28)$$

(1) Tire deflection (a measure of road holding and handling)

The road holding performance of a vehicle can be characterized in terms of its cornering, braking, and traction abilities. Generally, a suspension system keeps the tire in firm contact with the road (i.e., good road holding) under cornering and braking. Minimizing the variations in dynamic contact forces leads to improving cornering, braking, and traction. This is due to the fact that the lateral and longitudinal forces generated by a tire depend directly on the dynamic contact force. Since a tire roughly behaves like a spring in response to vertical forces, variations in dynamic contact forces can be directly related to vertical tire deflection ($z_u - z_0$). The dynamic contact force performance can therefore be quantified in terms of tire deflection multiplied by tire stiffness [Williams,1997]. The transfer function, which is the ratio of vertical tire deflection to the road input velocity, can be expressed by:

$$H_T(s) = \frac{z_u(s) - z_0(s)}{\dot{z}_0(s)} \quad (4.29)$$

where the tire deflection is the output of state-space.

(2) Suspension stroke (a measure of the rattle space requirement)

The rattle space requirement is kept small and is related to the power dissipated in the suspension. The suspension stroke can be quantified in terms of the suspension deflection ($z_s - z_u$). The transfer function, which is the ratio of suspension deflection to the road velocity input, is given by [Williams,1997]:

$$H_s(s) = \frac{z_s(s) - z_u(s)}{\dot{z}_0(s)} \quad (4.30)$$

(3) Sprung mass acceleration (a measure of ride comfort)

The ride comfort can be quantified by the vertical acceleration of a vehicle body. A well-designed suspension system isolates the sprung mass from road disturbances by reducing the vibratory forces transferred from the axle to the vehicle body, resulting in a smooth ride. This leads to reduced sprung mass acceleration. The transfer function, which is the ratio of sprung mass acceleration to the road velocity input, can be represented by the equation as follows [Williams,1997]:

$$H_A(s) = \frac{\ddot{z}_s(s)}{\dot{z}_0(s)} \quad (4.31)$$

Based on Table 4-2, the response of vehicle motion to random velocity input $w(t)$ is simulated as shown in Figure 4-11.

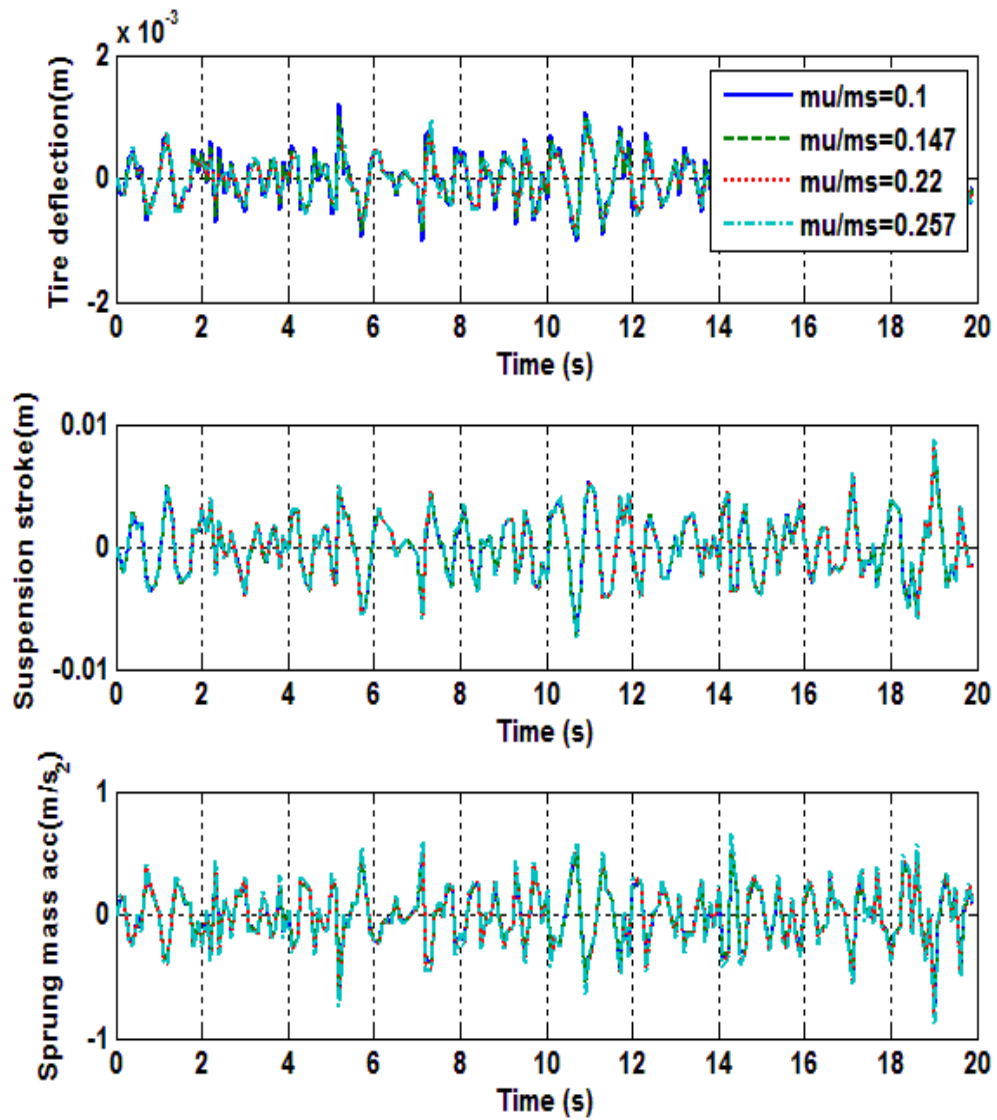


Figure 4-11: Effect of an increased unsprung mass on tire deflection, suspension stroke, and sprung mass acceleration versus time

The time response shows that the tire deflection, suspension stroke, and sprung mass acceleration increase slightly. However, the more useful plots are the frequency responses, below:

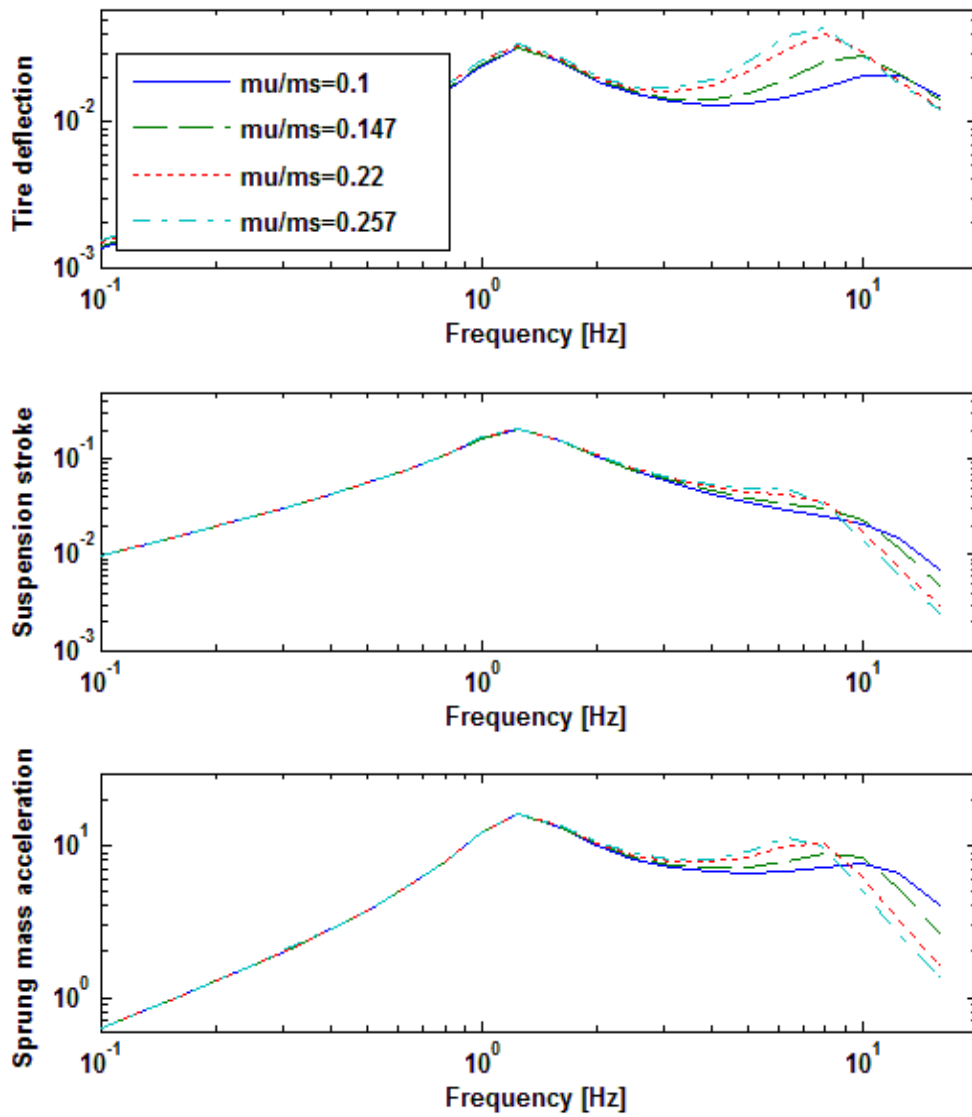


Figure 4-12: Frequency response of dynamic contact force, suspension stroke, and sprung mass acceleration with four different unsprung-to-sprung mass ratios under a random average (asphalt) road input and constant velocity 13.2 m/s

Figure 4-12 shows the frequency response of four different unsprung-to-sprung mass ratios under random, average (asphalt) road conditions and constant velocity of 13.2 m/s. The ratio of unsprung-to-sprung mass 0.147 corresponds to 50 kg (110 lb, 16 hp). The unsprung-to-sprung ratios 0.22 and 0.257 correspond to 75 kg (165 lb, 32 hp) and 87 kg (193 lb, 40 hp), respectively. The dynamic contact force, suspension stroke, and sprung mass acceleration are quantified as output of the analysis.

The dynamic contact force is related to the dynamic wheel load (road holding capability). Below the natural frequency of the sprung mass (1 Hz) and as the ratio of the unsprung-to-sprung mass increases (i.e., 0.1, 0.147, 0.22 and 0.27), it has little effect on dynamic contact force, suspension stroke, and unsprung mass acceleration. However, between the natural frequencies of the sprung mass (suspension mode) and the wheel hop frequency (wheel hop mode), the increased unsprung-to-sprung ratio increases the dynamic contact force, suspension stroke, and unsprung mass acceleration. After the wheel hop frequency (around 7 Hz ~ 12Hz), suspension stroke and unsprung mass acceleration decrease slightly, while it has an insignificant effect on the dynamic contact force.

Random vibration can be represented by a power spectral density (PSD) in the frequency domain. The PSD of input $S_g(f)$ to the vehicle system results in a PSD of output $S_v(f)$ through the square of the transfer function $|H(f)|$ for a linear system as follows:

$$S_v(f) = |H(f)|^2 S_g(f) \quad (4.32)$$

For instance, the unit of acceleration PSD is metric unit $\left(\text{m/s}^2\right)^2/\text{Hz}$ or g^2/Hz .

According to the statistical characteristic of random road excitation, the PSD of velocity input in the frequency domain is given by [Huang, Yu et al.,2010]:

$$S_g(w) = S_{\dot{x}_g}(f) = 4\pi^2 G p_0^2 v, [(m/s)^2 / \text{Hz}] \quad (4.33)$$

where G = road roughness

p_0 = reference spatial frequency(0.1)

v = vehicle forward velocity

f = corresponding time-domain frequency

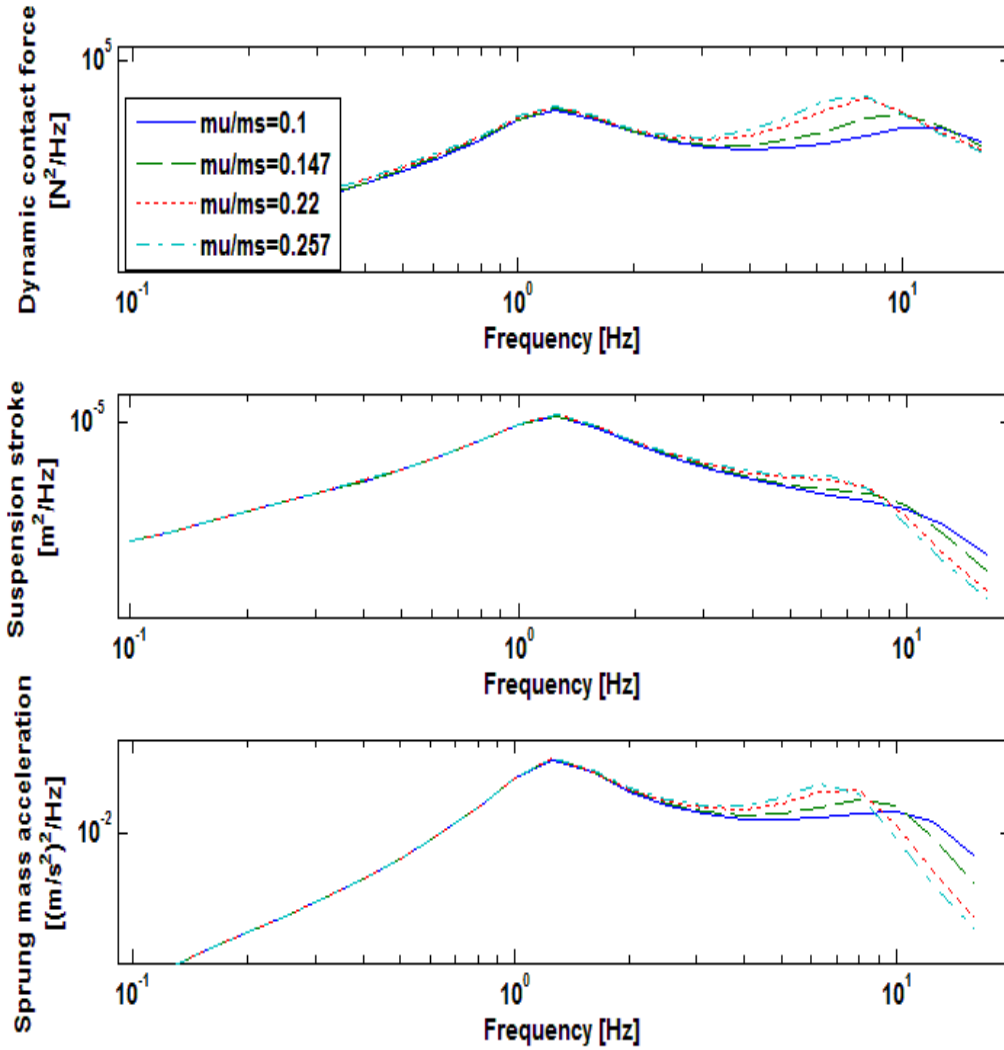


Figure 4-13: PSD of dynamic contact force, suspension stroke, and sprung mass acceleration with four different unsprung-to-sprung mass ratios under a random average (asphalt) road input and constant velocity 13.2 m/s

Figure 4-13 shows the PSDs of three criteria based on Equation (4.32). The PSDs show the distribution of energy across the frequency spectrum. The root mean square (RMS) acceleration can be obtained from the integral of the PSD over a frequency band.

The International Standard 2631-1 [ISO,1997] states that the human body's reaction to vibration is strongly directional and frequency dependent; motion sickness occurs in the frequency range 0.1 ~ 0.5 Hz, and whole-body resonance occurs when vibration falls within the critical range between 4 ~ 8 Hz. Therefore, the frequency-weighted RMS acceleration will be applied by weighting and one-third octave band data over the range of the frequency [Paddan and Griffin,2002; Paddan and Griffin,2002] (see Ch. 2 – Ride Comfort section). Since human beings are more sensitive to vibrations in the vertical direction, the emphasis is on the vertical direction in this research. In addition, road excitations ranging up to 20 Hz are directly transmitted to the passenger [Rojas, Niederkofler et al.,2010]. Figure 4-13 shows the PSD of three criteria based on Equation (4.32). The PSD shows the distribution energy across the frequency spectrum. The RMS acceleration can be obtained from the integral of the PSD over a frequency band.

4.2.1.1 Handling Performance Maps (Dynamic Contact Force)

Dynamic contact force is a measure of a vehicle's handling capability. It can be obtained by multiplying tire stiffness with tire deflection, which is a measure of road holding and handling. Figure 4-14 (a) shows the performance map of dynamic contact force output as a function of unsprung mass ratio and frequency for seven different speeds ranging from 4.4 m/s (10 mph) to 30.8 m/s (70 mph). This figure is derived from Equation (4.29) multiplied by tire stiffness and velocity input $2\pi n_0 \sqrt{Gv}$. Thus, the equation of dynamic contact force becomes as follows:

$$F_{def} = k_t H_T(s) \dot{z}_0(s) = k_t H_T(s) 2\pi n_0 \sqrt{Gv} \quad (4.34)$$

The results of the z-axis (dynamic contact force) and y-axis (unsprung ratio) in Figure 4-14 (a) are shown in Figure 4-14 (b).

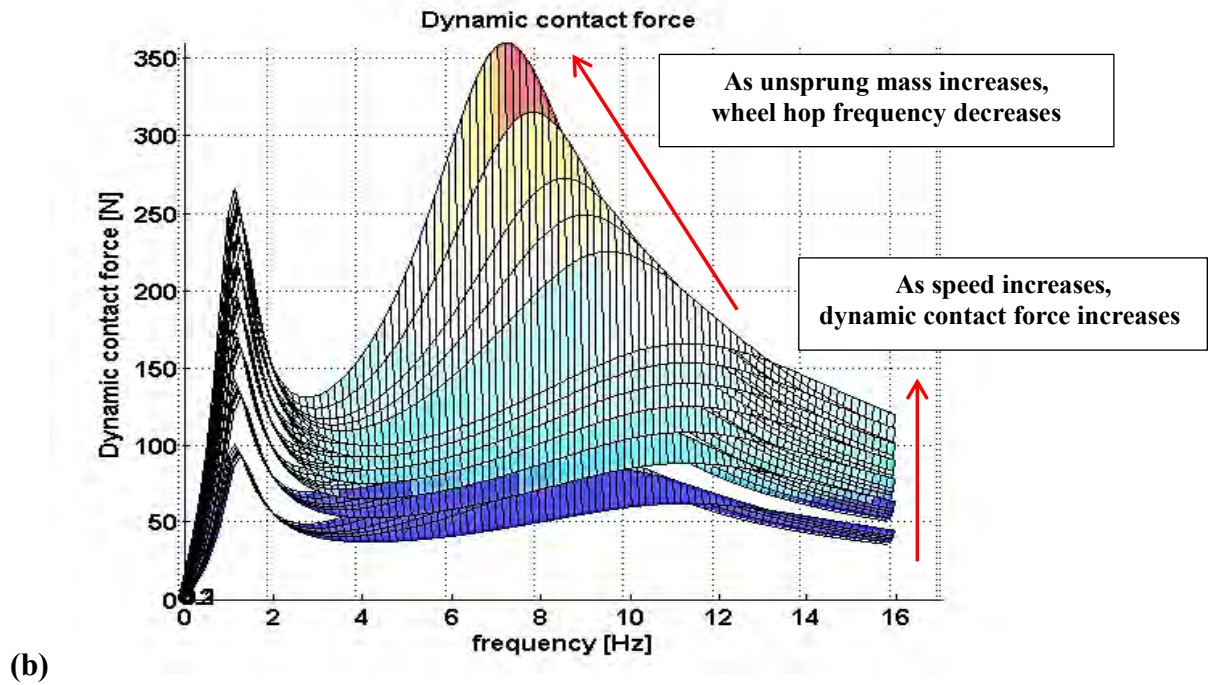
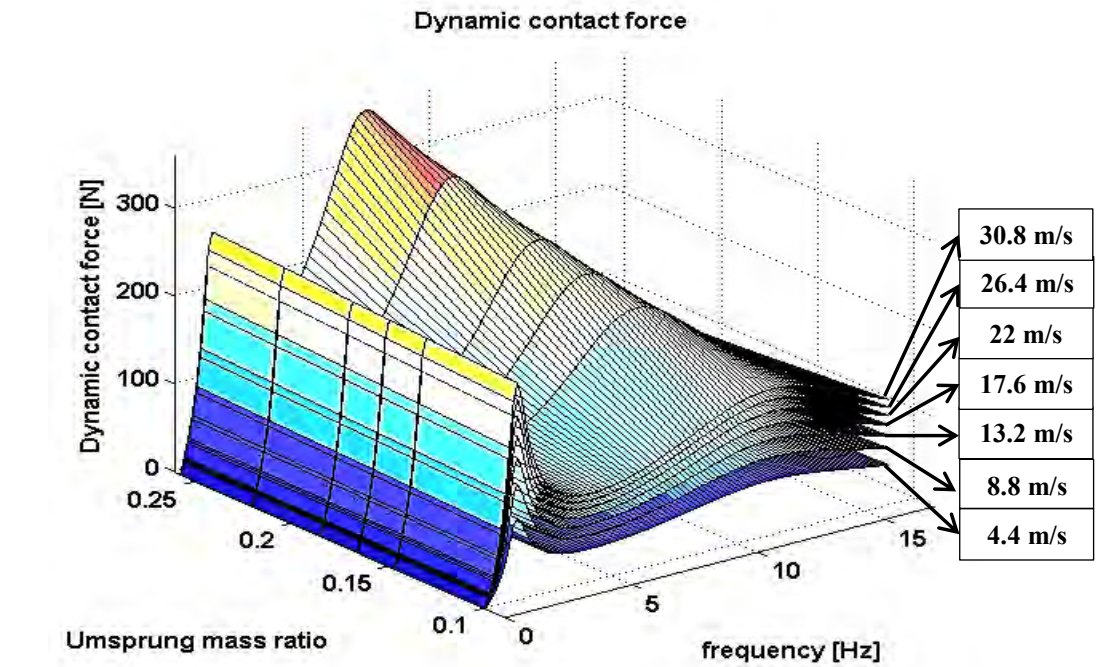


Figure 4-14: Dynamic contact force with six different unsprung-to-sprung mass ratios under a random average (asphalt) road input, as a speed increases from 4.4 m/s to 30.8 m/s

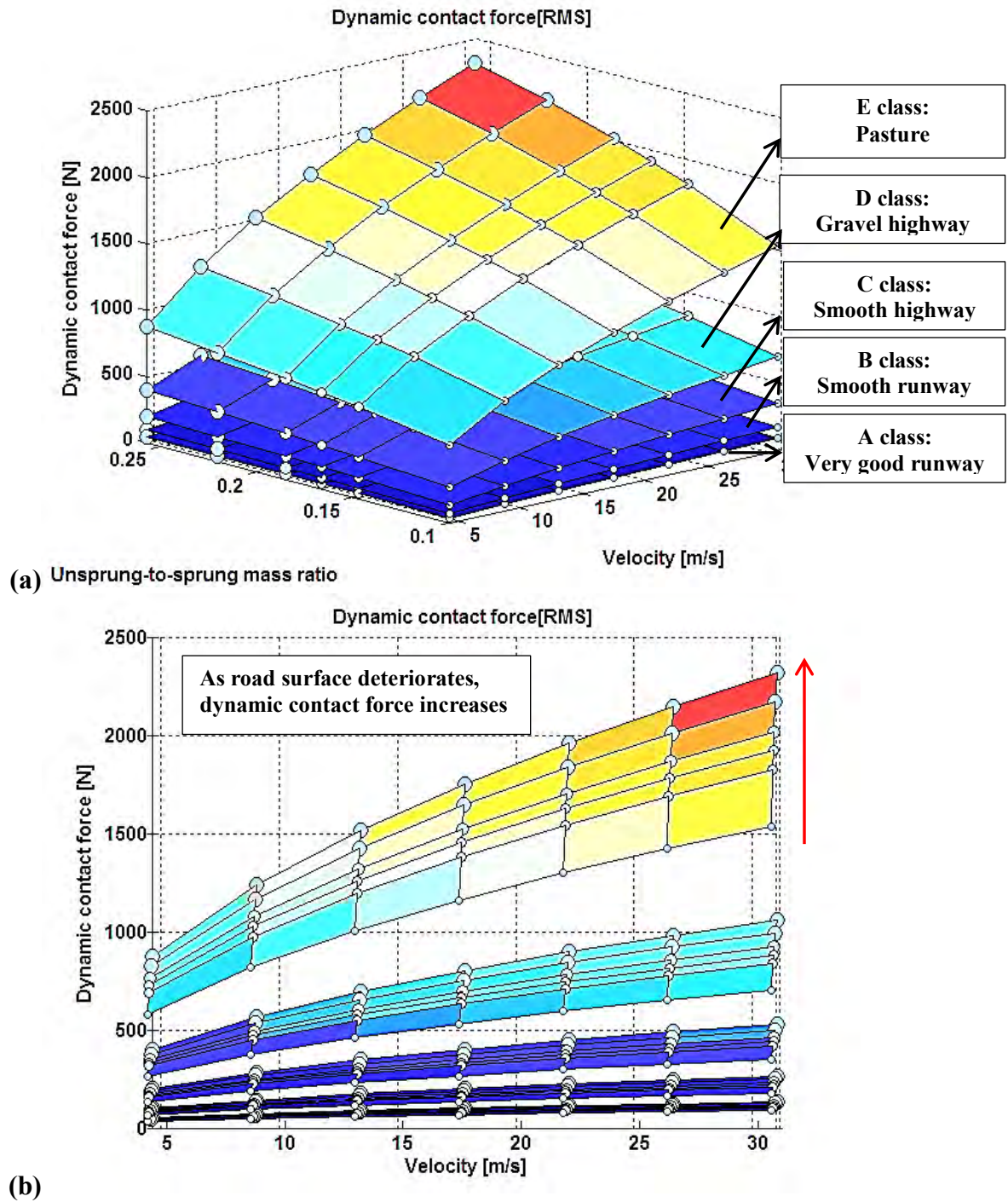


Figure 4-15: Handling performance map (dynamic contact force) with respect to six different unsprung-to-sprung mass ratios and velocity in terms of five classes of road surfaces

As the ratio of the sprung mass to the unsprung mass increases (i.e., 0.1, 0.147, 0.166, 0.185, 0.22, and 0.27), the second natural frequency which is the wheel hop frequency decreases. That is, when the ratio is 0.27 (i.e., unsprung mass 87 kg, sprung mass 340 kg per wheel), the wheel hop frequency is around 7.5 Hz, in contrast to 11.5 Hz when using the ratio of 0.1 (i.e., unsprung mass 34 kg, sprung mass 340 kg per wheel). Moreover, as the vehicle speed increases, the dynamic contact force increases with increased unsprung mass.

The ratio of the wheel hop frequency to the natural frequency of the sprung mass is around 10. However, as the unsprung mass increases, the two frequencies could move closer together. That is, the wheel hop frequency decreases. As a result, the large oscillations can cause the tires to lose traction and lose contact with the road in the worst case[Van Schalkwyk and Kamper,2006].

Figure 4-15 (a) shows the handling performance map (dynamic contact force(RMS)) as a function of the unsprung-to-sprung mass ratios and velocity in terms of five classes of road surfaces which were presented by the International Organization for Standardization (ISO) and classified as ISO 8608:1995[Wong,2008] (see Appendix A). The road surfaces are classified as follows: A class (very good runway), B class (smooth runway), C class (smooth highway), D class (gravel highway), and E class (pasture). The dynamic contact force (RMS) in this figure is obtained from the integral of the power spectral density over the frequency band as described in Figure 4-13.

We recall that minimizing the variations in the dynamic contact force results in improving cornering, braking, and traction. This is due to the fact that the lateral and longitudinal forces generated by a tire depend directly on the dynamic contact force. Figure 4-15 (b) is obtained from Figure 4-15 (a) after looking at z axis with respect to the y-axis. It can be seen that the dynamic contact force increases rapidly as the road

roughness deteriorates with increased unsprung mass as shown in Figure 4-15 (b). On a pasture conditions, the dynamic contact force (RMS) with increased unsprung mass varies from 1600N to 2300N given a velocity of 30.8 m/s (70 mph), and it varies from 300 N to 500 N at 30.8 m/s (70 mph) on a smooth highway. We can conclude that the handling performance of a vehicle worsens as the severity of the road increases. This [Vos, Besselink et al.,2010] paper also indicates the same results: the Belgian blocks is similar to the gravel highway in this research. They obtained the dynamic contact force (RMS) of approximately 750 ~ 900 N at the given 13.2 m/s velocity by simulating and conducting an experiment. Their result is similar to our result of 500 N, given 13.2 m/s and a gravel highway. The difference between the results is due to different vehicle parameters and road roughness (see Appendix A). To achieve the best road-holding performance (i.e., keep the tire in firm contact with the road), the suspension system should be designed to minimize the variation in dynamic contact forces under rough road conditions[Vos, Besselink et al.,2010].

4.2.1.2 Suspension Stroke Performance Maps (Suspension Stroke)

The suspension stroke is a measure of the rattle space requirement, which is relative displacement between the sprung mass (i.e., vehicle body) and unsprung mass (i.e., MDW). The suspension stroke output can be quantified in terms of the suspension deflection ($z_s - z_u$) multiplied by the velocity input of $2\pi n_0 \sqrt{Gv}$.

$$y_2 = H_S(s) \dot{z}_0(s) = H_S(s) 2\pi n_0 \sqrt{Gv} \quad (4.35)$$

Figure 4-16 shows the performance map of the suspension stroke output as a function of the unsprung-to-sprung mass ratios and frequency in terms of seven different speeds from 4.4 m/s (10 mph) to 30.8 m/s (70 mph).

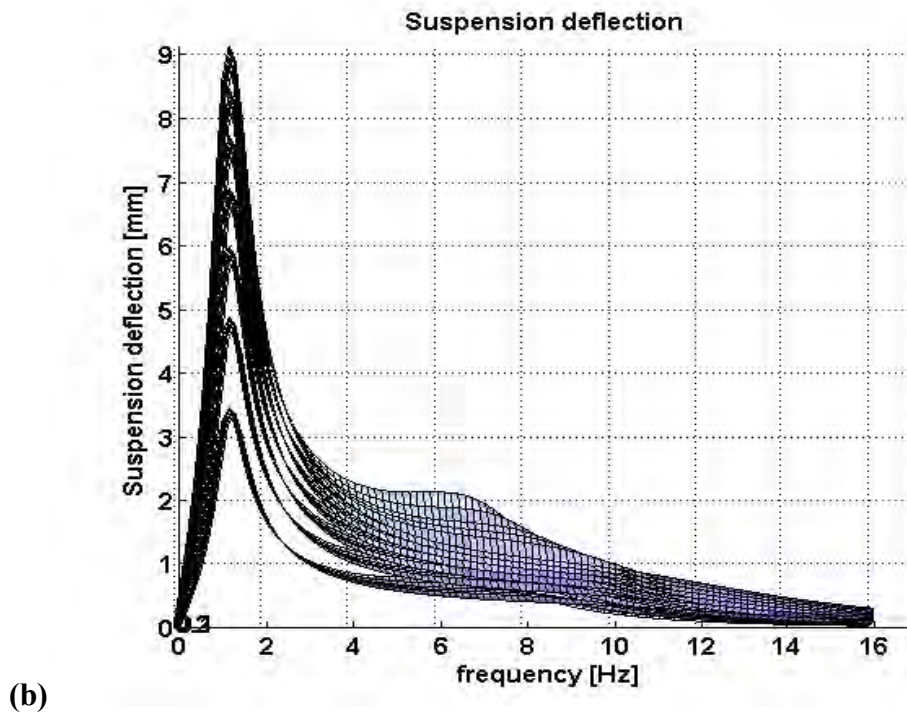
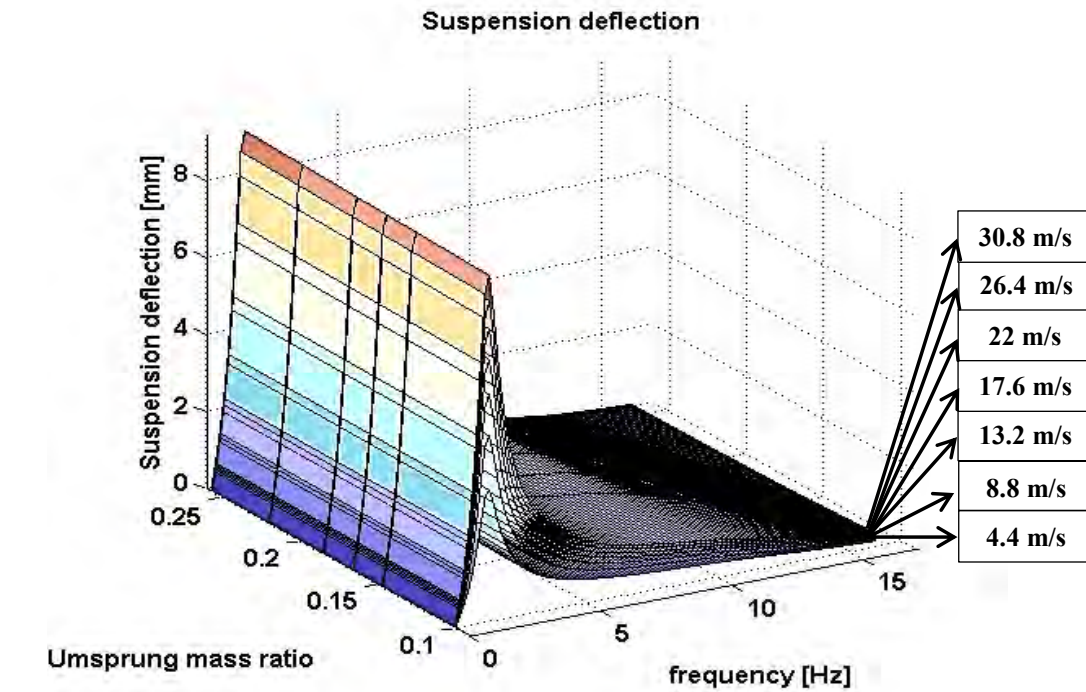


Figure 4-16: Suspension stroke with six different unsprung-to-sprung mass ratios under a random average (asphalt) road input, as a speed increases from 4.4 m/s to 30.8 m/s

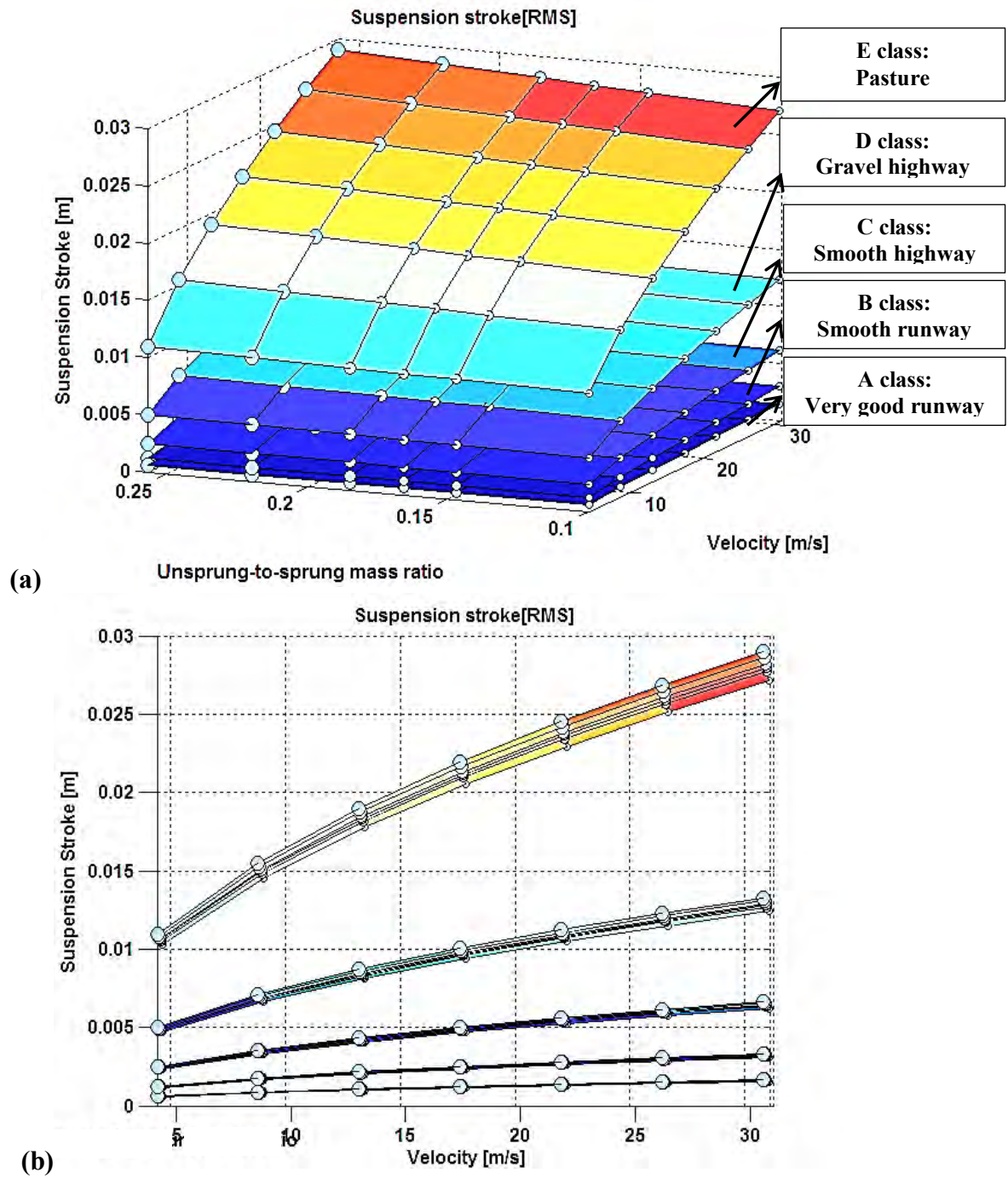


Figure 4-17: Suspension stroke performance map with respect to six different unsprung-to-sprung mass ratios and velocity in terms of five classes of road surfaces

This figure is derived from Equation (4.35). Then, we take the z-axis (suspension stroke) and y-axis (unsprung-to-sprung mass ratios) shown in Figure 4-15 (a) and plot them in Figure 4-16 (b). Increasing the ratio of the sprung mass to the unsprung mass has little effect on suspension stroke, compared to the dynamic contact force, as shown in Figure 4-14.

Figure 4-17 (a) shows the suspension stroke (RMS) performance map as a function of the unsprung-to-sprung mass ratios and velocity for five classes of road surfaces which were presented by the International Organization for Standardization (ISO) and classified as ISO 8608:1995[Wong,2008] (see Appendix A). Similarly, the suspension stroke (RMS) in this figure is obtained from the integral of the power spectral density over a frequency band as described in Figure 4-13. Figure 4-17 (b) is obtained from Figure 4-17 (a) by plotting the z-axis with respect to the y-axis. It can be seen that the suspension stroke increases, as the road surface deteriorates. However, the increased unsprung mass has little effect on suspension stroke as shown in Figure 4-17 (b). When driving on pastures, the suspension stroke (RMS) varies from 0.01 m to 0.028 m, whereas the variation is less on smooth runways and highways.

Previous research [Vos, Besselink et al.,2010] also indicates the same results: driving on Belgian blocks is similar to driving on the gravel highway used in this research. They obtained a suspension stroke (RMS) of 0.01 ~ 0.012 m at the given 13.2 m/s velocity. Their result compares to our result of 0.008 m, given 13.2 m/s and a gravel highway. The difference between the results is due to different vehicle parameters and road roughness (see Appendix A).

4.2.1.3 Ride Comfort Performance Maps (Sprung Mass Acceleration)

The sprung mass acceleration is a measure of how comfortable a car ride feels. The ride comfort can be quantified by the vertical acceleration of a vehicle body. Figure 4-17 (a) shows the performance map of the sprung mass acceleration output as a function of the unsprung mass ratio and frequency with seven different speeds from 4.4 m/s (10 mph) to 30.8 m/s (70 mph). This figure is derived from the Equation (4.31) multiplied by the velocity input $2\pi n_0 \sqrt{Gv}$. Thus, the equation of sprung mass acceleration becomes:

$$y_3 = H_A(s) \dot{z}_0(s) = H_A(s) 2\pi n_0 \sqrt{Gv} \quad (4.36)$$

As the ratio of the unsprung mass to the sprung mass increases, the second natural frequency, the wheel hop frequency, decreases. Also, as vehicle speed increases, the sprung mass acceleration increases with increased unsprung mass.

Figure 4-19 (a) shows the ride comfort performance map (frequency-weighted RMS sprung acceleration) as a function of the unsprung-to-sprung mass ratios and velocity for five classes of road surfaces which were presented by the International Organization for Standardization (ISO) and classified into ISO 8608:1995[Wong,2008] (see Appendix A). The frequency-weighted RMS sprung acceleration of this figure is obtained from the integral of the power spectral density over a frequency band as described in Figure 4-13.

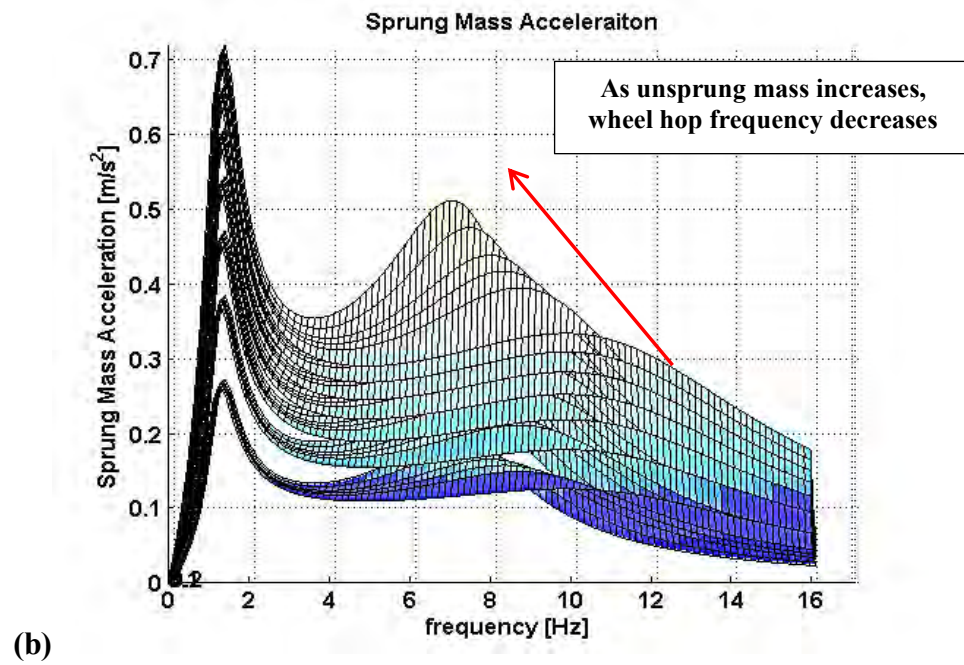
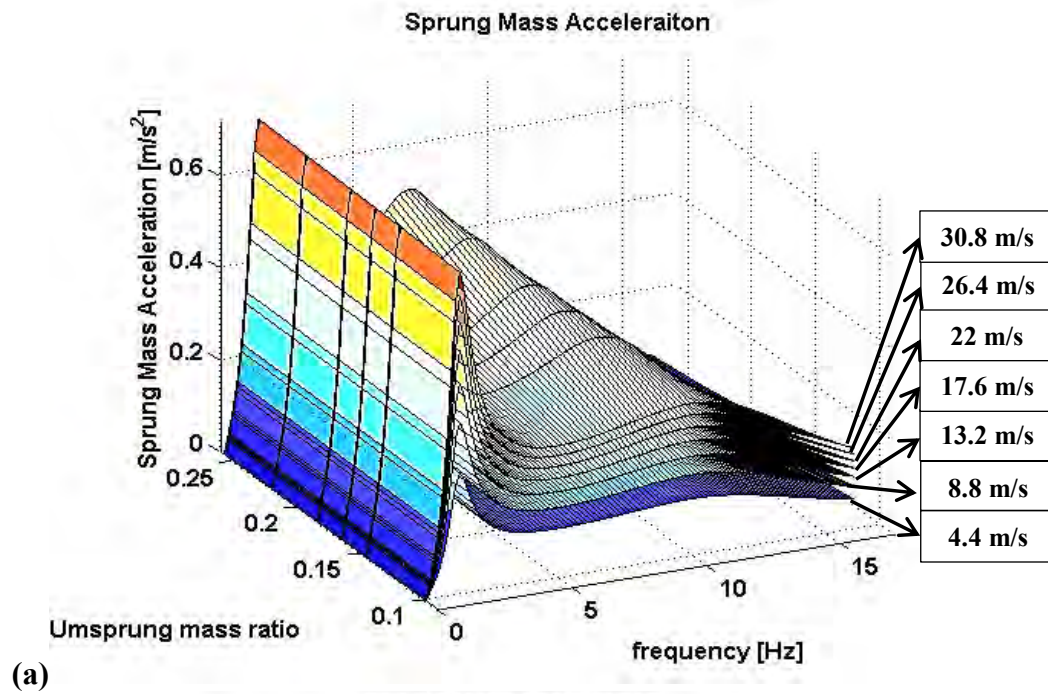


Figure 4-18: Sprung mass acceleration with six different unsprung-to-sprung mass ratios under a random average (asphalt) road input, as speed increases from 4.4 m/s to 30.8 m/s

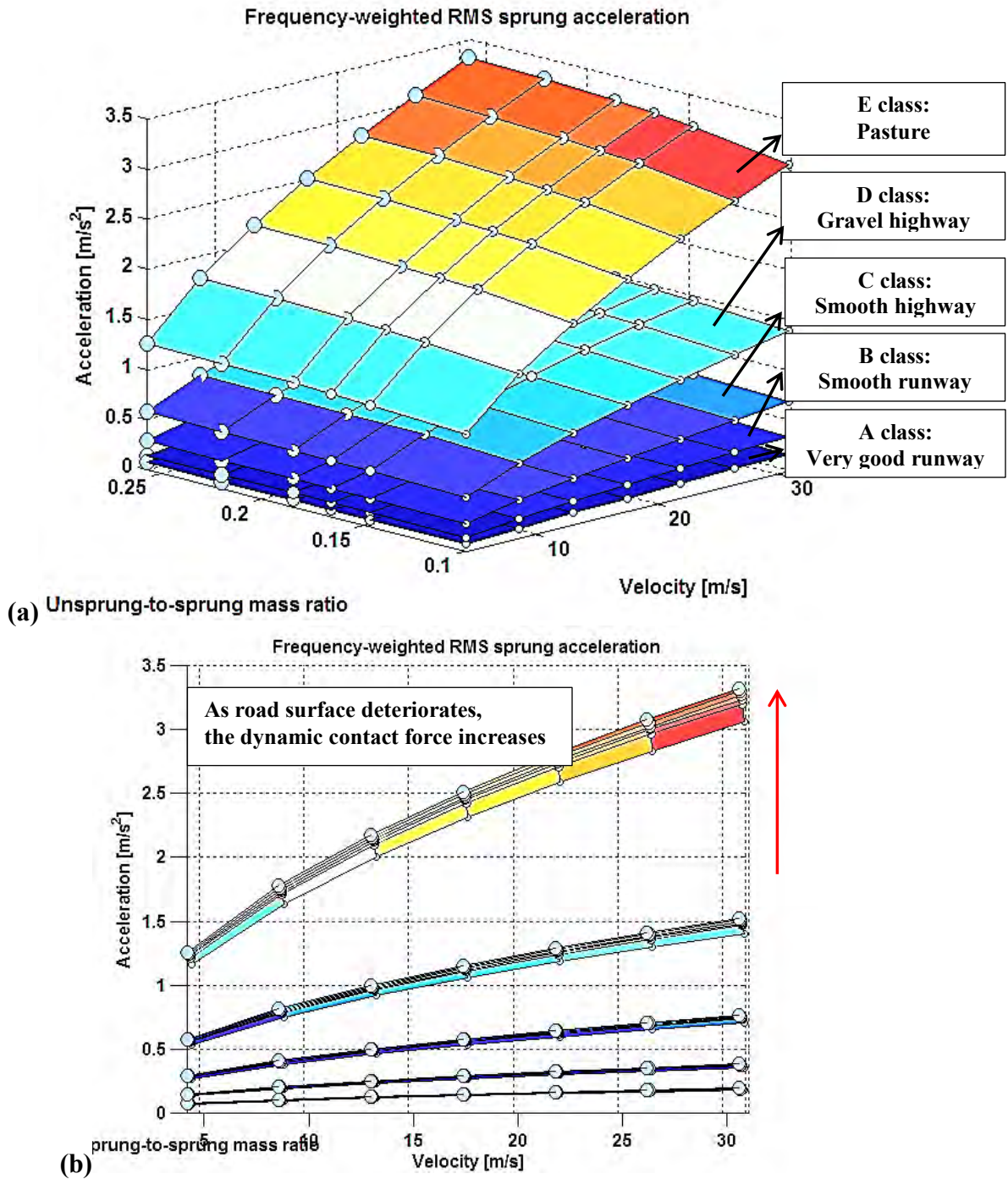


Figure 4-19: Ride comfort performance map (frequency weighted RMS sprung acceleration) with respect to six different unsprung-to-sprung mass ratios and velocity in terms of 5 classes of road surfaces

Figure 4-19 (b) is obtained from Figure 4-19 (a) by plotting the z-axis with respect to the y-axis. It can be seen that the frequency-weighted RMS sprung acceleration increases rapidly, as the road surface deteriorates with increased unsprung mass as shown in Figure 4-19 (b). On a pasture, the frequency-weighted RMS sprung acceleration with increased unsprung mass varies from 3 m/s^2 to 3.3 m/s^2 for a given 30.8 m/s (70 mph) velocity, while it is approximately 0.7 m/s^2 , given 30.8 m/s (70 mph) on a smooth highway.

Previous research [Vos, Besselink et al.,2010] shows similar results: driving on Belgian blocks is similar to driving on the gravel highway used in this research. They obtained the frequency-weighted RMS sprung acceleration of approximately $1.1 \sim 1.3 \text{ m/s}^2$ for a given 13.2 m/s velocity. Their result is similar to ours: 1 m/s^2 for a given 13.2 m/s on a gravel highway. The difference between results is due to different vehicle parameters and road roughness (see Appendix A).

This map can be used to determine ride comfort. On smooth highways, the level of comfort is acceptable, but it is uncomfortable on gravel highways and pasture. This is due to the fact that the range between 0.8 and 1.6 indicates uncomfortable as shown in Chapter 2 (see Ride Comfort section).

4.2.2 Half-Vehicle (4 DOF) Ride Model

A half-vehicle ride model accounts for both pitch and heave motions, in contrast to a quarter-vehicle ride model. As a result, it has four DOF including front / rear wheels (unsprung mass). This model can be used for simulating the ride characteristics of an whole vehicle[Cao, Liu et al.,2007; Cao, Liu et al.,2008]

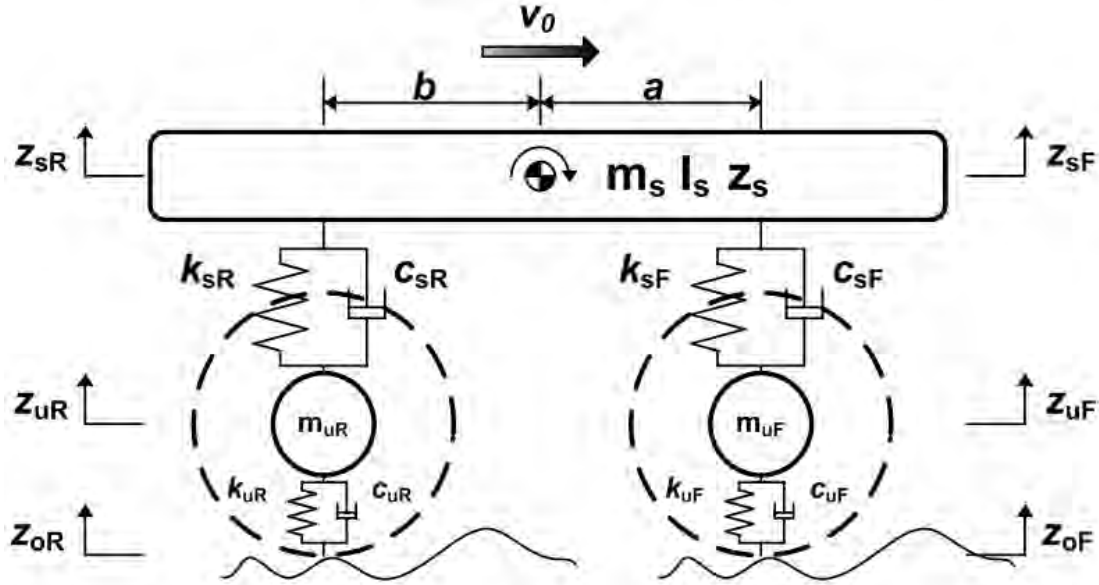


Figure 4-20: Half-vehicle model

Figure 4-20 shows the half-vehicle model. The z_{ij} is the vertical displacement. The subscript $i = s, u, o$ indicates sprung mass, unsprung mass, and road input, while $j = F, R$ represents front and rear wheel. The v_0 is constant forward velocity.

As can be seen in Figure 4-21, the total vertical forces acting on the sprung mass in the z -direction are given by:

$$\sum F_s = m_s \ddot{z}_s; \quad F_{sF} + F_{sR} = m_s \ddot{z}_s \quad (4.37)$$

where

$$F_{sF} = c_{sF} (\dot{z}_{uF} - \dot{z}_{sF}) + k_{sF} (z_{uF} - z_{sF})$$

$$F_{sR} = c_{sR} (\dot{z}_{uR} - \dot{z}_{sR}) + k_{sR} (z_{uR} - z_{sR})$$

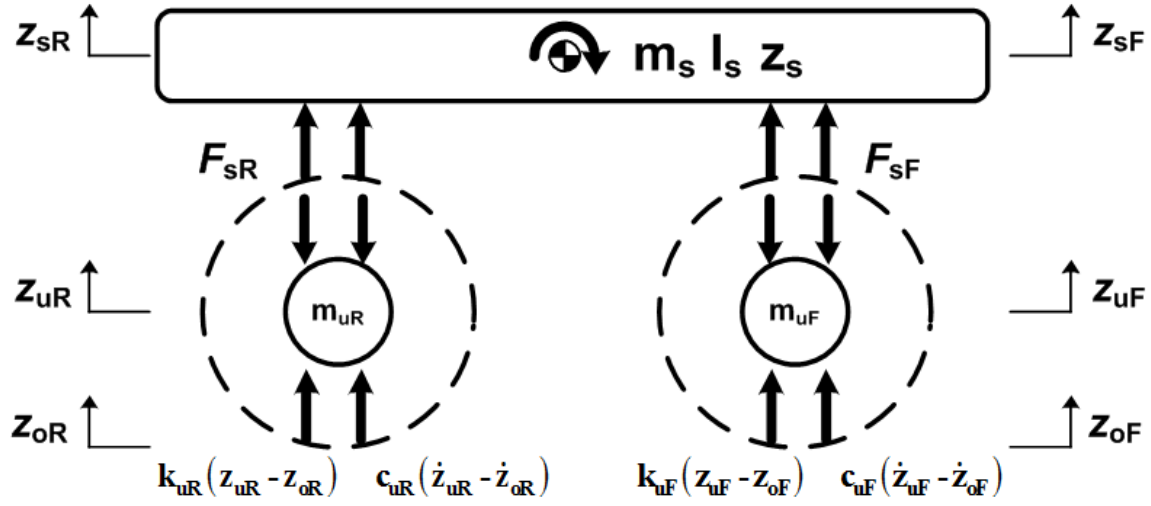


Figure 4-21: Free body diagram

F_{sF} and F_{sR} are the suspension forces at the front and rear wheels, respectively. The c_{ij} and k_{ij} indicates the stiffness and damping. The subscript $i = s, u$ indicates suspension and unsprung mass, while $j = F, R$ represents front and rear suspension stiffness and damping. When the vehicle body (sprung mass) moves up and down, it is subjected to the reaction force caused by the suspension forces (springs and shock absorbers).

The sum of the vertical forces of the front and rear wheels (unsprung masses) is given by:

$$\sum F_{uF} = m_{uF} \ddot{z}_{uF};$$

$$-c_{sF}(\dot{z}_{uF} - \dot{z}_{sF}) - k_{sF}(z_{uF} - z_{sF}) + c_{uF}(\dot{z}_{uF} - \dot{z}_{oF}) + k_{uF}(z_{uF} - z_{oF}) = m_{uF} \ddot{z}_{uF} \quad (4.38)$$

$$\sum F_{uR} = m_{uR} \ddot{z}_{uR};$$

$$-c_{sR}(\dot{z}_{uR} - \dot{z}_{sR}) - k_{sR}(z_{uR} - z_{sR}) + c_{uR}(\dot{z}_{uR} - \dot{z}_{oR}) + k_{uR}(z_{uR} - z_{oR}) = m_{uR} \ddot{z}_{uR}$$

where c_{sF} = front suspension damping

c_{sR} = rear suspension damping

k_{sF} = front suspension stiffness

k_{sR} = rear suspension stiffness

c_{uF} = front tire damping associated with unsprung mass
 c_{uR} = rear tire damping associated with unsprung mass
 k_{uF} = front tire stiffness associated with unsprung mass
 k_{uR} = rear tire stiffness associated with unsprung mass
 z_{uF} = displacement of front unsprung mass
 z_{uR} = displacement of rear unsprung mass
 \dot{z}_{uF} = velocity of front unsprung mass
 \dot{z}_{uR} = velocity of rear unsprung mass
 \ddot{z}_{uF} = acceleration of front unsprung mass
 \ddot{z}_{uR} = acceleration of rear unsprung mass
 z_{oF} = front road input
 z_{oR} = rear road input
 m_{uF} = front unsprung mass
 m_{uR} = rear unsprung mass

The total pitch moment around the y-axis acting on the half-vehicle is given by:

$$\sum M_s = I_s \ddot{\theta}_s; \quad F_{sR}b - F_{sF}a = I_s \ddot{\theta}_s \quad (4.39)$$

where a = distance from front axle to the CG

b = distance from rear axle to the CG

m_s = sprung mass

I_s = sprung moment of inertia

When the vehicle body pitches, it is influenced by the reaction force of the suspension forces. These reaction forces create the pitching moment to the vehicle body around its body center. In summary, the four equations of motion are given by [Soliman, Moustafa et al., 2008]:

$$\begin{aligned}
 m_s \ddot{z}_s &= c_{sF} (\dot{z}_{uF} - \dot{z}_{sF}) + k_{sF} (z_{uF} - z_{sF}) + c_{sR} (\dot{z}_{uR} - \dot{z}_{sR}) + k_{sR} (z_{uR} - z_{sR}) \\
 m_{uF} \ddot{z}_{uF} &= -c_{sF} (\dot{z}_{uF} - \dot{z}_{sF}) - k_{sF} (z_{uF} - z_{sF}) + c_{uF} (\dot{z}_{uF} - \dot{z}_{oF}) + k_{uF} (z_{uF} - z_{oF}) \\
 m_{uR} \ddot{z}_{uR} &= -c_{sR} (\dot{z}_{uR} - \dot{z}_{sR}) - k_{sR} (z_{uR} - z_{sR}) + c_{uR} (\dot{z}_{uR} - \dot{z}_{oR}) + k_{uR} (z_{uR} - z_{oR}) \\
 I_s \ddot{\theta}_s &= (c_{sR} (\dot{z}_{uR} - \dot{z}_{sR}) + k_{sR} (z_{uR} - z_{sR}))b - (c_{sF} (\dot{z}_{uF} - \dot{z}_{sF}) + k_{sF} (z_{uF} - z_{sF}))a
 \end{aligned} \quad (4.40)$$

4.2.3 Full-Vehicle (7 DOF) Ride Model

The full-vehicle ride model consists of four unsprung masses connected to a sprung mass by a vertical spring-damper system. The sprung mass has three motions such as roll, pitch, and bounce motion. The four unsprung masses have four vertical motions. As a result, this leads to full-vehicle (7DOF) ride model as shown in Figure 4-22 [Setiawan, Safarudin et al.,2009].

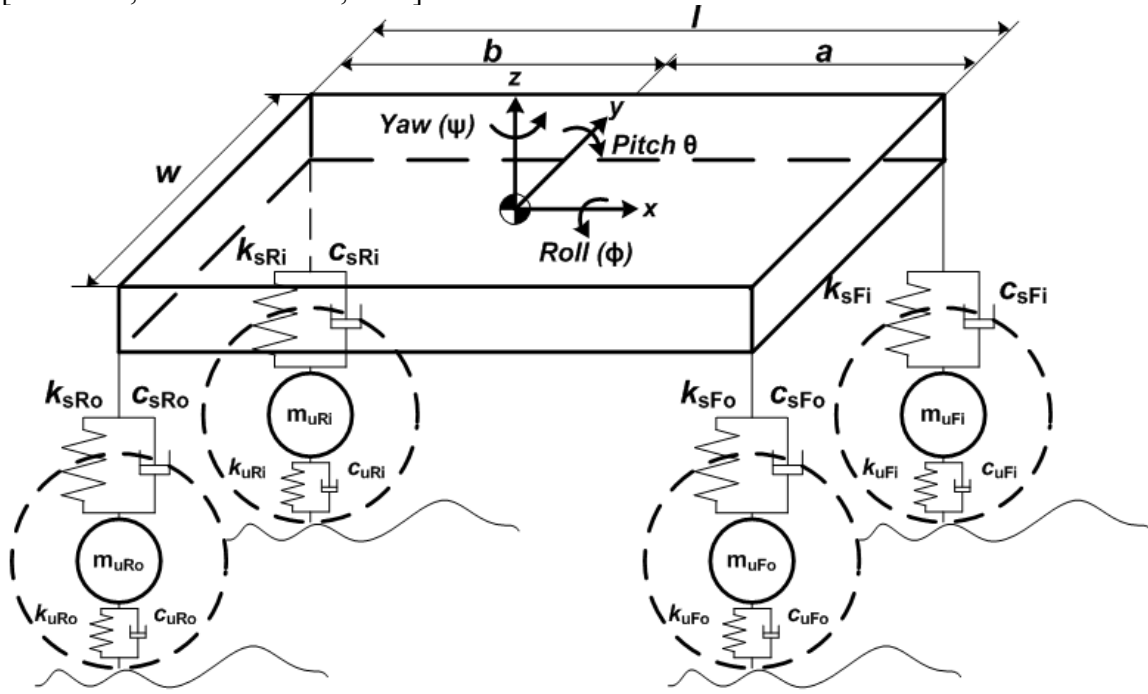


Figure 4-22: Full-vehicle model

To find out the equation of motion, we need the free body diagram. Figure 4-23 shows all forces acting on sprung and unsprung mass.

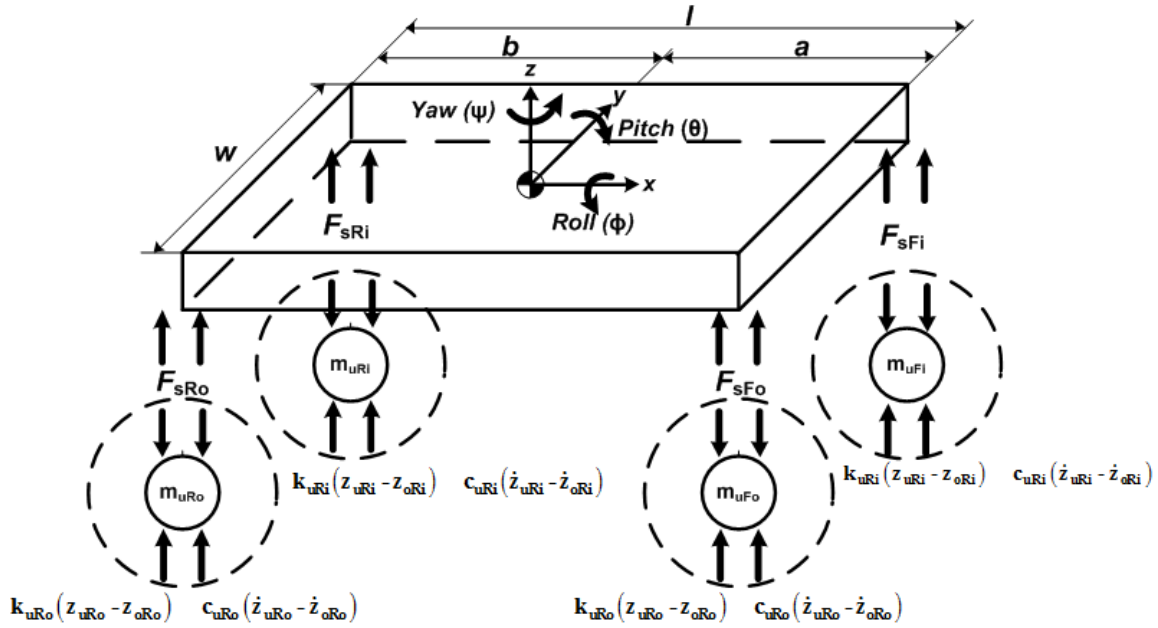


Figure 4-23: Free body diagram

With the free body diagram as above, the total vertical forces acting on the sprung mass in the z-direction are given by [Hudha, Kadir et al.,2009]:

$$\sum F_s = m_s \ddot{z}_s; \quad \left(\begin{matrix} F_{sFi} + F_{sFo} + F_{sRi} + F_{sRo} + \\ F_{aFi} + F_{aFo} + F_{aRi} + F_{aRo} \end{matrix} \right) = m_s \ddot{z}_s \quad (4.41)$$

where F_{sFi} = suspension force at the front-inside corner

F_{sFo} = suspension force at the front-outside corner

F_{sRi} = suspension force at the rear-inside corner

F_{sRo} = suspension force at the rear-outside corner

F_{aFi} = actuator force at the front-inside corner

F_{aFo} = actuator force at the front-outside corner

F_{aRi} = actuator force at the rear-inside corner

F_{aRo} = actuator force at the rear-outside corner

m_s = sprung mass

\ddot{z}_s = sprung mass acceleration at body CG

In this case, assuming a left turn maneuver, the front-left wheel is the front-inside wheel, while the front-right wheel is the front-outside wheel as shown in Figure 4-23. Under emergency maneuvers, the vehicle undergoes significant roll, pitch, and yaw associated with lateral force and reduced tire contact force which is the front-inside tire for a left turn maneuver. The sensors are available for measuring the contact and lateral force in real time. [Tesar,2011, August] suggests that using active suspension actuators (i.e., fully active suspension – no damping) is to balance the need for the undisturbed vehicle motion (i.e., ride comfort) and the need for maximizing the contact forces (i.e., drivability and safety), so that reducing wasteful tire slip leads to improved operational efficiency.

The Electro-Mechanical Actuator (EMA) drives the suspension system to stabilize the vehicle even under severe maneuvers, so that the ultimate goal of the vehicle experiences no acceleration in roll, pitch, and heave motion. By doing that, the force from the unsprung mass of the suspension is not transferred to the sprung mass. Furthermore, the intelligent corner decision making (in milli-sec) can maintain balance between reduced contact force and increased contact force so that available traction force can increase in curves or rough roads by perhaps 50% [Tesar,2011, August]. In this example, assuming no actuators at the suspension system, the above equation becomes:

$$F_{sFi} + F_{sFo} + F_{sRi} + F_{sRo} = m_s \ddot{z}_s \quad (4.42)$$

The suspension force is defined as follows:

$$\begin{aligned} F_{sFi} &= c_{sF} (\dot{z}_{uFi} - \dot{z}_{sFi}) + k_{sF} (z_{uFi} - z_{sFi}) \\ F_{sFo} &= c_{sF} (\dot{z}_{uFo} - \dot{z}_{sFo}) + k_{sF} (z_{uFo} - z_{sFo}) \\ F_{sRi} &= c_{sR} (\dot{z}_{uRi} - \dot{z}_{sRi}) + k_{sR} (z_{uRi} - z_{sRi}) \\ F_{sRo} &= c_{sR} (\dot{z}_{uRo} - \dot{z}_{sRo}) + k_{sR} (z_{uRo} - z_{sRo}) \end{aligned} \quad (4.43)$$

where c_{sFi} = front-inside suspension damping
 c_{sFo} = rear-outside suspension damping
 c_{sRi} = rear-inside suspension damping
 c_{sRo} = rear-outside suspension damping
 k_{sFi} = front-inside suspension stiffness
 k_{sFo} = rear-outside suspension stiffness
 k_{sRi} = rear-inside suspension stiffness
 k_{sRo} = rear-outside suspension stiffness
 z_{uFi} = displacement of front-inside unsprung mass
 z_{uFo} = displacement of front-outside unsprung mass
 z_{uRi} = displacement of rear-inside unsprung mass
 z_{uRo} = displacement of rear-outside unsprung mass
 \dot{z}_{uFi} = velocity of front-inside unsprung mass
 \dot{z}_{uFo} = velocity of front-outside unsprung mass
 \dot{z}_{uRi} = velocity of rear-inside unsprung mass
 \dot{z}_{uRo} = velocity of rear-outside unsprung mass

c_{ijk} and k_{ijk} indicate the stiffness and damping. The subscript $i = s$ indicates suspension stiffness and damping, while the subscript $i = u$ indicates tire stiffness and damping associated with unsprung mass. Second subscript $j = F, R$ represents front and rear suspension stiffness and damping. Finally, third subscript $k = i, o$ indicates inside and outside wheel of a vehicle. At each corner, the position of sprung mass can be written in terms of bounce, pitch and roll:

$$\begin{aligned}
z_{sFi} &= z_s - a \sin \theta + \frac{1}{2} w \sin \phi \\
z_{sFo} &= z_s - a \sin \theta - \frac{1}{2} w \sin \phi \\
z_{sRi} &= z_s + a \sin \theta + \frac{1}{2} w \sin \phi \\
z_{sRo} &= z_s + a \sin \theta - \frac{1}{2} w \sin \phi
\end{aligned} \tag{4.44}$$

Assuming small angles, the above equation is as follows:

$$\begin{aligned}
 z_{sFi} &= z_s - a\theta + \frac{1}{2}w\phi \\
 z_{sFo} &= z_s - a\theta - \frac{1}{2}w\phi \\
 z_{sRi} &= z_s + a\theta + \frac{1}{2}w\phi \\
 z_{sRo} &= z_s + a\theta - \frac{1}{2}w\phi
 \end{aligned} \tag{4.45}$$

where a = distance between the front of the vehicle and CG of sprung mass

b = distance between the rear of the vehicle and CG of sprung mass

θ = pitch angle at body center of body center of gravity

ϕ = roll angle at body center of body center of gravity

Taking derivative above equation is given by the following:

$$\begin{aligned}
 \dot{z}_{sFi} &= \dot{z}_s - a\dot{\theta} + \frac{1}{2}w\dot{\phi} \\
 \dot{z}_{sFo} &= \dot{z}_s - a\dot{\theta} - \frac{1}{2}w\dot{\phi} \\
 \dot{z}_{sRi} &= \dot{z}_s + a\dot{\theta} + \frac{1}{2}w\dot{\phi} \\
 \dot{z}_{sRo} &= \dot{z}_s + a\dot{\theta} - \frac{1}{2}w\dot{\phi}
 \end{aligned} \tag{4.46}$$

When we substitute Equation (4.45) and (4.46) into (4.43), the Equation (4.42) of motion of sprung mass including the resulting Equation (4.43) is given by [Ahmad, Hudha et al.,2009; Hudha, Kadir et al.,2009]:

$$\begin{aligned}
 m_s \ddot{z}_s &= -2(k_{sF} + k_{sR})z_s - 2(c_{sF} + c_{sR})\dot{z}_s \\
 &+ 2(ak_{sF} - bk_{sR})\theta + 2(ac_{sF} - bc_{sR})\dot{\theta} \\
 &+ k_{sF}z_{uFi} + c_{sF}\dot{z}_{uFi} + k_{sF}z_{uFo} + c_{sF}\dot{z}_{uFo} \\
 &+ k_{sR}z_{uRi} + c_{sR}\dot{z}_{uRi} + k_{sR}z_{uRo} + c_{sR}\dot{z}_{uRo}
 \end{aligned} \tag{4.47}$$

Similarly, the rotational equation of motion for roll motion is given by:

$$\begin{aligned}
I_{xx}\ddot{\phi} = & -\frac{w^2}{2}(k_{sF} + k_{sR})\phi - \frac{w^2}{2}(c_{sF} + c_{sR})\dot{\phi} \\
& + \frac{w}{2}(k_{sF}z_{uFi} + c_{sF}\dot{z}_{uFi} - k_{sF}z_{uFo} - c_{sF}\dot{z}_{uFo}) \\
& + \frac{w}{2}(k_{sR}z_{uRi} + c_{sR}\dot{z}_{uRi} - k_{sR}z_{uRo} - c_{sR}\dot{z}_{uRo})
\end{aligned} \tag{4.48}$$

Finally, the rotational equation of motion for pitch motion becomes as follows:

$$\begin{aligned}
I_{yy}\ddot{\theta} = & 2(ak_{sF} - bk_{sR})z_s + 2(ac_{sF} - bc_{sR})\dot{z}_s \\
& - 2(a^2k_{sF} + b^2k_{sR})\theta - 2(a^2c_{sF} + b^2c_{sR})\dot{\theta} \\
& - a(k_{sF}z_{uFi} + c_{sF}\dot{z}_{uFi} + k_{sF}z_{uFo} + c_{sF}\dot{z}_{uFo}) \\
& + b(k_{sR}z_{uRi} + c_{sR}\dot{z}_{uRi} + k_{sR}z_{uRo} + c_{sR}\dot{z}_{uRo})
\end{aligned} \tag{4.49}$$

where $\ddot{\phi}$ = roll angular acceleration at body CG

$\ddot{\theta}$ = pitch angular acceleration at body CG

I_{xx} = moment of inertia around roll axis

I_{yy} = rmoment of inertia around pitch axis

By applying Newton's second law of motion based on Free-body diagram shown in Figure 4-23, the sum of the vertical forces of the front / rear wheel (unsprung masses) is given by:

$$\begin{aligned}
\sum F_{uFi} &= m_{uFi}\ddot{z}_{uFi}; \\
-c_{sF}(\dot{z}_{uFi} - \dot{z}_{sFi}) - k_{sF}(z_{uFi} - z_{sFi}) + c_{uF}(\dot{z}_{uFi} - \dot{z}_{0Fi}) + k_{uF}(z_{uFi} - z_{0Fi}) &= m_{uFi}\ddot{z}_{uFi} \\
\sum F_{uFo} &= m_{uFi}\ddot{z}_{uFo}; \\
-c_{sF}(\dot{z}_{uFo} - \dot{z}_{sFo}) - k_{sF}(z_{uFo} - z_{sFo}) + c_{uF}(\dot{z}_{uFo} - \dot{z}_{0Fo}) + k_{uF}(z_{uFo} - z_{0Fo}) &= m_{uFo}\ddot{z}_{uFo} \\
\sum F_{uRi} &= m_{uRi}\ddot{z}_{uRi}; \\
-c_{sR}(\dot{z}_{uRi} - \dot{z}_{sRi}) - k_{sR}(z_{uRi} - z_{sRi}) + c_{uR}(\dot{z}_{uRi} - \dot{z}_{0Ri}) + k_{uR}(z_{uRi} - z_{0Ri}) &= m_{uRi}\ddot{z}_{uRi} \\
\sum F_{uRo} &= m_{uRi}\ddot{z}_{uR}; \\
-c_{sR}(\dot{z}_{uRo} - \dot{z}_{sRo}) - k_{sR}(z_{uRo} - z_{sRo}) + c_{uR}(\dot{z}_{uRo} - \dot{z}_{0Ro}) + k_{uR}(z_{uRo} - z_{0Ro}) &= m_{uRo}\ddot{z}_{uRo}
\end{aligned} \tag{4.50}$$

Assuming that the tire dampings (c_{uF}, c_{uR}) are neglected, we substitute equation (4.45) and (4.46) into (4.50). The resulting equations of motion are given by [Hudha, Kadir et al.,2009]:

$$\begin{aligned}
m_{uFi} \ddot{z}_{uFi} &= -a(k_{sF}\theta + c_{sF}\dot{\theta}) + \frac{w}{2}(k_{sF}\phi + c_{sF}\dot{\phi}) \\
&\quad + k_{sF}z_s + c_{sF}\dot{z}_s - (k_{sF} + k_{uF})z_{uFi} - c_{sF}\dot{z}_{uFi} + k_{uF}z_{0Fi} \\
m_{uFo} \ddot{z}_{uFo} &= -a(k_{sF}\theta + c_{sF}\dot{\theta}) - \frac{w}{2}(k_{sF}\phi + c_{sF}\dot{\phi}) \\
&\quad + k_{sF}z_s + c_{sF}\dot{z}_s - (k_{sF} + k_{uF})z_{uFo} - c_{sF}\dot{z}_{uFo} + k_{uF}z_{0Fo} \\
m_{uRi} \ddot{z}_{uRi} &= +a(k_{sR}\theta + c_{sR}\dot{\theta}) + \frac{w}{2}(k_{sR}\phi + c_{sR}\dot{\phi}) \\
&\quad + k_{sR}z_s + c_{sR}\dot{z}_s - (k_{sR} + k_{uR})z_{uRi} - c_{sR}\dot{z}_{uRi} + k_{uR}z_{0Ri} \\
m_{uRo} \ddot{z}_{uRo} &= +a(k_{sR}\theta + c_{sR}\dot{\theta}) - \frac{w}{2}(k_{sR}\phi + c_{sR}\dot{\phi}) \\
&\quad + k_{sR}z_s + c_{sR}\dot{z}_s - (k_{sR} + k_{uR})z_{uRo} - c_{sR}\dot{z}_{uRo} + k_{uR}z_{0Ro}
\end{aligned} \tag{4.51}$$

where \ddot{z}_{uFi} = acceleration of front-inside unsprung mass
 \ddot{z}_{uFo} = acceleration of front-outside unsprung mass
 \ddot{z}_{uRi} = acceleration of rear-inside unsprung mass
 \ddot{z}_{uRo} = acceleration of rear-outside unsprung mass
 z_{0Fi} = road input amplitude of front-inside unsprung mass
 z_{0Fo} = road input amplitude of front-outside unsprung mass
 z_{0Ri} = road input amplitude of rear-inside unsprung mass
 z_{0Ro} = road input amplitude of rear-outside unsprung mass

The Full-vehicle (7 DOF) model will be implemented to simulate the effect of different weight of wheels on performance criteria. Also, we compare the effect of various road conditions (i.e., dry, rain, ice, snow) and different road profiles (i.e., asphalt, gravel highway) on ride comfort and handling with increased unsprung mass.

4.3 VEHICLE HANDLING MODEL

The vehicle body can be considered by 6 DOF such as longitudinal, lateral, heave, roll, pitch, and yaw motions. In this section, bicycle (2 DOF) model which is one of the most popular models can be characterized by lateral and yaw motions. The horizontal (3 DOF) handling model is characterized by longitudinal, lateral, and yaw motions. On the other hand, the roll, pitch, and yaw motions are considered in the full-vehicle ride model.

4.3.1 Bicycle (2 DOF) Model

One of the most popular models in lateral vehicle dynamics is the bicycle model which used in analyzing vehicle handling characteristics as well as vehicle control. This is primarily due to simplicity and ability to predict actual handling behavior. The term “bicycle model” is due to the fact that the right and left wheels are collapsed into one as shown in Figure 4-10. For the analysis to be valid, the following assumptions must hold[Talukdar and Kulkarni,2011]:

- 1) The left and right steer angles (δ) of the front wheels must be approximately the same.
- 2) The radius of the turn (R) must be large compared to the vehicle wheelbase ($l = a + b$), and the vehicle track (t).
- 3) The slip angles of the front wheels (α_F) are equal, and the slip angles of the rear wheels (α_R) are equal.
- 4) The sideslip angle (β) at the CG is $\beta = \tan^{-1} \frac{v_y}{v_x} \approx \frac{v_y}{v_x}$.
- 5) The sideslip angle (β) and the yaw velocity ($\dot{\psi}$) are fixed in a steady turn so that the instantaneous speed tangent to the path at the CG is $v_{cg} = \dot{\psi} R$
- 6) The effect of vehicle roll is small

- 7) The chassis is modeled as a rigid beam
- 8) There are no aerodynamic effects
- 9) Small angle approximation are valid
- 10) The constant longitudinal speed (v_0)

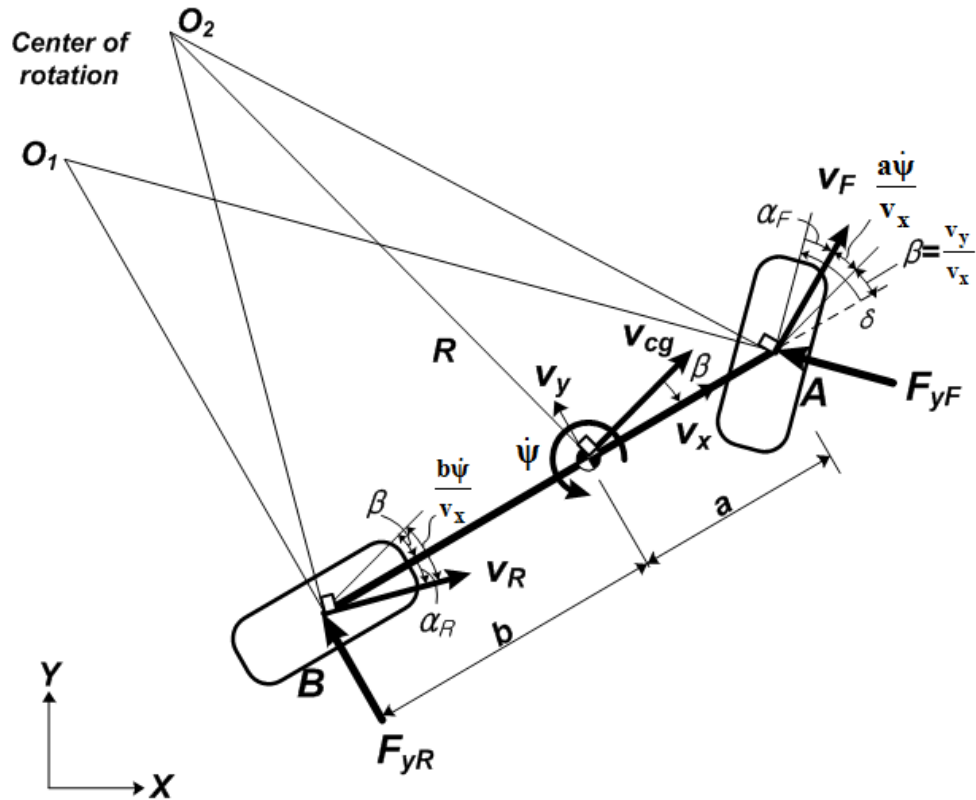


Figure 4-24: Bicycle Model

Figure 4-24 shows the schematic diagram of 2 DOF bicycle model which consists of lateral velocity and yaw rate. The XY coordinate is the global coordinate frame, while xy coordinate is a body coordinate frame (i.e., axis x – longitudinal direction, axis y – lateral direction). The point O_1 is the instantaneous center of zero velocity (IC), where it lies on the instantaneous axis. This axis is perpendicular to the plane of motion of a vehicle. At low speeds, the lateral force created by the tire slip angle is neglected (i.e.,

less than 5m/s)[Rajamani,2006]. The tire slip angle occurs due to the lateral elasticity of the tire. At high speed, the instantaneous center shifts from point O_1 to point O_2 due to tire slip angle which results in a lateral forces at the front wheels given the steering angle[Kim, Yi et al.,2010]. At the same time, the lateral and yaw accelerations will be present at the front wheels. After that, the vehicle body yaws, applying a slip angle at the rear wheels, resulting in a lateral force at the rear wheels. At the same time, the lateral acceleration increased, and yaw acceleration is decreased to zero. In addition, the slip angle on the rear wheels causes the sideslip angle at the CG to become negative. The lateral forces acting on the rear wheels build until they balance with those acting on the front. Finally, the vehicle reaches a steady state condition, after the front and rear tire forces become balanced [Gillespie,1992; Blundell and Harty,2004].

As can be seen Figure 4-24, the slip angles(α) can be defined as the angle between the heading direction of the tire and its travel direction which is the direction of the velocity vector. The side slip angle(β) is defined as the angle between the vehicle heading and the vehicle velocity direction due to the compliance of the pneumatic tire. Therefore, using the small angle approximation, the slip angles are given by:

$$\begin{aligned}\alpha_F &\approx \beta + \frac{a\dot{\psi}}{v_x} - \delta = \frac{v_y + a\dot{\psi}}{v_x} - \delta \\ \alpha_R &\approx \frac{v_y - b\dot{\psi}}{v_x}\end{aligned}\tag{4.52}$$

where v_x is the longitudinal velocity of the CG of the vehicle, and v_y is the lateral velocity of the CG of the vehicle. When a steering angle turns the heading of the tire by δ angle, the velocity vector(v_F) of the tire is lazier than the heading and turns by $(\beta + \frac{a\dot{\psi}}{v_x})$ angle (i.e., $(\beta + \frac{a\dot{\psi}}{v_x}) < \delta$). Therefore, a positive steer angle creates a

negative side slip angle. The difference between the front slip angle and rear slip angle becomes:

$$\alpha_F - \alpha_R = \delta - \frac{l}{R} \quad (4.53)$$

The above equation becomes:

$$\delta = \frac{l}{R} + \alpha_F - \alpha_R \quad (4.54)$$

The steering angle consists of the static part (l/R , known as the Ackermann angle) and dynamic part ($\alpha_F - \alpha_R$). If the front slip angle is larger than the rear slip angle, this condition is called understeer. If the rear slip angle is larger than the front slip angle, this condition is called oversteer. If they are equal, the steering angle is equal to the Ackerman angle, which condition is called neutral steer [Wong,2008].

Assuming linear tire model, the lateral tire force are directly proportional to the tire slip angles. The tire forces are given by:

$$\begin{aligned} F_{yF} &= -C_{\alpha F} \alpha_F = -C_{\alpha F} \left(\frac{v_y + a\dot{\psi}}{v_x} - \delta \right) \\ F_{yR} &= -C_{\alpha R} \alpha_R = -C_{\alpha R} \left(\frac{v_y - b\dot{\psi}}{v_x} \right) \end{aligned} \quad (4.55)$$

where $C_{\alpha F}$ and $C_{\alpha R}$ are the total front and rear cornering stiffness. By applying the Newton's Law, the equations of lateral motion and yaw motion are given by:

$$\begin{aligned} \sum F_y &= ma_y; \quad F_{yF} + F_{yR} = m(v_{x0}\dot{\psi} + \dot{v}_y) = m(v_{x0}\dot{\psi} + v_{x0}\dot{\beta}) \\ \sum M_z &= I_z \ddot{\alpha}_z; \quad aF_{yF} - bF_{yR} = I_z \ddot{\psi} \end{aligned} \quad (4.56)$$

As mentioned above assumption, we use $\beta = \tan^{-1} \frac{v_y}{v_x} \approx \frac{v_y}{v_x}$ or $v_y \approx \beta v_x$. We

substituted equation (4.55) into (4.56), and then a 2 DOF linear model for lateral dynamics can be written as [Jazar,2008]:

$$\begin{bmatrix} \dot{v}_y \\ \ddot{\psi} \end{bmatrix} = \begin{bmatrix} \frac{-(C_{\alpha F} + C_{\alpha R})}{mv_x} & \frac{-aC_{\alpha F} + bC_{\alpha R} - v_x}{mv_x} \\ -\frac{aC_{\alpha F} - bC_{\alpha R}}{I_z} & -\frac{a^2C_{\alpha F} + b^2C_{\alpha R}}{I_z v_x} \end{bmatrix} \begin{bmatrix} v_y \\ \dot{\psi} \end{bmatrix} + \begin{bmatrix} \frac{C_{\alpha F}}{m} \\ \frac{aC_{\alpha F}}{I_z} \end{bmatrix} \delta \quad (4.57)$$

where m is the mass of the vehicle and I_z is the moment of the inertia about the z -axis.

4.3.1.1 Simulation Results of Bicycle Model

Table 4-3 shows vehicle parameters. The passenger vehicle mass and yaw moment of inertia are 1360 kg and 2420 kg-m², respectively. The cornering stiffness of the front axle and the rear axle is 44000*2 and 47000*2 N/rad. Based on these parameters, simulation results are shown in Figure 4-25.

	Parameters	Value	Units	Value	Units
Vehicle mass	m	1360	kg	3000/g	slug
Yaw moment of inertia	I_z	2420	kg-m ²	1785	slug-ft ²
Cornering Stiffness	$C_{\alpha F}$	44000*2	N/rad	19783	lb/rad
Cornering Stiffness	$C_{\alpha R}$	47000*2	N/rad	21131	lb/rad
Steering Angle	δ	1	deg		

Table 4-3: Vehicle Parameters

The input variable is steering angle, and the output is lateral speed (v_y), yaw rate ($\dot{\psi}$), and lateral acceleration ($a_y = \dot{v}_y + a\dot{\psi}$) in terms of three longitudinal velocities ($v_x = u$). As the longitudinal velocity reaches 30.8 m/s (70 mph), the lateral speed is around negative 1 m/s.

Yaw rate and lateral acceleration is approximately 10 deg/s and 6 m/s², respectively. As mentioned above, the side slip angle (β) is defined as the angle between the vehicle heading and the vehicle velocity direction due to the compliance of pneumatic tire. The value of side slip angle becomes -0.0325 rad, as a result of $v_y / v_x (= -1/30.8)$.

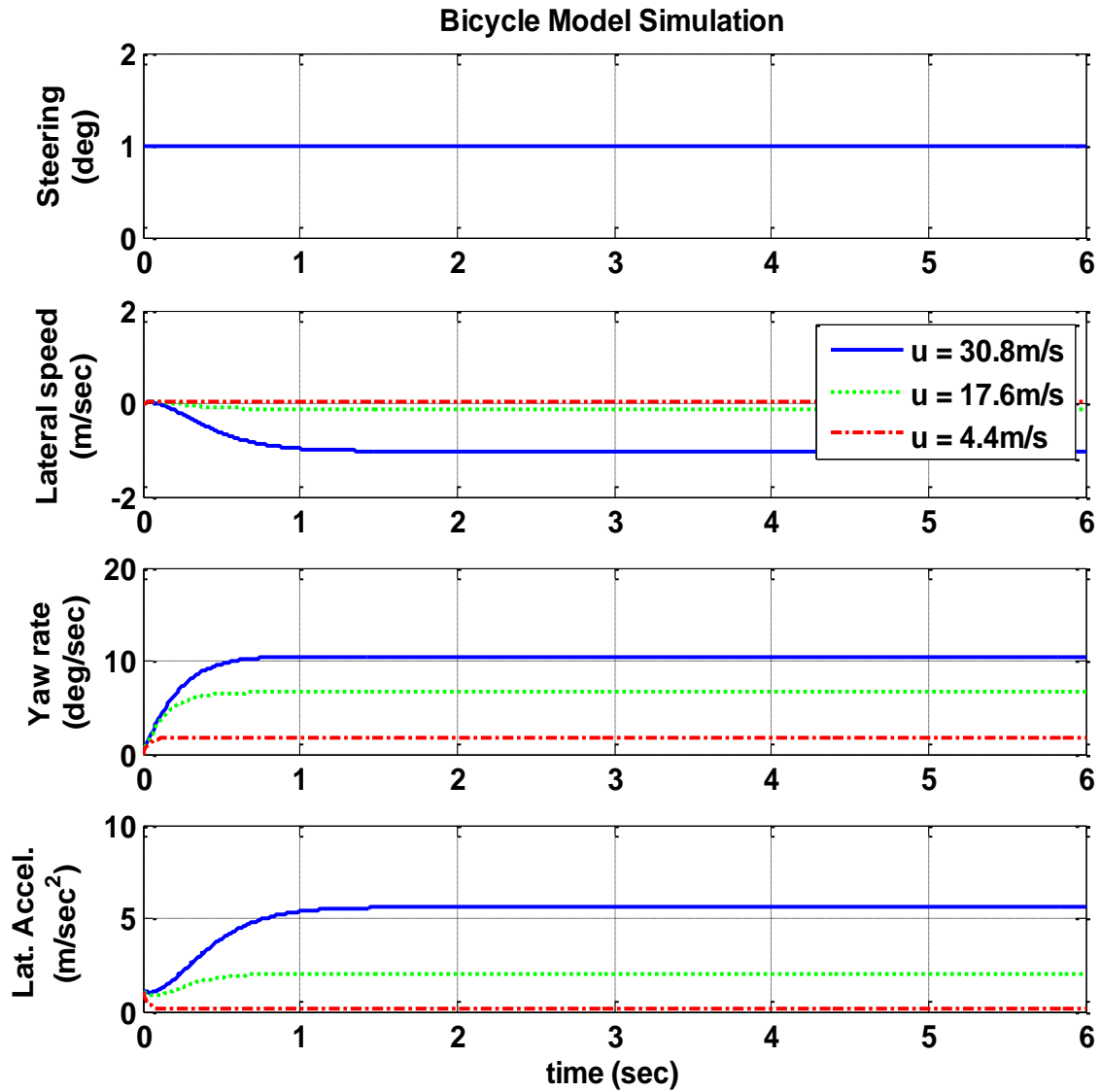


Figure 4-25: Simulation results based on the Bicycle Model

At low speed driving condition, the value of side slip angle becomes 0.009 rad, as a result of $v_y / v_x (= 1/4.4)$ because the lateral velocity is 1 m/s at longitudinal velocity of 4.4 m/s. In summary, the side slip angle is positive at low speed, while it is negative at high speed[Gillespie,1992; Barak and Tianbing,2003].

4.3.1.2 Four wheel steering

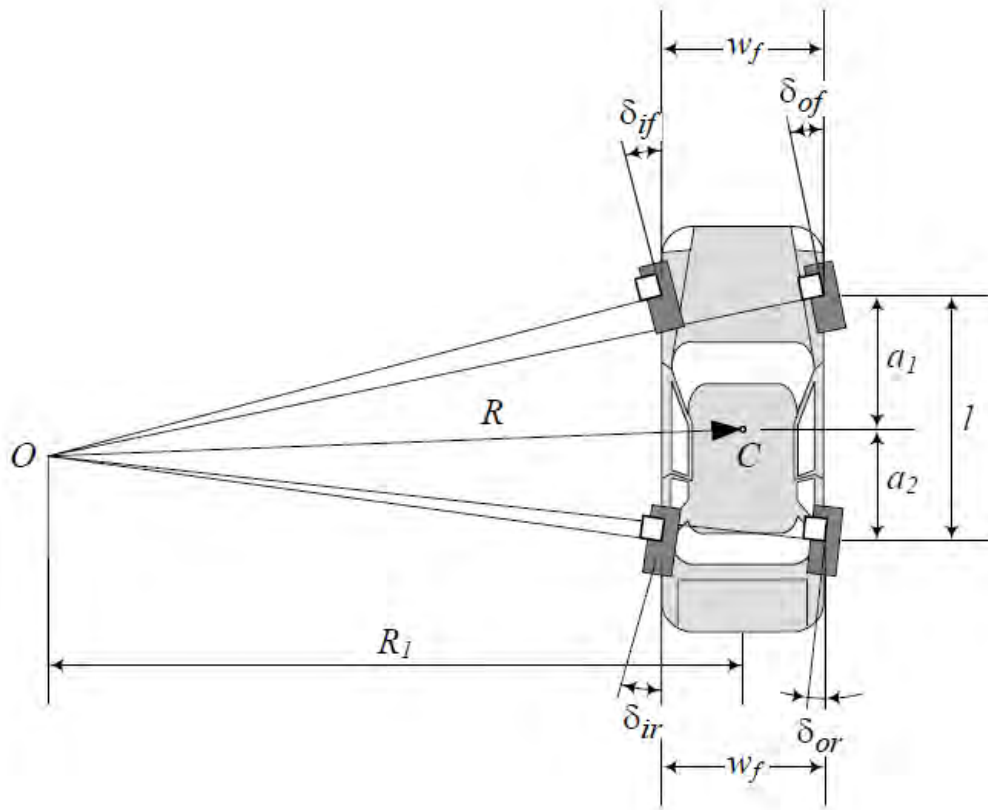


Figure 4-26: Four-wheel steering vehicle at low speeds

The four wheel steering reduces the side slip angle (lateral speed) to zero by adjusting the ratio of the rear wheel steer angle to the front wheel steer angle [Cariou, Lenain et al.,2008]. Figure 4-26 shows a four-wheel steering vehicle that the rear wheel is turned in the opposite direction to that of the front wheel. As a result, the positive side

slip angle becomes very small so that the maneuverability of the vehicle improves. That is, radius (R) of instantaneous center shown in Figure 4-24 becomes minimum radius [Huh, Kim et al.,2000; Jazar,2008].

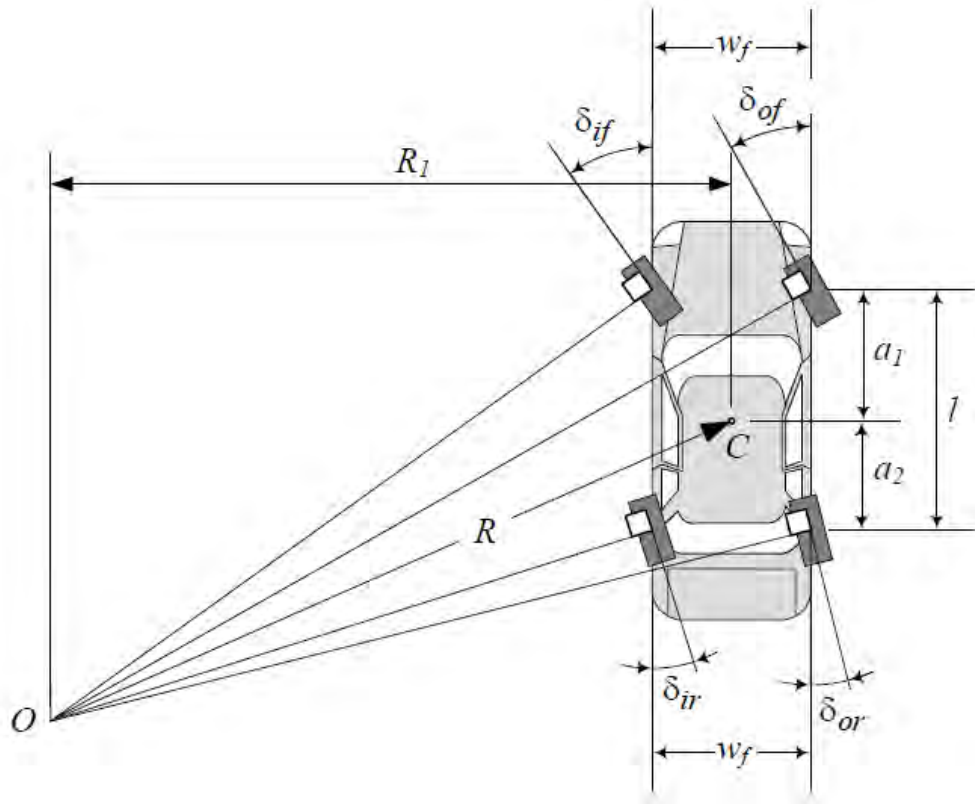


Figure 4-27: Four-wheel steering vehicle at high speeds

Figure 4-27 shows a four-wheel steering vehicle at high speeds that the rear wheel is turned in the same direction, so that the negative side slip angle becomes very small. This enables a vehicle to achieve good stability in the intermediate to high speed ranges during cornering and lane change [Nagai, Hirano et al.,1997; Jazar,2008].

4.3.2 Horizontal Handling (3 DOF) Model

The horizontal (3 DOF) handling model takes into account longitudinal, lateral, and yaw motions. Assuming that we consider the vehicle to be a rigid body, the global vehicle forces and moments act on the CG of a vehicle [Jonasson and Andreasson,2008; Jonasson, Andreasson et al.,2010; Jonasson, Andreasson et al.,2011]. The global force vector, $F_{global} = [F_x \ F_y \ F_z \ M_x \ M_y \ M_z]^T$, contains three forces and three moments. Three global forces become as follows [Jazar,2008]:

$$\begin{bmatrix} \sum F_x \\ \sum F_y \\ \sum F_z \end{bmatrix} = m\vec{a} = m(\dot{\vec{v}} + \vec{w} \times \vec{v}) = m \begin{bmatrix} \dot{v}_x + \dot{\theta}v_z - \dot{\psi}v_y \\ \dot{v}_y + \dot{\psi}v_x - \dot{\phi}v_z \\ \dot{v}_z + \dot{\phi}v_y - \dot{\theta}v_x \end{bmatrix} \quad (4.58)$$

The translational equations of motion states the sum of all the external forces acting on the body equals the acceleration of the body's CG [Hibbeler,2007]. Assuming the body coordinate system is the principal coordinate frame, the global moments become as follows:

$$\begin{bmatrix} \sum M_x \\ \sum M_y \\ \sum M_z \end{bmatrix} = \begin{bmatrix} I_{xx} & 0 & 0 \\ 0 & I_{yy} & 0 \\ 0 & 0 & I_{zz} \end{bmatrix} \begin{bmatrix} \ddot{\phi} \\ \ddot{\theta} \\ \ddot{\psi} \end{bmatrix} + \begin{bmatrix} \phi \\ \theta \\ \psi \end{bmatrix} \times \left(\begin{bmatrix} I_{xx} & 0 & 0 \\ 0 & I_{yy} & 0 \\ 0 & 0 & I_{zz} \end{bmatrix} \begin{bmatrix} \dot{\phi} \\ \dot{\theta} \\ \dot{\psi} \end{bmatrix} \right) \quad (4.59)$$

The above equation becomes:

$$\begin{bmatrix} \sum M_x \\ \sum M_y \\ \sum M_z \end{bmatrix} = \begin{bmatrix} I_{xx}\ddot{\phi} + (I_{zz} - I_{yy})\dot{\theta}\dot{\psi} \\ I_{yy}\ddot{\theta} + (I_{zz} - I_{xx})\dot{\psi}\dot{\phi} \\ I_{zz}\ddot{\psi} + (I_{yy} - I_{xx})\dot{\phi}\dot{\theta} \end{bmatrix} \quad (4.60)$$

Above equation is called Euler's rotational equations of motion, applying for the center of gravity [Hibbeler,2007].

To obtain the horizontal handling model, the following assumptions must hold:

- 1) The vehicle body is lumped into a single mass.
- 2) Neglect the roll (ϕ), pitch (θ), and vertical motions.
- 3) Neglect aerodynamic drag, rolling, and grade resistance.

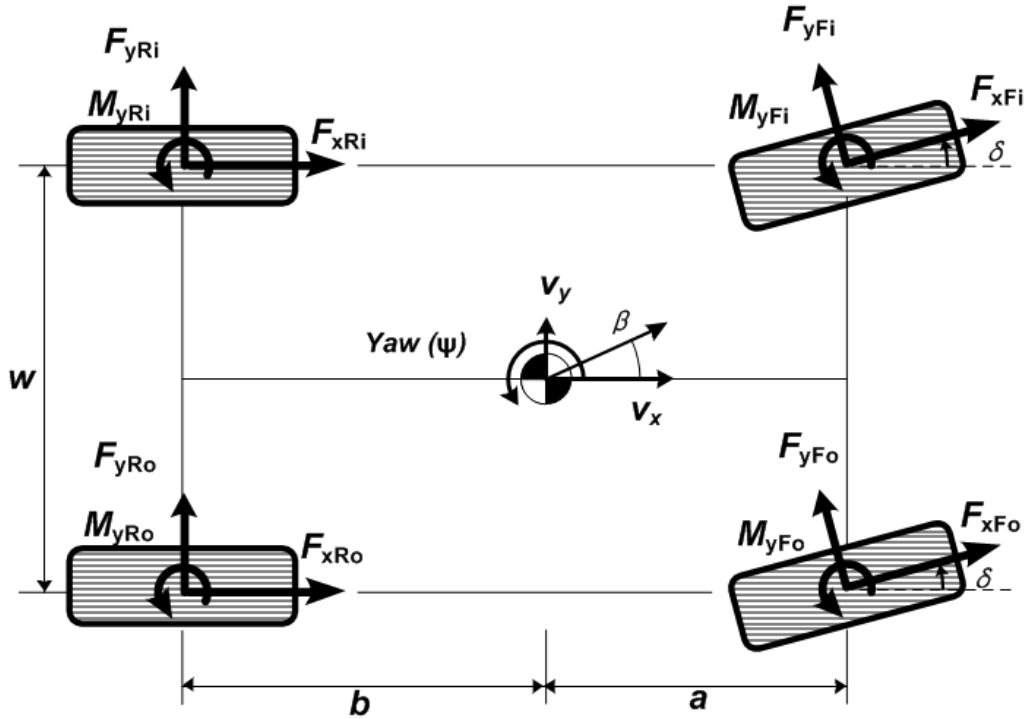


Figure 4-28: Horizontal Handling (3 DOF) Model

Figure 4-28 shows the schematic diagram of horizontal handling model. Considering that we assume above, the Equation (4.58) becomes as follows [Setiawan, Safarudin et al.,2009]:

$$m \begin{bmatrix} \dot{v}_x - \dot{\psi} v_y \\ \dot{v}_y + \dot{\psi} v_x \end{bmatrix} = \begin{bmatrix} F_{xFi} \cos \delta - F_{yFi} \sin \delta + F_{xFo} \cos \delta - F_{yFo} \sin \delta + F_{xRi} + F_{xRo} \\ F_{xFi} \sin \delta + F_{yFi} \cos \delta + F_{xFo} \sin \delta + F_{yFo} \cos \delta + F_{yRi} + F_{yRo} \end{bmatrix} \quad (4.61)$$

where v_x = longitudinal velocity of the CG of the vehicle

v_y = lateral velocity of the CG of the vehicle

δ = steering angle

The Equation (4.60) becomes as follows:

$$\begin{aligned}
I_{zz}\ddot{\psi} = & -\frac{w}{2}F_{xFi}\cos\delta + \frac{w}{2}F_{xFo}\cos\delta + \frac{w}{2}F_{yFi}\sin\delta - \frac{w}{2}F_{yFo}\sin\delta + \\
& aF_{xFi}\sin\delta + aF_{xFo}\sin\delta + aF_{yFi}\cos\delta + aF_{yFo}\cos\delta + \\
& \frac{w}{2}F_{xRi} + \frac{w}{2}F_{xRo} - bF_{yRi} - bF_{yRo} + \\
& M_{zFi} + M_{zFo} + M_{zRi} + M_{zRo}
\end{aligned} \tag{4.62}$$

where I_{zz} = moment of inertia of sprung mass around z-axis

 $\ddot{\psi}$ = yaw angular acceleration M_{zFi} = self-aligning moments of front-inside wheel M_{zFo} = self-aligning moments of front-outside wheel M_{zRi} = self-aligning moments of rear-inside wheel M_{zRo} = self-aligning moments of rear-outside wheel

The self-aligning moments are generated by lateral force acting at a moment arm defined as the pneumatic trail (see Sec. 4.4.3). They are assumed to have the same direction with the yaw motion.

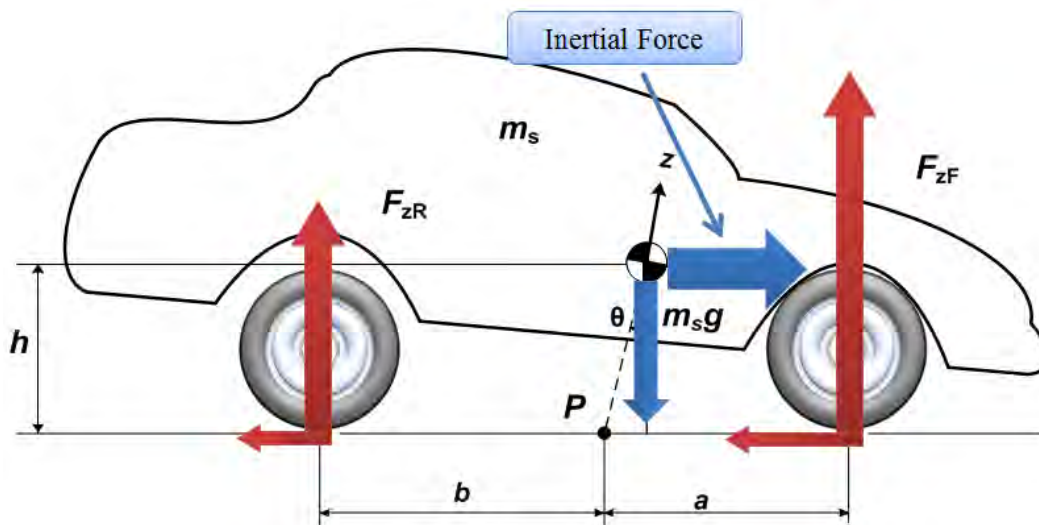


Figure 4-29: Pitch motion due to braking or traction

The longitudinal acceleration / deceleration lead to the pitch motion while the lateral acceleration contributes to the roll motion. Figure 4-29 shows longitudinal load transfer due to braking or traction, resulting in pitch motion. The sum of moment about the y-axis passing through pitch center (P) is given by [Setiawan, Safarudin et al.,2009]:

$$cw + \sum M_y = I_{yy} \ddot{\theta}; \quad m_s gh\theta - k_\theta \theta - c_\theta \dot{\theta} = (I_{yy} + m_s h^2) \ddot{\theta} - m_s a_x h \quad (4.63)$$

where I_{yy} = moment of inertia of sprung mass around y-axis

$\ddot{\theta}$ = pitch angular acceleration

h = CG height

a_x = longitudinal acceleration

k_θ = pitch stiffness

c_θ = pitch damping

The left side is equivalent to the sum of the “kinetic moments” of the components of $m_s a_x$ about P plus the “kinetic moment” of $(I_{yy} + m_s h^2) \ddot{\theta}$. The direction of $m_s a_x$ is directed in the negative x-axis direction, while the inertia force is directed in positive x-axis direction. The vector $m_s a_x$ is regarded as sliding vector which act at any point along its line of action[Hibbeler,2007].

The Equation (4.63) can be rearranged as:

$$(I_{yy} + m_s h^2) \ddot{\theta} = m_s a_x h + m_s gh\theta - k_\theta \theta - c_\theta \dot{\theta} \quad (4.64)$$

It should be noted that above equation is written by considering moments acting on the vehicle pitch center (P) than the CG of sprung mass. The pitch inertia of the sprung mass with respect to the vehicle pitch is considered in the above equation.

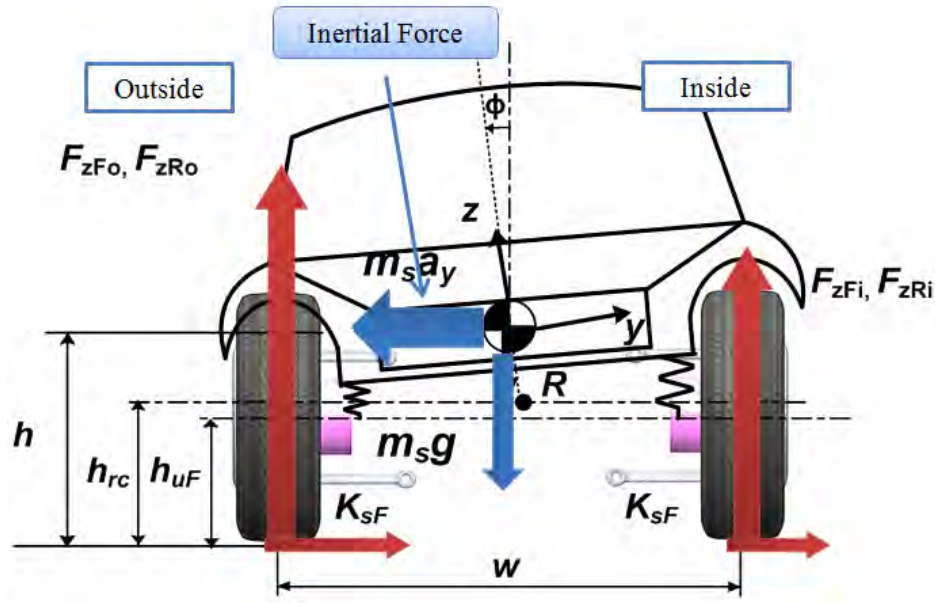


Figure 4-30: Roll motion due to a cornering maneuver

Figure 4-30 shows the lateral load transfer during a cornering maneuver. With the Free-body diagram shown in Figure 4-30, the roll equation of motion is derived by summing moments about the roll center of the vehicle as follows [Setiawan, Safarudin et al.,2009]:

$$ccw + \sum M_x = I_{xx} \ddot{\phi};$$

$$m_s g (h - h_{rc}) \sin \phi - k_{\phi} \phi - c_{\phi} \dot{\phi} = (I_{xx} + m_s (h - h_{rc})^2) \ddot{\phi} - m_s a_y (h - h_{rc}) \cos \phi \quad (4.65)$$

where I_{xx} = moment of inertia of sprung mass around x-axis

$\ddot{\phi}$ = roll angular acceleration

h = CG height

h_{rc} = roll center height

a_y = lateral acceleration

k_{ϕ} = roll stiffness

c_{ϕ} = roll damping

Assuming the sprung mass of a vehicle rotates about a kinematic roll center axis, the left side is equivalent to the sum of the “kinetic moments” of the components of $m_s a_y$ about vehicle roll center plus the “kinetic moment” of $\left(I_{xx} + m_s (h - h_{rc})^2\right) \ddot{\phi}$. The direction of $m_s a_y$ is directed in the positive y-axis direction, while the inertia force is directed in negative y-axis direction.

The Equation (4.65) can be rearranged as:

$$\left(I_{xx} + m_s (h - h_{rc})^2\right) \ddot{\phi} = m_s a_y (h - h_{rc}) \cos \phi + m_s g (h - h_{rc}) \sin \phi - k_\phi \phi - c_\phi \dot{\phi} \quad (4.66)$$

It should be noted that above equation is written by considering moments acting on the vehicle roll center than the CG of sprung mass. The roll inertia of the sprung mass with respect to the vehicle roll center is considered in above equation.

The normal force acting on the tire ground contact patch as shown in Figure 4-29 and Figure 4-30 will be explained in details in Section 4.5.

4.4 TIRE MODEL

Most forces and moments arise due to the tire-road contact (i.e., traction, braking, and handling). To find out these force and moments, we will discuss the tire (4 DOF) models associated with the angular velocities of the unsprung masses. The longitudinal slip and slip angle will be discussed. The Magic Formula is adopted as the model among friction coefficient, slip ratio, and slip angle, so that the lateral and longitudinal forces can be determined. First of all, we will discuss the tire coordinate system to understand the resulting forces and moments developed at the tire contact patch.

4.4.1 Tire Coordinate System

It is essential to define the tire coordinate system in order to describe the tire characteristics in terms of the forces and moments.

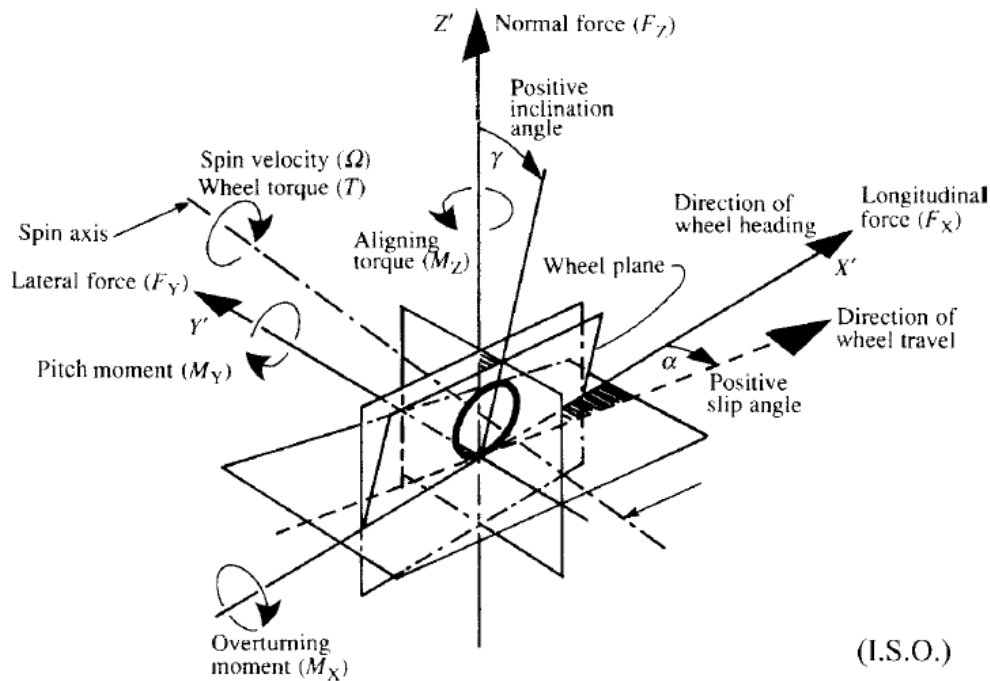


Figure 4-31: ISO coordinate system

Figure 4-31 shows the tire coordinate system with XYZ axis. Three forces ($F_{xjk}, F_{yjk}, F_{zjk}$) and moments ($M_{xjk}, M_{yjk}, M_{zjk}$) associated with the individual tire are defined in the axis directions. They are defined as [Dixon,2009]:

- 1) F_{xjk} – longitudinal force (tractive force) is the component in the X direction of the resultant force acting on the tire by the road
- 2) F_{yjk} – lateral force (cornering force) is the component in the Y direction of the resultant force acting on the tire by the road
- 3) F_{zjk} – normal force (contact force) is the component in the Y direction of the resultant force acting on the tire by the road
- 4) M_{xjk} – overturning moment is the moment about X axis acting on the tire by the road
- 5) M_{yjk} – rolling resistance moment is the moment about Y axis acting on the tire by the road
- 6) M_{zjk} – self-aligning moment is the moment about Z axis acting on the tire by the road

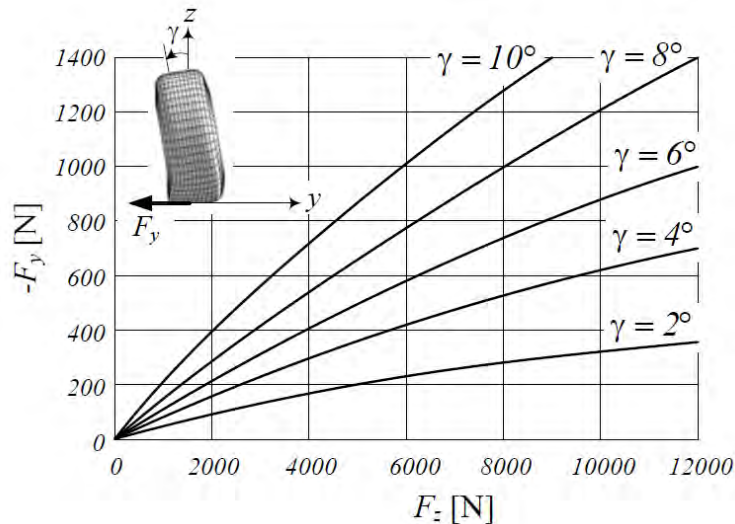


Figure 4-32: Lateral force as a function of normal force at different camber angles

In addition, the slip angle (α) is defined as the angle between the wheel heading and the wheel travel. Camber angle (γ) is the angle between the XZ plane and the wheel plane as shown in Figure 4-31. The lateral force (F_{yjk}) is influenced by the slip angle and the camber angle. Figure 4-32 shows the tire behaviors of a cambered tire which results in a lateral force as a function of normal force at different camber angles [Jazar,2008]. In this research, we assume that the wheel is vertical at all times with no camber angle so that there is no overturning moment acting in the x-axis direction.

4.4.2 Tire (4 DOF) Model

The mathematical model for tire (4 DOF) model is obtained from a one-wheel rotational dynamics.

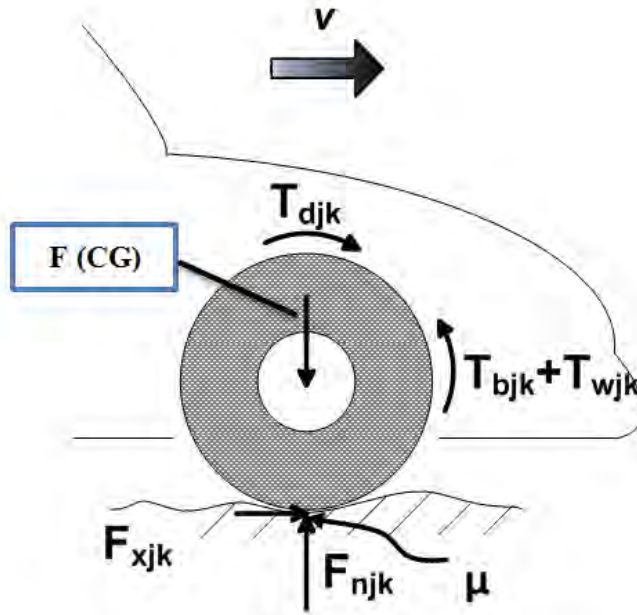


Figure 4-33: One-wheel rotational dynamics

Figure 4-33 shows Free-body diagram of one-wheel rotational dynamics. The $F(CG)$ depends on the location of the center of gravity (CG) associated with longitudinal acceleration, aerodynamic drag forces, and grade of the road. The $F_{\eta jk}$ indicates the normal force acting at tire contact patch associated with $F(CG)$. By applying Newton's second law of motion, the equation of motion for each wheel is given by[Calderón-Meza,2003]:

$$\begin{aligned}\sum M_y = J_{\eta jk} \ddot{\theta}; \quad & J_{wFi} \dot{\omega}_{wFi} = T_{dFi} - T_{bFi} - F_{xFi} r_w - T_{wFi}(\omega) \\ & J_{wFo} \dot{\omega}_{wFo} = T_{dFo} - T_{bFo} - F_{xFo} r_w - T_{wFo}(\omega) \\ & J_{wRi} \dot{\omega}_{wRi} = T_{dRi} - T_{bRi} - F_{xRi} r_w - T_{wRi}(\omega) \\ & J_{wRo} \dot{\omega}_{wRo} = T_{dRo} - T_{bRo} - F_{xRo} r_w - T_{wRo}(\omega)\end{aligned}\quad (4.67)$$

where ω_w = wheel rotational velocity

$J_{\eta jk}$ = wheel inertia

T_{djk} = motor torque

T_{bjk} = braking torque

r_w = wheel radius

F_{xjk} = traction (or braking when negative)

$T_{\eta jk}(\omega)$ = wheel friction torque

The subscript $j = F, R$ indicates front and rear wheel, while $k = i, o$ represents inside wheel and outside wheel, respectively. Many researchers have used one-wheel dynamics model without wheel friction torque. To simply analysis, the wheel friction torque is neglected.

The F_{xjk} represent traction force as follows:

$$\begin{aligned}F_{xjk} = \mu(s_F) \cdot F_{\eta jk}, \quad & \text{acceleratoin(slip)} \quad s_F = \left(\frac{r\omega_F - v_{xF}}{r\omega_F} \right) \times 100\% \quad (r\omega_F > v_{xF}) \\ \text{braking(skid)} \quad & s_F = \left(\frac{r\omega_F - v_{xF}}{v_{xF}} \right) \times 100\% \quad (r\omega_F < v_{xF})\end{aligned}\quad (4.68)$$

The traction force is friction force from the ground acting on the tires. It depends on the longitudinal slip/skid ratio, normal load on the tire, and the friction coefficient of the tire-road interface[Rajamani,2006]. The longitudinal slip/skid ratio will be discussed in next two sections.

4.4.3 Slip Angle

The slip angles (α) can be defined as the angle between the heading direction of the tire and its travel direction which is the direction of the velocity vector. The tire slip angle occurs due to the lateral elasticity of the tire [Wong,2008].

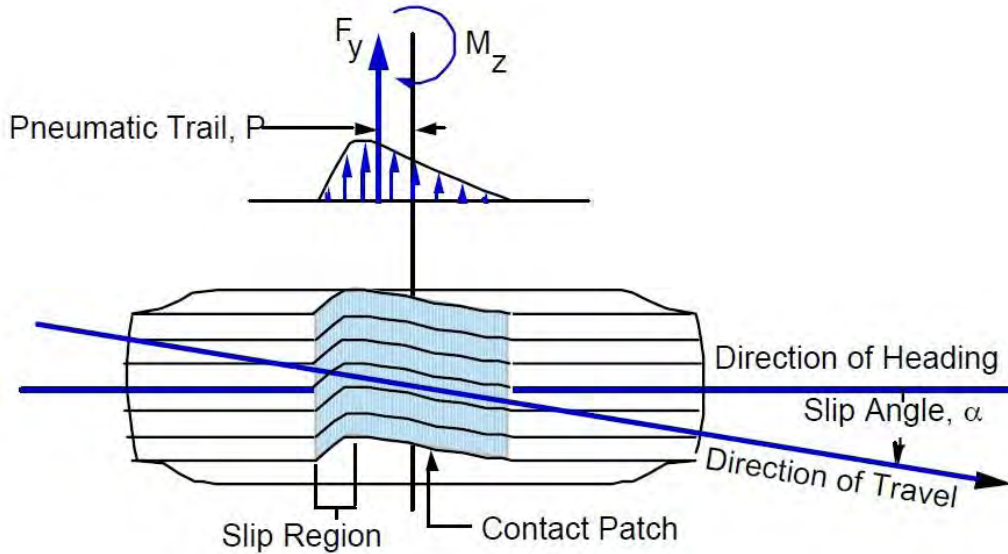


Figure 4-34: Slip angle induced tire self-aligning torque

The profile of lateral shear force over the tire contact patch is created, resulting in the resultant lateral force (F_y) which occurs by a distance of pneumatic trail (P). In addition, self-aligning torque (M_z) is generated by the pneumatic trail times the lateral force[Gillespie,1992]. The slip angle influenced by longitudinal velocity, lateral velocity, yaw rate, and steering angle of a vehicle is obtained by [Hudha, Ahmad et al.,2009]:

$$\alpha_F = \tan^{-1} \left(\beta + \frac{a\dot{\psi}}{v_x} \right) - \delta = \tan^{-1} \left(\frac{v_y + a\dot{\psi}}{v_x} \right) - \delta$$

$$\alpha_R = \tan^{-1} \left(\frac{v_y - b\dot{\psi}}{v_x} \right)$$
(4.69)

The front and rear slip angle will be used in the longitudinal slip / skid ratio.

4.4.4 Longitudinal Slip / Skid Ratio

Generally, applying a driving torque or a braking torque to a pneumatic tire produces tractive or braking force at the tire-ground contact patch. The driving torque creates compression at the tire tread in front of and within the contact patch. Therefore, the tire travels will be less than that in free rolling.

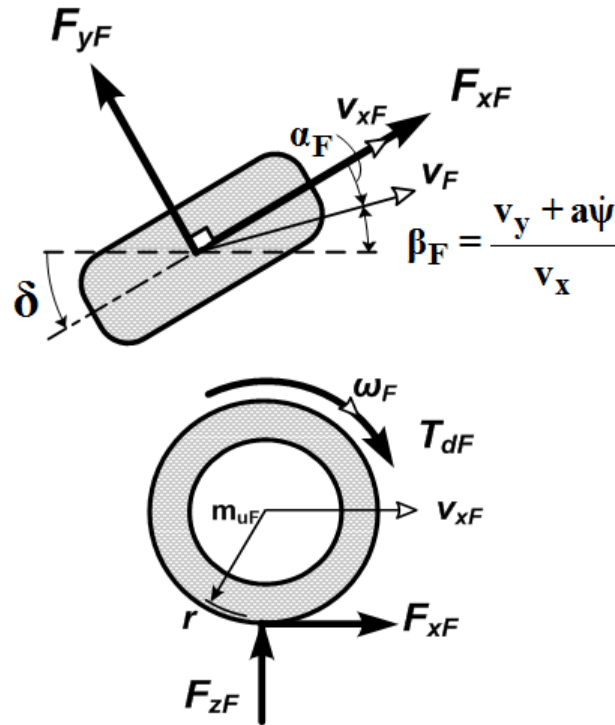


Figure 4-35: Longitudinal, lateral forces and velocity components

Similarly, applying a braking torque create tension at the tire tread within the contact patch. As a result, this tension causes the tire travels to be larger distance than in free rolling. This phenomenon is referred to as the wheel slip[Wong,2008].

Figure 4-35 shows the schematic diagram in terms of the longitudinal, lateral forces and velocity (see Figure 4-24). The longitudinal force (F_{xF}) and lateral force (F_{yF}) at the front wheel are generated from longitudinal slip ($s_F = \frac{r\omega_F - v_{xF}}{r\omega_F}$) and slip angle (α_F) with normal force (F_{zF}), respectively. The longitudinal velocity of the front wheel can be defined by [Hudha, Kadir et al.,2009]:

$$v_{xF} = v_F \cos \alpha_F = \sqrt{(v_y + a\dot{\psi})^2} + v_x \cos \alpha_F \quad (4.70)$$

where v_F is the speed of the front wheel, v_x and v_y are the longitudinal and later velocity at the CG, α_F is the slip angle at the front wheel. Similarly, the longitudinal velocity of the rear wheel can be written as:

$$v_{xR} = v_R \cos \alpha_R = \sqrt{(v_y - a\dot{\psi})^2} + v_x \cos \alpha_R \quad (4.71)$$

If a vehicle moves in a straight line, the lateral velocity and yaw rate will not occur so that the longitudinal velocity of the rear / front wheel can be equal to the longitudinal velocity of the CG.

Finally, assuming that the wheel's effective rolling radius is the same as the wheel radius, the longitudinal slip / skid at the front wheel are defined by:

$$\begin{aligned} \text{acceleratoin(slip)} \quad s_F &= \left(\frac{r\omega_F - v_{xF}}{r\omega_F} \right) \times 100\% \quad (r\omega_F > v_{xF}) \\ \text{braking(skid)} \quad s_F &= \left(\frac{r\omega_F - v_{xF}}{v_{xF}} \right) \times 100\% \quad (r\omega_F < v_{xF}) \end{aligned} \quad (4.72)$$

The longitudinal slip / skid at the rear wheel are similar to above equation. The longitudinal slip of the tire is 100%, indicating that tires are spinning while a vehicle doesn't move. For the skid, -100% represents a locked wheel while a vehicle moves.

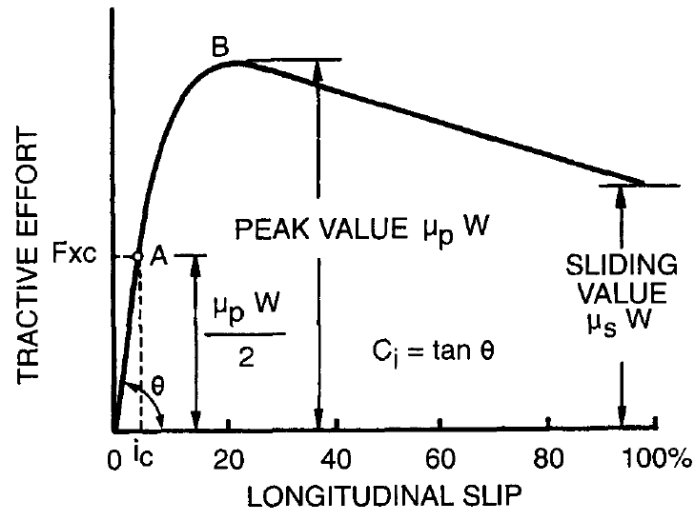


Figure 4-36: Variation of tractive effort with respect to longitudinal slip

Surface	Peak Value μ_p	Sliding Value μ_s
Asphalt and concrete (dry)	0.8–0.9	0.75
Asphalt (wet)	0.5–0.7	0.45–0.6
Concrete (wet)	0.8	0.7
Gravel	0.6	0.55
Earth road (dry)	0.68	0.65
Earth road (wet)	0.55	0.4–0.5
Snow (hard-packed)	0.2	0.15
Ice	0.1	0.07

Table 4-4: Average values of friction coefficient

The variation of tractive effort (traction force) as a function of longitudinal slip ratio is shown in Figure 4-36: Variation of tractive effort with respect to longitudinal slip. The traction force is proportional to the friction coefficient. The peak value (μ_p) of friction coefficient is associated with point 'B', while the sliding value (μ_s) of friction

coefficient is at 100%. Table 4-4 describes average values of friction coefficient [Wong,2008].

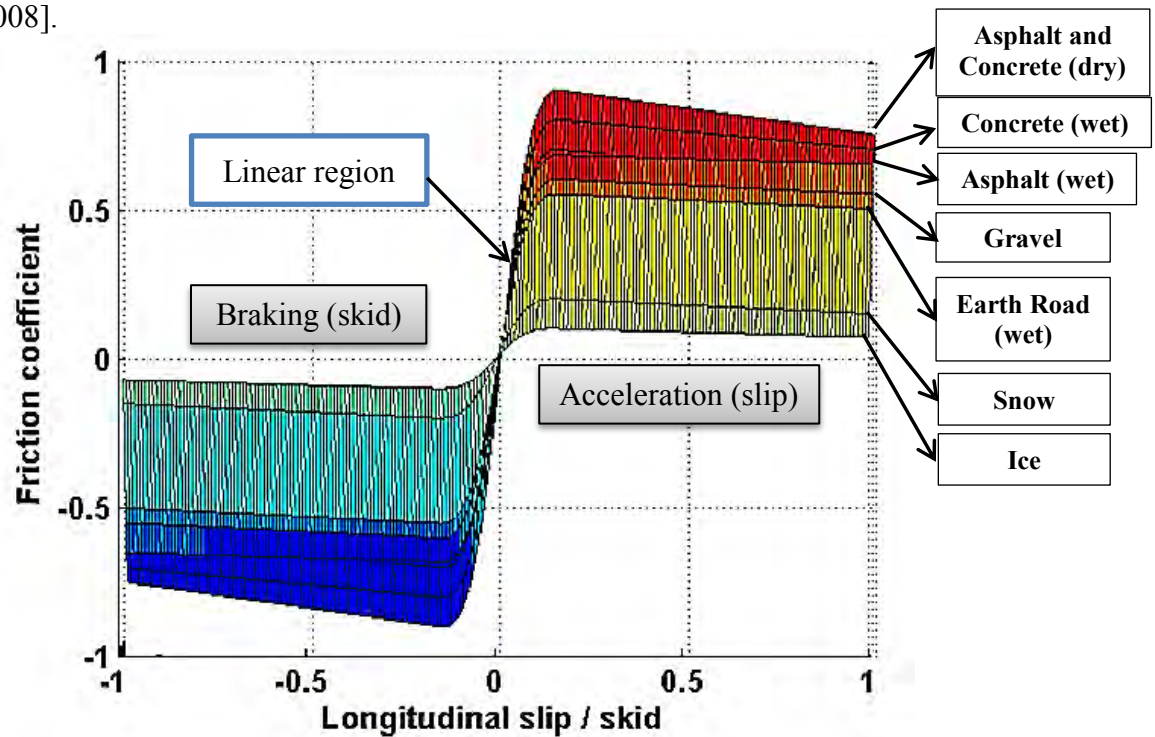


Figure 4-37: Friction coefficient versus longitudinal slip / skid ratio

Based on Table 4-4, the friction coefficient with respect to longitudinal slip / skid ratio is shown in Figure 4-37. The different road conditions have different friction coefficient which is the critical parameter to determine traction force. Figure 4-37 shows the relationship between friction coefficient and wheel longitudinal slip / skid ratio. For the wheel skid, the friction coefficient is negative. It can be seen that the larger the maximum torque, the less the wheel slip ratio (i.e., slip = 0.15). The maximum traction force can be constrained by the nature of tire-road interaction.[Kim and Kim,2007; Wong,2008].

4.4.5 Magic Formula

An empirical method to calculate steady-state tire force and moment as the Magic Formula has been used in vehicle dynamics. When the local shear forces are below the limit of friction force (μF_z), the tire elements adhere to the road surface. The Magic Formula gives us the longitudinal (F_x), and lateral (F_y , cornering) forces, and the self-aligning torque (M_z) based on slip angle and skid ratio. The general form of the formula is given by [Pacejka, 2006]:

$$y = D \sin \left[C \arctan \left\{ Bx - E \left(Bx - \arctan Bx \right) \right\} \right]$$

$$Y(X) = y(x) + S_v \quad (4.73)$$

$$x = X + S_h$$

where Y = output variable F_x , F_y , and M_z

X = input variable α and λ

B = stiffness factor

C = shape factor

D = peak value

E = curvature factor

S_h = horizontal shift

S_v = vertical shift

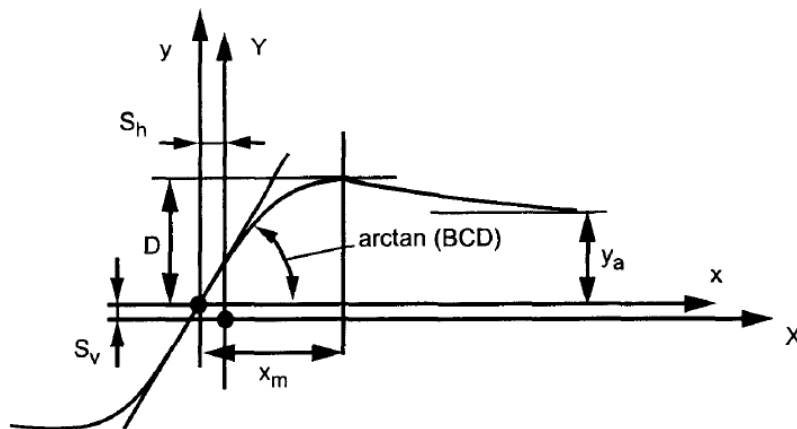


Figure 4-38: Tire characteristics of the Magic Formula for fitting tire test data

Figure 4-38 shows the tire characteristics of the Magic Formula associated with Equation (4.73). The peak factor D is a function of normal load F_z as follows:

$$D = a_1 F_z^2 + a_2 F_z \quad (4.74)$$

where a_1 and a_2 are empirical coefficients. Since the coefficient “D” is a function of normal force acting on the tire contact patch, we assume that the coefficient “D” corresponds to point “B” which is the peak value determined by friction force ($\mu_p F_z$) as shown in Figure 4-36.

	Load, F_z , kN	B	C	D	E	S_h	S_v	BCD
F_y , N	2	0.244	1.50	1936	-0.132	-0.280	-118	780.6
	4	0.239	1.19	3650	-0.678	-0.049	-156	1038
	6	0.164	1.27	5237	-1.61	-0.126	-181	1091
	8	0.112	1.36	6677	-2.16	0.125	-240	1017
M_z , N · m	2	0.247	2.56	-15.53	-3.92	-0.464	-12.5	-9.820
	4	0.234	2.68	-48.56	-0.46	-0.082	-11.7	-30.45
	6	0.164	2.46	-112.5	-2.04	-0.125	-6.00	-45.39
	8	0.127	2.41	-191.3	-3.21	-0.009	-4.22	-58.55
F_x , N	2	0.178	1.55	2193	0.432	0.000	25.0	605.0
	4	0.171	1.69	4236	0.619	0.000	70.6	1224
	6	0.210	1.67	6090	0.686	0.000	80.1	2136
	8	0.214	1.78	7711	0.783	0.000	104	2937

Table 4-5: Coefficient values in the Magic Formula for a vehicle tire

Table 4-5 shows coefficient values in the Magic Formula for a vehicle tire [Bakker, Nyborg et al.,1987; Wong,2008]. This empirical data was obtained from performing on a dry asphalt road condition. The Magic Formula provides the mathematical functions as follows:

$$\begin{aligned} F_{xjk} &= f(F_{zjk}, s_{jk}) \\ F_{yjk} &= f(F_{zjk}, \alpha_{jk}) \\ M_{yjk} &= f(F_{zjk}, \alpha_{jk}) \end{aligned} \quad (4.75)$$

The longitudinal force is a function of normal force and longitudinal slip. The lateral force and self-aligning moment is a function of normal force and slip angle.

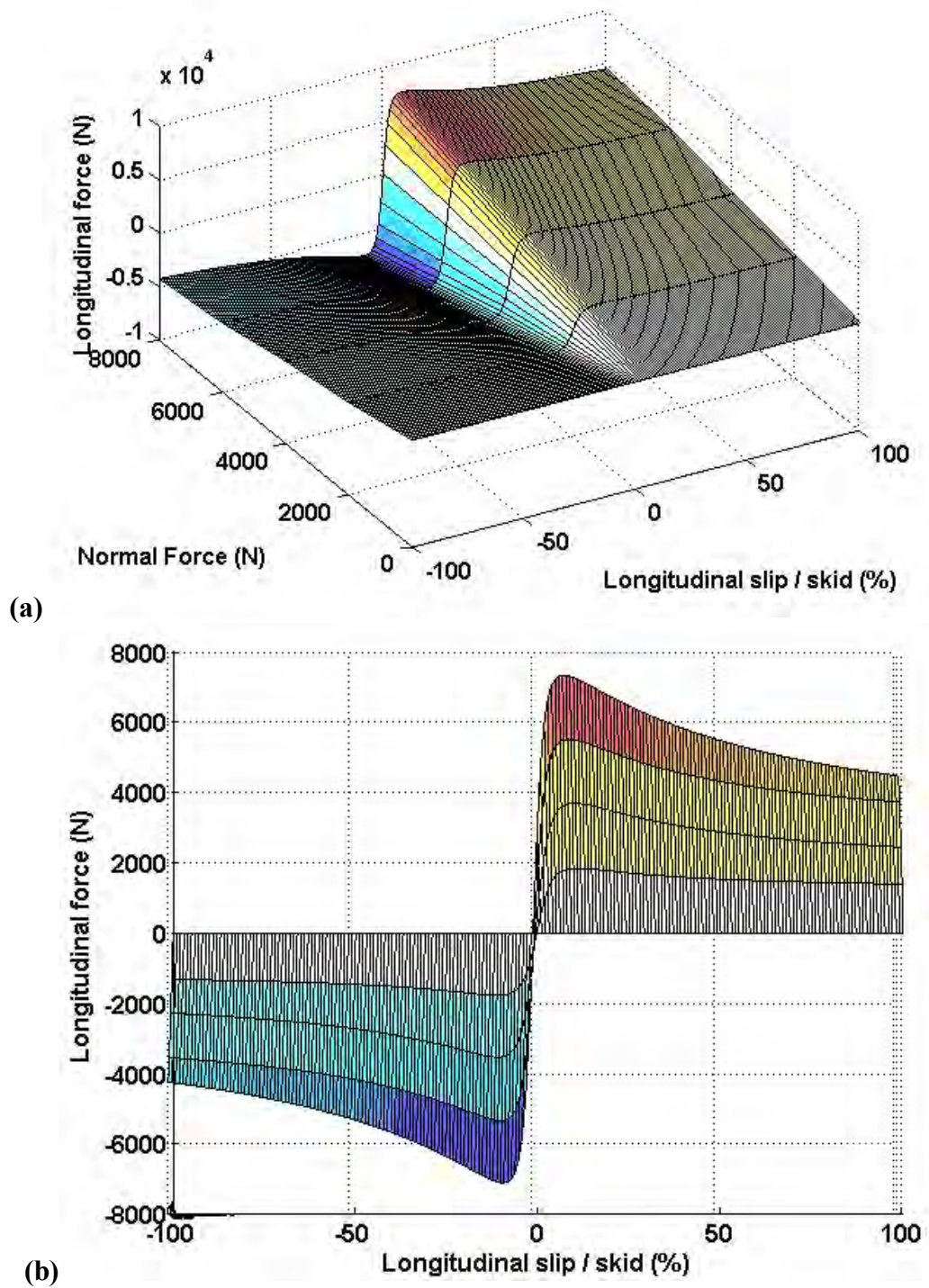


Figure 4-39: Longitudinal force w.r.t. normal force and longitudinal slip/skid

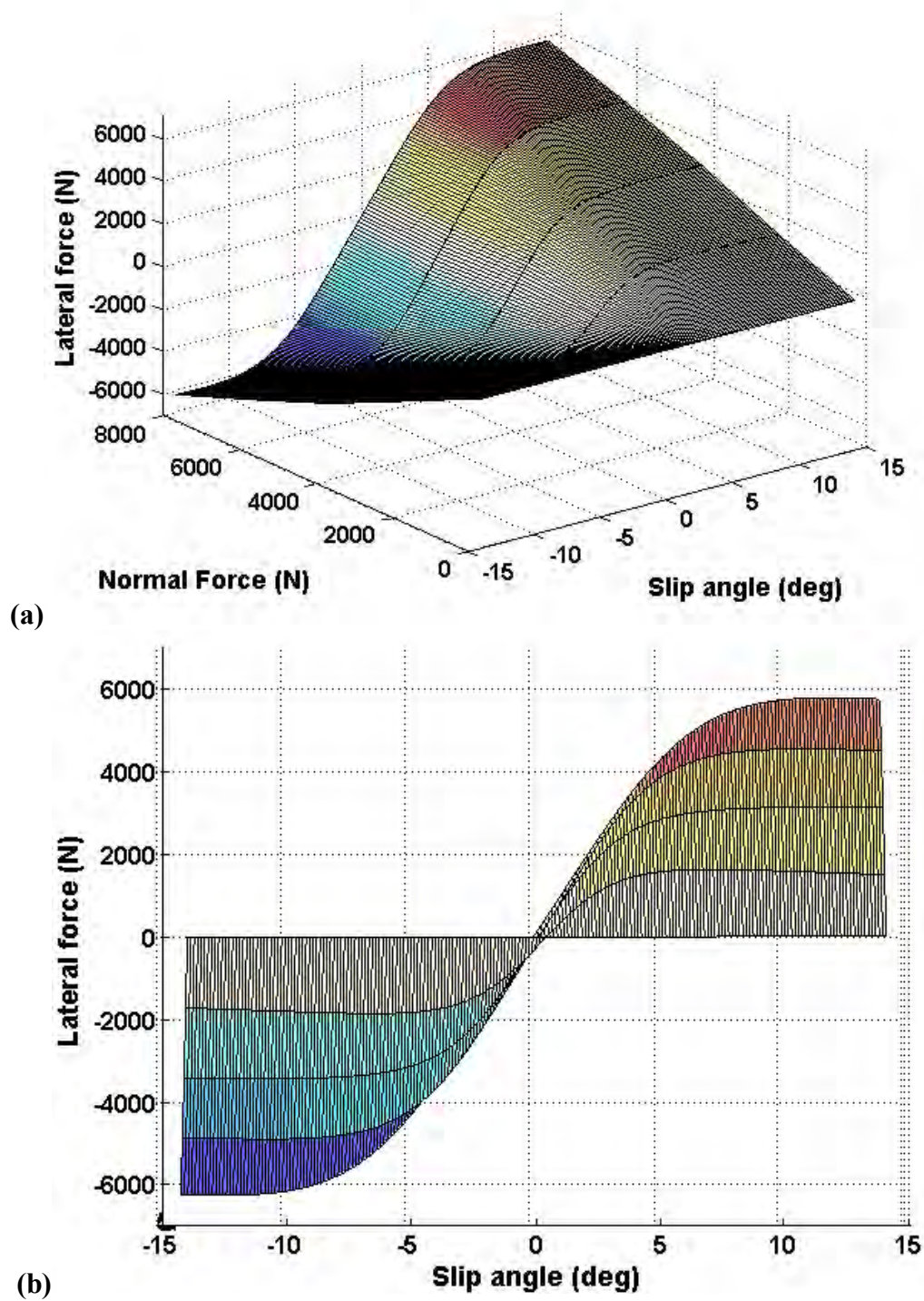
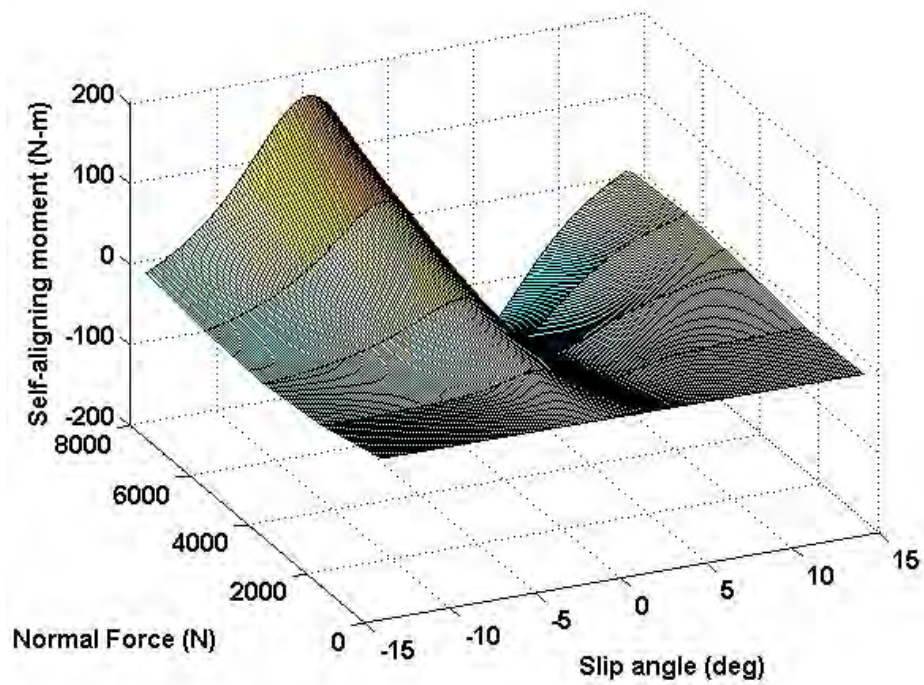
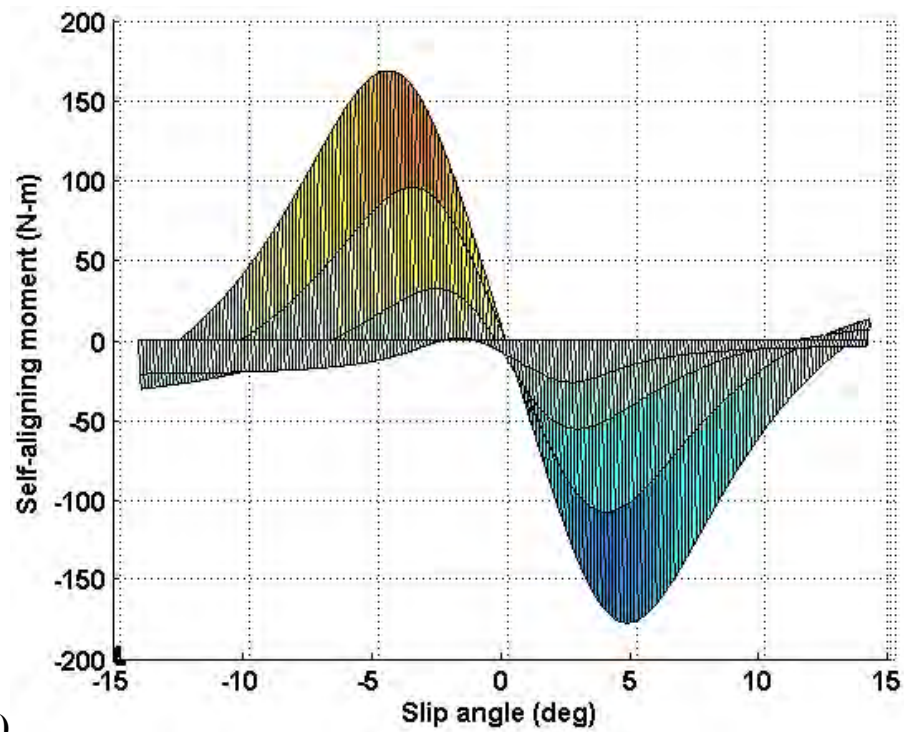


Figure 4-40: Lateral force w.r.t. normal force and slip angle



(a)



(b)

Figure 4-41: Self-aligning Moment w.r.t. normal force and slip angle

Figure 4-39, Figure 4-40, and Figure 4-41 show the longitudinal force, lateral force, and self-aligning moment with respect to normal force, longitudinal slip/skid and slip angle based on Table 4-5.[Wong,2008].

4.4.6 Friction Circle

The “friction circle” indicates the friction limit which is determined by the friction coefficient times the normal load as follows[Kim, Kim et al.,2010; Kim, Kang et al.,2011]:

$$F_{xjk}^2 + F_{yjk}^2 = (\mu F_{zjk})^2 \quad (4.76)$$

where F_{xjk} =longitudinal force (driving or braking force) at tire contact patch

F_{yjk} =lateral force (cornering force) at tire contact patch

F_{zjk} = normal force (contact force) at tire contact patch

μ = friction coefficient

The subscript $j = F, R$ represents front and rear wheel, while $k = i, o$ indicates inside and outside wheel of a vehicle, respectively.

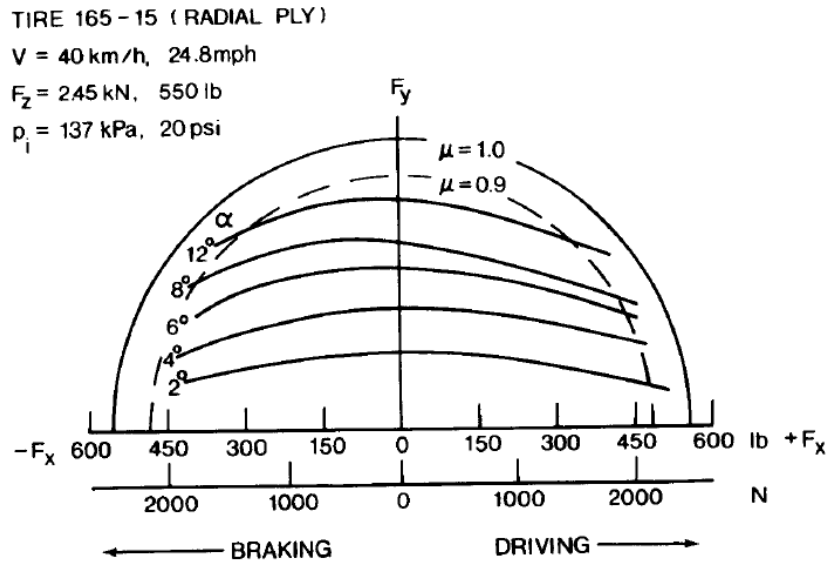


Figure 4-42: Lateral force versus longitudinal force at a given slip angle

Figure 4-42 shows lateral force (cornering force) with respect to longitudinal force (driving and braking force) for a range of slip angles[Wong,2008]. The maximum driving and braking force becomes radius of μF_z at the friction circle of each wheel which could be ‘friction ellipse’ as some tires have more traction and lateral capability associated with an elliptical boundary shape[Blundell and Harty,2004]

4.4.7 Force Margin

The normalized tire force margin related to traction force can be defined as:

$$F^m = \left(\frac{\mu F_{zjk} - \sqrt{F_{xjk}^2 + F_{yjk}^2}}{\mu F_{zjk}} \right) \times 100\% \quad (4.77)$$

Where F_{xjk} is the longitudinal force, F_{yjk} is the lateral force at each wheel, respectively. They are the operation forces acting at the tire ground contact patch of an electric vehicle. The μF_z is the available maximum traction force which constraints the maximum performance of an electric vehicle. The physical meaning of this equation as follows:

- 1) $FM = + \rightarrow$ associated wheel is operated below its maximum capability
- 2) $FM = 0 \rightarrow$ associated wheel is saturated
- 3) $FM = - \rightarrow$ associated wheel is operated with inefficient (spinning) slip

Most vehicles operate under the driving conditions of a given positive values of FM [Tesar,Nov 1, 2011].

Maximum performance of an electric vehicle is determined by one of two limitations such as traction limits or motor power to the wheels. The traction limits, influenced by various road conditions and poor weather, may be described by the available force margin, so that a driver can perceive situational awareness of all operational capability. As a result, it leads to improving mission choice and planning,

reducing vehicle rollovers, increasing fuel efficiency (range), and reducing unneeded vehicle traps. In addition, reduced tire slip/sliding will result in reducing energy consumption [Tesar,2011, August].

4.5 NONLINEAR 14 DEGREE-OF-FREEDOM FULL-VEHICLE MODEL

The nonlinear 14 DOF full-vehicle model consists of the vehicle ride (7DOF), horizontal handling (3 DOF), and tire (4 DOF) described by the Magic Formula. Before we discuss the full-vehicle model, we will discuss trajectory kinematics, anti-roll bars, center of gravity, and the normal forces of each wheel.

4.5.1 Trajectory Kinematics

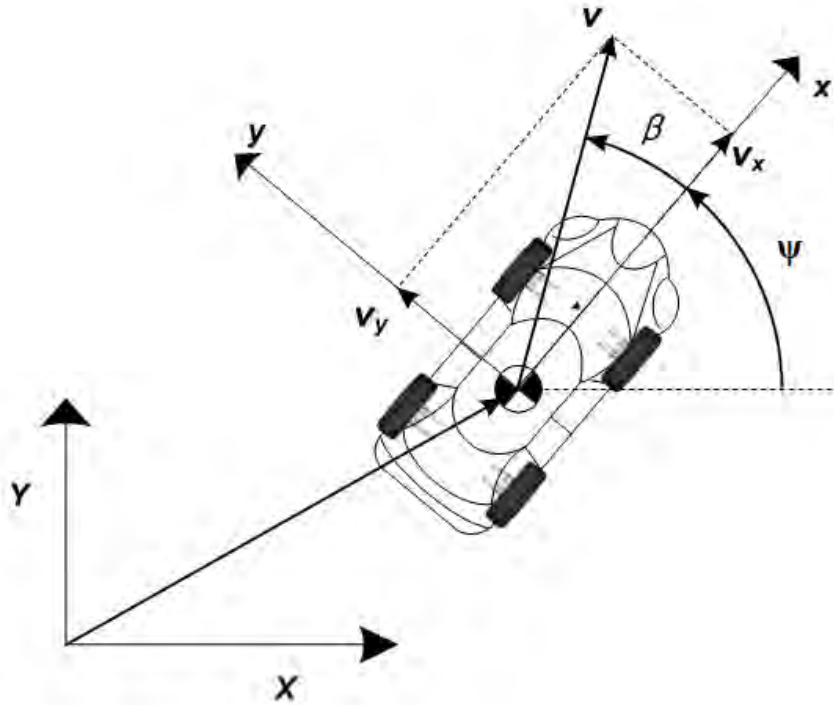


Figure 4-43: Rigid vehicle in a planar motion

A rigid vehicle in a planar motion is shown in Figure 4-43. The XY reference is the global coordinate frame, and the xy reference is a body fixed coordinate frame (i.e., axis x – longitudinal direction, axis y – lateral direction), which is attached to the CG of a vehicle. The rotation matrix from the body coordinate to the global coordinate can be expressed by:

$$R_{G \leftarrow B} = \begin{bmatrix} \cos \psi & -\sin \psi & 0 \\ \sin \psi & \cos \psi & 0 \\ 0 & 0 & 1 \end{bmatrix} \quad (4.78)$$

The CG velocity vector in global coordinates is given by:

$$V_{cg} = R_{G \leftarrow B} v_{cg} \quad (4.79)$$

The above equation becomes:

$$\begin{bmatrix} V_X \\ V_Y \\ 0 \end{bmatrix} = \begin{bmatrix} \cos \psi & -\sin \psi & 0 \\ \sin \psi & \cos \psi & 0 \\ 0 & 0 & 1 \end{bmatrix} \begin{bmatrix} v_x \\ v_y \\ 0 \end{bmatrix} = \begin{bmatrix} v_x \cos \psi - v_y \sin \psi \\ v_y \sin \psi + v_x \cos \psi \\ 0 \end{bmatrix} \quad (4.80)$$

The orientation angle (ψ) can be defined as the angle between the x and X axes. If we integrate the translational (V_X, V_Y) and rotational ($\dot{\psi}$) velocities of a rigid vehicle, the position of the vehicle is given by [Jazar, 2008]:

$$\psi(t) = \int \dot{\psi}(t) dt + \psi(t_0) \quad (4.81)$$

$$x(t) = \int (v_x \cos \psi - v_y \sin \psi) dt + x(t_0) \quad (4.82)$$

$$y(t) = \int (v_y \sin \psi + v_x \cos \psi) dt + y(t_0) \quad (4.83)$$

The cruise angle of the vehicle is the sum of the sideslip angle and the orientation angle as follows:

$$\text{Cruise angle} = \beta + \psi \quad (4.84)$$

4.5.2 Anti-Roll Bar

The stabilizer bar is called the anti-roll bar which reduces the roll of the vehicle during cornering maneuvers.

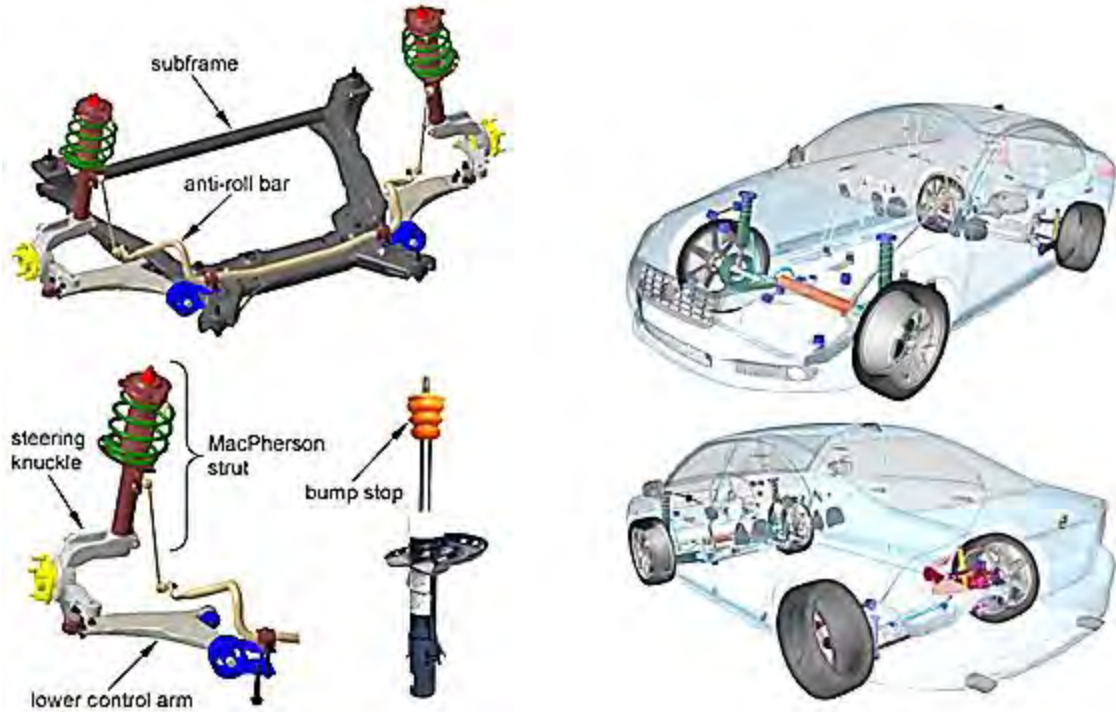


Figure 4-44: Volvo 80 MacPherson front wheel suspension and full-vehicle Adams Model[Wirje and Carlsson,2011]

Figure 4-44 shows a picture of the anti-roll bar (stabilizer bar) and suspension components. If the suspension on either the right side or the left side travels upward, the anti-roll bar twists along its length, resulting in torsional resistance. This is because of the fact that the anti-roll bar is anchored at each end to the suspension components. In this research, we neglect this anti-roll bar. We will discuss how to obtain the roll stiffness and damping from the suspension stiffness and damping.

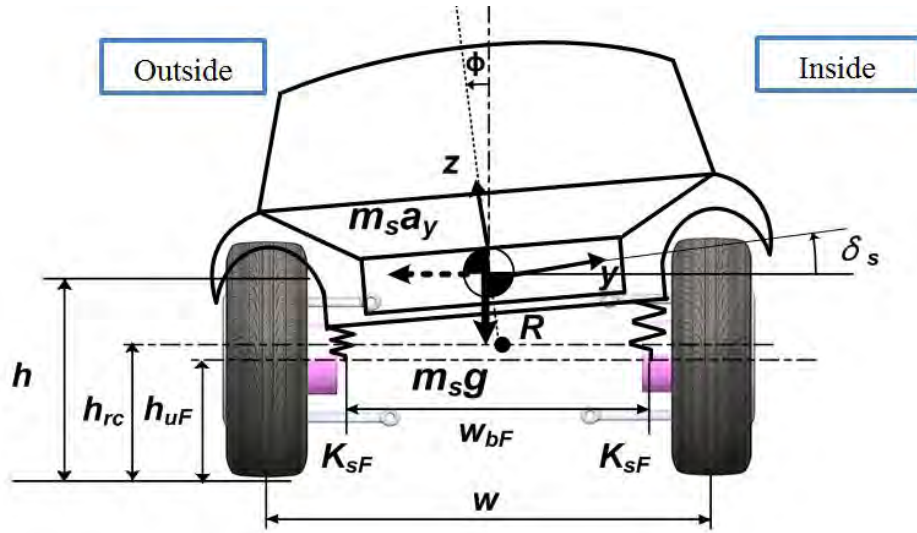


Figure 4-45: Roll moment of a vehicle in left cornering maneuver

Figure 4-45 shows the roll moment of a vehicle during a left cornering maneuver. The inertial force causes the sprung mass to rotate about the roll center (point R). The roll moment is given by:

$$M_{\theta} = m_s a_y (h - h_{rc}) \cos \phi + m_s g (h - h_{rc}) \sin \phi \quad (4.85)$$

where h = CG height

h_{rc} = roll center height

ϕ = rolling angle

If we neglect the roll angle because it is very small, the above equation becomes:

$$M_{\theta} = m_s a_y (h - h_{rc}) \quad (4.86)$$

The right-side of the first term can be expressed as:

$$m_s a_y (h - h_{rc}) = 2 \left[(k_{sF} \delta_s) \frac{w_{bF}}{2} + (k_{sR} \delta_s) \frac{w_{bR}}{2} \right] \quad (4.87)$$

where k_{sF} = suspension stiffness of front axle

k_{sR} = suspension stiffness of rear axle

w_{bF} = front wheel track between suspension

w_{bR} = rear wheel track between suspension

If deflection (δ) approximates $w_b\phi/2$, the roll angle becomes:

$$\phi = \frac{2(h - h_{rc})}{k_{sF}w_{bF}^2 + k_{sR}w_{bR}^2} m_s a_y \quad (4.88)$$

The roll stiffness associated with the suspension system is the roll moment divided by the roll angle as follows:

$$k_\phi = \frac{M_\phi}{\phi} \quad (4.89)$$

After we substitute Equation (4.86) and Equation (4.88) into Equation (4.89), the roll stiffness associated with the suspension system becomes [Gillespie,1992]:

$$k_\phi = \frac{1}{2} (k_{sF}w_{bF}^2 + k_{sR}w_{bR}^2) \quad (4.90)$$

In the same manner, the roll damping associated with the suspension system becomes:

$$c_\phi = \frac{1}{2} (c_{sF}w_{bF}^2 + c_{sR}w_{bR}^2) \quad (4.91)$$

It can be clearly seen that the roll stiffness is proportional to the square of the wheel track. That is, a large wheel track reduces the roll angle of a vehicle.

4.5.3 Center of Gravity

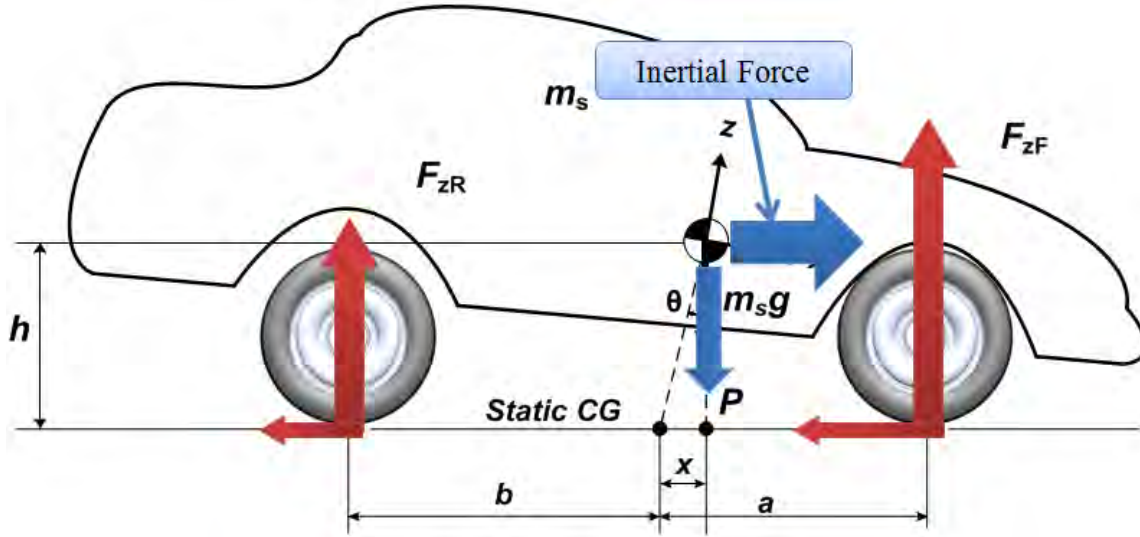


Figure 4-46: Shift of the CG in the x direction

Figure 4-46 shows the shift of the CG in the x direction due to braking. By summing the moments with respect to point P, the x position from the static CG can be obtained from:

$$\sum M_P = 0; \quad (\mu_{zRi} F_{zRi} + \mu_{zRo} F_{zRo})(b + x_{cg}) - (\mu_{zFi} F_{zFi} + \mu_{zFo} F_{zFo})(a - x_{cg}) = 0 \quad (4.92)$$

After solving for x, the above equation becomes:

$$x_{cg} = \frac{a(\mu_{zFi} F_{zFi} + \mu_{zFo} F_{zFo}) - b(\mu_{zRi} F_{zRi} + \mu_{zRo} F_{zRo})}{(\mu_{zFi} F_{zFi} + \mu_{zFo} F_{zFo}) + (\mu_{zRi} F_{zRi} + \mu_{zRo} F_{zRo})} \quad (4.93)$$

During severe acceleration and braking driving conditions, CG shifts to a position behind and ahead of the static CG, respectively.

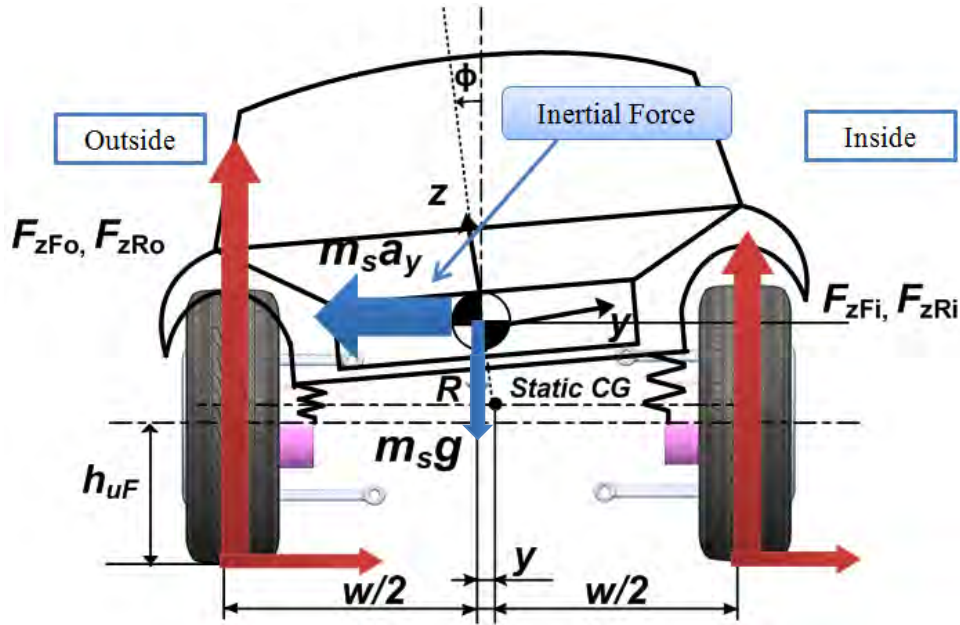


Figure 4-47: Shift of the CG in the y direction

Figure 4-47 shows the shift of the CG in the y direction due to a cornering maneuver. In this case, the CG shifts in the negative y direction. By summing the moments with respect to point R, the y position from the normal CG can be obtained from:

$$cw + \sum M_R = 0;$$

$$(\mu_{zFi} F_{zFi} + \mu_{zRi} F_{zRi}) \left(y_{cg} + \frac{w}{2} \right) - (\mu_{zRo} F_{zRo} + \mu_{zFo} F_{zFo}) \left(-y_{cg} + \frac{w}{2} \right) = 0 \quad (4.94)$$

After solving for y, the above equation becomes:

$$y_{cg} = \frac{\frac{w}{2} [(\mu_{zFi} F_{zFi} + \mu_{zRi} F_{zRi}) - (\mu_{zRo} F_{zRo} + \mu_{zFo} F_{zFo})]}{\mu_{zR} F_{zR} + \mu_{zF} F_{zF}} \quad (4.95)$$

During severe cornering maneuver, the position of CG shifts to outside or inside wheels from the static CG. Figure 4-47 shows that CG shifts to a position on the outside (right) of the static CG, based on the assumption that the vehicle is turning left.

4.5.4 Normal Forces of Each Wheel

The normal force (contact force at tire contact patch) is a vertical tire force (axle loads), which is normal to the ground plane. The resultant force acting on the tire by the road is positive if it is upward. In order to analyze the acceleration, braking, and cornering performance, it is necessary to determine the normal force. For instance, during a cornering maneuver, the load transfer occurs from the inside to the outside (or vice versa) because of the inertia force acting on the vehicle, so that the normal force varies from the static values by the amount of load transfer [Cho, Yoon et al.,2010]. The normal forces could be affected by five components [Shim and Ghike,2007; Wong,2008]:

- 1) Static normal loads (W_{sj} where $j = F, R \Rightarrow$ Front and Rear wheels)
- 2) Grade load transfer (W_{grade})
- 3) Aerodynamic load transfer (W_{aero})
- 4) Longitudinal load transfer (W_x)
- 5) Lateral load transfer (W_{yj})

Assuming that the grade and aerodynamic drag resistance is in the longitudinal direction, the normal force acting on the tire can be expressed in terms of the five components by the following equation:

$$\begin{aligned}
 F_{zFi} &= \frac{W_{sF}}{2} - \frac{(W_{aero} + W_{grade})}{2} - W_x - W_{yF} \\
 F_{zFo} &= \frac{W_{sF}}{2} - \frac{(W_{aero} + W_{grade})}{2} - W_x + W_{yF} \\
 F_{zRi} &= \frac{W_{sR}}{2} - \frac{(W_{aero} + W_{grade})}{2} + W_x - W_{yR} \\
 F_{zRo} &= \frac{W_{sR}}{2} - \frac{(W_{aero} + W_{grade})}{2} + W_x + W_{yR}
 \end{aligned} \tag{4.96}$$

In this case, assuming a left turn maneuver, the front-left wheel is the front-inside wheel, and the front-right wheel is the front-outside wheel. For instance, if we assume a constant longitudinal velocity (i.e., $W_x = 0$), and neglect aerodynamic drag and grade resistance, the normal force acting on the front-outside wheel (F_{zFo}) is larger than normal force acting on the front-inside wheel (F_{zFi}) owing to lateral load transfer. In addition, if the static normal force acting on the front-wheels (W_{sF}) is larger than the normal force acting on the rear-wheels (W_{sR}), the normal force acting on the rear-inside wheel is the smallest one of the four wheels under a cornering maneuver. We will discuss the details in Section 4.6.

4.5.4.1 Static Normal Force

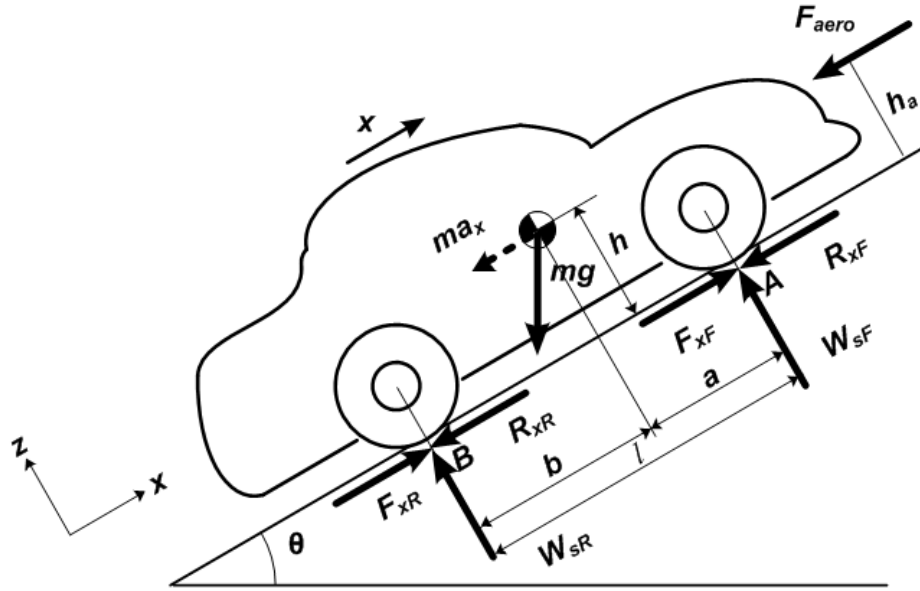


Figure 4-48: Forces acting on a vehicle

Consider a vehicle moving on an inclined road as shown in Figure 4-48. We assume that the longitudinal acceleration (a_x) is constant. That is, if the vehicle has constant pitch ($\ddot{\theta} = 0, \dot{\theta} = 0$), then these moments must sum to zero. By summing the moments with respect to point B, the static normal force on the rear axle can be obtained from:

$$cw + \sum M_B = I_{yy} \ddot{\theta} + ma_x h ; \quad (4.97)$$

$$mgb \cos \theta - mgh \sin \theta - F_{aero} h_a - W_{sF} l = ma_x h$$

The static normal force acting on the front axle becomes:

$$W_{sF} = \frac{(mgb \cos \theta - F_{grade} h - F_{aero} h_a - ma_x h)}{l} \quad (4.98)$$

Similarly, the static normal force acting on the rear axle becomes:

$$W_{sR} = \frac{(mga \cos \theta + F_{grade}h + F_{aero}h_a + ma_x h)}{l} \quad (4.99)$$

In this case, the cosine term is one and the sine term is zero on the ground level. Neglecting the aerodynamic drag force and the inertial terms, the static normal force acting on the front and rear axle is given by:

$$\begin{aligned} W_{sF} &= \frac{mgb}{l} \\ W_{sR} &= \frac{mga}{l} \end{aligned} \quad (4.100)$$

4.5.4.2 Grade Load Transfer

From Equation(4.98), it can be seen that the normal force due to the grade load transfer is given by:

$$W_{grade} = F_{grade} \frac{h}{l} = \frac{mgh \sin \theta}{l} \quad (4.101)$$

The slope angle is expressed in terms of the percent grade (%Grade = 100% $\times \tan(\theta)$).

In most cases, the approximations $\sin \theta \approx \tan \theta \approx \theta$ and $\cos \theta$ can be used.

4.5.4.3 Aerodynamic Load Transfer

From Equation(4.98), it can be seen that the normal force due to the aerodynamic load transfer can be expressed as:

$$W_{aero} = \frac{F_{aero}h_a}{l} = \frac{1}{2} \rho_a A_f C_d (v_v + v_w)^2 \frac{h_a}{l} \quad (4.102)$$

The aerodynamic drag force is proportional to the square of the vehicle velocity

4.5.4.4 Longitudinal Load Transfer

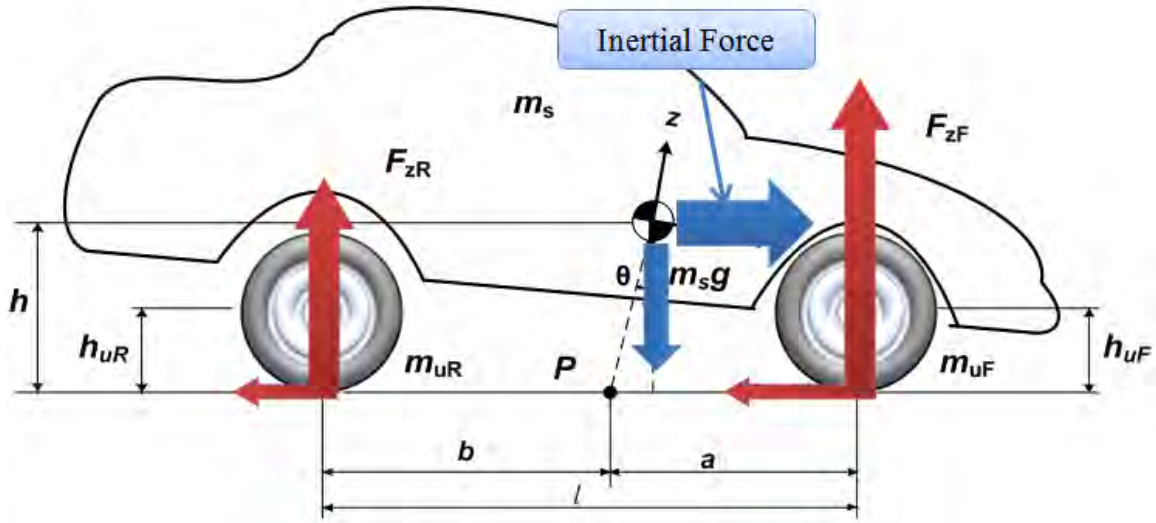


Figure 4-49: Longitudinal load transfer

During acceleration and braking operations, the load is transferred from the front axle to the rear axle (and vice versa), as shown in Figure 4-49. The longitudinal load transfer is given by:

$$W_x = \frac{(m_s h + m_{uF} h_{uF} + m_{uR} h_{uR})}{2l} (\dot{v}_x - \dot{\psi} v_y) \quad (4.103)$$

where m_s = vehicle sprung mass

m_{uF} = front unsprung mass

m_{uR} = rear unsprung mass

h = CG height

h_{uF} = height of front unsprung mass CG

h_{uR} = height of rear unsprung mass CG

l = wheel base

v_x = longitudinal velocity

v_y = lateral velocity

$\dot{\psi}$ = yaw angular velocity

4.5.4.5 Lateral Load Transfer

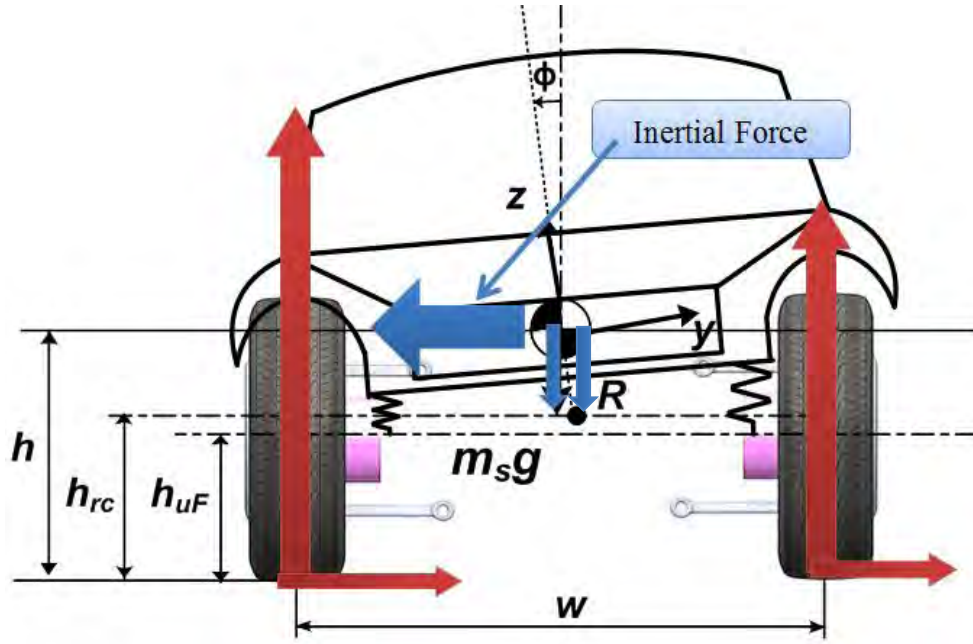


Figure 4-50: Lateral load transfer

The total lateral load transfer of the front and rear suspension systems occurs because of the roll center height, unsprung mass, and body roll as follows:

$$\begin{aligned} W_{yF} &= W_{rF} + W_{uF} + W_{bF} \\ W_{yR} &= W_{rR} + W_{uR} + W_{bR} \end{aligned} \quad (4.104)$$

where W_{yF}, W_{yR} = total front / rear lateral load transfer

W_{rF}, W_{rR} = front / rear lateral load transfer due to rolling center height

W_{uF}, W_{uR} = front / rear lateral load transfer due to unsprung mass

W_{bF}, W_{bR} = front / rear lateral load transfer due to body roll

Figure 4-50 shows the lateral load transfer. The lateral load transfer due to the rolling center height is given by:

$$\begin{aligned}
W_{rF} &= \frac{m_s b (h_{cg} - h_{rcF})}{wl} (\dot{v}_y + \dot{\psi} v_x) \\
W_{rR} &= \frac{m_s a (h_{cg} - h_{rcF})}{wl} (\dot{v}_y + \dot{\psi} v_x)
\end{aligned} \tag{4.105}$$

The lateral load transfer due to the unsprung mass becomes:

$$\begin{aligned}
W_{uF} &= \frac{m_{uF} h_{uF}}{w} (\dot{v}_y + \dot{\psi} v_x) \\
W_{uR} &= \frac{m_{uR} h_{uR}}{w} (\dot{v}_y + \dot{\psi} v_x)
\end{aligned} \tag{4.106}$$

The lateral load transfer due to body roll for both suspensions can be expressed as:

$$W_{bF} = \frac{(k_{\phi} \phi + c_{\phi} \dot{\phi})}{w} \tag{4.107}$$

Because the combined roll stiffness and damping is largely due to the suspension spring and absorbers, we can substitute Equation (4.90) and (4.91) into Equation (4.107). Assuming that the rear and front wheel tracks are the same, the resulting equation can be expressed as:

$$W_{bF} = \frac{\left(\frac{1}{2} (k_{sF} w_{bF}^2 + k_{sR} w_{bR}^2) \phi + \frac{1}{2} (c_{sF} w_{bF}^2 + c_{sR} w_{bR}^2) \dot{\phi} \right)}{w} \tag{4.108}$$

If the stiffness and damping of the front and rear corners are the same, the above equation becomes:

$$W_{bF} = \frac{1}{w} (k_{sF} w_{bF}^2 \phi + c_{sF} w_{bF}^2 \dot{\phi}) \tag{4.109}$$

When we substitute Equation (4.105), (4.106), and (4.109) into Equation (4.104), the resulting equation becomes:

$$\begin{aligned}
W_{yF} &= \left\{ \frac{m_s b (h_{cg} - h_{rcF})}{wl} + \frac{m_{uF} h_{uF}}{w} \right\} (\dot{v}_y + \dot{\psi} v_x) + \frac{1}{w} (k_{sF} w_{bF}^2 \phi + c_{sF} w_{bF}^2 \dot{\phi}) \\
W_{yR} &= \left\{ \frac{m_s a (h_{cg} - h_{rcR})}{wl} + \frac{m_{uR} h_{uR}}{w} \right\} (\dot{v}_y + \dot{\psi} v_x) + \frac{1}{w} (k_{sF} w_{bF}^2 \phi + c_{sF} w_{bF}^2 \dot{\phi})
\end{aligned} \tag{4.110}$$

Consequently, combining Equations (4.100), (4.101), (4.102), (4.103), and (4.110)

into Equation (4.96), the resulting normal force of each wheel becomes:

$$\begin{aligned}
F_{zFi} &= \left(\frac{m_s g b}{2l} + m_{uF} g \right) - \left\{ \frac{1}{2} \rho_a A_f C_d (v_x + v_w)^2 + mg \sin \theta \right\} \frac{h}{2l} \\
&\quad - \frac{(m_s h + m_{uF} h_{uF} + m_{uR} h_{uR})}{2l} (\dot{v}_x - \dot{\psi} v_y) \\
&\quad - \left\{ \frac{m_s b (h_{cg} - h_{rcF})}{wl} + \frac{m_{uF} h_{uF}}{w} \right\} (\dot{v}_y + \dot{\psi} v_x) - \frac{1}{w} (k_{sF} w_{bF}^2 \phi + c_{sF} w_{bF}^2 \dot{\phi}) \\
F_{zFo} &= \left(\frac{m_s g b}{2l} + m_{uF} g \right) - \left\{ \frac{1}{2} \rho_a A_f C_d (v_x + v_w)^2 + mg \sin \theta \right\} \frac{h}{2l} \\
&\quad - \frac{(m_s h + m_{uF} h_{uF} + m_{uR} h_{uR})}{2l} (\dot{v}_x - \dot{\psi} v_y) \\
&\quad + \left\{ \frac{m_s b (h_{cg} - h_{rcF})}{wl} + \frac{m_{uF} h_{uF}}{w} \right\} (\dot{v}_y + \dot{\psi} v_x) + \frac{1}{w} (k_{sF} w_{bF}^2 \phi + c_{sF} w_{bF}^2 \dot{\phi}) \\
F_{zRi} &= \left(\frac{m_s g a}{2l} + m_{uR} g \right) + \left\{ \frac{1}{2} \rho_a A_f C_d (v_x + v_w)^2 + mg \sin \theta \right\} \frac{h}{2l} \\
&\quad + \frac{(m_s h + m_{uF} h_{uF} + m_{uR} h_{uR})}{2l} (\dot{v}_x - \dot{\psi} v_y) \\
&\quad - \left\{ \frac{m_s a (h_{cg} - h_{rcF})}{wl} + \frac{m_{uR} h_{uR}}{w} \right\} (\dot{v}_y + \dot{\psi} v_x) - \frac{1}{w} (k_{sF} w_{bF}^2 \phi + c_{sF} w_{bF}^2 \dot{\phi}) \\
F_{zRo} &= \left(\frac{m_s g a}{2l} + m_{uR} g \right) + \left\{ \frac{1}{2} \rho_a A_f C_d (v_x + v_w)^2 + mg \sin \theta \right\} \frac{h}{2l} \\
&\quad + \frac{(m_s h + m_{uF} h_{uF} + m_{uR} h_{uR})}{2l} (\dot{v}_x - \dot{\psi} v_y) \\
&\quad + \left\{ \frac{m_s a (h_{cg} - h_{rcF})}{wl} + \frac{m_{uR} h_{uR}}{w} \right\} (\dot{v}_y + \dot{\psi} v_x) + \frac{1}{w} (k_{sF} w_{bF}^2 \phi + c_{sF} w_{bF}^2 \dot{\phi})
\end{aligned} \tag{4.111}$$

Based on the suspension force from Equation (4.43), the above equations are equivalent to the following equations:

$$\begin{aligned}
F_{zFi} &= \left(\frac{m_s g b}{2l} + m_{uF} g \right) - \left\{ \frac{1}{2} \rho_a A_f C_d (v_x + v_w)^2 + mg \sin \theta \right\} \frac{h}{2l} \\
&\quad + c_{sF} (\dot{z}_{uFi} - \dot{z}_{sFi}) + k_{sF} (z_{uFi} - z_{sFi}) \\
F_{zFo} &= \left(\frac{m_s g b}{2l} + m_{uF} g \right) - \left\{ \frac{1}{2} \rho_a A_f C_d (v_x + v_w)^2 + mg \sin \theta \right\} \frac{h}{2l} \\
&\quad + c_{sF} (\dot{z}_{uFo} - \dot{z}_{sFo}) + k_{sF} (z_{uFo} - z_{sFo}) \\
F_{zRi} &= \left(\frac{m_s g a}{2l} + m_{uR} g \right) + \left\{ \frac{1}{2} \rho_a A_f C_d (v_x + v_w)^2 + mg \sin \theta \right\} \frac{h}{2l} \\
&\quad + c_{sR} (\dot{z}_{uRi} - \dot{z}_{sRi}) + k_{sR} (z_{uRi} - z_{sRi}) \\
F_{zRo} &= \left(\frac{m_s g a}{2l} + m_{uR} g \right) + \left\{ \frac{1}{2} \rho_a A_f C_d (v_x + v_w)^2 + mg \sin \theta \right\} \frac{h}{2l} \\
&\quad + c_{sR} (\dot{z}_{uRo} - \dot{z}_{sRo}) + k_{sR} (z_{uRo} - z_{sRo})
\end{aligned} \tag{4.112}$$

4.5.5 Nonlinear 14 Degree-of-Freedom Full-Vehicle Model

The nonlinear 14 DOF full-vehicle model consists of the vehicle ride (7DOF) model, horizontal handling (3 DOF) model, and tire (4 DOF) model with the Magic Formula [Setiawan, Safarudin et al.,2009]. The input to the full-vehicle model is composed of driver inputs (i.e., steering angle, torque, and brake) and road conditions (i.e., concrete, asphalt, gravel, and poor weather) [Kadir, Hudha et al.,2011]. As can be seen in Figure 4-51, a small block diagram is the ride model, handling model, tire model, slip ratio, slip angle, and magic formula.

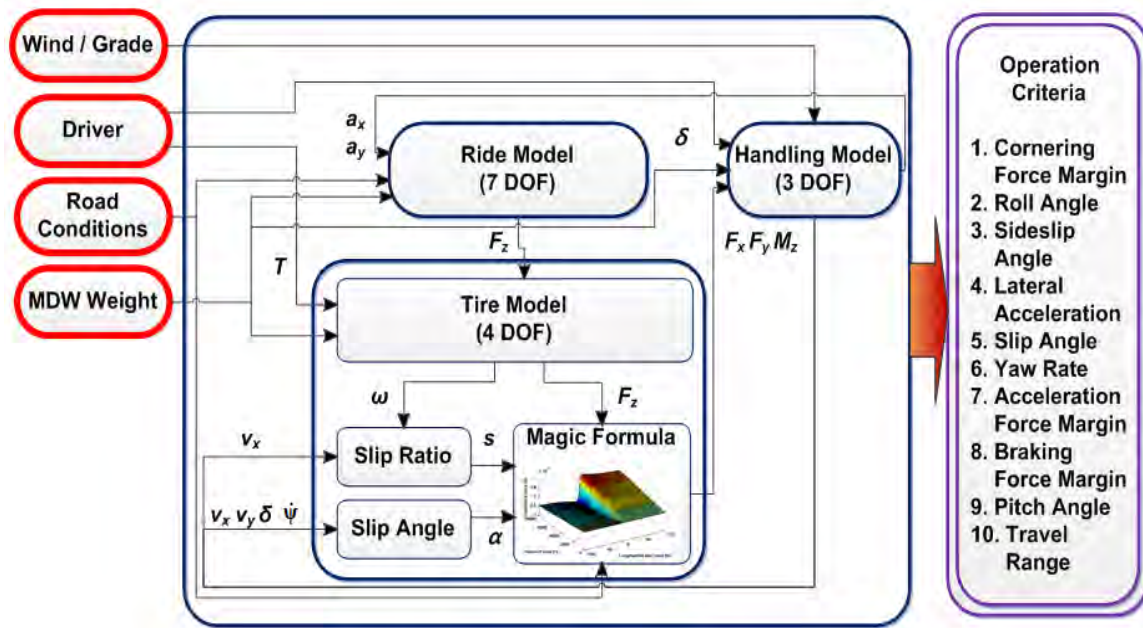


Figure 4-51: Schematic diagram of 14 DOF full-vehicle model consisting of block diagrams in MATLAB/SIMULINK

The control parameters are wind / grade, driver (i.e. torque, steering angle), road conditions, and MDW weight. The operation performance criteria such as cornering force

margin, roll angle, sideslip angle, lateral acceleration, slip angle, yaw rate, acceleration force margin, braking force margin, pitch angle, and travel range can be affected through the nonlinear 14 DOF full-vehicle model, which is governed by the input control parameters.

As shown in Figure 4-51, the horizontal handling (3 DOF) model takes the steering angle (δ) determined by the driver as well as the longitudinal (F_x), lateral (F_y) forces, and self-aligning moment (M_z) as input and determines the vehicle's longitudinal (a_x) and lateral (a_y) acceleration. In addition, it determines the longitudinal (v_x) velocity, lateral (v_y) velocity, and yaw angular velocity ($\dot{\psi}$).

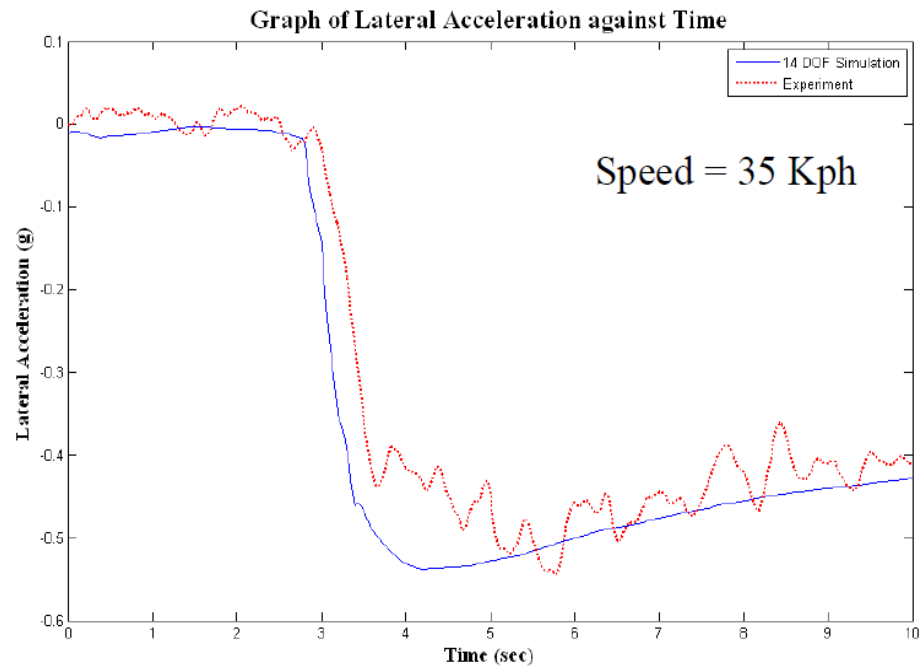
Second, the vehicle ride (7 DOF) model takes longitudinal (a_x) and lateral (a_y) acceleration and road conditions as input. It determines the normal force (F_z). Last, the tire (4 DOF) model takes the normal force (F_z) and motor torque (T) as input to estimate the wheel angular velocity (ω). The block diagram for the slip ratio determines a slip ratio (s) which is determined by the wheel angular velocity and longitudinal velocity, whereas the block diagram of a slip angle determines a slip angle (α) which is affected by the longitudinal velocity, lateral velocity, yaw angular velocity, and steering angle. The block diagram for the Magic Formula takes the normal force, slip ratio, and slip angle as input and determines the longitudinal, lateral forces, and self-aligning moment to the horizontal handling model.

4.5.6 Validation of a Nonlinear 14 Degree-of-Freedom Full-Vehicle Model

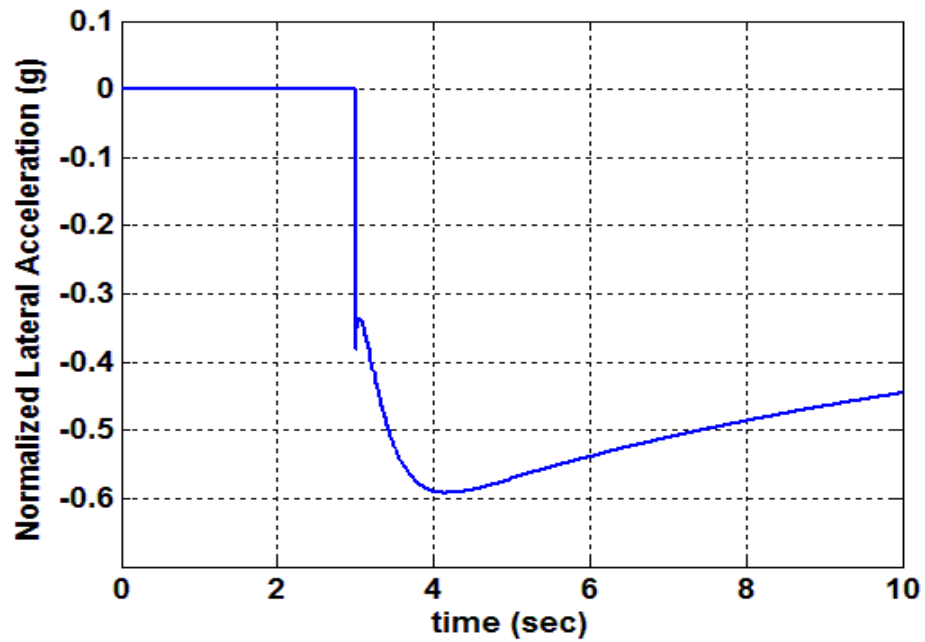
The nonlinear 14 DOF full-vehicle model used in this research was implemented in a MATLAB/SIMULINK environment. The simulation results have been compared and validated based on a previous research paper [Setiawan, Safarudin et al., 2009], which performed experimental work using an instrumented experimental vehicle.

The modeling assumptions for the validation are as follows:

- 1) The vehicle body (sprung mass) and wheel (unsprung mass) are lumped as single masses, respectively
- 2) Aerodynamic drag, grade, and rolling resistance are neglected
- 3) Suspensions are modeled as passive viscous dampers and springs
- 4) The outer and inner steering angle are the same
- 5) Suspension systems keep the four tires in firm contact with the road (i.e., good road holding) under cornering and braking.
- 6) The steering system is modeled as a constant gear ratio (18:1) between the steering wheel angle and steering angle of a tire
- 7) Neglect steering inertia and the stabilizer bar effect
- 8) The vehicle is moving on a flat road during step steer

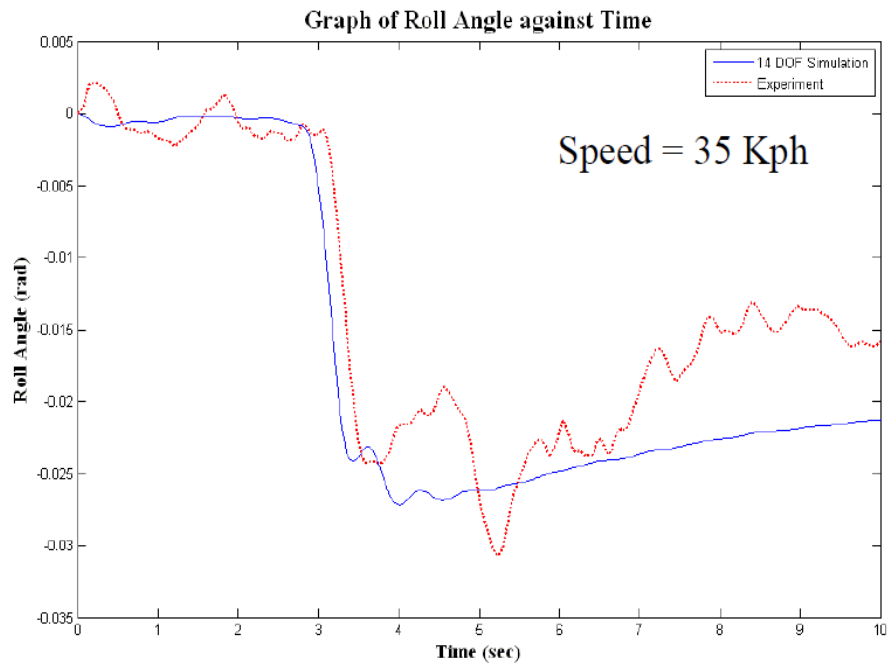


(a) Lateral acceleration response to a 180° step steer[Setiawan, Safarudin et al.,2009]

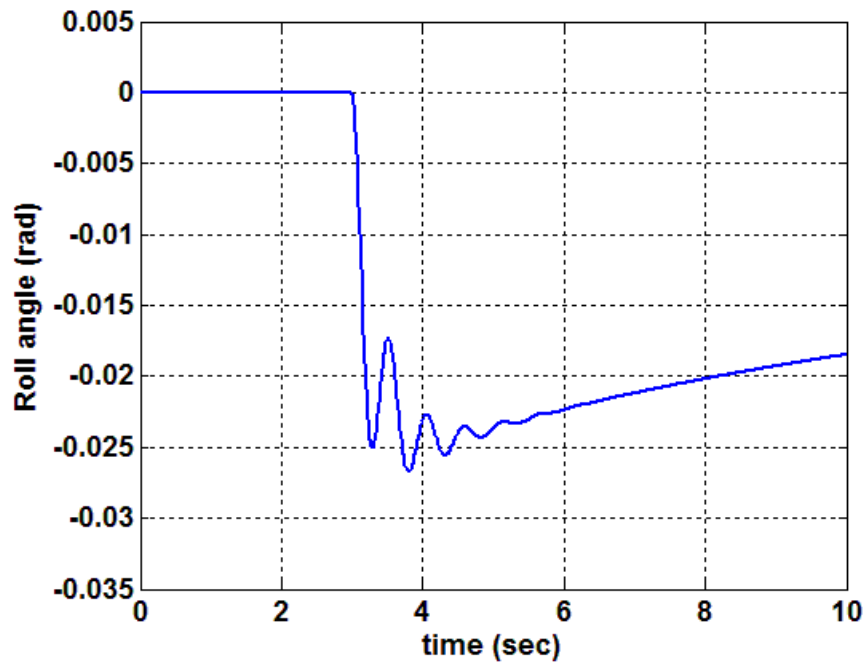


(b) Simulation result of lateral acceleration to a 180° step steer

Figure 4-52: Validation of lateral acceleration response



(a) Lateral acceleration response to a 180° step steer [Setiawan, Safarudin et al., 2009]



(b) Simulation result of lateral acceleration response to a 180° step steer

Figure 4-53: Validation of roll angle response

The step steer test can be used for evaluating the transient response of the vehicle under the steering wheel angle input. The 180° step steer was performed at 35 kph (22 mph) [Setiawan, Safarudin et al.,2009]. Assuming that the steering gear ratio is 18 to 1, the steering angle will be 10° as a result of the steering wheel angle (180°) being divided by the steering gear ratio (18). We used 10° as the steering angle to match the parameters of the reference paper. Since we assume a counter-clock wise steering angle as positive, the input (-10°) indicates a clockwise steering angle, resulting in a negative lateral acceleration and roll angle. In other words, the vehicle experiences a right cornering maneuver rather than a left cornering maneuver.

Figure 4-52 shows the validation of the lateral acceleration in response to a 180° step steer. The simulation result of a Simulink model is shown in Figure 4-52 (b), and the previous result is shown in Figure 4-52 (a). A step steering wheel angle of 180° is applied to the 14 DOF vehicle model at 3 s. The simulation result of the lateral acceleration reached -5.9 m/s^2 , and then decreased to 4.5 m/s^2 . This simulation result is closely matched with that of the research paper, as shown in Figure 4-52 (a). The existing discrepancies may come from differences in the Magic Formula data: we use the Magic Formula data [Bakker, Nyborg et al.,1987; Wong,2008], where this empirical data was obtained from performing on a dry asphalt road condition.

Figure 4-53 shows the validation of the roll angle in response to a 180° step steer. Figure 4-53 (a) and (b) shows the paper's result and the simulation result of a Simulink model, respectively. Under the same conditions, the simulation result of a roll angle varied from 0.027 rad (1.55°) to 0.018 rad (1°). This simulation result is closely matched with that of the paper as shown in Figure 4-53 (a).

It can be concluded that the nonlinear 17 DOF full-vehicle model, which is implemented in a MATLAB/SIMULINK environment, is valid because the response of

this model closely follows the response generated by [Setiawan, Safarudin et al.,2009]. Therefore, we can conclude that the vehicle model of this research is acceptable and valid.

4.5.7 Transient and Steady State Response

Many studies have been evaluated for the roll angle and lateral acceleration response to step steer [Ghike and Shim,2006; Shim and Ghike,2007; Zhao, Chen et al.,2011]. These researchers evaluated the roll angle response based on a 14 DOF model, CARSIM, and the ADAMS/Car program.

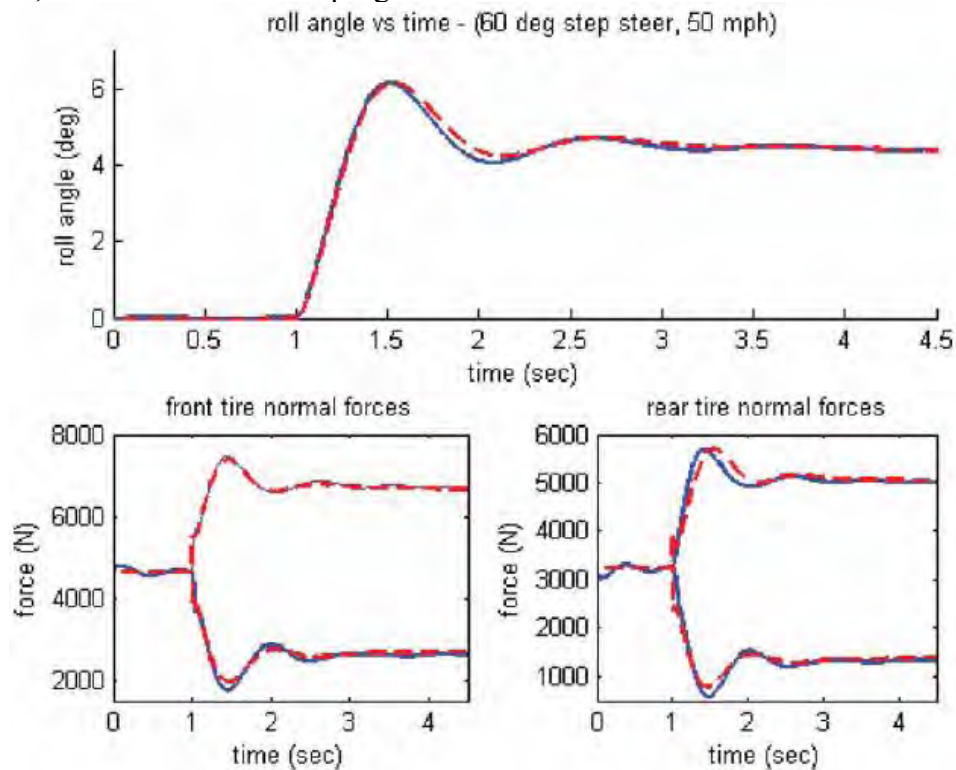


Figure 4-54: Comparative responses to step steer (14 DOF and 8 DOF models)
[Shim and Ghike,2007]

Figure 4-54 shows the comparative responses to a 60° step steer. It can be seen that the transient response occurs from 1 to 3 s, and then the roll angle reaches 4° as a steady state response. In contrast, the roll angle of our Simulink model decreased as shown in Figure 4-53.

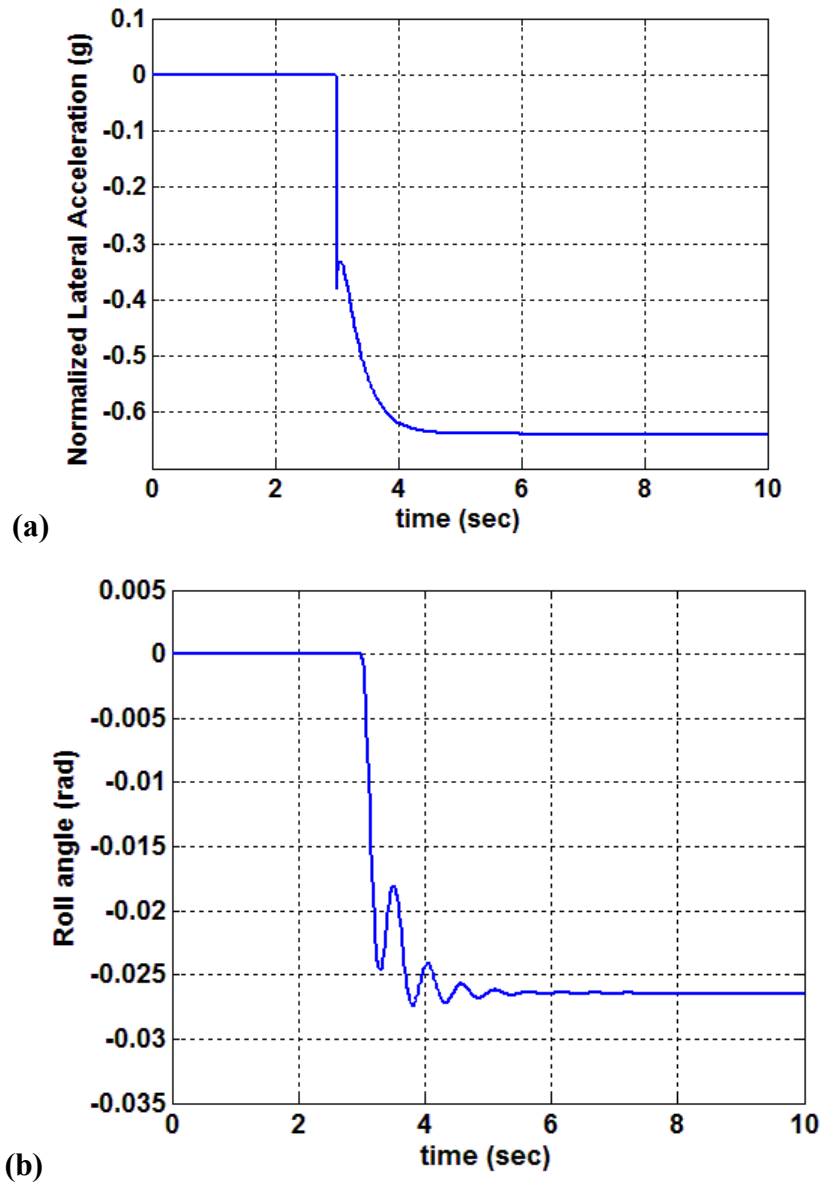


Figure 4-55: Validation of lateral acceleration and roll angle response to a step steer

The differences may come from the nonlinearity of the different tire models: we use the Magic Formula data [Bakker, Nyborg et al.,1987; Wong,2008]. To examine the vehicle roll response at steady state, we modified the Simulink model so that constant longitudinal velocity is maintained during the simulation. Therefore, the normalized lateral acceleration and lateral roll angle respond to 180° step steer as shown in Figure 4-55.

It can be seen that the normalized lateral acceleration and roll angle values rise toward the equilibrium points of -0.63 and -0.227 rad, respectively. If the steering angle is positive, the results will be a positive normalized lateral acceleration and roll angle, respectively. Lateral acceleration is related to the rollover threshold which is “ t over $2h$ ”. For instance, rollover threshold of a passenger car with a CG height (h) of 24 inch and wheel tread (t) of 60 inch is around 1.25 g. The rollover threshold is different for different vehicle sizes. The decreasing the CG height and increasing the track width lead to the rollover threshold increases. [Gillespie,1992; Marimuthu, Andres et al.,2005].

4.6 CHAPTER SUMMARY

In this chapter, we discussed the handling and ride comfort performance map (Sec. 4.2.1). The handling performance map is evaluated based on the dynamic contact force, which is a measure of road holding. The ride comfort performance map is evaluated based on the frequency weighted RMS sprung acceleration. We conclude that the worst disadvantage is to increase the dynamic contact force, which deteriorate the handling characteristics. As mentioned previously, minimizing the variations in the dynamic contact force leads to improving cornering, braking, and traction.

Second, we discussed the nonlinear 14 DOF full-vehicle model consisting of block diagrams which are the ride model, handling model, tire model, slip ratio, slip

angle, and magic formula (Sec. 4.5.5.). Each block diagram in this research is implemented in a MATLAB/SIMULINK environment. The simulation results have been compared and validated based on previous research paper [Setiawan, Safarudin et al.,2009]. The control parameters are wind / grade, driver (i.e. torque, steering angle), road conditions, and MDW weight. We will simulate the vehicle modeling how these control parameters affect the performance criteria such as acceleration, braking, and force margin in handling. The various road conditions are the dry asphalt, wet asphalt, and snowy road, resulting in different friction coefficient (μ). The MDW weight is associated with different weight of wheels such as 16, 20, 24, 32, up to 40 hp which would become customer choices.

Chapter 5. Vehicle Simulation Results

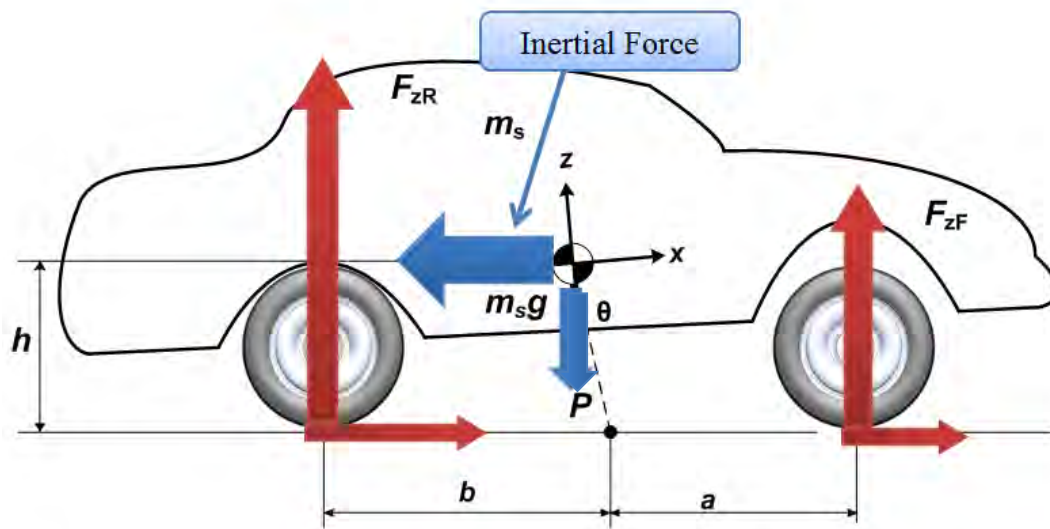
Equation Chapter 5 Section 1 In this chapter, the simulation results were performed through the nonlinear 14 DOF full vehicle model. The effects of unsprung mass on performance criteria such as acceleration, braking, and cornering maneuver (i.e., step steer and single-lane change) are presented in Sec. 5.1. The effects of increased unsprung mass under various road conditions such as dry asphalt, wet asphalt, and a snowy road will be explained in Sec. 5.2. The vehicle behaviors will be examined by simulation results in terms of acceleration, braking, and cornering maneuver. The cornering force margin performance maps are explained in Sec. 5.3. and Sec. 5.4., under the different vehicle weight and same vehicle weight.

5.1 EFFECTS OF UNSPRUNG MASS ON PERFORMANCE CRITERIA

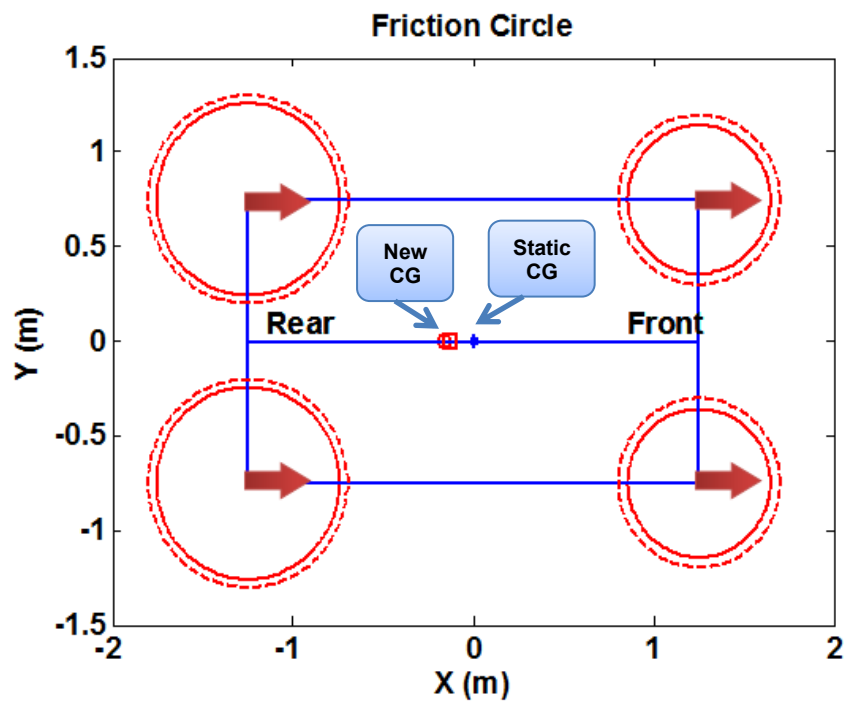
The Multi-Speed Hub Drive Wheels (MDWs), which are unsprung masses, will have different wheel sizes depending on the power size, such as 16, 20, 24, 32, and up to 40 hp which would become a customer choice. In this section, we discuss the effects of unsprung mass on performance criteria such as acceleration, braking, and cornering maneuvers.

5.1.1 Acceleration

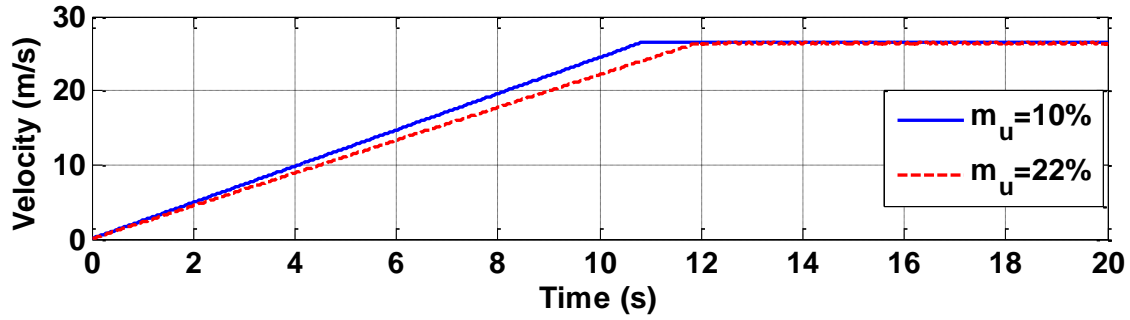
The acceleration of an electric vehicle depends primarily on the torque generated by the motor. From the customer point of view, acceleration is judged by the time required to go from 0 to 60 mph.



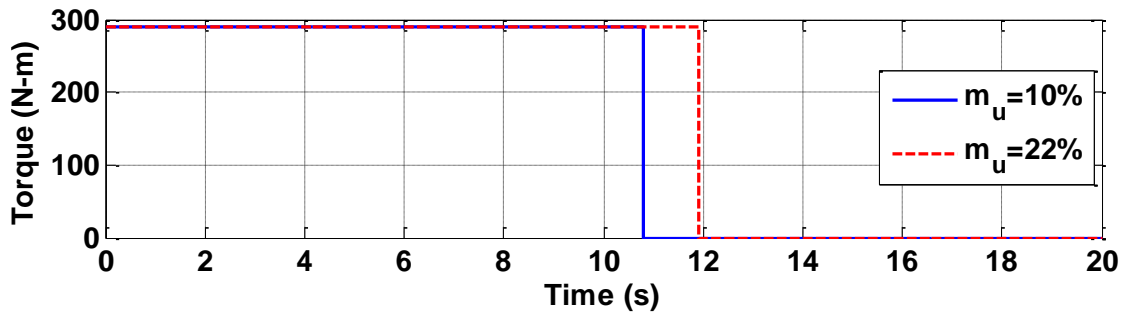
(a) Vehicle motion due to longitudinal acceleration



(b) Friction circles of each wheel (top view)



(c) Velocity profile



(d) Wheel torque command

Figure 5-1: Simulation results for acceleration of 0-60 mph

A vehicle with $m_u = 10\%$ reaches a velocity of 26.4 m/s (60 mph) from rest with constant acceleration (0.25g) for $t = 10.8$ s, while a vehicle with $m_u = 22\%$ reaches a velocity of 26.4 m/s from rest with constant acceleration (0.233g) for $t = 11.9$ s with same wheel torque command. At that time, the vehicle experiences rear squatting, as shown in Figure 5-1 (a), owing to the acceleration inertial force. Figure 5-1 (b) shows what the friction circles look like at that time. Figure 5-1 (c) and (d) shows the velocity profile and wheel torque, respectively, based on the 14 DOF full-vehicle model. In the Simulink simulation, it is assumed that the vehicle is simulated with the fixed sprung mass, while unsprung mass increases in terms of the unsprung-to-sprung mass ratio such as 10% and 22%, as described in Table 5-1. As a result, the total weight of a vehicle increases as

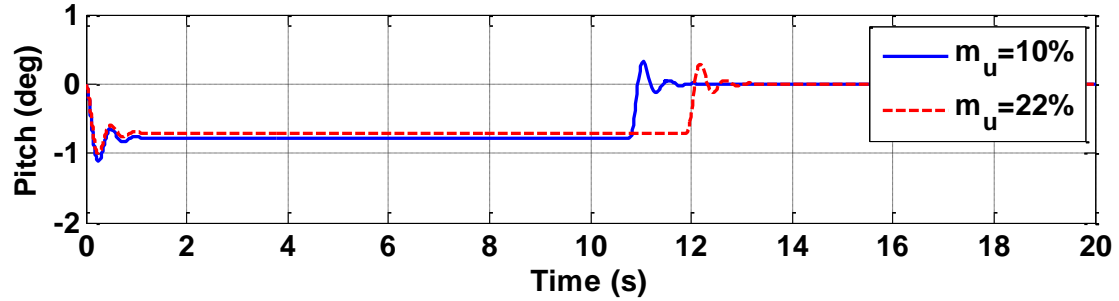
unsprung mass increases. We will discuss the simulation results that the total weight of a vehicle doesn't vary, as unsprung mass increases in Sec. 4.8 chapter summary.

	Parameters	Value	Units	Value	Units
Vehicle sprung mass	m_s	1360	kg	3000/g	slug
Unsprung mass (0.1, reference car)	m_u	136	kg	300	lb
Unsprung mass (0.22, MDW 32 hp)	m_u	300	kg	660	lb
Distance from front axle to vehicle CG	a	1.25	m	49.2	in
Distance from rear axle to vehicle CG	b	1.25	m	49.2	in
Vehicle track width	w	1.5	m	59	in
Vehicle CG	h	0.61	m	24	in
Rolling center height	h_{ra}	0.3	m	15.7	in
Yaw moment of inertia	I_z	3190	kg-m ²	2353	slug-ft ²
Roll moment of inertia	I_{xx}	400	kg-m ²	295	slug-ft ²
Pitch moment of inertia	I_{yy}	400	kg-m ²	295	slug-ft ²
Suspension damping	c_s	1.5	kN-s/m	8.53	lb-s/in
Suspension stiffness	k_s	35	kN/m	199	lb/in

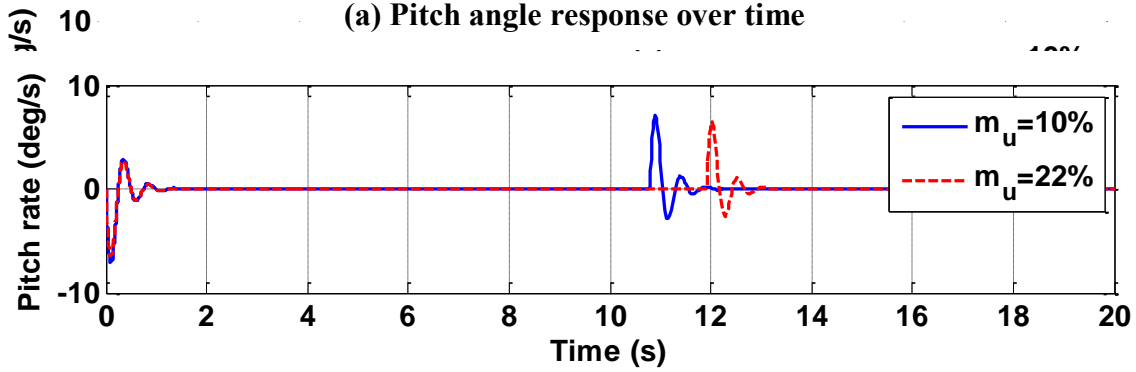
Table 5-1: Vehicle parameters used in simulation

Figure 5-1 (c) shows that a vehicle with an unsprung-to-sprung mass ratio of 0.1 is faster than that with an unsprung-to-sprung mass ratio of 0.22; 0-60 mph (26.4 m/s) acceleration times for a vehicle ($m_u/m_s = 0.1$) are around $t = 10.8$ s, and a vehicle with a $m_u/m_s = 0.22$ reaches in $t = 11.9$ s. The wheel torque command is 290 N-m (214 ft-lb), as

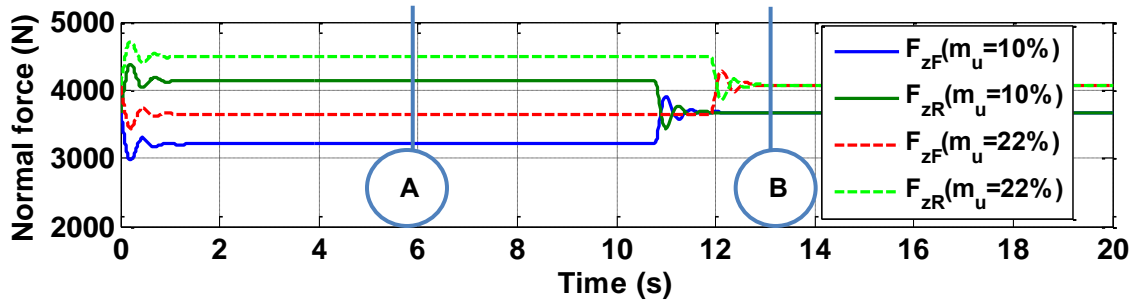
shown in Figure 5-1 (d). For comparison purposes, we do not consider aerodynamic, rolling, and grade resistances in this analysis.



(a) Pitch angle response over time



(b) Pitch rate response over time



(c) Normal force of front and rear wheels response over time

Figure 5-2: Simulation results of vehicle response for acceleration of 0–60 mph

Figure 5-2 (a) - (c) shows plots of pitch angle, pitch rate, and normal force of front and rear wheels based on the 14 DOF full-vehicle model, respectively. As can be

seen in Figure 5-2 (a), the pitch angle of a vehicle with a $m_u = 10\%$ is larger than that of a vehicle with a $m_u = 22\%$, and the associated pitch rate is shown in Figure 5-2 (b). During acceleration, the dynamic load is transferred from the front axle to the rear axle, as shown in Figure 5-2 (c). The normal force is defined a vertical force acting on the tire by the road

	Rear wheels (F_{zR})				Front wheels (F_{zF})			
	$m_u = 10\%$		$m_u = 22\%$		$m_u = 10\%$		$m_u = 22\%$	
A (t = 6s)	4139	N	4493	N	3207	N	3650	N
{Acceleration}	930	lb	1010	lb	721	lb	821	lb
B (t = 13s)	3673	N	4072	N	3673	N	4072	N
	826	lb	915	lb	826	lb	915	lb

Table 5-2: Normal forces of each wheel during acceleration

Regarding a vehicle with a $m_u = 10\%$, the load starts transferring from the front axle to the rear axle around 466 N (105 lb), which is calculated by 4139 N (A, t = 6 s) minus 3673 N (B, t = 13 s) as tabled in Table 5-2. The longitudinal load transfer can be approximated by Equation as follows:

$$W_x = \frac{(m_s h + m_{uF} h_{uF} + m_{uR} h_{uR})}{2l} (0.25g) \quad (5.1)$$

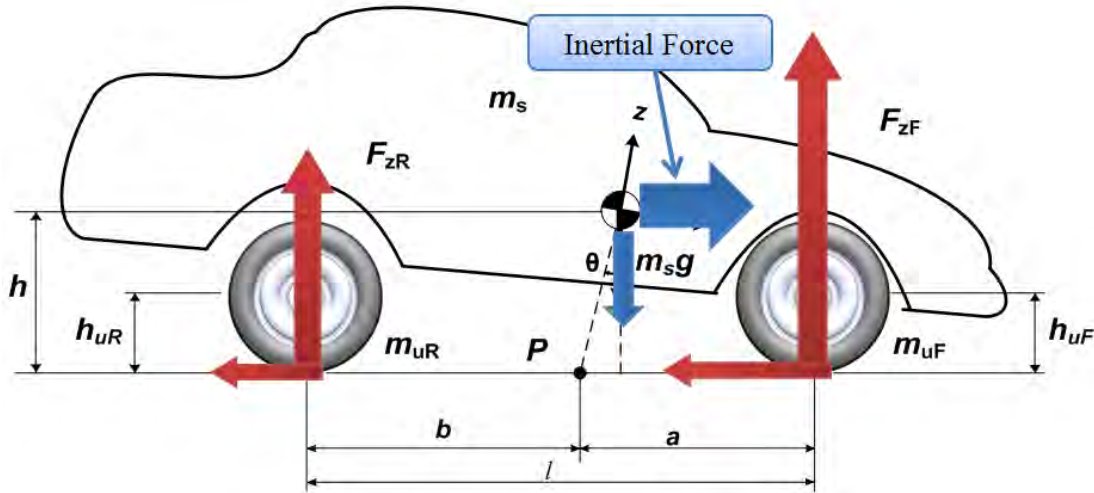
The symbol ‘A’ and ‘B’ indicate t = 6 s and t = 13 s, respectively. Regarding a vehicle with a $m_u = 22\%$, the transferred load is around 421 N (95 lb), which is obtained from 4493 N (1010 lb) minus 4072 N (915 lb). The detailed numerical numbers are tabled in Table 5-2.

5.1.2 Braking

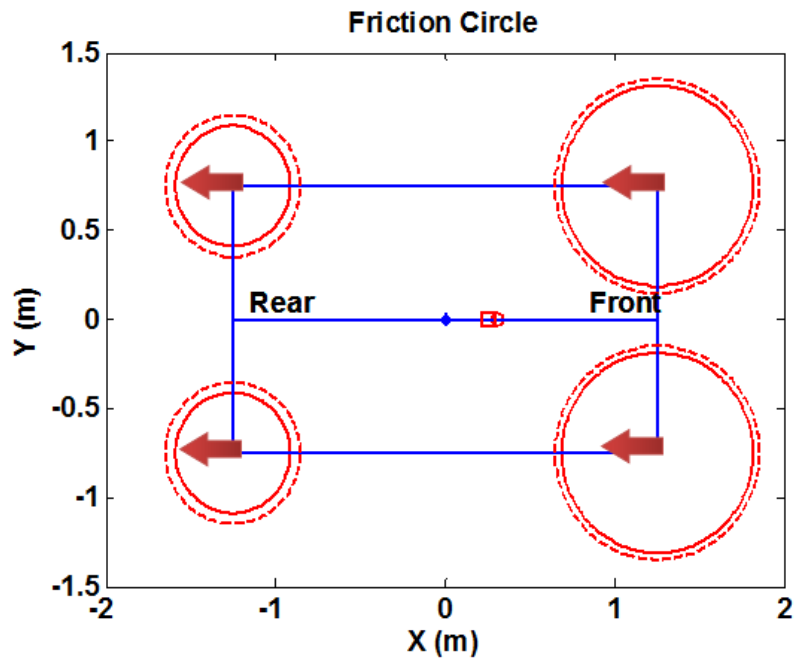
The braking performance can be a measure of stopping distance. According to [Wei and Rizzoni,2004], stopping distance consists of reaction distance and braking distance. The former is the distance from the time a driver perceives a hazard to the time he/she steps on the brake. The latter is the distance a vehicle travels from the time that a driver applies the brake until the vehicle comes to a complete stop. With full braking on dry, level asphalt and an average perception-reaction time of 1.5 s, the formula is given by:

$$\text{stopping distance} = 2.2V + 0.048V^2 \quad (5.2)$$

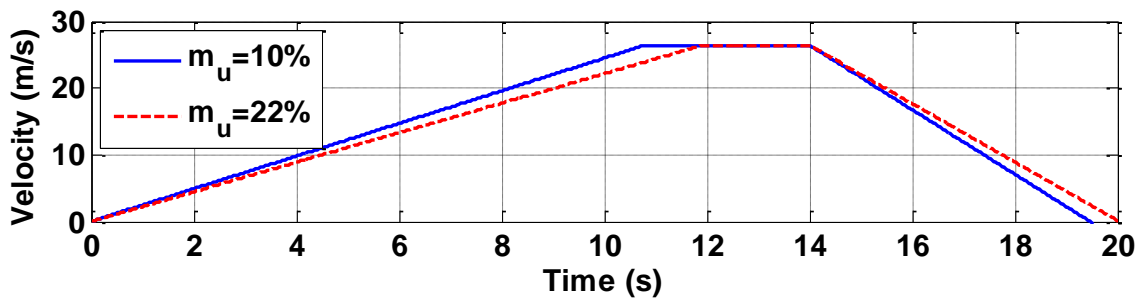
where stopping distance is in feet and velocity is in mph.



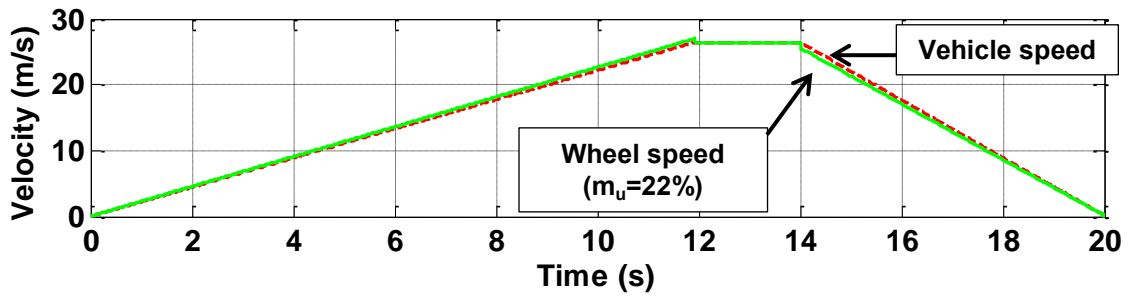
(a) Vehicle motion due to braking



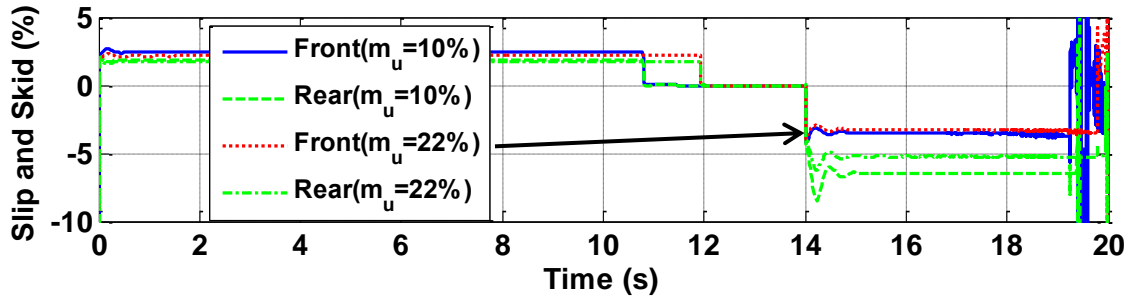
(b) Friction circle of each wheel (top view)



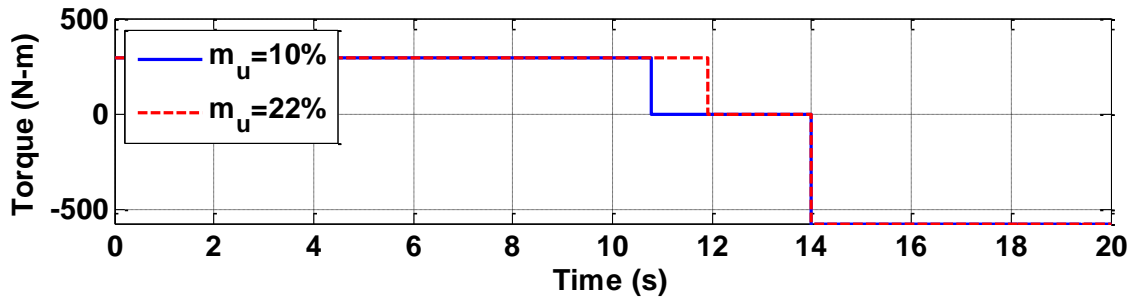
(c) Velocity profile



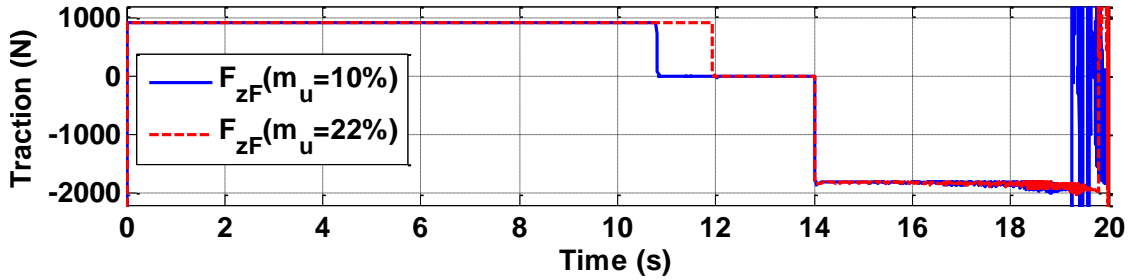
(d) Wheel speed and vehicle speed for $m_u = 22\%$



(e) Longitudinal slip (traction) and skid (braking) ratio



(f) Wheel torque command



(g) Front wheel traction

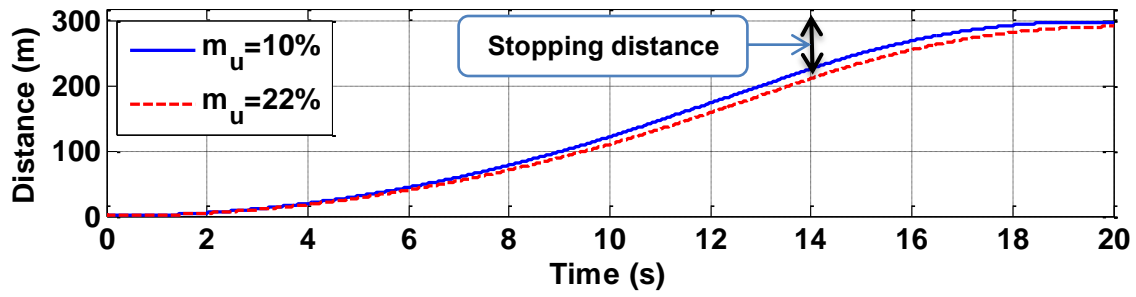
Figure 5-3: Simulation results for braking 60–0 mph

Consider braking distance as stopping distance. While braking from 14 to 19.5 s, the vehicle experiences front diving, as shown Figure 5-3 (a). This occurs because of the forward inertial force. Figure 5-3 (b) shows the friction circles of each wheel of a vehicle at that time.

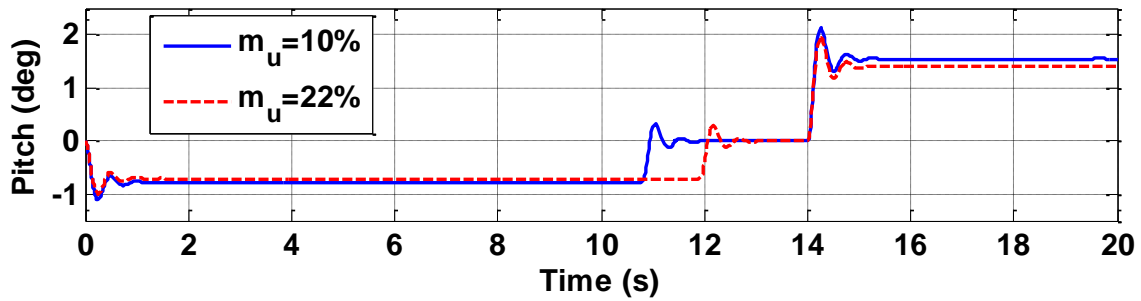
The front wheels have large friction circles due to high normal force acting on the tire contact patch. Figure 5-3 (c) – (g) shows the velocity profile, wheel speed and vehicle speed for $m_u = 22\%$ longitudinal slip (traction), and skid (braking) ratio, wheel torque, and front wheel traction as simulation results, based on 14 DOF full-vehicle model, respectively. At first, the vehicle is decelerated by the braking wheel torque that causes the wheel to stop from 14 to 19.5 s. Finally, the vehicle with a $m_u = 10\%$ is stopped at 19.5 s, while the vehicle with a $m_u = 22\%$ is stopped at 20 s.

Figure 5-3 (c) shows that a vehicle with a $m_u = 10\%$ is shorter than that with a $m_u = 22\%$; the deceleration of each one is 0.5 g and 0.45 g, given the same braking torque, respectively. Figure 5-3 (d) is the comparison plot between a wheel speed and a vehicle speed.

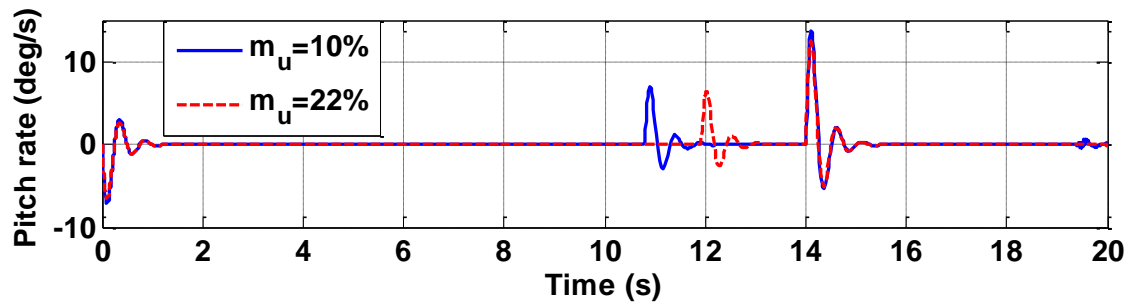
As can be seen in Figure 5-3 (e), the difference between wheel speed and vehicle speed indicates the skid ratio, representing a 3% skid ratio for the front ($m_u = 22\%$) from 14 to 19.5 s. In other words, the front ($m_u = 22\%$) means a front tire of a vehicle with a $m_u = 22\%$. As can be seen in Figure 5-3 (f), the wheel torque as an input produces 570 N-m (420 ft-lb) from 14 to 19.5 s. The front wheel braking traction is around 1850 N (416 lb), as shown in Figure 5-3 (g).



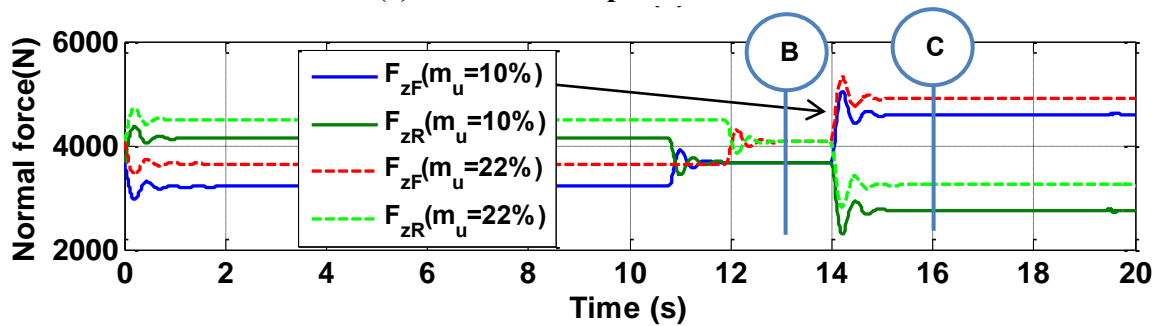
(a) Distance



(b) Pitch angle response over time



(c) Pitch rate response over time



(d) Normal force of front and rear wheels response over time

Figure 5-4: Simulation results of vehicle response for braking 60-0 mph

Figure 5-4 (a) – (d) shows plots of distance, pitch angle, pitch rate and normal force of the front and rear tires. During braking, the stopping distance is 73 m (240 ft), as shown in Figure 5-4 (a). Alternatively, given constant deceleration of 0.5g, the stopping distance can be obtained from:

$$SD = \frac{v^2}{2a} = \frac{(60 \times 1.4667)^2}{2(32.2 \times 0.5)} = 240 \text{ ft} (73 \text{ m}) \quad (5.3)$$

The stop time is 5.5 s, which is given by $t_s = v_x / (0.5g)$. For a vehicle with a $m_u = 22\%$, the stop time is 6 s, which is given by $t_s = v_x / (0.45g)$, resulting in 266 ft (81m). The stopping distance is proportional to the square of the velocity, whereas the stop time is proportional to the velocity. In terms of passenger vehicles, the performance metric of braking distance (60–0 mph) is 130 ~ 145 ft [Wei and Rizzoni,2004].

The consumer reports [Consumer-Reports,2012] shows that the braking performance of passenger cars is around 135 ft: Hyundai Sonata (134 ft), Toyota Camry (130 ft), and Chevrolet Equinox (138 ft). From Equation (5.3), it can be seen that the deceleration of these vehicles would be 0.9 g.

The pitch angle of a vehicle with a $m_u = 10\%$ is larger than that of a vehicle with a $m_u = 22\%$, as shown in Figure 5-4 (b), and the associated pitch rate is shown in Figure 5-4 (c). During deceleration, the dynamic load is transferred from the rear axle to the front axle, as shown in Figure 5-4 (d).

	Rear wheels (F_{zR})				Front wheels (F_{zF})			
	$m_u = 10\%$		$m_u = 22\%$		$m_u = 10\%$		$m_u = 22\%$	
B (t = 13s)	3673	N	4072	N	3673	N	4072	N
	826	lb	915	lb	826	lb	915	lb
C (t = 16s)	2755	N	3241	N	4591	N	4902	N
{Braking}	619	lb	729	lb	1032	lb	1102	lb

Table 5-3: Normal forces of each wheel during braking

The load is transferred from the rear axle to the front axle around 918N (206 lb), which is obtained from 4591 N (C, t = 16 s) minus 3673 N (B, t = 13 s) as tabled in Table 5-2. The longitudinal load transfer can be approximated by Equation as follows:

$$W_x = \frac{(m_s h + m_{uF} h_{uF} + m_{uR} h_{uR})}{2l} (0.5g) \quad (5.4)$$

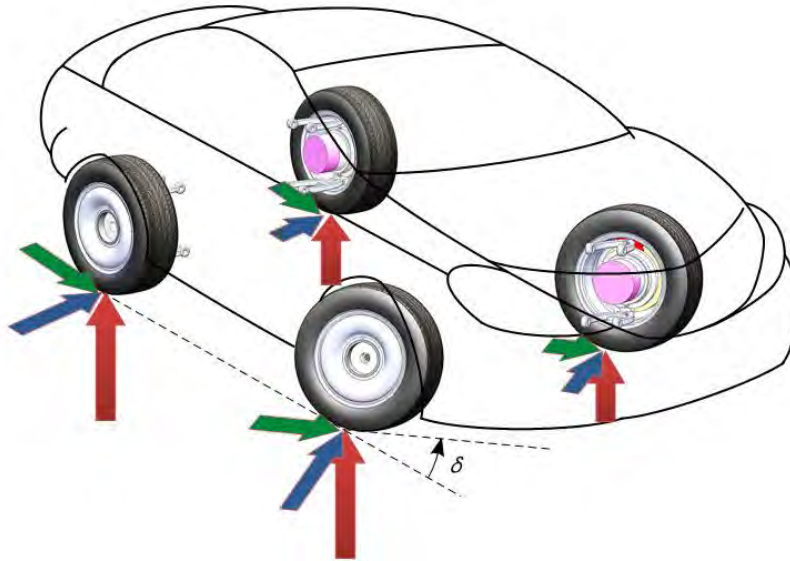
As can be seen Figure 5-4 (d), the symbol ‘B’ and ‘C’ indicate t = 13 s and t = 16 s, respectively. The numerical numbers are tabled in Table 5-3. Regarding a vehicle with a $m_u = 22\%$, the transferred load is around 830 N (187 lb), which is obtained from 4902 N (1102 lb) minus 4072 N (915 lb). In summary, as the unsprung mass increases, the longitudinal load transfer decreases, given the same braking wheel torque.

5.1.3 Cornering Maneuver

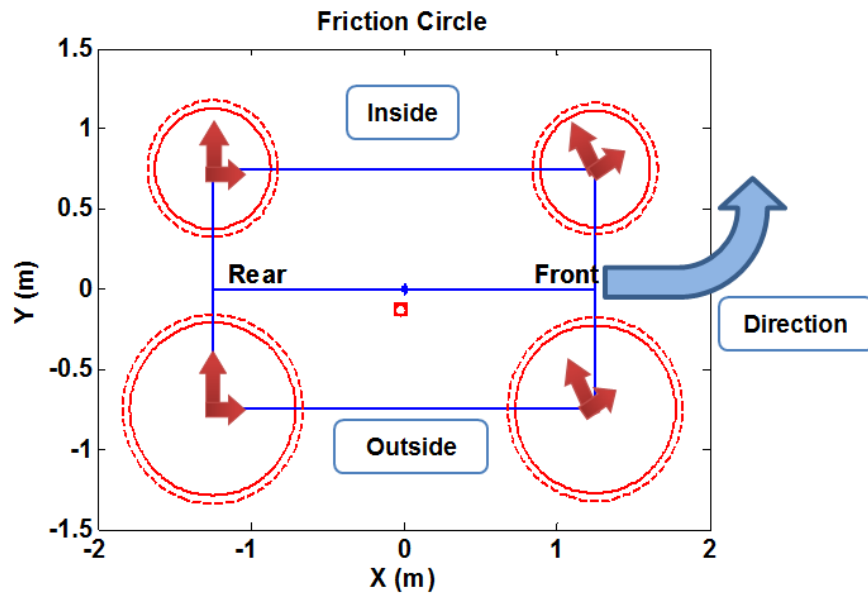
The cornering maneuver can be evaluated by a step steer input, a single-lane change, and double-lane change [Xiong and Yu,2009; Ghoneim,2011]. We will simulate a vehicle response to a step steer input and single lane change.

5.1.3.1 Step Steer

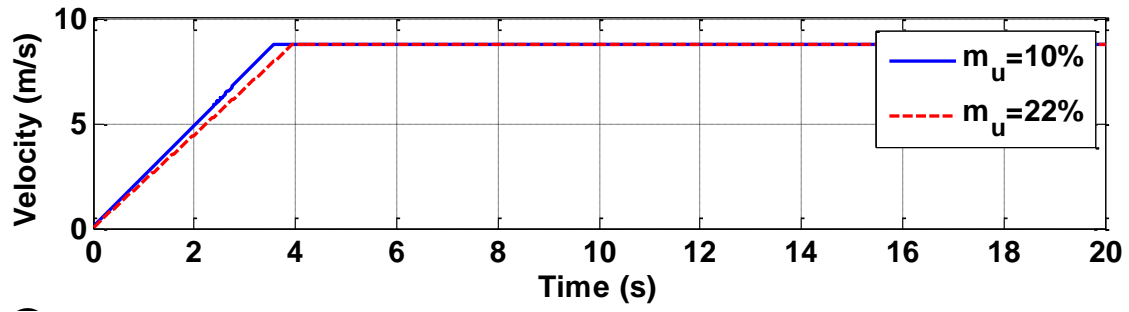
The dynamic response to a step steer input is a standard test to investigate the vehicle's behavior. The step steer input is a sudden change from zero to certain constant value as shown in Figure 5-5 (d).



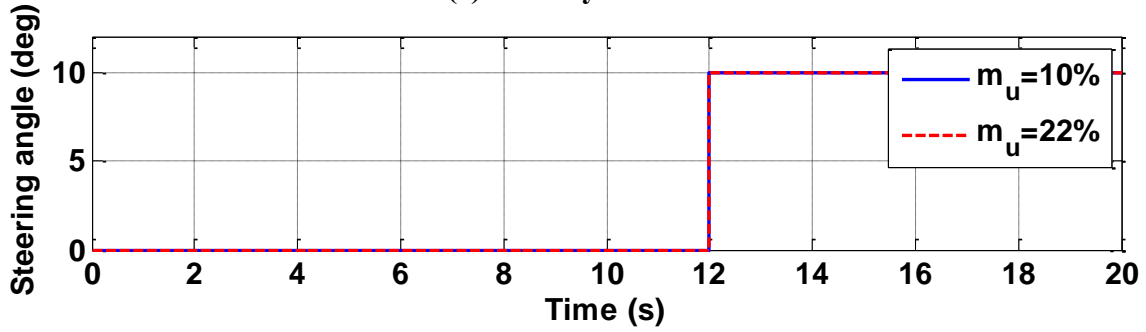
(a) Vehicle motion due to a cornering maneuver



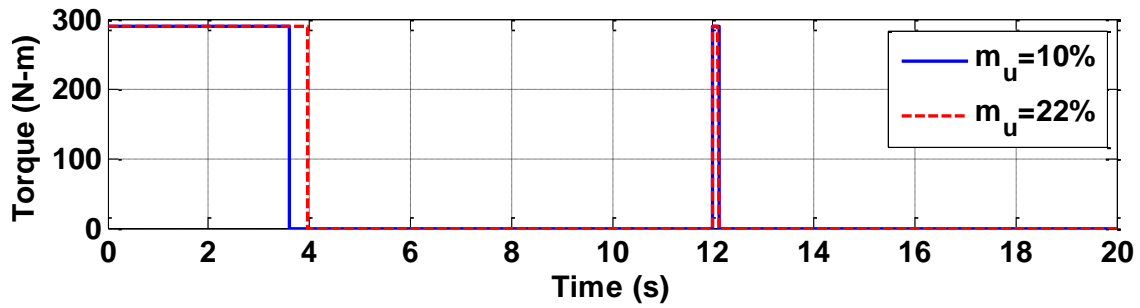
(b) Friction circle of each wheel during left cornering (top view)



(c) Velocity Profile



(d) Steering angle command



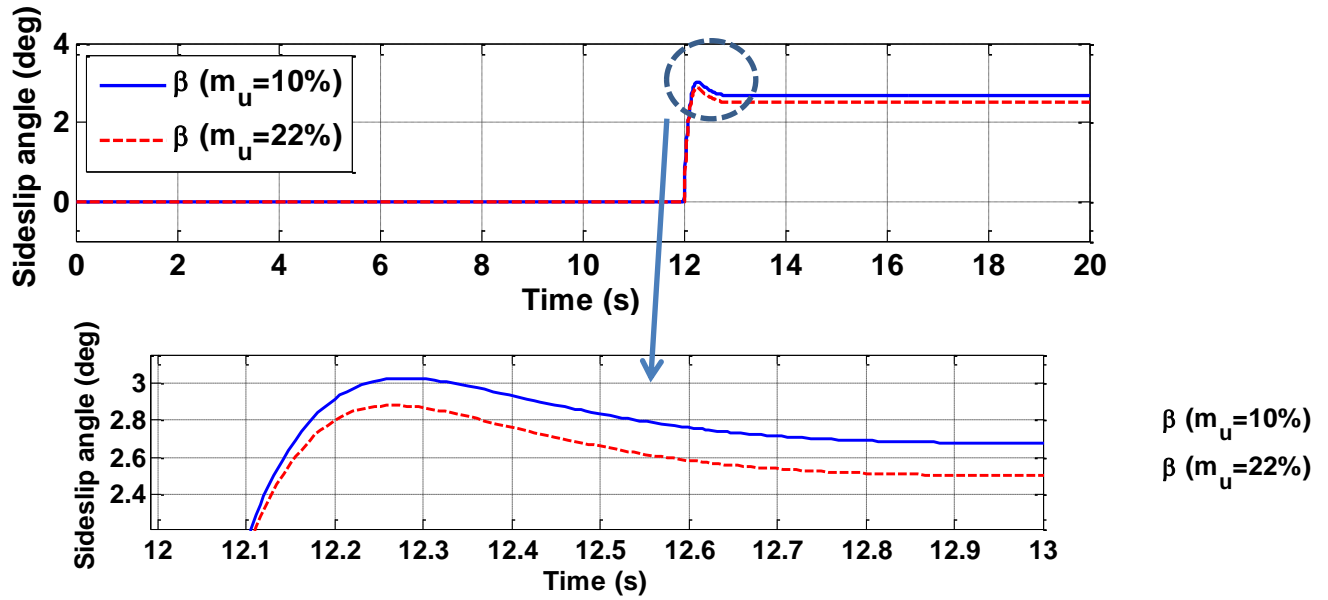
(e) Wheel torque command

Figure 5-5: Simulation results for a cornering maneuver (step steer 10°)

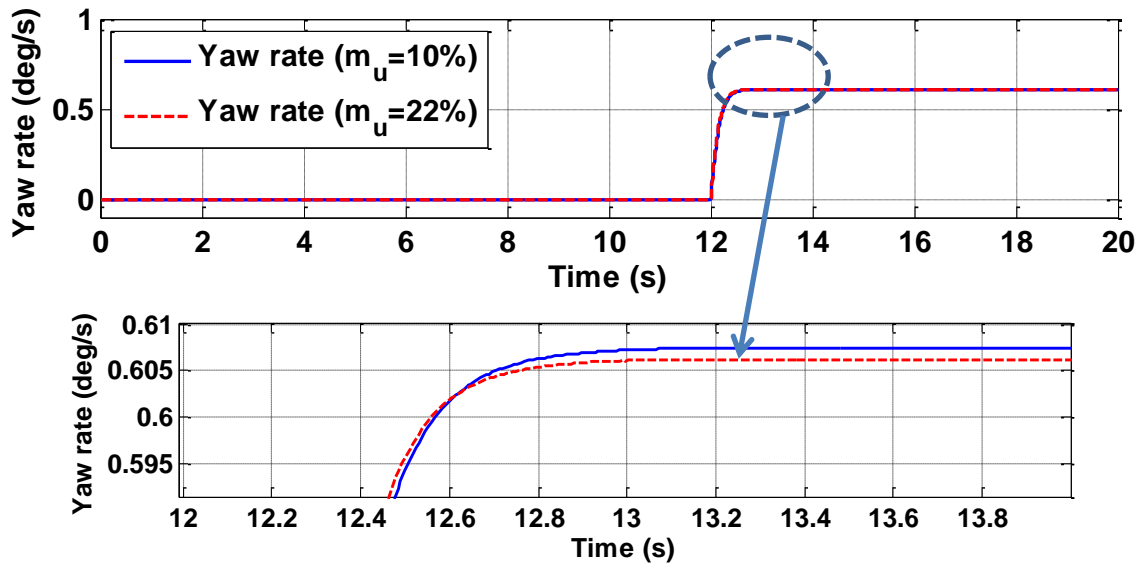
Under a cornering maneuver at 12 s, the vehicle experiences a rolling motion, resulting in increased outside wheel force, as shown in Figure 5-5 (a), owing to the outward inertial force. Figure 5-5 (b) shows the friction circles of each wheel of a vehicle at that time. The outside wheels have large friction circles owing to high normal force

acting on the tires. Figure 5-5 (c) – (e) shows the velocity profile, steering angle, and wheel torque command as simulation results based on the 14 DOF full-vehicle model, respectively.

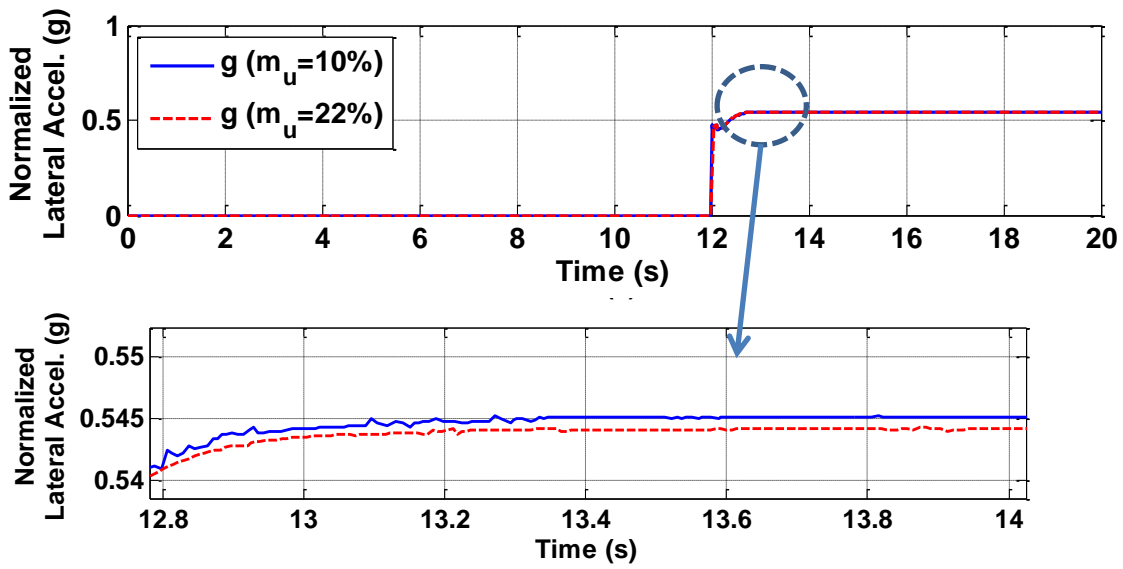
Figure 5-5 (c) shows that a vehicle with an unsprung-to-sprung mass ratio of 0.1 is faster than that with an unsprung-to-sprung mass ratio of 0.22. As can be seen in Figure 5-5 (d), the steering angle command as input is simulated at 12 s with a steering angle of 10° . In order to obtain a velocity of 8.8 m/s (20 mph), the wheel torque as input produces 290 N-m (207 ft-lb), as shown in Figure 5-5 (e).



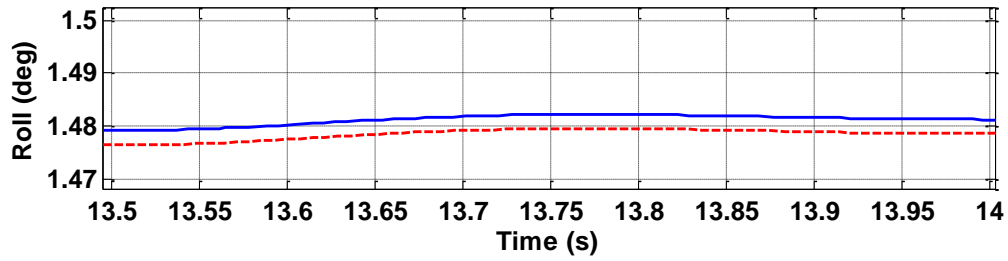
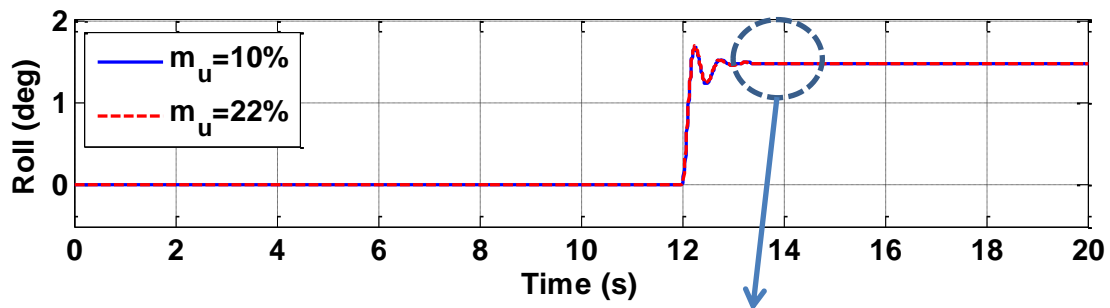
(a) Sideslip angle response over time



(b) Yaw rate response over time



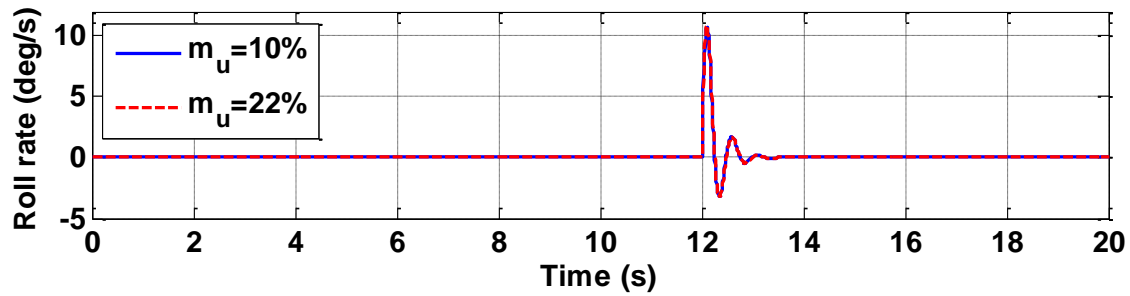
(c) Normalized lateral acceleration response over time



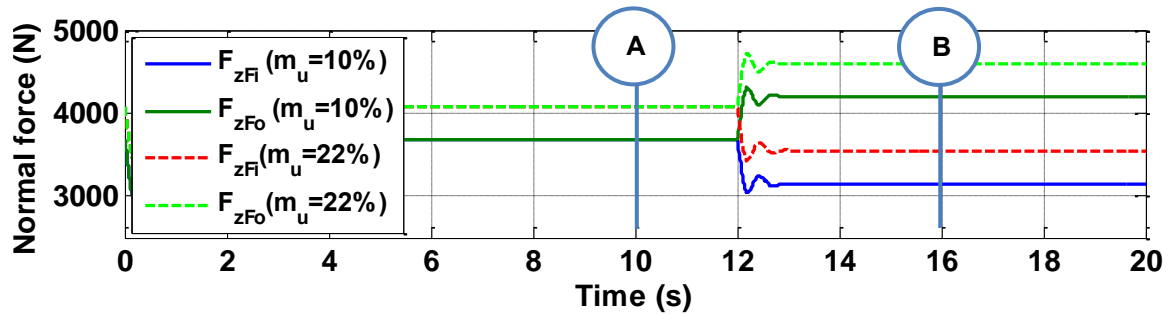
$m_u = 10\%$

$m_u = 22\%$

(d) Roll angle response over time



(e) Roll rate response over time



(f) Normal force of front and rear wheels response over time

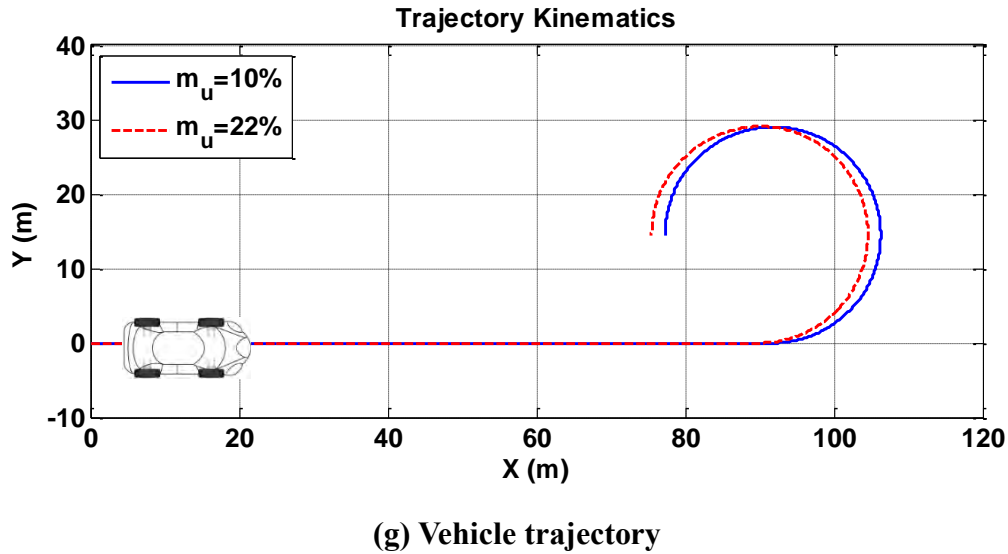


Figure 5-6: Simulation results of vehicle response for a cornering maneuver (10°)

Figure 5-6 (a) – (g) shows plots of sideslip angle, yaw rate, normalized lateral acceleration, roll angle, roll rate, normal forces of the front and rear wheels, and vehicle trajectory, respectively. As the unsprung mass increases, the sideslip angle, yaw rate, and lateral acceleration decrease, as shown in Figure 5-6 (a) – (c).

The roll angle of a vehicle with a $m_u = 10\%$ is larger than that of a vehicle with a $m_u = 22\%$, as shown in Figure 5-6 (d), and the associated roll rate is shown in Figure 5-6 (e). During cornering at $t = 12$ s, the dynamic load is transferred from the inside wheel to the outside wheel, as shown in Figure 5-1 (f). The vehicle trajectory is shown in Figure 5-1 (g).

The numerical numbers are tabled in Table 5-4. In terms of a vehicle with a $m_u = 10\%$, the dynamic load is transferred from the inside wheel to the outside wheel around 529 N (119 lb), which is obtained from 4202 N (B, $t = 16$ s) minus 3673 N (A, $t = 10$ s). the lateral load transfer can be approximated by Equation as follows:

$$\begin{aligned}
W_{yF} &= \left\{ \frac{m_s b (h_{cg} - h_{rcF})}{wl} + \frac{m_{uF} h_{uF}}{w} \right\} (0.55g) + \frac{1}{w} (k_{sF} w_{bF}^2 \phi + c_{sF} w_{bF}^2 \dot{\phi}) \\
W_{yR} &= \left\{ \frac{m_s a (h_{cg} - h_{rcR})}{wl} + \frac{m_{uR} h_{uR}}{w} \right\} (0.55g) + \frac{1}{w} (k_{sF} w_{bF}^2 \phi + c_{sF} w_{bF}^2 \dot{\phi})
\end{aligned} \tag{5.5}$$

As can be seen Figure 5-4 (d), the symbol ‘A’ and ‘B’ indicate $t = 10$ s and $t = 16$ s, respectively.

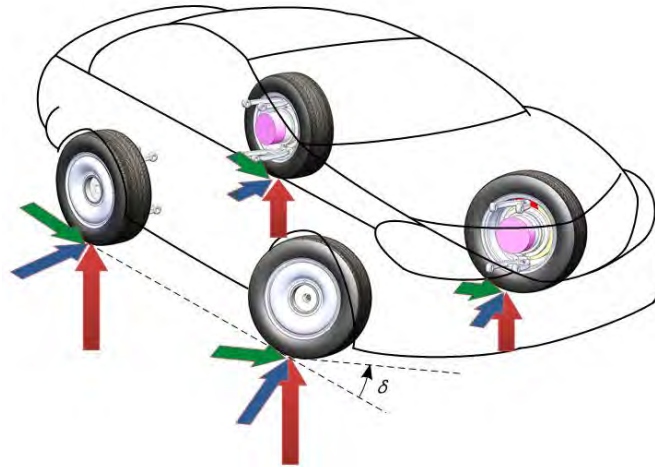
	Inside wheels (F_{zFi}, F_{zRi})				Outside wheels (F_{zFo}, F_{zRo})			
	$m_u = 10\%$		$m_u = 22\%$		$m_u = 10\%$		$m_u = 22\%$	
A ($t = 10$ s)	3673	N	4072	N	3673	N	4072	N
	826	lb	915	lb	826	lb	915	lb
B ($t = 16$ s)	3144	N	3544	N	4202	N	4599	N
{Cornering}	707	lb	797	lb	944	lb	1034	lb

Table 5-4: Normal forces of each wheel during step steer

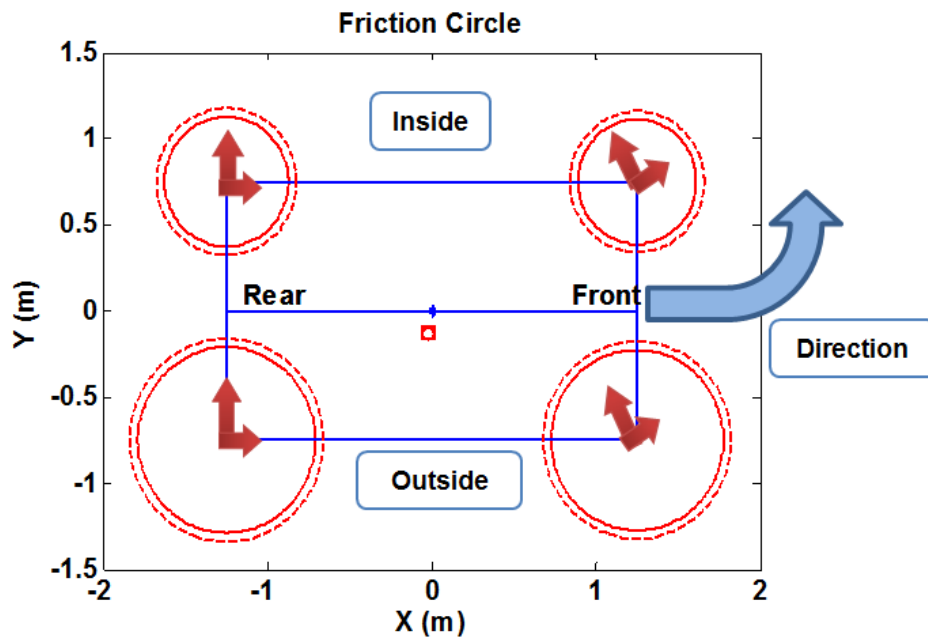
In terms of a vehicle with a $m_u = 22\%$, the transferred load is around 527 N (118 lb), which is obtained from 4599 N (1034 lb) minus 4072 N (915 lb). In summary, as the unsprung mass increases, it has little effect on the lateral load transfer.

5.1.3.2 Single-Lane Change

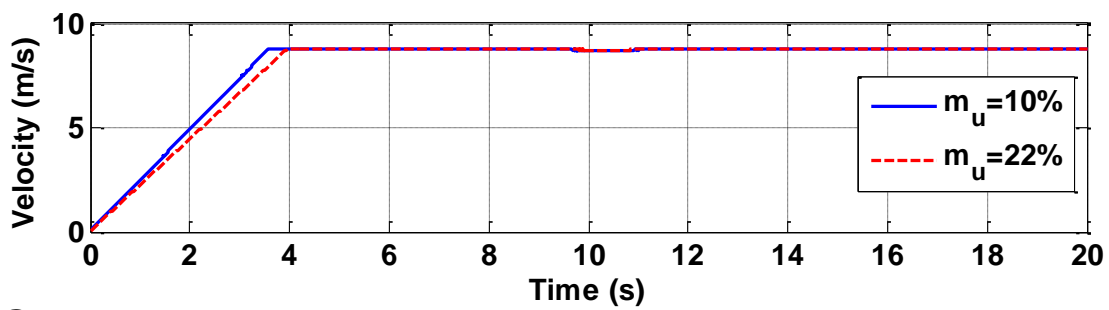
Many researchers used single-lane change maneuvers to examine a vehicle's dynamic responses [Kim and Kim,2006; Lee, Lee et al.,2008; Backmark, Karlsson et al.,2009].



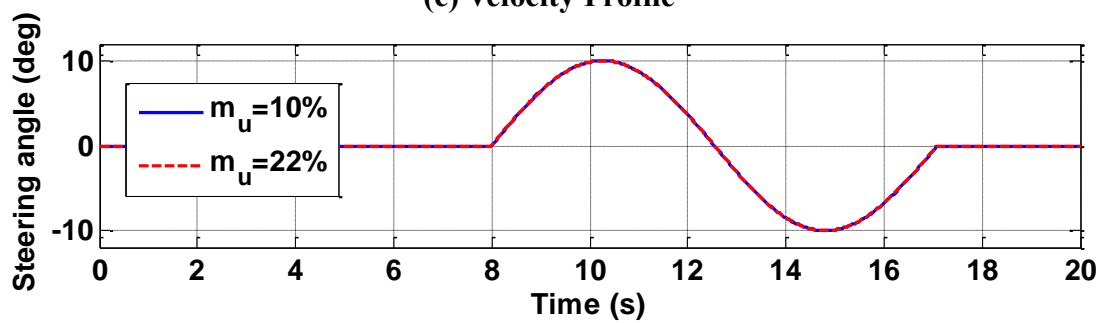
(a) Vehicle motion due to a cornering maneuver



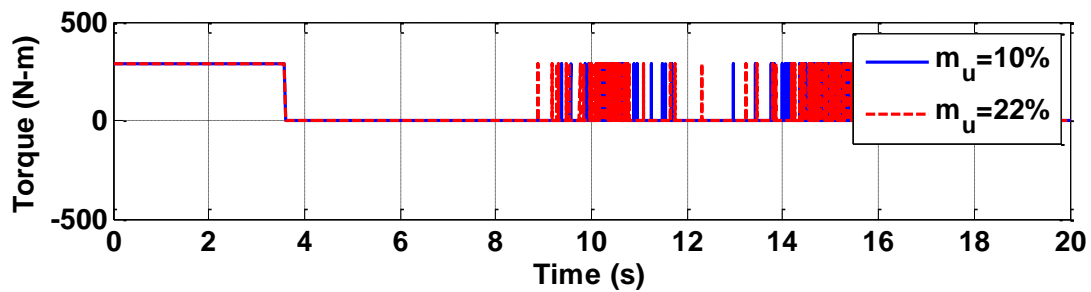
(b) Friction circle of each wheel during left cornering (top view)



(c) Velocity Profile



(d) Steering angle command



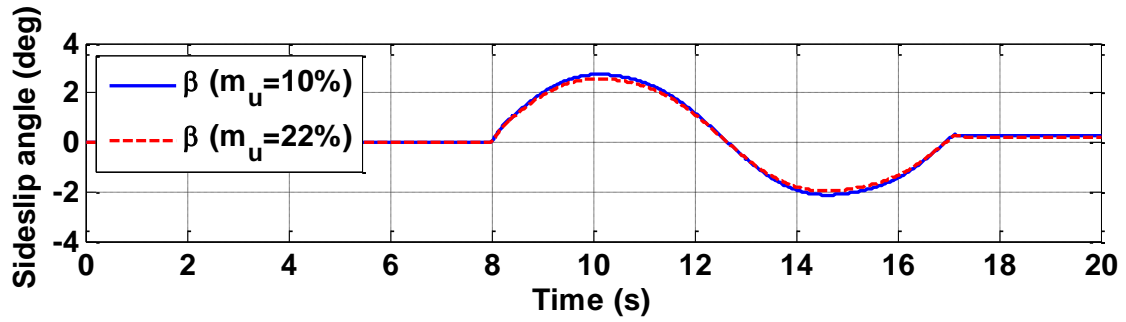
(e) Wheel torque command

Figure 5-7: Simulation results for single-lane change maneuver

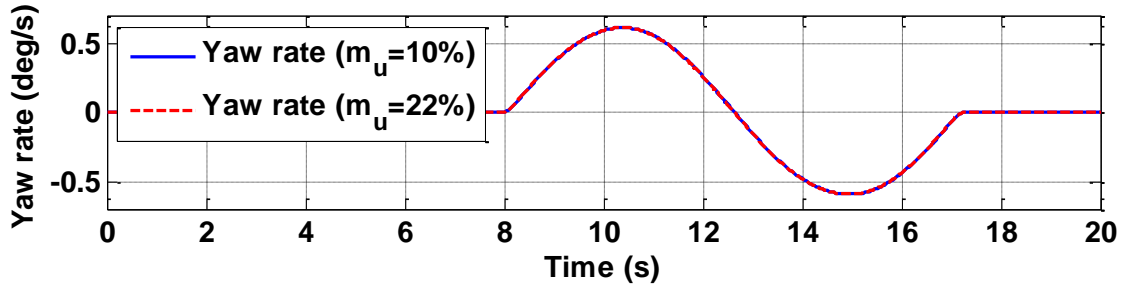
The single sinusoidal wave can be used for a single-lane change. Therefore, a single sinusoidal wave can be expressed as [Ackermann and Bunte,1998]:

$$\delta(t) = \begin{cases} \delta_0 \sin\left(\frac{2\pi v_x}{L}(t-t_0)\right), & t_0 < t < \frac{2\pi}{w}\left(= \frac{L}{v_x}\right) \\ 0, & \text{otherwise} \end{cases} \quad (5.6)$$

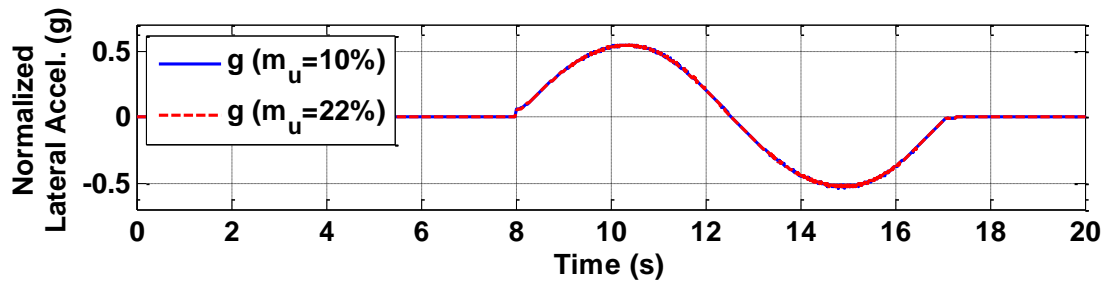
where L is the wave length which is assumed to be 70 m. The amplitude of δ_0 is 0.175 rad (10°), and the longitudinal velocity of v_x is 8.8 m/s (20 mph). Figure 5-7 (c) shows the steering angle command based on Equation (5.6). Figure 5-7 (a) shows the vehicle motions during a single-lane change. The wheel torque is produced to maintain the vehicle's velocity during the single-lane change, as shown in Figure 5-7 (e).



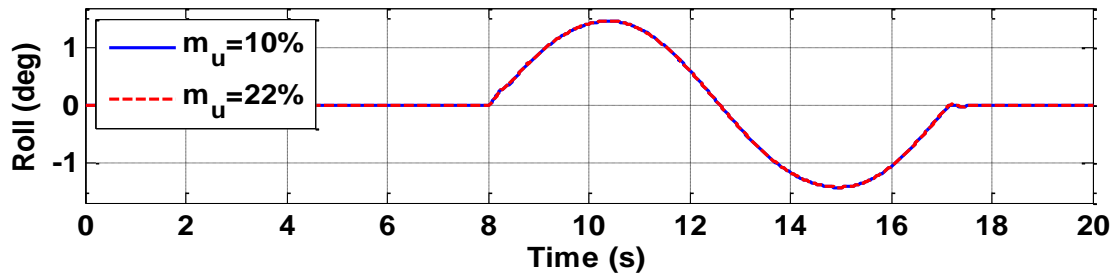
(a) Sideslip angle response over time



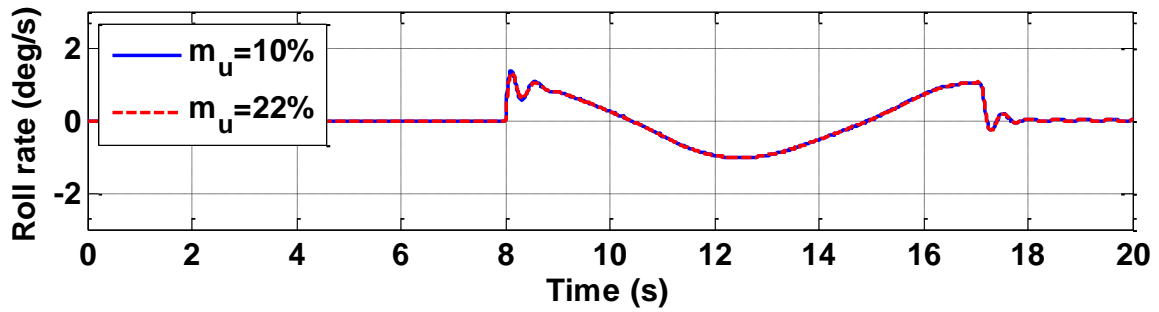
(b) Yaw rate response over time



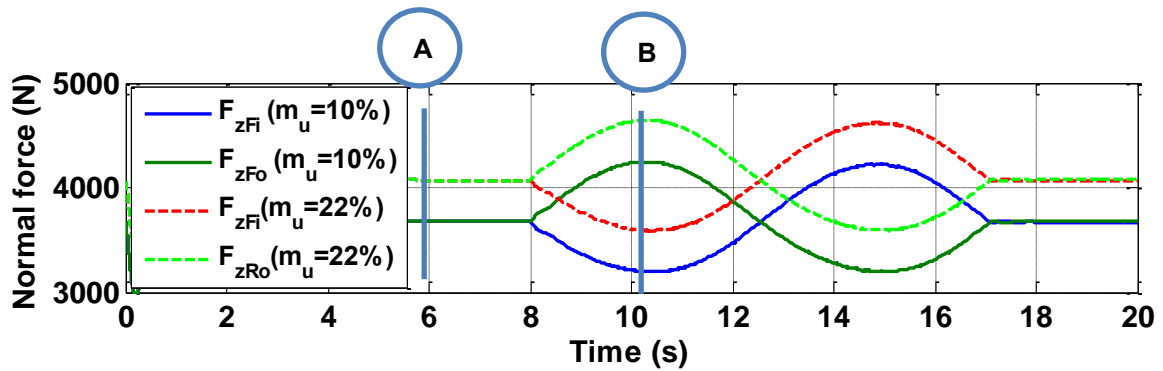
(c) Normalized Lateral Acceleration response over time



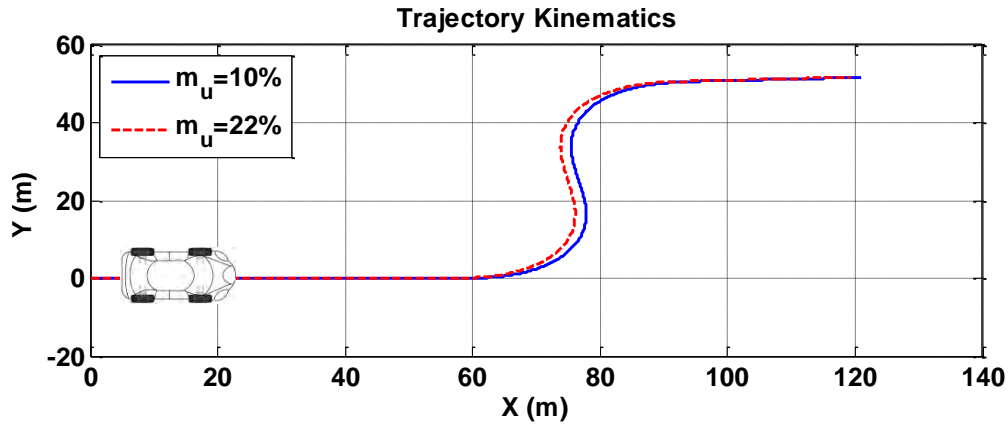
(d) Roll angle response over time



(e) Roll rate response over time



(f) Normal force of front and rear wheels



(g) Vehicle trajectory

Figure 5-8: Simulation results of vehicle response for single-lane change maneuver

Figure 5-8 (a) – (g) shows plots of sideslip angle, yaw rate, normalized lateral acceleration, roll angle, roll rate, normal forces of front and rear wheels, and vehicle trajectory, respectively. As unsprung mass increases, the sideslip angle, yaw rate, and lateral acceleration slightly decreases, as shown in Figure 5-8 (a) – (c). The increased unsprung mass decreases slightly roll motion, as shown in Figure 5-6 (d), and the associated roll rate is shown in Figure 5-8 (e). During cornering from 12 seconds, the dynamic load is transferred from the inside wheel to the outside wheel as shown in Figure 5-8 (f).

The numerical numbers are tabled in Table 5-5. As can be seen Figure 5-8 (f), the symbol ‘A’ and ‘B’ indicate $t = 6$ s and $t = 10.4$ s, respectively. In terms of a vehicle with a $m_u = 10\%$, the dynamic load is transferred from the inside wheel to the outside wheel around 575 N (129 lb), which is obtained from 4248N (B, $t = 10.4$ s) minus 3673 N (A, $t = 10$ s).

	Inside wheels (F_{zFi}, F_{zRi})				Outside wheels (F_{zFo}, F_{zRo})			
	$m_u = 10\%$		$m_u = 22\%$		$m_u = 10\%$		$m_u = 22\%$	
A (t = 6s)	3673	N	4072	N	3673	N	4072	N
	826	lb	915	lb	826	lb	915	lb
B (t = 10.4s)	3196	N	3588	N	4248	N	4642	N
{Cornering}	719	lb	807	lb	955	lb	1044	lb

Table 5-5: Normal forces of each wheel during single-lane change

In terms of a vehicle with a $m_u = 22\%$, the transferred load is around 570 N (128 lb), which is obtained from 4642N (1044 lb) minus 4072 N (915 lb).

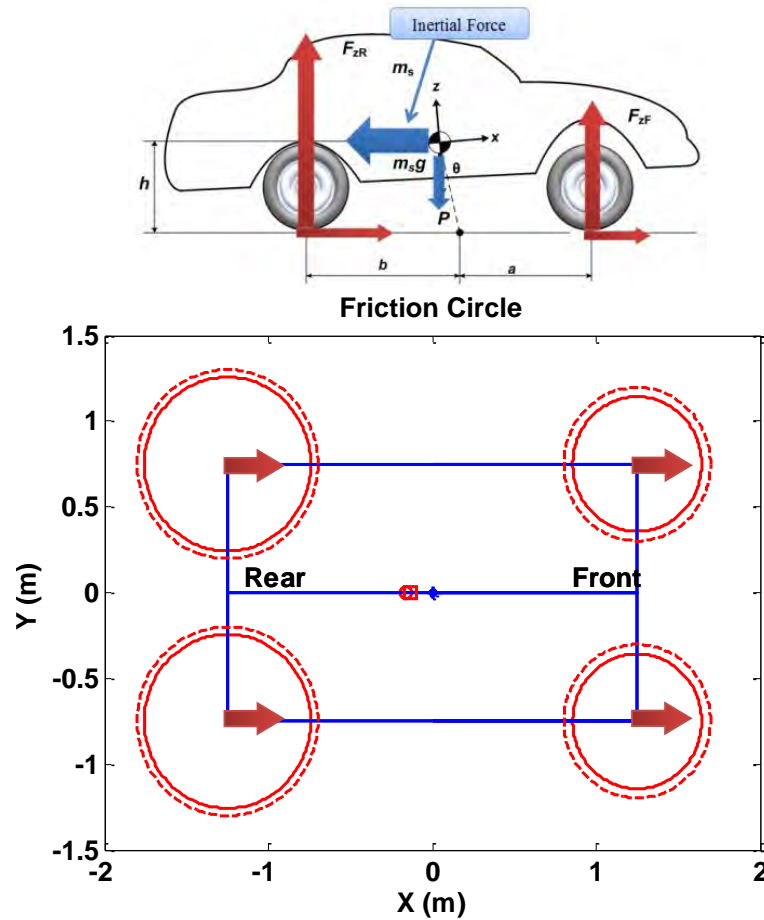
5.2 EFFECTS OF INCREASED UNSPRUNG MASS UNDER VARIOUS ROAD CONDITIONS

In this section, we discuss the effects of increased unsprung mass on performance criteria under various road conditions: dry asphalt, wet asphalt, and snowy road.

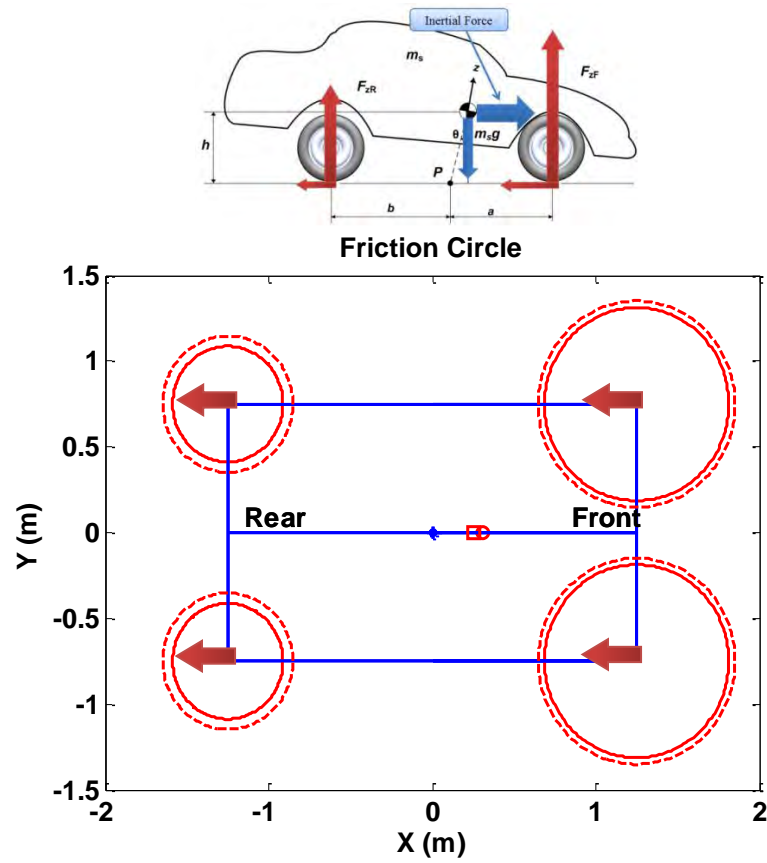
5.2.1 Dry Asphalt Road

5.2.1.1 Acceleration and Braking

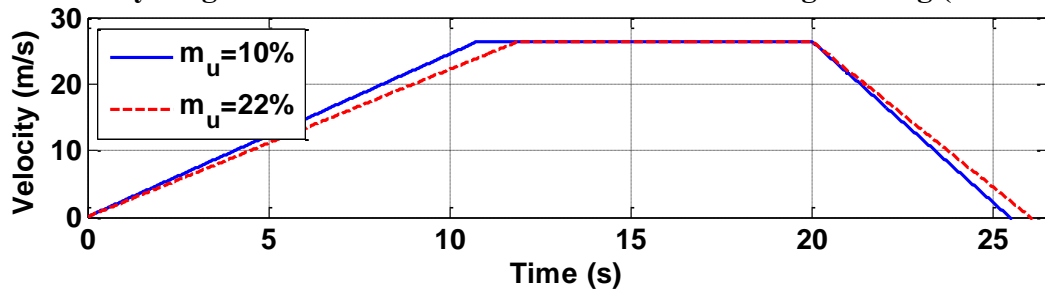
We discussed the effect of unsprung mass on acceleration and braking in Secs. 4.6.1 and 4.6.2. Simulations of the vehicle response subjected to acceleration and braking have been carried out as shown below in Figure 5-9.



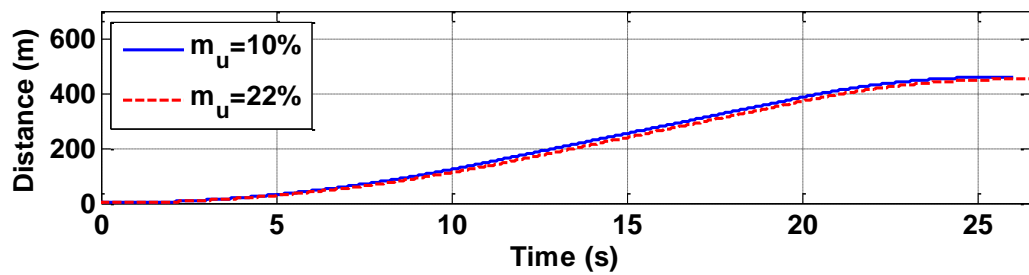
(a) Free-body diagram and friction circle of each wheel during acceleration(0-11 s)



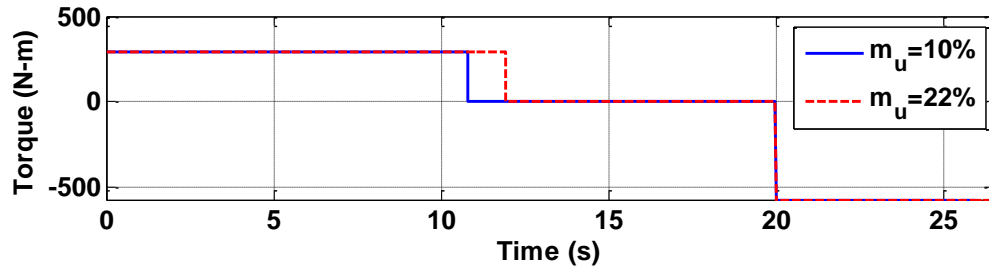
(b) Free-body diagram and friction circle of each wheel during braking (20-25.5 s)



(c) Velocity Profile



(d) Distance



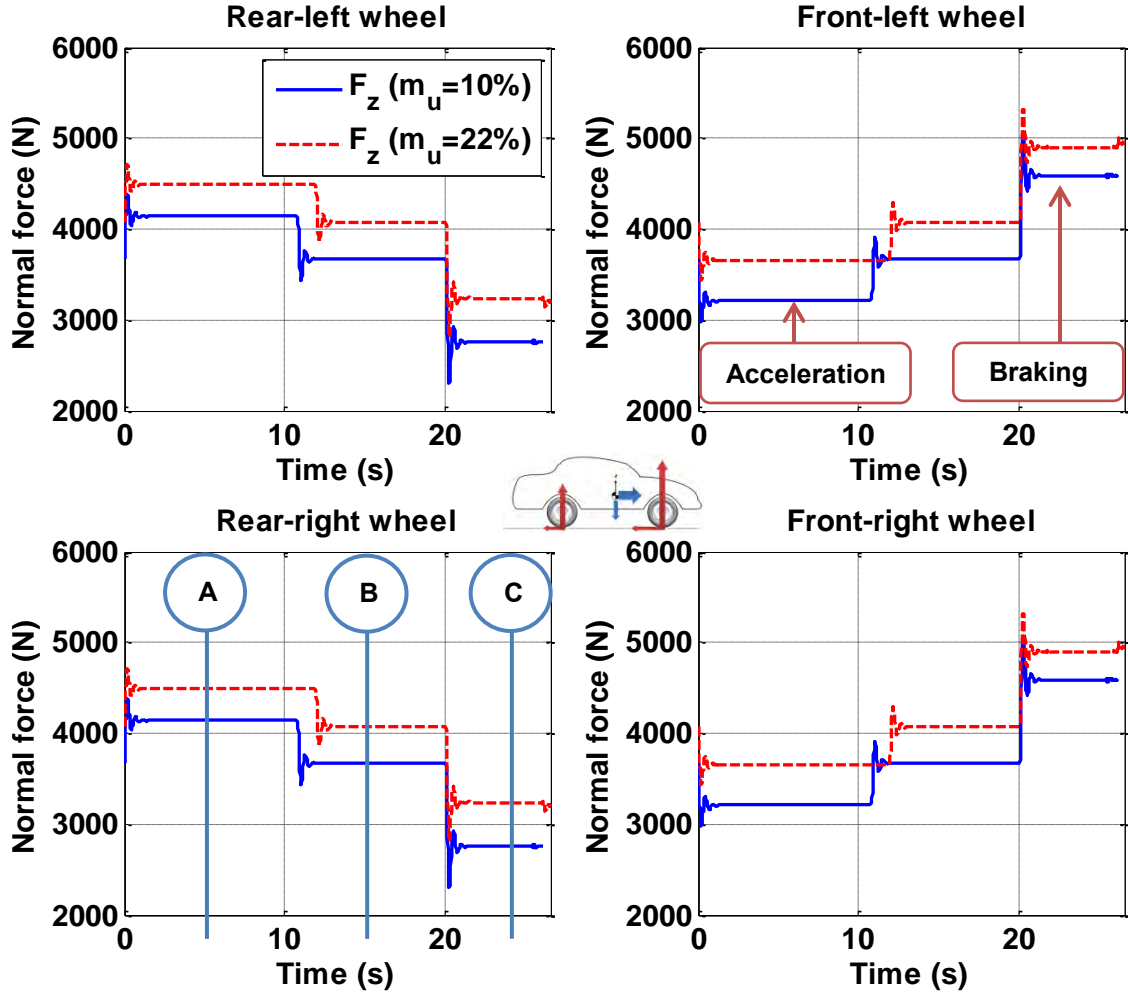
(e) Wheel torque command

Figure 5-9: Simulation results for acceleration and braking on dry asphalt ($\mu = 0.9$)

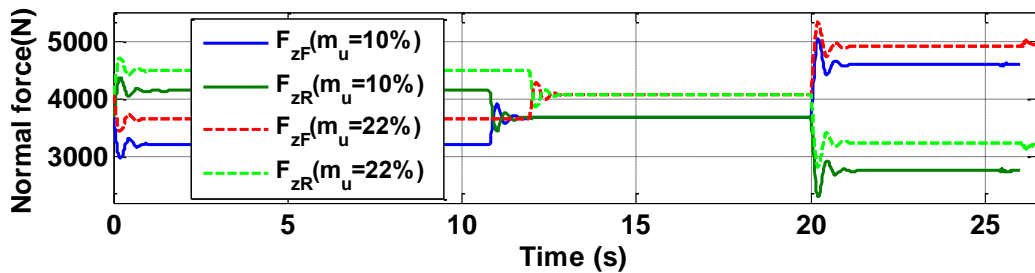
The torque command as input is performed at $t = 0$ s with positive 290 N-m (214 ft-lb) and $t = 20$ s with negative 570 N-m, which are associated with acceleration and braking, respectively. Figure 5-9 (a) and (b) shows the free-body diagram and friction circles, which are visualized at each wheel during acceleration and braking. The solid line and dashed line circles are associated with vehicles where $m_u = 10\%$ and $m_u = 22\%$, respectively. Clearly, it can be seen that the friction circles of the rear wheels during acceleration are larger than those of the front wheels due to backward inertial force. Conversely, during braking, the friction circles of the front wheels are larger than those of the rear wheels due to forward inertial force, as shown in Figure 5-9 (b).

According to research by Toyota Motor Company regarding in-wheel motor (IWM) [Katsuyama and CORPORATION,2011; Murata,2011], a large vertical force component of driving force on tires is generated during acceleration. Since the instantaneous center of the suspension cannot be changed for braking attitude and ride comfort, a larger vertical component of driving force can be used for vertical body motion control. In addition, with the capability of generating forward and reverse torque, IWMs can improve performance during driving, turning, stopping, and also improve ride comfort. As shown in Figure 5-9 (a) and (b), the larger normal force due to the increased unsprung mass improve acceleration and braking and provide better vehicle control.

Also, as a result of wheel torque, the velocity profile and distance can be determined as shown in Figure 5-9 (c) and (d), respectively.



(a) Normal forces of each wheel



(b) Comparison of normal forces

Figure 5-10: Normal forces during acceleration and braking on dry asphalt ($\mu = 0.9$)

As mentioned in Secs. 5.1.1 and 5.1.2, the dynamic load is transferred from the front axle to the rear axle (or vice versa) during acceleration and braking due to the inertial force acting on the vehicle, so that the normal force varies from static values by the amount of dynamic load transfer. Figure 5-10 (a) shows the normal forces of each wheel during acceleration (0 – 12 s) and braking (20 – 26 s): rear-left wheel, front-left wheel, rear-right wheel, and front-left wheel. Figure 5-10 (b) shows the comparison of normal forces in terms of $m_u = 10\%$ and $m_u = 22\%$. The numerical numbers of this plot can be seen in Table 5-6.

	A (t = 5s) B (t = 15s) C (t = 23s)						A (t = 5s) B (t = 15s) C (t = 23s)					
	{Accel.}			{Braking}			{Accel.}			{Braking}		
	<u>Rear-left wheel</u> (F_{zRl})						<u>Front-left wheel</u> (F_{zFl})					
m _u =22%	4493	N	4072	N	3241	N	3650	N	4072	N	4902	N
	1010	lb	915	lb	729	lb	821	lb	915	lb	1102	lb
m _u =10%	4139	N	3673	N	2755	N	3207	N	3673	N	4591	N
	930	lb	827	lb	619	lb	721	lb	826	lb	1032	lb
	<u>Rear-right wheel</u> (F_{zRr})						<u>Front-right wheel</u> (F_{zFr})					
m _u =22%	Same as above						Same as above					
m _u =10%	Same as above						Same as above					

Table 5-6: Normal forces of each wheel

As shown in Figure 5-8 (f), the symbol ‘A’, ‘B’, and ‘C’ corresponds to $t = 5$ s, $t = 15$ s, and $t = 23$ s, respectively. During acceleration (A), the maximum normal forces of the rear wheels in terms of $m_u = 22\%$ and $m_u = 10\%$ are 4493 N and 4139 N, respectively. During constant velocity (B), the normal forces of the all wheels are 4072 N and 3673 N,

respectively. During braking (C), the maximum normal forces of the front wheels in terms of $m_u = 22\%$ and $m_u = 10\%$ are 4902 N and 4591 N, respectively.

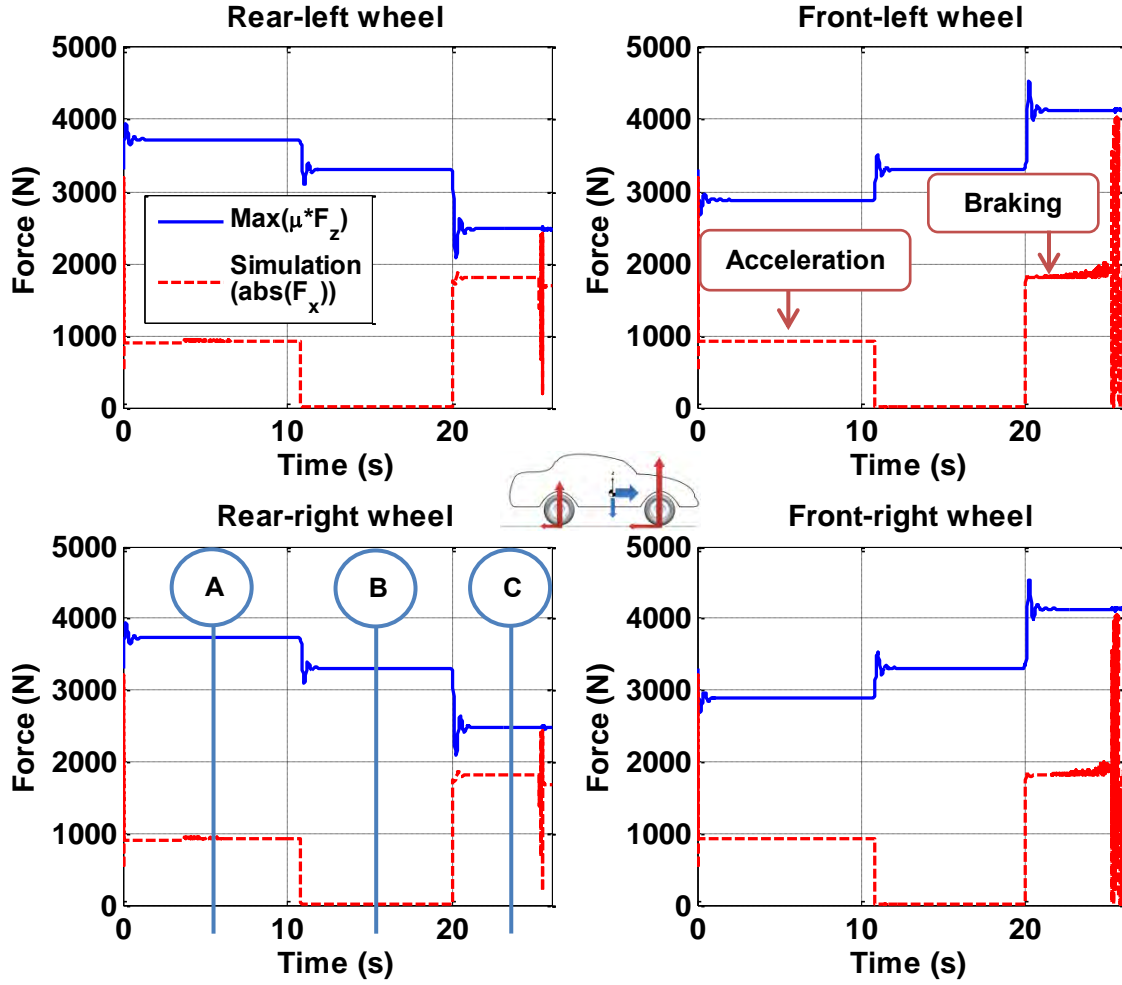


Figure 5-11: Traction and braking forces on dry asphalt ($m_u = 10\%$, $\mu = 0.9$)

As previously mentioned, the input is the wheel torque, while the outputs are longitudinal forces on all four wheels: there are no lateral forces because of the absence of a steering angle. The longitudinal forces must satisfy specified equality constraints as follows:

$$F_{xjk}^2 + F_{yjk}^2 \leq (\mu F_{zjk})^2 \quad (5.7)$$

This equation is related to the friction circle. Since the lateral force does not exist, the above equation becomes:

$$F_{xjk} \leq (\mu F_{zjk}) \quad (5.8)$$

Figure 5-11 shows the traction force and braking forces of a vehicle ($m_u = 10\%$). The solid and dashed lines represent available maximum traction force and simulated traction force, respectively. As shown in Figure 5-11, the symbol ‘A’, ‘B’, and ‘C’ corresponds to $t = 5$ s, $t = 15$ s, and $t = 23$ s, respectively. The numerical numbers associated with these plots can be seen in Table 5-7.

	A (t = 5s) B (t = 15s) C (t = 23s)						A (t = 5s) B (t = 15s) C (t = 23s)					
	{Accel.}						{Braking}					
	{Accel.}						{Braking}					
	<u>Rear-left Wheel</u> (F_{zRl})						<u>Front-left wheel</u> (F_{zFl})					
Max	3725	N	3306	N	2479	N	2886	N	3306	N	4132	N
(μ*F _z)	837	lb	743	lb	557	lb	649	lb	743	lb	929	lb
Simulation	919	N	3	N	1807	N	919	N	3	N	1830	N
(abs(F _x))	207	lb	0.7	lb	406	lb	207	lb	0.7	lb	411	lb
	<u>Rear-right wheel</u> (F_{zRr})						<u>Front-right wheel</u> (F_{zFr})					
Max	Same as above						Same as above					
(μ*F _z)												
Simulation	Same as above						Same as above					
(abs(F _x))												

Table 5-7: Traction and braking forces of each wheel ($m_u = 10\%$)

During acceleration (A), the maximum traction forces and the simulated traction of the rear wheels are 3725 N and 919 N, respectively. During constant velocity (B), the

maximum traction forces and the simulated traction of all wheels are 3306 N and 3 N, respectively. During braking (C), the maximum traction forces and the simulated traction of the front wheels are 4132 N and 1830 N, respectively. In other words, the vehicle is simulated with traction forces of 919 N for all wheels during acceleration, and simulated with braking forces of 1830 N for all wheels during braking. For purposes of comparison, the absolute value of the braking force is used.

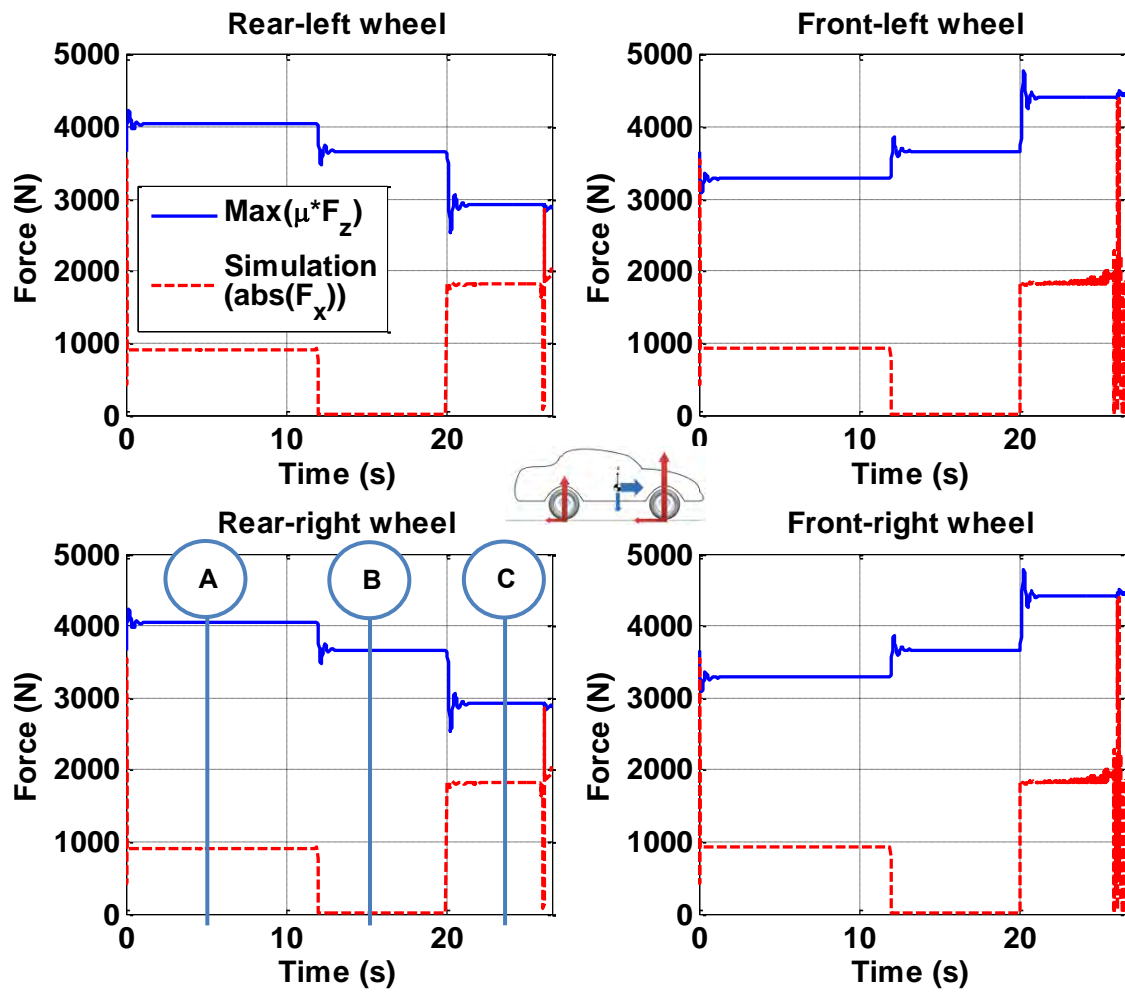


Figure 5-12: Traction and braking forces on dry asphalt ($m_u = 22\%$, $\mu = 0.9$)

Given unsprung mass of $m_u = 22\%$, traction and braking forces on dry asphalt are simulated as shown in Figure 5-12. The symbol ‘A’, ‘B’, and ‘C’ correspond to $t = 5$ s, $t = 15$ s, and $t = 23$ s, respectively. The numerical numbers associated with these plots can be seen in Table 5-8.

	A (t = 5s)			B (t = 15s)			C (t = 23s)			A (t = 5s)			B (t = 15s)			C (t = 23s)		
	{Accel.}			{Braking}			{Accel.}			{Braking}			{Accel.}			{Braking}		
	<u>Rear-left wheel</u> (F_{zRl})									<u>Front-left wheel</u> (F_{zFl})								
Max	4044	N	3664	N	2917	N	3285	N	3664	N	4412	N						
($\mu * F_z$)	909	lb	824	lb	656	lb	739	lb	824	lb	992	lb						
Simulation	919	N	6	N	1807	N	919	N	6	N	1813	N						
(abs(F_x))	207	lb	1.4	lb	406	lb	207	lb	1.4	lb	408	lb						
	<u>Rear-right wheel</u> (F_{zRr})									<u>Front-right wheel</u> (F_{zFr})								
Max	Same as above									Same as above								
($\mu * F_z$)																		
Simulation	Same as above									Same as above								
(abs(F_x))																		

Table 5-8: Traction and braking forces of each wheel ($m_u = 22\%$)

During acceleration (A), the maximum traction forces and the simulated traction of the rear wheels are 4044 N and 909 N, respectively. During constant velocity (B), the maximum traction forces and the simulated traction of all wheels are 3664 N and 6 N, respectively. During braking (C), the maximum traction forces and the simulated traction of the front wheels are 4412 N and 1813 N, respectively.

The difference between the maximum traction from Table 5-7 and the maximum traction from Table 5-8 during the constant velocity (B) is due to the increased unsprung

mass that varies from 10% (136 kg) to 22% (300 kg). The increased unsprung mass of each wheel is around 41 kg (90 lb). Taking into account the friction coefficient ($\mu = 0.9$), the increased normal force becomes 360 N (90 lb). That is, the maximum traction of 3306 N tabled in Table 5-7 becomes a value of 3664 N, as shown in Table 5-8. The simulated force of 6 N is attributed to the tire slip in spite of constant velocity.

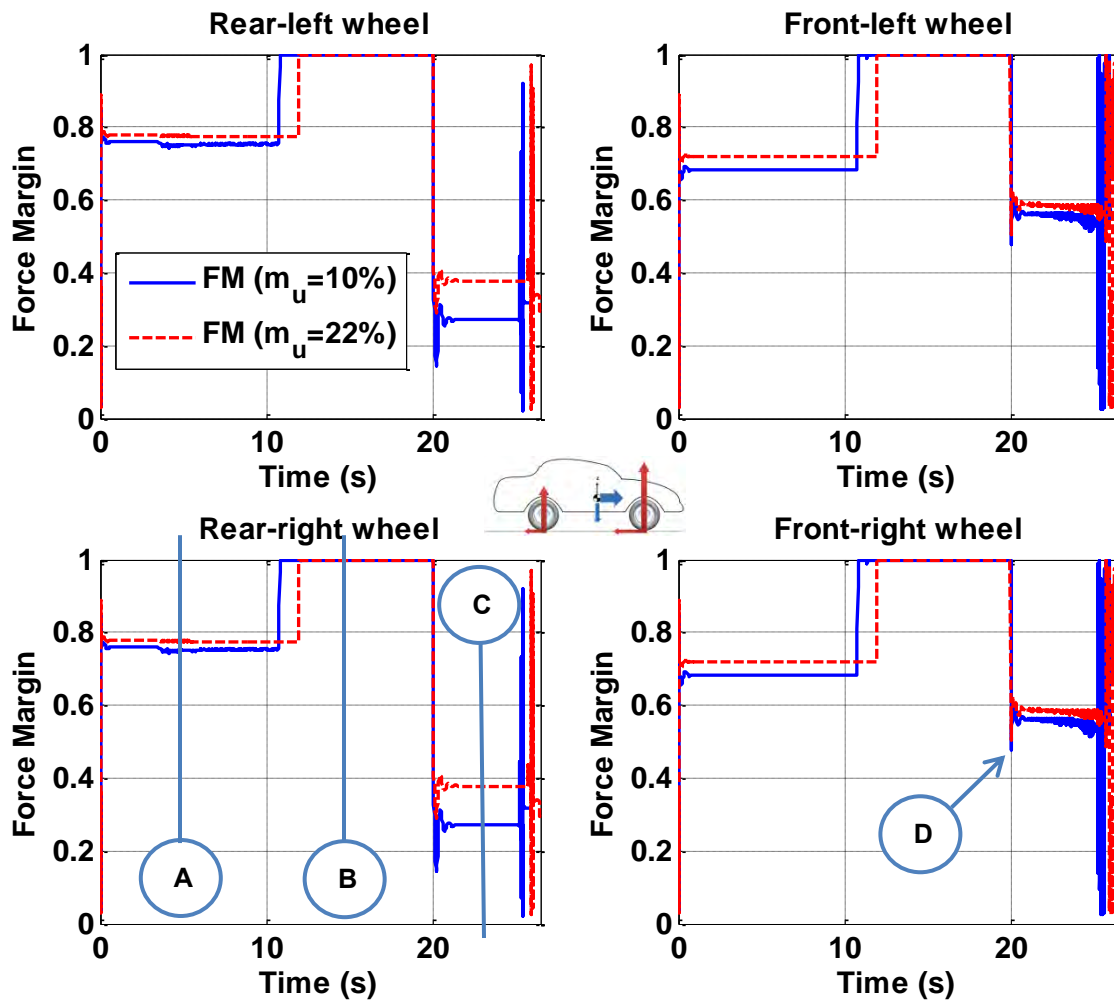


Figure 5-13: Effect of unsprung mass on force margin on dry asphalt ($\mu = 0.9$)

The force margin can be defined as follows:

$$FM = \left(\frac{\mu F_{zjk} - \sqrt{F_{xjk}^2 + F_{yjk}^2}}{\mu F_{zjk}} \right) \times 100\% \quad (5.9)$$

Using the information from maximum traction force (μF_{zjk}) and simulated traction force (F_{xjk}) for each wheel, the force margin of each wheel can be calculated. For instance, the maximum traction force and simulated traction force are 3725 N and 919 N, respectively, from the rear-left wheel plot as shown in Figure 5-11. Therefore, Equation (5.9) above becomes:

$$FM_{wRl} = \left(\frac{3725 - 919}{3725} \right) \times 100\% = 75\% \quad (5.10)$$

The minimum force margin of the rear-left wheel for a vehicle with $m_u = 0.1$ becomes 0.75, which indicates an available traction force of 76 %; a value of zero indicates traction saturation. The minimum force margin of a vehicle with $m_u = 0.22$ is around 0.77. As shown in Figure 5-13, the symbol ‘A’, ‘B’, and ‘C’ corresponds to $t = 5$ s, $t = 15$ s, and $t = 23$ s, respectively. The symbol ‘D’ indicates the minimum force margin during braking. The numerical numbers associated with these plots can be seen in Table 5-9.

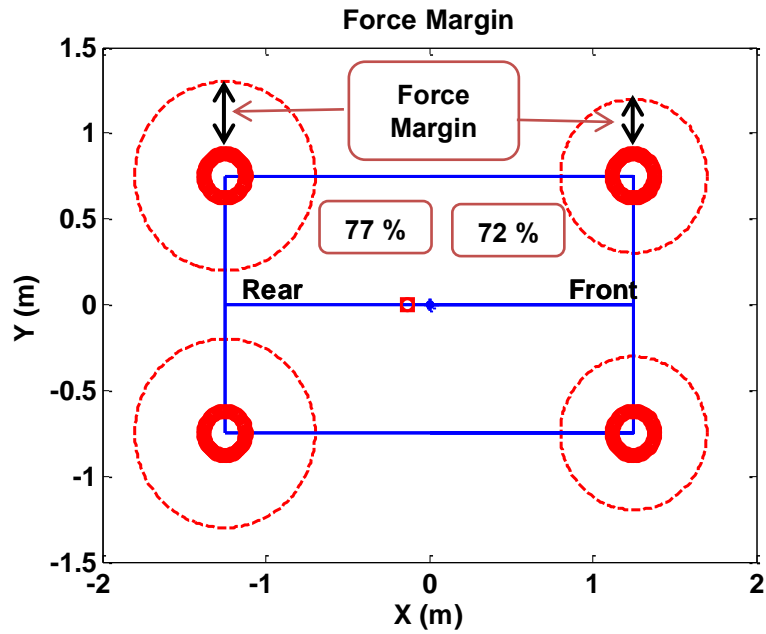
	A (t=5s) {Accel.}	B(t=15s)	C (t=23s) {Braking}	D (min)	A (t=5s) {Accel.}	B(t=15s)	C (t=23s) {Braking}	D (min)
	<u>Rear-left wheel</u> (F_{zRl})				<u>Front-left wheel</u> (F_{zFl})			
$m_u=22\%$	0.77	1	0.38	0.29	0.72	1	0.59	0.50
$m_u=10\%$	0.75	1	0.27	0.15	0.68	1	0.57	0.48
	<u>Rear-right wheel</u> (F_{zRr})				<u>Front-right wheel</u> (F_{zFr})			
$m_u=22\%$	Same as above				Same as above			
$m_u=10\%$	Same as above				Same as above			

Table 5-9: Force margins of each wheel

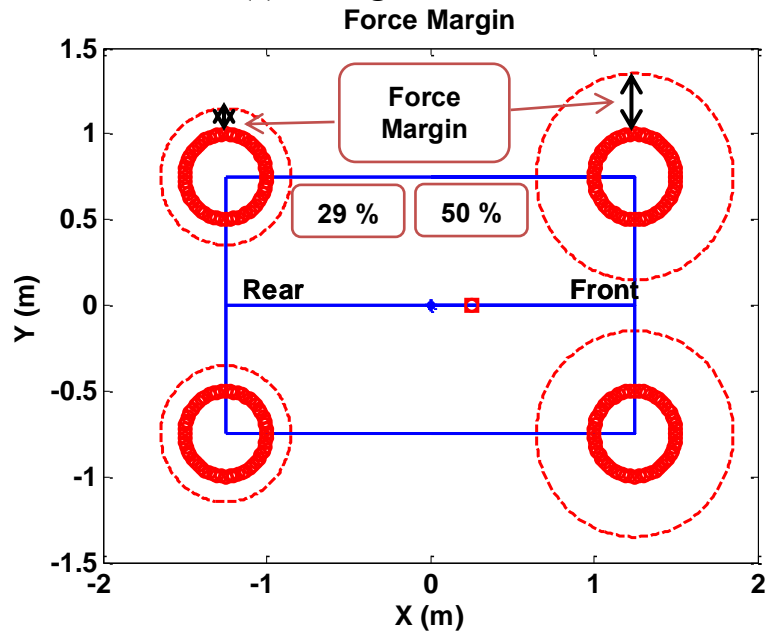
During constant velocity, the force margin becomes 1, indicating that the available maximum traction force of a vehicle is 100% at each wheel. The maximum traction force of a vehicle can be determined by one of two constraints: traction limits and motor power on the wheels.

During braking, the force margin of the rear wheels is 0.38 ($m_u = 22\%$) and 0.27 ($m_u = 10\%$), while the force margin of the front wheels is 0.59 ($m_u = 22\%$) and 0.57 ($m_u = 10\%$). The reason that the force margins of front wheels are larger than those of rear wheels is due to large normal forces on the front wheels that result from the forward inertial force caused by braking of the vehicle.

In addition, the minimum force margin of the rear wheels is 0.29 ($m_u = 22\%$) and 0.15 ($m_u = 10\%$), while the force margin of the front wheels is 0.5 ($m_u = 22\%$) and 0.48 ($m_u = 10\%$). These are the maximum overshoot due to braking torque input. Overall, the increased unsprung mass increases the force margin of each wheel, given the same wheel torque condition.



(a) During acceleration



(b) During braking ($t = 23$ s)

Figure 5-14: Force margins of each wheel on dry asphalt ($m_u = 0.22$, $\mu = 0.9$)

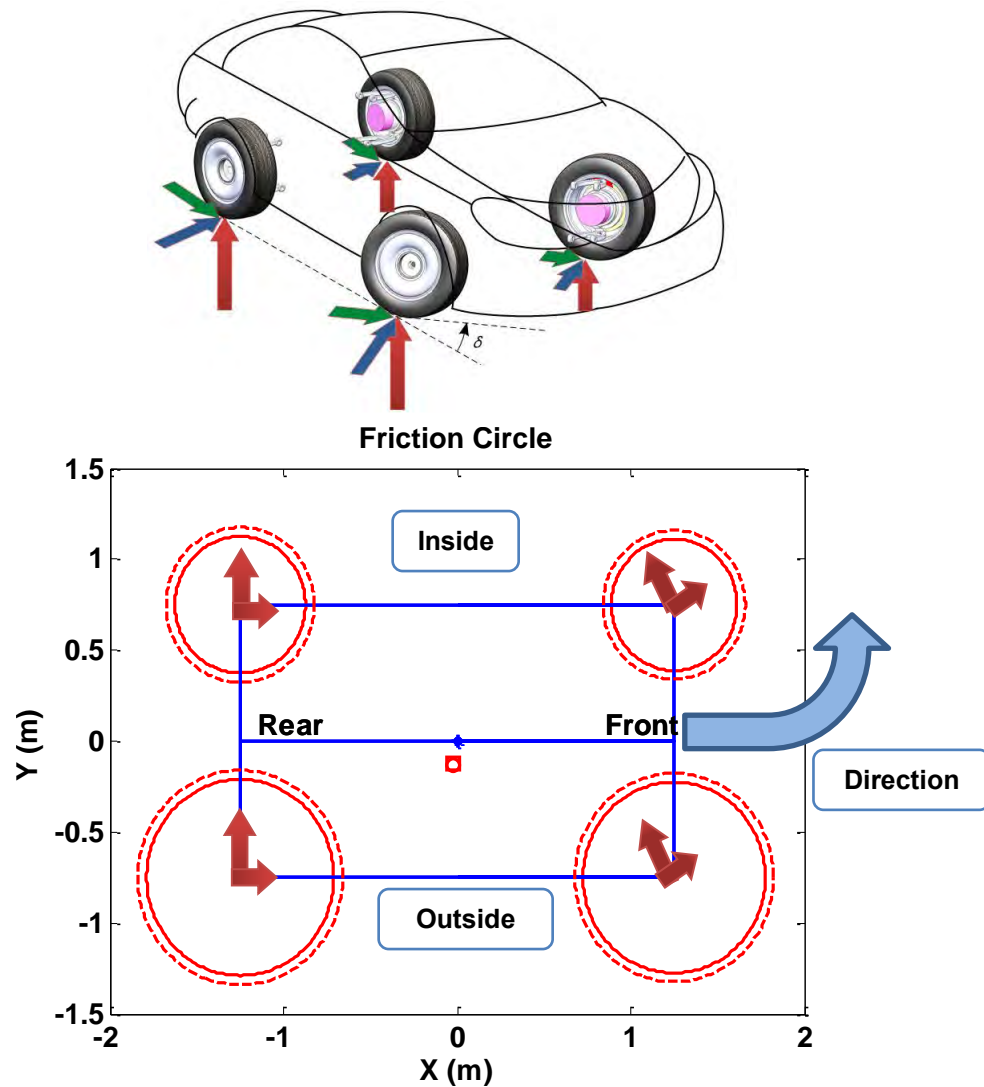
Figure 5-14 shows the force margins which are visualized by using the friction circle of each wheel. The dashed and heavy circles indicate maximum and simulated friction circle, respectively. As can be seen in Figure 5-14, the force margin of each wheel during acceleration is large (i.e., 77% and 72%).

This is attributed to low torque input of 290 N-m (214 ft-lb). If a vehicle moves with a high acceleration of 1 g, the required torque input may be 1120 N-m (826 ft-lb), so that force margin would become very small. As shown in Figure 5-14 (b), the force margin of each wheel during deceleration is relatively small, compared to Figure 5-14 (a). This is due to the braking torque input being larger than the acceleration torque input; the braking torque input is 570 N-m (420 ft-lb).

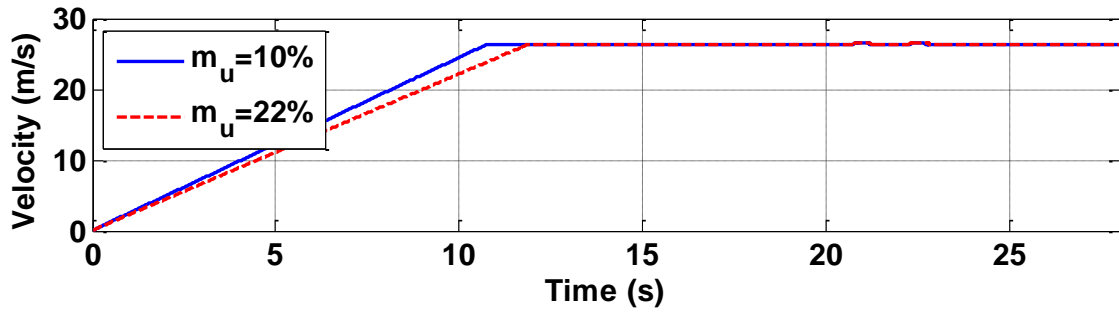
In addition, the force margin is large on the wheel that has a large normal force. In other words, during acceleration, the force margin of the rear wheels is larger than that of front wheels. In contrast, during braking, the force margin of front wheels is larger than that of rear wheels. If a vehicle use the available force margin (i.e. front wheels during braking, rear wheels during acceleration), the traction and braking capability will be maximized.

5.2.1.2 Cornering Maneuver

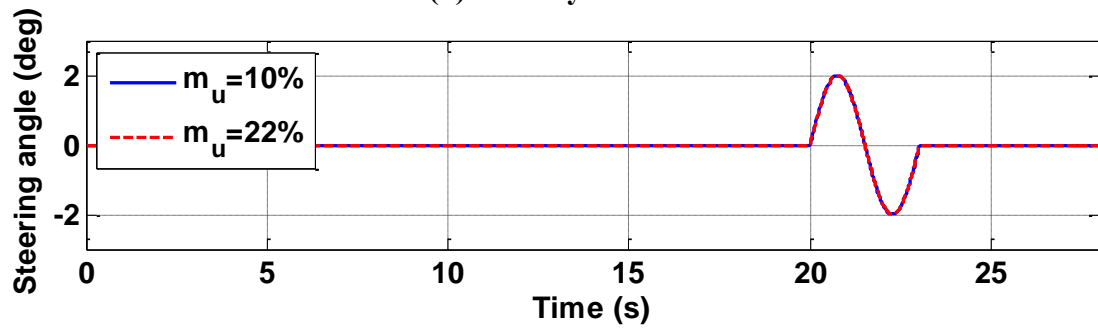
We discussed the effect of unsprung mass on the cornering maneuver such as a step steer and a single-lane change in Secs. 4.6.3. The single-lane change maneuver is chosen as a cornering maneuver in this simulation. Simulations of the vehicle's response subjected to a single-lane change are carried out as shown in Figure 5-15.



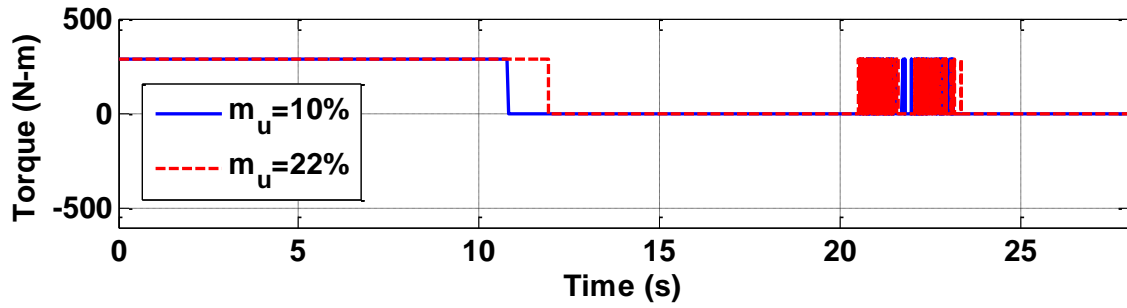
(a) Free-body diagram and friction circle of each wheel during cornering



(b) Velocity Profile



(c) Steering angle command



(d) Wheel torque command

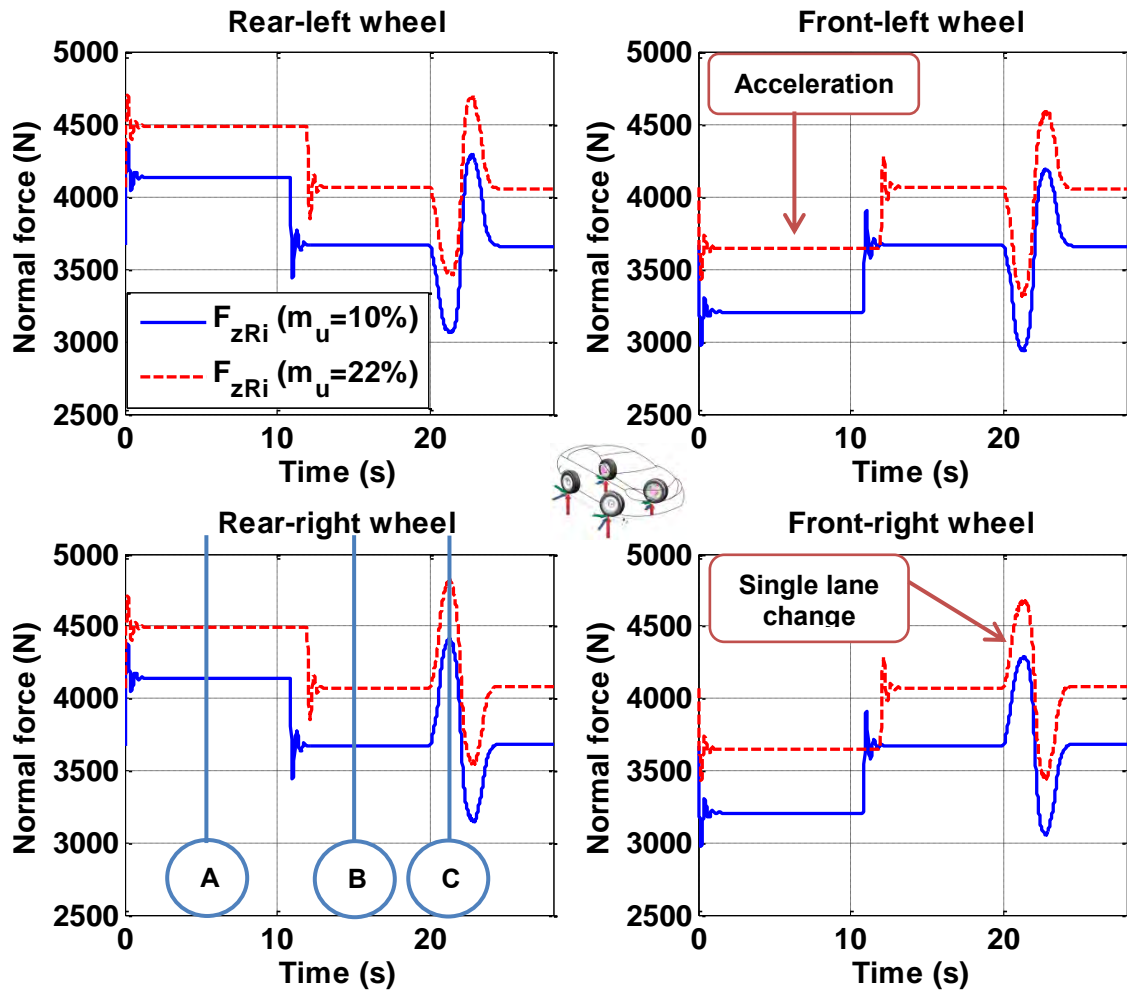
Figure 5-15: Simulation results for a single-lane change on dry asphalt ($\mu = 0.9$)

Figure 5-15 (a) shows a free-body diagram and the friction circles visualized at each wheel, when a vehicle reaches a steering angle of 2° at $t = 20.8$ s, as shown in Figure 5-15 (c).

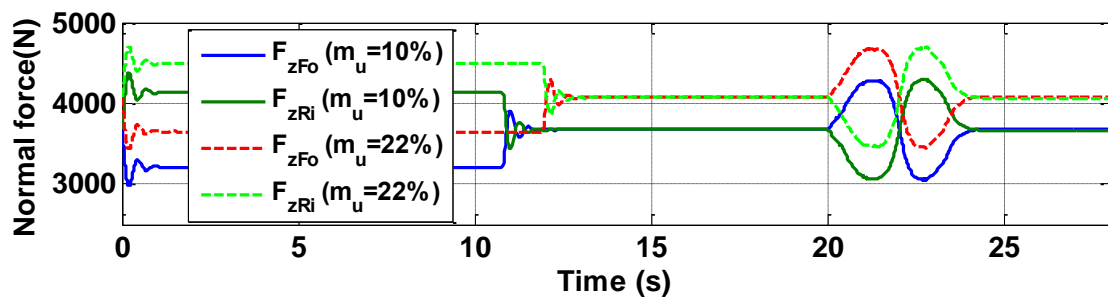
The friction circles of front-outside (front-left) and rear-outside (rear-left) wheels are larger than those of front-inside (front-right) and rear-inside (rear-right) wheels. This occurs because of the right-outward inertial force. On the other hand, when a vehicle reaches a steering angle of -2° at $t = 22.3$ s, the opposite phenomenon occurs.

As can be seen in Figure 5-15 (a), the solid and dashed circles are associated with vehicles for $m_u = 10\%$ and $m_u = 22\%$, respectively. It can be clearly seen that the friction circles of the outside wheels are larger than those of the inside wheels due to outward inertial force.

In addition, the increased unsprung mass increases the size of a friction circle. As shown in Figure 5-15 (d), the wheel torque is produced to maintain the longitudinal velocity of 26.4 m/s (60 mph) during a single-lane change. The steering angle commands are shown in Figure 5-15 (c).



(a) Normal forces of each wheel



(b) Comparison of normal forces

Figure 5-16: Normal forces for a single-lane change on dry asphalt ($\mu = 0.9$)

As mentioned in Secs. 5.1.3, during a cornering maneuver, the dynamic load transfer occurs from the inside to the outside (or vice versa) because of the inertia force acting on the vehicle, so that the normal force varies from the static values by the amount of load transfer. Figure 5-16 (a) shows the normal forces of each wheel for a single-lane change on dry asphalt, and Figure 5-16 (b) shows the comparison of normal forces between the front-outside (F_{zFo}) wheel and the rear-inside (F_{zRi}) wheel in terms of unsprung masses of 10% and 22%. The numerical numbers associated with these plots can be seen in Table 5-10.

	A (t = 5s) {Accel.}	B (t = 15s)	C (t=21.2s) {SLC}	A (t = 5s) {Accel.}	B (t = 15s)	C (t=21.2s) {SLC}
	<u>Rear-left wheel</u> (F_{zRl})			<u>Front-left wheel</u> (F_{zFl})		
$m_u=22\%$	4493 N 1010 lb	4072 N 915 lb	3473 N 781 lb	3650 N 821 lb	4072 N 915 lb	3319 N 746 lb
$m_u=10\%$	4139 N 930 lb	3673 N 827 lb	3067 N 689 lb	3207 N 721 lb	3673 N 826 lb	2936 N 660 lb
	<u>Rear-right wheel</u> (F_{zRr})			<u>Front-right wheel</u> (F_{zFr})		
$m_u=22\%$	Same as above			Same as above		
$m_u=22\%$	Same as above			Same as above		
$m_u=10\%$	Same as above			Same as above		

Table 5-10: Normal forces of each wheel

As shown in Figure 5-16 (a), the symbol ‘A’, ‘B’, and ‘C’ corresponds to $t = 5$ s, $t = 15$ s, and $t = 21.2$ s, respectively. During acceleration (A), the maximum normal forces

of the rear wheels in terms of $m_u = 22\%$ and $m_u = 10\%$ are 4493 N and 4139 N, respectively. During constant velocity (B), the normal forces of the all wheels are 4072 N and 3673 N, respectively. During a single-lane change (SLC, 'C'), the maximum normal forces of the front-right and rear-right wheel in terms of $m_u = 22\%$ are 4824 N and 4410 N, and the maximum normal forces of the front-right and rear-right wheel in terms of $m_u = 10\%$ are 4410 N and 4280 N respectively.

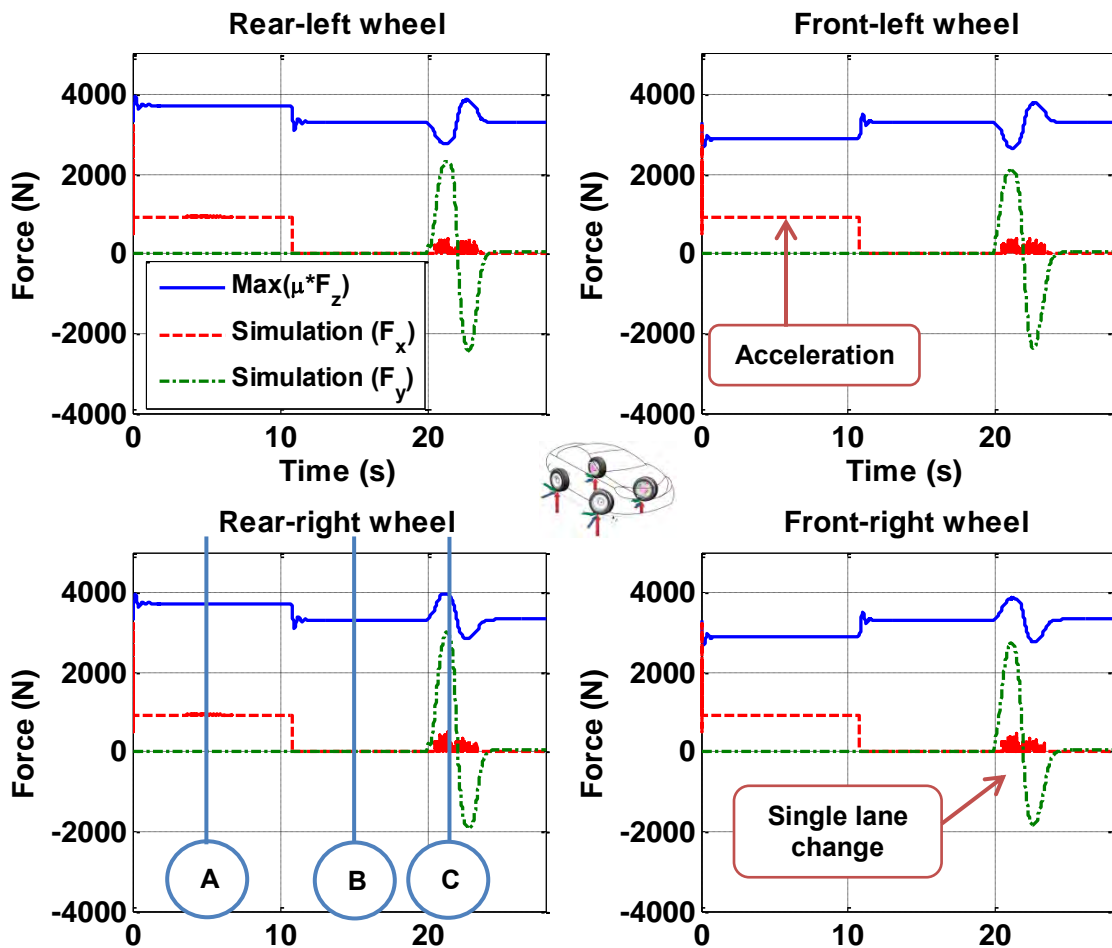


Figure 5-17: Longitudinal and lateral forces on dry asphalt ($m_u = 10\%$, $\mu = 0.9$)

With regard to a single-lane change, the input is the steering angle. This generates a slip angle and results in lateral forces on all four wheels. The longitudinal and lateral forces have to satisfy specified equality constraints, as shown in Equation (5.7). Figure 5-17 shows the longitudinal and lateral forces of each wheel on a vehicle with $m_u = 10\%$. The solid, dashed, and dash-dot line indicates available maximum traction force, simulated longitudinal force, and simulated lateral force. As shown in Figure 5-17, the symbol ‘A’, ‘B’, and ‘C’ corresponds to $t = 5$ s, $t = 15$ s, and $t = 21.2$ s, respectively. The numerical numbers associated with these plots can be seen in Table 5-11.

	A (t = 5s) B (t = 15s)				C (t = 21.2s)		A (t = 5s) B (t = 15s)				C (t = 21.2s)	
	{Accel.}				{SLC}		{Accel.}				{SLC}	
	<u>Rear-left wheel</u> (F_{zRl})						<u>Front-left wheel</u> (F_{zFl})					
Max	3725	N	3306	N	2765	N	2886	N	3306	N	2642	N
(μ *F _z)	837	lb	743	lb	622	lb	649	lb	743	lb	594	lb
Simulation	919	N	3	N	352	N	915	N	3	N	345	N
(abs(F _x))	207	lb	0.7	lb	79	lb	206	lb	0.7	lb	55	lb
Simulation	0	N	0	N	2305	N	0	N	0	N	2111	N
(F _y)	0	lb	0	lb	518	lb	0	lb	0	lb	475	lb
	<u>Rear-right wheel</u> (F_{zRr})						<u>Front-right wheel</u> (F_{zFr})					
Max	Same as above				3967	N	Same as above				3855	N
(μ *F _z)					892	lb					867	lb
Simulation	Same as above				453	N	Same as above				467	N
(abs(F _x))					102	lb					105	lb
Simulation	Same as above				2943	N	Same as above				2719	N
(F _y)					662	lb					611	lb

Table 5-11: Traction and braking forces of each wheel ($m_u = 10\%$, $\mu = 0.9$)

During acceleration (A), the maximum traction forces and the simulated traction of the rear wheels are 3725 N and 919 N, respectively. During constant velocity (B), the maximum traction forces and the simulated traction of all wheels are 3306 N and 3 N, respectively. During a single-lane change (SLC, 'C'), the maximum traction forces, simulated longitudinal force, and lateral force of the rear-right wheels are 3967 N, 453 N, and 2943 N, respectively. In addition, the maximum traction forces, simulated longitudinal force, and lateral force of the front-right wheels are 3855 N, 467 N, and 2719 N, respectively.

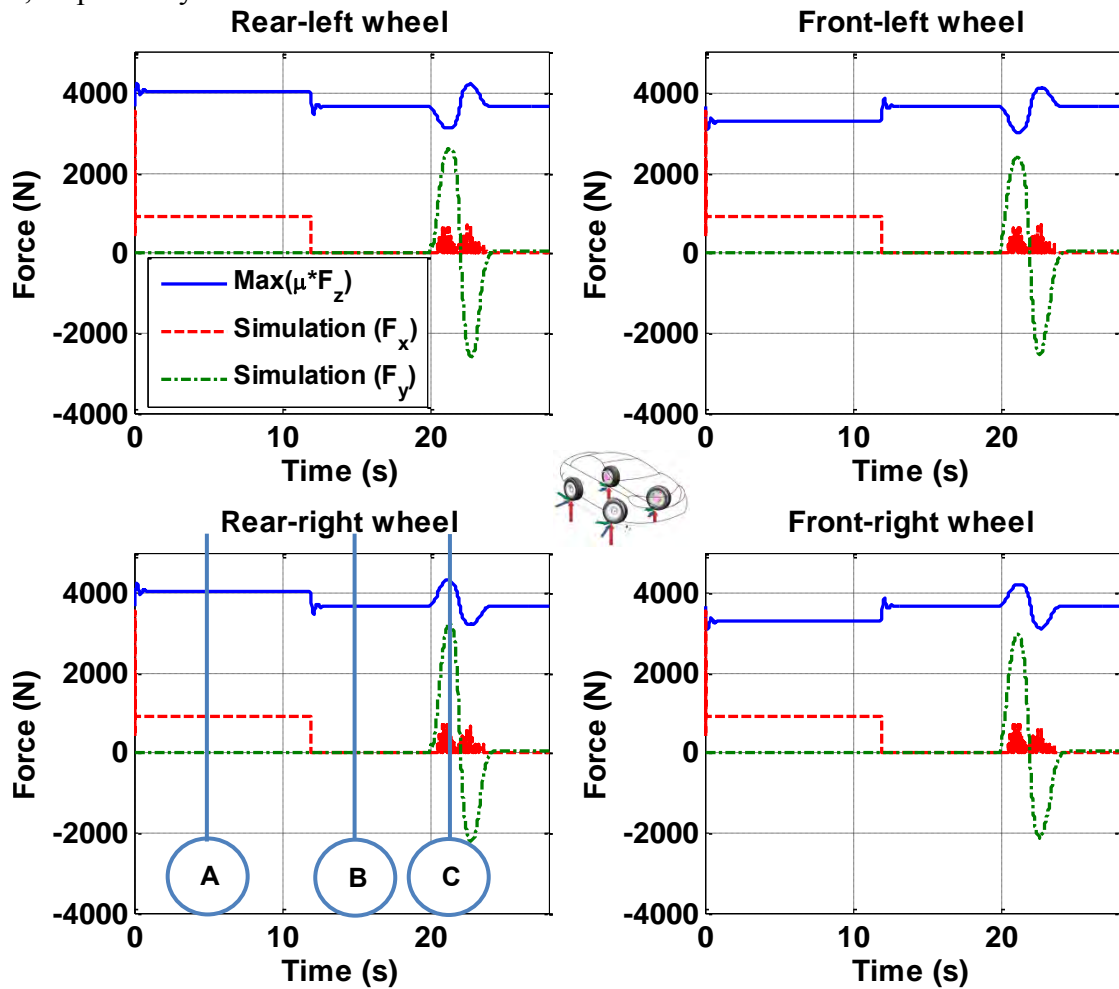


Figure 5-18: Longitudinal and lateral forces on dry asphalt ($m_u = 22\%$, $\mu = 0.9$)

Given unsprung mass ($m_u = 22\%$), the longitudinal and lateral forces on dry asphalt are simulated as shown in Figure 5-18. The symbol ‘A’, ‘B’, and ‘C’ corresponds to $t = 5$ s, $t = 15$ s, and $t = 21.2$ s, respectively. The numerical numbers associated with these plots can be seen in Table 5-12.

During acceleration (A), the maximum traction forces and the simulated traction of the rear wheels are 4044 N and 915 N, respectively. During constant velocity (B), the maximum traction forces and the simulated traction of all wheels are 3664 N and 6 N, respectively.

	A (t = 5s) B (t = 15s)				C (t = 21.2s)		A (t = 5s) B (t = 15s)				C (t = 21.2s)	
	{Accel.}				{SLC}		{Accel.}				{SLC}	
	<u>Rear-left wheel</u> (F_{zRl})						<u>Front-left wheel</u> (F_{zFl})					
Max	4044	N	3664	N	3131	N	3285	N	3664	N	2988	N
(μ*F _z)	909	lb	824	lb	704	lb	739	lb	824	lb	672	lb
Simulation	915	N	6	N	300	N	919	N	6	N	610	N
(abs(F _x))	206	lb	1.4	lb	67	lb	207	lb	1.4	lb	137	lb
Simulation	0	N	0	N	2595	N	0	N	0	N	2380	N
(F _y)	0	lb	0	lb	583	lb	0	lb	0	lb	535	lb
	<u>Rear-right wheel</u> (F_{zRr})						<u>Front-right wheel</u> (F_{zFr})					
Max	Same as above				4341	N	Same as above				4211	N
(μ*F _z)					976	lb					947	lb
Simulation	Same as above				710	N	Same as above				700	N
(abs(F _x))					160	lb					157	lb
Simulation	Same as above				3235	N	Same as above				2964	N
(F _y)					727	lb					666	lb

Table 5-12: Traction and braking forces of each wheel ($m_u = 22\%$, $\mu = 0.9$)

During a single-lane change (SLC, 'C'), the maximum traction forces, simulated longitudinal force, and lateral force of the rear-right wheels are 4341 N, 710 N, and 3235 N, respectively. In addition, the maximum traction forces, simulated longitudinal force, and lateral force of the front-right wheels are 4211 N, 157 N, and 666 N, respectively

The difference between the maximum traction from Table 5-11 and the maximum traction from Table 5-12 during the constant velocity (B) is due to the increased unsprung mass which is from 10% (136 kg) to 22% (300 kg).

The increased unsprung mass of each wheel is around 41 kg (90 lb). Taking into account the friction coefficient ($\mu = 0.9$), the increased normal force becomes 360 N (90 lb). That is, the maximum traction of 3306 N tabled in Table 5-11 becomes a value of 3664 N, as shown in Table 5-12. The simulated force of 6 N is attributed to the tire slip in spite of constant velocity.

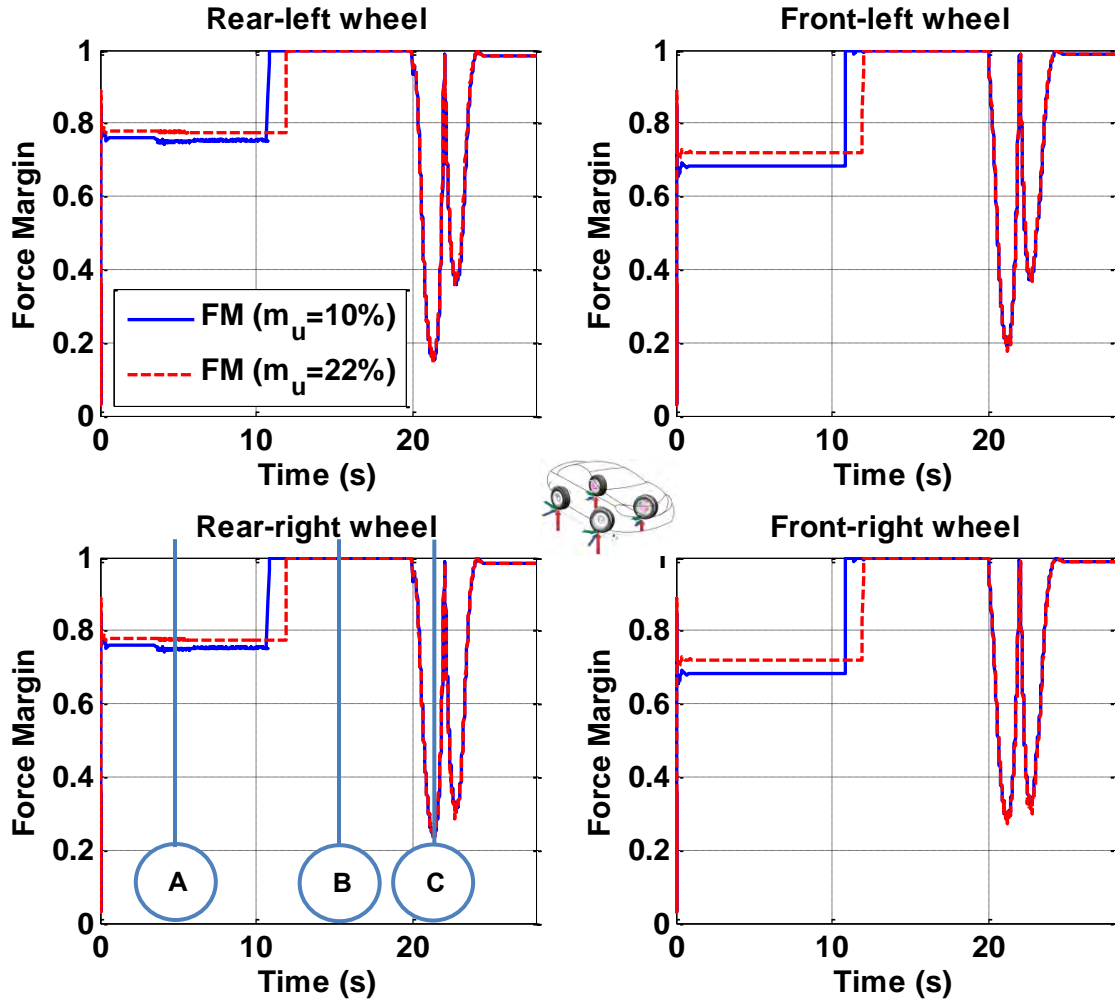


Figure 5-19: Effect of unsprung mass on force margin on dry asphalt ($\mu = 0.9$)

Figure 5-19 shows the variation of force margin subjected to a single-lane change from $t = 20$ s to $t = 25$ s. It can be seen that the increased unsprung mass gives little effect on the force margin. The dashed line is superimposed on the solid line.

The force margin of each wheel can be calculated by knowing the information of maximum traction force (μF_{zjk}) and simulated longitudinal force (F_{xjk}) and lateral force (F_{yjk}) of each wheel. For instance, the maximum traction force, simulated lateral

force, and simulated longitudinal force are 2765 N, 2305 N, and 352 N from the rear-left wheel plot, as shown in Figure 5-17. Therefore, Equation (5.9) becomes:

$$FM = \left(\frac{2765 - \sqrt{352^2 + 2305^2}}{2765} \right) \times 100\% = 16\% \quad (5.11)$$

The force margin of the rear-left wheel of a vehicle with a $m_u = 10\%$ becomes 0.16, which indicates an available traction force of 16 %: a value of zero indicates saturation of the traction force. The force margin of a vehicle with $m_u = 22\%$ increase slightly. As shown in Figure 5-19, the symbol ‘A’, ‘B’, and ‘C’ correspond to $t = 5$ s, $t = 15$ s, and $t = 21.2$ s, respectively. The numerical numbers associated with these plots can be seen in Table 5-13.

	A (t = 5s) {Accel.}	B (t = 15s)	C (t = 21.2s) {SLC}	A (t = 5s) {Accel.}	B (t = 15s)	C (t = 21.2s) {SLC}
	<u>Rear-left wheel</u> (F_{zRl})			<u>Front-left wheel</u> (F_{zFl})		
$m_u=22\%$	0.77	1	0.16	0.72	1	0.20
$m_u=10\%$	0.75	1	0.16	0.68	1	0.19
	<u>Rear-right wheel</u> (F_{zRr})			<u>Front-right wheel</u> (F_{zFr})		
$m_u=22\%$	Same as above		0.25	Same as above		0.29
$m_u=10\%$	Same as above		0.24	Same as above		0.28

Table 5-13: Force margins of each wheel

During constant velocity, the force margin becomes 1, indicating that the available maximum traction force of a vehicle is 100% at each wheel. During a single-lane change, the force margins of the outside wheels (i.e., 0.24, 0.28) are larger than those

of the inside wheels (i.e., 0.16, 0.19). This is attributed that the normal forces of the outside wheels are larger than those of the inside wheels, which result from the inertial force caused by cornering.

In addition, the force margins of the rear wheels (i.e., 0.16, 0.24) are smaller than those of the front wheels (i.e., 0.19, 0.28). This occurs because the later acceleration at the CG causes the rear slip angle to increase more than the front slip angle, as shown in Figure 5-20. This condition is termed oversteer.

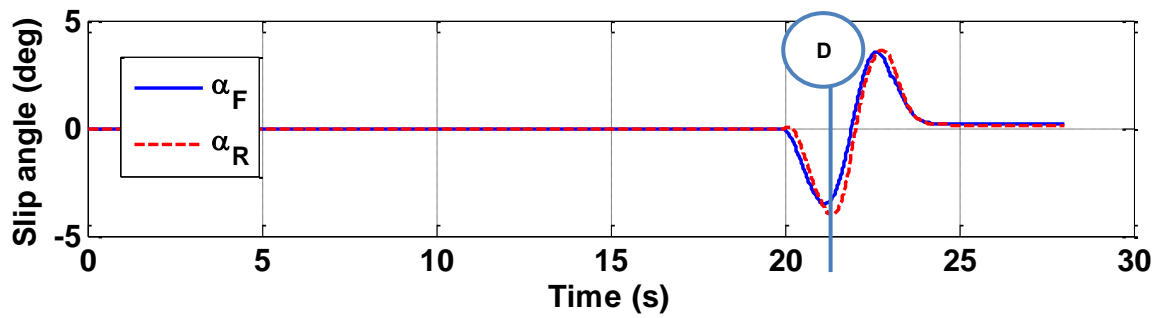


Figure 5-20: Front and rear slip angle

At the symbol 'D' ($t = 21.2$ s), the front slip angle (α_F) and rear slip angle (α_R) are 3.3° and 4° , respectively. As a result, the rear lateral force is larger than the front lateral force, resulting in the decreased force margin.

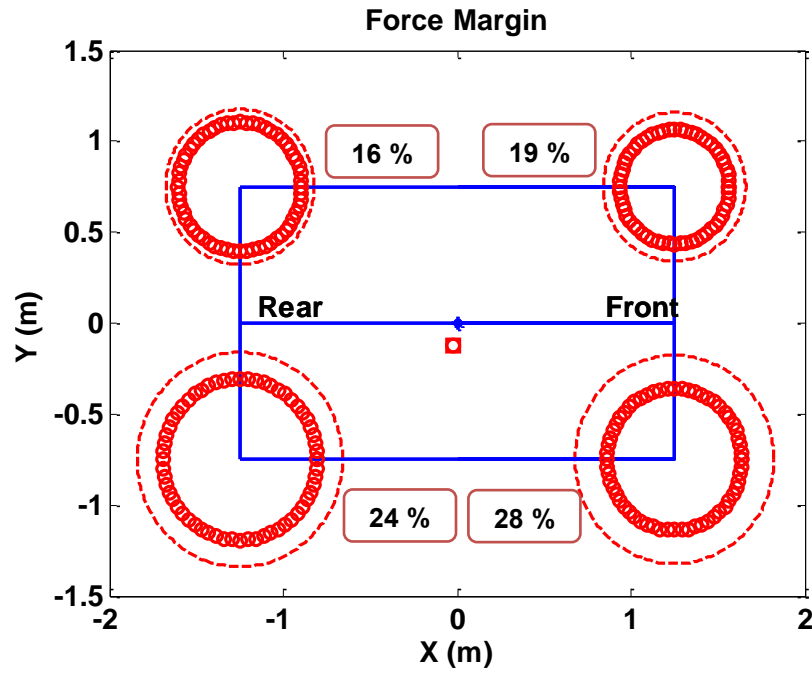


Figure 5-21: Force margin of each wheel on dry asphalt ($\mu = 0.9$)

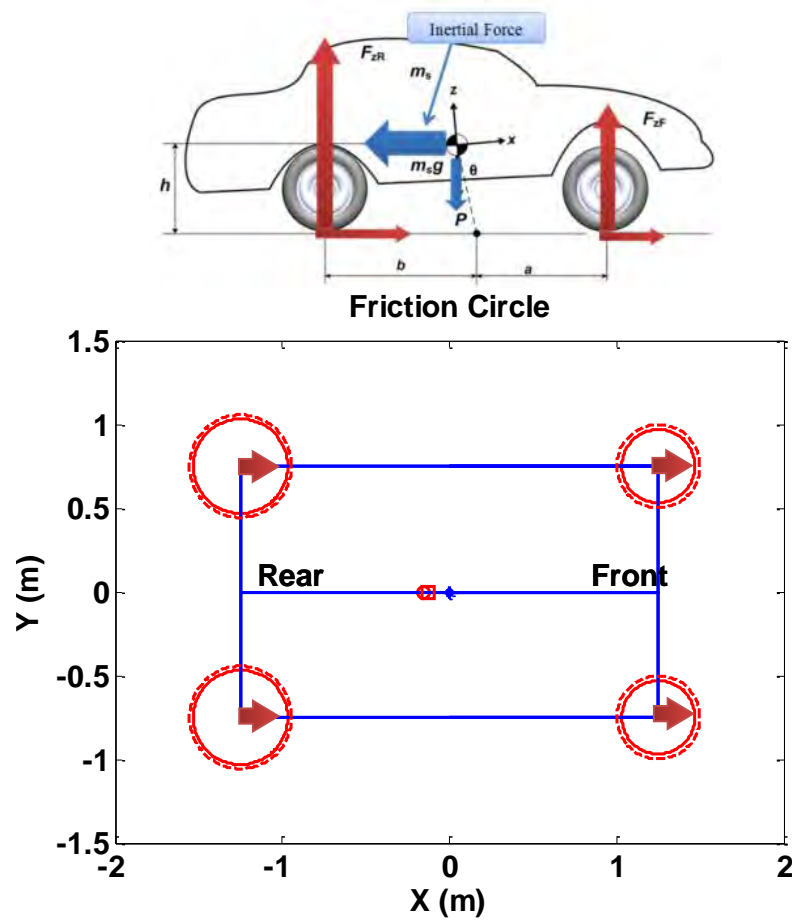
Figure 5-21 shows force margins which are visualized by using a friction circle for each wheel. The dashed and thick circle lines indicate the maximum friction circle and simulated friction circle, respectively.

Clearly, it can be seen that the force margins of rear-right (rear-outside) and front-right (front-outside) wheels are larger than those of rear-left (rear-inside) and front-left (front-inside) wheels.

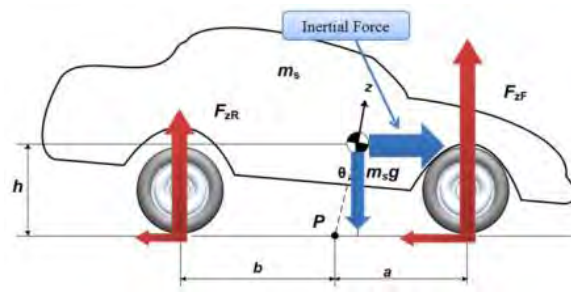
5.2.2 Wet Asphalt Road

5.2.2.1 Acceleration and Braking

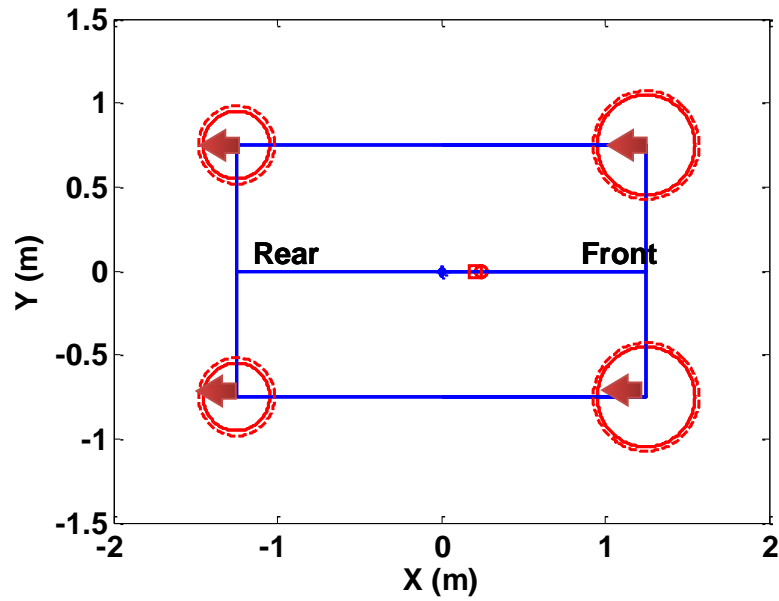
A wet asphalt road ($\mu = 0.5$) affects a vehicle's performance such as acceleration and braking. Simulations of the vehicle response subjected to acceleration and braking have been carried out as shown in Figure 5-22.



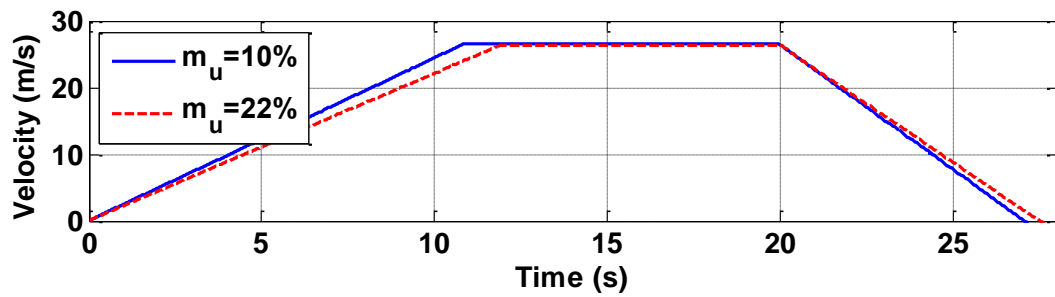
(a) Free-body diagram and friction circle of each wheel during acceleration (0-12s)



Friction Circle



(b) Free-body diagram and friction circle of each wheel during braking (20-27 s)



(c) Velocity Profile

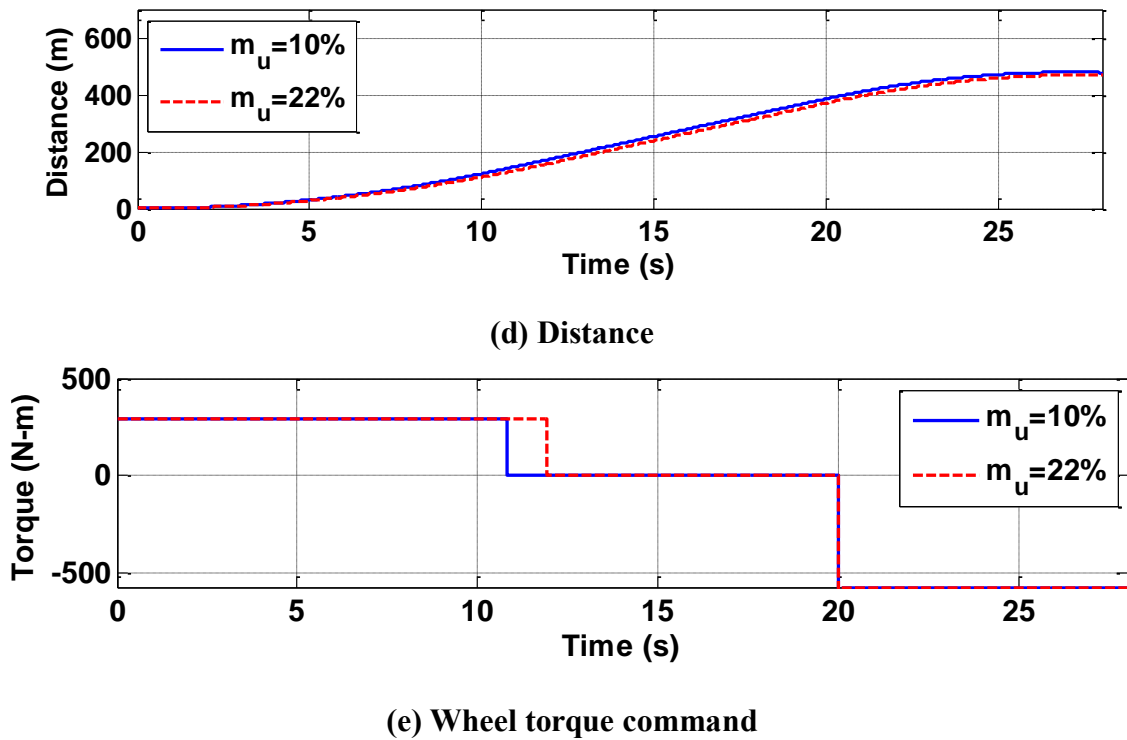


Figure 5-22: Simulation results for acceleration and braking on wet asphalt ($\mu = 0.5$)

The torque command as input is performed at $t = 0$ s with positive 290 N-m (214 ft-lb), and $t = 20$ s with negative 570 N-m, which are associated with acceleration and braking, respectively. Figure 5-22 (a) and (b) shows the free-body diagram and friction circles which are visualized at each wheel during acceleration and braking. The solid and dashed circles are associated with vehicles where $m_u = 10\%$ and $m_u = 22\%$, respectively.

Compared to the dry road at Sec 5.2.1.1, it can be seen that the friction circles of each wheel become smaller because of the decreased friction force caused by a lower friction coefficient (wet $\mu = 0.5$). In addition, the stopping distance becomes somewhat longer as shown in Figure 5-22 (d); stopping distance is 92 m (302 ft) on the wet road, while the stopping distance is 73 m (240 ft) on a dry road. As a result of wheel torque, the

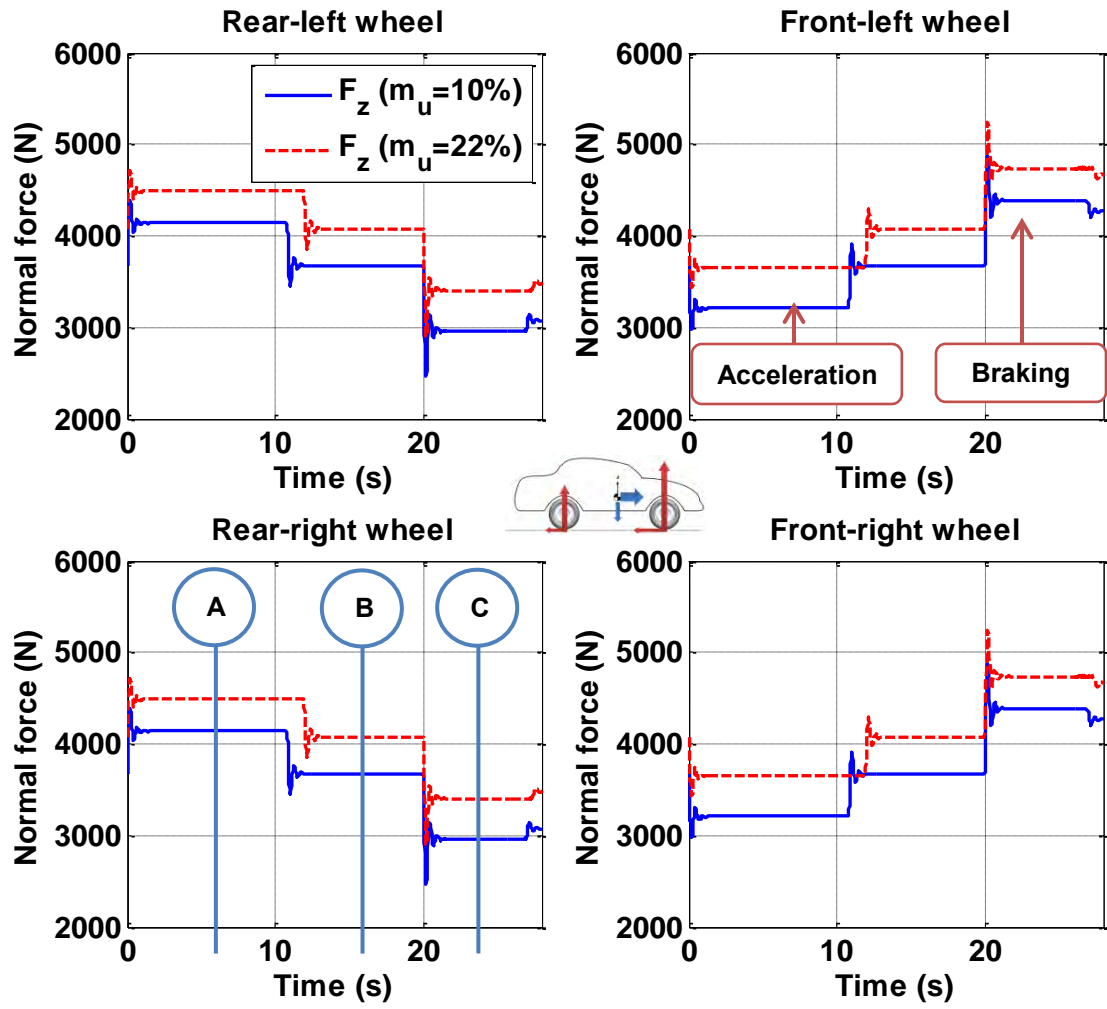
velocity profile and distance are determined as shown in Figure 5-22 (c) and (d), respectively.

		0-60 mph acceleration		60-0 mph braking	
		Dry asphalt	Wet asphalt	Dry asphalt	Wet asphalt
$m_u=22\%$	time	11.9 s	11.9 s	6 s	7.5 s
	accel.	0.23 g	0.23 g	0.45 g	0.36 g
	distance	143 m(ft)	158 (518) m(ft)	80(263) m(ft)	99(325) m(ft)
$m_u=10\%$	time	10.8 s	10.8 s	5.5 s	7 s
	accel.	0.25 g	0.25 g	0.5 g	0.38 g
	distance	143 m(ft)	143 (469) m(ft)	73(240) m(ft)	93(305) m(ft)

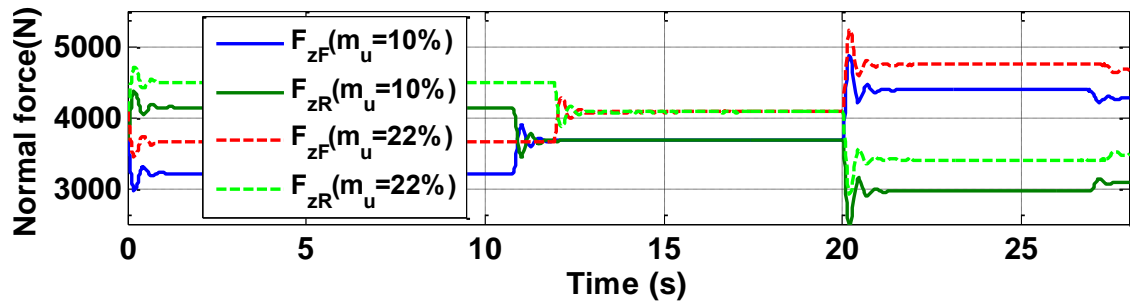
Table 5-14: Comparison of acceleration and braking

Table 5-14 shows the comparison of time, acceleration / deceleration, and distance during acceleration and braking in terms of $m_u = 10\%$ and $m_u = 22\%$. The 0-60 mph acceleration time is $t = 11.9$ s and $t = 10.8$ s, and the corresponding acceleration level is 0.23 g and 0.25 g in terms of $m_u = 22\%$ and $m_u = 10\%$, regardless of the dry and wet asphalt.

Under the dry asphalt condition, the 60-0 mph braking stopping time is $t = 6$ s and $t = 5.5$ s, and the corresponding deceleration level is 0.45 g and 0.5 g, and the stopping distance is $SD = 80$ m and $SD = 73$ m in terms of $m_u = 22\%$ and $m_u = 10\%$. Under the wet asphalt condition, the 60-0 mph braking stopping time is $t = 7.5$ s and $t = 7$ s, and the corresponding deceleration level is 0.36 g and 0.38 g, and the stopping distance is $SD = 99$ m and $SD = 63$ m in terms of $m_u = 22\%$ and $m_u = 10\%$.



(a) Normal forces of each wheel



(b) Comparison of normal forces

Figure 5-23: Normal forces during acceleration and braking on wet asphalt ($\mu = 0.5$)

Figure 5-23 (a) shows the normal forces of each wheel during acceleration (0 – 12 s) and braking (20 – 27.5 s): rear-left wheel, front-left wheel, rear-right wheel, and front-left wheel. Figure 5-23 (b) shows the comparison of normal forces in terms of $m_u = 10\%$ and $m_u = 22\%$. The numerical numbers associated with these plots can be seen in Table 5-15.

	A (t = 5s) {Accel.}	B (t = 15s)	C (t = 23s) {Braking}	A (t = 5s) {Accel.}	B (t = 15s)	C (t = 23s) {Braking}
	<u>Rear-left wheel</u> (F_{zRl})			<u>Front-left wheel</u> (F_{zFl})		
$m_u=22\%$	4493 N	4072 N	3404 N	3650 N	4072 N	4739 N
	1010 lb	915 lb	765 lb	821 lb	915 lb	1065 lb
$m_u=10\%$	4139 N	3673 N	2962 N	3207 N	3673 N	4383 N
	930 lb	827 lb	666 lb	721 lb	826 lb	985 lb
	<u>Rear-right wheel</u> (F_{zRr})			<u>Front-right wheel</u> (F_{zFr})		
$m_u=22\%$	Same as above			Same as above		
$m_u=10\%$	Same as above			Same as above		

Table 5-15: Normal forces of each wheel

As shown in Figure 5-23 (f), the symbol ‘A’, ‘B’, and ‘C’ corresponds to $t = 5$ s, $t = 15$ s, and $t = 23$ s, respectively. During acceleration (A), the maximum normal forces of the rear wheels in terms of $m_u = 22\%$ and $m_u = 10\%$ are 4493 N and 4139 N, respectively. During constant velocity (B), the normal forces of the all wheels are 4072 N and 3673 N, respectively. During braking (C), the maximum normal forces of the front wheels in terms of $m_u = 22\%$ and $m_u = 10\%$ reduced to 4739 N and 4383 N, due to the decreased deceleration, respectively.

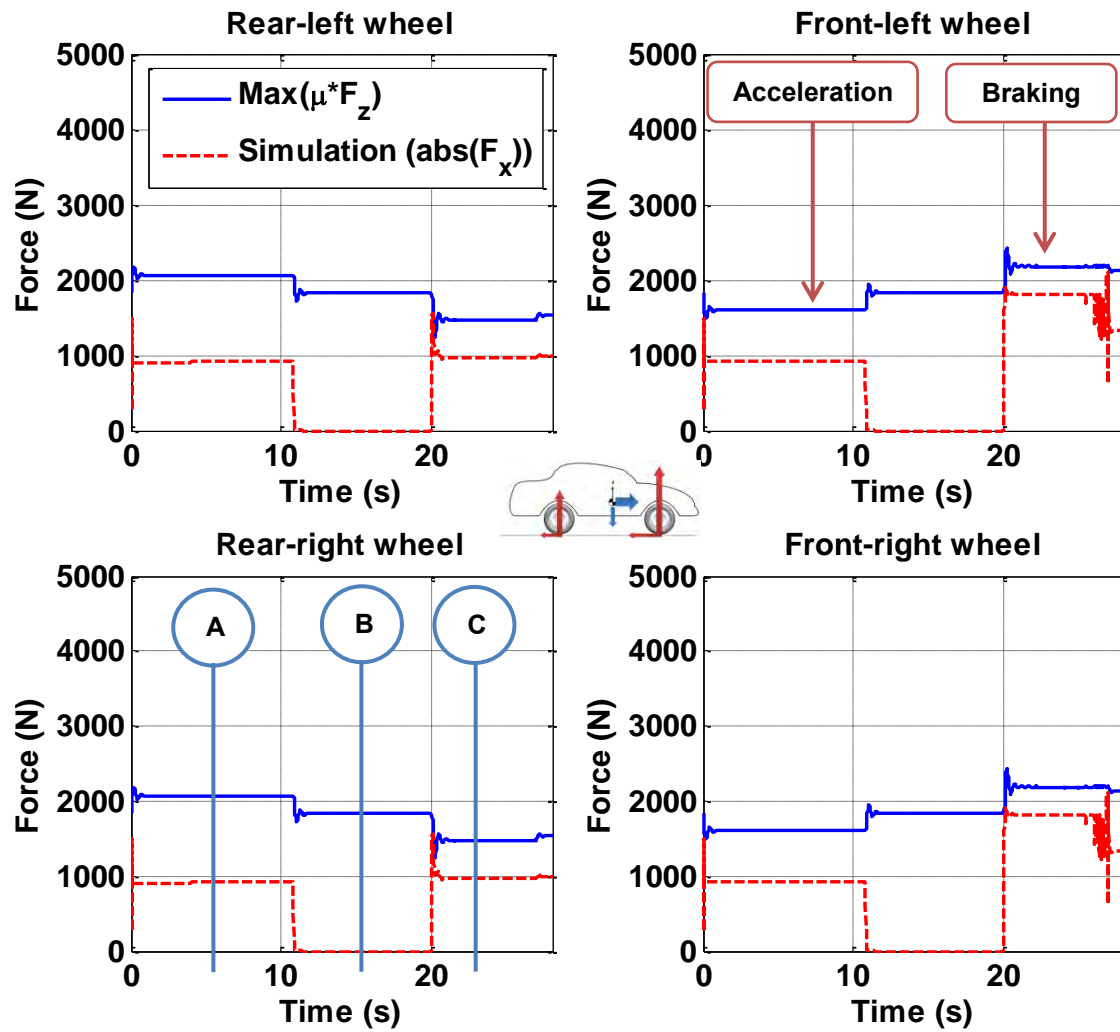


Figure 5-24: Traction and braking forces on wet asphalt ($m_u = 10\%$, $\mu = 0.5$)

Figure 5-24 shows the traction force and braking forces of a vehicle with $m_u = 10\%$. The solid and dashed lines represent available maximum traction force and simulated traction force, respectively. As shown in Figure 5-24, the symbol ‘A’, ‘B’, and ‘C’ corresponds to $t = 5$ s, $t = 15$ s, and $t = 23$ s, respectively. The numerical numbers associated with these plots can be seen in Table 5-16.

	A (t = 5s)			B (t = 15s)			C (t = 23s)			A (t = 5s)			B (t = 15s)			C (t = 23s)		
	{Accel.}			{Braking}			{Accel.}			{Braking}			{Accel.}			{Braking}		
	<u>Rear-left Wheel</u> (F_{zRl})						<u>Front-left wheel</u> (F_{zFl})											
Max	2069	N	1836	N	1481	N	1604	N	1836	N	2192	N						
($\mu * F_z$)	465	lb	413	lb	333	lb	361	lb	413	lb	493	lb						
Simulation	919	N	0	N	972	N	919	N	0	N	1822	N						
(abs(F_x))	207	lb	0	lb	219	lb	207	lb	0	lb	410	lb						
	<u>Rear-right wheel</u> (F_{zRr})						<u>Front-right wheel</u> (F_{zFr})											
Max	Same as above						Same as above											
($\mu * F_z$)																		
Simulation	Same as above						Same as above											
(abs(F_x))																		

Table 5-16: Traction and braking forces of each wheel ($m_u = 10\%$, $\mu = 0.5$)

During acceleration (A), the maximum traction forces and the simulated traction of the rear wheels are 2069 N and 919 N, respectively. During constant velocity (B), the maximum traction forces and the simulated traction of all wheels are 1836 N and 0 N, respectively. During braking (C), the maximum traction forces and the simulated traction of the front wheels are 2192 N and 1822 N, respectively. For purposes of comparison, the absolute value of the braking force is used.

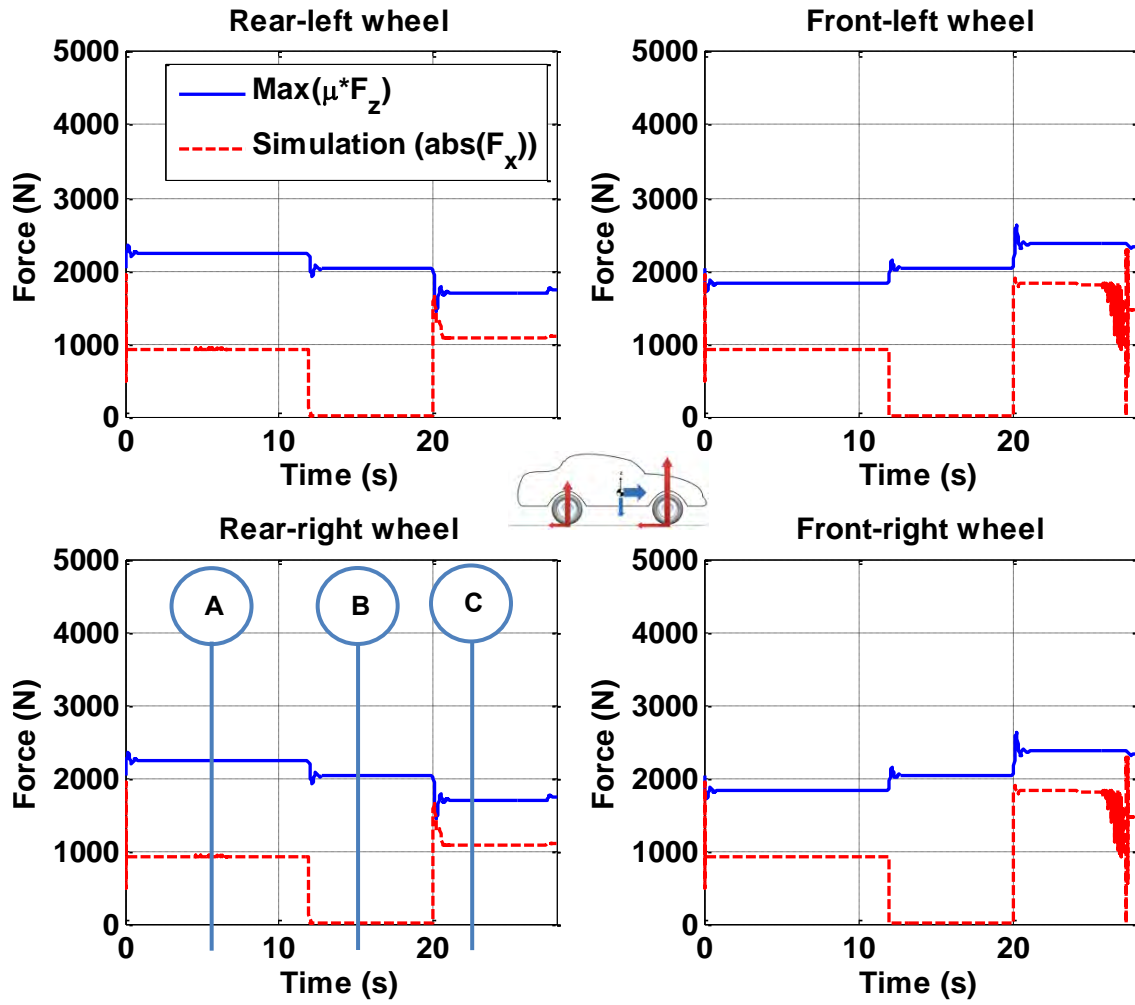


Figure 5-25: Traction and braking forces on wet asphalt ($m_u = 22\%$, $\mu = 0.5$)

Given unsprung mass of $m_u = 22\%$, traction and braking forces on wet asphalt are simulated as shown in Figure 5-25. The symbol ‘A’, ‘B’, and ‘C’ correspond to $t = 5$ s, $t = 15$ s, and $t = 23$ s, respectively. The numerical numbers associated with these plots can be seen in Table 5-17.

	A (t = 5s) B (t = 15s) C (t = 23s)						A (t = 5s) B (t = 15s) C (t = 23s)					
	{Accel.}											

Table 5-17: Traction and braking forces of each wheel ($m_u = 22\%$, $\mu = 0.5$)

During acceleration (A), the maximum traction forces and the simulated traction of the rear wheels are 2247 N and 919 N, respectively. During constant velocity (B), the maximum traction forces and the simulated traction of all wheels are 2036 and 0 N, respectively. During braking (C), the maximum traction forces and the simulated traction of the front wheels are 2369 N and 1824 N, respectively.

The difference between the maximum traction from Table 5-16 and the maximum traction from Table 5-17 during the constant velocity (B) is due to the increased unsprung mass that varies from 10% (136 kg) to 22% (300 kg). The increased unsprung mass of each wheel is around 41 kg (90 lb). Taking into account the friction coefficient ($\mu = 0.5$), the increased normal force becomes 200 N (45 lb). That is, the maximum traction of 1836 N tabled in Table 5-16 becomes a value of 2036 N, as shown in Table 5-17.

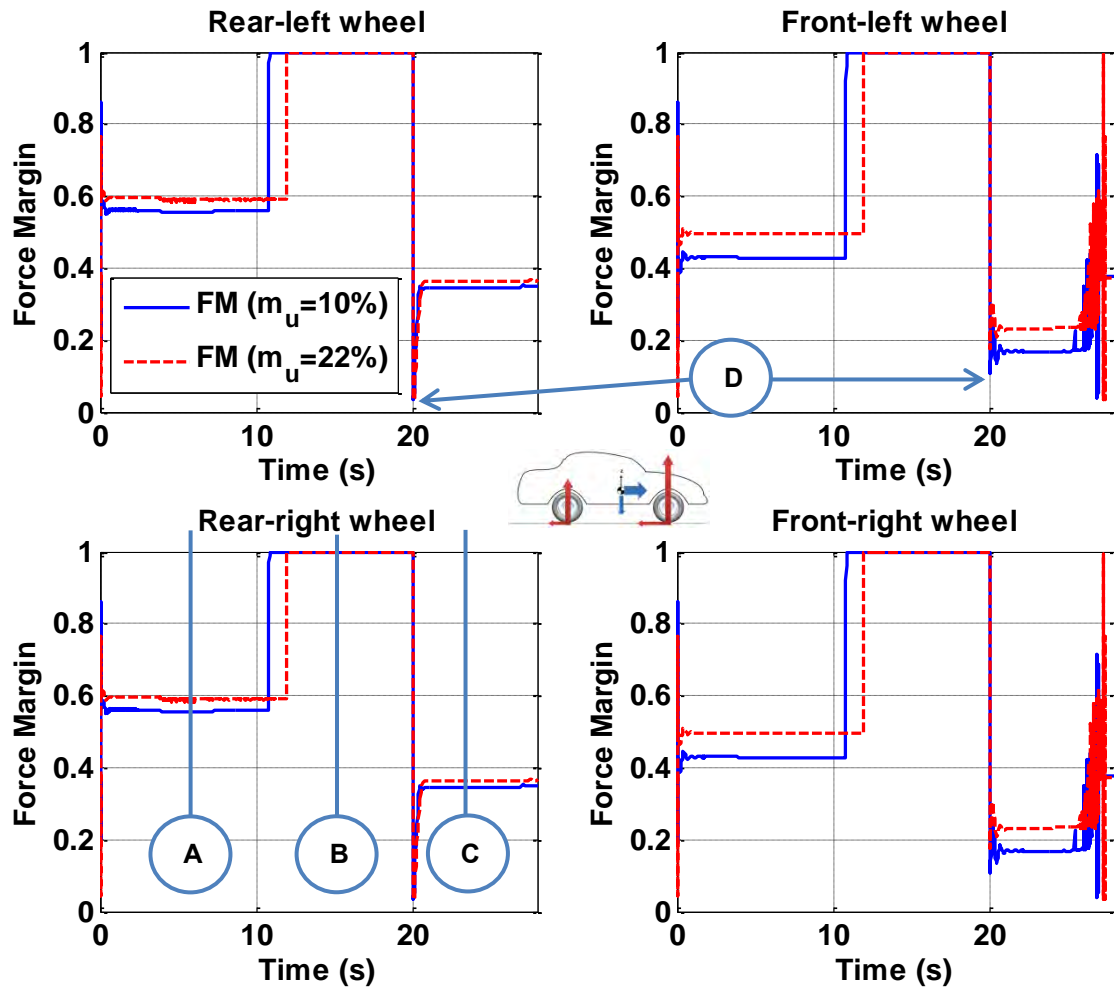


Figure 5-26: Effect of unsprung mass on force margin on wet asphalt ($\mu = 0.5$)

As can be seen from the data in Figure 5-24 and Figure 5-25, the force margins of each wheel are determined as shown in Figure 5-26. The variation of force margin during acceleration and braking are shown in terms of $m_u = 10\%$ and $m_u = 20\%$. The symbol ‘A’, ‘B’, and ‘C’ corresponds to $t = 5$ s, $t = 15$ s, and $t = 23$ s, respectively. The symbol ‘D’ indicates a minimum point of force margin. The numerical numbers associated with these plots can be seen in Table 5-18.

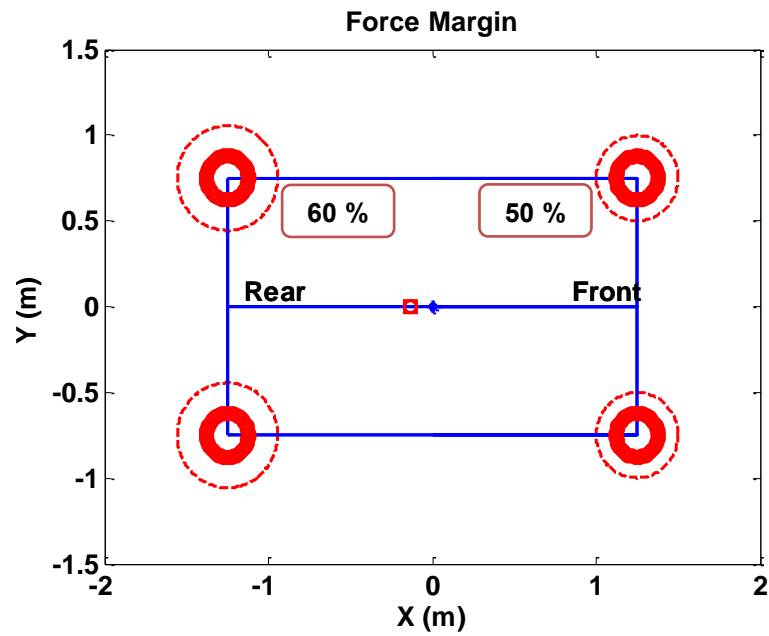
	A (t=5s) {Accel.}	B(t=15s)	C (t=23s) {Braking}	D (min)	A (t=5s) {Accel.}	B(t=15s)	C (t=23s) {Braking}	D (min)
	<u>Rear-left wheel</u> (F_{zRl})				<u>Front-left wheel</u> (F_{zFl})			
$m_u=22\%$	0.60	1	0.36	0.03	0.50	1	0.23	0.18
$m_u=10\%$	0.56	1	0.34	0.03	0.43	1	0.17	0.11
	<u>Rear-right wheel</u> (F_{zRr})				<u>Front-right wheel</u> (F_{zFr})			
$m_u=22\%$	Same as above				Same as above			
$m_u=10\%$	Same as above				Same as above			

Table 5-18: Force margins of each wheel

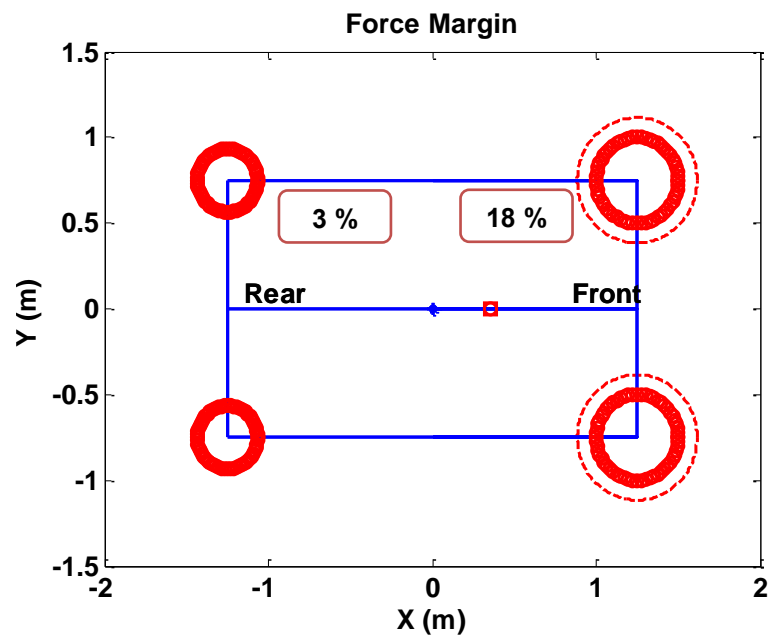
During acceleration, the force margin of the rear wheels is 0.60 ($m_u = 22\%$) and 0.56 ($m_u = 10\%$), and the force margin of the front wheels is 0.50 ($m_u = 22\%$) and 0.40 ($m_u = 10\%$). During constant velocity, the force margin becomes 1, indicating that the available maximum traction force of a vehicle is 100% at each wheel.

The maximum traction force of a vehicle can be determined by one of two constraints: traction limits and motor power on the wheels. During braking, the force margin of the rear wheels is 0.36 ($m_u = 22\%$) and 0.34 ($m_u = 10\%$), while the force margin of the front wheels is 0.23 ($m_u = 22\%$) and 0.17 ($m_u = 10\%$). In addition, the minimum force margin of the rear wheels is 0.03 regardless of unsprung masses, while the minimum force margin of the front wheels is 0.18 ($m_u = 22\%$) and 0.11 ($m_u = 10\%$). These are the maximum overshoot due to braking torque input.

In comparison with Table 5-9 (dry road) for $m_u = 22\%$, during acceleration, the force margins of the rear and front wheels are reduced to 0.6 and 0.5, respectively. In addition, during braking, the minimum force margins of rear and front wheels are reduced to 0.03 and 0.18, respectively. Overall, the increased unsprung mass increases the force margin of each wheel, given the same wheel torque condition.



(a) During acceleration



(b) During braking

Figure 5-27: Minimum Force margins of each wheel on wet asphalt ($m_u = 0.22$, $\mu = 0.5$)

Figure 5-27 shows the force margins which are visualized by using the friction circle of each wheel under $m_u = 0.22$ and $\mu = 0.5$. The dashed and heavy circles indicate maximum and simulated friction circle, respectively.

As can be seen in Figure 5-27 (a), the force margin of each wheel during acceleration is large (i.e., 60% and 50%). As shown in Figure 5-27 (b), the minimum force margin of each wheel during deceleration is relatively small (i.e., 3% and 18%), compared to Figure 5-27 (a). This is due to the braking torque input being larger than the acceleration torque input; the braking torque input is 570 N-m (420 ft-lb).

It can be seen that the force margin of each wheel decreases as the friction circle of each wheel decreases, given acceleration and braking torque. If the force margin becomes zero, the friction force reaches the saturation of the tire so that a vehicle might skid, which causes unstable vehicle motion.

5.2.2.2 Cornering Maneuver

The wet asphalt road affects a vehicle's performance especially in cornering maneuver. The single-lane change maneuver is chosen as a cornering maneuver. Simulations of the vehicle's response subjected to single lane change have been carried out as shown in Figure 5-28.

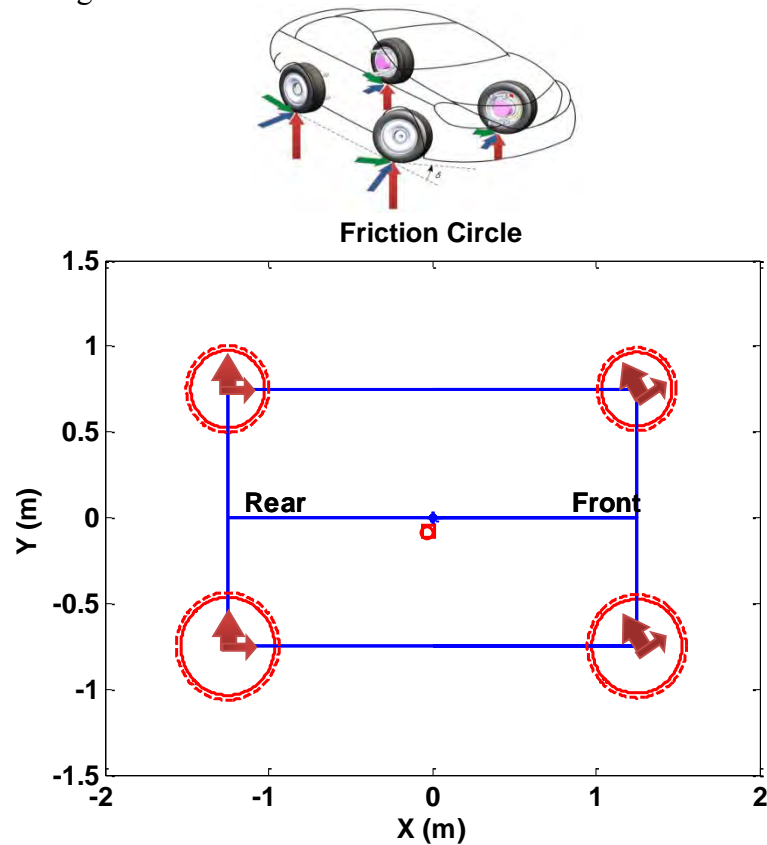
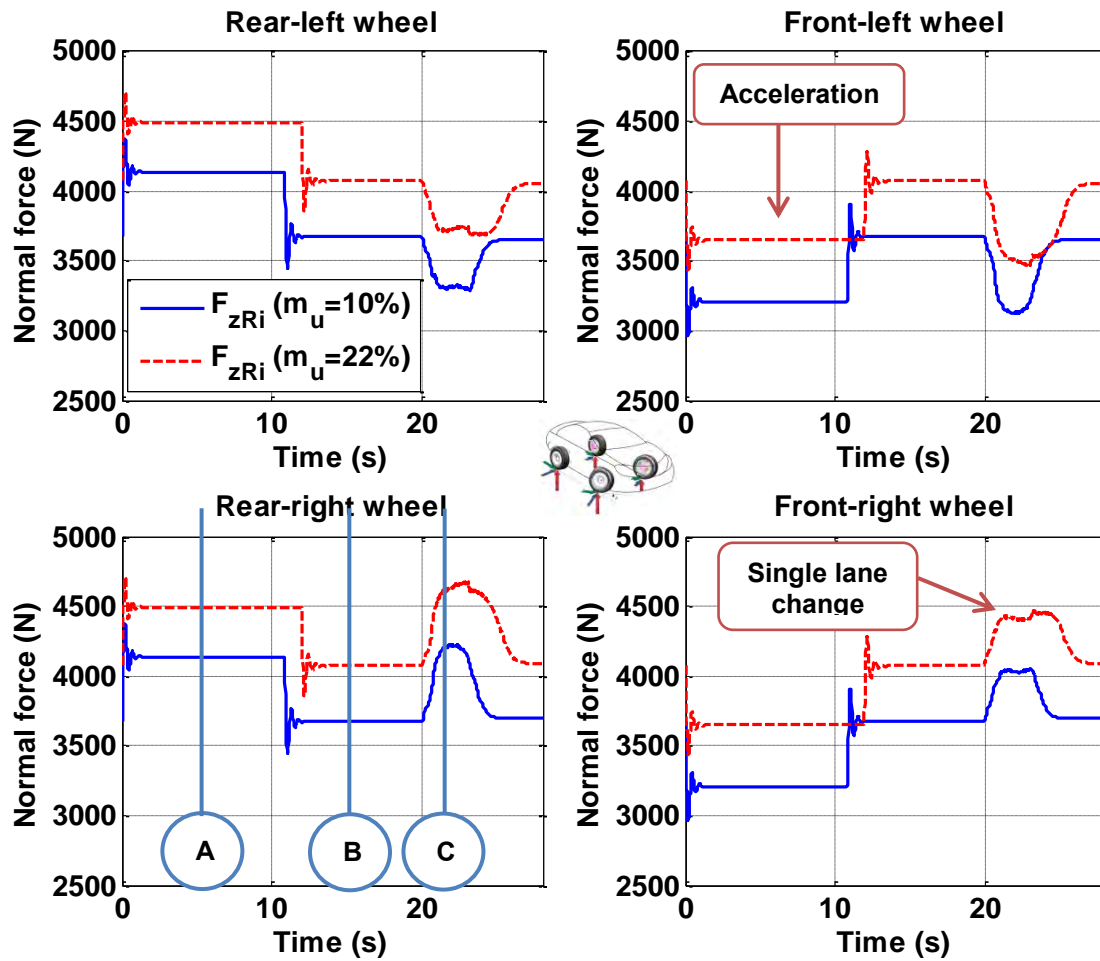
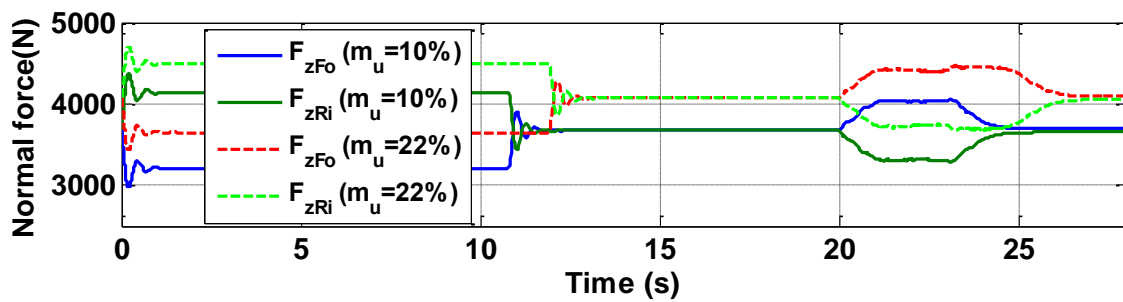


Figure 5-28: Friction circles of each wheel on wet asphalt ($\mu = 0.5$)

Figure 5-28 shows the friction circles which are visualized at each wheel, when a vehicle reaches a steering angle of 2° at $t = 20.8$ s. In comparison with Figure 5-15, it can be clearly seen that the friction circles of each wheel become smaller, as the friction coefficient decreases. The following analysis was performed under the same basic conditions in Sec.5.2.1.2.



(a) Normal forces of each wheel



(b) Comparison of normal forces

Figure 5-29: Normal forces for a single-lane change on wet asphalt ($\mu = 0.5$)

Figure 5-29 (a) shows the normal forces of each wheel for a single-lane change on a wet asphalt road, and Figure 5-29 (b) shows the comparison of normal forces between the front-outside (F_{zFo}) wheel and the rear-inside (F_{zRi}) wheel in terms of unsprung masses of 10% and 22%. The numerical numbers associated with these plots can be seen in Table 5-19.

	A (t = 5s) B (t = 15s) C (t=21.2s)			A (t = 5s) B (t = 15s) C (t=21.2s)		
	{Accel.}			{SLC}		
	<u>Rear-left wheel</u> (F_{zRl})			<u>Front-left wheel</u> (F_{zFl})		
$m_u=22\%$	4493 N	4072 N	3723 N	3650 N	4072 N	3556 N
	1010 lb	915 lb	837 lb	821 lb	915 lb	799 lb
$m_u=10\%$	4139 N	3673 N	3309 N	3207 N	3673 N	3164 N
	930 lb	827 lb	744 lb	721 lb	826 lb	711 lb
	<u>Rear-right wheel</u> (F_{zRr})			<u>Front-right wheel</u> (F_{zFr})		
$m_u=22\%$	Same as above			Same as above		
$m_u=10\%$	Same as above			Same as above		

Table 5-19: Normal forces of each wheel

As shown in Figure 5-29 (a), the symbol ‘A’, ‘B’, and ‘C’ corresponds to $t = 5$ s, $t = 15$ s, and $t = 21.2$ s, respectively. During acceleration (A), the maximum normal forces of the rear wheels in terms of $m_u = 22\%$ and $m_u = 10\%$ are 4493 N and 4139 N, respectively. During constant velocity (B), the normal forces of the all wheels are 4072 N and 3673 N, respectively. During a single-lane change (SLC, ‘C’), the maximum normal

forces of the front-right and rear-right wheel in terms of $m_u = 22\%$ are 4593 N and 4188 N, and the maximum normal forces of the front-right and rear-right wheel in terms of $m_u = 10\%$ are 4188 N and 4036 N, respectively.

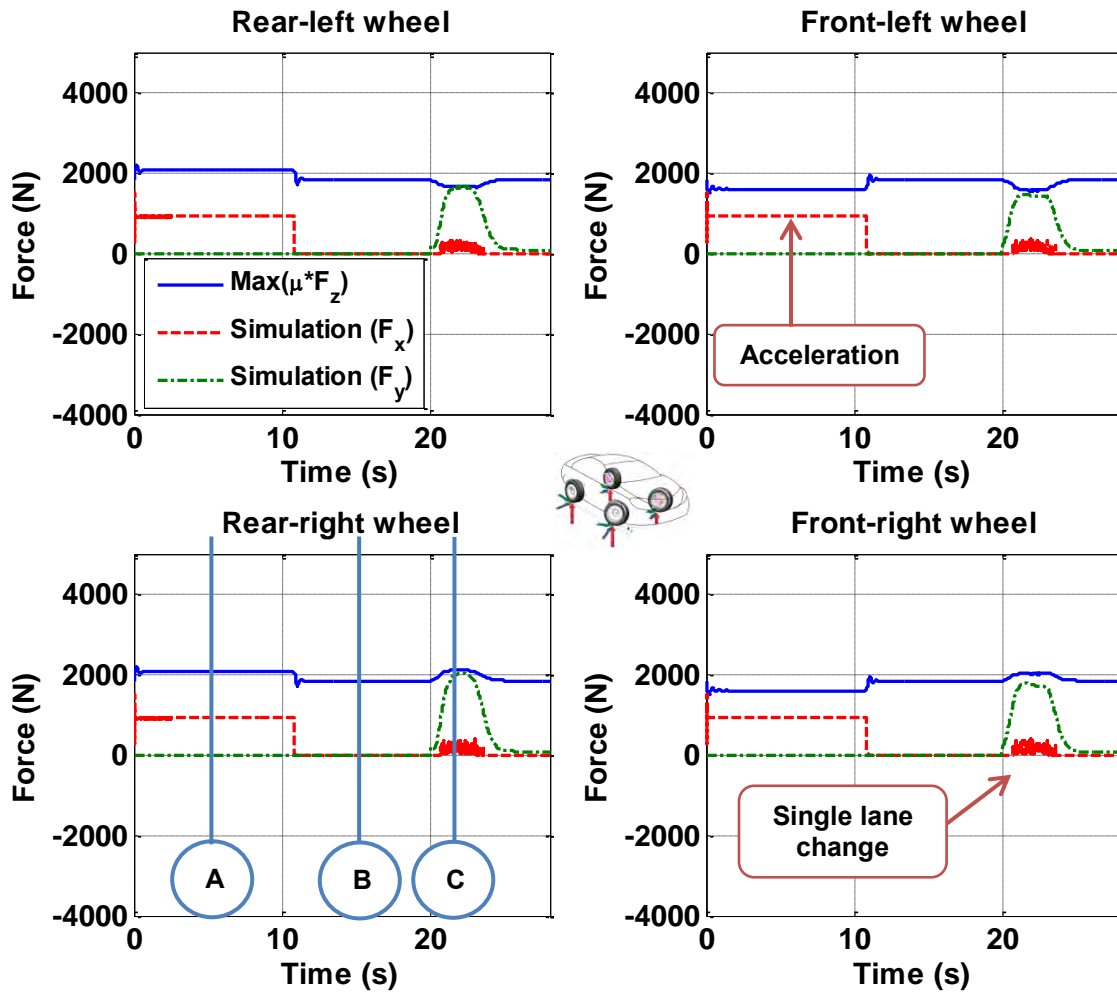


Figure 5-30: Longitudinal and lateral forces on wet asphalt ($m_u = 10\%$, $\mu = 0.5$)

With regard to a single-lane change, the input is the steering angle. This generates a slip angle and results in lateral forces on all four wheels. The longitudinal and lateral forces must satisfy specified equality constraints, as shown in Equation (5.7). Figure

5-30 shows the longitudinal and lateral forces of each wheel on a vehicle with $m_u = 10\%$. The solid, dashed, and dash-dot line indicate available maximum traction force, simulated longitudinal force, and simulated lateral force. As shown in Figure 5-30, the symbol ‘A’, ‘B’, and ‘C’ corresponds to $t = 5$ s, $t = 15$ s, and $t = 21.2$ s, respectively. The numerical numbers associated with these plots can be seen in Table 5-20.

	A (t = 5s) B (t = 15s)				C (t = 21.2s)		A (t = 5s) B (t = 15s)				C (t = 21.2s)	
	{Accel.}				{SLC}		{Accel.}				{SLC}	
	<u>Rear-left wheel</u> (F_{zRl})						<u>Front-left wheel</u> (F_{zFl})					
Max	2069	N	1836	N	1655	N	2069	N	1836	N	1582	N
(μ *F _z)	465	lb	413	lb	372	lb	465	lb	413	lb	356	lb
Simulation	919	N	0	N	300	N	915	N	0	N	212	N
(abs(F _x))	207	lb	0	lb	67	lb	206	lb	0	lb	48	lb
Simulation	0	N	0	N	1513	N	0	N	0	N	1444	N
(F _y)	0	lb	0	lb	340	lb	0	lb	0	lb	325	lb
	<u>Rear-right wheel</u> (F_{zRr})						<u>Front-right wheel</u> (F_{zFr})					
Max	Same as above				2086	N	Same as above				2017	N
(μ *F _z)					469	lb					453	lb
Simulation	Same as above				323	N	Same as above				318	N
(abs(F _x))					73	lb					71	lb
Simulation	Same as above				1818	N	Same as above				1742	N
(F _y)					409	lb					392	lb

Table 5-20: Traction and braking forces of each wheel ($m_u = 10\%$, $\mu = 0.5$)

During acceleration (A), the maximum traction forces and the simulated traction of the rear wheels are 2069 N and 919 N, respectively. During constant velocity (B), the maximum traction forces and the simulated traction of all wheels are 1836 N and 0 N,

respectively. During a single-lane change (SLC, 'C'), the maximum traction forces, simulated longitudinal force, and lateral force of the rear-right wheels are 2086 N, 323 N, and 1818 N, respectively. In addition, the maximum traction forces, simulated longitudinal force, and lateral force of the front-right wheels are 2017 N, 318 N, and 1742 N, respectively.

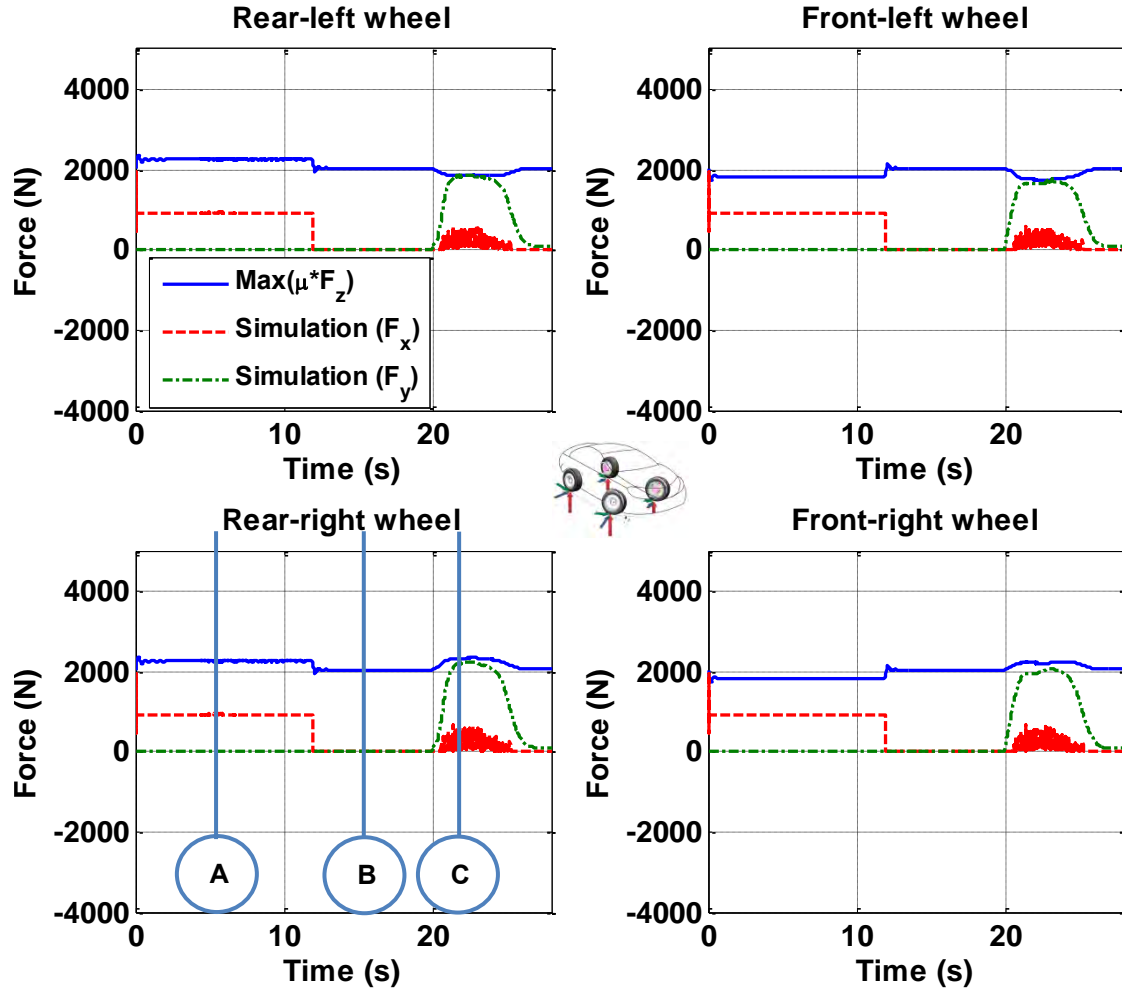


Figure 5-31: Longitudinal and lateral forces on wet asphalt ($m_u = 22\%$, $\mu = 0.5$)

Given unsprung mass ($m_u = 22\%$), the longitudinal and lateral forces on wet asphalt are simulated as shown in Figure 5-31. The symbol 'A', 'B', and 'C' corresponds

to $t = 5$ s, $t = 15$ s, and $t = 21.2$ s, respectively. The numerical numbers associated with these plots can be seen in Table 5-21.

	A (t = 5s) B (t = 15s)				C (t = 21.2s)		A (t = 5s) B (t = 15s)				C (t = 21.2s)	
	{Accel.}				{SLC}		{Accel.}				{SLC}	
	<u>Rear-left wheel</u> (F_{zRl})						<u>Front-left wheel</u> (F_{zFl})					
Max	2247	N	2036	N	1861	N	1835	N	2036	N	1781	N
(μ*F _z)	505	lb	458	lb	418	lb	413	lb	458	lb	400	lb
Simulation	915	N	0	N	331	N	919	N	0	N	300	N
(abs(F _x))	206	lb	0	lb	74	lb	207	lb	0	lb	67	lb
Simulation	0	N	0	N	1736	N	0	N	0	N	1614	N
(F _y)	0	lb	0	lb	390	lb	0	lb	0	lb	363	lb
	<u>Rear-right wheel</u> (F_{zRr})						<u>Front-right wheel</u> (F_{zFr})					
Max	Same as above				2296	N	Same as above				2211	N
(μ*F _z)					516	lb					497	lb
Simulation	Same as above				353	N	Same as above				350	N
(abs(F _x))					79	lb					79	lb
Simulation	Same as above				2023	N	Same as above				1895	N
(F _y)					455	lb					426	lb

Table 5-21: Traction and braking forces of each wheel ($m_u = 10\%$, $\mu = 0.5$)

During acceleration (A), the maximum traction forces and the simulated traction of the rear wheels are 2247 N and 915 N, respectively. During constant velocity (B), the maximum traction forces and the simulated traction of all wheels are 2036 N and 0 N, respectively. During braking (C), the maximum traction forces, simulated longitudinal force, and lateral force of the rear-right wheels are 2296 N, 353 N, and 2023 N,

respectively. In addition, the maximum traction forces, simulated longitudinal force, and lateral force of the front-right wheels are 2211 N, 350 N, and 1895 N, respectively

The difference between the maximum traction from Table 5-20 and the maximum traction from Table 5-21 during the constant velocity (B) is due to the increased unsprung mass which is from 10% (136 kg) to 22% (300 kg). The increased unsprung mass of each wheel is around 41 kg (90 lb). Taking into account the friction coefficient ($\mu = 0.5$), the increased normal force becomes 200 N (46 lb). That is, the maximum traction of 1836 N tabled in Table 5-20 becomes a value of 2036 N, as shown in Table 5-21.

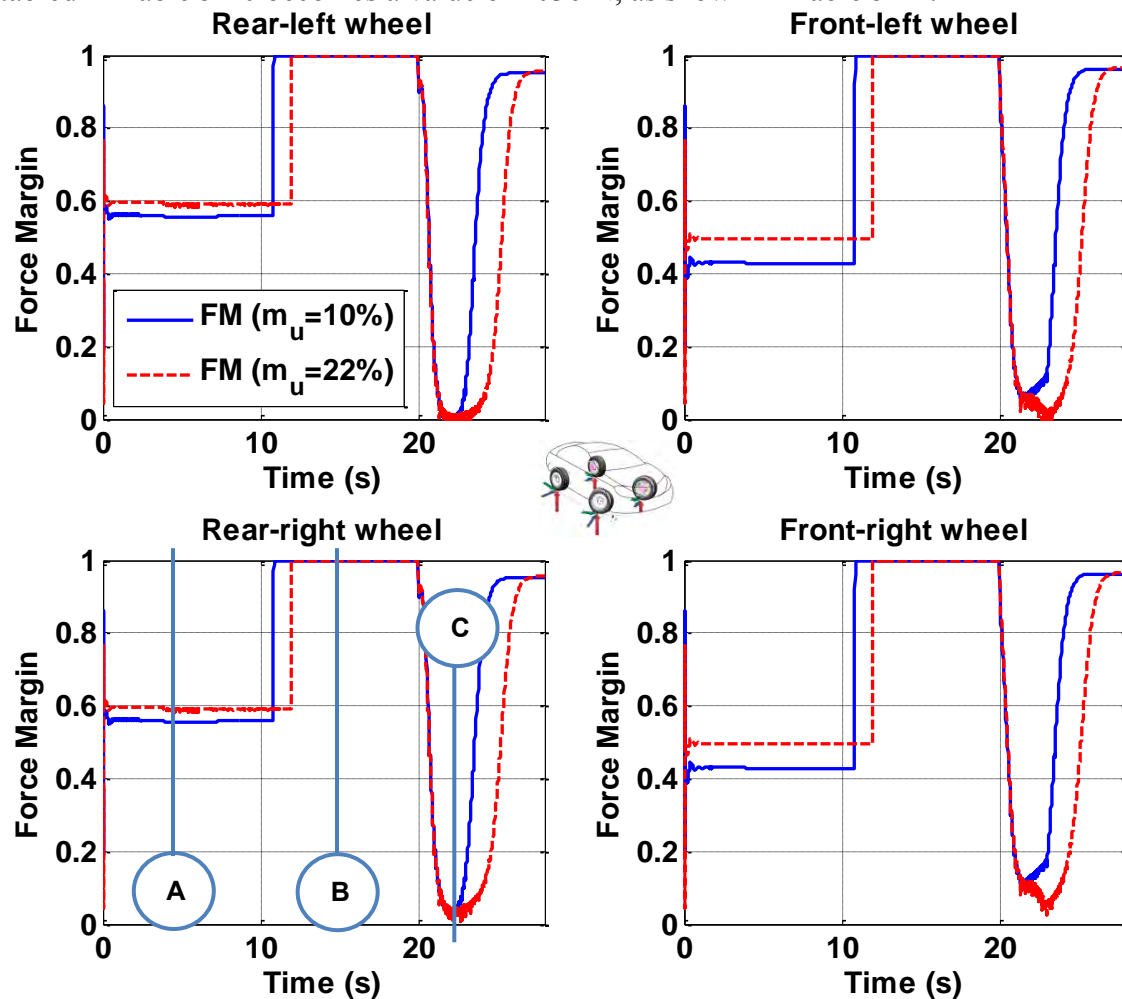


Figure 5-32: Effect of unsprung mass on force margin on wet asphalt ($\mu = 0.5$)

Figure 5-32 shows the variation of force margin subjected to a single-lane change from $t = 20$ s to $t = 25$ s. It can be seen that the increased unsprung mass leads to the decreased force margin. The force margin of each wheel can be calculated by knowing the information of maximum traction force (μF_{zjk}) and simulated longitudinal force (F_{xjk}) and lateral force (F_{yjk}) of each wheel, as shown in Figure 5-30 and Figure 5-31.

As shown in Figure 5-32, the symbol ‘A’, ‘B’, and ‘C’ correspond to $t = 5$ s, $t = 15$ s, and $t = 22.7$ s, respectively. The numerical numbers associated with these plots can be seen in Table 5-22.

	A (t = 5s) B (t = 15s)		C (t = 22.7s)	A (t = 5s) B (t = 15s)		C (t = 22.7s)
	{Accel.}		{SLC}	{Accel.}		{SLC}
	<u>Rear-left wheel</u> (F_{zRl})			<u>Front-left wheel</u> (F_{zFl})		
$m_u=22\%$	0.59	1	0	0.50	1	0
$m_u=10\%$	0.56	1	0	0.43	1	0.1
	<u>Rear-right wheel</u> (F_{zRr})			<u>Front-right wheel</u> (F_{zFr})		
$m_u=22\%$	Same as above		0.01	Same as above		0.03
$m_u=10\%$	Same as above		0.1	Same as above		0.15

Table 5-22: Force margins of each wheel

During constant velocity, the force margin becomes 1, indicating that the available maximum traction force of a vehicle is 100% at each wheel. During a single-lane change, the minimum force margins of the outside wheels (i.e., 0.1 and 0.15 for $m_u = 10\%$, 0.01 and 0.03 for $m_u = 22\%$) are larger than those of the inside wheels (i.e., 0 and 0.1 for $m_u = 10\%$, 0 and 0 for $m_u = 22\%$). This is attributed that the normal forces of the

outside wheels are larger than those of the inside wheels, which result from the inertial force caused by cornering.

In addition, the minimum force margins of the rear wheels (i.e., 0.01, 0.1) are smaller than those of the front wheels (i.e., 0.03, 0.15). This occurs because the later acceleration at the CG causes the rear slip angle to increase more than the front slip angle, as shown in Figure 5-33.

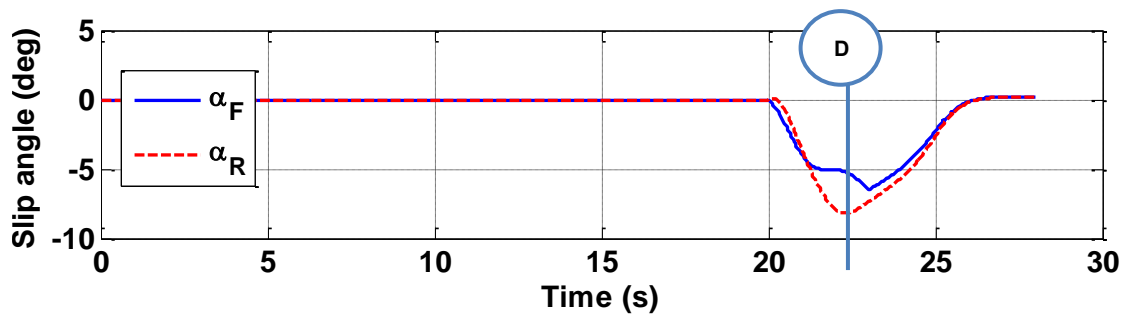


Figure 5-33: Front and rear slip angle

At the symbol 'D' ($t = 22.7\text{s}$), the front slip angle (α_F) and rear slip angle (α_R) are 5.5° and 8° , respectively. As a result, the rear lateral force is larger than the front lateral force, resulting in the decreased force margin.

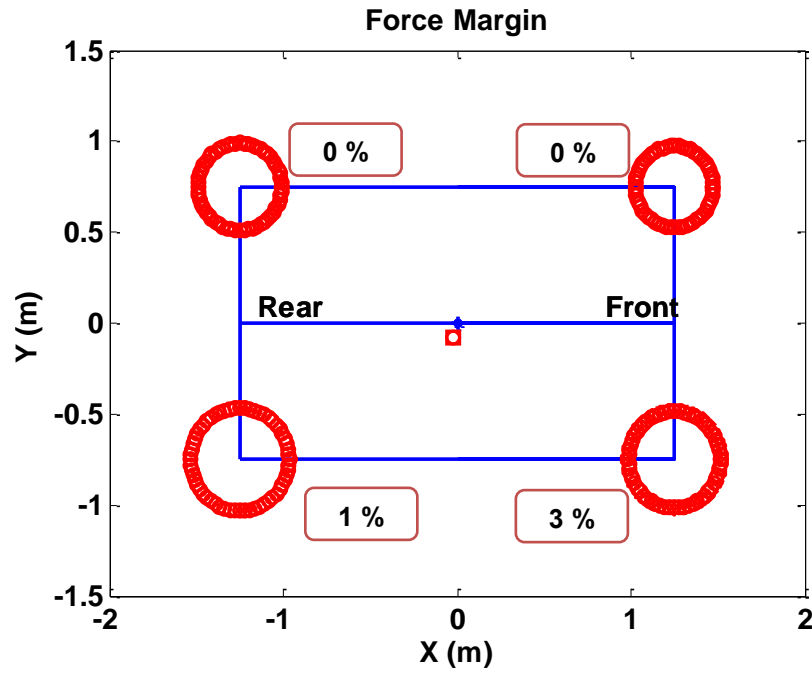


Figure 5-34: Force margins of each wheel on wet asphalt ($m_u = 22\%$, $\mu = 0.5$)

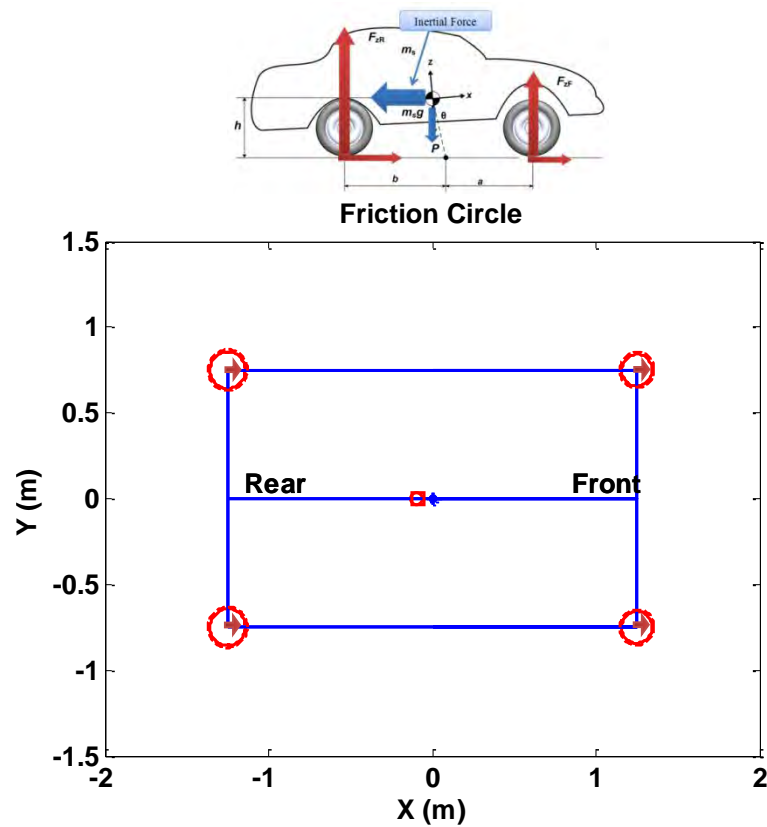
Figure 5-34 (a) and (b) shows force margins which are visualized by using a friction circle for each wheel in terms of $m_u = 10\%$ and $m_u = 22\%$. The dashed and thick circle lines indicate the maximum friction circle and simulated friction circle, respectively.

In comparison with Figure 5-21, it can be seen that the force margins becomes smaller, as the friction circles decreases due to friction coefficient of $\mu = 0.5$. The force margin of 0 indicates that the wheel's traction force is saturated so that a vehicle starts skidding, and this leads to unstable vehicle motion.

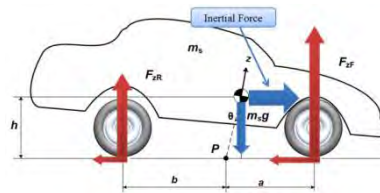
5.2.3 Snowy Road

5.2.3.1 Acceleration and Braking

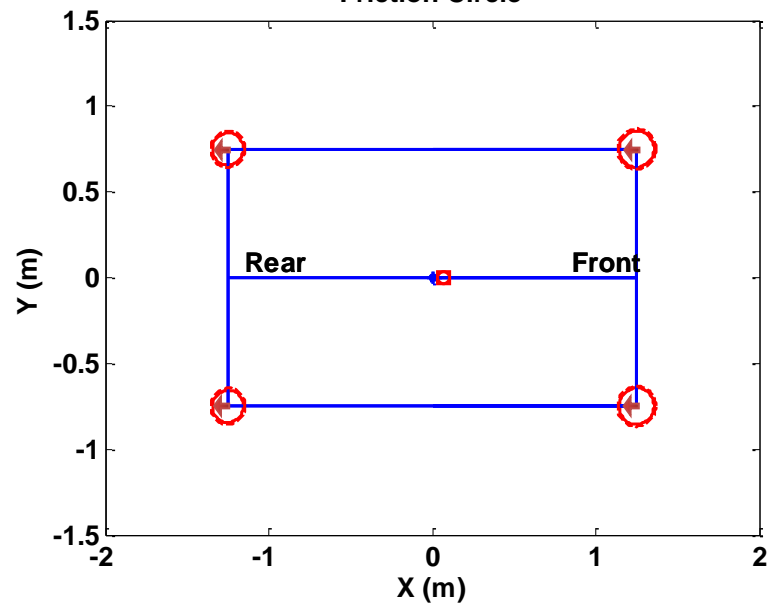
A snowy asphalt road ($\mu = 0.2$) affects a vehicle's performance such as acceleration and braking. Simulations of the vehicle response subjected to acceleration and braking have been carried out as shown in Figure 5-35.



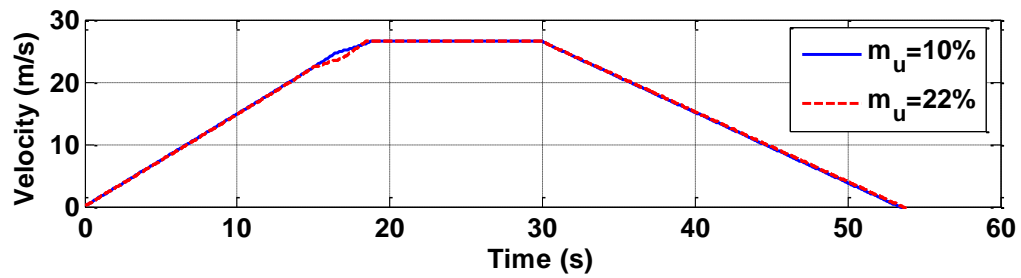
(a) Free-body diagram and friction circle of each wheel during acceleration (0-12s)



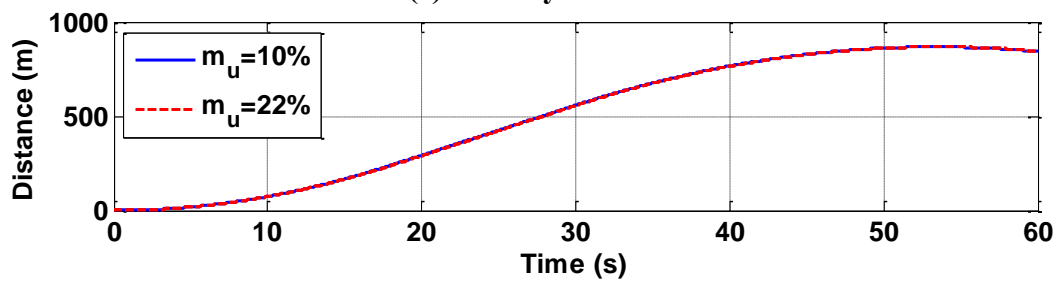
Friction Circle



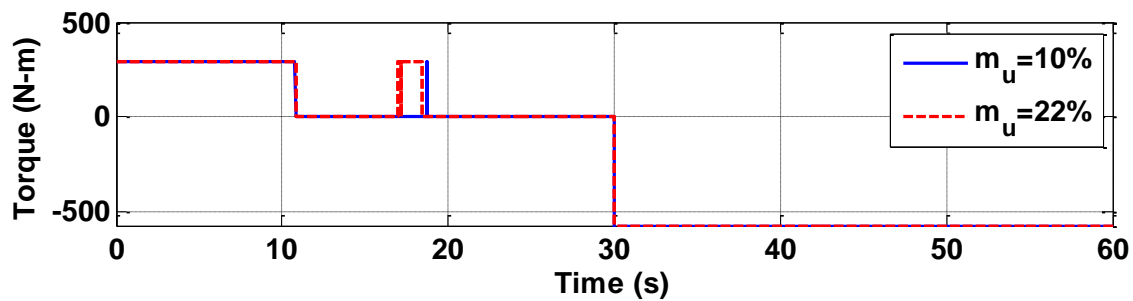
(b) Free-body diagram and friction circle of each wheel during braking (30-53.6 s)



(c) Velocity Profile



(d) Distance



(e) Wheel torque command

Figure 5-35: Simulation results for acceleration and braking on snowy road ($\mu = 0.2$)

The torque command as input is performed at $t = 0$ s with positive 290 N-m (214 ft-lb), and $t = 30$ s with negative 570 N-m, which are associated with acceleration and braking, respectively. Figure 5-35 (a) and (b) shows the free-body diagram and friction circles which are visualized at each wheel during acceleration and braking. The solid and dashed circles are associated with vehicles where $m_u = 10\%$ and $m_u = 22\%$, respectively.

Compared to the dry asphalt road (Sec 5.2.1.1) and the wet asphalt road (Sec 5.2.2.1), it can be seen that the friction circles of each wheel become smaller because of the decreased friction force caused by a lower friction coefficient (wet $\mu = 0.2$). In addition, the stopping distance becomes somewhat longer as shown in Figure 5-35 (d). As a result of wheel torque, the velocity profile and distance are determined as shown Figure 5-35 (c) and (d), respectively.

Table 5-23 shows the comparison of time, acceleration / deceleration, and distance during acceleration and braking in terms of $m_u = 10\%$ and $m_u = 22\%$, when a vehicle moves on the dry asphalt, wet asphalt, and snowy road. The 0-60 mph acceleration time is $t = 11.9$ s and $t = 10.8$ s, and the corresponding acceleration level is 0.23 g and 0.25 g in terms of $m_u = 22\%$ and $m_u = 10\%$, regardless of the dry and wet asphalt. However, on snowy road, the 0-60 mph acceleration time is $t = 18.46$ s and $t =$

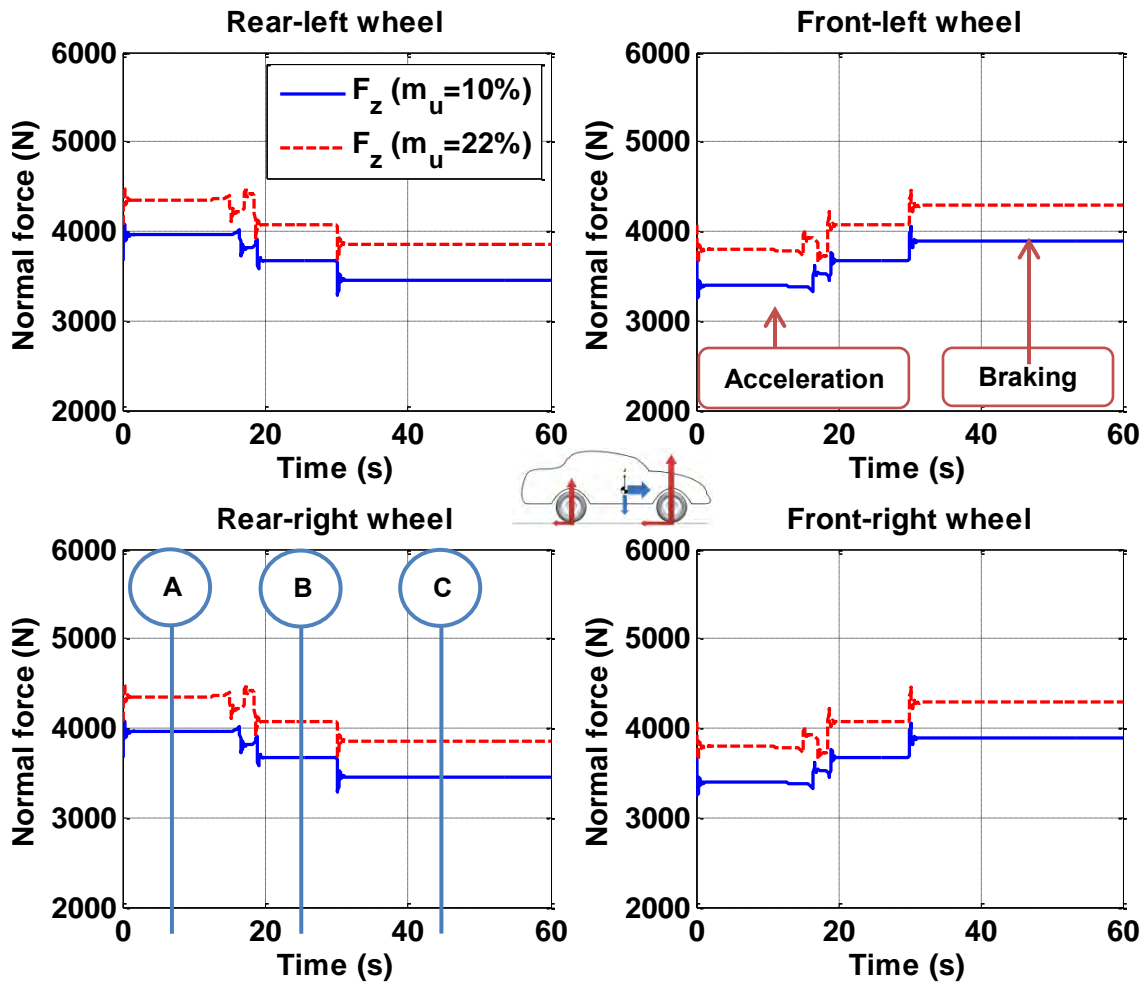
18.8 s, and the corresponding acceleration level is 0.151 g and 0.152 g in terms of $m_u = 22\%$ and $m_u = 10\%$.

		0-60 mph acceleration			60-0 mph braking			unit
		Dry asphalt	Wet asphalt	Snowy road	Dry asphalt	Wet asphalt	Snowy road	
$m_u=22\%$	time	11.9	11.9	18.46	6	7.5	23.6	s
	accel.	0.23	0.23	0.151	0.45	0.36	0.114	g
	distance	143 (469)	158 (518)	249 (817)	80 (263)	99 (325)	312 (1024)	m (ft)
$m_u=10\%$	time	10.8	10.8	18.8	5.5	7	23.4	s
	accel.	0.25	0.25	0.152	0.5	0.38	0.115	g
	distance	143 (469)	143 (469)	260 (853)	73 (240)	93 (305)	310 (1017)	m (ft)

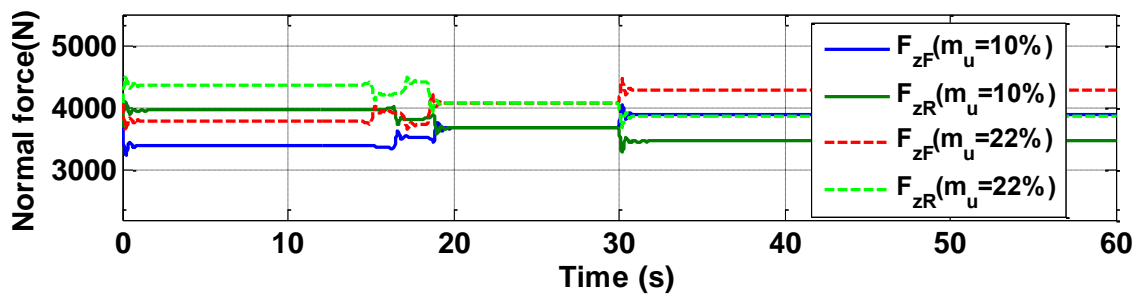
Table 5-23: Comparison of acceleration and braking

Under the dry asphalt condition, the 60-0 mph braking stopping time is $t = 6$ s and $t = 5.5$ s, and the corresponding deceleration level is 0.45 g and 0.5 g, and the stopping distance is $SD = 80$ m and $SD = 73$ m in terms of $m_u = 22\%$ and $m_u = 10\%$. Under the wet asphalt condition, the 60-0 mph braking stopping time is $t = 7.5$ s and $t = 7$ s, and the corresponding deceleration level is 0.36 g and 0.38 g, and the stopping distance is $SD = 99$ m and $SD = 63$ m in terms of $m_u = 22\%$ and $m_u = 10\%$.

Under the snowy condition, the 60-0 mph braking stopping time is $t = 23.6$ s and $t = 23.4$ s, and the corresponding deceleration level is 0.114 g and 0.115 g, and the stopping distance is $SD = 312$ m and $SD = 310$ m in terms of $m_u = 22\%$ and $m_u = 10\%$. In summary, as unsprung mass increases, the acceleration and braking time increases slightly on both dry asphalt road and wet asphalt road, while they decreases slightly on a snowy road, given the constant wheel torque and braking torque.



(a) Normal forces of each wheel



(b) Comparison of normal forces

Figure 5-36: Normal forces during acceleration and braking on a snowy road ($\mu = 0.2$)

Figure 5-36 (a) shows the normal forces of each wheel during acceleration (0 – 12 s) and braking (20 – 27.5 s): rear-left wheel, front-left wheel, rear-right wheel, and front-left wheel. Figure 5-36 (b) shows the comparison of normal forces in terms of $m_u = 10\%$ and $m_u = 22\%$. The numerical numbers associated with these plots can be seen in Table 5-24.

	A (t = 5s) B (t = 25s) C (t = 45s)						A (t = 5s) B (t = 25s) C (t = 45s)					
	{Accel.}			{Braking}			{Accel.}			{Braking}		
	<u>Rear-left wheel</u> (F_{zRl})						<u>Front-left wheel</u> (F_{zFl})					
m _u =22%	4353	N	4072	N	3858	N	3790	N	4072	N	4285	N
	979	lb	915	lb	867	lb	852	lb	915	lb	963	lb
m _u =10%	3955	N	3673	N	3457	N	3390	N	3673	N	3888	N
	889	lb	827	lb	777	lb	762	lb	826	lb	874	lb
	<u>Rear-right wheel</u> (F_{zRr})						<u>Front-right wheel</u> (F_{zFr})					
m _u =22%	Same as above						Same as above					
m _u =10%	Same as above						Same as above					

Table 5-24: Normal forces of each wheel

As shown in Figure 5-36 (a), the symbol ‘A’, ‘B’, and ‘C’ corresponds to $t = 5$ s, $t = 25$ s, and $t = 45$ s, respectively. During acceleration (A), the maximum normal forces of the rear wheels in terms of $m_u = 22\%$ and $m_u = 10\%$ are 4353 N and 3955 N, respectively. During constant velocity (B), the normal forces of the all wheels are 4072 N and 3673 N, respectively. During braking (C), the maximum normal forces of the front wheels in terms of $m_u = 22\%$ and $m_u = 10\%$ reduced to 4285 N and 3888 N, due to the decreased deceleration, respectively.

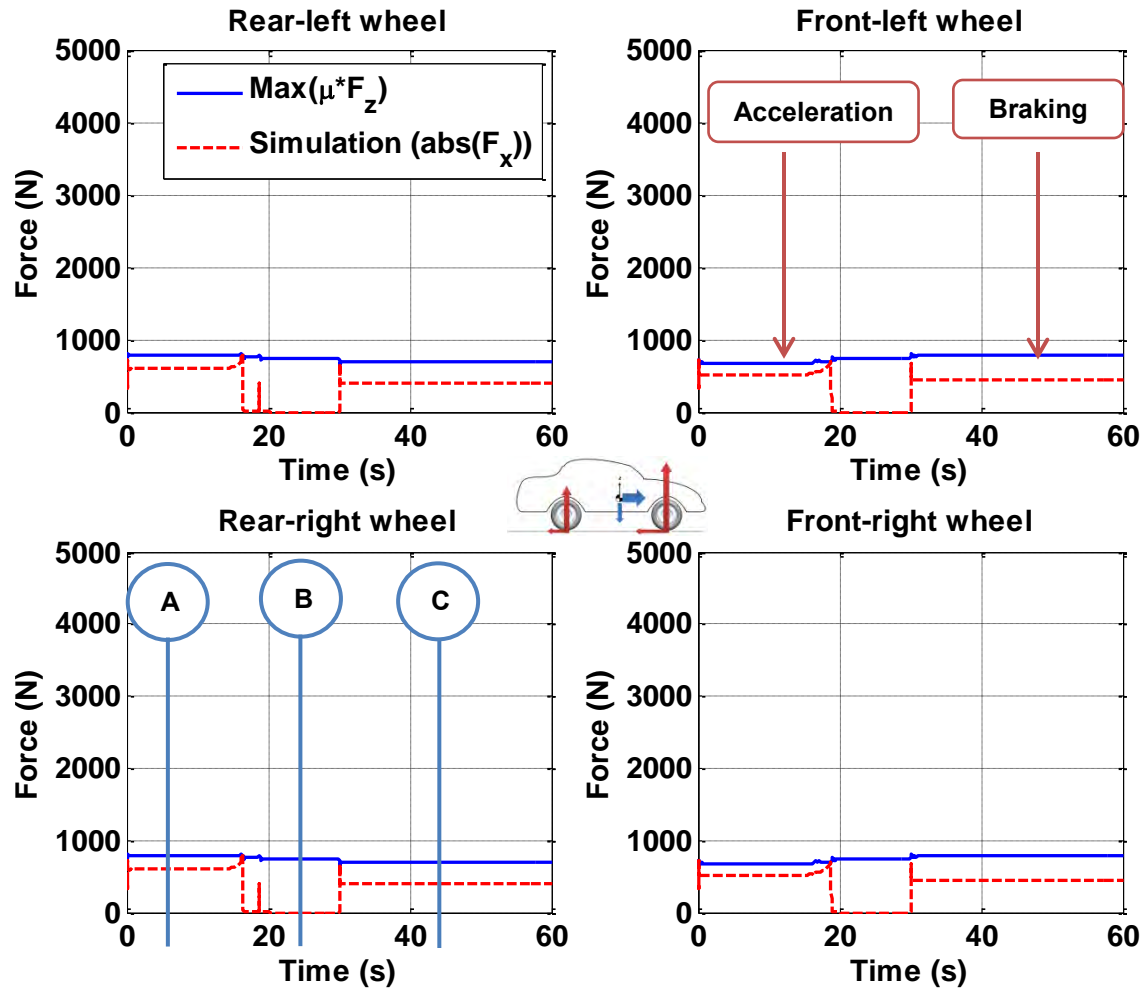


Figure 5-37: Traction and braking forces on a snowy road ($m_u = 10\%$, $\mu = 0.2$)

Figure 5-37 shows the traction force and braking forces of a vehicle with $m_u = 10\%$. The solid and dashed lines represent available maximum traction force and simulated traction force, respectively. As shown in Figure 5-37, the symbol ‘A’, ‘B’, and ‘C’ corresponds to $t = 5$ s, $t = 25$ s, and $t = 45$ s, respectively. The numerical numbers associated with these plots can be seen in Table 5-25.

	A (t = 5s)			B (t = 25s)			C (t = 45s)			A (t = 5s)			B (t = 25s)			C (t = 45s)		
	{Accel.}						{Braking}			{Accel.}						{Braking}		
	<u>Rear-left Wheel</u> (F_{zRl})						<u>Front-left wheel</u> (F_{zFl})											
Max	791	N	735	N	692	N	678	N	735	N	778	N						
($\mu * F_z$)	178	lb	165	lb	156	lb	152	lb	165	lb	175	lb						
Simulation	595	N	0	N	134	N	516	N	0	N	116	N						
(abs(F_x))	404	lb	0	lb	91	lb	442	lb	0	lb	99	lb						
	<u>Rear-right wheel</u> (F_{zRr})						<u>Front-right wheel</u> (F_{zFr})											
Max	Same as above						Same as above											
($\mu * F_z$)																		
Simulation	Same as above						Same as above											
(abs(F_x))																		

Table 5-25: Traction and braking forces of each wheel ($m_u = 10\%$, $\mu = 0.2$)

During acceleration (A), the maximum traction forces and the simulated traction of the rear wheels are 791 N and 595 N, respectively. During constant velocity (B), the maximum traction forces and the simulated traction of all wheels are 735 N and 0 N, respectively. During braking (C), the maximum traction forces and the simulated traction of the front wheels are 778 N and 116 N, respectively. For the purpose of comparison, the absolute value of the braking force is used.

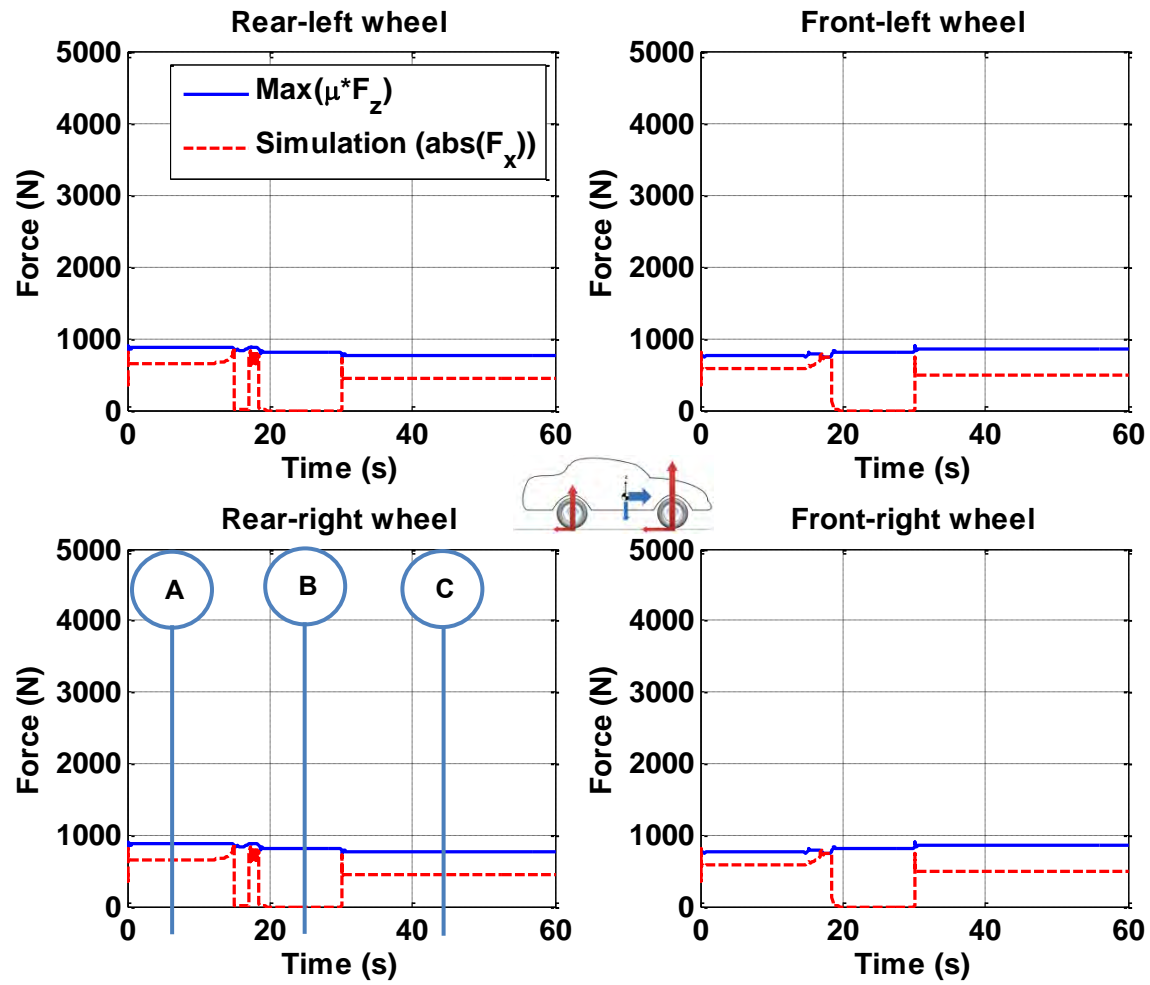


Figure 5-38: Traction and braking forces on a snowy road ($m_u = 22\%$, $\mu = 0.2$)

Given unsprung mass of $m_u = 22\%$, traction and braking forces on a snowy road are simulated as shown in Figure 5-38. The symbol 'A', 'B', and 'C' correspond to $t = 5$ s, $t = 25$ s, and $t = 45$ s, respectively. The numerical numbers associated with these plots can be seen in Table 5-26.

	A (t = 5s) B (t = 25s) C (t = 45s)						A (t = 5s) B (t = 25s) C (t = 45s)																	
	{Accel.}						{Braking}						{Accel.}						{Braking}					
	<u>Rear-left wheel</u> (F_{zRl})												<u>Front-left wheel</u> (F_{zFl})											
Max	871	N	815	N	772	N	758	N	815	N	857	N												
($\mu * F_z$)	196	lb	183	lb	174	lb	170	lb	183	lb	193	lb												
Simulation	654	N	0	N	440	N	572	N	0	N	491	N												
(abs(F_x))	147	lb	0	lb	99	lb	129	lb	0	lb	110	lb												
	<u>Rear-right wheel</u> (F_{zRr})												<u>Front-right wheel</u> (F_{zFr})											
Max	Same as above												Same as above											
($\mu * F_z$)																								
Simulation	Same as above												Same as above											
(abs(F_x))																								

Table 5-26: Traction and braking forces of each wheel ($m_u = 22\%$, $\mu = 0.2$)

During acceleration (A), the maximum traction forces and the simulated traction of the rear wheels are 871 N and 654 N, respectively. During constant velocity (B), the maximum traction forces and the simulated traction of all wheels are 814 and 0 N, respectively. During braking (C), the maximum traction forces and the simulated traction of the front wheels are 857 N and 491 N, respectively.

The difference between the maximum traction from Table 5-25 and the maximum traction from Table 5-26 during the constant velocity (B) is due to the increased unsprung mass that varies from 10% (136 kg) to 22% (300 kg). The increased unsprung mass of each wheel is around 41 kg (45 lb). Taking into account the friction coefficient ($\mu = 0.2$), the increased normal force becomes 80 N (18 lb). That is, the maximum traction of 735 N tabled in Table 5-25 becomes a value of 815 N, as shown in Table 5-26.

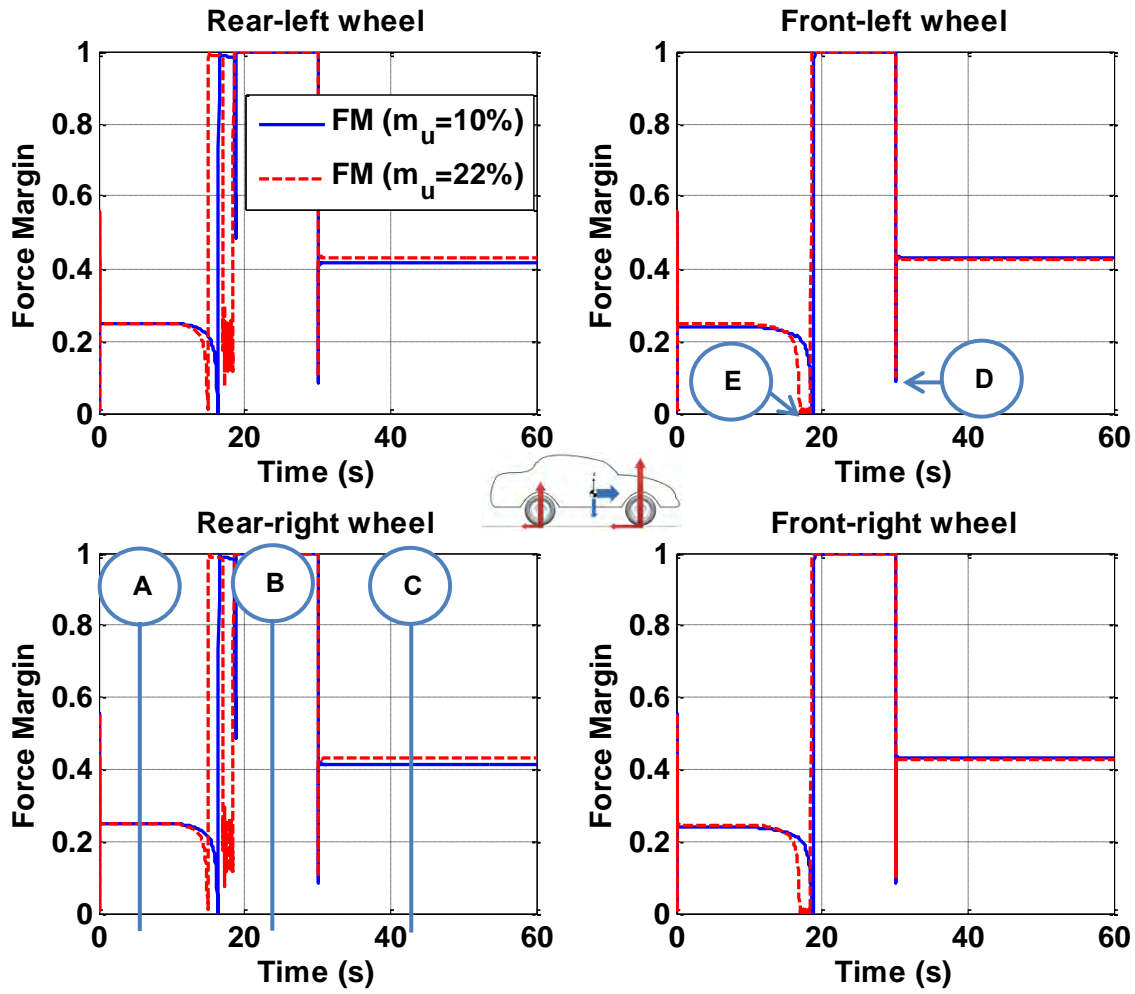


Figure 5-39: Effect of unsprung mass on force margin on a snowy road ($\mu = 0.2$)

As can be seen from the data in Figure 5-37 and Figure 5-38, the force margins of each wheel are determined as shown in Figure 5-39. The variation of force margin during acceleration and braking are shown in terms of $m_u = 10\%$ and $m_u = 20\%$. The symbol 'A', 'B', and 'C' corresponds to $t = 5$ s, $t = 15$ s, and $t = 23$ s, respectively. The symbol 'D' and 'E' indicates the minimum point during braking and acceleration, respectively. The numerical numbers associated with these plots can be seen in Figure 5-27.

	A (t = 5s) {Accel.}	B (t = 15s)	C (t = 23s) {Braking}	A (t = 5s) {Accel.}	B (t = 15s)	C (t = 23s) {Braking}
	<u>Rear-left wheel</u> (F_{zRl})			<u>Front-left wheel</u> (F_{zFl})		
$m_u=22\%$	0.25	1	0.43	0.25	1	0.43
$m_u=10\%$	0.25	1	0.41	0.24	1	0.426
	<u>Rear-right wheel</u> (F_{zRr})			<u>Front-right wheel</u> (F_{zFr})		
$m_u=22\%$	Same as above			Same as above		
$m_u=10\%$	Same as above			Same as above		

Table 5-27: Force margins of each wheel ($\mu = 0.2$)

During acceleration, the force margin of the rear wheels is 0.25 ($m_u = 22\%$) and 0.25 ($m_u = 10\%$), and the force margin of the front wheels is 0.25 ($m_u = 22\%$) and 0.24 ($m_u = 10\%$).

During constant velocity, the force margin becomes 1, indicating that the available maximum traction force of a vehicle is 100% at each wheel. The maximum traction force of a vehicle can be determined by one of two constraints: traction limits and motor power on the wheels.

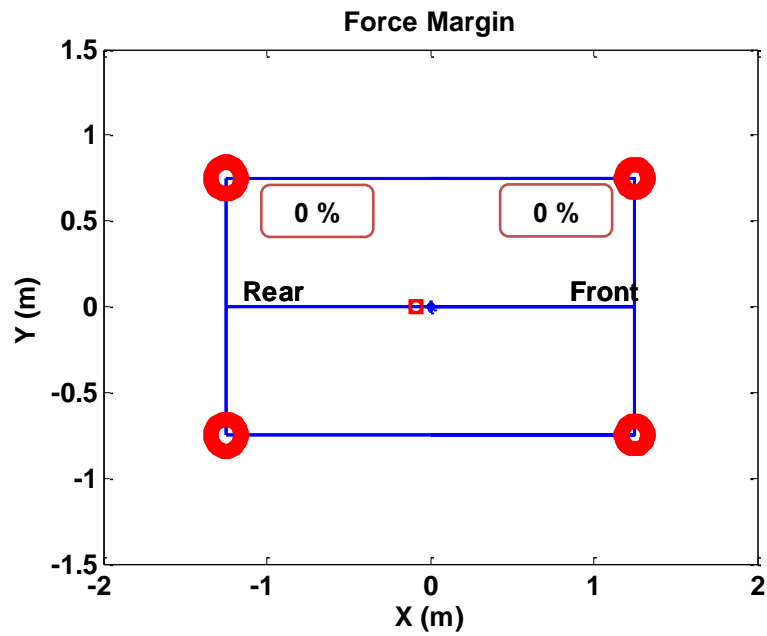
During braking, the force margin of the rear wheels is 0.43 ($m_u = 22\%$) and 0.41 ($m_u = 10\%$), while the force margin of the front wheels is 0.43 ($m_u = 22\%$) and 0.426 ($m_u = 10\%$). As can be seen in Figure 5-39, the minimum force margin indicated by symbol ‘D’ and ‘E’ are seen in Table 5-28.

	E (min) {Accel.}	D (min) {Braking}	E (min) {Accel.}	D (min) {Braking}
	<u>Rear-left wheel</u> (F_{zRl})		<u>Front-left wheel</u> (F_{zFl})	
$m_u=22\%$	0	0.08	0	0.08
$m_u=10\%$	0	0.06	0	0.06
	<u>Rear-right wheel</u> (F_{zRr})		<u>Front-right wheel</u> (F_{zFr})	
$m_u=22\%$	Same as above		Same as above	
$m_u=10\%$	Same as above		Same as above	

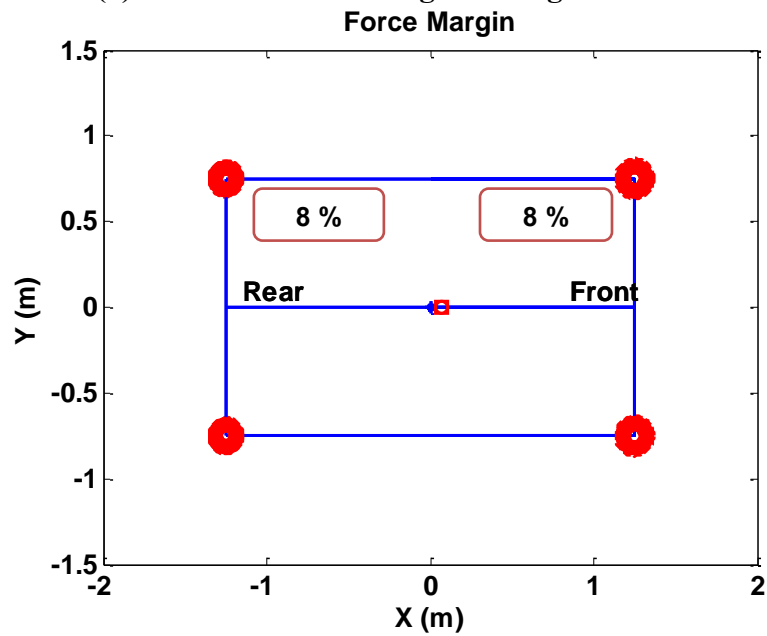
Table 5-28: Minimum force margins of each wheel ($\mu = 0.2$)

During acceleration, the minimum force margin of the rear wheels is 0, and the minimum force margin of the front wheels is 0 regardless of unsprung masses. This means that the friction force reaches the saturation of the tire so that a vehicle might skid, which causes unstable vehicle motion. In addition, the minimum force margin of the rear and front wheels during braking is 0.08 ($m_u = 22\%$) and 0.06 ($m_u = 10\%$). These are the maximum overshoot due to braking torque input.

In comparison with Table 5-9 (dry road) and Table 5-18 (wet road), the minimum force margins of the rear and front wheels during acceleration are reduced to 0. In addition, during braking, the force margins of rear and front wheels are reduced to 0.08.



(a) Minimum force margin during acceleration



(b) Minimum force margin during braking

Figure 5-40: Force margins of each wheel on a snowy road ($m_u = 0.22$, $\mu = 0.2$)

Figure 5-40 shows the minimum force margins which are visualized by using the friction circle of each wheel under $m_u = 0.22$ and $\mu = 0.2$. The dashed and heavy circles indicate maximum and simulated friction circle, respectively. As can be seen in Figure 5-40 (a), the force margin of each wheel during acceleration becomes zero. As shown in Figure 5-40 (b), the force margin of each wheel during deceleration also becomes 0.08%.

It can be seen that the force margin of each wheel decreases as the friction circle of each wheel decreases, given acceleration and braking torque. If the force margin becomes zero, the friction force reaches the saturation of the tire so that a vehicle might skid, which causes unstable vehicle motion.

5.2.3.2 Cornering Maneuver

A snowy road affects a vehicle's performance such as a cornering maneuver. The single-lane change maneuver is chosen as a cornering maneuver. Simulations of the vehicle response subjected to single lane change have been carried out as shown Figure 5-41

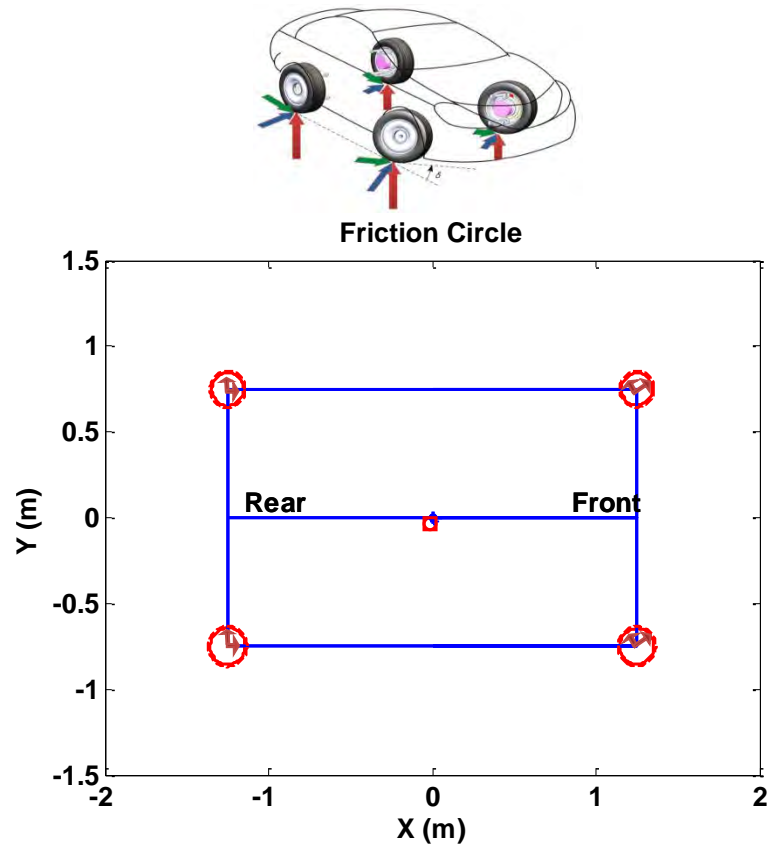
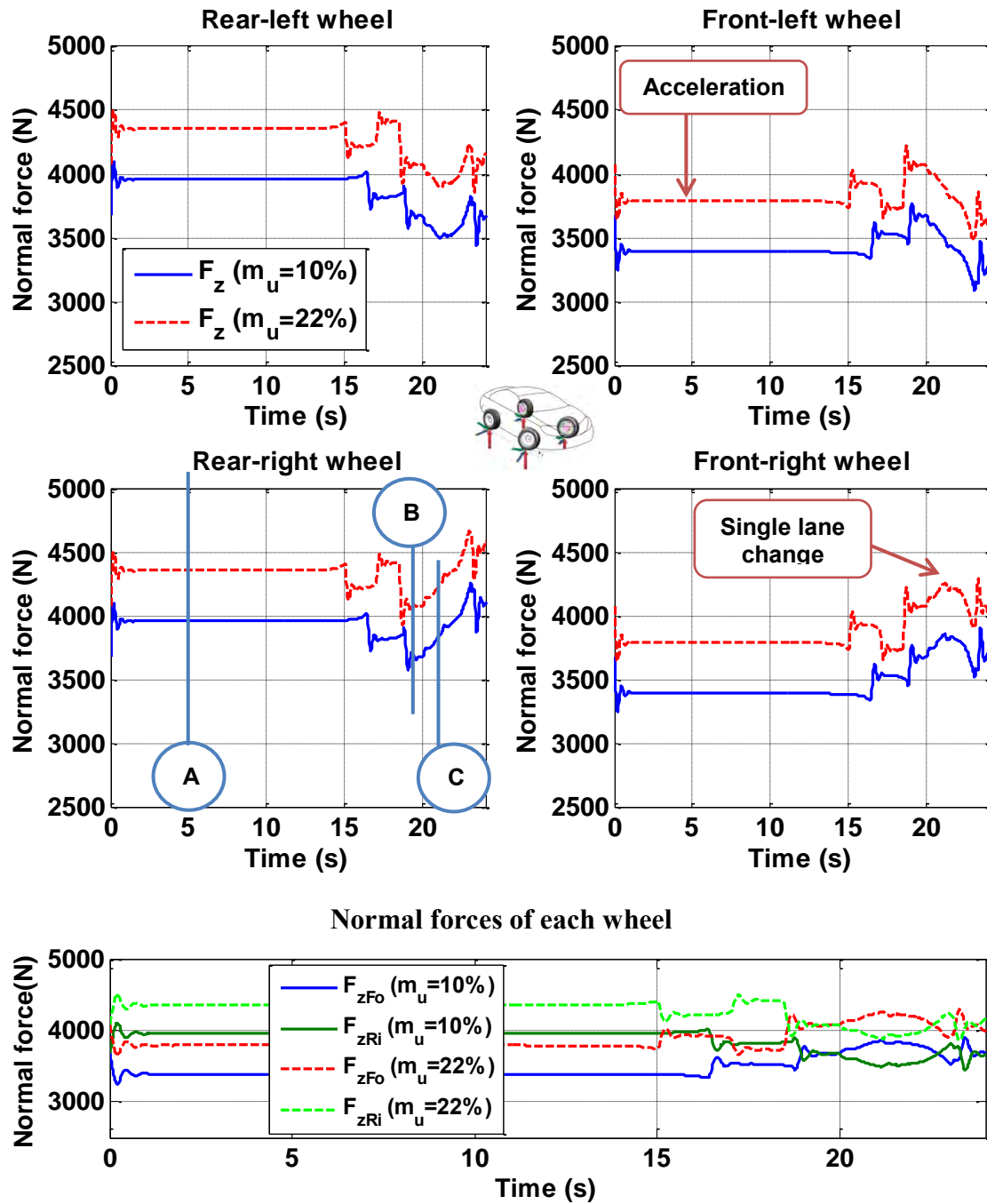


Figure 5-41: Friction circles of each wheel on a snowy road ($\mu = 0.2$)

Figure 5-41 shows the friction circles which are visualized at each wheel, when a vehicle reaches a steering angle of 2° at $t = 20.8$ s. In comparison with Figure 5-15 and Figure 5-28, it can be clearly seen that the friction circles of each wheel become smaller, as the friction coefficient decreases. The following analysis was performed under the same basic conditions in Sec.5.2.1.2.



Comparison of normal forces

Figure 5-42: Normal forces for a single-lane change on a snowy road ($\mu = 0.2$)

Figure 5-42 (a) shows the normal forces of each wheel for a single-lane change on a wet asphalt road, and Figure 5-42 (b) shows the comparison of normal forces between the front-outside (F_{zFo}) wheel and the rear-inside (F_{zRi}) wheel in terms of unsprung masses of 10% and 22%. The numerical numbers associated with these plots can be seen in Table 5-29.

	A (t = 5s) {Accel.}	B(t= 19.5s)	C (t=21.2s) {SLC}	A (t = 5s) {Accel.}	B (t = 19.5s)	C (t=21.2s) {SLC}
	<u>Rear-left wheel</u> (F_{zRl})			<u>Front-left wheel</u> (F_{zFl})		
$m_u=22\%$	4353 N 979 lb	4072 N 915 lb	3897 N 876 lb	3790 N 852 lb	4072 N 915 lb	3894 N 875 lb
$m_u=10\%$	3955 N 889 lb	3673 N 827 lb	3491 N 785 lb	3390 N 762 lb	3673 N 826 lb	3425 N 770 lb
	<u>Rear-right wheel</u> (F_{zRr})			<u>Front-right wheel</u> (F_{zFr})		
$m_u=22\%$	Same as above		4257 N 957 lb	Same as above		4255 N 957 lb
$m_u=10\%$	Same as above		3866 N 869 lb	Same as above		3850 N 865 lb

Table 5-29: Normal forces of each wheel

As shown in Figure 5-42 (a), the symbol ‘A’, ‘B’, and ‘C’ corresponds to $t = 5$ s, $t = 19.5$ s, and $t = 21.2$ s, respectively. During acceleration (A, $t = 0$ s ~ 19 s), the normal forces of the rear wheels in terms of $m_u = 22\%$ and $m_u = 10\%$ are 4353 N and 3955 N, respectively. During constant velocity (B, $t = 19$ s ~ 20 s), the normal forces of the all wheels are 4072 N and 3673 N, respectively. During a single-lane change (SLC, ‘C’, $t = 20$ s ~ 24 s), the maximum normal forces of the front-right and rear-right wheel in terms of

$m_u = 22\%$ are 4255 N and 4257 N, and the maximum normal forces of the front-right and rear-right wheel in terms of $m_u = 10\%$ are 3850 N and 3866 N, respectively.

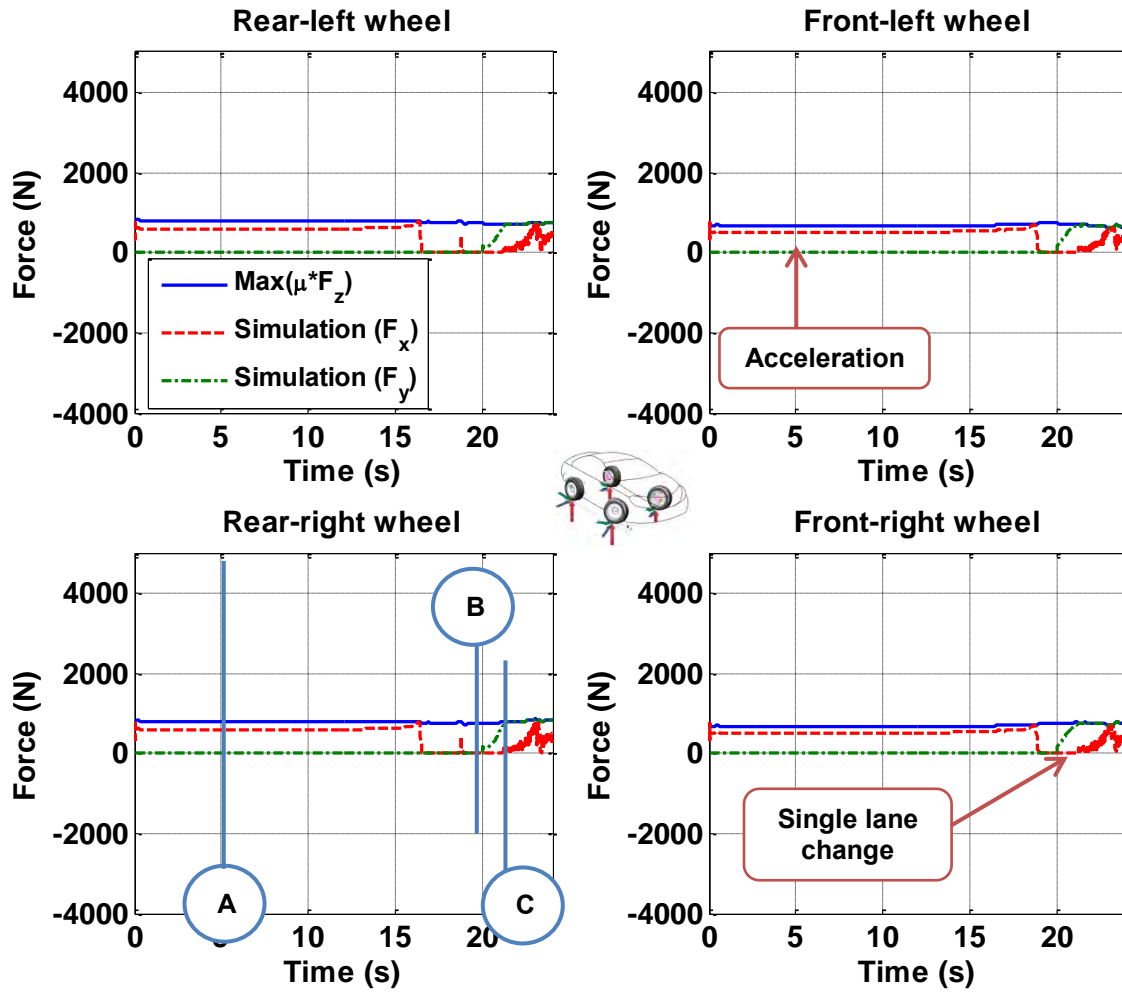


Figure 5-43: Longitudinal and lateral forces on a snowy road ($m_u = 10\%$, $\mu = 0.2$)

With regard to a single-lane change, the input is the steering angle. This generates a slip angle and results in lateral forces on all four wheels. The longitudinal and lateral forces must satisfy specified equality constraints, as shown in Equation (5.7). Figure 5-43 shows the longitudinal and lateral forces of each wheel on a vehicle with $m_u = 10\%$.

The solid, dashed, and dash-dot line indicate available maximum traction force, simulated longitudinal force, and simulated lateral force. As shown in Figure 5-43, the symbol ‘A’, ‘B’, and ‘C’ corresponds to $t = 5$ s, $t = 19.5$ s, and $t = 21.2$ s, respectively. The numerical numbers associated with these plots can be seen in Table 5-30.

	A (t = 5s) B(t= 19.5s)				C (t=21.2s)		A (t = 5s) B (t=19.5s)				C (t=21.2s)	
	{Accel.}				{SLC}		{Accel.}				{SLC}	
	<u>Rear-left wheel</u> (F_{zRl})						<u>Front-left wheel</u> (F_{zFl})					
Max	791	N	736	N	702	N	678	N	737	N	672	N
($\mu * F_z$)	178	lb	165	lb	158	lb	152	lb	165	lb	151	lb
Simulation	595	N	0	N	48	N	516	N	0	N	92	N
(abs(F_x))	134	lb	0	lb	11	lb	116	lb	0	lb	21	lb
Simulation	0	N	0	N	637	N	0	N	0	N	650	N
(F_y)	0	lb	0	lb	143	lb	0	lb	0	lb	146	lb
	<u>Rear-right wheel</u> (F_{zRr})						<u>Front-right wheel</u> (F_{zFr})					
Max	Same as above				771	N	Same as above				770	N
($\mu * F_z$)					173	lb					173	lb
Simulation	Same as above				126	N	Same as above				724	N
(abs(F_x))					28	lb					163	lb
Simulation	Same as above				695	N	Same as above				125	N
(F_y)					156	lb					28	lb

Table 5-30: Traction and braking forces of each wheel ($m_u = 10\%$, $\mu = 0.2$)

During acceleration (A), the maximum traction forces and the simulated traction of the rear wheels are 791 N and 595 N, respectively. During constant velocity (B), the maximum traction forces and the simulated traction of all wheels are 736 N and 0 N,

respectively. During a single-lane change (SLC, 'C'), the maximum traction forces, simulated longitudinal force, and lateral force of the rear-right wheels are 771 N, 126 N, and 695 N, respectively. In addition, the maximum traction forces, simulated longitudinal force, and lateral force of the front-right wheels are 770 N, 724 N, and 125 N, respectively.

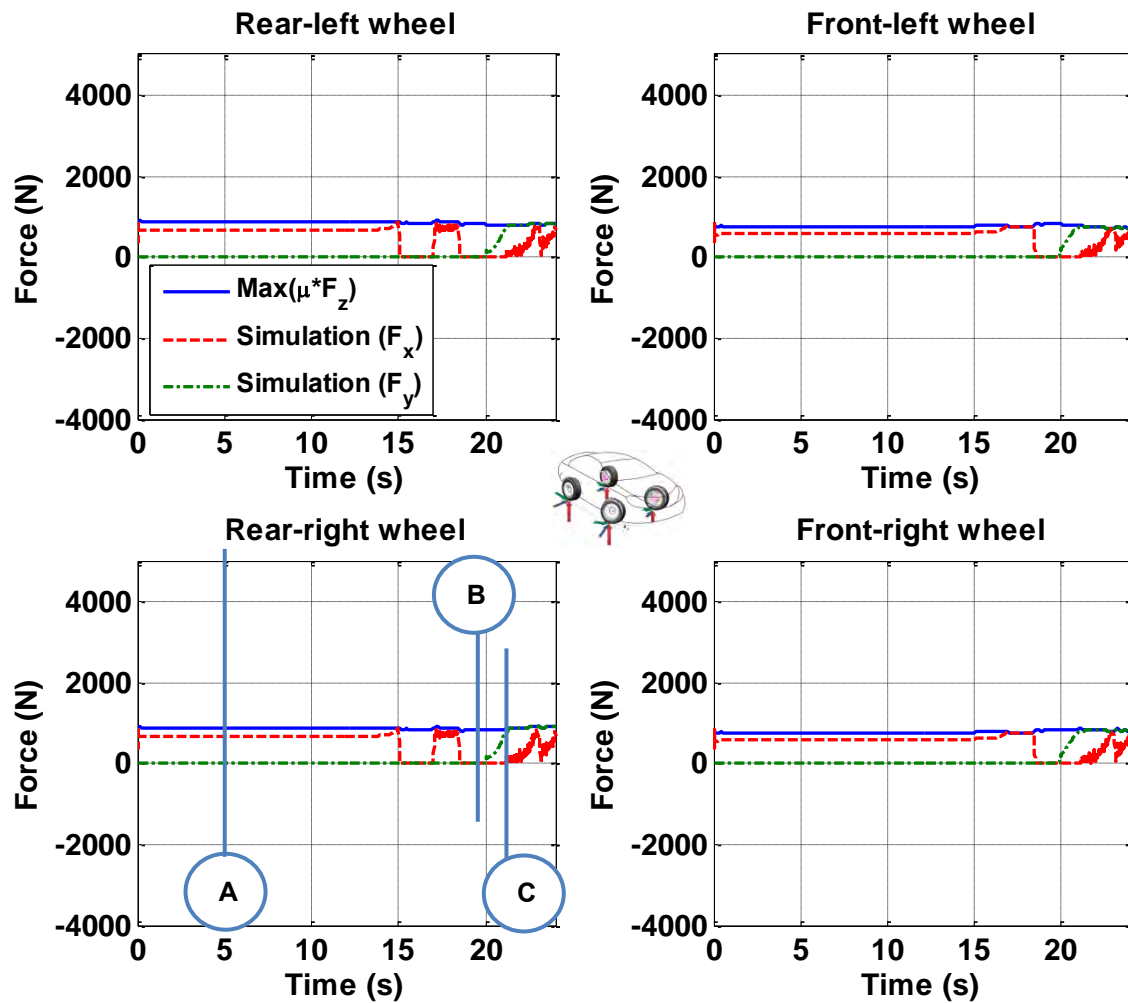


Figure 5-44: Longitudinal and lateral forces on a snowy road ($m_u = 22\%$, $\mu = 0.2$)

Given unsprung mass ($m_u = 22\%$), the longitudinal and lateral forces on wet asphalt are simulated as shown in Figure 5-44. The symbol ‘A’, ‘B’, and ‘C’ corresponds to $t = 5$ s, $t = 19.5$ s, and $t = 21.2$ s, respectively. The numerical numbers associated with these plots can be seen in Table 5-31.

	A (t = 5s) B(t=19.5s)				C (t=21.2s)		A (t = 5s) B (t=19.5s)				C (t=21.2s)	
	{Accel.}				{SLC}		{Accel.}				{SLC}	
	<u>Rear-left wheel</u> (F_{zRl})						<u>Front-left wheel</u> (F_{zFl})					
Max	870	N	816	N	778	N	758	N	816	N	778	N
(μ*F _z)	196	lb	183	lb	175	lb	170	lb	183	lb	175	lb
Simulation	654	N	0	N	716	N	572	N	0	N	748	N
(abs(F _x))	147	lb	0	lb	161	lb	129	lb	0	lb	168	lb
Simulation	0	N	0	N	167	N	0	N	0	N	166	N
(F _y)	0	lb	0	lb	38	lb	0	lb	0	lb	37	lb
	<u>Rear-right wheel</u> (F_{zRr})						<u>Front-right wheel</u> (F_{zFr})					
Max	Same as above				850	N	Same as above				851	N
(μ*F _z)					191	lb					191	lb
Simulation	Same as above				753	N	Same as above				792	N
(abs(F _x))					169	lb					178	lb
Simulation	Same as above				178	N	Same as above				178	N
(F _y)					40	lb					40	lb

Table 5-31: Traction and braking forces of each wheel ($m_u = 22\%$, $\mu = 0.2$)

During acceleration (A), the maximum traction forces and the simulated traction of the rear wheels are 870 N and 654 N, respectively. During constant velocity (B), the maximum traction forces and the simulated traction of all wheels are 816 N and 0 N, respectively. During a single-lane change (SLC, 'C'), the maximum traction forces, simulated longitudinal force, and lateral force of the rear-right wheels are 850 N, 753 N, and 178 N, respectively. In addition, the maximum traction forces, simulated longitudinal force, and lateral force of the front-right wheels are 851 N, 792 N, and 178 N, respectively

The difference between the maximum traction from Table 5-30 and the maximum traction from Table 5-31 during the constant velocity (B) is due to the increased unsprung mass which is from 10% (136 kg) to 22% (300 kg).

The increased unsprung mass of each wheel is around 41 kg (90 lb). Taking into account the friction coefficient ($\mu = 0.2$), the increased normal force becomes 80 N (18 lb). That is, the maximum traction of 736 N tabled in Table 5-30 becomes a value of 816 N, as shown in Table 5-31.

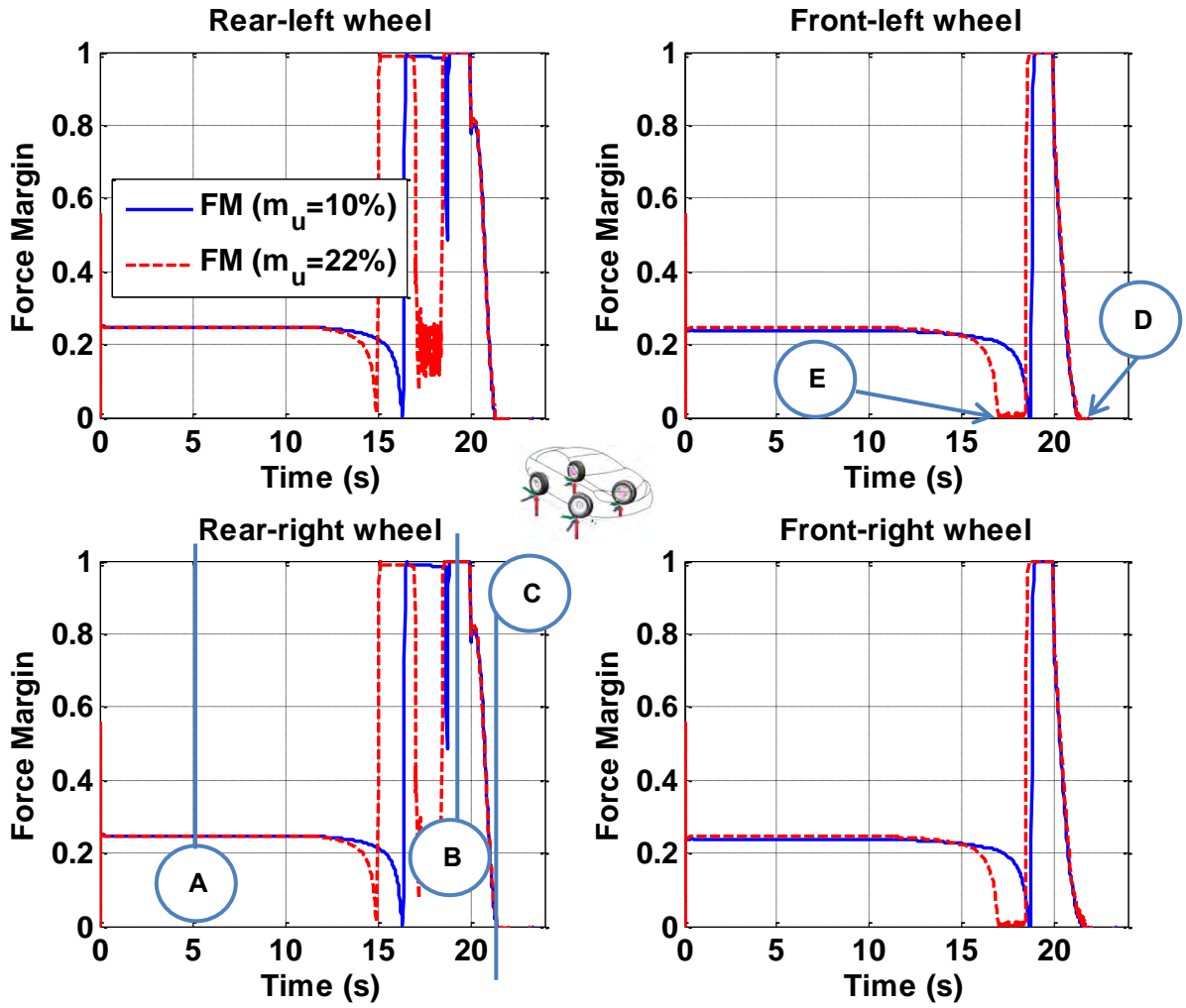


Figure 5-45: Effect of unsprung mass on force margin on a snowy road ($\mu = 0.2$)

Figure 5-45 shows the variation of force margin subjected to a single-lane change from $t = 20$ s to $t = 25$ s. The force margin of each wheel can be calculated by knowing the information of maximum traction force (μF_{zjk}) and simulated longitudinal force (F_{xjk}) and lateral force (F_{yjk}) of each wheel, as shown in Figure 5-43 and Figure 5-44.

As shown in Figure 5-45, the symbol ‘A’, ‘B’, and ‘C’ correspond to $t = 5$ s, $t = 19.5$ s, and $t = 21.2$ s, respectively. The symbol ‘D’ indicates a minimum force margin. The numerical numbers associated with these plots can be seen in Table 5-32.

	A (t=5s) {Accel.}	B(t=19.5s)	C (t=21.2s) {SLC}	A (t=5s) {Accel.}	B(t=19.5s)	C (t=21.2s) {SLC}
	<u>Rear-left wheel</u> (F_{zRl})			<u>Front-left wheel</u> (F_{zFl})		
$m_u=22\%$	0.25	1	0.04	0.25	1	0.01
$m_u=10\%$	0.25	1	0.04	0.24	1	0.01
	<u>Rear-right wheel</u> (F_{zRr})			<u>Front-right wheel</u> (F_{zFr})		
$m_u=22\%$	Same as above		0.09	Same as above		0.06
$m_u=10\%$	Same as above		0.09	Same as above		0.06

Table 5-32: Force margins of each wheel

During constant velocity, the force margin becomes 1, indicating that the available maximum traction force of a vehicle is 100% at each wheel. During a single-lane change, the force margins of the outside wheels (i.e., 0.09 and 0.06) are larger than those of the inside wheels (i.e., 0.04 and 0.01). This is attributed that the normal forces of the outside wheels are larger than those of the inside wheels, which result from the inertial force caused by cornering. As can be seen in Figure 5-45, the minimum force margin indicated by symbol ‘D’ and ‘E’ are seen in Table 5-33.

	E (min) {Accel.}	D (min) {SLC}	E (min) {Accel.}	D (min) {SLC}
	<u>Rear-left wheel</u> (F_{zRl})		<u>Front-left wheel</u> (F_{zFl})	
$m_u=22\%$	0	0	0	0
$m_u=10\%$	0	0	0	0
	<u>Rear-right wheel</u> (F_{zRr})		<u>Front-right wheel</u> (F_{zFr})	
$m_u=22\%$	Same as above		Same as above	
$m_u=10\%$	Same as above		Same as above	

Table 5-33: Minimum force margins of each wheel ($\mu = 0.2$)

During acceleration, the minimum force margin of the rear wheels is 0, and the minimum force margin of the front wheels is 0 regardless of unsprung masses. This means that the friction force reaches the saturation of the tire so that a vehicle might skid, which causes unstable vehicle motion. In addition, the minimum force margin of the rear and front wheels is 0.08 ($m_u = 22\%$) and 0.06 ($m_u = 10\%$). These are the maximum overshoot due to braking torque input.

In comparison with Table 5-9 (dry road) and Table 5-18 (wet road), the minimum force margins of the rear and front wheels during acceleration are reduced to 0. In addition, during SLC, the force margins of rear and front wheels are reduced to 0.

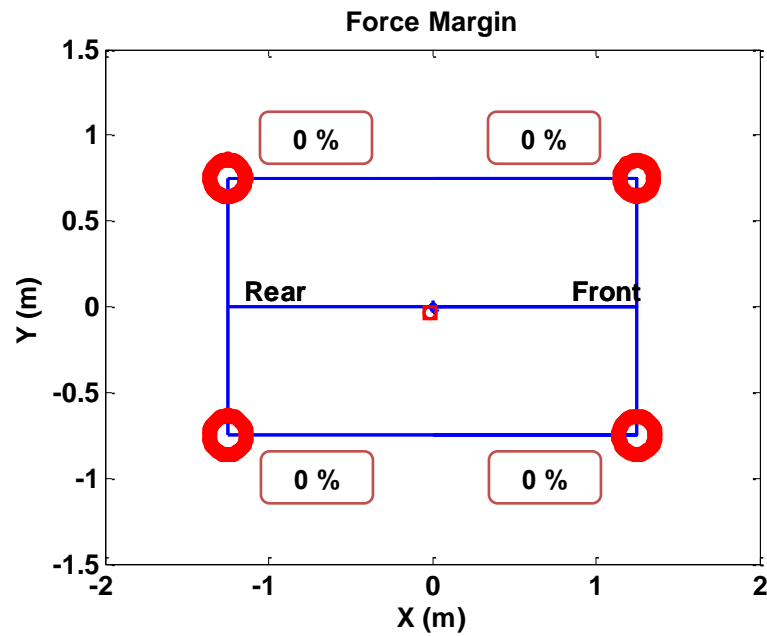


Figure 5-46: Force margin of each wheel on snowy road ($m_u = 0.22$, $\mu = 0.2$)

Figure 5-46 shows force margins that can be visualized by friction circles of each wheel. The force margin of each wheel is zero because the traction force exceeds the saturation point and the vehicle starts skidding, which occurs during cornering. Furthermore, if the road condition is icy ($\mu = 0.1$), the vehicle also spin out of control. The icy road condition will be simulated in the performance maps in the next section.

5.3 PERFORMANCE MAPS FOR DIFFERENT VEHICLE WEIGHT

We discussed the effects of increased unsprung mass ($m_u = 10\%$ and $m_u = 22\%$) on acceleration, braking, and force margin on cornering maneuver, under various road conditions such as dry asphalt road, wet asphalt road, and snowy road. Based on the previous sections, we expand this into acceleration, braking, and force margin performance maps.

5.3.1 Acceleration Performance Map

The acceleration performance map can be defined as the 0-60 mph acceleration time which describes how fast a vehicle moves. Two control parameters are chosen: unsprung mass ratios (from 10% to 26%) and various road conditions. Vehicle parameters used in simulation can be seen in Table 5-34.

The sprung mass is constant, while the unsprung mass varies based on different sizes of MDW such as 16, 20, 24, 32, up to 40 hp which would become customer choices. For instance, the total weight of a standard vehicle is 3300 lb; sprung mass (3000/g) and unsprung mass ($m_u=10\%$, 300/g). In addition, the total weight of a vehicle containing four MDW (32 hp) becomes 3660 lb; sprung mass (3000/g) and unsprung mass ($m_u=22\%$, 660/g).

Figure 5-47 shows the acceleration performance map with respect to unsprung mass ratio and various road conditions. For instance, the friction coefficients of dry asphalt, wet asphalt, and snowy road are $\mu = 0.9$, $\mu = 0.5$, and $\mu = 0.2$, respectively. Each point is simulated through the 14 DOF full-vehicle Simulink model, corresponding to two control parameters.

	Parameters	Value	Units	Value	Units
Vehicle sprung mass	m_s	1361	kg	3000/g	slug
Unsprung mass		136		300	
{Total Vehicle Mass} (m_u =10%, reference car)	m_u	{1497}	kg	{3300}	lb/g
Unsprung mass		200		440	
{Total Vehicle Mass} (m_u =14.7%, MDW 16 hp)	m_u	{1560}	kg	{3440}	lb/g
Unsprung mass		225.6		496	
{Total Vehicle Mass} (m_u =16.6%, MDW 20 hp)	m_u	{1586}	kg	{3496}	lb/g
Unsprung mass		251.2		552	
{Total Vehicle Mass} (m_u =18.5%, MDW 24 hp)	m_u	{1611}	kg	{3552}	lb/g
Unsprung mass		300		660	
{Total Vehicle Mass} (m_u =22%, MDW 32 hp)	m_u	{1660}	kg	{3660}	lb/g
Unsprung mass		350		770	
{Total Vehicle Mass} (m_u =25.7%, MDW 40 hp)	m_u	{1710}	kg	{3770}	lb/g

Table 5-34: Vehicle parameters used in simulation

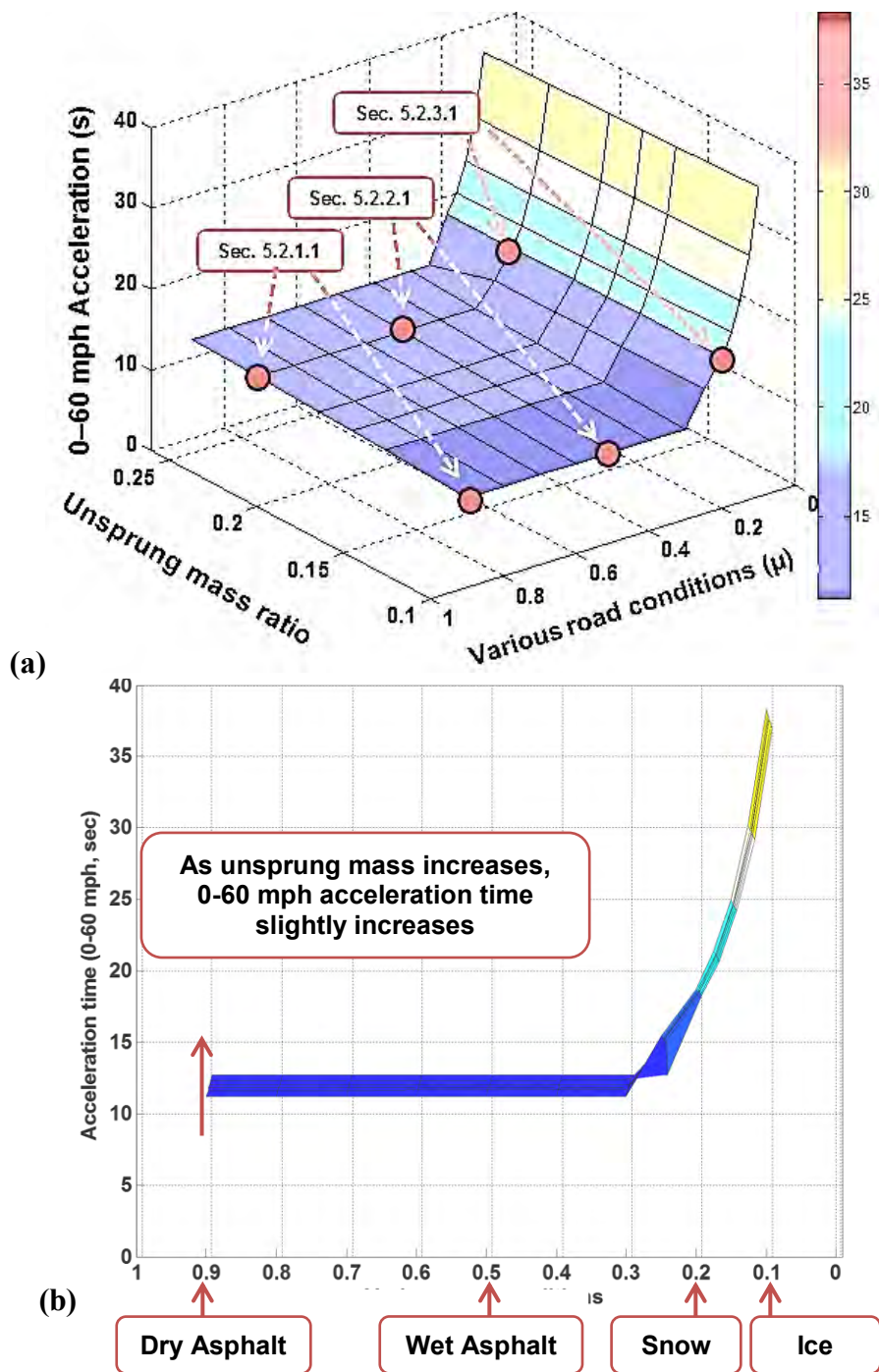


Figure 5-47: Acceleration performance map given constant torque (290 N-m (214 ft-lb))

The circles indicate corresponding sections that has been simulated with two control parameters such as unsprung mass ratio and various road conditions (i.e. different

friction coefficient μ). As the ratio of the sprung mass to the unsprung mass increases (i.e., 0.1, 0.147, 0.166, 0.185, 0.22, and 0.26), 0-60 mph acceleration time increases slightly on the dry and wet asphalt road. However, on the snow ($\mu = 0.2$) and ice ($\mu = 0.1$) roads, the increased unsprung mass has an insignificant effect on the acceleration performances.

When the vehicle moves on the slippery road condition ($\mu = 0.3$), the wheel torque exceeds the limit of friction force between tire and road surfaces. In other words, the associated wheel is operated under inefficient traction resulting in (spinning) slip. In order to avoid this situation, simulations of the vehicle's response subjected to acceleration have been carried out based on the limitation of various road conditions, resulting in maintaining a force margin of 5 ~ 40 %. This leads to a lower torque than the original torque of 290 N-m (214 ft-lb), thus increasing the 0-60 acceleration time. On an icy road, the 0-60 acceleration time is around 38 s, while it is around 11 s on the dry road. Since an icy road has less friction, the 0-60 acceleration time on an icy road is around 2 times longer than that on a snowy road; an icy road (38 s) and a snowy road (18 s)

5.3.2 Braking Performance Map

The braking performance map can be defined as the 60-0 mph braking time which describes how fast a vehicle stops. Two control parameters are chosen as unsprung mass ratio from 10 % to 26 % and various road conditions. Figure 5-48 shows the braking performance map with respect to unsprung mass ratio and various road conditions. As the ratio of the sprung mass to the unsprung mass increases, the 60-0 mph braking time increases slightly on dry asphalt road ($\mu = 0.9$ and $\mu = 0.8$). However, it decreases for the road conditions ($\mu = 0.7 \sim 0.1$) as shown in Figure 5-48 (b).

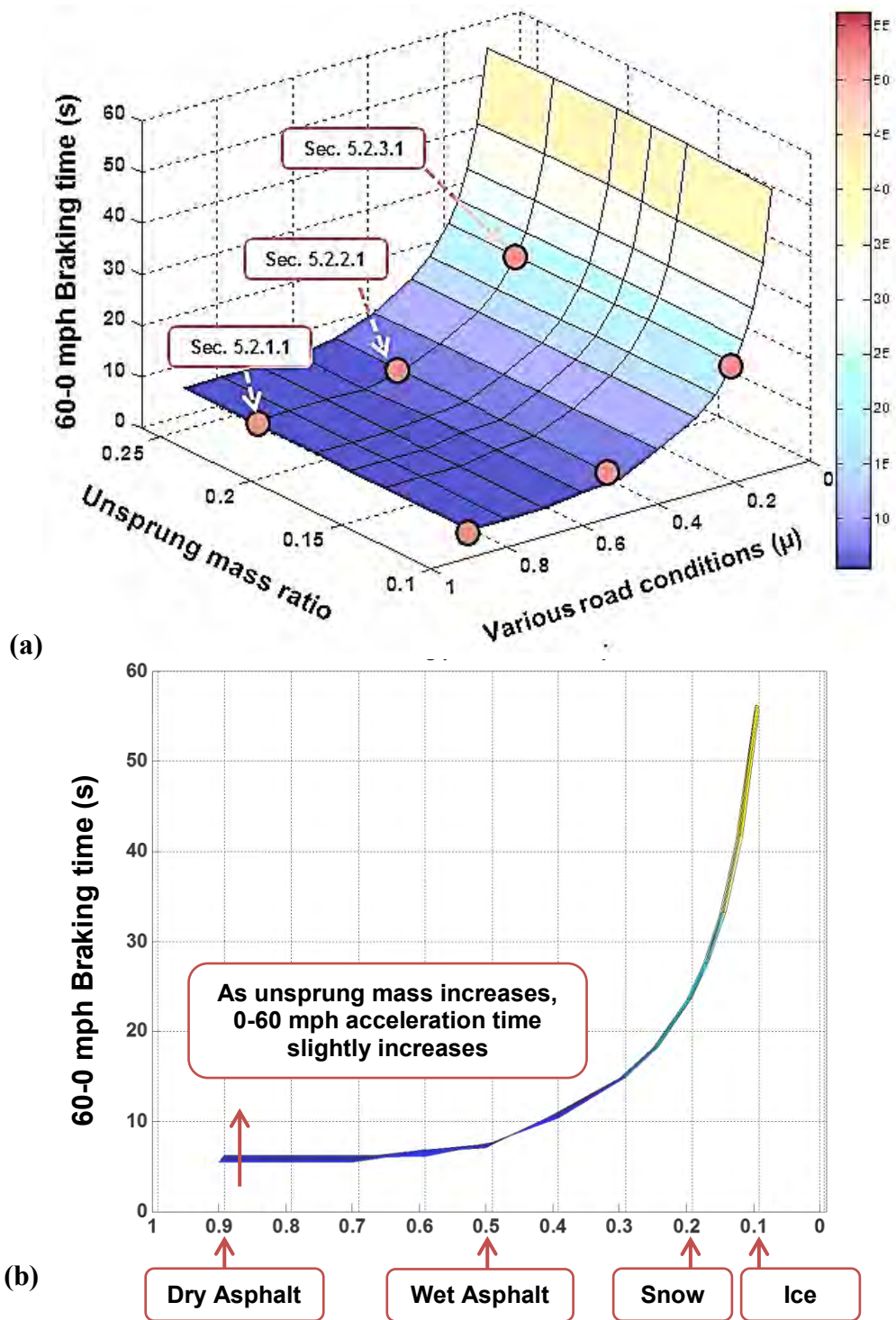


Figure 5-48: Braking performance map given constant torque (570 N-m(420 ft-lb))

When a vehicle brakes on a road condition $\mu = 0.7$, the wheel braking torque exceeds the limit of friction force between the tire and road surface. Once the wheel exceeds the saturation limit, the vehicle's wheels are locked and wheel sliding occurs. From the force margin point of view, the associated wheel is operated under inefficient traction to cause a skid (skidding/sliding).

In order to avoid this situation, simulations of the vehicle's response subjected to braking have been carried out based on the limitation of various road conditions, resulting in maintaining a force margin of 5 ~ 40 %. This leads to a lower braking torque than the original braking torque of 570 N-m, so that the 60-0 mph braking time increases rapidly.

On the icy road, the 60-0 braking time is around 55 s, while it is around 5.5 s on the dry road. Since an icy road has less friction, the 0-60 acceleration time on an icy road is approximately 2.3 times longer than that on a snowy road; an icy road (58 s) and a snowy road (25 s).

5.3.3 Force Margin Performance Map during a Cornering Maneuver

The force margin performance map during cornering maneuver can be defined as how much traction force is available for control purpose. Two control parameters are chosen, such as unsprung mass ratios from 10% to 26% and various road. The circles indicate corresponding sections that were simulated with two control parameters such as unsprung mass ratios and various road conditions (i.e. with different friction coefficients μ).

Figure 5-49 shows the force margin performance map of a front-inside wheel during a cornering maneuver in a single-lane change. The increased unsprung mass increases slightly the force margin for a single-lane change.

When a vehicle runs on a road of $\mu = 0.4$, the force margin becomes zero. That is, the wheel's traction force is saturated so that a vehicle starts skidding, and this leads to unstable vehicle motion. Figure 5-49 (b) shows the force margin map in x-z coordinates, which is the force margin as a function of various road conditions.

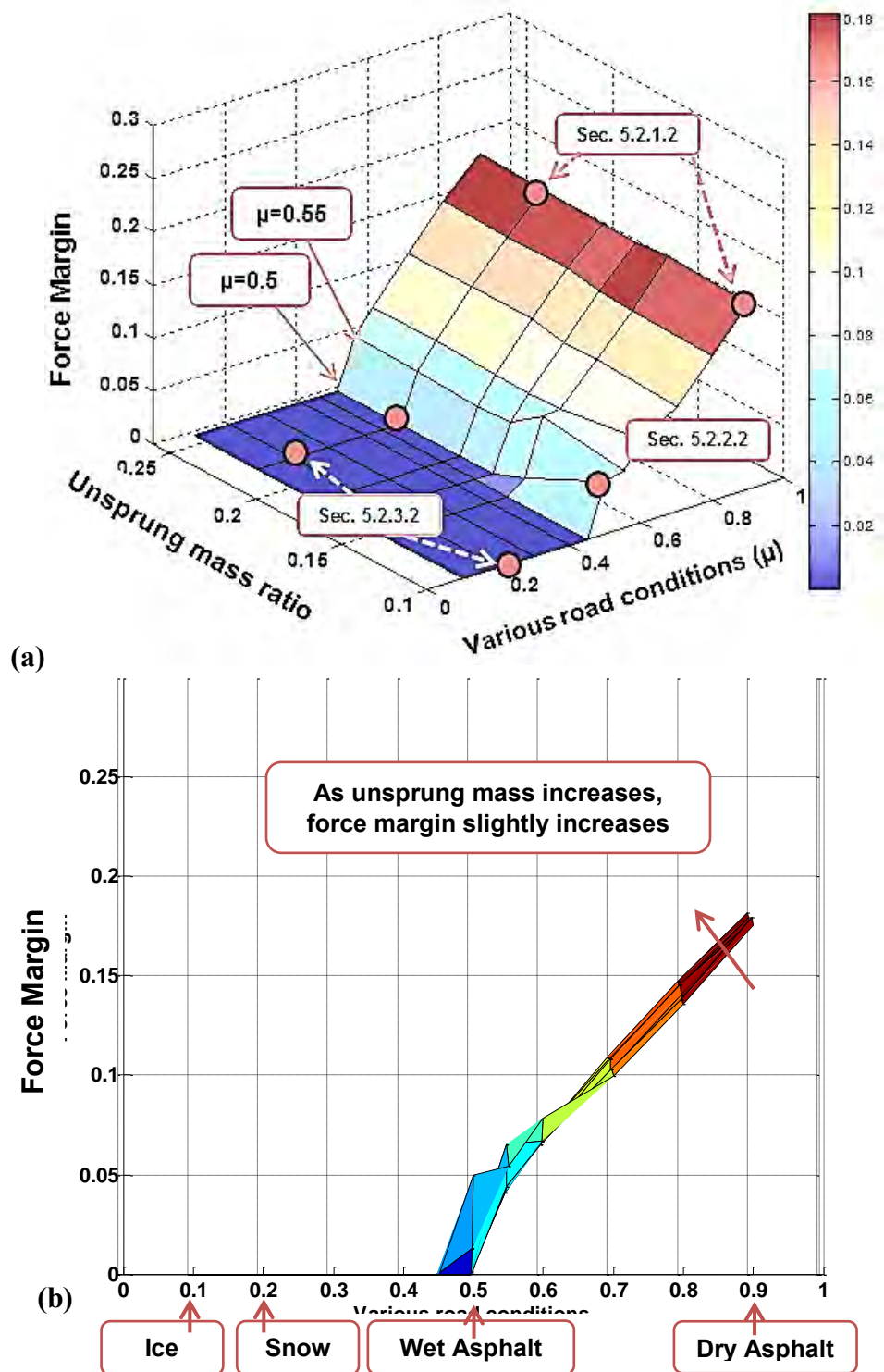


Figure 5-49: Force margin performance map (front-inside) for a single-lane change

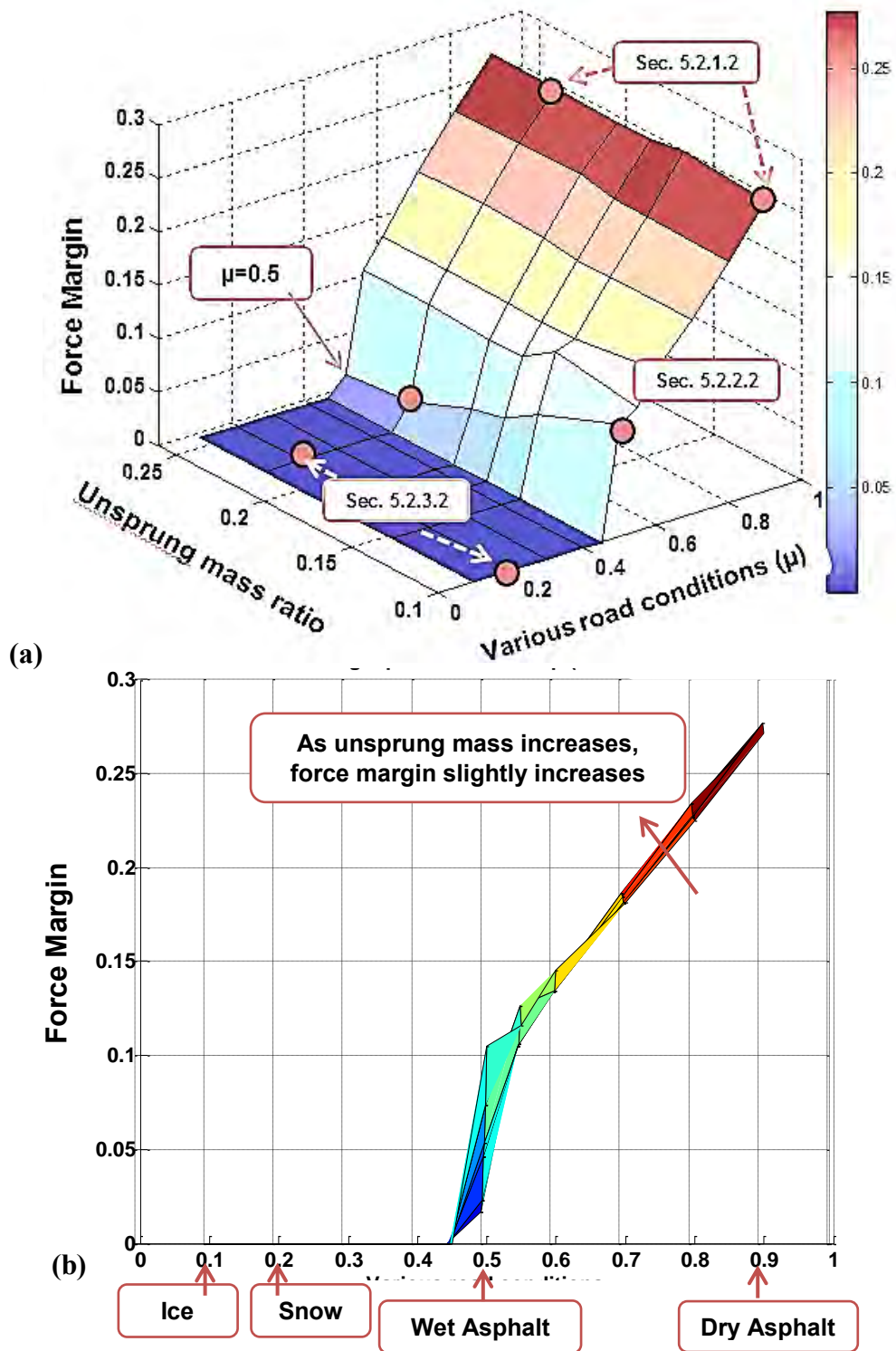
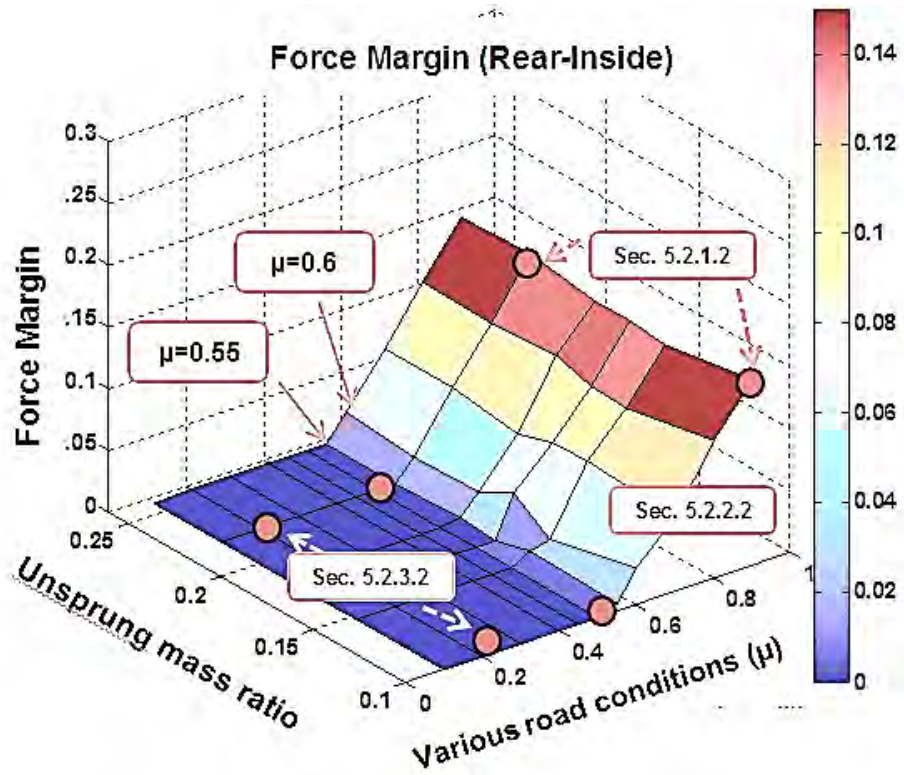
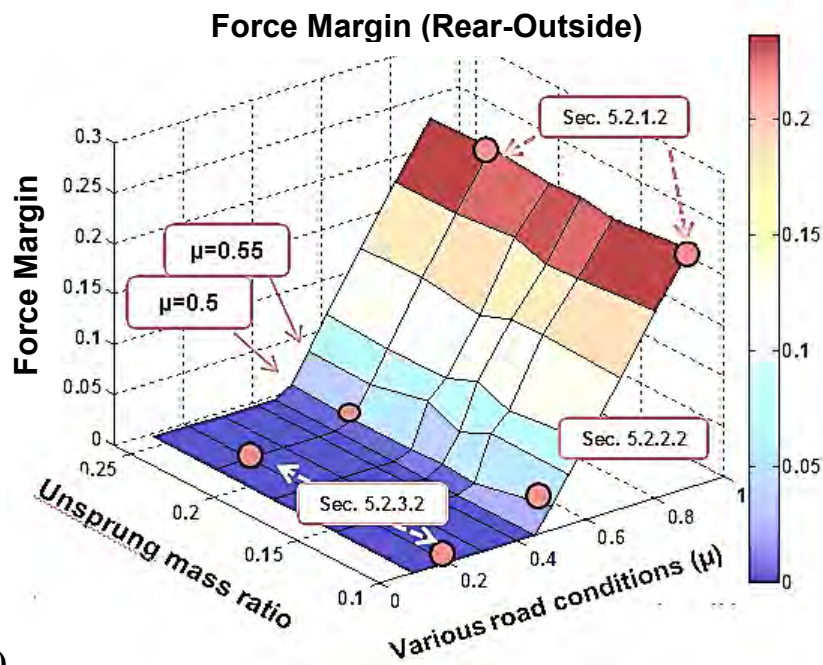


Figure 5-50: Force margin performance map (front-outside) for a single-lane change



(a)



(b)

Figure 5-51: Force margin performance map of rear-inside and rear-outside wheels

Figure 5-50 (a) shows the force margin performance map of a front-outside wheel during a cornering maneuver in a single-lane change. Figure 5-50 (b) shows the force margin map in x-z coordinates, which is the force margin as a function of various road conditions. The increased unsprung increases slightly the force margin for a single-lane change.

Figure 5-51 shows the force margin performance maps that describe how much force is available at the rear-inside and rear-outside wheels. As can be seen in Figure 5-51 (a), the force margin of a rear-inside wheel becomes zero on a slippery road of $\mu = 0.55$, while the force margin of a rear-outside wheel becomes zero on a slippery road of $\mu = 0.5$.

This occurs because the normal force of a rear-outside wheel is larger than that of a rear-inside wheel (see Sec. 5.2.2.2.). In comparison with Figure 5-50 (a) and Figure 5-51 (b) (i.e., $\mu = 0.5$ and $m_u = 10\%$), the force margins of a front-outside and rear-outside wheel are 0.1 and 0.02, respectively. This occurs when the lateral acceleration at the CG causes the rear slip angle to increase more than the front slip angle, resulting in oversteer behavior.

5.4 PERFORMANCE MAPS FOR THE SAME VEHICLE WEIGHT

In this section, we will discuss the effects of increased unsprung mass on acceleration, braking, and force margin on cornering maneuver, under the same vehicle weight. Acceleration, braking, and force margin performance maps are generated under the various road conditions.

5.4.1 Acceleration Performance Map

The acceleration performance map can be defined as the 0-60 mph acceleration time which describes how fast a vehicle moves. Two control parameters are chosen: unsprung mass ratios (from 10% to 26%) and various road conditions. Vehicle parameters used in simulation can be seen in Table 5-35.

The sprung mass is constant, while the unsprung mass varies based on different sizes of MDW such as 16, 20, 24, 32, up to 40 hp which would become customer choices. For instance, the total weight of a standard vehicle is 3300 lb; sprung mass (3000/g) and unsprung mass ($m_u=10\%$, 300/g). In addition, the total weight of a vehicle containing four MDW (32 hp) becomes about 3300 lb; sprung mass (2700/g) and unsprung mass ($m_u=22\%$, 594/g).

	Parameters	Value	Units	Value	Units
Total Vehicle mass	m_s	1497	kg	3300/g	slug
Unsprung mass		136		300	
{Sprung Mass}	m_u	{1361}	kg	{3000}	lb/g
(m_u =10%, reference car)					
Unsprung mass		192		422	
{Sprung Mass}	m_u	{1305}	kg	{2871}	lb/g
(m_u =14.7%, MDW 16 hp)					
Unsprung mass		213		469	
{Sprung Mass}	m_u	{1284}	kg	{2825}	lb/g
(m_u =16.6%, MDW 20 hp)					
Unsprung mass		234		514	
{Sprung Mass}	m_u	{1263}	kg	{2779}	lb/g
(m_u =18.5%, MDW 24 hp)					
Unsprung mass		270		594	
{Sprung Mass}	m_u	{1227}	kg	{2700}	lb/g
(m_u =22%, MDW 32 hp)					
Unsprung mass		306		673	
{Sprung Mass}	m_u	{1191}	kg	{2620}	lb/g
(m_u =25.7%, MDW 40 hp)					

Table 5-35: Vehicle parameters used in simulation

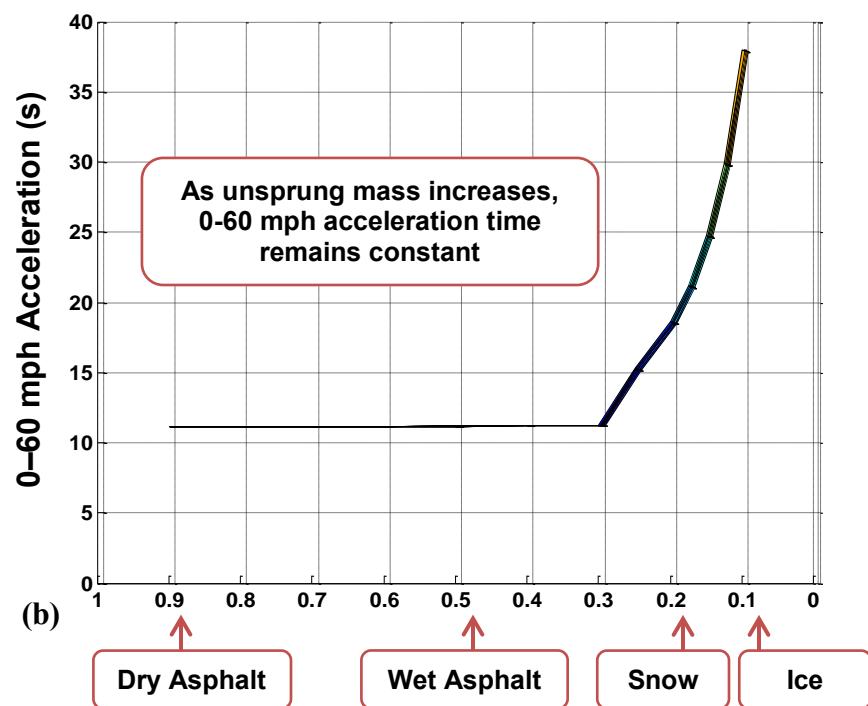
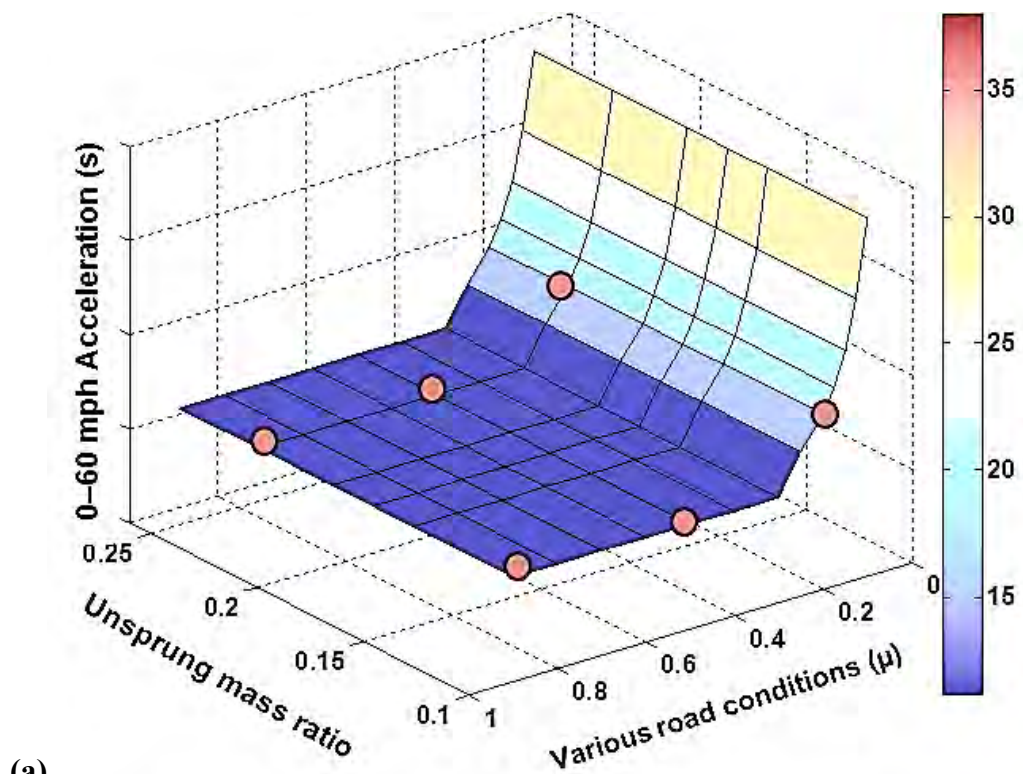


Figure 5-52: Acceleration performance map given constant torque (290 N-m (214 ft-lb))

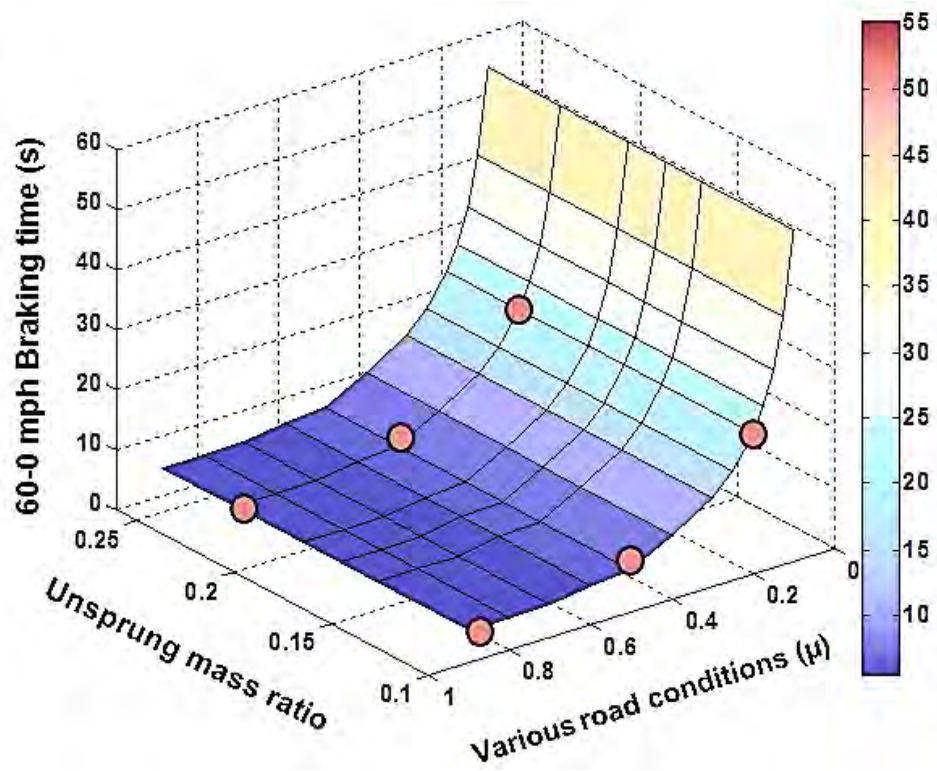
Figure 5-52 shows the acceleration performance map with respect to unsprung mass ratio and various road conditions. For instance, the friction coefficients of dry asphalt, rain asphalt, and snowy road are $\mu = 0.9$, $\mu = 0.5$, and $\mu = 0.2$, respectively. Each point is simulated through the 14 DOF full-vehicle Simulink model, corresponding to two control parameters. The circles indicate corresponding sections that has been simulated with two control parameters such as unsprung mass ratio and various road conditions (i.e. different friction coefficient μ).

As the ratio of the sprung mass to the unsprung mass increases (i.e., 0.1, 0.147, 0.166, 0.185, 0.22, and 0.26), the 0-60 mph acceleration time remains constant on the dry, wet asphalt, and snow ($\mu = 0.2$) road. The increased unsprung mass has an insignificant effect on the acceleration performances. On an icy road, the 0-60 acceleration time is around 38 s, while it is around 11 s on the dry road. Since an icy road has less friction, the 0-60 acceleration time on an icy road is around 2 times longer than that on a snowy road; an icy road (38 s) and a snowy road (18 s)

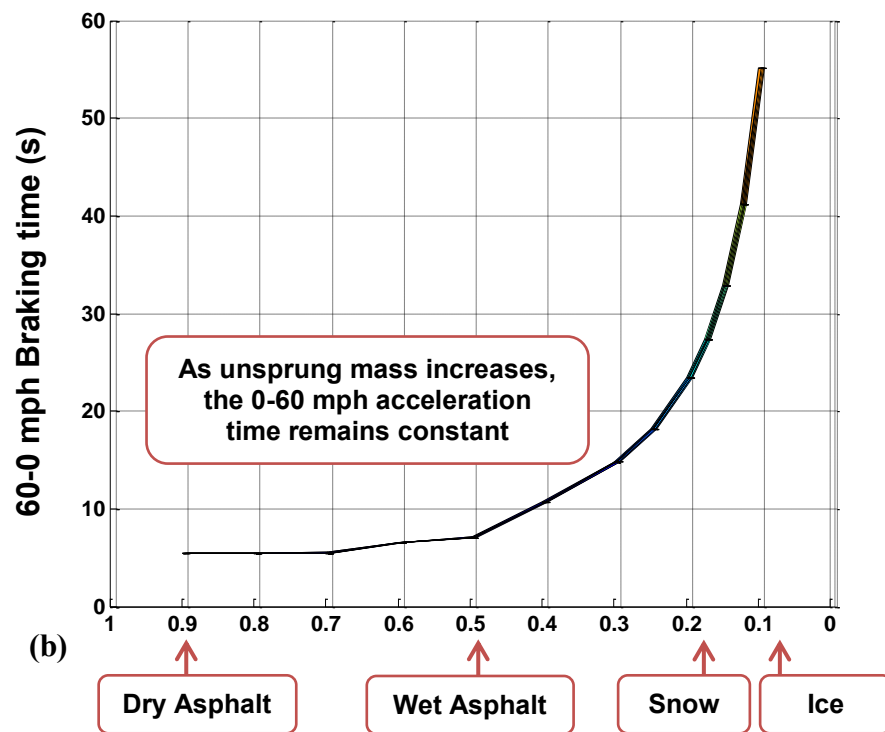
5.4.2 Braking Performance Map

The braking performance map can be defined as the 60-0 mph braking time which describes how fast a vehicle stops. Two control parameters are chosen as unsprung mass ratio from 10 % to 26 % and various road.

Figure 5-53 shows the braking performance map with respect to unsprung mass ratio and various road conditions. As the ratio of the sprung mass to the unsprung mass increases, the 60-0 mph braking time remains constant on various road conditions, as shown in Figure 5-53(b).



(a)



(b)

Figure 5-53: Braking performance map given constant torque (570 N-m(420 ft-lb))

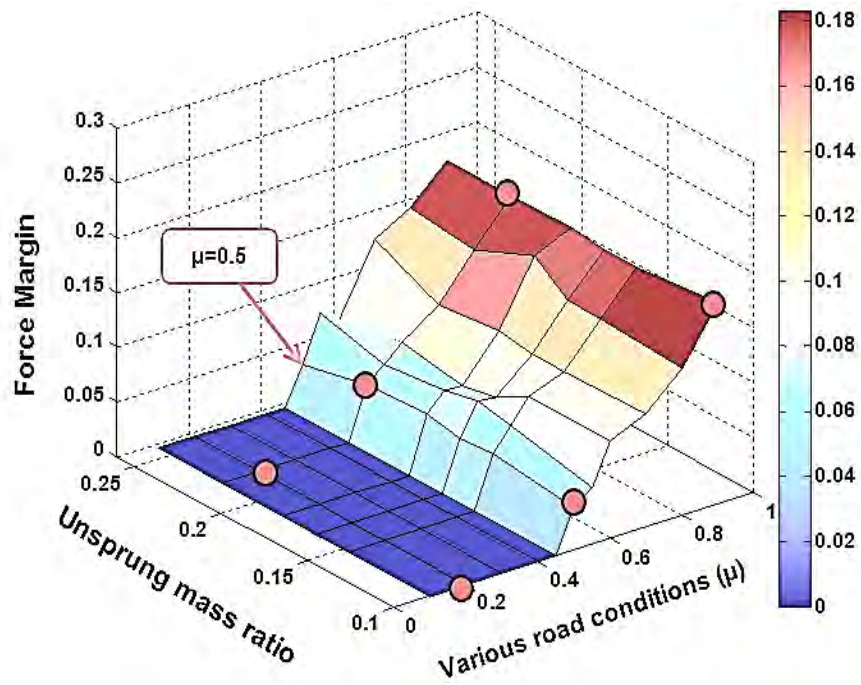
On the icy road, the 60-0 braking time is around 55 s, while it is around 5.5 s on the dry road. Since an icy road has less friction, the 0-60 acceleration time on an icy road is approximately 2.3 times longer than that on a snowy road; an icy road (58 s) and a snowy road (25 s).

5.4.3 Force Margin Performance Map during a Cornering Maneuver

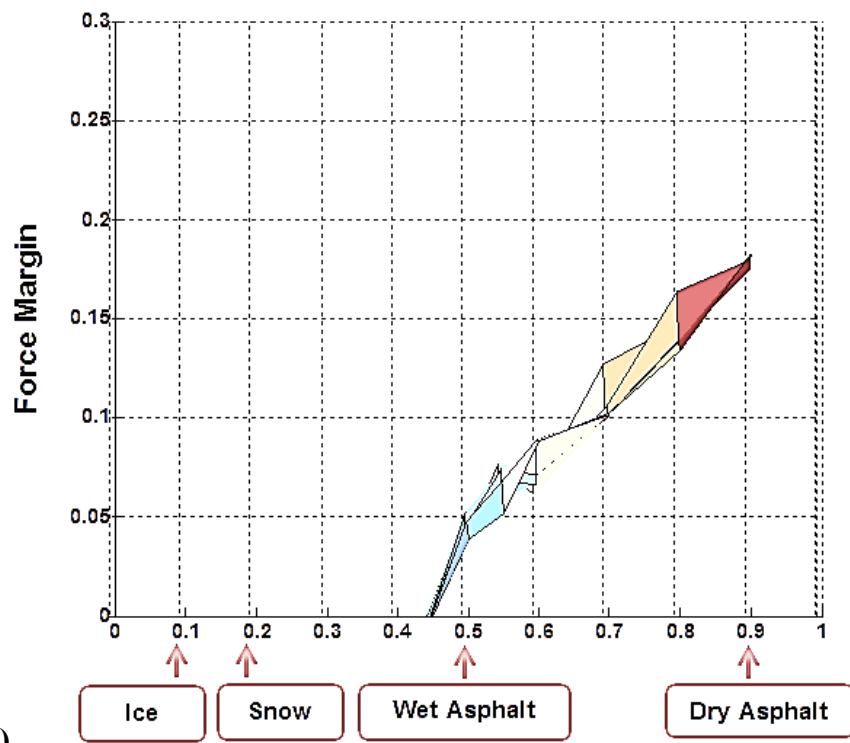
The force margin performance map during cornering maneuver can be defined as how much traction force is available for control purpose. Two control parameters are chosen, such as unsprung mass ratios from 10% to 26% and various road. The circles indicate corresponding sections that were simulated with two control parameters such as unsprung mass ratios and various road conditions (i.e. with different friction coefficients μ).

Figure 5-54 shows the force margin performance map of a front-inside wheel during a cornering maneuver in a single-lane change. When a vehicle runs on a road of $\mu = 0.4$, the force margin becomes zero. That is, the wheel's traction force is saturated so that a vehicle starts skidding, and this leads to unstable vehicle motion.

Figure 5-49 (b) shows the force margin map in x-z coordinates, which is the force margin as a function of various road conditions. The increased unsprung mass has little effect on the force margin of a front-inside wheel of a vehicle.

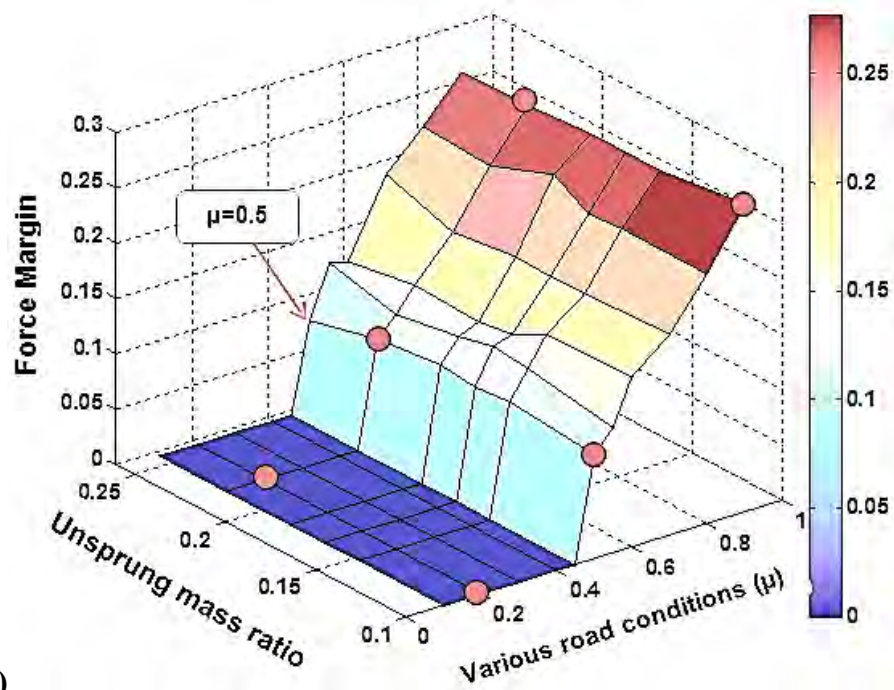


(a)

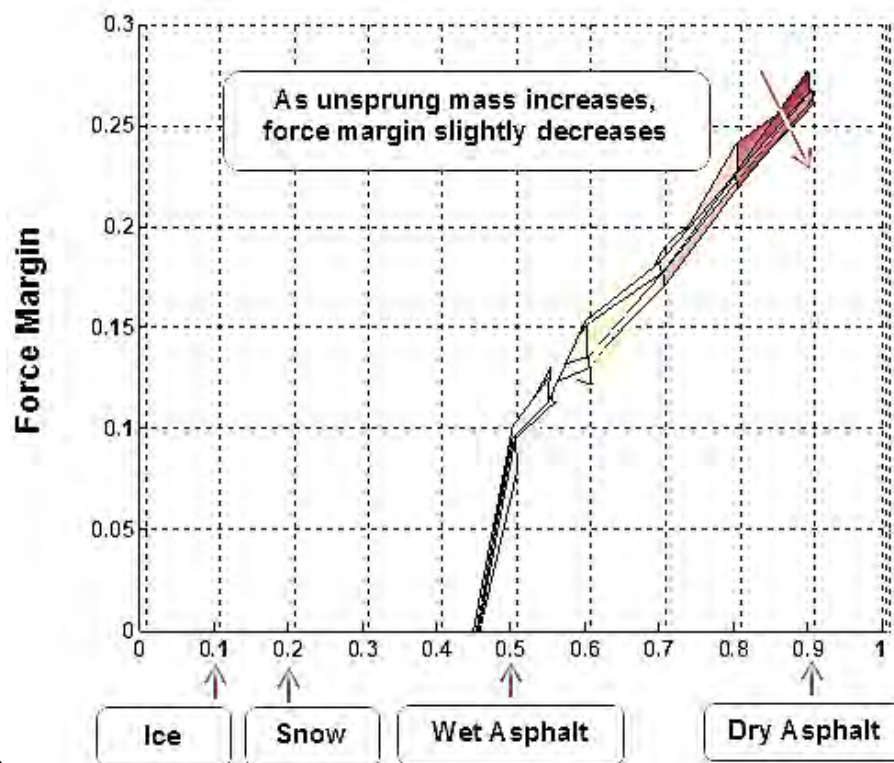


(b)

Figure 5-54: Force margin performance map (front-inside) for a single-lane change



(a)



(b)

Figure 5-55: Force margin performance map (front-outside) for a single-lane change

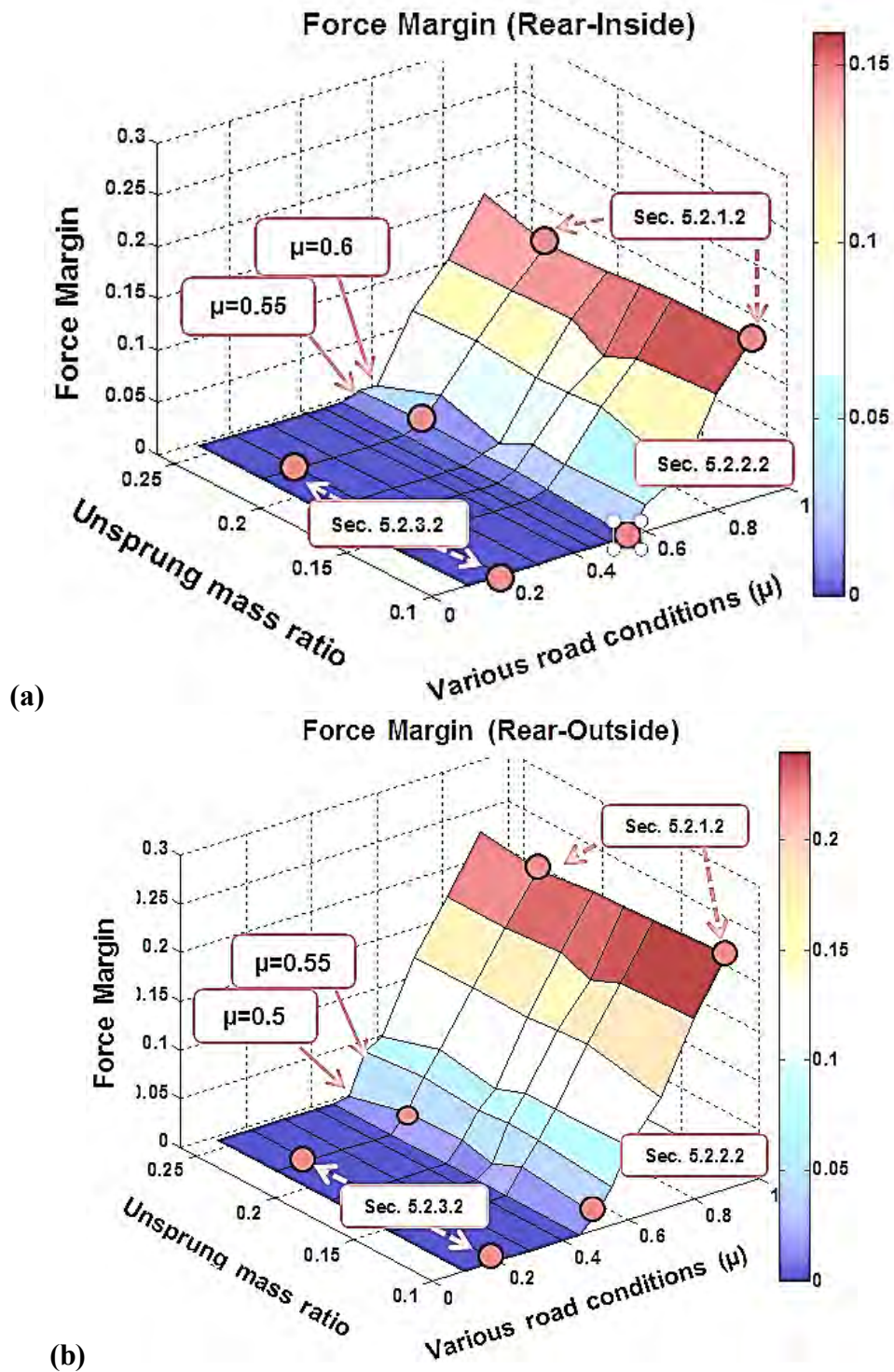


Figure 5-56: Force margin performance map of rear-inside and rear-outside wheels

Figure 5-55 (a) shows the force margin performance map of a front-outside wheel during a cornering maneuver in a single-lane change. Figure 5-55 (b) shows the force margin map in x-z coordinates, which is the force margin as a function of various road conditions. The increased unsprung mass has little effect on the force margin for a single-lane change.

Figure 5-56 shows the force margin performance maps that describe how much force is available at the rear-inside and rear-outside wheels. As can be seen in Figure 5-56 (a), the force margin of a rear-inside wheel becomes zero on a slippery road of $\mu = 0.55$, while the force margin of a rear-outside wheel becomes zero on a slippery road of $\mu = 0.5$. This occurs because the normal force of a rear-outside wheel is larger than that of a rear-inside wheel (see Sec. 5.2.2.2.).

In comparison with Figure 5-55 (a) and Figure 5-56 (b) (i.e., $\mu = 0.55$ and $m_u = 10\%$), the force margins of the front-outside and rear-outside wheel are 0.1 and 0.015, respectively. This occurs when the lateral acceleration at the CG causes the rear slip angle to increase more than the front slip angle, resulting in oversteer behavior.

5.5 CHAPTER SUMMARY

Maximum performance of an electric vehicle is determined by one of two constraints such as traction limits or motor power on the wheels. In this chapter, assuming there is an adequate power from the motor, the traction limit is influenced by various road conditions (i.e. friction coefficient between the tire and road).

With these constraints, the performance maps are generated based on the Simulink model of a 14 DOF full-vehicle model. Therefore, from an operational standpoint, a driver can perceive situational awareness of all operational capability. In

addition, the force margin performance maps during acceleration and braking can be used as operational criteria.

In the next chapter, we will discuss the limitation of motor power on the wheels based on individual demand cycles so that another version of performance maps can be developed based on performance criteria with respect to different size wheels and various road conditions.

Chapter 6. Duty / Demand Cycles

Equation Chapter 6 Section 1 Optimal sizing of in-wheel drive, choice of battery and capacity, development of controllers, and realistic charging scenarios requires a discussion of vehicle duty cycles [Liaw and Dubarry,2007; Shahidinejad, Bibeau et al.,2010]. In this research, the demand cycle refers to the individual's driving history and can be described by a speed versus time curve. The duty cycle refers to a vehicle's history of power usage and the manufacturer can use it to design the drive wheel actuator. As a result, the components of the actuator will be sized to meet the duty cycle.

For instance, an aggressive driver might want 0-60 mph acceleration time in 5 s, but an efficiency-priority driver will want high efficiency instead of the quick 0-60 mph acceleration time. The demand cycle, depending on the customer, will be determined by the driver history's speed versus time curve. Consequently, manufacturers can configure specific driving cycles for each particular customer. Based on their driving cycles, the actuator components will be tailored to that particular customer. This could lead to a more optimized actuator so that the customer can be best satisfied with their purchase. We will discuss in detail how to evaluate, classify, and satisfy these individual customers in Sec. 6.2. In addition, we will analytically demonstrate how the selection of the design components of MDWs differs for different types of customers such as an aggressive driver vs. an efficiency-priority driver, and describe design specifications such as different g levels, gear ratio, continuous torque, peak torque, power rating, battery resource management etc.

This chapter begins with duty cycle analysis based on existing driving cycles in Sec. 6.1. Energy consumption analysis is explained in Sec. 6.2. The individual demand cycles will be presented in Sec. 6.3. We will evaluate what the demands are on actuators

according to the specific operational demands on a passenger car. The chapter summary will be given in Sec. 6.4.

6.1 DUTY CYCLE ANALYSIS BASED ON EXISTING DUTY CYCLES

The duty cycle is a standardized driving pattern that represents typical operation of a passenger vehicle. Representative duty cycles include stop-go city driving, highway cruising, and combined city/highway driving conditions. There are 17 types of road driving patterns documented by the U.S. Environmental Protection Agency (EPA)[EPA; Davis, Diegel et al.,2011]. In addition, Berry proposed the effects of these duty cycles on the real-world fuel consumption of U.S. light-duty vehicles [Berry,2010].

6.1.1 Standard Duty Cycles

The duty cycles are used to assess vehicle fuel economy and emissions. Moreover, in order to develop the automotive power trains, they are used as a valuable design evaluation tool. EPA dynamometer driving schedules list 17 types of road driving cycles[EPA]:

Driving Cycles
Inspection and Maintenance (IM240)
Urban Dynamometer Driving Schedule (UDDS)
Federal Test Procedure (FTP)
Highway Fuel Economy Driving Schedule (HWFET)
New York City Cycle (NYCC)
Aggressive Driver (US06)
Air Conditioning Driving Cycle (SC03)
Heavy Duty Urban Dynamometer Driving Schedule (HUDDS)
LA92
LA92Short
Economic Commission of Europe (ECE)
Extra Urban Driving Cycle (EUDC)
Extra-Urban Driving Cycle (Low Powered Vehicles)(EUDC_LP)
New European Driving Cycle (NEDC)
Japan 10-Mode
Japan 15-Mode
Japan 1015-Mode

We selected three driving cycles to simulate the vehicle performance: Urban Dynamometer Driving Schedule (UDDS), Highway Fuel Economy Driving Schedule

(HWFET), and US06. We will discuss UDDS, HWFET, and US06. The rest of the duty cycles are plotted in the Appendix B.

6.1.1.1 Urban Dynamometer Driving Schedule (UDDS)

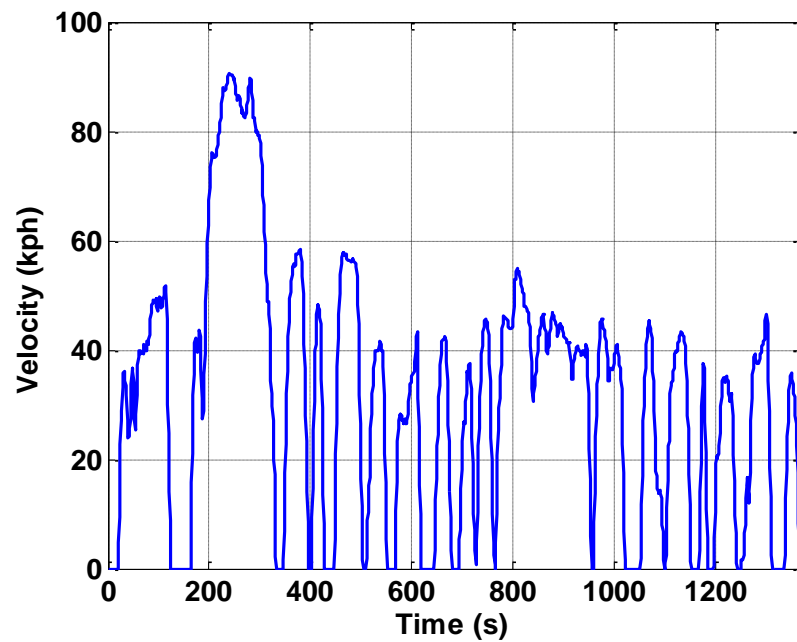


Figure 6-1: Driving cycle (UDDS)

The Urban Dynamometer Driving Schedule (UDDS) is called “LA4” or the “city test” and represents a city duty cycle with continuous stop-start operation, as shown in Figure 6-1. The UDDS can be used for light duty vehicle testing. This duty cycle results in a length of 7.45 miles, test duration of 1369 sec, top speed of 56.7 mph, and an average speed of 19.59 mph.

6.1.1.2 Highway Fuel Economy Test (HWFET)

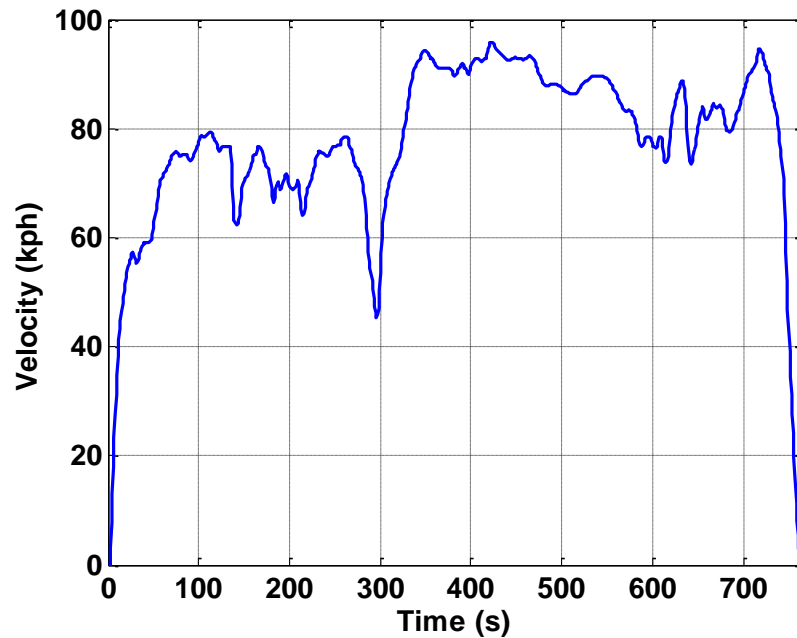


Figure 6-2: Driving cycle (HWFET)

The Highway Fuel Economy Test (HWFET) can be used for highway driving conditions under 100 kph, as shown in Figure 6-2. This cycle results in a cycle length of 10.26 miles, test duration of 765 sec, top speed of 59.9 mph, and an average speed of 48.3 mph.

6.1.1.3 Aggressive Driver (US06)

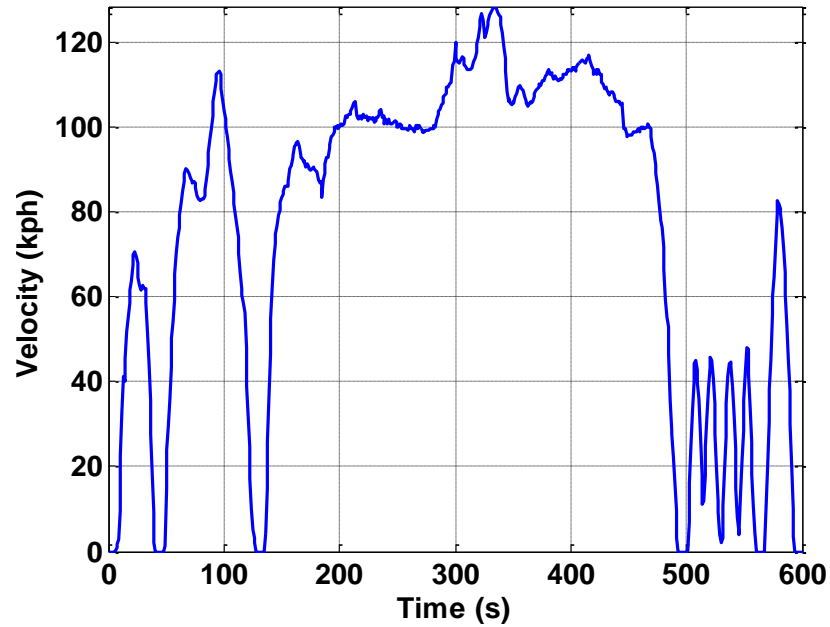


Figure 6-3: Driving cycle (US06)

The US06 represents a high acceleration driving schedule which can be used to represent for an aggressive driver, as shown in Figure 6-3. This duty cycle results in a cycle length of 8.01 miles, test duration of 596 sec, top speed of 80 mph, and an average speed of 48.37 mph.

6.1.2 Total Wheel Torque and Power

The equation of motion along a vehicle's longitudinal direction is used for analyzing vehicle performance, as shown in Equation (4.23) as follows [Larminie and Lowry, 2003; Vandana and Fernandes, 2010] (see Section 4.1.6):

$$\begin{aligned}\tau_m &= \frac{\tau_{tw}}{N_w g_r \eta_g} = \frac{r_w F_t}{N_w g_r \eta_g} \\ &= \frac{r_w}{N_w g_r \eta_g} \left[\left\{ m_c + \frac{N_w}{r_w^2} \left(I_w + g_r^2 \frac{I_m}{\eta_g} \right) \right\} a_{car} + \left\{ \frac{1}{2} \rho_a A_f C_d (v_v + v_w)^2 + C_r m_c g \cos \theta + m_c g \sin \theta \right\} \right] \quad (6.1)\end{aligned}$$

For a short period of time, the speed is assumed to be linear with time. In other words, the acceleration is constant during this time. These acceleration can be estimated by the following equation [Ehsani, Gao et al., 2009]:

$$a_{car} = \frac{dV}{dt} = \frac{V_{k+1} - V_k}{t_{k+1} - t_k} \quad (k = 1, 2, \dots, n; n = \text{total number of points}) \quad (6.2)$$

It should be noted that the time step of existing duty cycles is 1 Hz data (1 s). Since we use one-second time intervals, the power is equal to the energy consumed. Substituting Equation (6.2) into Equation (6.1) yields:

$$\begin{aligned}\tau_m &= \frac{\tau_{tw}}{N_w g_r \eta_g} = \frac{r_w F_t}{N_w g_r \eta_g} \\ &= \frac{r_w}{N_w g_r \eta_g} \left[\left\{ m_c + \frac{N_w}{r_w^2} \left(I_w + g_r^2 \frac{I_m}{\eta_g} \right) \right\} \left(\frac{V_{k+1} - V_k}{t_{k+1} - t_k} \right) + \left\{ \frac{1}{2} \rho_a A_f C_d (v_v + v_w)^2 + C_r m_c g \cos \theta + m_c g \sin \theta \right\} \right] \quad (6.3)\end{aligned}$$

In this next section, we show how to estimate motor torque (τ_m) for a given duty cycle.

	Parameters	Value	Units	Value	Units
Number of wheels	N_w	4			
Vehicle mass	m_c	1497	kg	3300/g	slug
Moment of inertia of the wheel	I_w	1.28	kg-m ²	0.944	slug-ft ²
Moment of inertia of motor rotor	I_m	6.03E-6	kg-m ²	4.45E-6	slug-ft ²
Gear system efficiency	η_g	1			
Head wind velocity	v_w	0	m/s	0	ft/s
Wheel radius	r_w	0.305	m	12	in
Air density	ρ_a	1.23	kg/m ³	0.0024	slug/ft ³
Frontal area	A_f	1.3	m ²	14	ft ²
Drag coefficient	C_d	0.3			
Rolling coefficient	C_r	0.007			
Gear ratio	g_{r1}, g_{r2}	49,14			

Table 6-1: Vehicle Parameters

Table 6-1 shows the vehicle system parameters which were used in this report for the vehicle simulation based on the UDDS driving cycle.

6.1.2.1 Urban Dynamometer Driving Schedule (UDDS)

A UDDS driving cycle is translated into wheel speed, total wheel torque, and total wheel power requirement, as shown in Figure 6-4 (a), (b), and (c), respectively. The wheel speed plot, as shown in Figure 6-4 (a), can be obtained from the following equation:

$$n_w = \frac{v}{r_w} \left(\frac{60}{2\pi} \right) \quad (6.4)$$

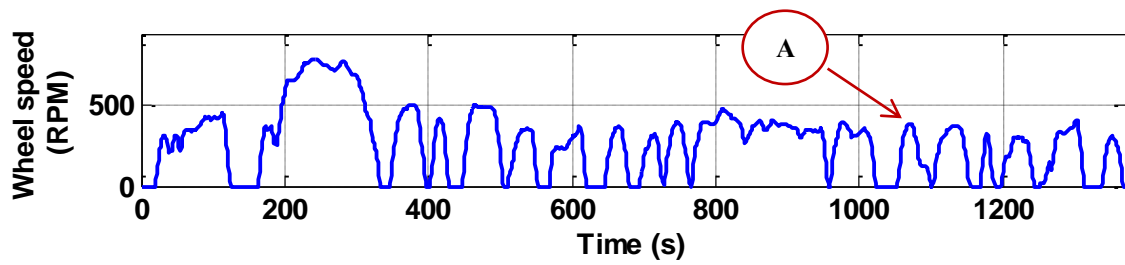
where velocity (v) comes from the duty cycle plot. As can be seen in Figure 6-4 (b), the total wheel torque (τ_{tw}) required in any instant in a duty cycle can be calculated based on Equation(6.3) as follows:

$$\tau_{tw} = r_w \left[\left\{ m_c + \frac{N_w}{r_w^2} \left(I_w + g_r^2 \frac{I_m}{\eta_g} \right) \right\} \left(\frac{V_{k+1} - V_k}{t_{k+1} - t_k} \right) + \left\{ \frac{1}{2} \rho_a A_f C_d (v_v + v_w)^2 + C_r m_c g \cos \theta + m_c g \sin \theta \right\} \right] \quad (6.5)$$

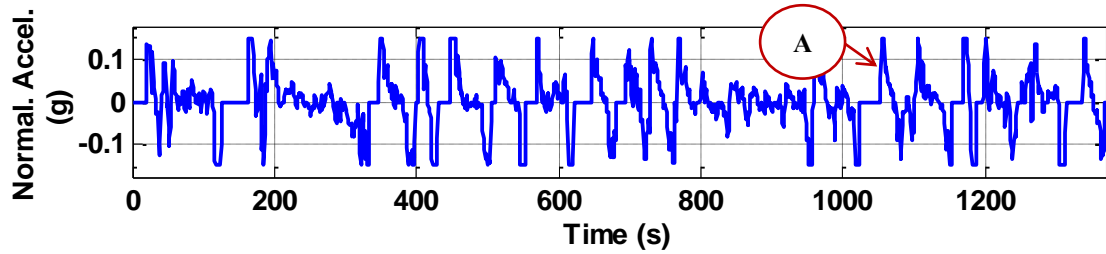
The total wheel power (kw) is calculated by:

$$P_{tw} = \frac{(2\pi n_w) \tau_{tw}}{60} \quad (6.6)$$

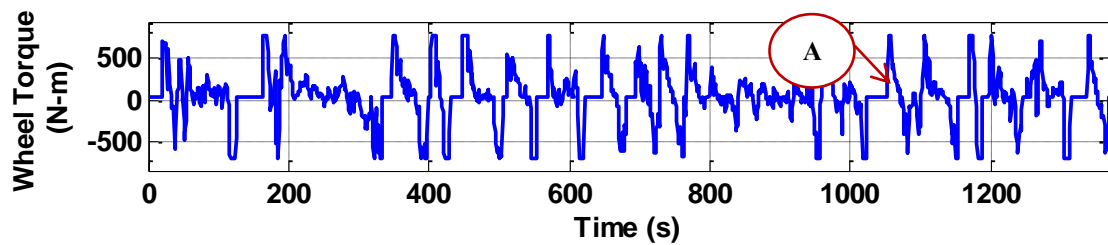
where τ_{tw} is the total wheel torque, n_w is the wheel speed, P_{tw} is the total wheel power.



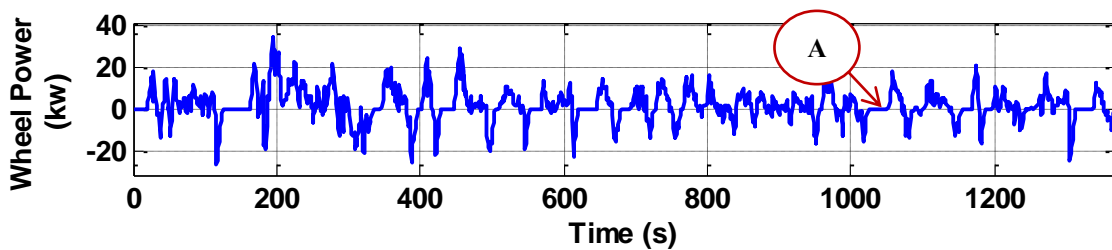
(a) Wheel speed over time



(b) Normalized acceleration over time



(c) Total wheel torque over time



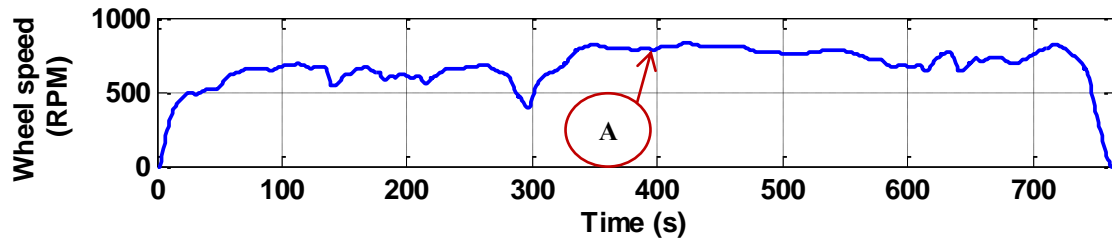
(d) Total wheel power over time

Figure 6-4: Total wheel torque and power requirement derived from duty cycle (UDDS)

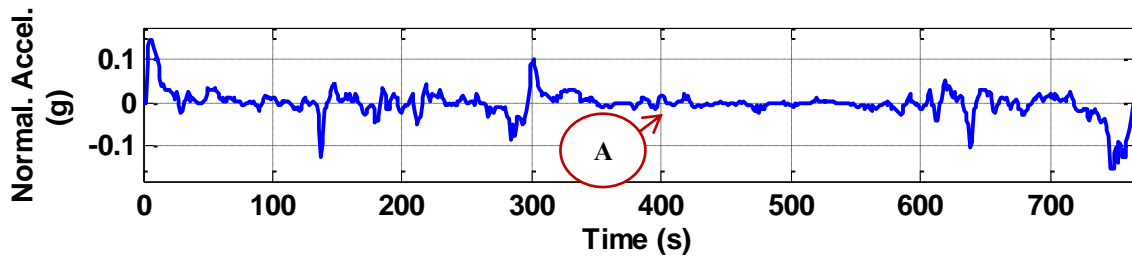
As seen at symbol 'A' shown in Figure 6-4 (a), the wheel speed accelerates from 0 to 400 RPM (28 mph). From the corresponding total wheel torque and power shown in

Figure 6-4 (c) and (d), it is concluded that the peak torque and power are strongly associated with acceleration events shown in Figure 6-4 (b).

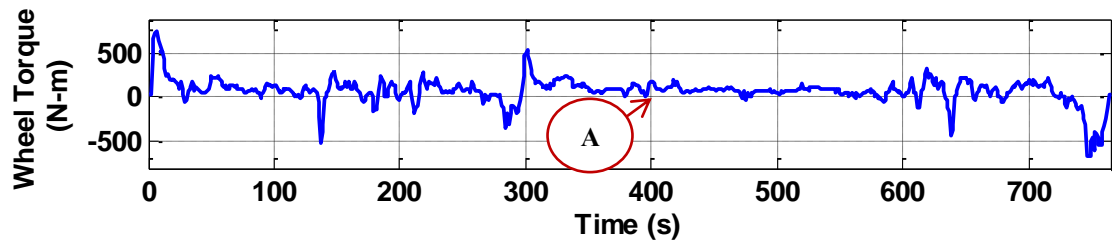
6.1.2.2 Highway Fuel Economy Test (HWFET)



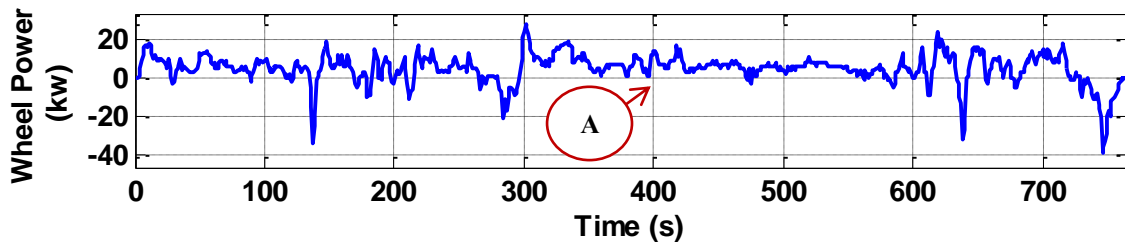
(a) Wheel speed over time



(b) Normalized acceleration over time



(c) Total wheel torque over time



(d) Total wheel power over time

Figure 6-5: Total wheel torque and power requirement derived from duty cycle (HWFET)

An HWFET driving cycle is translated into wheel speed, normalized acceleration, total wheel torque, and total wheel power requirement, as shown in Figure 6-5 (a) – (d), respectively. As seen at symbol ‘A’ shown in Figure 6-5 (a), the wheel speed is around 800 RPM (56 mph) and normalized acceleration is 0.02 g. The continuous torque and power are 170 N-m and 13.6 kw during cruising.

6.1.2.3 Aggressive Driver (US06)

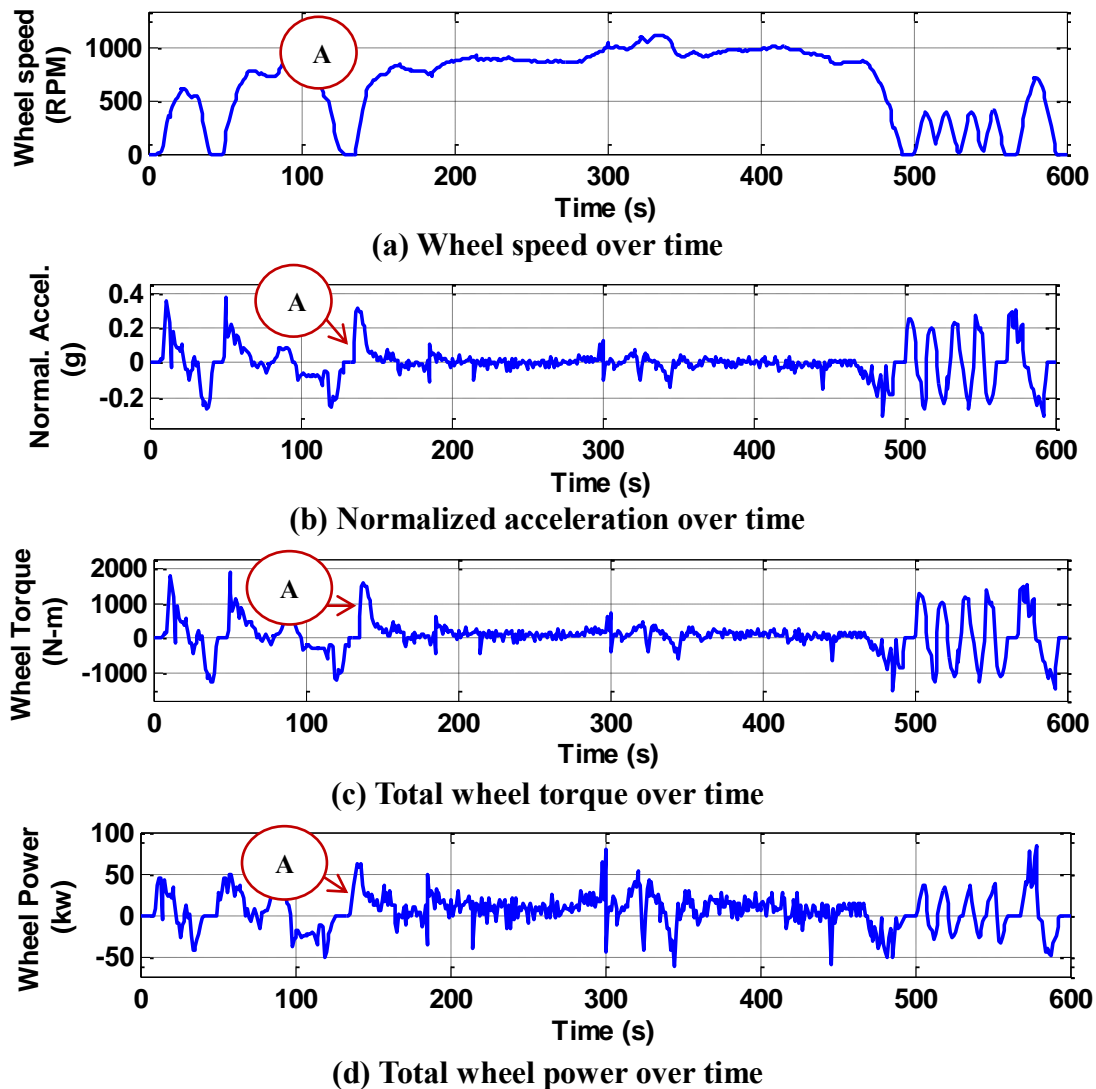


Figure 6-6: Total wheel torque and power requirement derived from duty cycle (US06)

A US06 duty cycle is translated into wheel speed, normalized acceleration, total wheel torque, and total wheel power requirement, as shown in Figure 6-6 (a) - (d), respectively. As seen at symbol 'A' shown in Figure 6-6 (a), the wheel speed rapidly accelerates from 0 to 400 RPM. This behavior indicates characteristics of an aggressive driver. At that time, peak torque and power are around 1557 N-m and 63 kw. The normalized acceleration is around 0.3 g. Clearly, it is evident that the instantaneous torque and power are strongly dependent on acceleration events. The variation of total wheel torque and power shows how the aggressive driver behaves and what he / she expects (wants).

6.1.3 Speed-Acceleration Frequency Distribution

The required information about the time proportions of individual duty cycles can be obtained from the Speed-Acceleration Frequency Distribution (SAFD) [Shahidinejad, Bibeau et al.,2010]. In addition, this plot provides a visual picture of each duty cycle, and hence, this 3D map can illustrate whether the duty cycle is biased in terms of speed or acceleration regions.

6.1.3.1 Urban Dynamometer Driving Schedule (UDDS)

Figure 6-7 shows a 3D map of speed-acceleration frequency distribution with respect to normalized acceleration level and velocity. This map helps us to understand how the duty cycle is biased. In other words, this map describes the range and distribution of time spent at different speeds and acceleration. For instance, duty cycles regarding urban driving conditions represent a city cycle with continuous stop-go operation. With regard to UDDS, it is apparent that there is a bias around 40 kph (25 mph) and 80 kph (50 mph). Furthermore, as can be seen in Figure 6-7 (b), the plot shows

that there is significant time spent idling around 0 kph due to a city cycle with continuous stop-start operation. The peak acceleration and deceleration are around 0.15 g, as shown in Figure 6-7 (a). Their limited acceleration and deceleration were artificially produced by the traction limits of the chassis dynamometer.

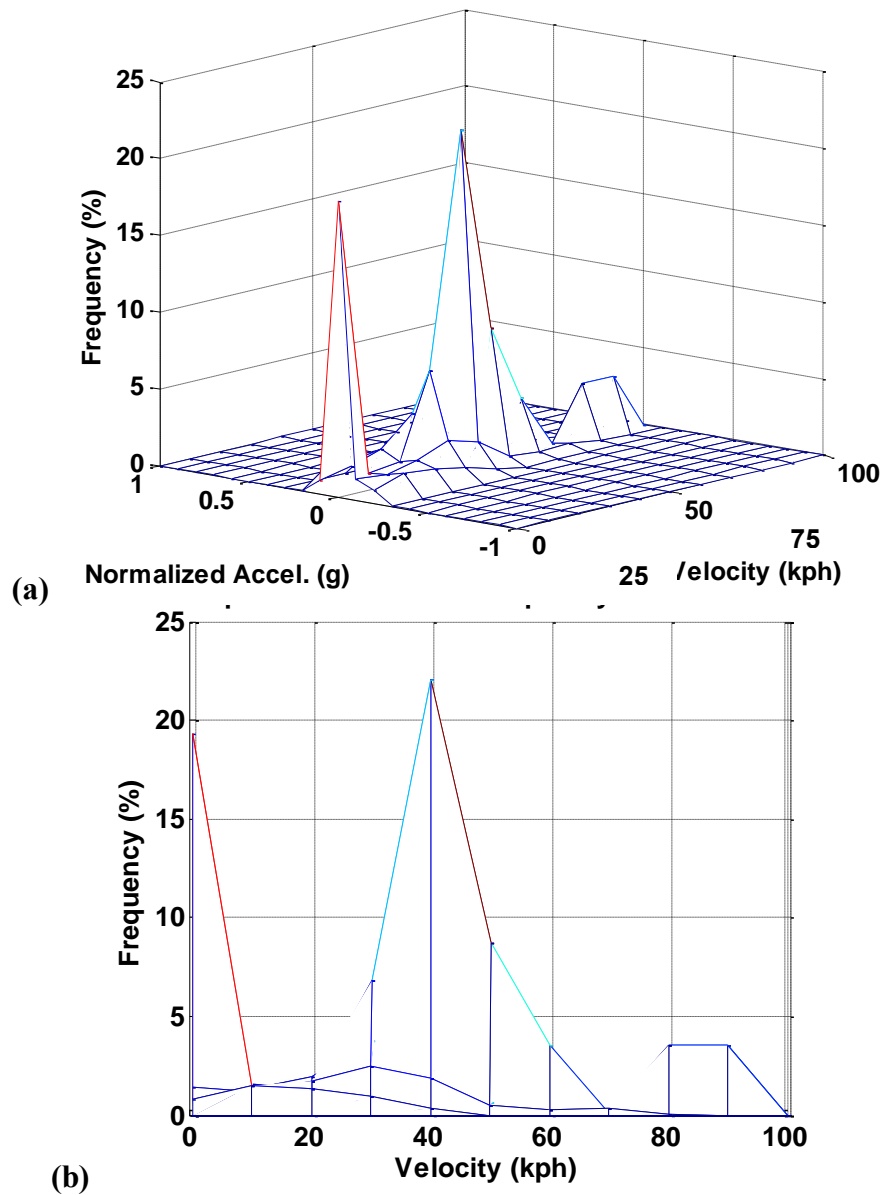


Figure 6-7: Speed-acceleration frequency distribution plot (UDDS)

6.1.3.2 Highway Fuel Economy Test (HWFET)

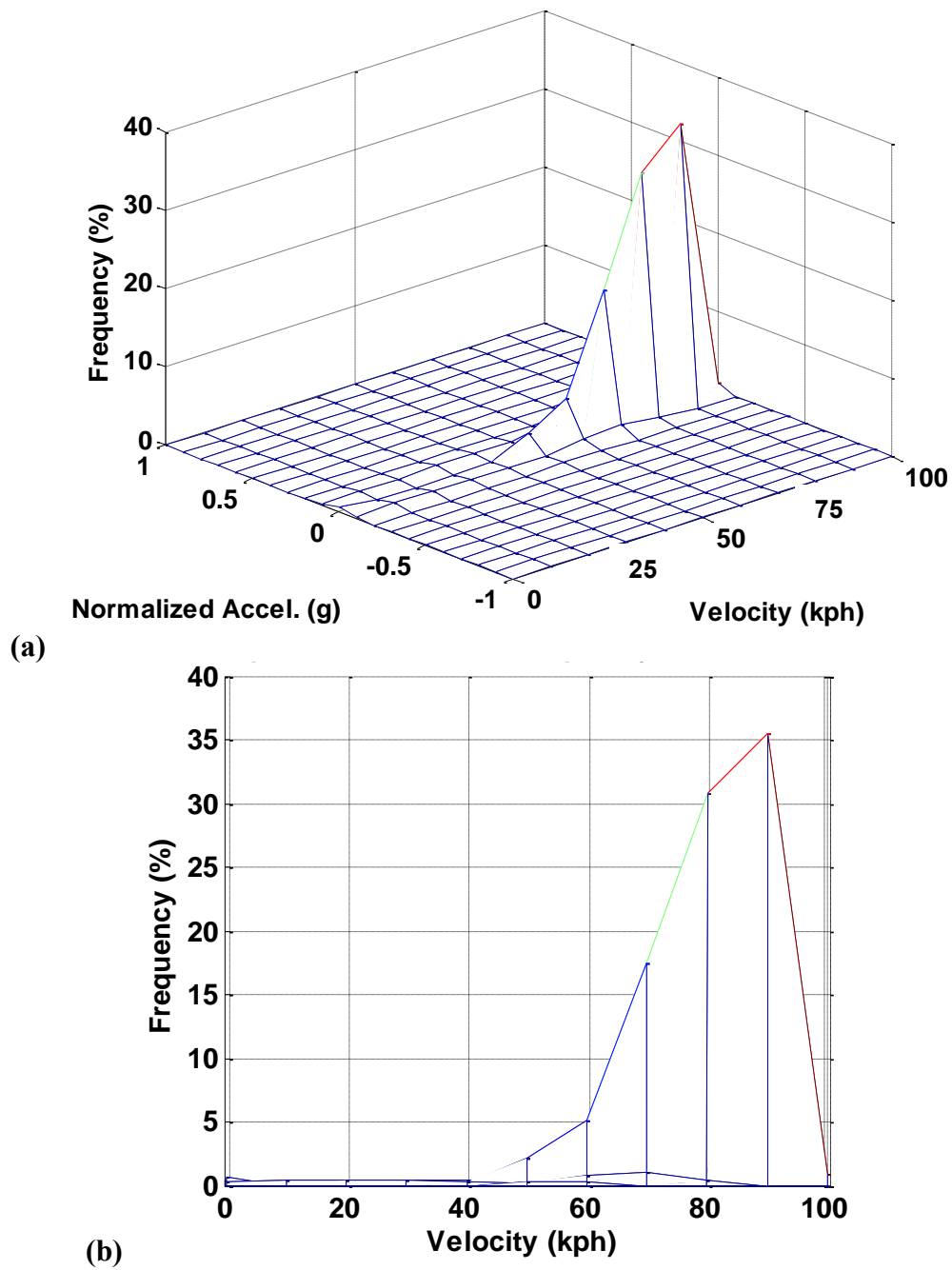


Figure 6-8: Speed-acceleration frequency distribution plot (HWFET)

Since the HWFET is used for highway driving conditions under 100 kph, the most frequent speeds (frequency (%)) are from 60 to 100 kph (63 mph), as shown in Figure 6-8.

6.1.3.3 Aggressive Driver (US06)

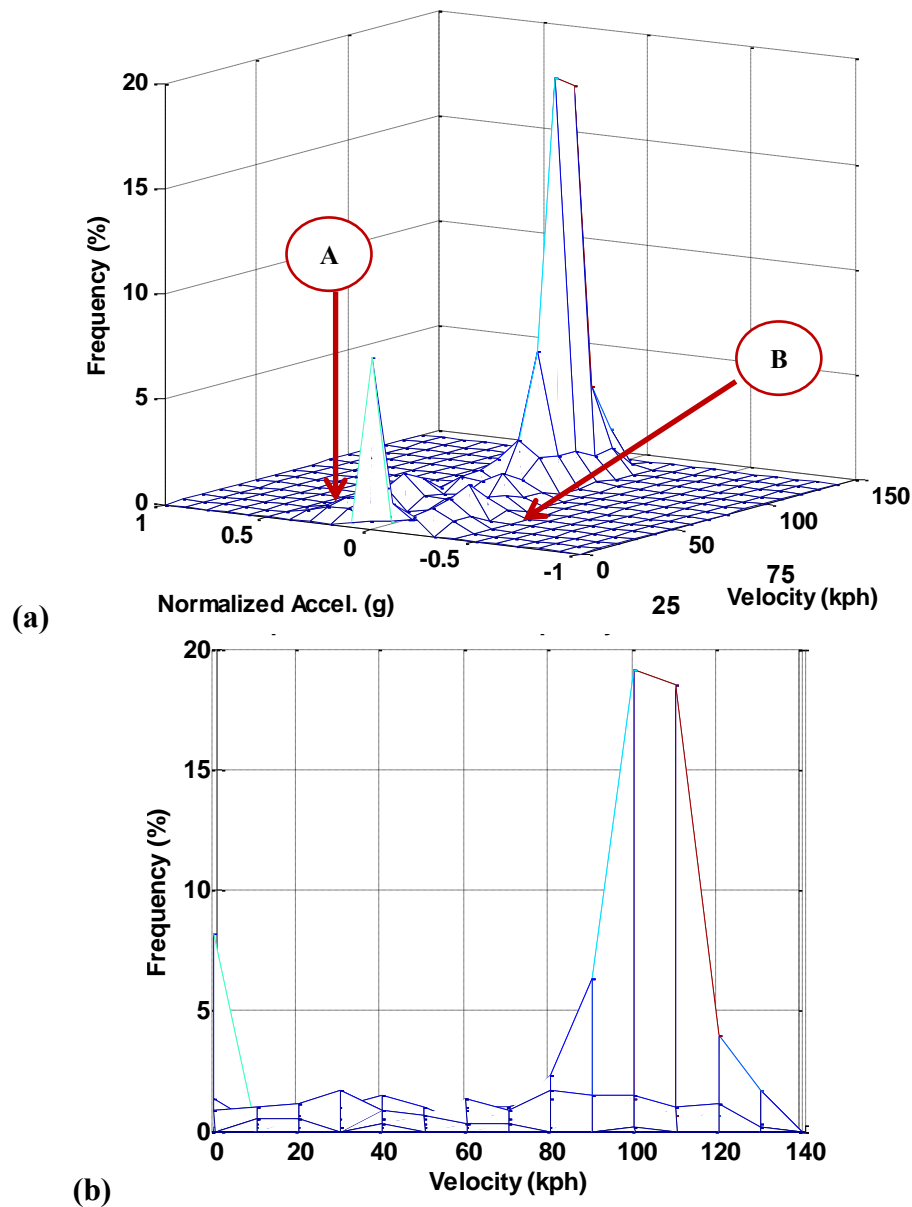


Figure 6-9: Speed-acceleration frequency distribution plot (US06)

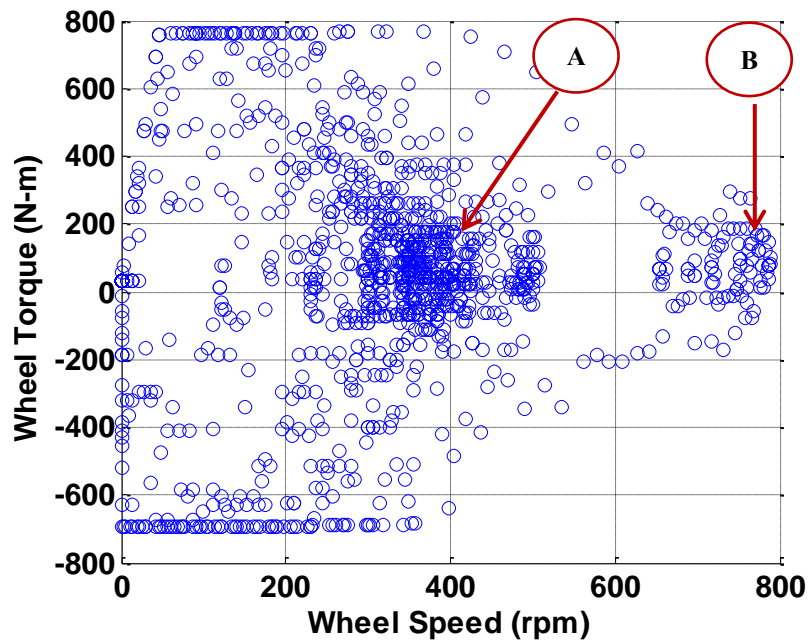
Figure 6-9 shows the 3D map of speed-acceleration frequency distribution with respect to normalized acceleration level and velocity. Compared to Figure 6-7 and Figure 6-8, the US06 is the much higher rates of acceleration and deceleration. The symbol 'A' and 'B' indicate a peak acceleration of 0.35 g and a peak deceleration of 0.3 g, respectively. This is a characteristic of an aggressive driver.

6.1.4 Wheel Torque-Speed

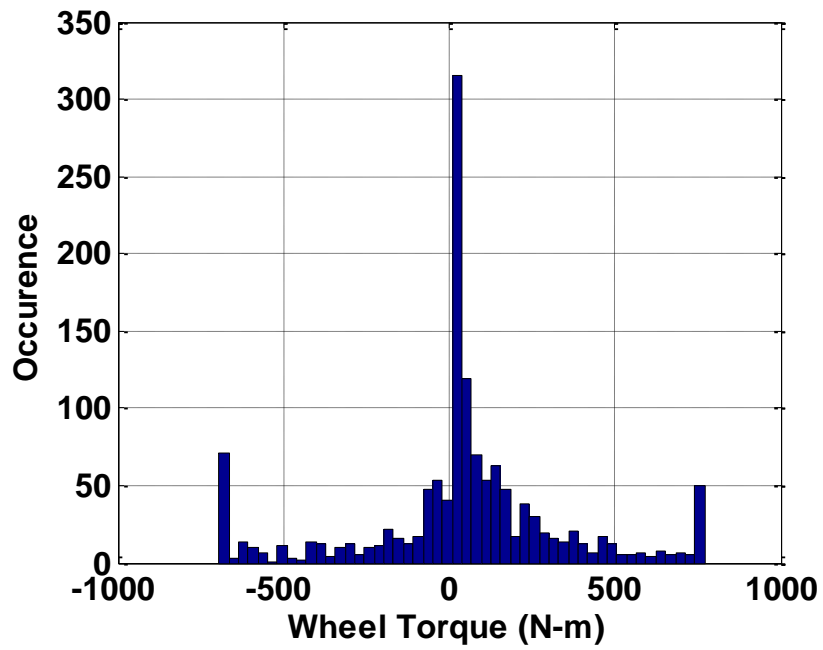
Some research studies show the torque-speed characteristics of the driving cycles[Ren, Crolla et al.,2009; Greaves, Walker et al.,2011]. This section will discuss the wheel torque-speed scatter plots in terms of UDDS, HWFET, and US06 conditions.

6.1.4.1 Urban Dynamometer Driving Schedule (UDDS)

Torque-speed characteristics play an important role in designing the proper motor power rating, which is the primary consideration with respect to performance specifications. Figure 6-10 (a) and (b) show the total wheel torque vs. speed scatter plot and the number of occurrence vs. total wheel torque histogram, respectively, for the UDDS driving cycle. As can be seen in Figure 6-10 (a), each circle is the operating point associated with the UDDS duty cycle and is plotted based on Equation(6.5). As seen at symbol ‘A’ and ‘B’ in Figure 6-10 (a), two significant findings are highlighted. First, the symbol ‘A’ (40 kph (25 mph)) represents characteristics of downtown driving (i.e., stop and go operation). Second, symbol ‘B’ (80 kph (50 mph)) indicates that the operating points move away from the center due to the quadratic aerodynamic drag force as wheel speed increases[Greaves, Walker et al.,2011]. In order to find out the continuous torque and peak torque specifications, it is necessary to obtain a histogram in terms of the number of occurrences vs. total wheel torque, as shown in Figure 6-10 (b). The majority of the energy consumed corresponds to those occurrences that occur at low torque levels between 0 and 100 N-m. Given four-independent drive wheels, the total continuous wheel torque is 400 N-m (i.e., 100 N-m per wheel) and total peak wheel torque is 1000 N-m (i.e., 250 N-m per wheel).



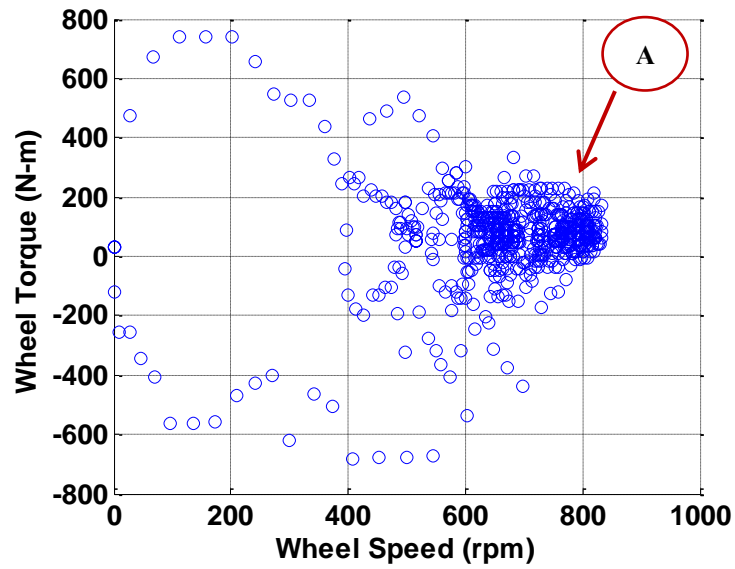
(a) Total wheel torque-speed scatter plot



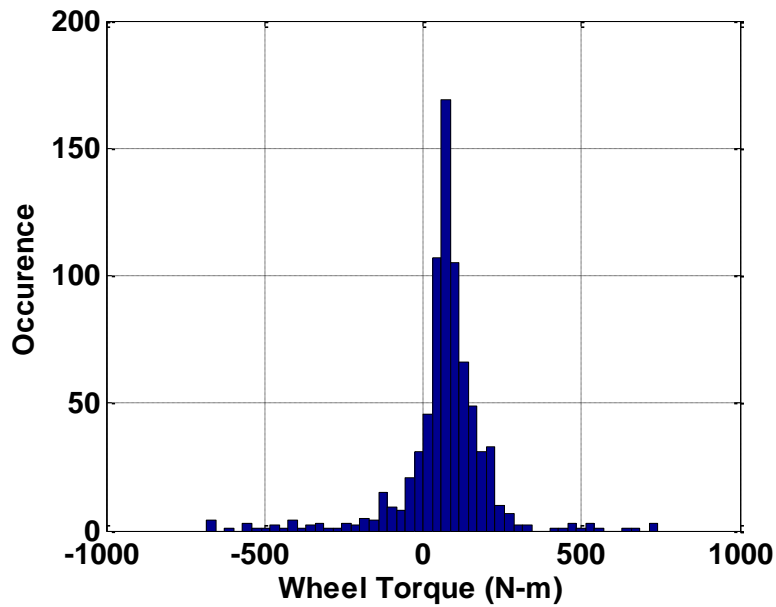
(b) Occurrence – total wheel torque histogram

Figure 6-10: Total wheel torque-speed (UDDS)

6.1.4.2 Highway Fuel Economy Test (HWFET)



(a) Total wheel torque-speed scatter plot



(b) Occurrence – total wheel torque histogram

Figure 6-11: Total wheel torque-speed (HWFET)

Compared to the UDDS, many operating points occur around 700 RPM (50 mph) due to highway driving conditions, as seen at symbol ‘A’ shown in Figure 6-11.

6.1.4.3 Aggressive Driver (US06)

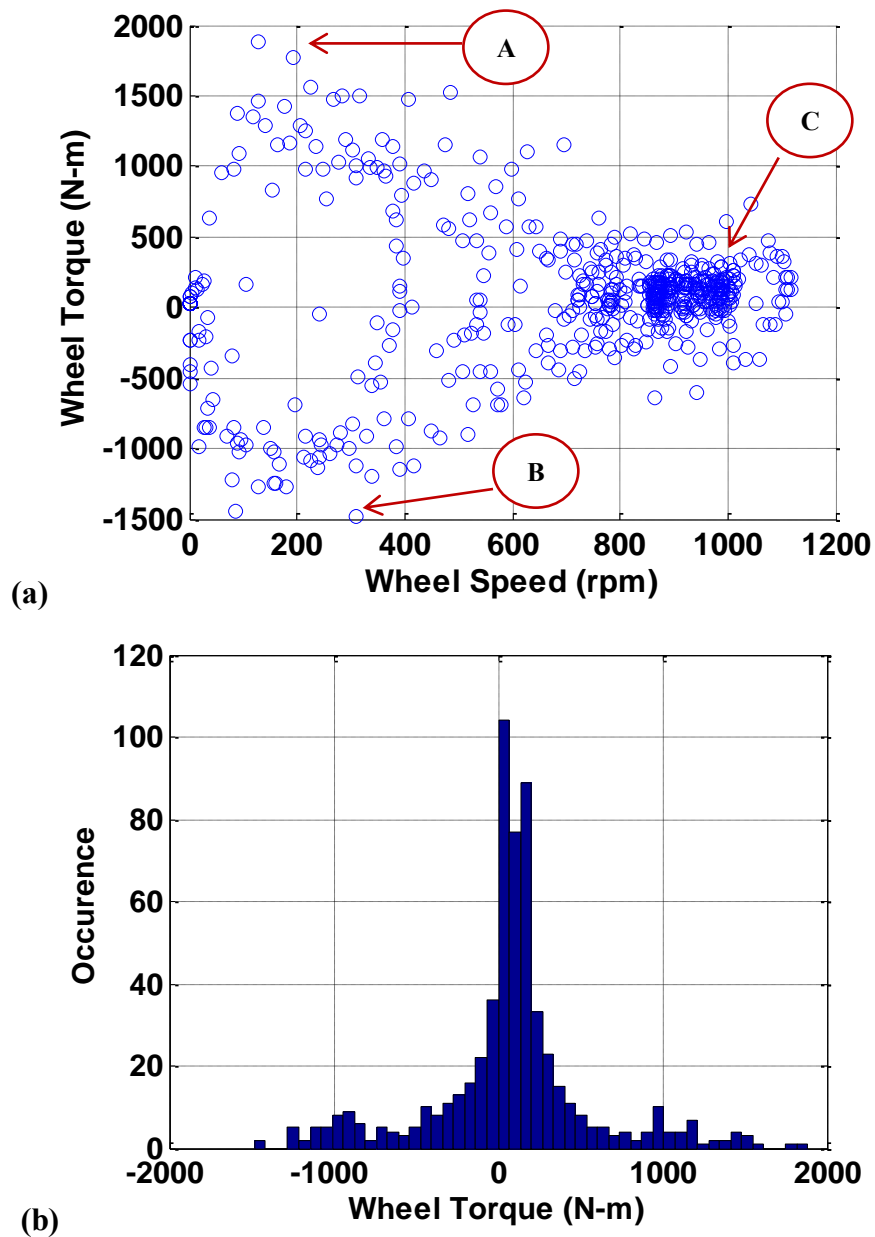


Figure 6-12: Total wheel torque-speed (US06)

Figure 6-12 (a) and (b) show the total wheel torque-speed scatter plot and the number of occurrences vs. total wheel torque histogram, respectively, for the US06 driving cycle. As can be seen in Figure 6-12 (a), each circle is the operating point associated with a US06 driving cycle. As seen at symbols 'A', 'B', and 'C' in Figure 6-12 (a), three significant findings are highlighted.

First, symbol 'A' indicates that high acceleration levels for the aggressive driver occur at low speed, and are relatively short in duration. Second, symbol 'B' indicates that high deceleration levels for the aggressive driver also occur at low speeds. Third, the symbol 'C' indicates that the operating points move away from the center due to the quadratic aerodynamic drag force, as wheel speed increases [Greaves, Walker et al., 2011].

As shown in Figure 6-12 (b), the majority of the energy consumed occurs at low torque levels between 0 and 400 N-m wheel torque. Given four independent drive wheels, the total continuous wheel torque is 1600 N-m (i.e., 400 N-m per wheel) and total peak wheel torque is 2400 N-m (i.e., 600 N-m per wheel). The peak wheel torque is limited by the power rating of the drive wheel.

6.1.5 Motor Output Torque and Power

The MDW has four distinct speeds (two electrical and two mechanical) in order to improve efficiency and enhance drivability such as acceleration, braking, and climbing a hill on the command of the operator.

Since the MDW has four distinct speeds, the g (acceleration) level will have four different levels that are associated with four distinct speed ranges: g_1 (0 – 10 mph), g_2 (11 – 20 mph), g_3 (21 – 40 mph), and g_4 (41 mph – 70 mph). The clutch shift occurs at 20 mph from 49-to-1 (for low speed and high torque) to 14-to-1 (for high speed and low torque) for the two mechanical speeds. One controller configuration operates the g_1 and

g_3 regimes at low power while the other controller configuration operates the g_2 and g_4 regimes at higher power for the two electrical speeds. Hence, the MDW has four choices regarding efficiency and drivability. [Tesar and Ashok, May, 2011].

Assuming four independent drive wheels, the motor characteristics can be determined in terms of motor speed, torque, and power of the MDW of an electric vehicle. We will discuss the motor speed, torque, and power in terms of the 4 operating regimes of the MDW.

6.1.5.1 Urban Dynamometer Driving Schedule (UDDS)

With regard to the MDW, the first and second speed ranges would be 0-20 mph, and the third and fourth speed ranges would be 21-70 mph. The MDW operates from 0 to 13,726 RPM in the first/second motor speed range based on the first gear ratio of 49-to-1 (for low speed and high torque). After a changeover due to clutch shift at 20 mph, the MDW operates from 4,118 to 13,726 RPM corresponding to 21 to 70 mph (for high speed and low torque). Figure 6-13 shows motor output speed, acceleration torque, and power derived from Figure 6-4 considering the four-independent drive wheels. The motor speed required to produce the wheel speed is given by:

$$\begin{aligned} n_{m1} &= n_{w1} \times g_{r1} \\ n_{m2} &= n_{w2} \times g_{r2} \end{aligned} \tag{6.7}$$

where n_{w1} and n_{m1} are the wheel speed (RPM) and motor speed (RPM) associated with a gear ratio of g_{r1} (49:1), and n_{w2} and n_{m2} are the wheel speed (RPM) and motor speed (RPM) associated with a gear ratio of g_{r2} (14:1).

As seen at symbol ‘A’ in Figure 6-13 (a), a sudden peak speed occurs before the clutch shift. At that time, the wheel speed is 280 RPM (20 mph) and the motor speed is 13726 RPM with an acceleration of 0.15 g as shown in Figure 6-13 (b). As can be seen in

Figure 6-13 (c) and (d), the motor output torque and power can be obtained from the total wheel torque and power divided by the number of wheels as follow:

$$\begin{aligned} \tau_{m1} &= \frac{\tau_{tw}}{N_w g_{r1} \eta_g}, \quad \tau_{m2} = \frac{\tau_{tw}}{N_w g_{r2} \eta_g} \\ P_{m1} &= \frac{(2\pi n_{m1}) \tau_{m1}}{60 N_w}, \quad P_{m2} = \frac{(2\pi n_{m2}) \tau_{m2}}{60 N_w} \end{aligned} \quad (6.8)$$

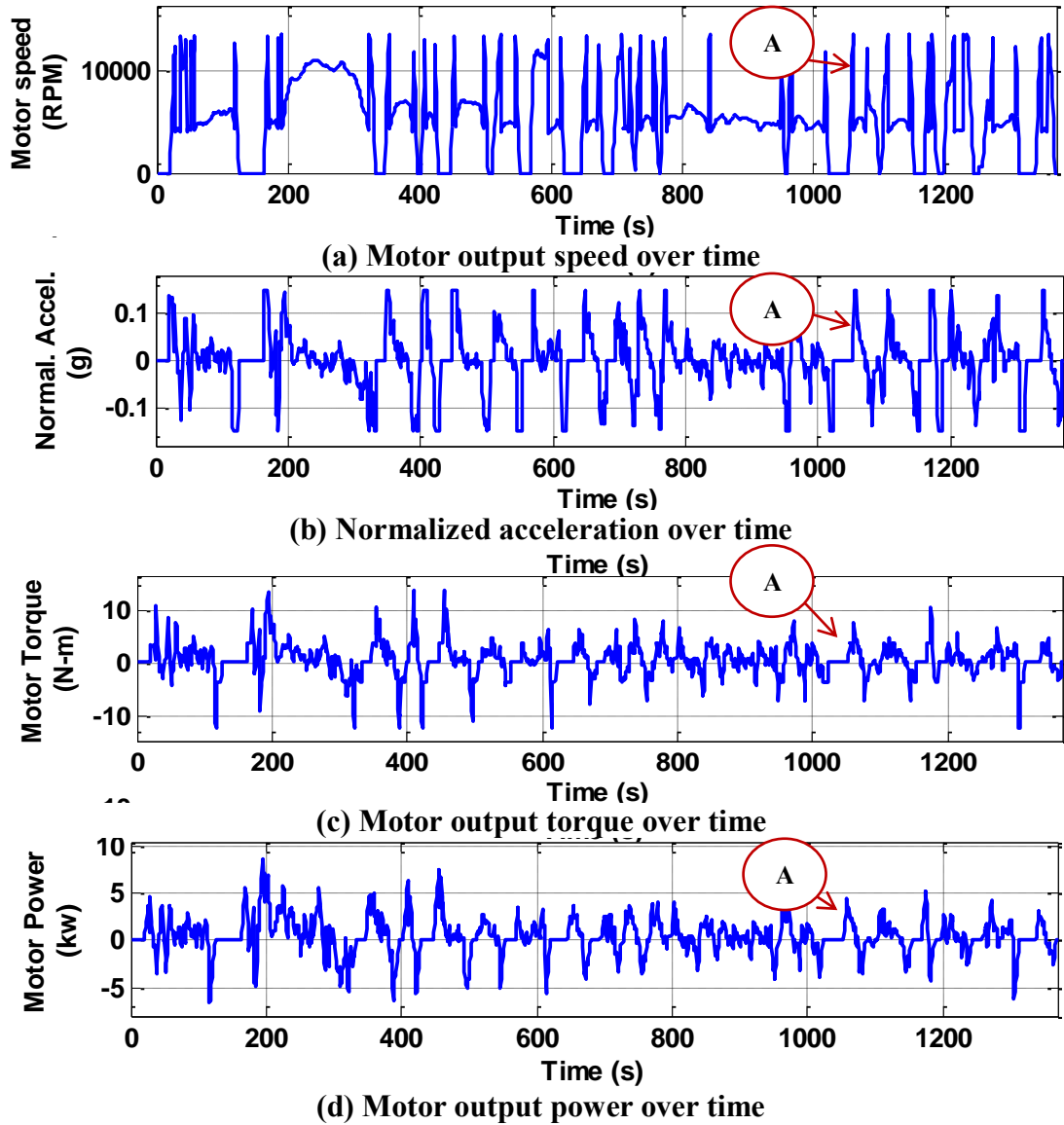
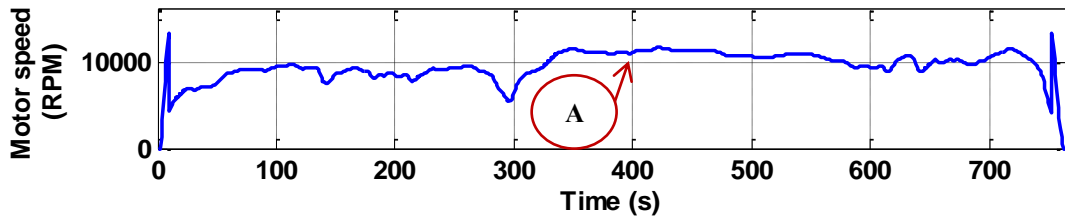


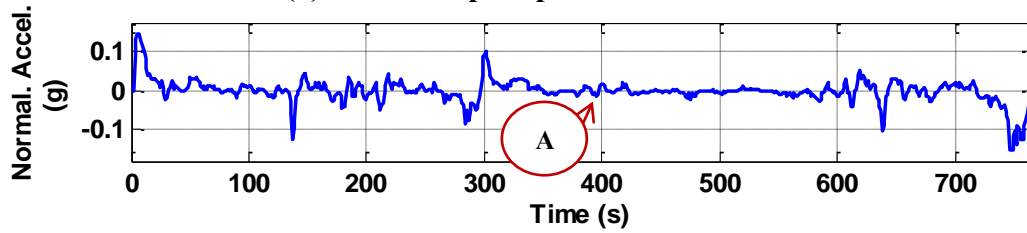
Figure 6-13: Motor output speed, acceleration, torque, and power (UDDS)

From Equation (6.8), τ_{m1} and P_{m1} are the motor output speed (RPM) and motor output power (kw) associated with a gear ratio of g_{r1} (49:1), and τ_{m1} and P_{m1} are the motor output speed (RPM) and motor output power (kw) associated with a gear ratio of g_{r2} (14:1). As seen at symbol 'A' in Figure 6-13 (b), it is concluded that the peak torque and power are strongly associated with acceleration events.

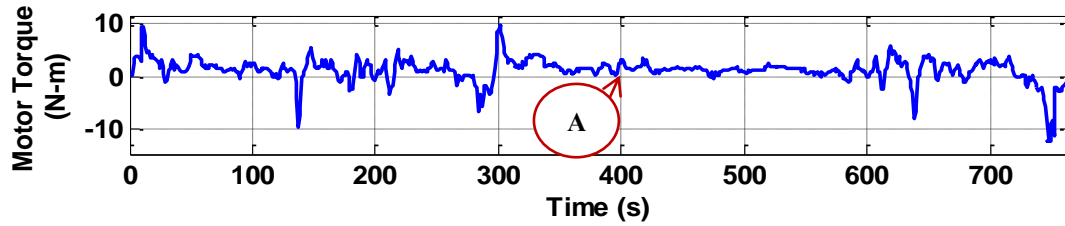
6.1.5.2 Highway Fuel Economy Test (HWFET)



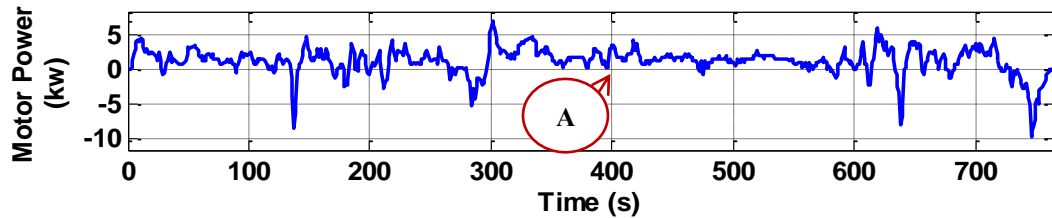
(a) Motor output speed over time



(b) Normalized acceleration over time



(c) Motor output torque over time



(d) Motor output power over time

Figure 6-14: Motor output speed, acceleration, torque, and power (HWFET)

Figure 6-14 shows motor output speed, normalized acceleration, torque, and power derived from Figure 6-5. These plots are derived by Equation (6.7) and (6.8). As seen symbol ‘A’ shown in Figure 6-14 (a), the motor output speed is 11100 RPM with a corresponding wheel speed around 800 RPM (56 mph). The torque and power are 3.5 N-m and 3.4 kw. The 3.5 N-m is from 170 N-m divided by gear ratio (14:1) and four wheels. The 3.4 kw is from 13.6 kw divided by four wheels (see Section 6.1.2.2).

6.1.5.3 Aggressive Driver (US06)

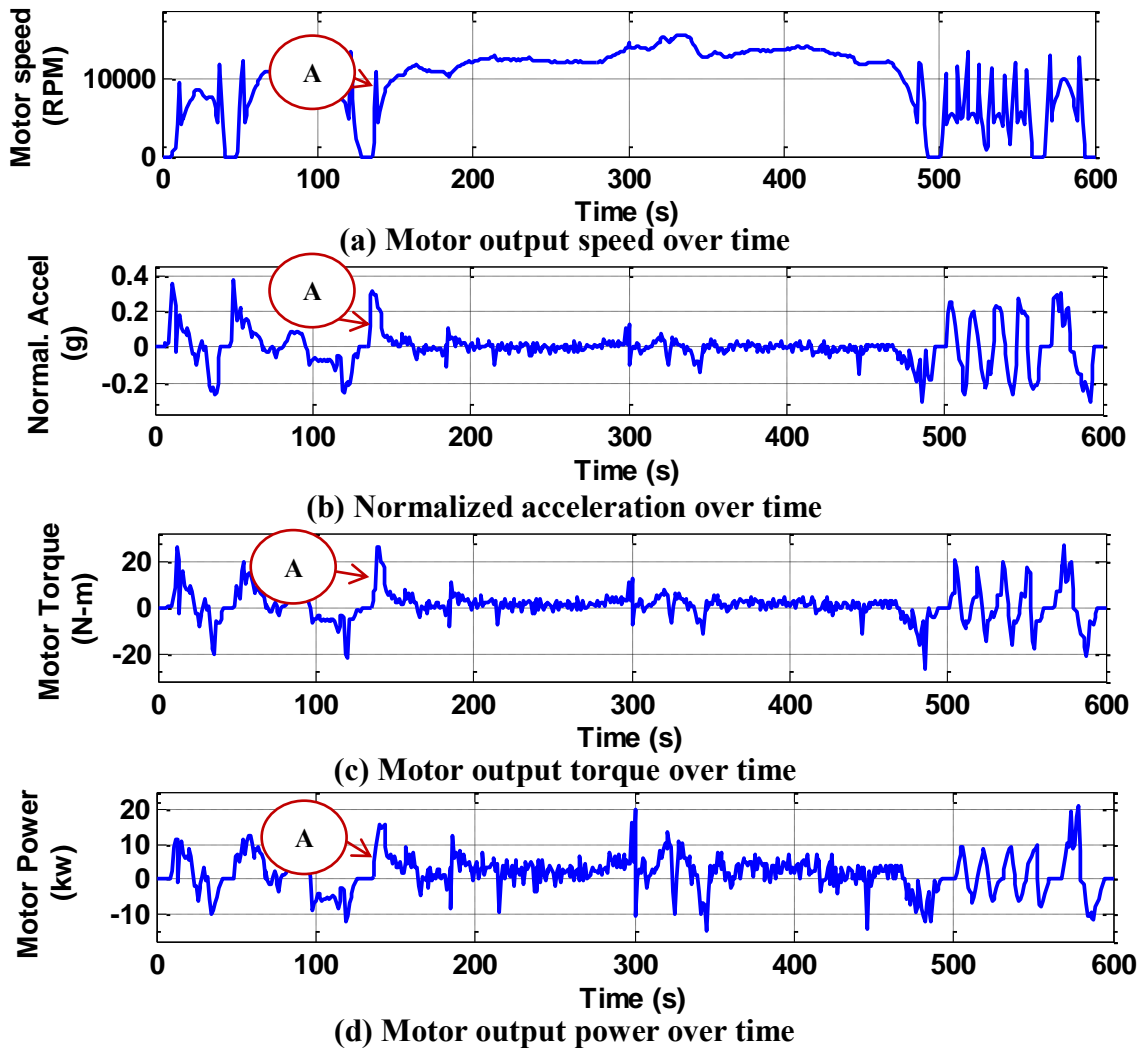


Figure 6-15: Motor output speed, acceleration, torque, and power (US06)

Figure 6-15 shows motor output speed, normalized acceleration, torque, and power derived from Figure 6-6 considering the four-independent drive wheels. These plots are derived by Equation (6.7) and (6.8). As seen at symbol 'A' shown in Figure 6-15 (a), the motor speed is rapidly accelerated from 0 to 6000 RPM (30 mph) through the clutch shift at 20 mph. This behavior indicates characteristics of an aggressive driver. The normalized acceleration is around 0.3 g. At that time, peak motor output torque and power associated with each wheel are around 27 N-m and 16 kw. The 27 N-m is from 1557 N-m divided by gear ratio (14:1) and four wheels. The 16 kw is from 13.6 kw divided by four wheels (see Section 6.1.2.3). Clearly, it is evident that the instantaneous torque and power are strongly dependent on acceleration events shown in Figure 6-15 (b). Also, as seen in Figure 6-15 (a), the sudden spike of motor torque and power shows how the aggressive driver wants to operate.

6.1.6 Motor Power Demand

The motor input power demand can be obtained from the motor output power divided by motor efficiency as follows[Koran and Tesar,2008]:

$$P_{m-in} = P_{m-out} / \eta_m \quad (6.9)$$

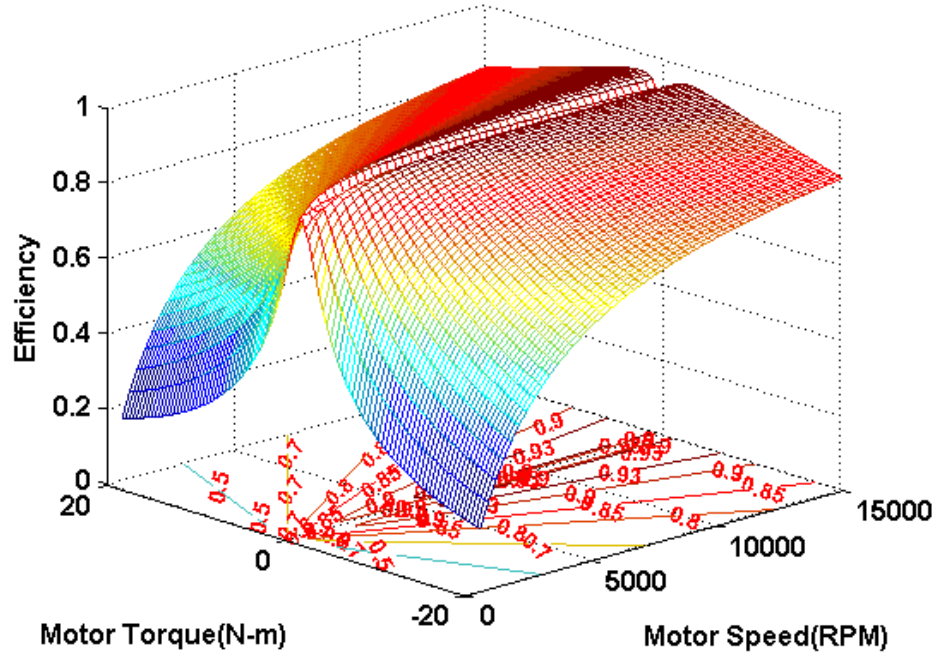


Figure 6-16: Efficiency map of a motor

Figure 6-16 shows the efficiency map of a motor at different operation points. This map describes how efficiency varies with respect to motor torque and motor speed. The motor efficiency, which is described in Chapter 2, can be defined as the ratio given by[Larminie and Lowry,2003; Gantt,2011]:

$$\eta_m = \frac{T\omega}{T\omega + Total_Losses(k_c T^2 + k_i \omega + k_w \omega^3 + C)} \quad (6.10)$$

The motor efficiency is the ratio of the power output to the input power. The copper losses are caused by electrical resistance of the wires of the motor, resulting in heating

(I^2R). This is proportional to the torque ($k_c T^2$). The constant k_c is selected as 16. The iron losses are caused by magnetic effects in the iron of the motor. It is proportional to the frequency with which magnetic field changes related to the speed of the rotor ($k_i \omega$). The constant k_i is selected as 0.005. The windage losses increase with the increased speed of the rotor ($k_w \omega^3$). The constant of k_w is dependent on the size and shape of the rotor. It is selected as 1.0×10^{-11} . Finally, the constant loss coefficient (C) is chosen as 0.2.

Even though this efficiency equation can be used for determining the efficiency of a brushed DC motor, this equation is true for all types of motor to obtain a good approximation, which allows us to predict the motor losses[Larminie and Lowry,2003]. In this research, this efficiency equation assumed to be related to a switched reluctance motor (SRM).

Negative motor torque to the driven wheels is due to the regenerative braking system which utilizes the electric motor, converting kinetic energy to electrical energy for recharging the battery[Gantt, Perkins et al.,2011].

6.1.7 MDW Specification

We discussed motor power demand, motor output torque and power, wheel torque-speed, speed-acceleration frequency distribution, total wheel torque and power, and standard driving cycles in terms of UDDS, HWFET, and US06. Based on this previous analysis, we will discuss what MDW specification is suitable to UDDS, HWFET, and US06. The MDW user choice specifications will be different g levels, 0-60 acceleration time, power rating, MDW size, optimal gear ratio, and clutch shift point.

6.1.7.1 UDDS – How to Maximize efficiency in terms of a MDW?

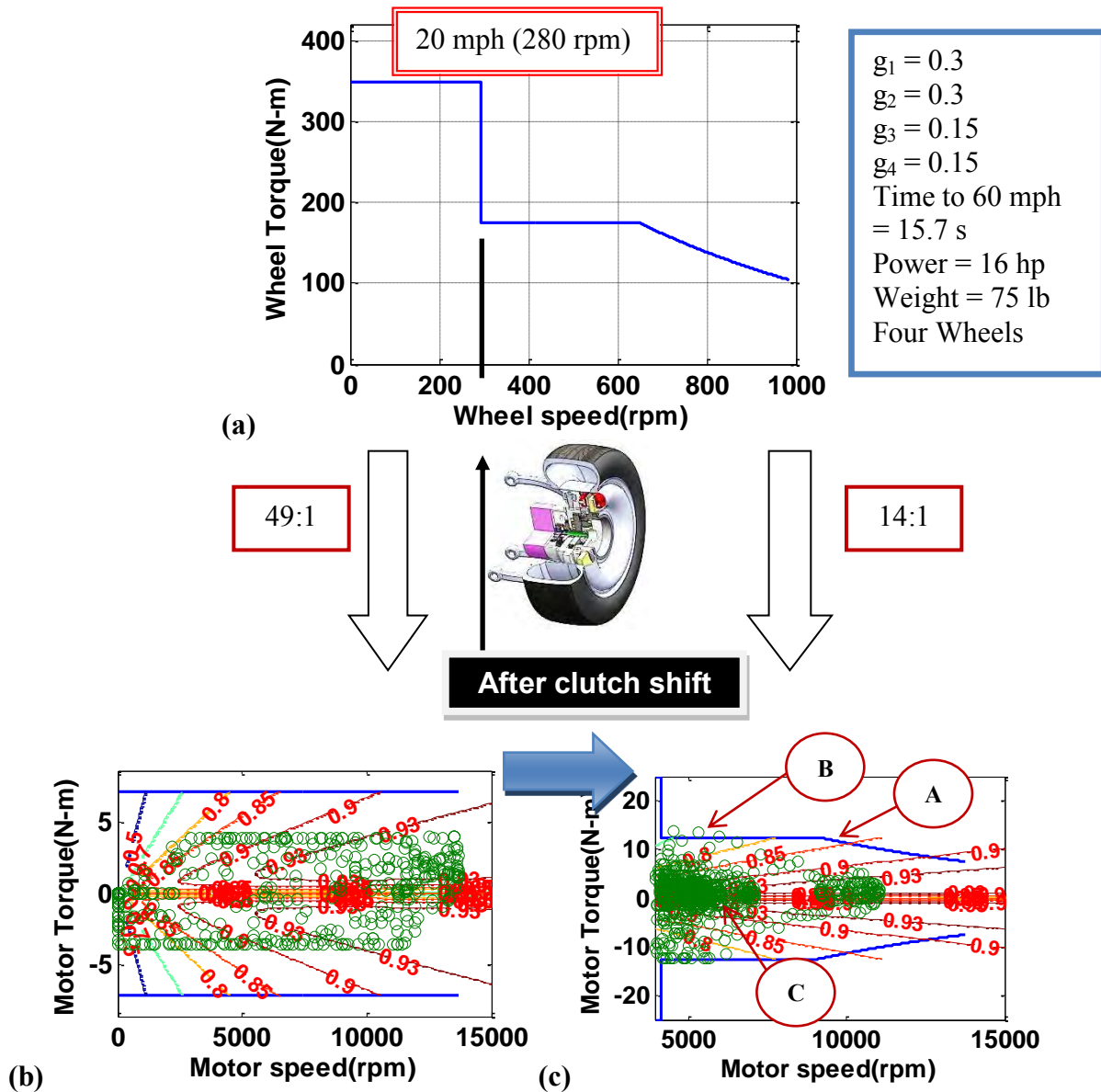


Figure 6-17: Mapping wheel torque into motor torque w.r.t first and second stages (UDDS)

Figure 6-17 (a) shows the wheel torque-speed curve of the MDW in correspondence with the speed ranges of the first and second stages. In this case, the

wheel torque-speed curve is defined as the design envelope for the given constraints, which are different g levels: $g_1 = 0.3$, $g_2 = 0.3$, $g_3 = 0.15$, $g_4 = 0.15$.

Given four-independent wheels, the power rating of each wheel is selected as 16 hp. The clutch shift occurs at 20 mph (280 RPM). Before the clutch shift, given the gear ratio (49:1), the design envelope of 350 N-m in the wheel domain is translated into the design envelope of 7.14 N-m in the motor domain, as shown in Figure 6-17 (b). The Negative motor torque to the driven wheels is due to the regenerative braking system. After the clutch shift, given the gear ratio (14:1), the design envelope of 179 N-m in the wheel domain is translated into the design envelope of 12.5 N-m in the motor domain, as shown in Figure 6-17 (c).

Figure 6-17 (b) and (c) show mapping of the wheel torque into motor torque with respect to the speed range of the first stage and the speed range of the second stage. That is, two maps, which are the motor efficiency map and scatter map superimposed. As shown in Figure 6-17 (b), the scatter map in the motor domain is transformed from Figure 6-10 in the wheel domain. In other words, the wheel torque – wheel speed (0 – 280 RPM) is transformed into motor torque – motor speed (0 – 13726 RPM) through the gear ratio (49:1).

Assuming that the controller efficiency equals 1, the motor efficiency is transformed from Figure 6-16. In the same manner, as shown in Figure 6-17 (b), the wheel torque – wheel speed (280 – 1000 RPM) is transformed into motor torque – motor speed (4118 – 13726 RPM) through the gear ratio (14:1). The corresponding motor efficiency map is transformed from Figure 6-16.

From design point of view, the question arises: does the MDW's design envelope cover the desired operating points? How do we find the optimal gear ratio and clutch shift point?. The symbol 'A' in Figure 6-17 (b) indicates the MDW's design envelop. As seen

at symbol ‘B’, some scattered operating points of the UDDS driving cycle exceed the MDW’s capability. That is, the MDW design somewhat fails to satisfy the customer. For the purpose of analysis, even though this is acceptable through the maximum power rating for a short period of time, the MDW design should be modified to cover all reasonable operating points. We will demonstrate how the selection of the design components of MDWs matches to the driver whose duty cycle is the UDDS.

Due to one-second time intervals, the power equals to the energy consumed. That is, the energy required for a vehicle to move for one second is equal to the power [Larminie and Lowry,2003]. The net energy consumption from the batteries can be expressed as [Ehsani, Gao et al.,2009] :

$$E_{out} = \int_{traction} \left(\frac{P_{m-out}}{\eta_m} \right) dt + \int_{braking} \left(\frac{\alpha P_{m-out}}{\eta_m} \right) dt \quad (6.11)$$

Where P_{m-out} is the motor power output, η_m is the motor efficiency, and α varies from 0 to 1, which is the percentage of the total braking energy that can be regenerated by the electric motor. The α is called the regenerative braking factor as a function of the design and control of the braking system. It should be noted that the second term (braking power) on the right side has a negative sign. The detailed discussion will be explained in Section 6.2.

As can be seen in Figure 6-17 (b) and (c), each operating point has a corresponding efficiency. The overall efficiency can be obtained from the sum of all operating points divided by the number of operating points. The overall efficiency including the speed ranges of the first and second stages is around 88.6%. Also, regarding the clutch operation to the speed range of the second stage, the total number of clutch shift events on a given UDDS is around 40 events, corresponding to sudden peaks at motor speed vs. time plot as shown in Figure 6-13.

- How to Maximize Efficiency in terms of the MDW?

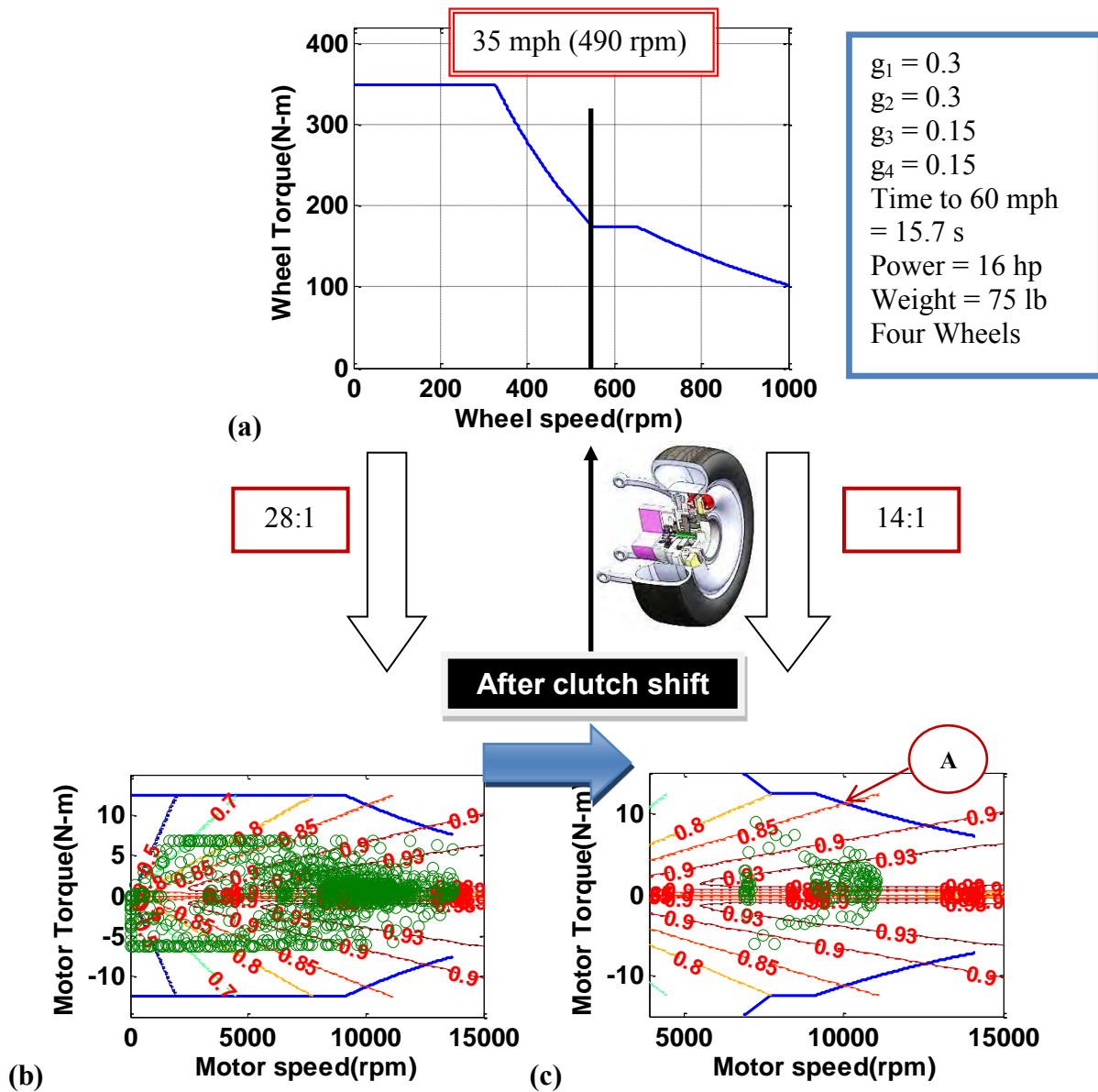


Figure 6-18: Mapping wheel torque into motor torque w.r.t first and second stages (UDDS)

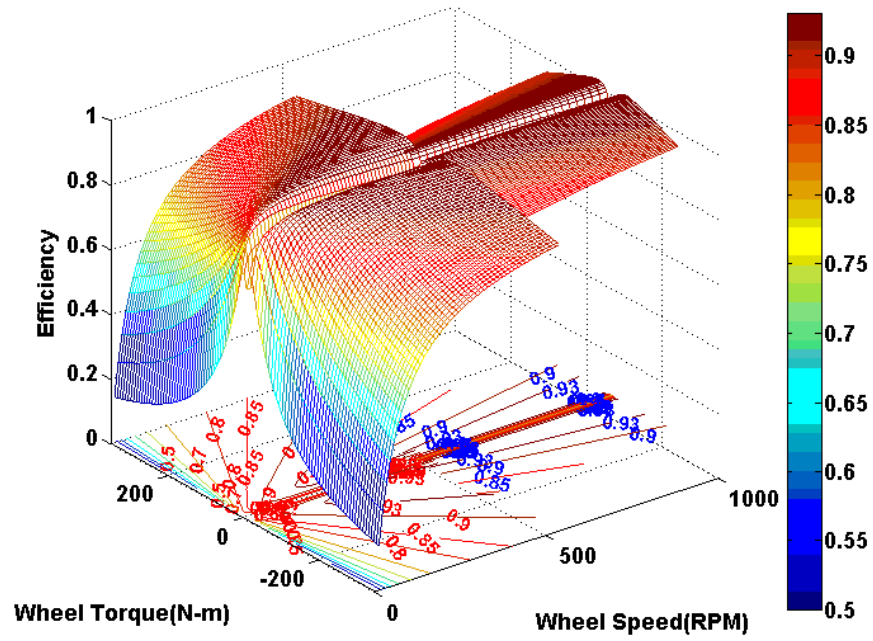
Ren develops and predicts EV energy consumption with a variable and fixed ratio gearbox over a standard driving cycle to obtain useful efficiency estimates [Ren, Crolla et

al.,2009]. In order to maximize the efficiency, the MDW should be optimized for the highest efficiency. As seen at symbol 'C' shown in Figure 6-17 (c), the driving operating points between 20 and 35 mph occur frequently.

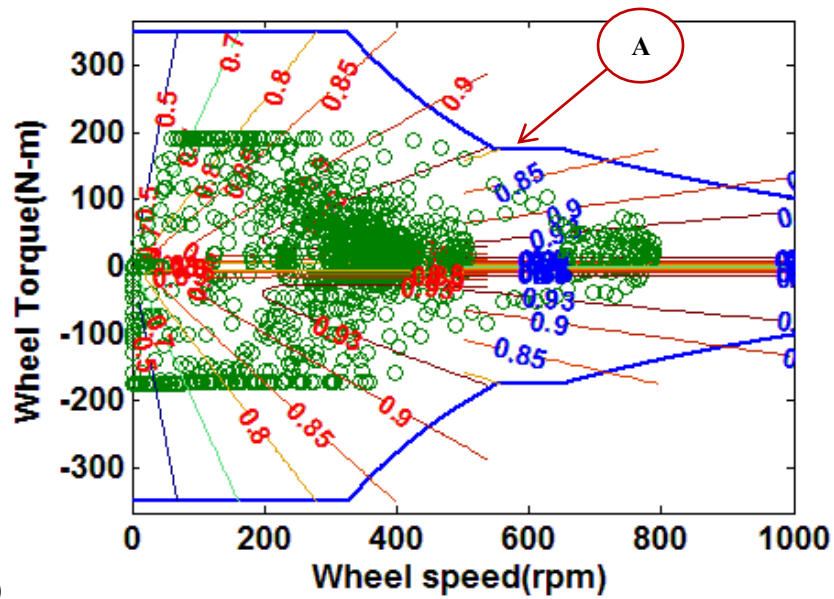
To cover these operating points, the clutch shift point of a MDW should be redesigned. After the MDW redesign, Figure 6-18 shows the configuration of the MDW optimized for maximizing efficiency by choosing the first stage gear ratio (28:1 => front end (2:1) and back end (14:1)) and second stage gear ratio (14:1). In addition, the clutch shift point of the MDW is chosen as 35 mph (i.e., motor speed = 13720 RPM). These MDW parameters will be chosen by the customer who prefers efficiency as his priority. As seen at symbol 'A' shown in Figure 6-18 (c), the design envelope now covers all operating points.

Consequently, the overall efficiency including the speed ranges of the first and second stage is around 88.7% which is a slight higher than previous efficiency (88.6%). Furthermore, regarding the clutch operation to the speed range of the second stage, the total number of clutch shift events on a given UDDS is around 7 events, which is 5 times less than previous MDW design (40 events). This leads to decreasing the energy consumption and improving the MDW's durability because the clutch actuator is used less. Despite a minor difference of efficiency, it is necessary to pursue this reduced need to shift. In addition, the paper [Qian, Xu et al.,2010] confirms that an energy management strategy based on optimal driving torque distribution improves the efficiency by 27.4%, given four-independent wheels. The work by Qian and Xu show that additional efficiency benefits occur by managing in real time the actual traction forces on each independently controlled electric wheel drive. This result adds to the importance of the present work, especially for those cases where traction varies a great deal or is uncertain.

In this case, two torque-speed regions based on the mechanical clutch operation were considered, while assuming that the efficiency of controller equals one. On the other hand, with a reconfigurable power controller, the MDW would have higher efficiency over its entire torque-speed profile by flattening out the efficiency sweet spot. In other words, by choosing appropriate controller components, the overall efficiency can be further improved to meet the customer requirements for different purposes of the system in real time. The electric motor would be driven under two controller configurations, resulting in two additional speed domains. Hence, four distinct operational regimes are created (with a mechanical clutch shift) [Tesar and Ashok, May, 2011].



(a)



(b)

Figure 6-19: Overall efficiency map w.r.t wheel torque and wheel speed (UDDS)

In order to understand visually in the wheel domain instead of the motor domain, it is essential to visualize the efficiency map with respect to wheel torque and wheel speed. Figure 6-19 (a) shows the overall efficiency map of the MDW as a function of wheel torque and wheel speed. Also, Figure 6-19 (b) shows overall efficiency map of the MDW in a 2D contour plot.

The symbol 'A' shown in Figure 6-19 (b) indicates the design envelope in the wheel domain. The contour lines represent efficiency values at different wheel torques and speeds in terms of the speed ranges of the first and second stage. The scatter points are the operating points associated with the urban duty cycle (UDDS).

Clearly, it can be seen that the MDW design capacity covers all operating points. In addition, it is more efficient because it is possible to keep the MDW within the most efficient RPM range. Therefore, we can now suggest the MDW specifications which are appropriate to the driver (UDDS). Given four-independent wheels, the power rating of the MDW will be 16 hp. The different g levels become $g_1 = 0.3$, $g_2 = 0.3$, $g_3 = 0.15$, and $g_4 = 0.15$. The 0-60 mph acceleration time becomes 15.2s. The weight of the MDW is estimated at 75 lb[Tesar and Ashok,May, 2011]. The optimal clutch shift point will be 35 mph.

In this case, we assume that the design envelope ('A') is related to the maximum torque, and the second quadrant (generator mode) is mirrored by the first quadrant (motor mode)[Guzzella and Sciarretta,2005]. Furthermore, the efficiency of controller and gear train is assumed to be one. For the purpose of analysis, the design envelope should cover all scattered operating points. In practice, for a short period of time, electric motors can be operated at higher than their designed power rating. According to [Vagati, Pellegrino et al.,2010], overload torque and power are acceptable for a couple of minutes and are limited by the inverter and battery maximum ratings. That is, the maximum torque is

determined by the inverter current, and the maximum power is limited by the battery unless we also use a super capacitor.

6.1.7.2 Highway Fuel Economy Test (HWFET)

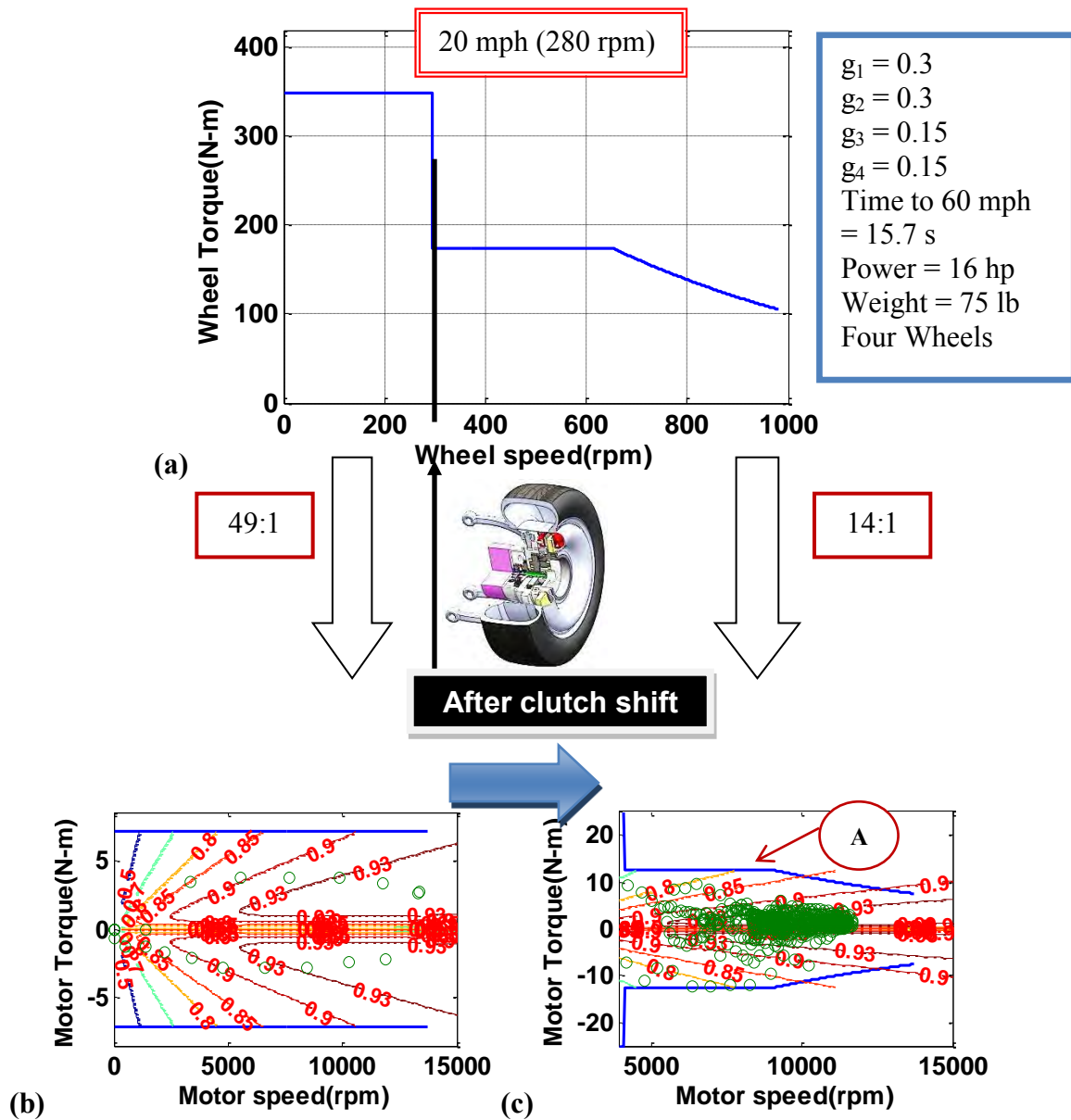


Figure 6-20: Mapping wheel torque into motor torque w.r.t first and second stages (HWFET)

Figure 6-20 (a) shows the wheel torque-speed curve of the MDW in correspondence with the speed ranges of the first and second stages. In the same manner, the design envelope is generated by different g levels: $g_1 = 0.3$, $g_2 = 0.3$, $g_3 = 0.15$, $g_4 = 0.15$. Given four-independent wheels, the power rating of each wheel is selected as 16 hp. The clutch shift occurs at 20 mph (280 RPM). Before the clutch shift, given the gear ratio (49:1), the design envelope of 350 N-m in the wheel domain is translated into the design envelope of 7.14 N-m in the motor domain, as shown in Figure 6-20 (b). After the clutch shift, given the gear ratio (14:1), the design envelope of 175 N-m in the wheel domain is translated into the design envelope of 12.5 N-m in the motor domain, as shown in Figure 6-20 (c).

Figure 6-20 (b) and (c) show mapping of the wheel torque into motor torque with respect to the speed range of the first stage and the speed range of the second stage. That is, two maps, which are the motor efficiency map and scatter map, are superimposed. As shown in Figure 6-20 (b), the scatter map in the motor domain is transformed from Figure 6-11 in the wheel domain. In other words, the wheel torque – wheel speed (0 – 280 RPM) is transformed into motor torque – motor speed (0 – 13726 RPM) through the gear ratio (49:1). Assuming that the controller efficiency equals 1, the motor efficiency is transformed from Figure 6-16. In the same manner, as shown in Figure 6-20 (c), the wheel torque – wheel speed (280 – 1000 RPM) is transformed into motor torque – motor speed (4118 – 13726 RPM) through the gear ratio (14:1). The corresponding motor efficiency map is transformed from Figure 6-16.

Figure 6-21 (a) shows the overall efficiency map of the MDW as a function of wheel torque and wheel speed. Also, Figure 6-21 (b) shows overall efficiency map of the MDW based on 2D. The symbol ‘A’ shown in Figure 6-21 (b) indicates the design envelope in the wheel domain. The contour lines represent an efficiency value at different

wheel torque and speed in terms of the speed ranges of the first and second stages. The scatter points are the operating points associated with the driving cycle (HWFET). Clearly, it is evident that the design envelope covers all operating points. Therefore, the MDW of 16 hp is acceptable to the driving cycle (HWFET).

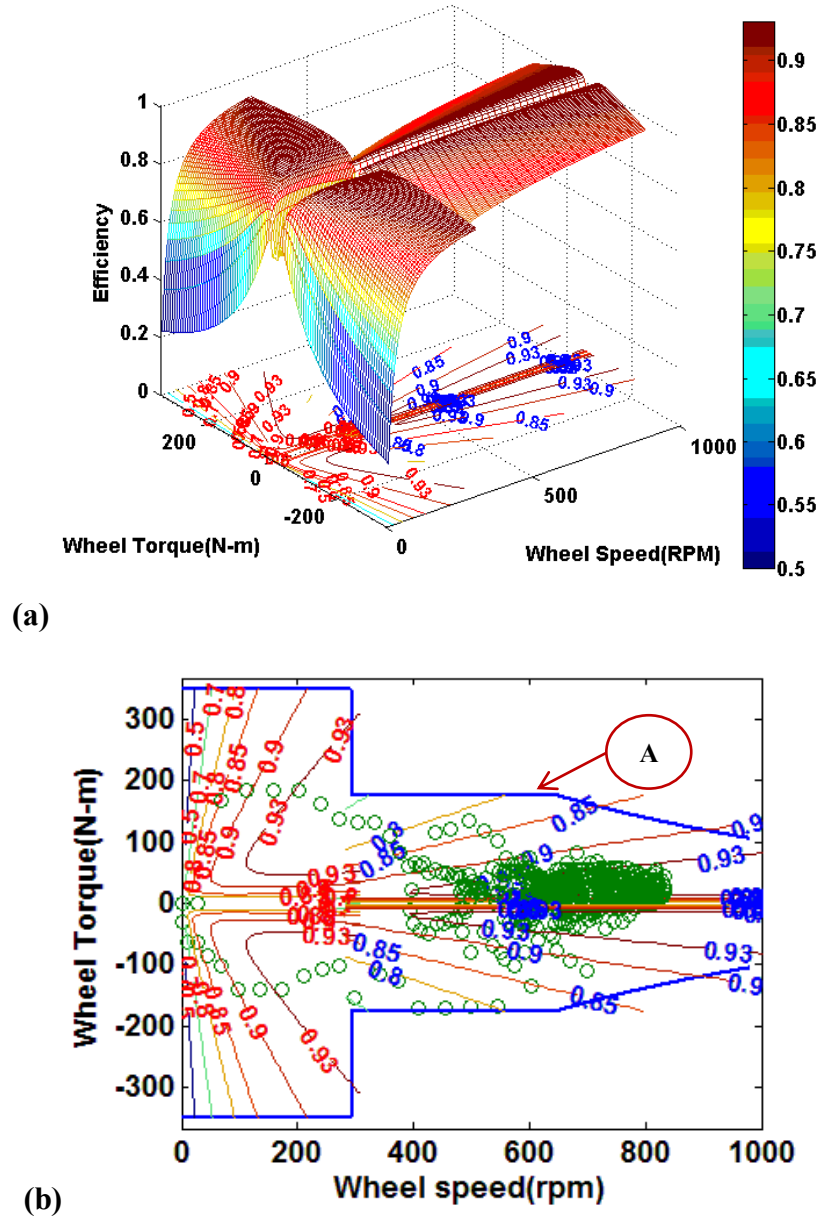


Figure 6-21: Overall efficiency map w.r.t wheel torque and wheel speed (HWFET)

6.1.7.3 US06 - How to Maximize Drivability in terms of a MDW?

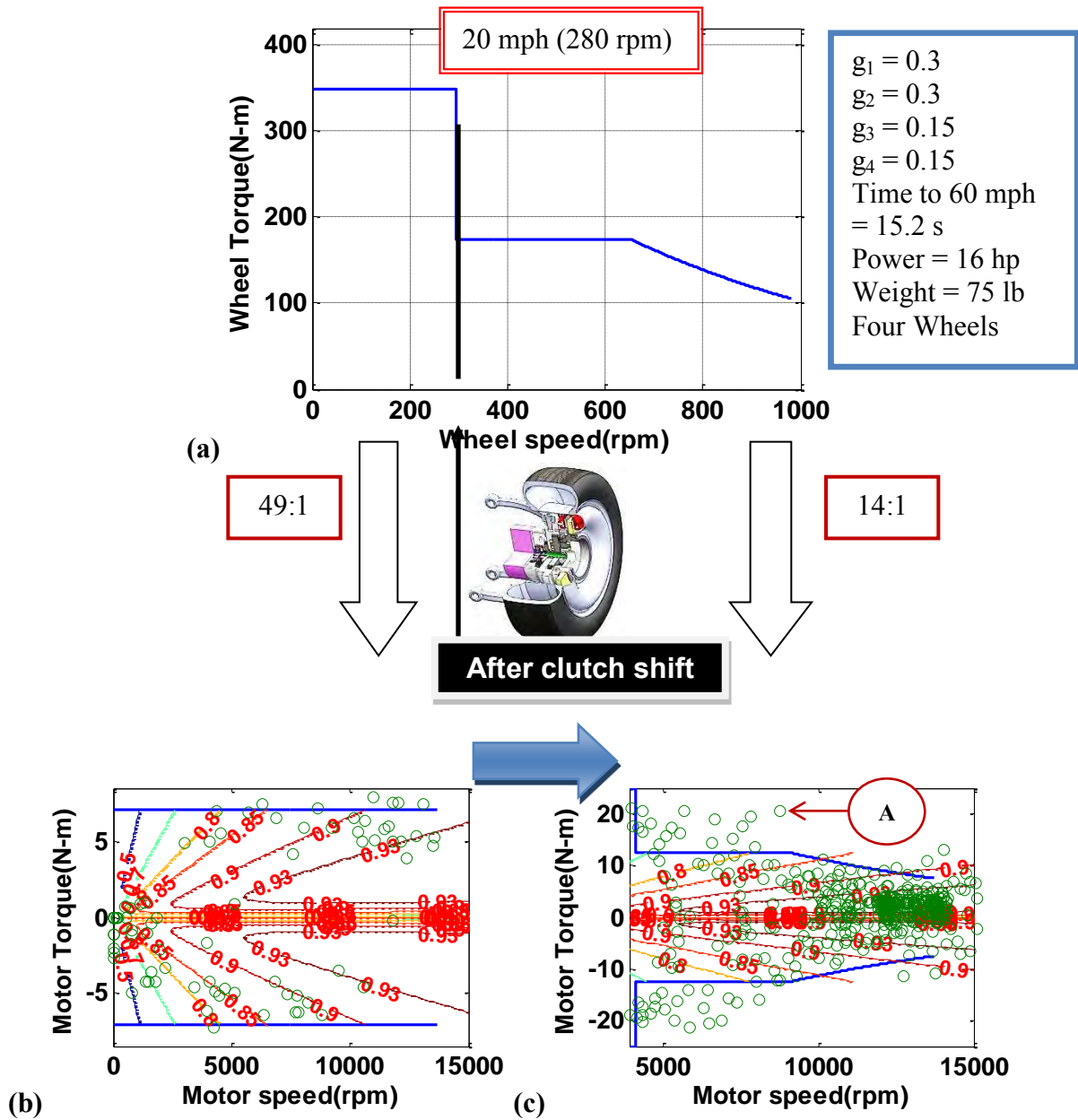


Figure 6-22: Mapping wheel torque into motor torque w.r.t first and second stages (US06)

With the same scenario based on Sec. 6.1.7.2, the simulation results are shown in Figure 6-22 (a) regarding the wheel torque-speed curve of the MDW in correspondence with the speed range of the first and second stages. In the same manner, the design envelope is generated by different g levels: $g_1 = 0.3$, $g_2 = 0.3$, $g_3 = 0.15$, $g_4 = 0.15$. As seen at symbol 'A' in Figure 6-22 (c), the scattered operating points exceed the MDW design capacity. Since the US06 represents the aggressive driver, the MDW design should focus on drivability such as acceleration, resulting in a higher power rating. In the next section, we show how to maximize drivability to meet the customer (US06) needs.

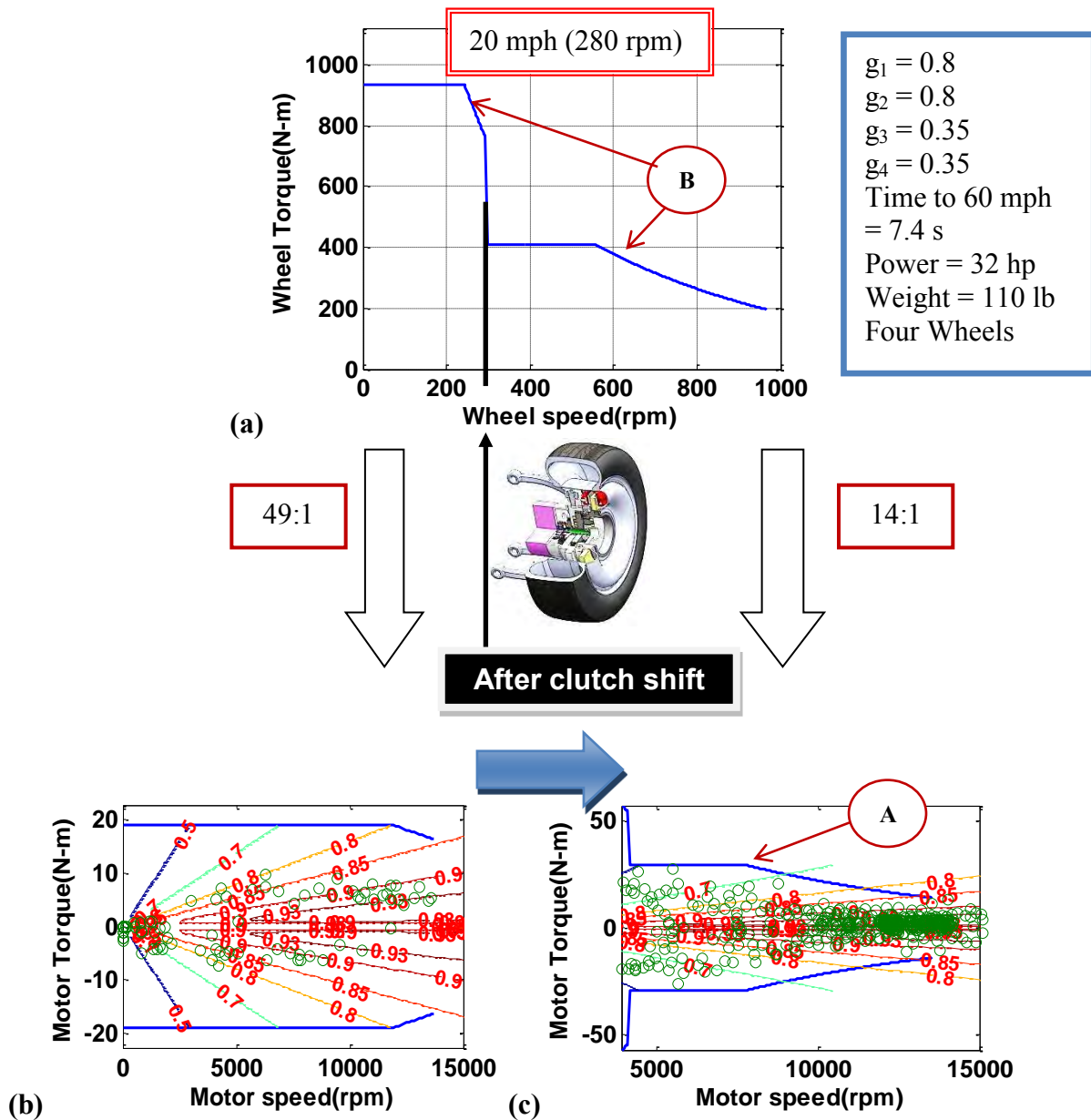


Figure 6-23: Mapping wheel torque into motor torque w.r.t first and second stages
 (US06)

- **How to Maximize Drivability in terms of the MDW?**

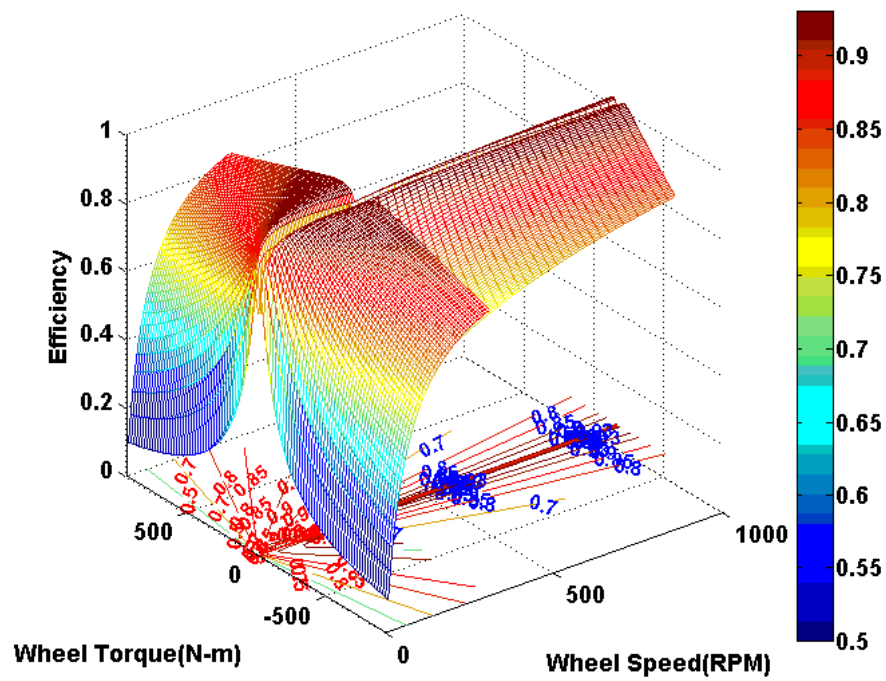
In order to maximize drivability to meet the aggressive customer needs, the power rating of the MDW should be increased. Given the power rating of 30 hp with different g levels, simulation results are shown in Figure 6-23 to cover all operating points.

Figure 6-23 (a) shows the wheel torque-speed curve of the MDW in correspondence with the speed ranges of the first and second stages. The clutch shift occurs at 20 mph (280 RPM). Before the clutch shift, given the gear ratio (49:1), the design envelope of 933 N-m in the wheel domain is translated into the design envelope of 19 N-m in the motor domain, as shown in Figure 6-23 (b).

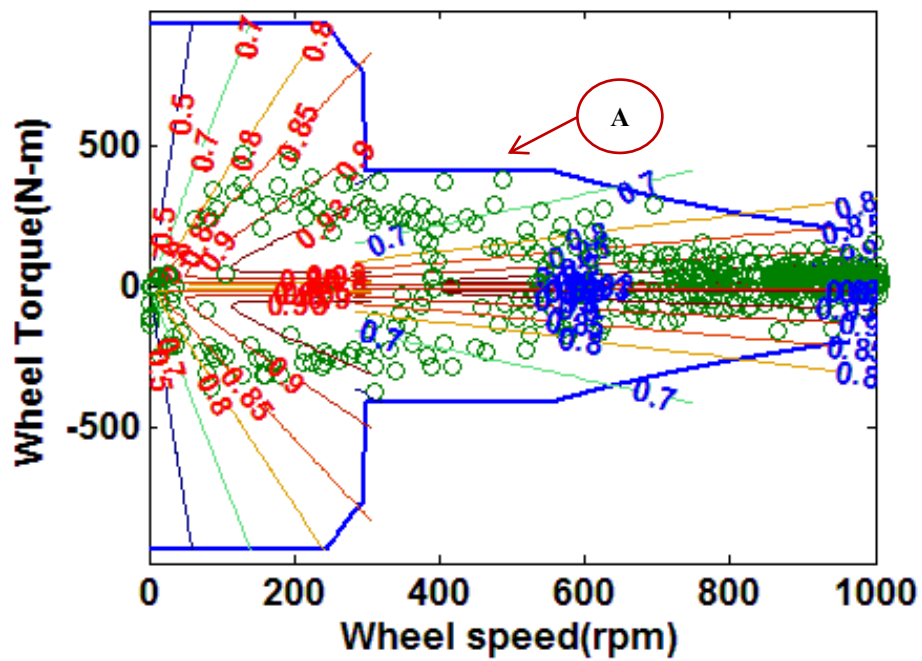
After the clutch shift, given the gear ratio (14:1), the design envelope of 408 N-m in the wheel domain is translated into the design envelope of 29.2 N-m in the motor domain, as shown in Figure 6-23 (c).

The curves seen at symbol 'B' represent the constant power region. Figure 6-23 (b) and (c) show mapping of the wheel torque into motor torque with respect to the speed range of the first stage and the speed range of the second stage. That is, two maps, which are the motor efficiency map and scatter map, are superimposed.

In brief, compared to Figure 6-22, the power rating required increases from 16 hp to 32 hp. The different g levels become $g_1 = 0.8$, $g_2 = 0.8$, $g_3 = 0.35$, and $g_4 = 0.35$. The 0-60 mph acceleration time becomes 7 s. **The overall efficiency is around 86.6%.** It is apparent that US06 duty cycle has a lower efficiency than the UDDS duty cycle.



(a)



(b)

Figure 6-24: Overall efficiency map w.r.t wheel torque and wheel speed (US06)

Figure 6-24 (a) shows overall efficiency map of the MDW as a function of wheel torque and wheel speed. Also, Figure 6-24 (b) shows overall efficiency map of the MDW in a 2D contour plot. The symbol 'A' shown in Figure 6-24 (b) indicates the design envelope in the wheel domain.

The contour lines represent an efficiency value at different wheel torques and speeds in terms of the speed range of the first and second stages. The scatter points are the operating points associated with the duty cycle (US06).

Clearly, it can be seen that the MDW design capacity covers all operating points. Therefore, we can suggest the MDW specifications which are appropriate to the driver (US06). Given four-independent wheels, the power rating of the MDW will be 32 hp. The different g levels become $g_1 = 0.8$, $g_2 = 0.8$, $g_3 = 0.35$, and $g_4 = 0.35$. The 0-60 mph acceleration time becomes 7.4 s. The weight of each MDW becomes 110 lb.

6.2 ENERGY CONSUMPTION ANALYSIS

6.2.1 Estimating Input Power Demands from Output Power

As mentioned in Section 6.1.6, the motor input power demand can be estimated from the motor output power divided by motor efficiency.

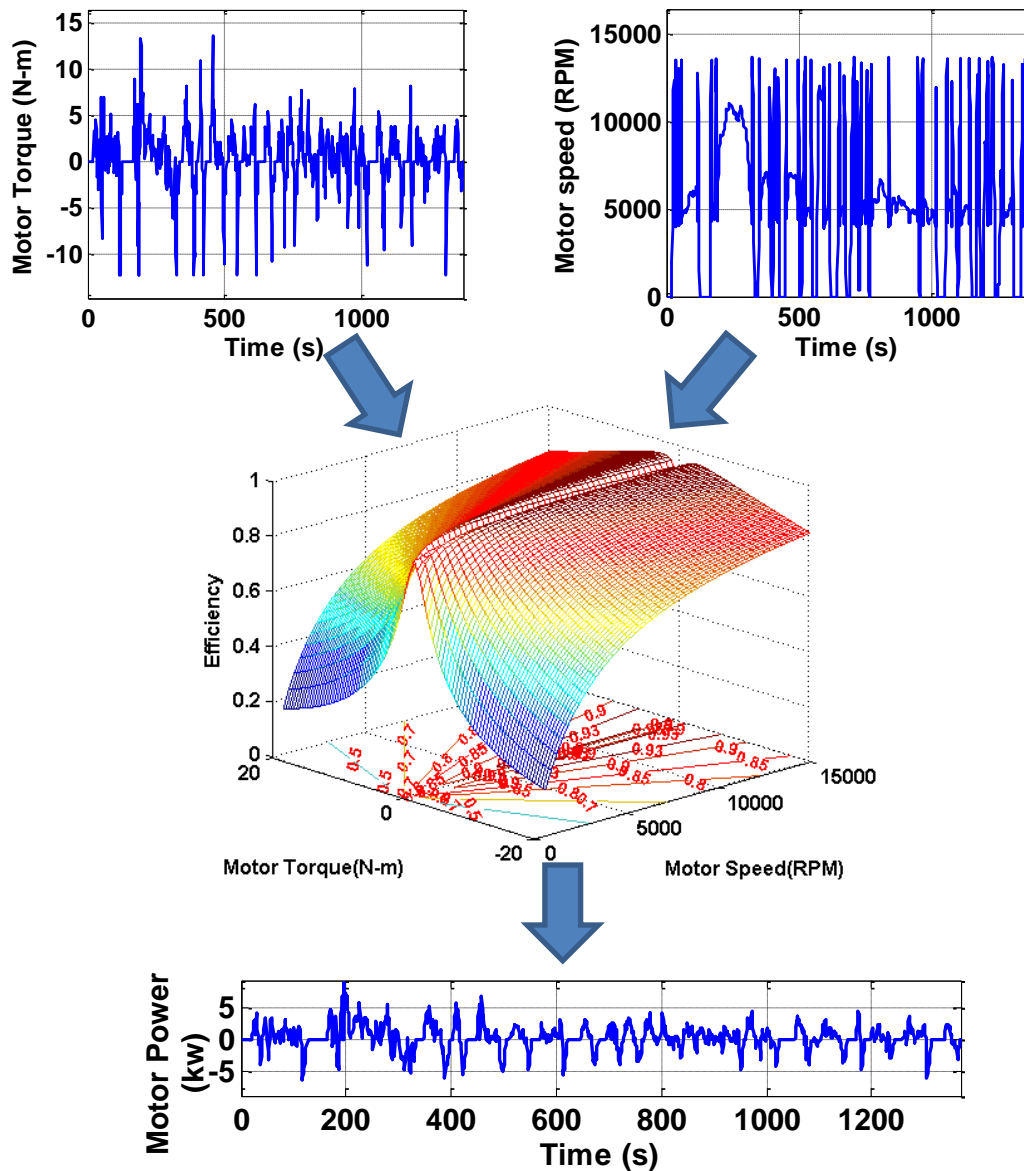


Figure 6-25: Mapping Output Requirement to Input Demand (UDDS)

The motor output power is the product of the motor torque and the motor speed.

RRG research[Koran and Tesar,2008] presented the mapping output requirements to prospective input requirements. Figure 6-25 shows the process of how to obtain motor input power demand from motor output torque and speed through the overall efficiency of a MDW. The motor output torque and speed are from Section 6.15.

The motor input power demand can be obtained from the motor output power divided by motor efficiency as follows:

$$P_{m-in} = \frac{P_{m-out}}{\eta_m} \quad (6.12)$$

This indicates that the electrical power is larger than the mechanical output power. Regarding regenerative power which is negative power, the efficiency works in the opposite sense. The electrical power required is decreased, so that the equation becomes [Larminie and Lowry,2003]:

$$P_{m-in} = P_{m-out} \times \eta_m \quad (6.13)$$

6.2.2 Traction and Braking Energy Dissipation at Motor Output Power

As a vehicle operates on a road, there are two kinds of energy such as traction energy and braking energy. The integration of the positive and negative power over the driving cycle provides the traction energy and braking energy, respectively[Ehsani, Gao et al.,2009].

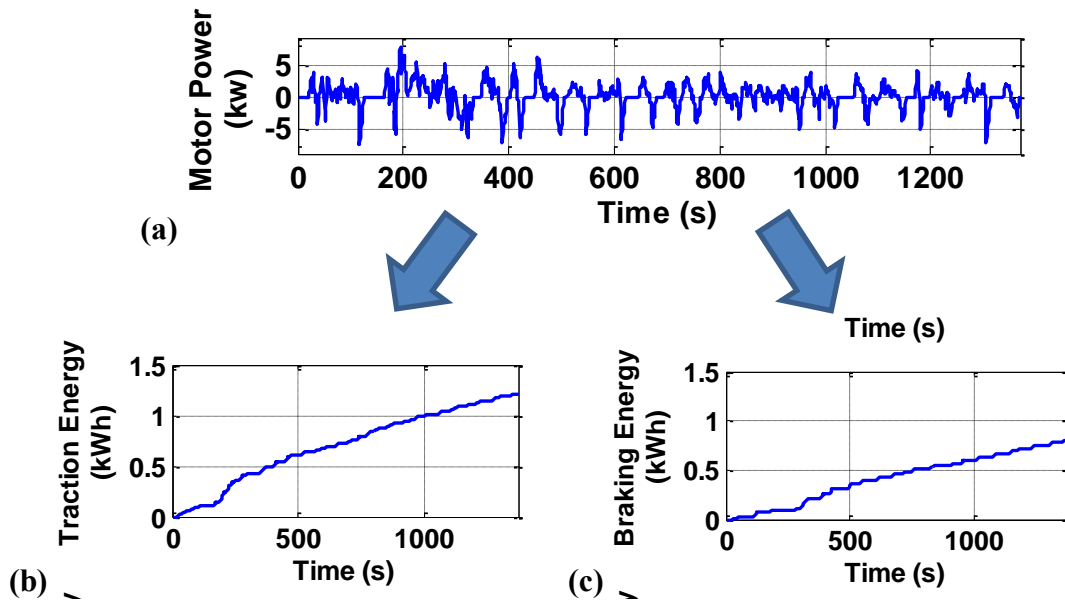


Figure 6-26: Traction and braking energy extracted from motor output power (UDDS)

Figure 6-26 (a) shows the motor output power versus time. From this plot, the traction and braking energy can be obtained as shown in Figure 6-26 (b) and (c), respectively. The maximum traction and braking energy are 1.22 kWh and 0.81 kWh, respectively.

6.2.3 Traction and Braking Energy Dissipation at Motor Input Power

Figure 6-27 (a) shows the motor input power over time. Also, the traction and braking energy plots are simulated as shown in Figure 6-27 (b) and (c).

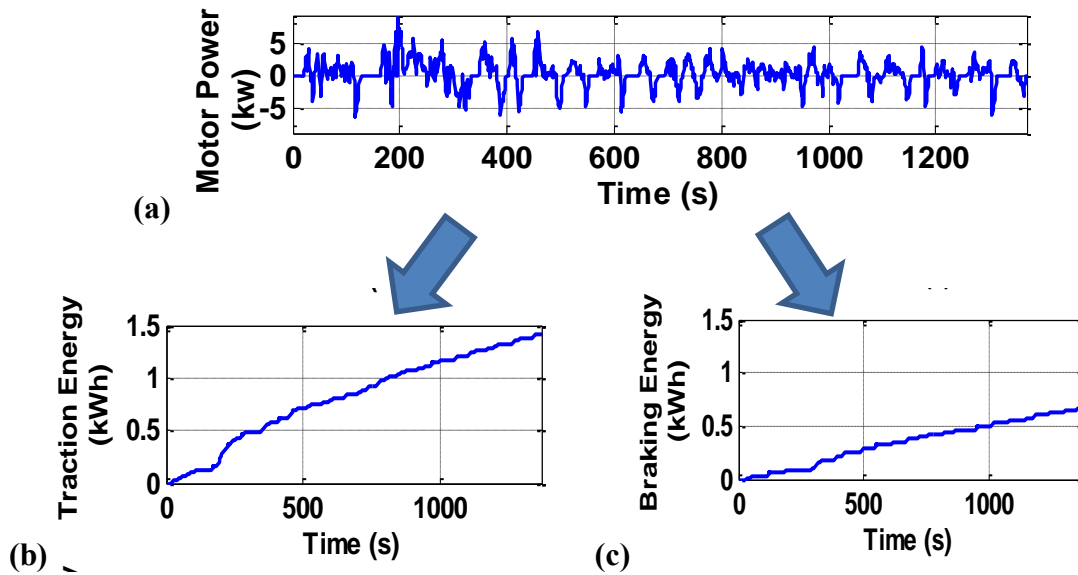


Figure 6-27: Traction and braking energy extracted from motor input power (UDDS)

The maximum traction and braking energy are 1.42 kWh and 0.67 kWh, respectively. From the duty cycle information, we can estimate how much heat is generated. The difference between traction at the motor output power and the motor input power represents heat which the drive component must dissipate [Koran and Tesar,2008].

6.2.4 Efficiency Based on Input Energy and Heat Energy

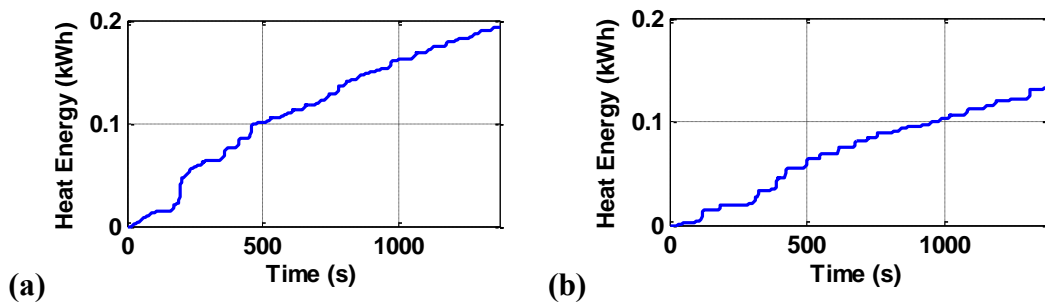


Figure 6-28: Heat energy lost due to inefficiencies (UDDS)

Figure 6-28 (a) and (b) show the heat energy lost due to inefficiencies during traction and braking. The heat energy during traction is 0.19 kWh, and the heat energy during braking is 0.13 kWh. The combined heat energy lost becomes 0.32 kWh. Using the input energy and losses, the efficiency becomes:

$$\eta = \frac{\text{Input Energy} - \text{losses}}{\text{Input Energy}} = \frac{(1.42 + 0.67) - 0.32}{(1.42 + 0.67)} = 0.85 \quad (6.14)$$

The net energy consumption from the batteries can be expressed as[Ehsani, Gao et al.,2009]:

$$E_{out} = \int_{traction} \left(\frac{P_{m-out}}{\eta_m} \right) dt + \int_{braking} \left(\frac{\alpha P_{m-out}}{\eta_m} \right) dt \quad (6.15)$$

Where P_{m-out} is the motor power output, η_m is the motor efficiency, and α varies from 0 to 1, which is the percentage of the total braking energy that can be regenerated by the electric motor. The α is called the regenerative braking factor as a function of the design and control of the braking system. It should be noted that the second term (braking power) on the right side has a negative sign. Assuming the regenerative braking factor equals 0.5, the net energy consumption from the batteries becomes 1.0 kWh (i.e., 1.36-0.5*0.71).

Parameters	Values (kWh)
Input Energy	2.07
Heat Energy	0.236
Efficiency	88.6%
Energy Consumption (kWh/mph)	0.248
Net Energy Consumption	1.0

Table 6-2: Simulation results

6.3 COMPARISON OF A MDW AND PROTEAN'S IN-WHEEL MOTOR

6.3.1 Comparison of Two Speed Regimes and One Speed Regime

6.3.1.1 Urban Duty Cycle (UDDS)

In this section, the comparison of a MDW and Protean's in-wheel motor is made in terms of efficiency based on the UDDS duty cycle.

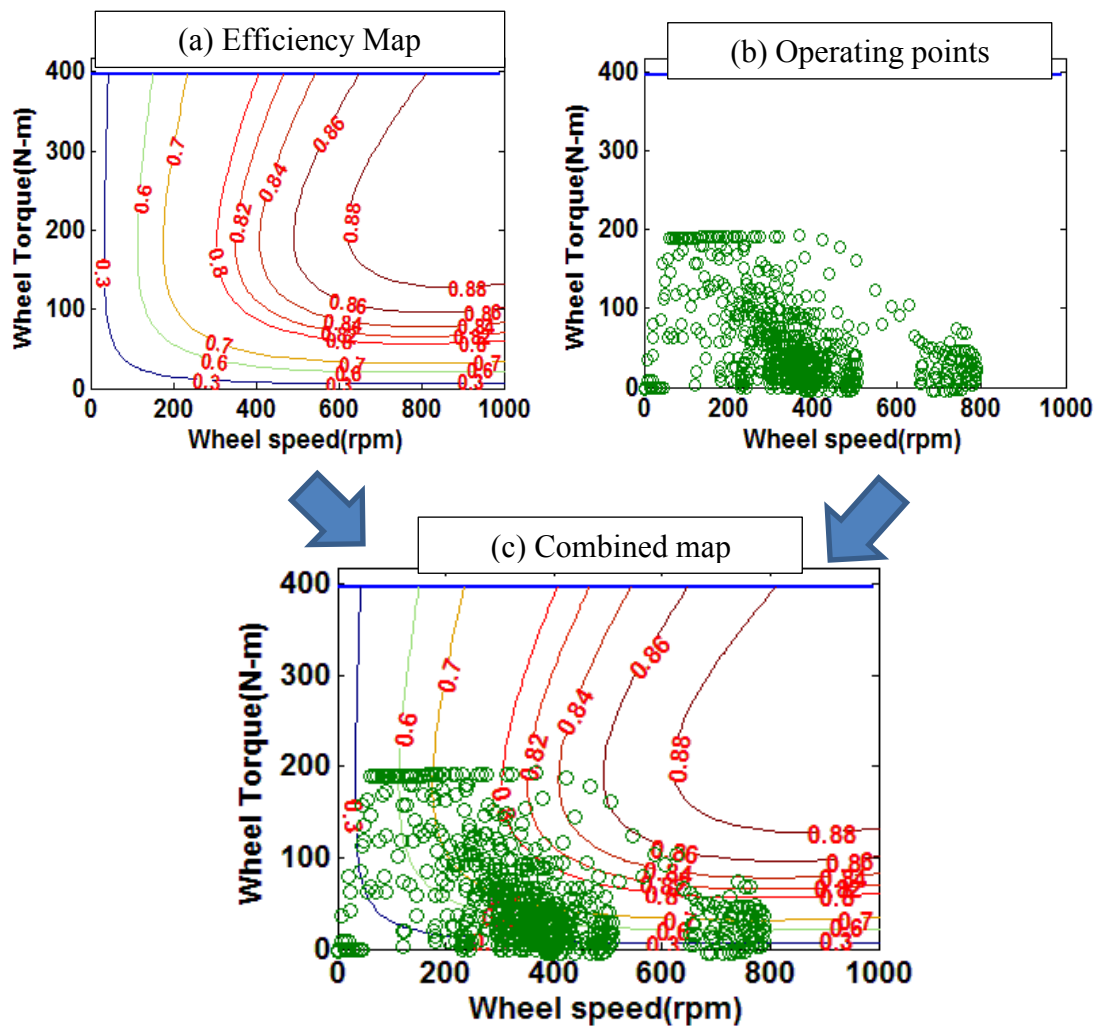


Figure 6-29: Combined efficiency map of Protean's in- wheel motor during urban driving

Figure 6-29 (a) shows the efficiency map of Protean's in-wheel motor [Watts, Vallance et al.,2010]. As mentioned in Section 6.1.6, this efficiency map is generated based on Equation (6.10). The motor power rating is 110 hp. The copper loss constant k_c and iron loss constant k_i are selected as 0.022 and 0.001, respectively. The windage loss constant k_w and is selected as 8.0×10^{-7} . Finally, the constant loss coefficient (C) is chosen as 700.

Figure 6-29 (b) shows the operating point associated with the UDDS duty cycle. Two maps are combined as shown in Figure 6-29 (c). For the purpose of comparison, we only consider the motor efficiency. The overall efficiency for the UDDS duty cycle is around 73.8%.

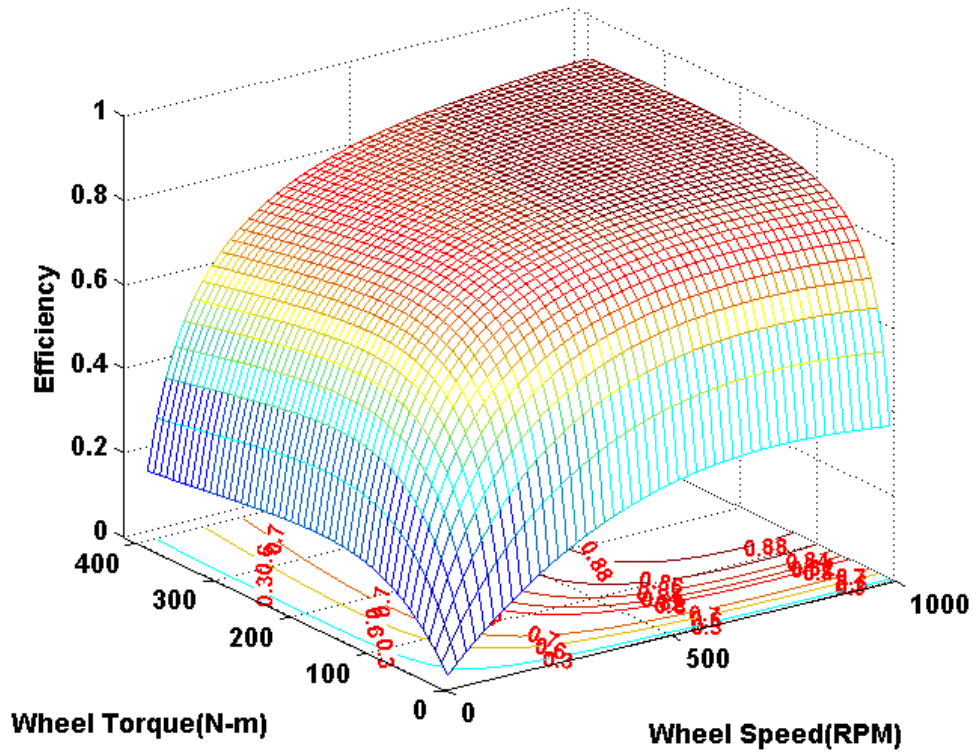


Figure 6-30: Efficiency map of Protean's in-wheel motor

The efficiency map of Protean's in-wheel motor with respect to wheel torque and wheel speed is shown in Figure 6-30. It is apparent that efficiency is low at low speeds.

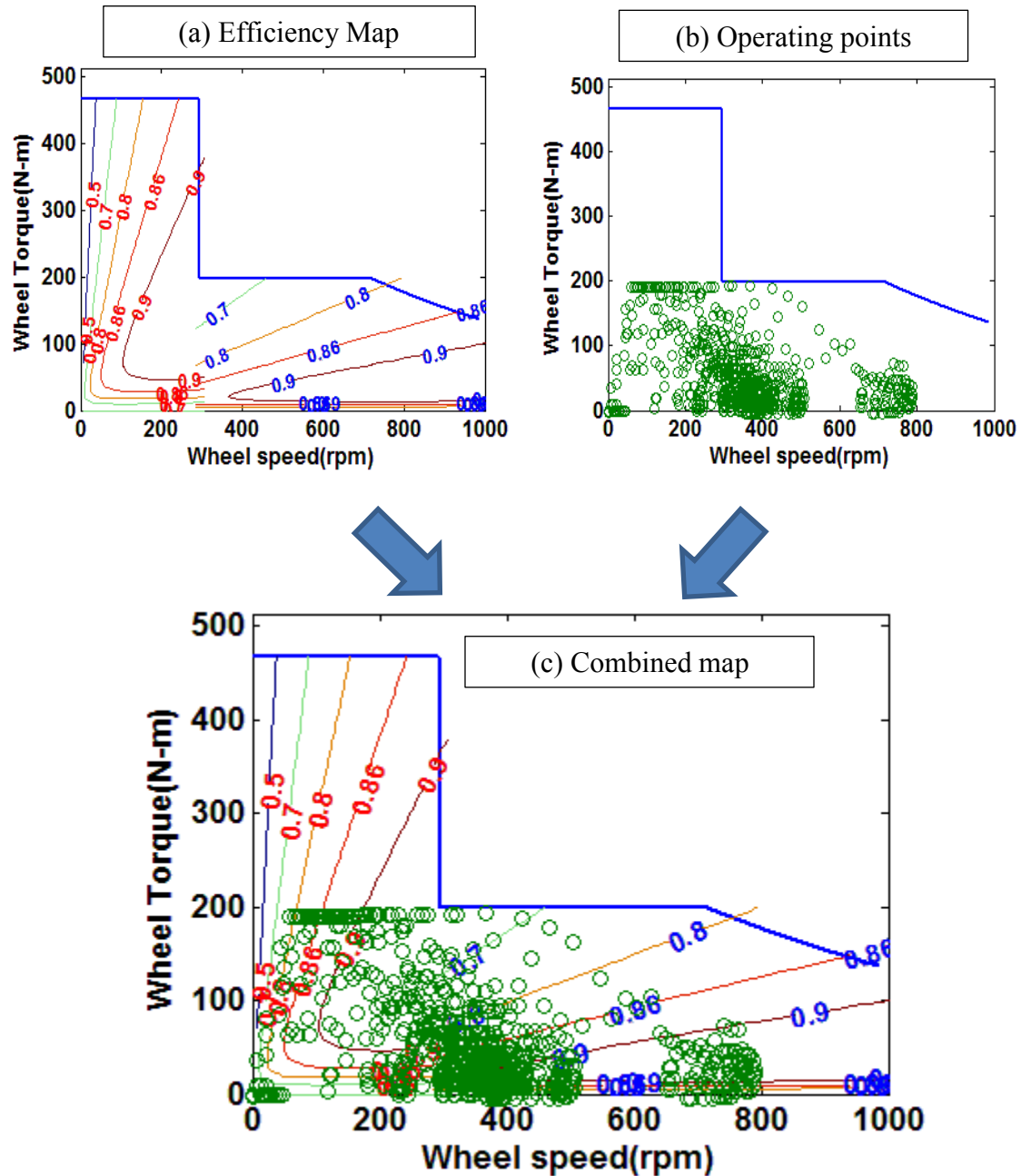


Figure 6-31: Combined Efficiency map of a MDW

Figure 6-31 (a) shows the assumed efficiency map of an MDW. As mentioned in Section 6.1.6, this efficiency map is generated based on Equation (6.10). The motor power rating is 20 hp. The copper loss constant k_c and iron loss constant k_i are selected as 20 and 0.008, respectively. The windage loss constant k_w and is selected as 1.0×10^{-11} . Finally, the constant loss coefficient (C) is chosen as 2. The wheel torque-speed curve is defined as the design envelope for the given constraints, which are different g levels: $g_1 = 0.4$, $g_2 = 0.4$, $g_3 = 0.17$, $g_4 = 0.17$.

Figure 6-31 (b) shows the operating point associated with the UDDS duty cycle. Two maps are combined as shown in Figure 6-31 (c). The overall efficiency including the speed range of the first and second stages is around 85.8%, which is around 12% higher than efficiency (73.8%) of Protean's in-wheel motor. Clearly, it can be seen that efficiency of two speed regimes improves, compared to the efficiency of one speed regime.

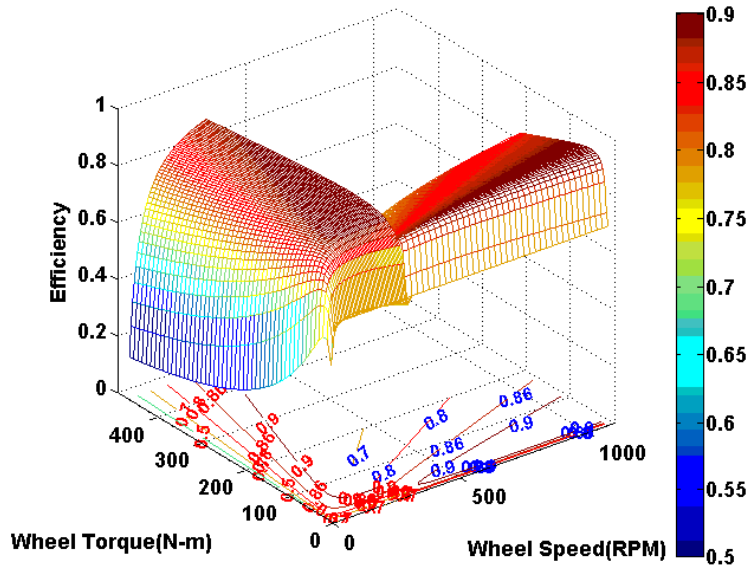


Figure 6-32: Efficiency map of a MDW

The efficiency map of an MDW with respect to wheel torque and wheel speed is shown in Figure 6-32. This efficiency map of an MDW is identical to Figure 6-31 (c). Compared to the Figure 6-30, Figure 6-32 has a somewhat higher and flatten sweet spot area. Certainly, urban driving requires the capability to operate efficiently at low speed and low torque. Therefore, the MDW which has high efficiency in low speed and low torque is great a choice for the customers who drive in the city.

6.3.1.2 Highway Duty Cycle (HWFET)

In this section, the comparison of a MDW and an in-wheel motor is made in terms of efficiency based on the HWFET duty cycle.

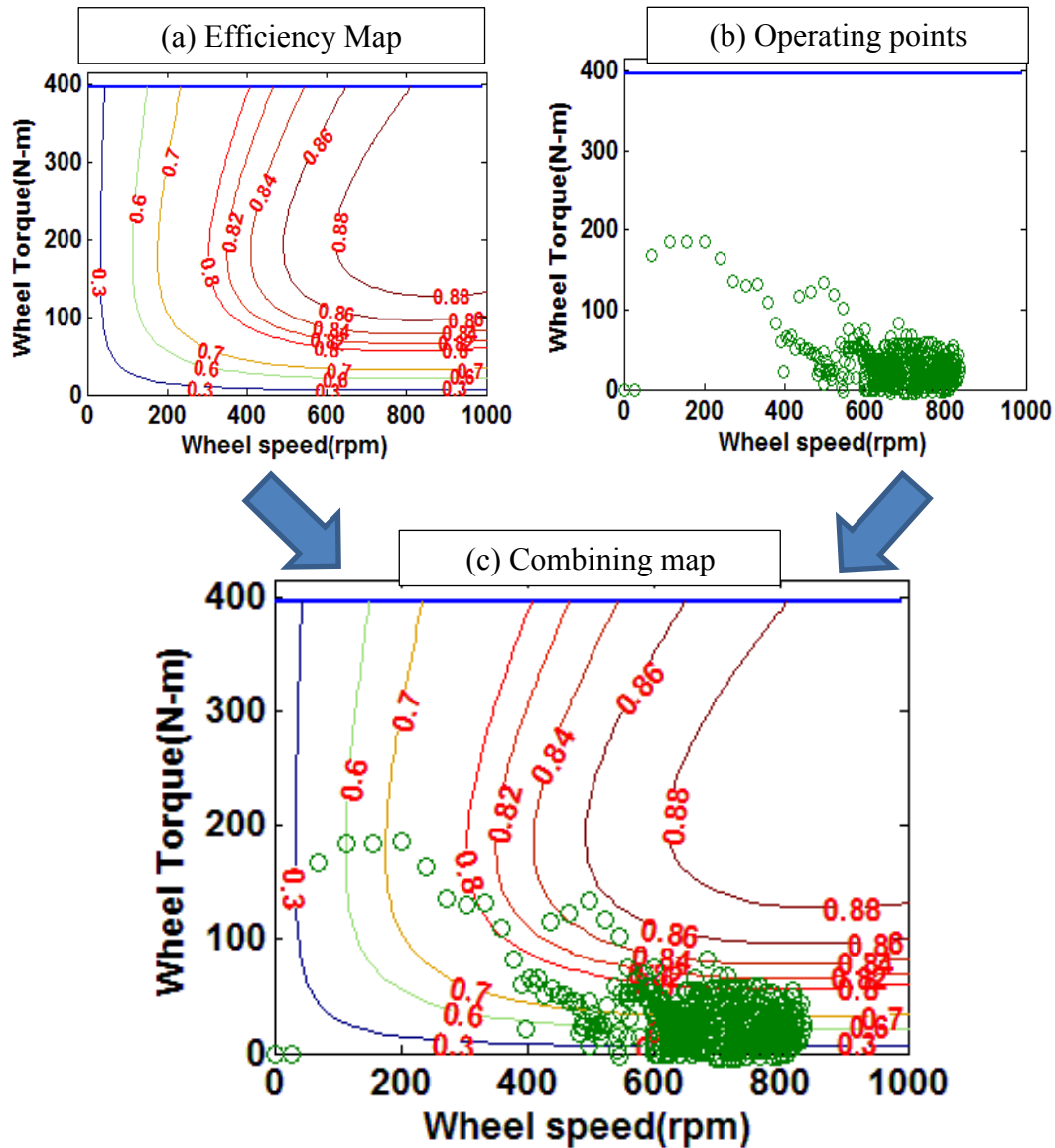


Figure 6-33: Combined efficiency of an in- wheel motor during highway driving

Figure 6-33 (a) shows the efficiency map of Protean's in-wheel motor. Figure 6-33 (b) shows the operating points associated with the HWFET duty cycles. The two maps are combined as shown in Figure 6-33 (c). For the purpose of comparison, we only consider the motor efficiency. The overall efficiency including the speed ranges of the first and second stages is around 81.5%.

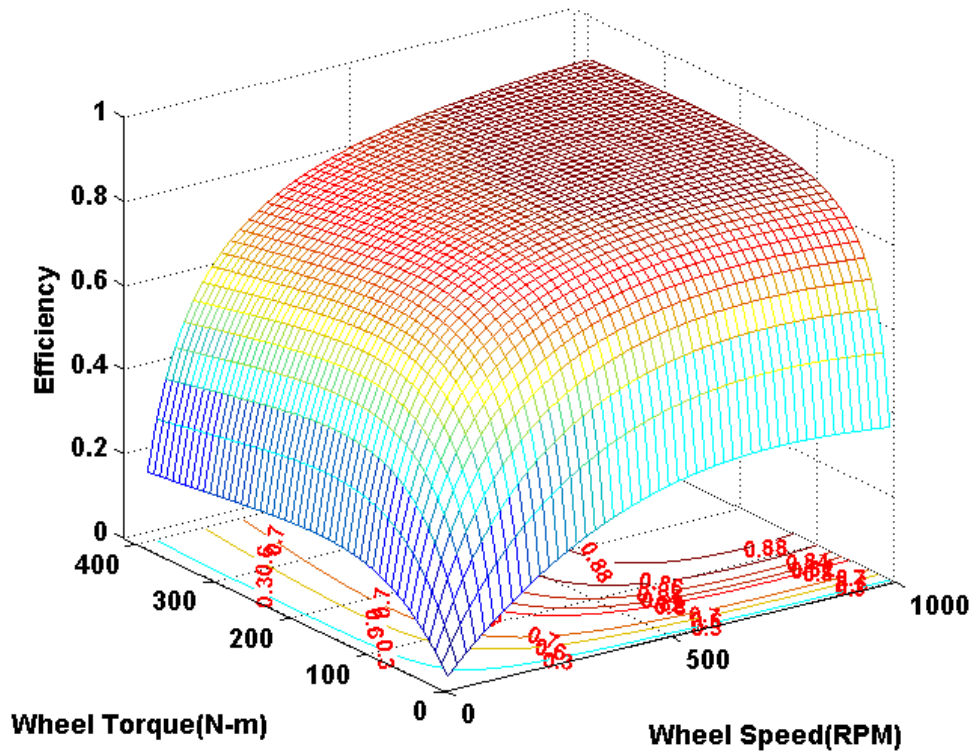


Figure 6-34: Efficiency map of Protean's in-wheel motor

The efficiency map of an in-wheel motor with respect to wheel torque and wheel speed is shown in Figure 6-34.

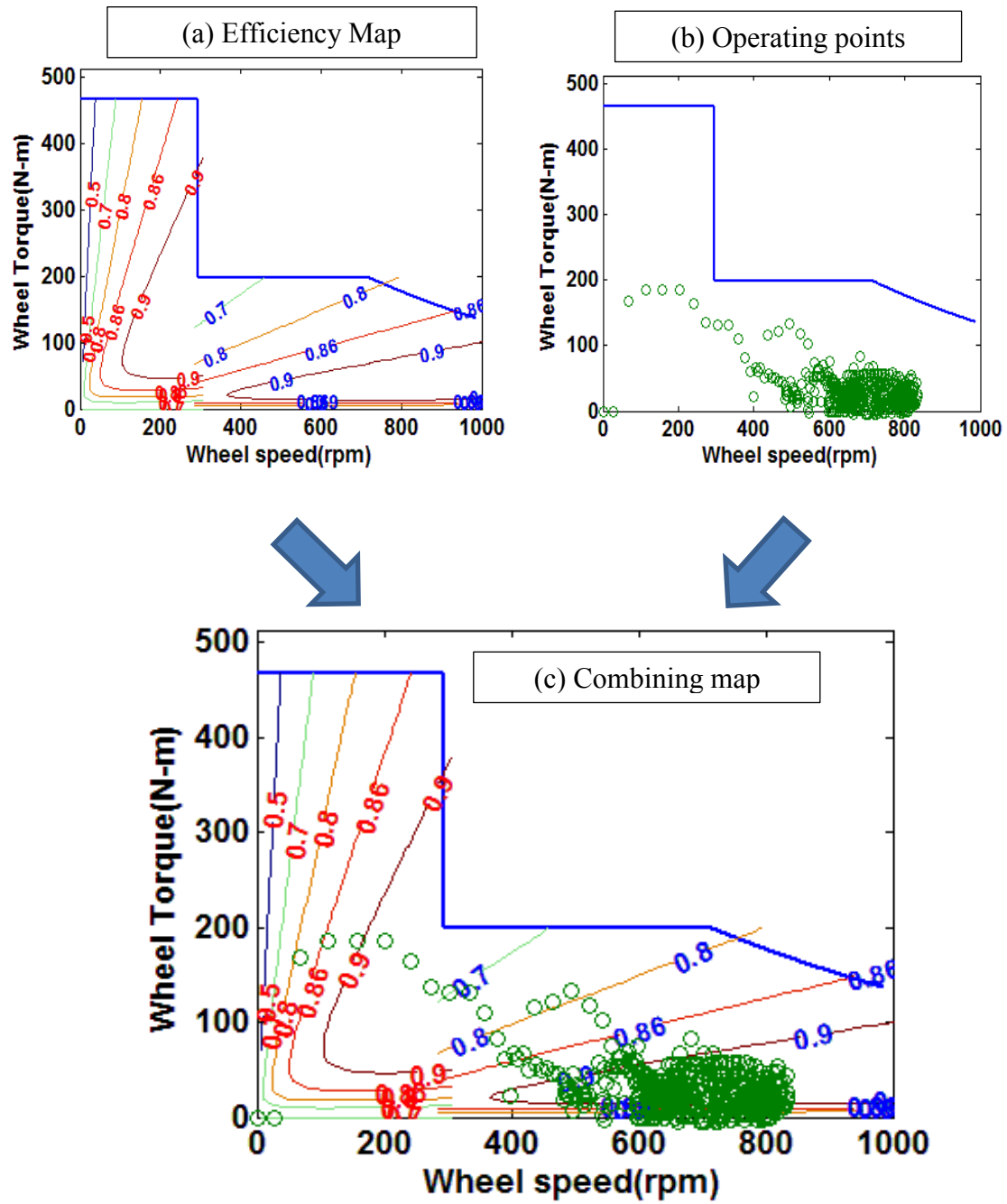


Figure 6-35: Combined Efficiency map of an MDW

Figure 6-35 (a) shows the assumed efficiency map of an MDW. As mentioned in Section 6.1.6, this efficiency map is generated based on Equation (6.10). Figure 6-35 (b) shows the operating point associated with the HWFET duty cycles. The two maps are combined as shown in Figure 6-35 (c). The overall efficiency including the speed ranges of the first and second stages is around 89.6%, which is around 8.1% higher than efficiency (81.5%) of Protean's in-wheel motor. Clearly, it can be seen that the efficiency of two speed regimes improves, compared to the efficiency of one speed regime.

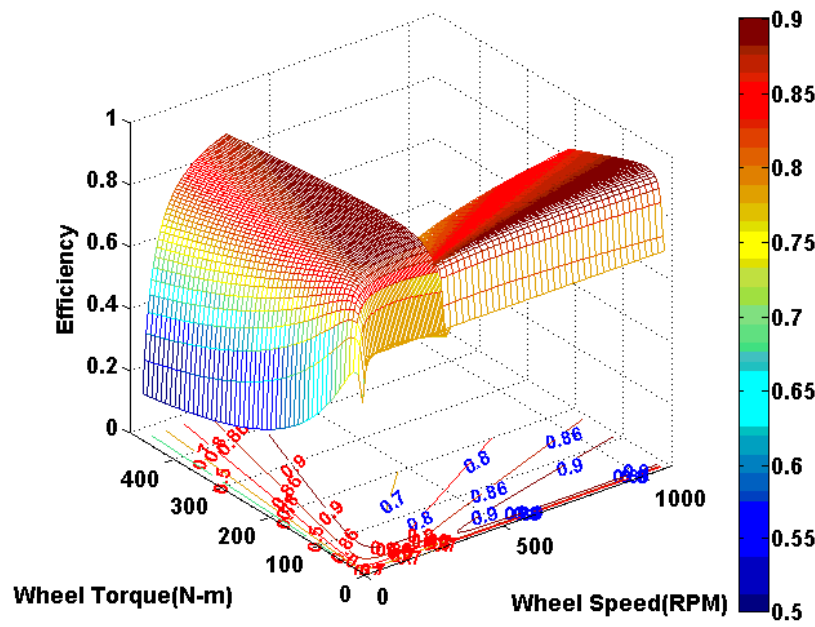


Figure 6-36: Efficiency map of an MDW

The efficiency map of an MDW with respect to wheel torque and wheel speed is shown in Figure 6-36. This efficiency map of an MDW is identical to Figure 6-35 (c). Highway driving requires the capability to operate in high speed and low torque. Therefore, the MDW which has high efficiency in high speed and low torque is a great choice for the customers who drive in the highway as well.

	Protean's IWM (%)	MDW (%)	Difference (%)	Loss Improvement Ratio
Urban Driving (UDDS)	73.8	85.8	12.0	1.9
Highway Driving (HWFET)	81.5	89.6	8.1	1.8

Table 6-3: Simulation results

Efficiency comparisons between the in-wheel motor and the MDW are made in Table 6-3, in terms of an urban driving and a highway driving. Clearly, it is concluded that the MDW has the capability to have high efficiency not only for urban driving but also for highway driving, compared to Protean's single speed in-wheel motor. The loss improvement ratio indicates that the losses of a MDW are lower than that of Protean's IWM, by a factor of approximately two. As a simulation result, we proved that efficiency of the MDW is significantly higher than that of Protean's in-wheel motor. The MDW has four speed regimes, just as transmission has 5 or 6 speeds to increase efficiency [Tesar and Ashok, May, 2011]. Now we will discuss the comparison of a MDW with a reconfigurable controller.

6.3.2 Comparison of a MDW with a Reconfigurable Controller

With a reconfigurable power controller, we project that the MDW can have a high efficiency over its entire torque-speed profile by raising and flattening the sweet spot. In other words, by choosing appropriate controller components, the overall efficiency can be further improved to meet the customer requirements for different purposes of the system in real time. The electric motor would be driven under two controller configurations, resulting in two additional speed regimes. Hence, four distinct "speeds" are created with a mechanical clutch shift [Tesar and Ashok, May, 2011]

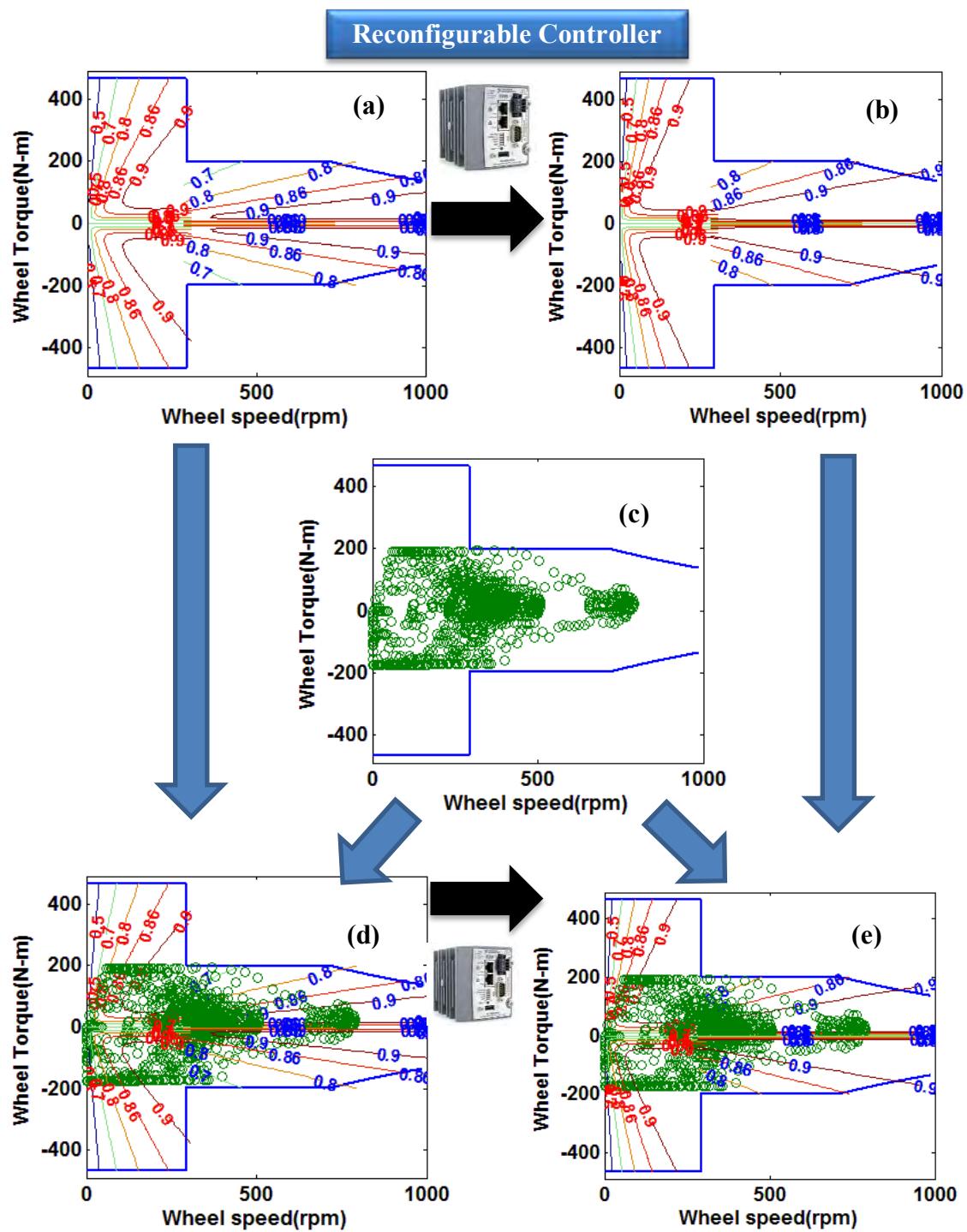


Figure 6-37: Efficiency maps of an MDW without & with a reconfigurable controller

Figure 6-37 (a) is simulated based on a clutch shift point at 20 mph considering motor mode and generator mode. Other constraints remain the same as Figure 6-31. This figure shows the efficiency map of a MDW without a reconfigurable controller. Figure 6-37 (b) shows the hypothetical efficiency map of a MDW with a reconfigurable controller which expands and raises the efficiency sweet spot. Figure 6-37 (c) shows the scatter points associated with UDDS duty cycle. Each point is the operating point. Figure 6-37 (d) and (e) show the combined map including efficiency map and scatter map, which presents the efficiency of an MDW with and without a reconfigurable controller, respectively. The efficiency of an MDW with and without a reconfigurable controller is calculated as 85.8% and 88.2%. It is suggested then that the MDW with a reconfigurable controller has a higher efficiency by a further 2.4% (i.e., loss improvement = 1.2x).

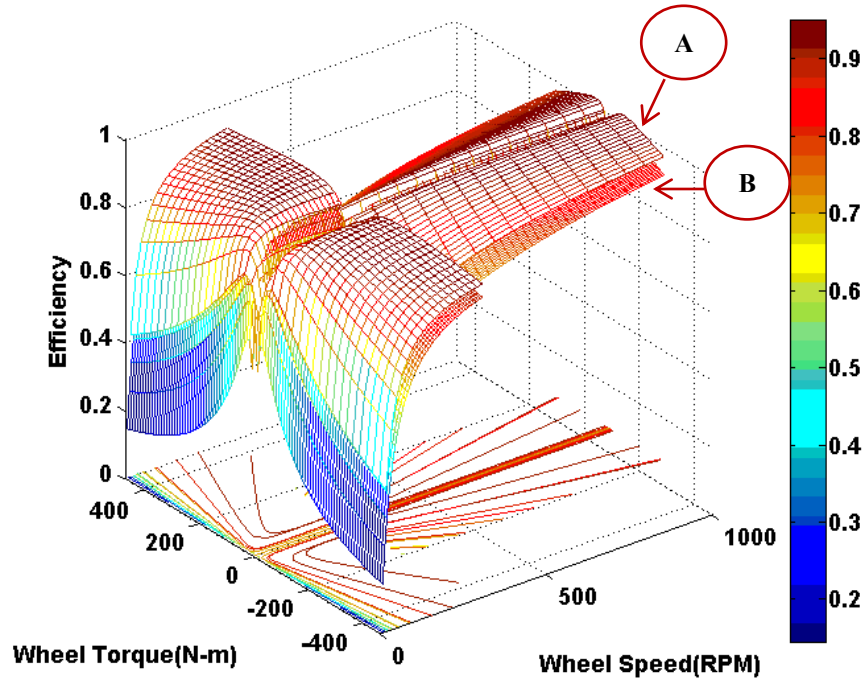


Figure 6-38: Efficiency maps of an MDW without & with a reconfigurable controller

Simulated efficiency maps of an MDW without & with a reconfigurable controller are shown in Figure 6-38. As seen at symbol 'A' shown in Figure 6-38, this is the improved efficiency map of an MDW with a reconfigurable controller. Without a reconfigurable controller, the symbol 'B' indicates the efficiency map of an MDW.

6.4 INDIVIDUAL DEMAND CYCLES

We demonstrated how the selection of the components of MDWs matches to the driver whose driving cycles are UDDS, HWFET, and US06. These driving cycles would be average driving style of ordinary people. The individual demand cycle can be defined as the driving cycle associated with a particular customer[Cunningham and Tesar,2011]. Customer's demand cycle is critical for their desired drivability and efficiency. The question arises: how to measure a customer?, how to classify a customer?, and how to satisfy a customer?.

To address these problems, an automobile company will provide a customer with a representative vehicle to obtain the individual demand cycles. The customer will drive for two weeks. Whenever he drives, numerous many sensors equipped in the vehicle will keep taking information, so that all operational parameters can be recorded. After that, a third-party "software application" analyzes specific duty cycle for that driver. Consequently, we can use the customer's duty cycle to predict what the customer wants, and thus electric vehicles will be customized to suit the customer's demand style, so that the customer can be satisfied with their purchase [Tesar and Ashok,May, 2011].

The performance of an electric vehicle is usually evaluated by its acceleration time, maximum speed, and gradeability. The power rating and gear ratios are the primary considerations to satisfy these performance specifications. These parameters are

influenced by the torque-speed characteristics of the traction motor[Ehsani, Gao et al.,2009].

In this research, the maximum vehicle speed is determined by the maximum speed of the traction motor. Therefore, in this design the maximum speed of the MDW is constrained by 70 mph (i.e., SRM motor speed 13000 ~ 15000 RPM). According to this constraint [Ashok and Tesar,2002], if the motor operates above 15000 RPM (which can be regarded as high speed), it is important to evaluate the effects of hoop stress, inertia, and critical speed.

The demand cycles determine the vehicle performance of a specific set of tasks: 0-60 acceleration time, cruising speed, climbing a hill of a certain grade at a specified speed, etc. It can be used for design goals for motor power rating, maximum torque, and speed [Cunningham and Tesar,2011]. With regard to the M-ATV (Mine-resistant Ambush Protected All-Terrain Vehicle), the author characterized and evaluated the motor torque required for three demand cycles: acceleration from a stop (0-30 mph), maintain cruising speed while climbing a specified grade, maximum gradeability from a stop.

In the same manner, an electric vehicle equipped with four independent MDWs was simulated based on vehicle parameters as listed in Table 6-4. The five demand cycles are specified as follows:

1. 0-60 mph acceleration time
2. Maintaining cruising speed
3. Maximum gradeability
4. Acceleration from 30 to 50 mph
5. Acceleration from 50 to 70 mph

Since we have five different types of the MDWs (16 hp, 20 hp, 24 hp, 32 hp, and 40 hp), the simulation will be carried out in terms of five types of the electric vehicles equipped with four independent MDWs.

	Parameters	Value	Units	Value	Units
Number of wheels	N_w	4			
Vehicle mass	m_c	1497	kg	3300/g	slug
Moment of inertia of the wheel	I_w	1.28	kg-m ²	0.944	slug-ft ²
Moment of inertia of motor rotor	I_m	6.03E-6	kg-m ²	4.45E-6	slug-ft ²
Gear system efficiency	η_g	1			
Head wind velocity	v_w	0	m/s	0	ft/s
Wheel radius	r_w	0.305	m	12	in
Air density	ρ_a	1.23	kg/m ³	0.0024	slug/ft ³
Frontal area	A_f	1.3	m ²	14	ft ²
Drag coefficient	C_d	0.3			
Rolling coefficient	C_r	0.007			
Gear ratio	g_{r1}, g_{r2}	49,14			
Clutch shift point	C_{sp}	20	mph		
Acceleration levels (16 hp)	g_1, g_2, g_3, g_4	0.3, 0.3, 0.15, 0.15			
Acceleration levels (20 hp)	g_1, g_2, g_3, g_4	0.4, 0.4, 0.17, 0.17			
Acceleration levels (24 hp)	g_1, g_2, g_3, g_4	0.5, 0.5, 0.2, 0.2			
Acceleration levels (32 hp)	g_1, g_2, g_3, g_4	0.8, 0.8, 0.3, 0.3			
Acceleration levels (40 hp)	g_1, g_2, g_3, g_4	1, 1, 0.4, 0.4			

Table 6-4: Vehicle Parameters

6.4.1 Acceleration Time of 0-60 mph

The 0-60 mph acceleration time is used as a classical vehicle performance reference. According to consumer's reports[Consumer-Reports,2012], the 0-60 mph acceleration time of Nissan Leaf (power rating: 107 hp) which is a pure electric vehicle is 10.3 s. The 0-60 mph acceleration time of Tesla roadster (power rating: 288 hp) is 3.9 sec [Wikipedia; Hayes, de Oliveira et al.,2011].

As mentioned in Secs. 6.1.5, the MDW has four different g levels: g_1 (0 – 10 mph), g_2 (11 – 20 mph), g_3 (21 – 40 mph), and g_4 (41 mph – 70 mph). The clutch shift occurs at 20 mph from 49-to-1 (for low speed and high torque) to 14-to-1 (for high speed and low torque) for two mechanical speeds.

As listed in Table 6-4, assuming different g levels which are determined by customer choice, the demand torque will be determined, so that the 0-60 mph acceleration time can be simulated as shown in Figure 6-39 (a). Each MDW is constrained by its rated motor power.

As can be seen in Figure 6-39 (b), given the four independent MDWs, the 0-60 mph acceleration times of the MDW (16 hp) and MDW (20 hp) are 15.4 s and 12.9 s, respectively. The 0-60 mph acceleration times corresponding to the MDW (24hp, 32hp, and 40hp) are 10.8 s, 7.3 s, and 5.7 s. That is, the electric vehicle equipped with the four independent MDW requires the motor power rating of 160 hp to achieve the 0-60 mph acceleration time of 5.7 s.

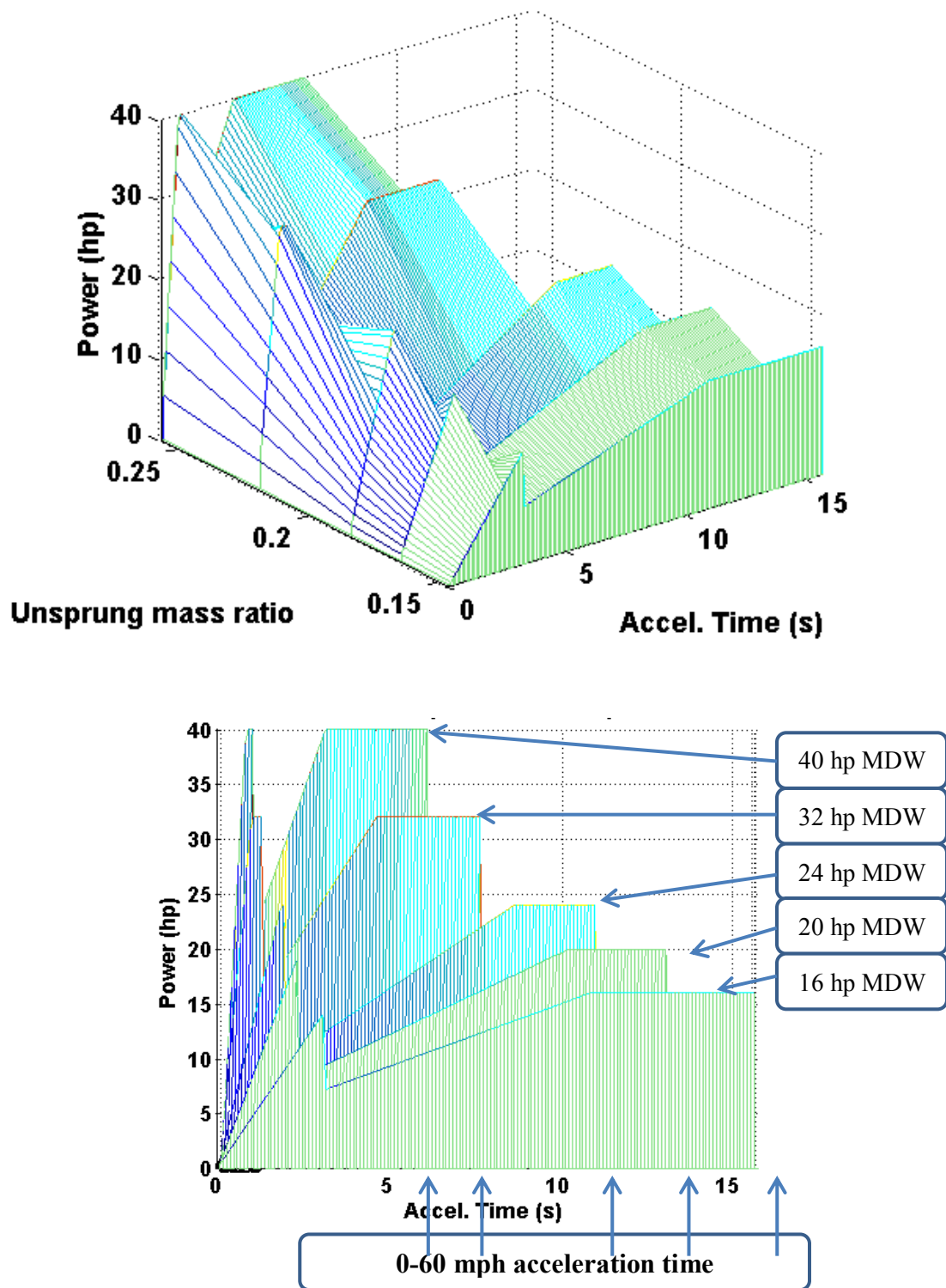


Figure 6-39: Power performance map w.r.t. unsprung mass ratio and time

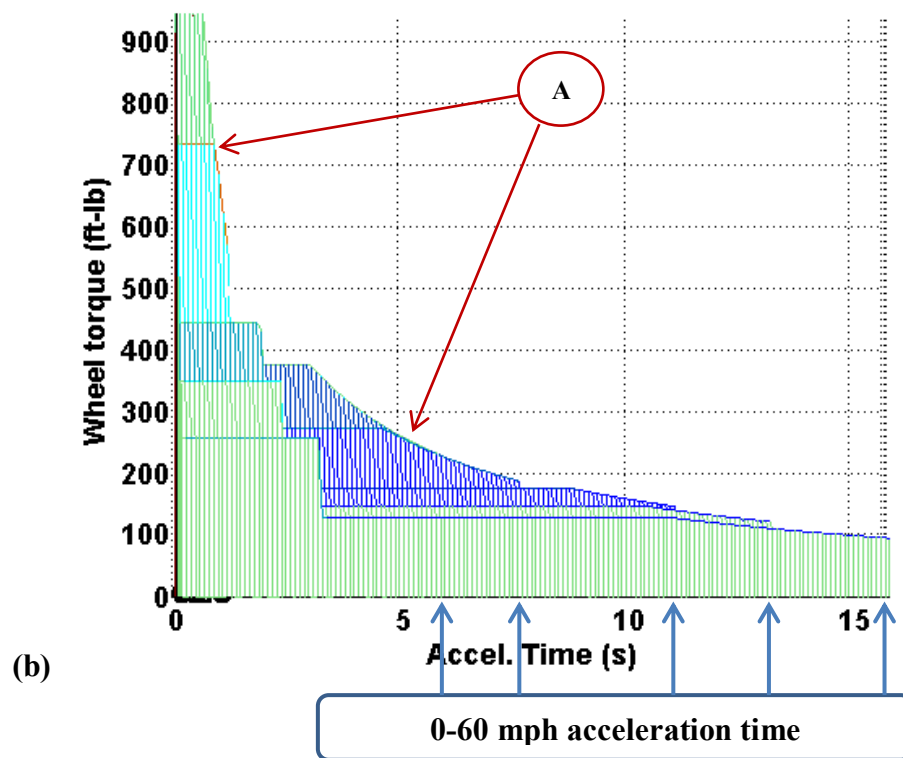
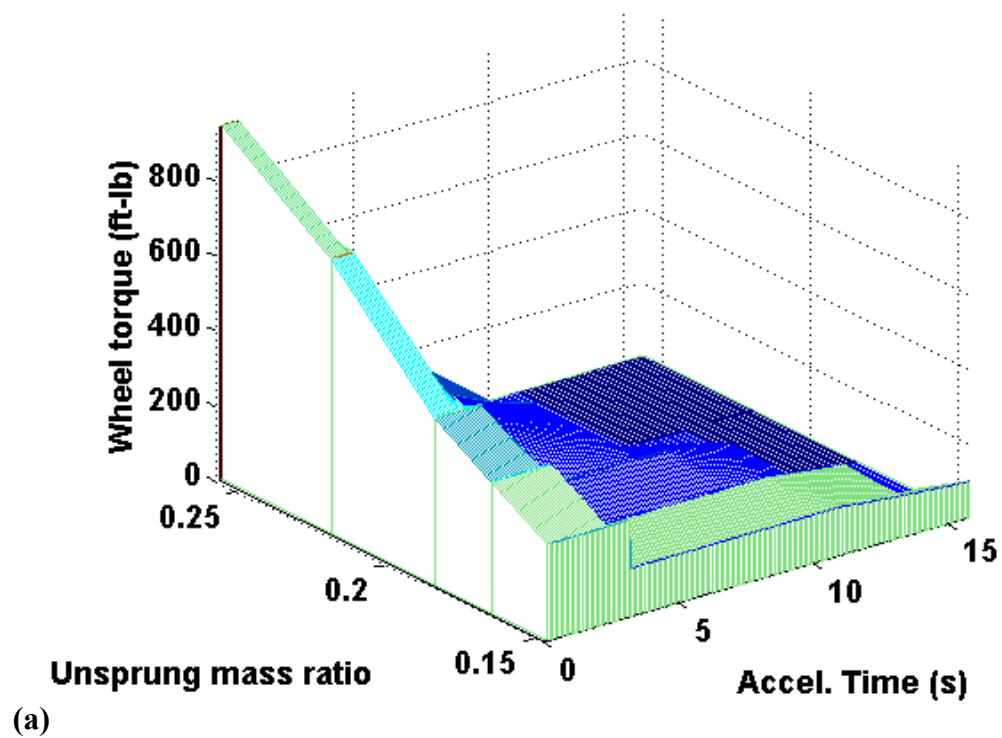


Figure 6-40: Wheel torque performance map w.r.t. unsprung mass ratio and time

Figure 6-40 (a) shows the wheel torque performance with respect to unsprung mass ratio and time. As can be seen in Figure 6-40 (b), the MDW (40 hp) shows high wheel torque associated with first acceleration level of $g_1 = 1$ (826 ft-lb). The wheel torque of g_1 of MDW (32 hp, 24 hp, 20 hp, and 16 hp) is 660 ft-lb, 413 ft-lb, 330 ft-lb, and 248 ft-lb. It should be noted that the curves seen at symbol 'A' occurs due to constant power limitation. In sum, if a customer want the 0-60 mph acceleration time to be less than 6 s, the electric vehicle equipped with four independent MDWs (40 hp) is suitable for that particular customer. If a customer wants the cheapest electric vehicle out of the five models, the electric vehicle equipped with four independent MDWs (16 hp) is suitable for that customer.

6.4.2 Maintaining Cruising Speed

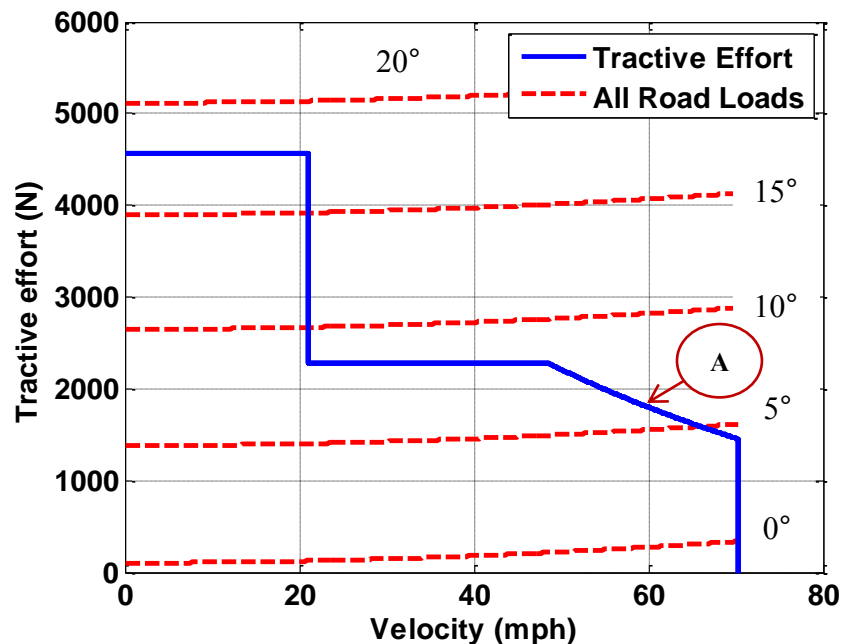


Figure 6-41: Tractive effort versus velocity (MDW, 16 hp)

Maintaining cruising speed, while climbing a hill, is an important consideration for the design of the motor drive and power supply [Cunningham and Tesar,2011]. At a given rated motor power (16 hp), Figure 6-41 shows the performance characteristics of tractive effort and all road loads which contain aerodynamic, rolling, and grade resistance. The tractive effort is plotted based on different g levels: $g_1 = 0.15$, $g_2 = 0.15$, $g_3 = 0.3$, and $g_4 = 0.3$. The each dotted line indicates all road loads corresponding to the grade of 0° , 5° , 10° , 15° , and 20° . As seen at symbol 'A' in Figure 6-41, the grade, while maintaining the cruising speed (60 mph), is around 7° which is determined by the net tractive effort which is the difference between tractive effort and sum of rolling resistance and aerodynamic resistance.

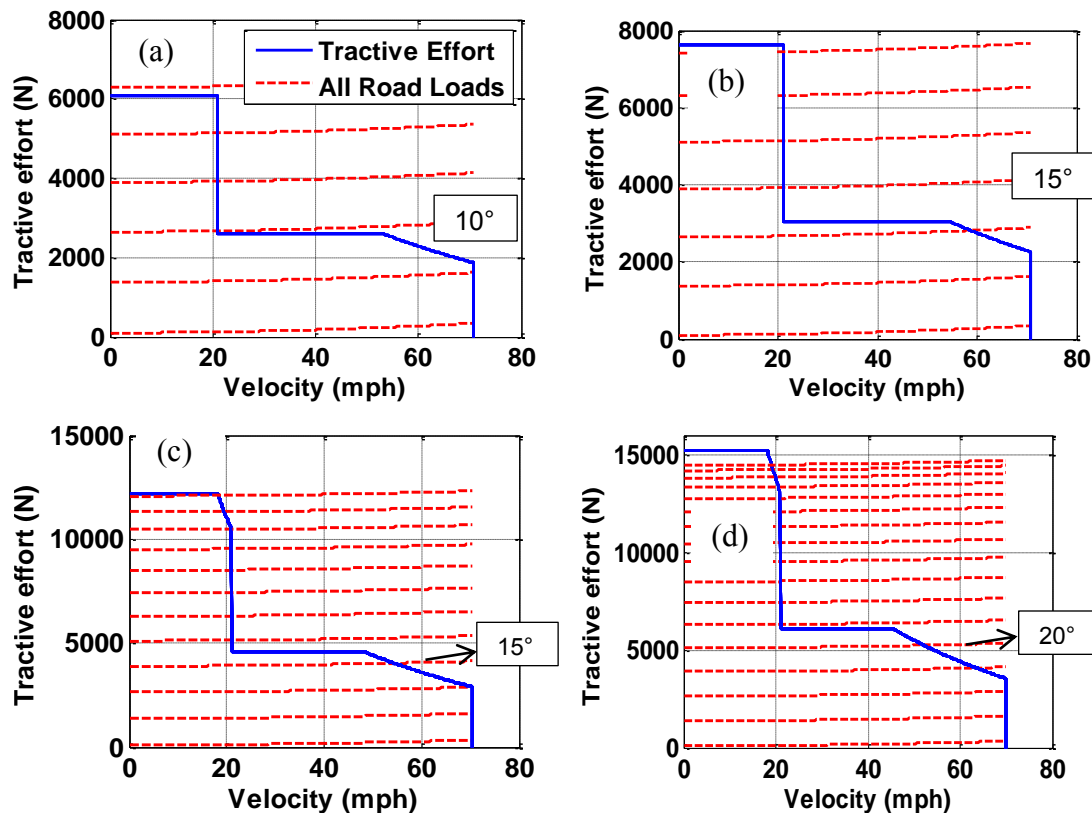


Figure 6-42: Tractive effort versus velocity (a) 20 hp, (b) 24 hp, (c) 32 hp, (d) 40 hp

Figure 6-42 shows the performance characteristics of tractive effort and all road loads. Figure 6-42 (a) – (d) are simulated based on the rated motor power of 20 hp, 24 hp, 32 hp, and 40 hp, respectively. Due to the four independent MDWs, the resulting power levels are 80 hp, 96 hp, 128 hp, and 160 hp. As can be seen in Figure 6-42 (a) and (b), the grade, while maintaining the cruising speed (60 mph), is around 8° and 10° , respectively. The grade, while maintaining the cruising (60 mph), is around 13° and 16° as shown in Figure 6-42 (c) and (d), respectively.

6.4.3 Maximum gradeability

Maximum gradeability can be defined as the maximum grade that the electric vehicle can overcome at a certain constant speed. From equation (6.1), The maximum grade can be obtained by[Ehsani, Gao et al.,2009]:

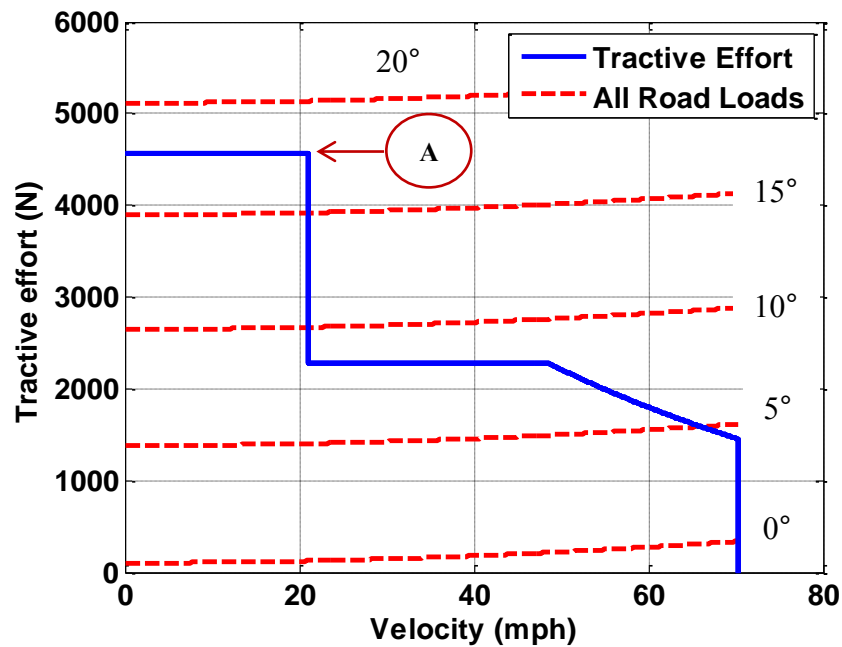


Figure 6-43: Tractive effort versus velocity (MDW, 16 hp)

$$\theta = \sin^{-1} \frac{F_t - \left\{ \frac{1}{2} \rho_a A_f C_d (v_v + v_w)^2 + C_r m_c g \cos \theta \right\}}{m_c g} \quad (6.16)$$

The F_t is the tractive effort of the electric vehicle equipped with four independent wheels.

The realistic performance goals of passenger car and van is around 30 % (17.3°) and 20-25 % (11.5° ~ 14.4°), respectively. The goals of the minibus and urban bus is around 15-20 % and 12-15%, respectively [Chan,1993].

At a given rated motor power (16 hp), Figure 6-43 shows the performance characteristics of tractive effort and all road loads which contain aerodynamic, rolling, and grade resistance. The tractive effort is plotted based on different g levels: $g_1 = 0.15$, $g_2 = 0.15$, $g_3 = 0.3$, and $g_4 = 0.3$. The each dotted line indicates all road loads corresponding to the grade of 0°, 5°, 10°, 15°, and 20°. As seen at symbol 'A' in Figure 6-43, the maximum gradeability could be around 17° which is determined by the net tractive effort which is the difference between tractive effort and sum of rolling resistance and aerodynamic resistance.

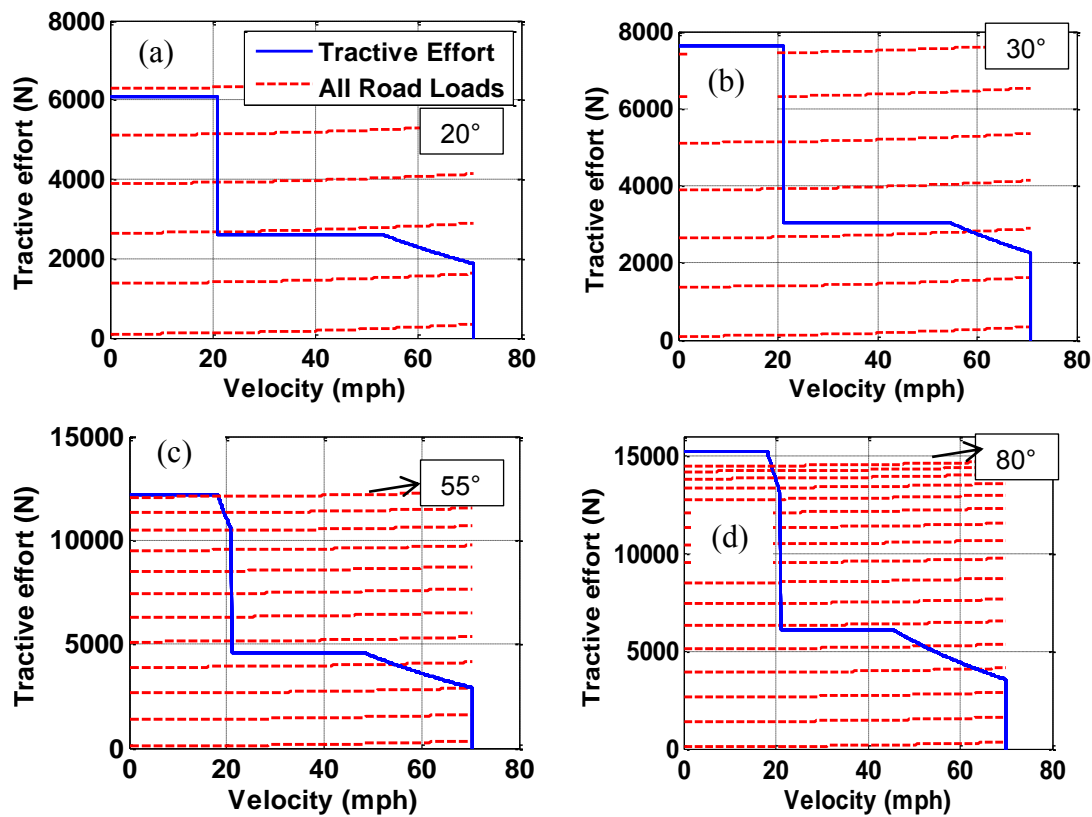


Figure 6-44: Tractive effort versus velocity (a) 20 hp, (b) 24 hp, (c) 32 hp, (d) 40 hp

Figure 6-44 shows the performance characteristics of tractive effort and all road loads. Figure 6-44 (a) – (d) are simulated based on the rated motor power of 20 hp, 24 hp, 32 hp, and 40 hp, respectively. As can be seen in Figure 6-44 (a) and (b), the maximum gradeability could be around 24° and 31°, respectively. As shown in Figure 6-44 (c) and (d), the maximum gradeability could be around 55° and 80°, respectively.

6.4.4 Acceleration from 30 to 50 mph

Acceleration from 30 to 50 mph can be used for evaluating the ability to merge onto a highway entrance ramp. From a two-seater to full-size SUVs, the acceleration time

from 30 to 50 mph is approximately 1.6 s to 4.9 s [Wei and Rizzoni, 2004; Cunningham and Tesar, 2011].

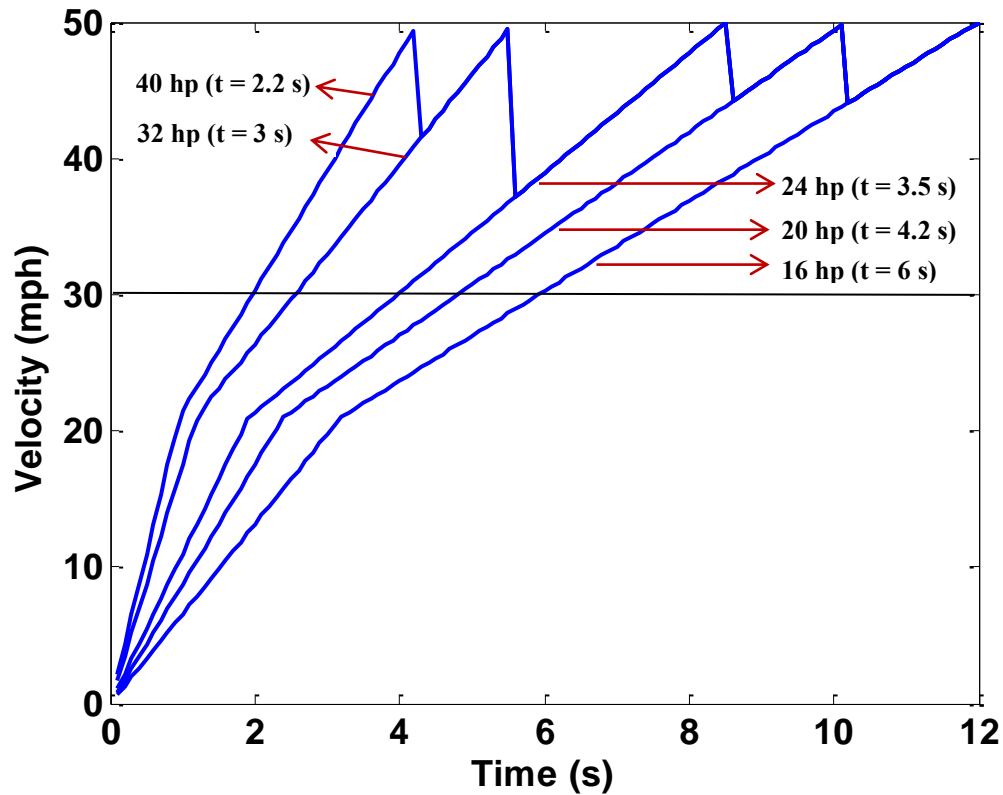


Figure 6-45: 30 – 50 mph acceleration time of the MDWs

Figure 6-45 shows the 30-50 mph acceleration time with respect to 16 hp, 20 hp, 24 hp, 32 hp, and 40 hp. The 30-50 mph acceleration times of the electric vehicle equipped with four independent MDWs (16 hp, 20 hp, and 24 hp) are around 6 s, 4.2 s, and 3.5 s, respectively. In terms of the electric vehicles equipped with four independent MDWs (32 hp and 40 hp), the 30-50 mph acceleration times are around 3 s and 2.2 s.

6.4.5 Acceleration from 50 mph to 70 mph

A passing maneuver on the highway is significant to evaluate vehicle performance in terms of passenger vehicle. From a two-seater to full-size SUVs, the acceleration time from 50 to 70 mph is approximately from 2.9 s to 7.1 s [Wei and Rizzoni,2004; Cunningham and Tesar,2011]

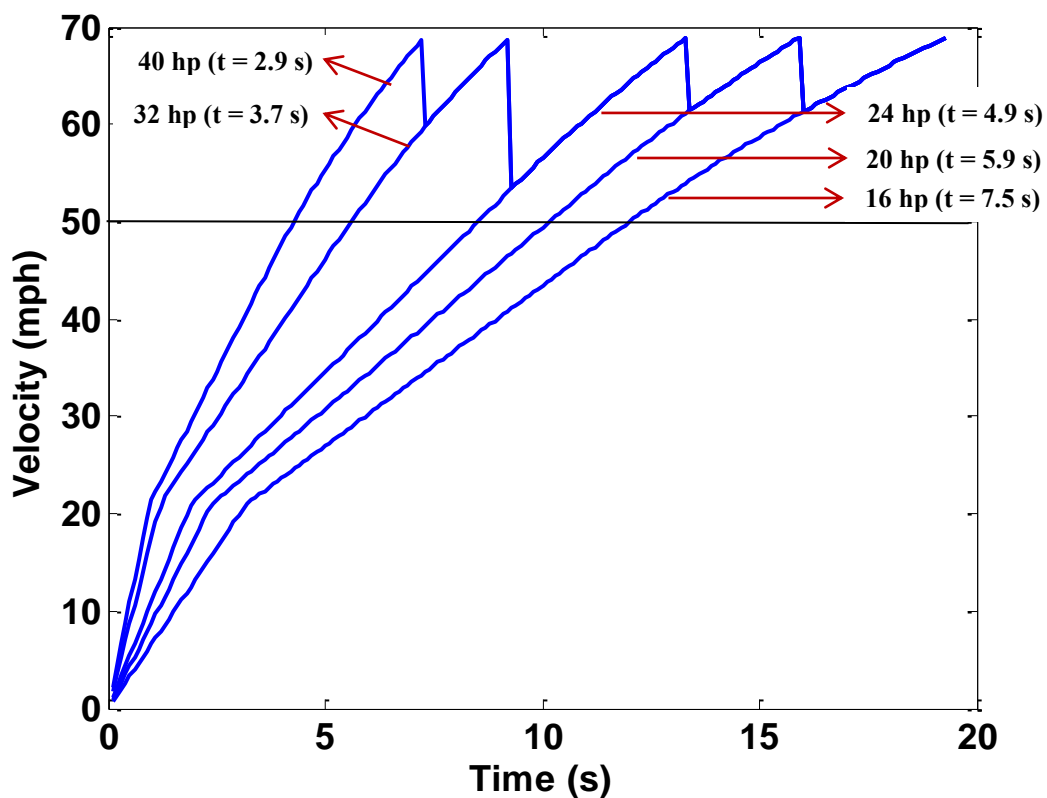


Figure 6-46: 50 – 70 mph acceleration time of the MDWs

Figure 6-46 shows the 50-70 mph acceleration time with respect to 16 hp, 20 hp, 24 hp, 32 hp, and 40 hp. The 50-70 mph acceleration times of the electric vehicle equipped with four independent MDWs (16 hp, 20 hp, and 24 hp) are around 7.5 s, 5.9 s,

and 4.9 s, respectively. In terms of the electric vehicles equipped with four independent MDWs (32 hp and 40 hp), the 50-70 mph acceleration times are around 3.7 s and 2.9 s. Clearly, it can be seen that the 50-70 mph acceleration time of the electric vehicle equipped with four independent MDWs of 40 hp is over two times faster than that of the electric vehicle equipped with four independent MDWs of 16 hp

6.5 CHAPTER SUMMARY

In order to design a customer-focused MDW, the duty cycle question must be answered and analyzed on a higher level to become competitive products. Vehicle duty cycles play a significant role in designing the appropriate MDW to meet average human needs. In this chapter, we developed a procedure for the duty cycle analysis of the driving cycles in order to obtain not only how to maximize efficiency but also how to maximize drivability, based on the existing driving cycles: Urban Dynamometer Driving Schedule (UDDS), Highway Fuel Economy Test (HWFET), and Aggressive Driver (US06).

First, given the driving cycles, the total wheel torque and power requirement were evaluated to investigate the variation of peak torque and power (Sec. 6.1.2). Second, speed-acceleration frequency distribution provided insight to a designer as an illustration whether the driving cycle was biased in terms of speed or acceleration regions (Sec. 6.1.3). Third, the wheel torque-speed characteristics considering scatter plots and histogram enable a designer to determine the continuous wheel torque and peak wheel torque (Sec. 6.1.4). Forth, the motor output torque and power requirement were evaluated to meet the duty cycles (Sec. 6.1.5). Fifth, the motor power demand can be obtained from the motor output power divided by motor efficiency (Sec. 6.1.6). We then demonstrated how the selection of the components of MDWs can be used to match the driver whose driving cycles are Urban Dynamometer Driving Schedule (UDDS), Highway Fuel

Economy Test (HWFET), and Aggressive Driver (US06) (Sec. 6.1.7). In this research, the MDW specification is defined as different g levels, 0-60 acceleration time, power rating, MDW size, optimal gear ratio, and clutch shift point.

We evaluated the required input power demands from output power, and traction and braking energy dissipation were also evaluated from the input power demands and output power, so that we can obtain the heat energy. Furthermore, the net energy consumption is determined from traction and braking energy (Sec. 6.2). The comparison of a MDW and an in-wheel motor are made in terms of the urban duty cycle (UDDS) and the highway duty cycle (HWFET) (Sec. 6.3.1). In addition, we presented the comparison of a MDW with and without a reconfigurable controller (Sec. 6.3.2).

Existing driving cycles might be average driving style of ordinary people. The individual demand cycle can be defined as the driving cycle associated with a particular customer. For the purpose of analysis, five individual demand cycles are specified in terms of five different electric vehicles equipped with four independent MDWs (16 hp, 20 hp, 24 hp, 32 hp, and 40 hp). Five individual demand cycles are 0-60 mph acceleration time, maintain cruising speed, maximum gradeability, acceleration from 30 to 50 mph, and acceleration from 50 to 70 mph. We have demonstrated that maximum performance of an electric vehicle is constrained by rated motor power on the wheels. It should be noted that total motor power ratings of the electric vehicles equipped with four independent MDWs (16 hp, 20 hp, 24 hp, 32 hp, and 40 hp) becomes 64 hp, 80 hp, 96 hp, 128 hp, and 160 hp. In the next chapter, we will discuss customer needs from the viewpoint of purchase, operation, maintenance, and refreshment.

Chapter 7. Purchase / Operation / Maintenance / Refreshment Standpoints

Equation Chapter 7 Section 1 This chapter will discuss how to satisfy a customer in terms of the Multi-speed hub Drive Wheel (MDW) of a hybrid electric vehicle. First of all, it is essential to know what the customer needs are in terms of purchase, operation, maintenance, and refreshment point of view. Satisfying human needs means to respond directly to human commands / objectives at the time of purchase, in real time operation, and maintenance / tech mods over the life history of the vehicle. This leads to maximizing human choice. To meet human choice means not only to keep the human fully informed on a series of choices, but also to maximize their self-awareness [Tesar, Dec 11, 2011].

In order for the customers to make the right choices as to what they want, it is necessary to have visual decision surfaces (maps) which can be used to aid decision making. The question raised is what maps are of interest to the customers? We will discuss maps with regard to purchase, operation, maintenance, and refreshment.

7.1 PURCHASE CRITERIA

7.1.1 Cost

Cost is a major factor for customers in the purchase a hybrid electric vehicle. Clearly, characteristics of the MDW become choices. Zeraoulia proposes a simple comparative study in terms of a selection of different electric motors such as DC motors (DC), Induction Motor (IM), Brushless DC Motor (BLDC), and Switched Reluctance Motor (SRM) [Cuenca, Gaines et al.,2000; Zeraoulia, Benbouzid et al.,2006; Hashemnia and Asaei,2008]

	Vehicle Configuration	Unit(Costs)	Car with 4 wheels
	Vehicle sprung mass (16 hp) (Including battery/super cap, engine, generator, skateboard chassis, car bodies, etc.)	\$ 10,000	
	Same as above (20 hp)	\$ 10,500	
	Same as above (24 hp)	\$ 11,000	
	Same as above (32 hp)	\$ 12,000	
	Same as above (40 hp)	\$ 13,000	
1	Drive Wheel 16 hp with a controller (w/o clutch)	\$ 750	\$ 13,000
	Same as above (20 hp)	\$ 850	\$ 13,900
	Same as above (24 hp)	\$ 950	\$ 14,800
	Same as above (32 hp)	\$ 1050	\$ 16,200
	Same as above (40 hp)	\$ 1150	\$ 16,600
2	MDW 16 hp with a controller (with clutch)	\$ 1,000	\$ 14,000
	Same as above (20 hp)	\$ 1,100	\$ 14,900
	Same as above (24 hp)	\$ 1,200	\$ 15,800
	Same as above (32 hp)	\$ 1,300	\$ 17,200
	Same as above (40 hp)	\$ 1,350	\$ 17,400
3	MDW 16 hp with a reconfigurable controller (with clutch) (i.e., reconfigurable controller \$ 300)	\$ 1,300	\$ 15,200
	Same as above (20 hp)	\$ 1,400	\$ 16,100
	Same as above (24 hp)	\$ 1,500	\$ 17,000
	Same as above (32 hp)	\$ 1,600	\$ 18,200
	Same as above (40 hp)	\$ 1,650	\$ 18,400
4	MDW 16 hp with a reconfigurable controller/Intelligent corner (i.e., Intelligent corner cost = \$ 2,000)	\$ 3,300	\$ 23,200
	Same as above (20 hp)	\$ 3,400	\$ 24,100
	Same as above (24 hp)	\$ 3,500	\$ 25,000
	Same as above (32 hp)	\$ 3,600	\$ 26,200
	Same as above (40 hp)	\$ 3,650	\$ 26,400

Table 7-1: Assumed component cost list

The cost effective and rugged SRM of the MDW uses standard materials in place of rare earth materials which are very unstable in future cost estimates. In addition, the motor module can be considered as a plug-on module of two diameters (diameter 1-16, 20, 24 hp and diameter 2 – 32, 40 hp) to reduce cost by using the minimum set of laminate / wiring combinations simply by using three MDW lengths for the first diameter and two MDW lengths for the second diameter. With this reduction to two geometric patterns for the production of 5 unique MDW power levels, it is expected that cost will be continuously lowered by mass production [Tesar and Ashok, May, 2011].

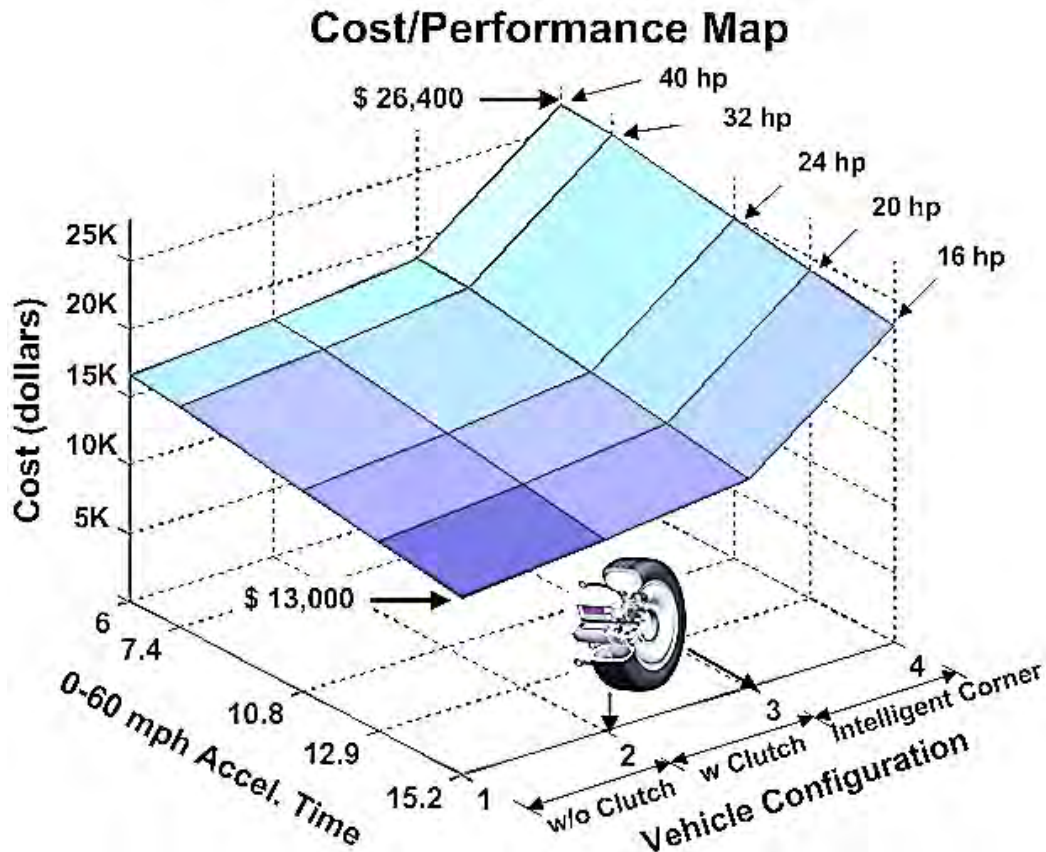


Figure 7-1: Cost estimate map with respect to 0-60 mph acceleration time and vehicle components considering four independent wheels

For the purpose of analysis, Table 7-1 shows a reasonable set of costs such as a drive wheel without clutch, MDW (including a clutch) with a controller, MDW with a reconfigurable power controller, and MDW with a reconfigurable power controller and intelligent corner system including camber/active suspension [Tesar,2011, August].

Based on information as listed in Table 7-1, Figure 7-1 shows a cost performance map as a function of the acceleration time (see Section 6.4.1) and the cost of vehicle components. In this case, assuming four independent wheels, the 0-60 acceleration time is associated with 15.2 s (16 hp), 12.9 s (20 hp), 10.8 s (24 hp), 7.4 s (32 hp), and 6.0 s (40 hp). Including the vehicle sprung mass, the vehicle configuration ‘1’ and ‘2’ represent use of a Drive Wheel with a controller (without clutch) and MDW with a controller (with clutch), respectively. In addition, the vehicle configuration ‘3’ and ‘4’ indicate use of a MDW with a reconfigurable controller (with clutch) and a MDW with a reconfigurable controller / intelligent corner, respectively. As the rated power increases with vehicle configuration from ‘1’ to ‘4’, the customer must pay the associated increased cost for the increased performance (from \$ 13,000 up to \$ 26,400).

7.1.2 Weight

The Robotics Research Group (RRG) has designed the MDW which is estimated to weigh 95 lb. In the future, this weight of the 16 hp version will become around 62.5 lb by using high-end aluminum shell, higher-quality gear materials, careful helix angle selection, etc. [Tesar and Ashok,May, 2011]. The unsprung mass (or the unsprung weight) also includes the sum of the masses associated with the following components: tires, brakes, wheel hubs, and some of the weight of spring (1/3), shock absorber (1/2 if needed), and perhaps 1/3 of the suspension link.[Wikipedia; R.Q. Riley,2005].

■ Drive Wheel (DW), Multi-speed hub Drive Wheel (MDW), Unsprung Weight (UW), Sprung Weight (SW), Intelligent Corner (IC), unsprung-to-sprung mass ratio (%)

	Value	Units	Value	Units
Vehicle sprung weight (16 hp)	1225	kg	2700	lb
Same as above (20 hp)	1259	kg	2775	lb
Same as above (24 hp)	1293	kg	2850	lb
Same as above (32 hp)	1338	kg	2950	lb
Same as above (40 hp)	1429	kg	3150	lb
Moment of inertia of motor rotor (16 hp)	6.03E-6	kg-m ²	4.45E-6	slug-ft ²
Same as above (20 hp)	7.24E-6	kg-m ²	5.34E-6	slug-ft ²
Same as above (24 hp)	8.44E-6	kg-m ²	6.23E-6	slug-ft ²
Same as above (32 hp)	10.85E-6	kg-m ²	8.01E-6	slug-ft ²
Same as above (40 hp)	12.06E-6	kg-m ²	8.90E-6	slug-ft ²
Drive Wheel 16 hp (w/o clutch)	28.3	kg	62.5	lb
Same as above (20 hp)	31.8	kg	70	lb
Same as above (24 hp)	35.4	kg	78	lb
Same as above (32 hp)	38.5	kg	85	lb
Same as above (40 hp)	43.1	kg	95	lb
Unsprung weight (DW 16 hp, 13.0%)	34.0	kg	75	lb
Same as above (DW 20 hp, 14.1%)	38.5	kg	85	lb
Same as above (DW 24 hp, 15.2%)	43.1	kg	95	lb
Same as above (DW 32 hp, 16.1%)	49.9	kg	110	lb
Same as above (DW 40 hp, 16.8%)	56.7	kg	125	lb
MDW 16 hp (with clutch)	34	kg	75	lb
Same as above (20 hp)	37.4	kg	82.5	lb
Same as above (24 hp)	40.8	kg	90	lb
Same as above (32 hp)	45.9	kg	101.3	lb
Same as above (40 hp)	51.0	kg	112.5	lb
Unsprung weight (MDW 16 hp, 14.8%)	45.4	kg	100	lb
Same as above (MDW 20 hp, 15.9%)	50.0	kg	110	lb
Same as above (MDW 24 hp, 16.8%)	54.4	kg	120	lb
Same as above (MDW 32 hp, 18.3%)	61.2	kg	135	lb
Same as above (MDW 40 hp, 19.1%)	68.0	kg	150	lb

	Value	Units	Value	Units
Total weight of a vehicle (16 hp, DW + Added UW)	1361	kg	3000	lb
Same as above (20 hp)	1413	kg	3115	lb
Same as above (24 hp)	1465	kg	3230	lb
Same as above (32 hp)	1537	kg	3390	lb
Same as above (40 hp)	1665	kg	3650	lb
Total weight of a vehicle (16 hp, MDW + Added UW)	1401	kg	3100	lb
Same as above (20 hp)	1458	kg	3215	lb
Same as above (24 hp)	1510	kg	3330	lb
Same as above (32 hp)	1583	kg	3490	lb
Same as above (40 hp)	1701	kg	3750	lb

Table 7-2: Vehicle weight parameters in terms of DW and MDW

As can be seen from the data in Table 7-2, vehicle sprung weight and the rotary inertia of motor rotor are estimated based on different power ratings such as 16 hp, 20 hp, 24 hp, 32 hp, and 40 hp which would become customer choices. Also, Drive Wheel (DW) (without clutch), MDW (with clutch), unsprung weight, and intelligent corner weight are also estimated for different power ratings. For instance regarding the MDW (16 hp), the unsprung weight is assumed to be 100 lb, which is the sum of the MDW (75 lb) and the related weights (25 lb). Regarding the MDW (32 hp), the unsprung weight is taken to be 135 lb, which is the sum of the MDW itself (101.3 lb) and the other related weights (33.7 lb).

Then, the total weight of a vehicle based on the five drive wheel (DW) choice becomes 3000 lb, 3115 lb, 3230 lb, 3390 lb, and 3650 lb depending on different types of the power ratings. In addition, the total weight of a vehicle based on the MDW becomes 3100 lb, 3215 lb, 3330 lb, 3490 lb, and 3750 lb.

	Value	Units	Value	Units
Vehicle sprung weight (IC, 16 hp)	1361	kg	3000	lb
Same as above (IC, 20 hp)	1395	kg	3075	lb
Same as above (IC, 24 hp)	1429	kg	3150	lb
Same as above (IC, 32 hp)	1519	kg	3350	lb
Same as above (IC, 40 hp)	1610	kg	3550	lb
Unsprung weight (IC 16 hp, 17.3%)	59.0	kg	130	lb
Same as above (IC 20 hp, 18.2%)	63.5	kg	140	lb
Same as above (IC 24 hp, 19.1%)	68.0	kg	150	lb
Same as above (IC 32 hp, 20.3%)	77.1	kg	170	lb
Same as above (IC 40 hp, 20.9%)	83.9	kg	185	lb
Total weight of a vehicle (16 hp,MDW+Added UW+IC+Added SW)	1596	kg	3520	lb
Same as above (20 hp)	1649	kg	3635	lb
Same as above (24 hp)	1701	kg	3750	lb
Same as above (32 hp)	1828	kg	4030	lb
Same as above (40 hp)	1946	kg	4290	lb

Table 7-3: Vehicle weight parameters in terms of the Intelligent Corner

Vehicle sprung and unsprung weights with a full intelligent corner are estimated in Table 7-3. Due to the active suspension, the increased sprung weight becomes 3000 lb to 3550 lb based on different sizes of the MDW power ratings. In addition, due to the steering, camber and active suspension actuators, the increased unsprung weight becomes 130 lb to 185 lb associated with different sizes of the power ratings at each wheel. Then, the total weight of a vehicle ranges from 3520 lb to 4290 lb.

In brief, there are three types of a total weight of a vehicle: a) an electric vehicle equipped with four independent Drive Wheels (DW, without clutch), b) an electric vehicle equipped with four independent MDW (with clutch), c) an electric vehicle equipped with four independent MDW (with clutch) and complete intelligent corner.

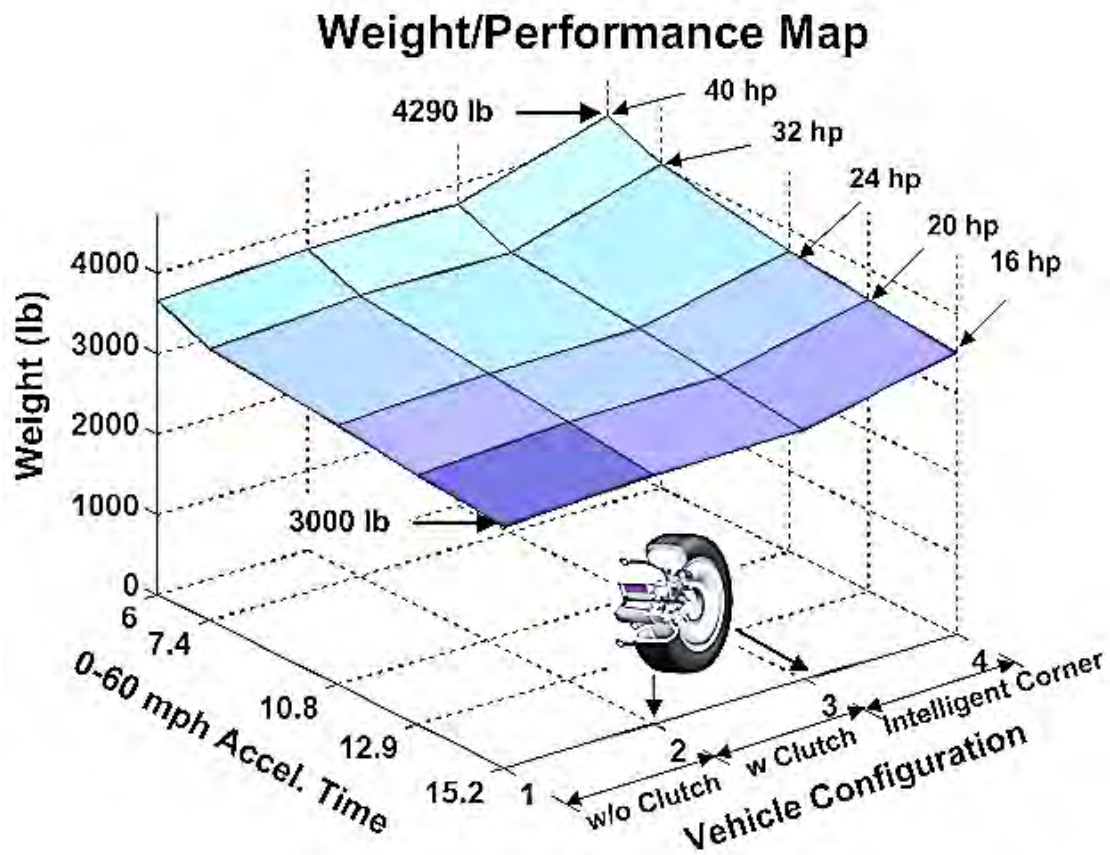


Figure 7-2: Weight map with respect to 0-60 mph acceleration time and vehicle components considering four independent wheels

Based on information as listed in Table 7-2 and Table 7-3, Figure 7-2 shows the weight performance map as a function of the acceleration time and selected vehicle components. As the rated power increases and vehicle configuration from '1' to '4' is selected, the associated vehicle weight increases. We note that there is nominal weight difference between vehicle configuration '2' and '3'.

7.1.3 Power

The Robotics Research Group (RRG) at the University of Texas at Austin has designed a first generation of the Multi-speed Hub Drive Wheel (MDW). The suggested motor powers of the MDW are 16, 20, 24, 32, up to 40 hp. Total effective power utilization rating of the hybrid electric vehicles equipped with four-independent MDWs are 64, 80, 96, 128, up to 160 hp.

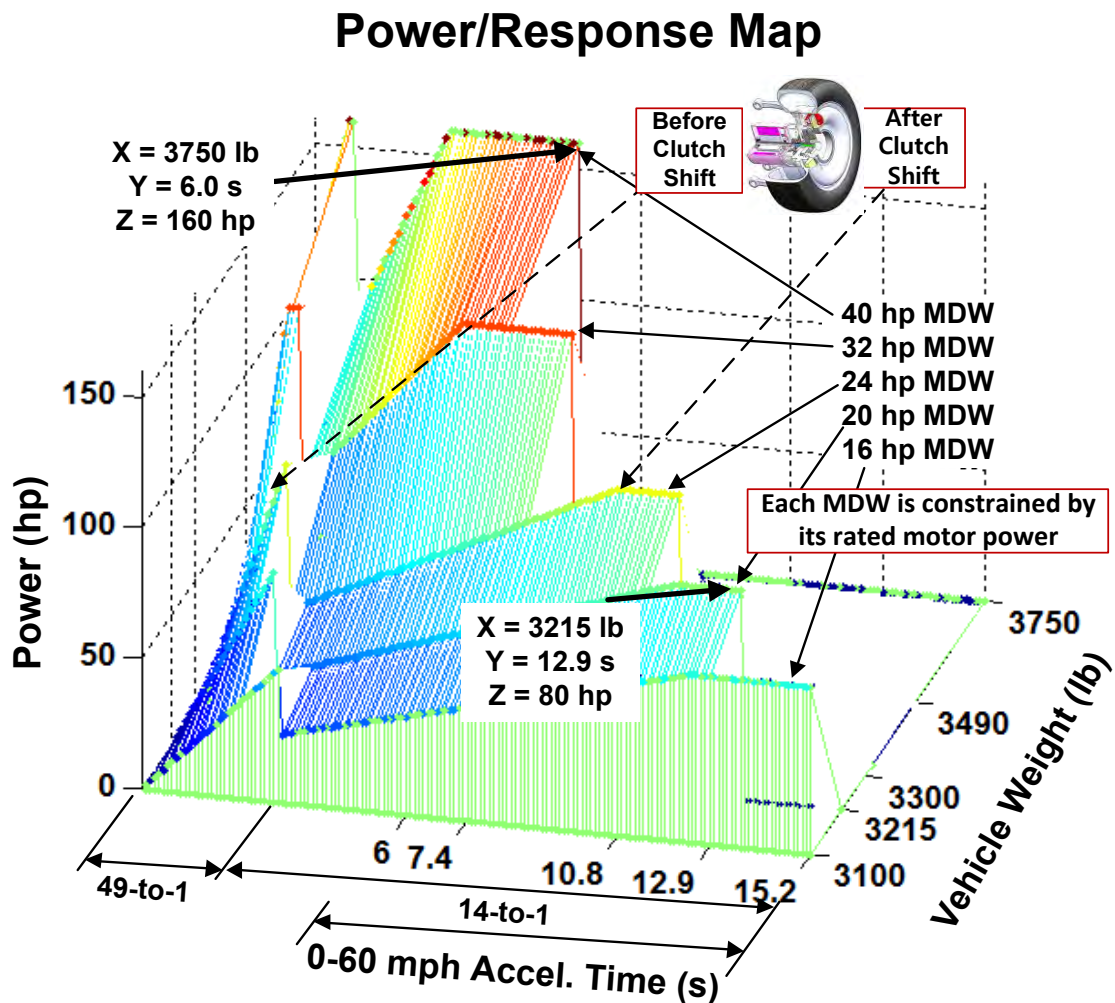


Figure 7-3: Power/Response map with respect to 0-60 acceleration time and vehicle weight considering four independent drive wheels

Assuming the electric vehicle is equipped with four independent MDW drive wheels, the power performance map as a function of vehicle weight and acceleration time is shown in Figure 7-3. In this figure, the rated power is assumed to be the maximum power.

In practice, electric motors can be operated at higher than their designed power rating for a short period of time[Guzzella and Sciarretta,2005]. According to [Vagati, Pellegrino et al.,2010], overload torque and power are acceptable for a couple of minutes and are limited by the inverter and battery maximum ratings and the effect of temperature rise. Temperature may be managed by on-demand cooling. That is, the maximum torque is determined by the inverter current, and the maximum power is limited by the battery unless we also use a super capacitor.

As mentioned in Section 6.4, the simulation has been carried out based on the different g levels corresponding to the power ratings. As the total power rating of a hybrid electric vehicle increases, the weight of the vehicle will necessarily also increase. Here, the power ratings are constrained by 64 hp to 160 hp. In this case, assuming four independent wheels, the 0-60 acceleration time is associated with 15.2 s (64 hp), 12.9 s (80 hp), 10.8 s (96 hp), 7.4 s (128 hp), and 6.0 s (160 hp).

From the power/response map as shown in Figure 7-3, it is clear that a very direct relationship exists between the power level choice and the customer desired acceleration (responsiveness).

7.1.4 Acceleration

From the customer point of view, acceleration is judged by the time required to go from 0 to 60 mph. As mentioned in Section 6.2, the 0-60 mph acceleration time can be simulated as shown in Figure 7-4. Given four independent MDWs, the 0-60 mph

acceleration times of the MDW (16 hp, 20 hp, and 24 hp) are 15.2 s, 12.9 s, and 10.8 s, respectively. The 0-60 mph acceleration times corresponding to the MDW (32hp) and MDW (40hp) are 7.3 s and 6.0 s. That is, the electric vehicle equipped with the four independent MDWs requires the motor power rating of 160 hp to achieve the very respectable 0-60 mph acceleration time of 6.0 s.

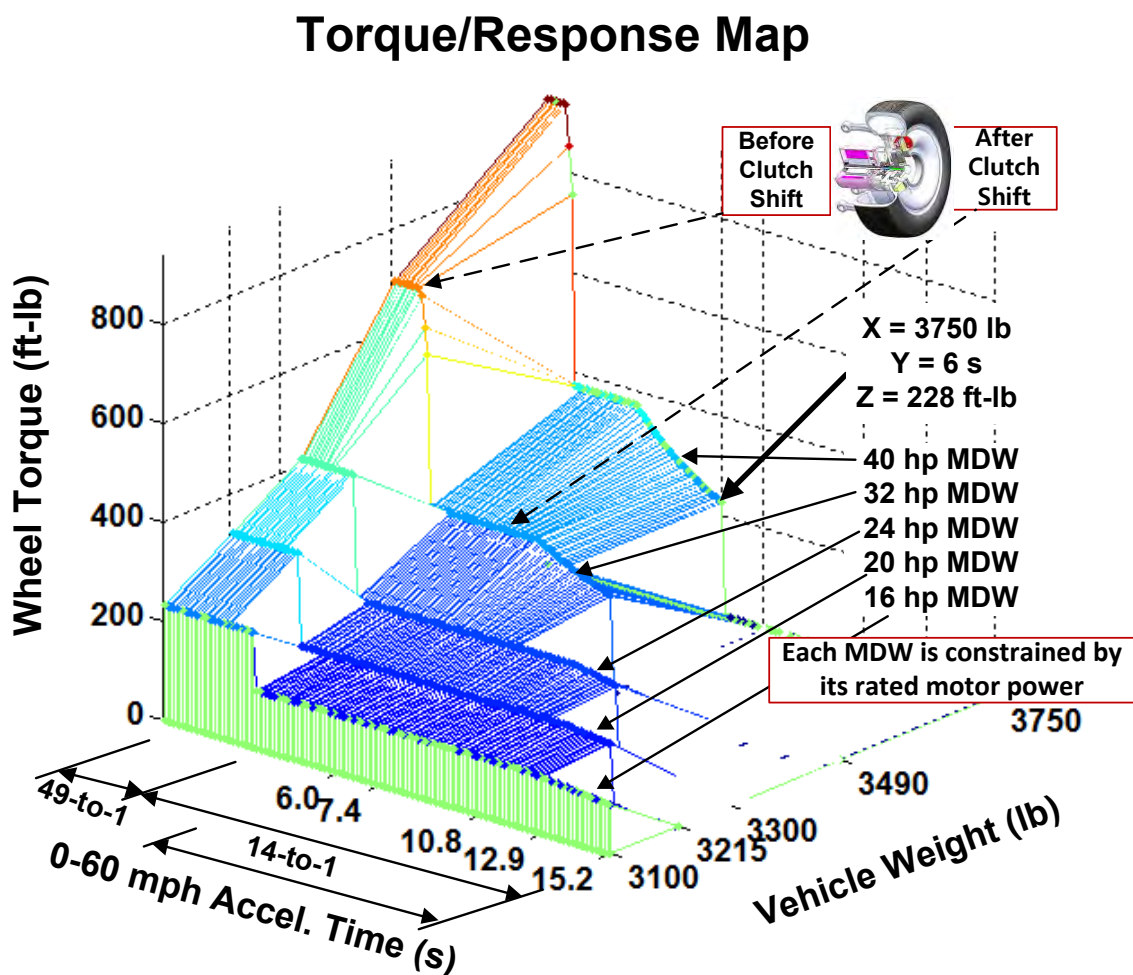


Figure 7-4: Torque/response map with respect to 0-60 acceleration time and vehicle weight considering four independent wheels

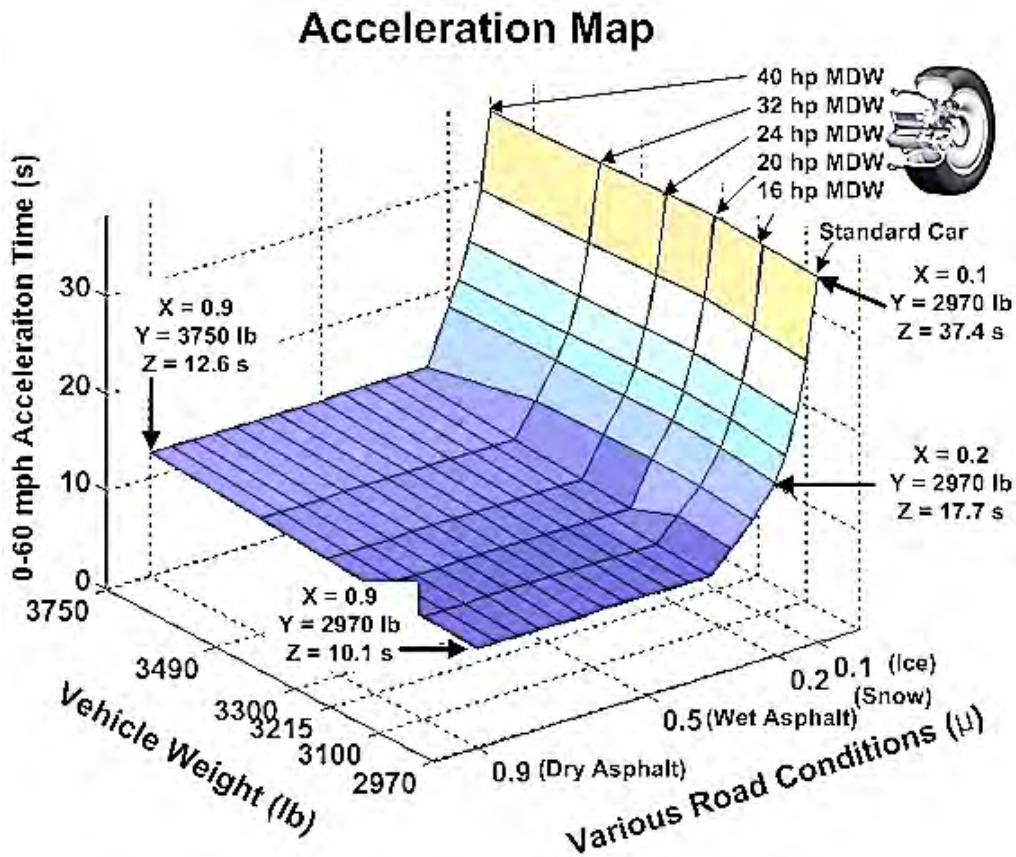


Figure 7-5: Acceleration map with respect to vehicle weight and various road conditions given constant torque (290 N-m (214 ft-lb))

As mentioned in Section 5.3.1 and 5.4.1, another acceleration performance map with respect to vehicle weight and various road conditions is shown in Figure 7-5. When the vehicle moves on a slippery road ($\mu = 0.35$), the wheel torque exceeds the limit of friction force between tire and road surfaces. In other words, the associated wheel is operated under inefficient traction resulting in (spinning) slip. In order to avoid this situation, simulations of the vehicle's response subjected to acceleration have been carried out based on the limitation of various road conditions, resulting in maintaining a force margin of 5 ~ 40 % (see Sections 4.4.7., 5.3.1 and 5.4.1). This leads to a lower

torque than the original torque of 290 N-m (214 ft-lb), thus increasing the 0-60 acceleration time. On an icy road ($\mu=0.1$), the 0-60 mph acceleration time of a standard car (2970 lb) is around 37.4 s, while the 0-60 acceleration time of a vehicle (3750 lb) is around 10.1 s on the dry asphalt road ($\mu=0.9$). Since an icy road has less friction, the 0-60 mph acceleration time on an icy road ($\mu=0.1$) is around 2 times longer than that on a snowy road ($\mu=0.2$); i.e., for the icy road (37.4 s) and for the snowy road (17.7 s). On the dry asphalt road, the 0-60 acceleration time of a standard car (2970 lb) is around 10.1 s, while the 0-60 acceleration time of a vehicle (3750 lb) is around 12.6 s.

7.1.5 Gradeability

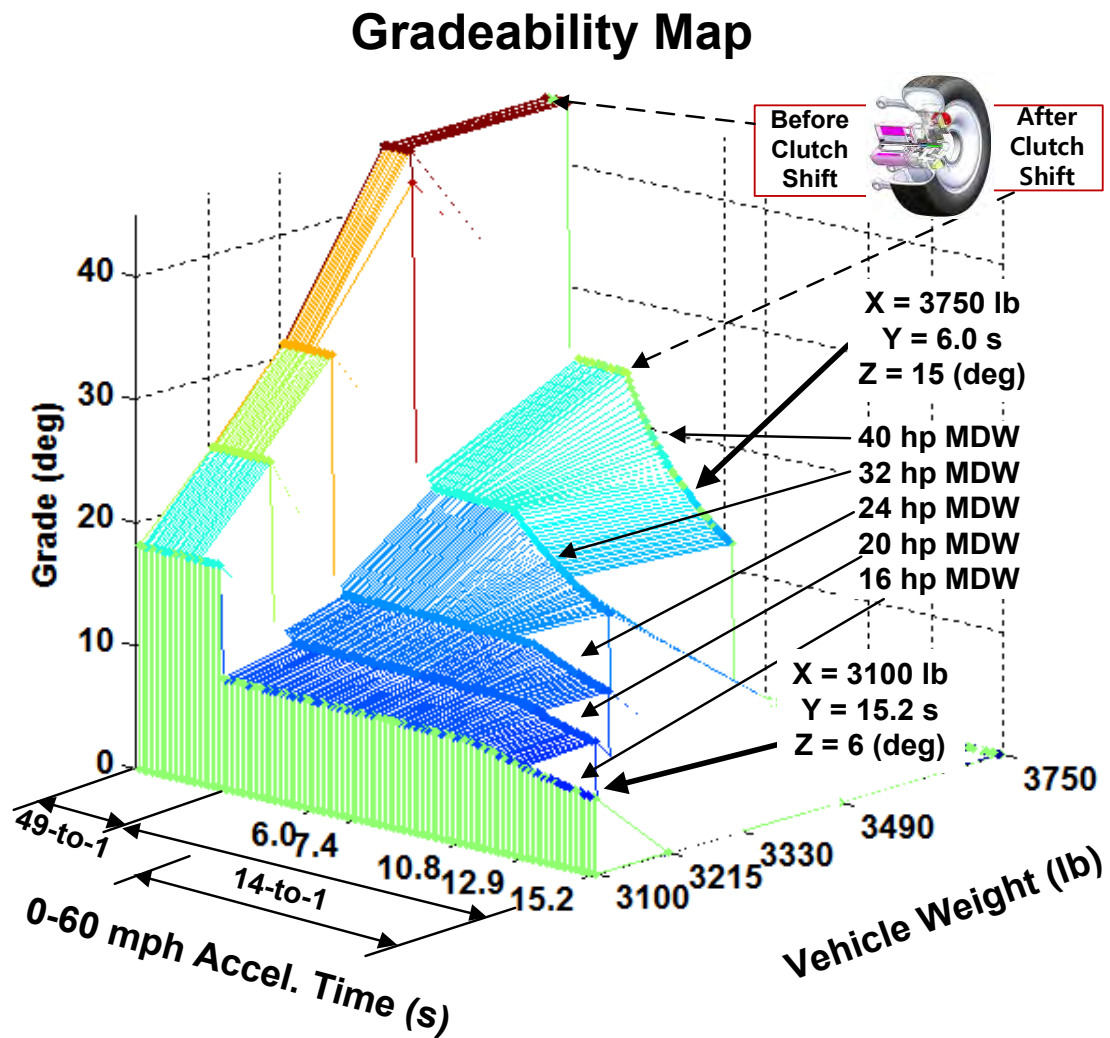


Figure 7-6: Gradeability map with respect to 0-60 mph acceleration time and vehicle weight considering four independent wheels

As mentioned in Section 6.4.2 and 6.4.3, the gradeability can be defined as the grade that the electric vehicle can manage at a certain constant speed. The maximum gradeability as a function of 0-60 mph acceleration time and vehicle weight is shown in Figure 7-6.

The maximum gradeability can be achieved using the 49-to-1 gear ratio. Maintaining cruising speed, while climbing a hill, is an important consideration for the design of the motor drive and power supply. At a given rated motor power (16 hp), while maintaining the cruising speed (60 mph), the maximum grade would be around 6°. This results from the net tractive effort (see Sections 6.4.2 and 4.1) which is the difference between tractive effort and sum of rolling resistance and aerodynamic resistance.

At a given rated motor power (40 hp), the maximum gradeability can be as high as 45° based on 49-to-1 gear ratio, which is before the clutch shift at 20 mph. After the clutch shift, the maximum grade can be around 29° based on 14-to-1 gear ratio. Furthermore, while maintaining the cruising speed (60 mph), the maximum grade can be around 15°, as shown in Figure 7-6.

7.1.6 Braking

7.1.6.1 Normal Braking (420 ft-lb)

The braking performance map can be defined as the 60-0 mph braking time which describes how fast a vehicle stops. Figure 7-7 shows the braking performance map with respect to vehicle weight and various road conditions. The constant braking torque of 420 ft-lb is assumed to be generated from both the caliper brake and the wheel motor.

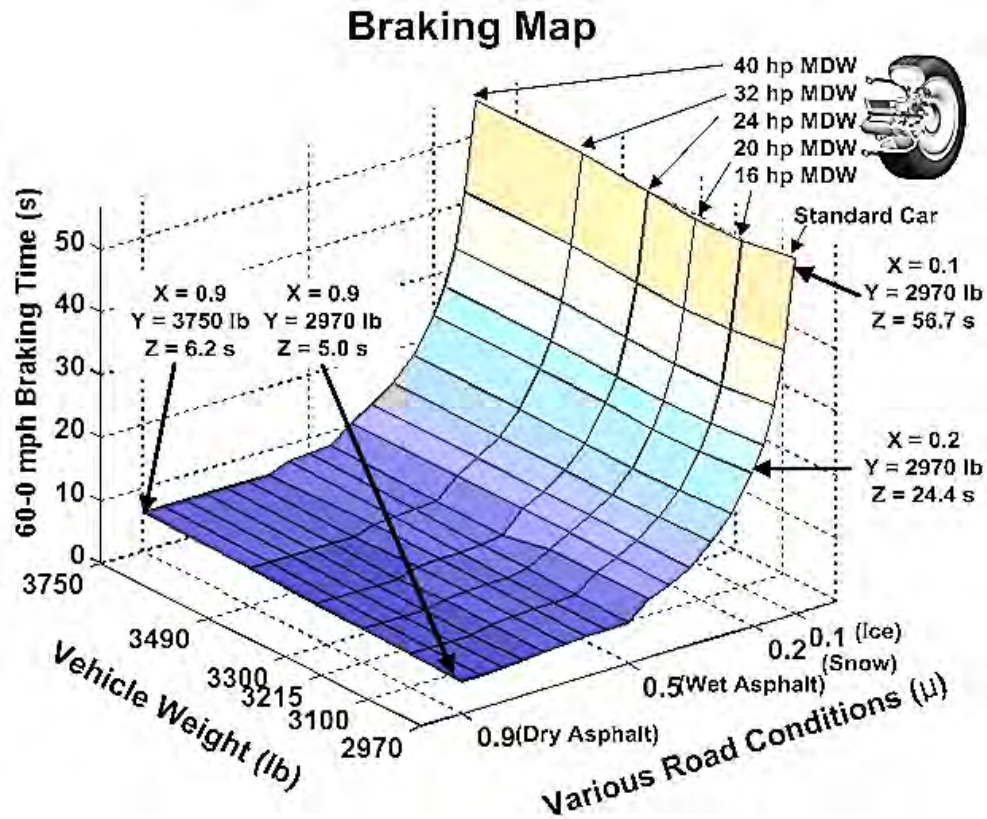


Figure 7-7: Braking map with respect to vehicle weight and various road conditions given constant braking torque (570 N-m(420 ft-lb))

As mentioned in Section 5.3.2 and 5.3.3, when a vehicle brakes on a road with a friction condition of $\mu = 0.7$, the wheel braking torque will exceed the limit of friction force between the tire and road surface. Once the wheel exceeds the saturation limit, the vehicle's wheels are locked and wheel sliding occurs. From the force margin point of view, the associated wheel is operated under insufficient traction which causes a skid (skidding/sliding). In order to avoid this situation, simulations of the vehicle's response subjected to braking have been carried out based on the limitation of various road conditions, resulting in maintaining a force margin of 5 ~ 40 % (see Sections 4.4.7., 5.3.2 and 5.4.2). This leads to a lower braking torque than the original braking torque of 420 ft-

lb, so that the 60-0 mph braking time increases rapidly. The force margin of each wheel on dry asphalt ($\mu = 0.9$) and snowy road ($\mu = 0.2$) are simulated as shown in Figure 7-8.

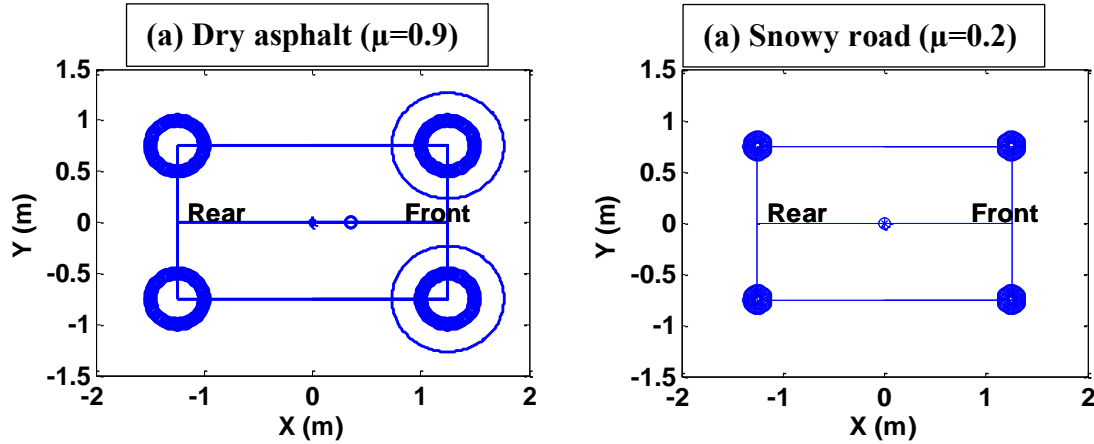


Figure 7-8: Force margin of each wheel on dry asphalt ($\mu=0.9$) and snowy road ($\mu=0.2$)

Figure 7-8 (a) shows the force margins which are visualized by using the friction circle of each wheel. The outside circle and thick circle indicate maximum and simulated friction circle, respectively (see Sections 5.2.1.1, 5.2.2.1, and 5.2.3.1). The difference between maximum and simulated friction circle indicates the force margin which represents the available traction force on each wheel of a vehicle.

Given the braking torque of 420 ft-lb and the dry asphalt road, the braking torque of 405 ft-lb is applied. The difference between 420 ft-lb and 405 ft-lb is due to the skid ratio (0.036), which is the ratio of the skid velocity as a percentage of the free rolling velocity (i.e., $\text{braking}(\text{skid}) = (v - r\omega) / v$) (see Section 4.4.4). This leads to braking time of 5 sec with a deceleration of 0.55 g, and stopping distance of 215 ft. On a snowy road of $\mu = 0.2$, the friction circle of each wheel becomes much smaller, resulting in a decreased braking torque of 87 ft-lb. This leads to braking time of 24.4 s with a deceleration of 0.11 g, and stopping distance of 1128 ft. On the icy road, the 60-0 braking

time is around 56.7 s, while it is around 5 s on the dry road. Since an icy road has less friction, the 0-60 acceleration time on an icy road is approximately 2 times longer than that on a snowy road on an icy road (56.7 s) and a snowy road (24.4 s).

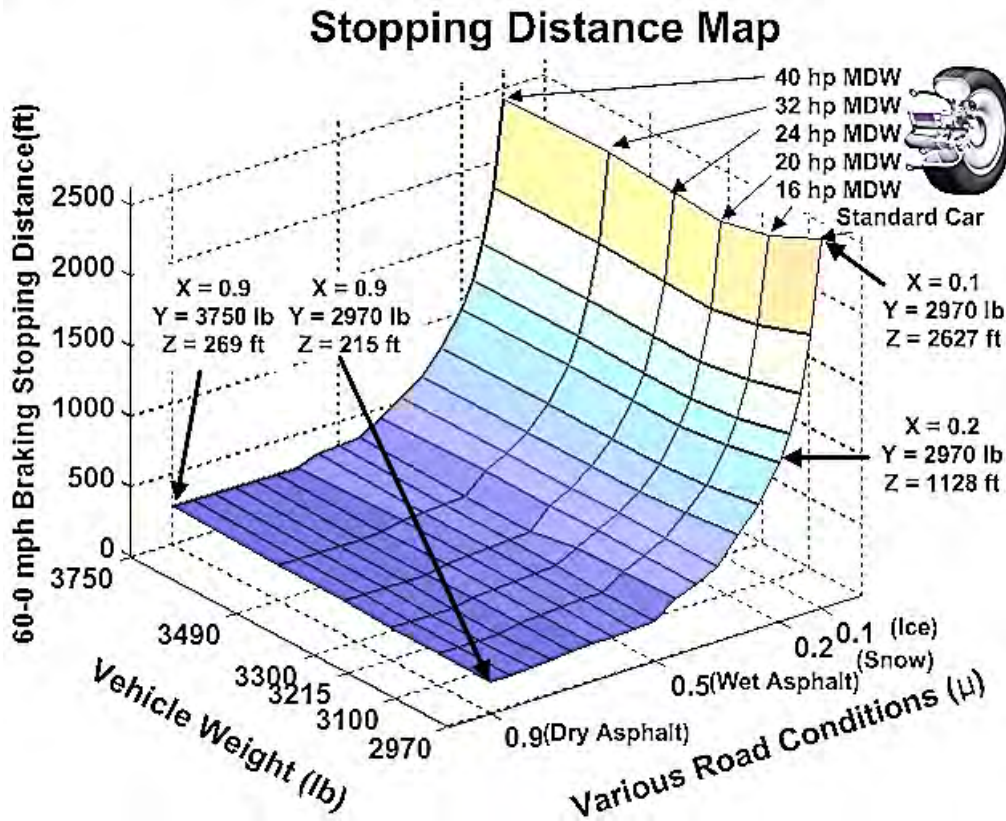


Figure 7-9: Stopping distance map with respect to vehicle weight and various road conditions given constant braking torque (570 N-m(420 ft-lb))

Figure 7-9 shows the stopping distance map as a function of vehicle weight and various road conditions given constant torque. On the dry asphalt road of $\mu=0.9$ and given vehicle weight of 2970 lb, stopping distance is around 215 ft, while it is around 269 ft given a vehicle weight of 3750 lb. On the snow road of $\mu=0.2$ and given a vehicle weight of 2970 lb, stopping distance is around 1128 ft. On the icy road of $\mu=0.1$ and

given a vehicle weight of 2970 lb, stopping distance is around 2627 ft (essentially uncontrolled stopping)

As mentioned in Section 5.1.2, the performance metric of braking distance (60-0 mph) is 130 ~ 145 ft in terms of passenger vehicles [Wei and Rizzoni,2004]. Consumer Reports [Consumer-Reports,2012] shows that the braking performance of passenger vehicles is around 135 ft (41 m): Hyundai Sonata (134 ft), Toyota Camry (130 ft), and Chevrolet Equinox (138 ft). The deceleration of these vehicles would be 0.9 g.

7.1.6.2 Emergency Braking (840 ft-lb)

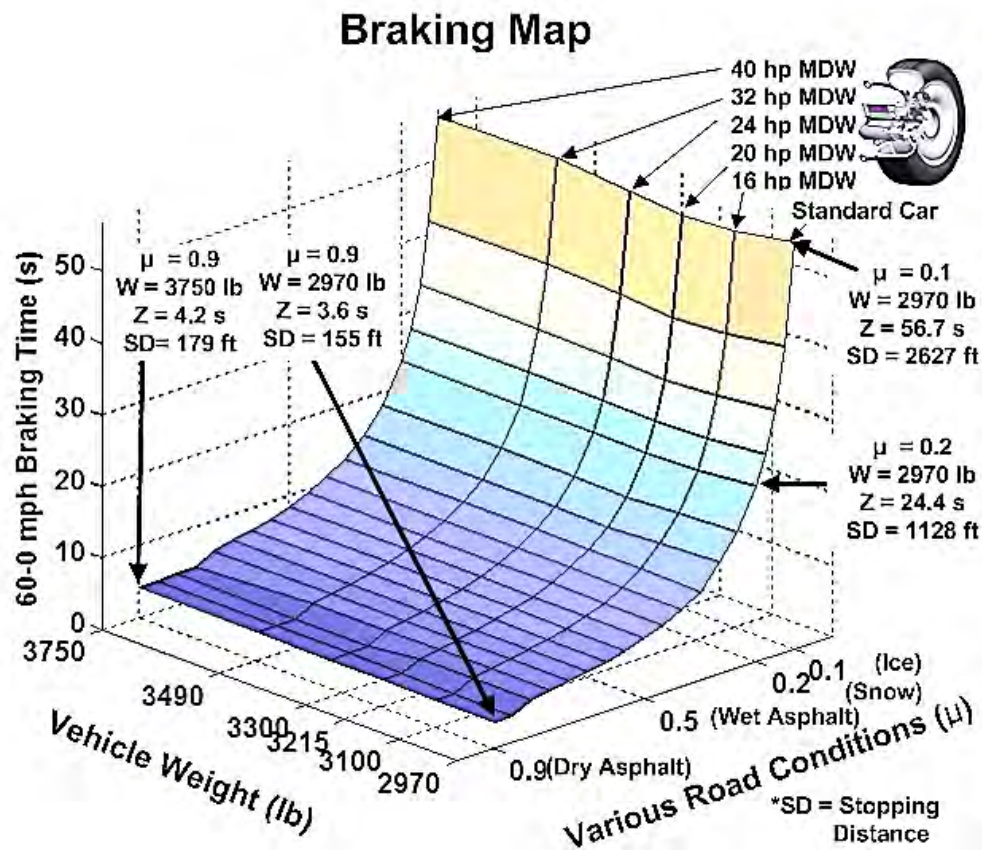


Figure 7-10: Braking map with respect to vehicle weight and various road conditions given constant braking torque (1140 N-m (840 ft-lb))

Figure 7-10 shows the braking performance map with respect to vehicle weight and various road conditions. Considering emergency braking, simulations of the vehicle's response subjected to braking have been carried out based on the braking torque of 840 ft-lb. In the same manner, the force margin of each wheel on dry asphalt and snowy road are simulated as shown in Figure 7-11.

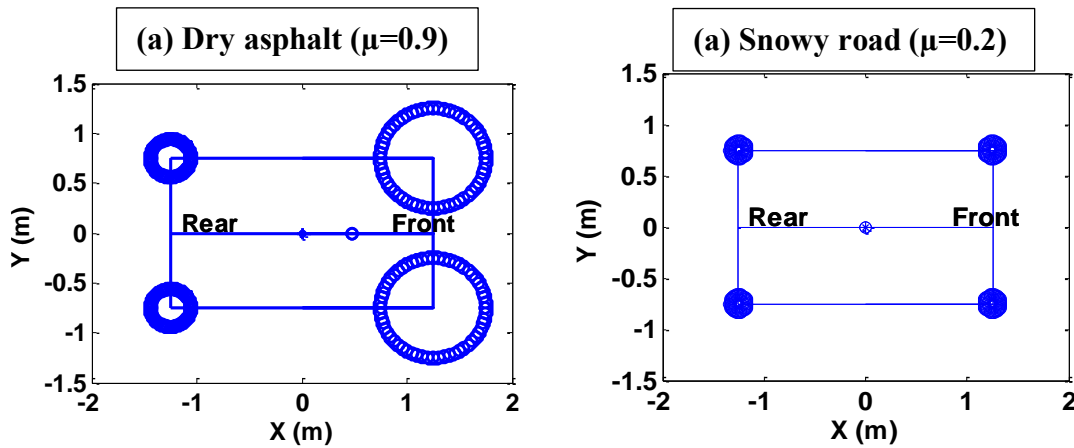


Figure 7-11: Force margin of each wheel on dry asphalt ($\mu=0.9$) and snowy road ($\mu=0.2$)

Figure 7-11 (a) shows the force margins which are visualized by using the friction circle of each wheel. Given the braking torque of 840 ft-lb and the dry asphalt road, the braking torque of 820 ft-lb is applied to the front wheels and the braking torque of 302 ft-lb is applied to the rear wheels. This occurs because the available traction on the front wheels is significantly larger than that on the rear wheels.

This leads to braking time of 3.6 s, a deceleration of 0.76 g, and a stopping distance of 154 ft. When it comes to a snowy road of $\mu = 0.2$ and an icy road of $\mu=0.1$, simulation results are the same as previous results.

Figure 7-12 shows the stopping distance map as a function of vehicle weight and various road conditions given constant braking torque of 840 ft-lb. On a dry asphalt road

of $\mu = 0.9$ and given a vehicle weight of 2970 lb, stopping distance is around 155 ft, while it is around 179 ft given a vehicle weight of 3750 lb. Simulation results on the snowy road of $\mu = 0.2$ and the icy road of $\mu = 0.1$ are the same result in Section 7.1.6.1.

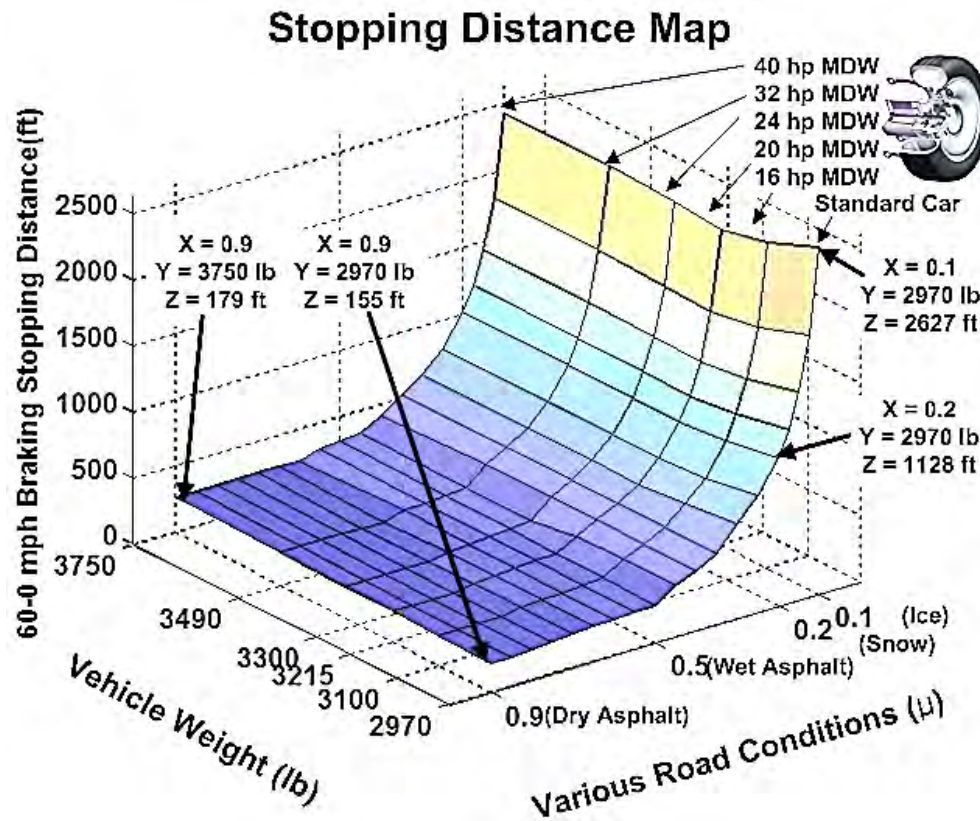


Figure 7-12: Stopping distance map with respect to vehicle weight and various road conditions given constant braking torque (570 N-m(420 ft-lb))

As mentioned in Section 5.1.2, the stopping distance can be obtained from $SD = v^2 / 2a$, where v is the velocity (ft/s), and a is the acceleration. The stopping distance is proportional to the square of the initial velocity.

Stopping Distance Map

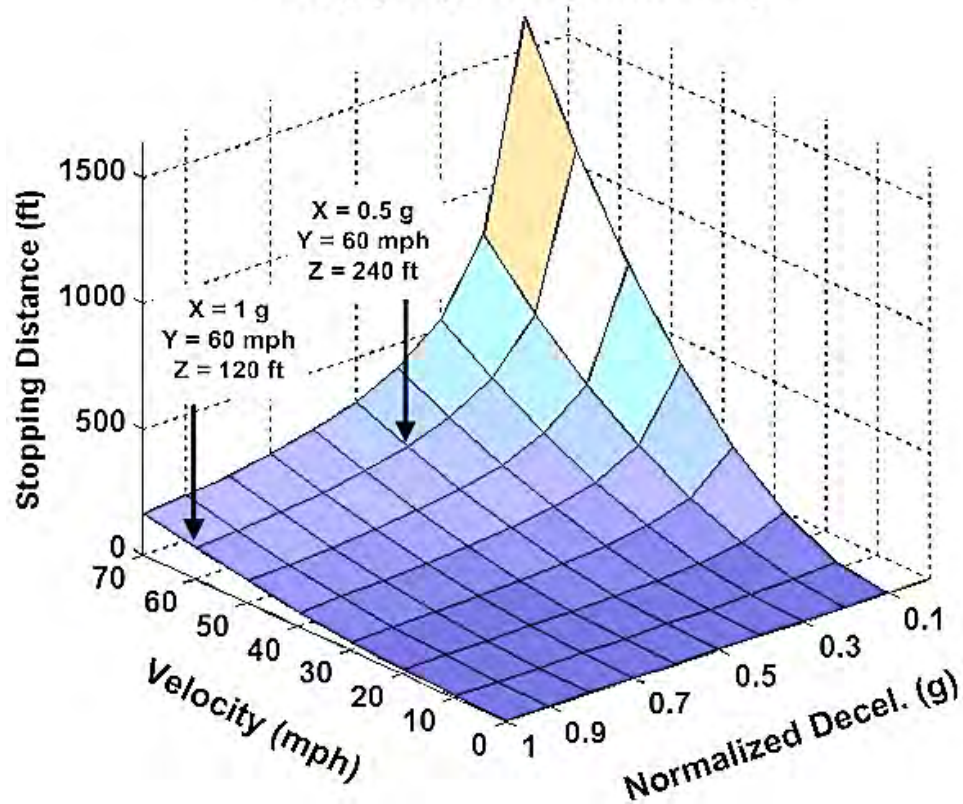


Figure 7-13: Stopping distance map with respect to velocity and normalized deceleration

Using simple equation, Figure 7-13 shows the stopping distance map as a function of velocity and normalized deceleration. Given the normalized deceleration of 1 g, the 60-0 mph stopping distance is around 120 ft. Given the normalized deceleration of 0.5 g, the stopping distance is 240 ft.

7.1.7 Handling

As mentioned in Section 4.2.1.1, dynamic contact force is a measure of a vehicle's handling capability. It conceptually can be obtained by multiplying tire stiffness with tire deflection, which is a useful measure of road holding and handling.

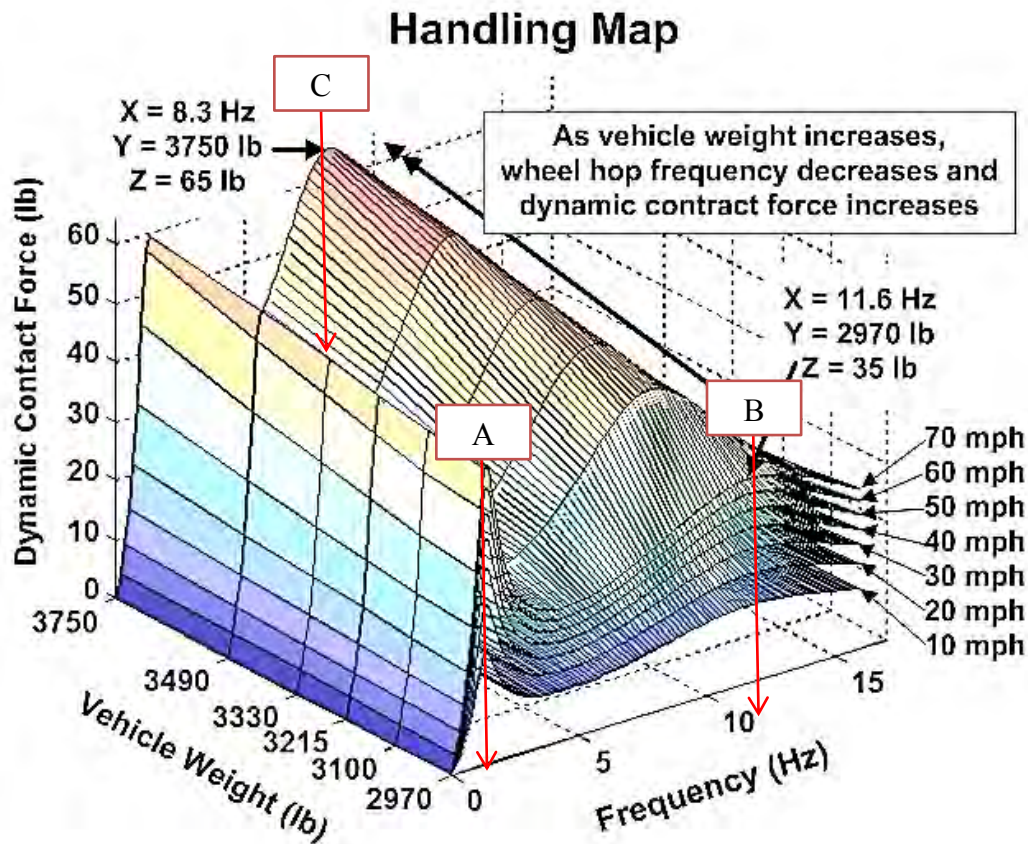


Figure 7-14: Dynamic contact force with six different vehicle weights under a random average (asphalt) road input, as speed increases from 10 mph to 70 mph

Figure 7-14 shows the frequency response of dynamic contact force output as a function of vehicle weight and frequency for seven different speeds ranging from 10 mph to 70 mph. As the vehicle weight increases, the second natural frequency which is the wheel hop frequency decreases and the dynamic contact force increases. The increased

dynamic contact force leads to deteriorating traction required for acceleration, braking, or cornering.

	A (1.3 Hz)	B (11.6 Hz)	C (8.3 Hz)
70 mph	50.3	34.5	65.2
60 mph	46.6	32.0	60.4
50 mph	42.5	29.1	55.0
40 mph	37.8	26.1	49.3
30 mph	32.7	22.6	42.7
20 mph	26.7	18.5	34.8
10 mph	19.0	13.1	24.4

Table 7-4: Speed Related Performance Values

The performance values indicated by symbol ‘A’, ‘B’, and ‘C’ in Figure 7-14 are listed in Table 7-4. The symbol ‘A’ is associated with sprung mass natural frequency given a standard car (2970 lb). The symbol ‘B’ and ‘C’ are associated with wheel hop frequency of vehicle weight of 2970 lb and 3750 lb, respectively. Regarding the sprung mass natural frequency, dynamic contact force under the 70 mph condition is 2.5 times larger than that for 10 mph. In addition, as the vehicle weight increases, dynamic contact force increases at the wheel hop frequency. This means that the traction force margin goes down as the dynamic contact force goes up.

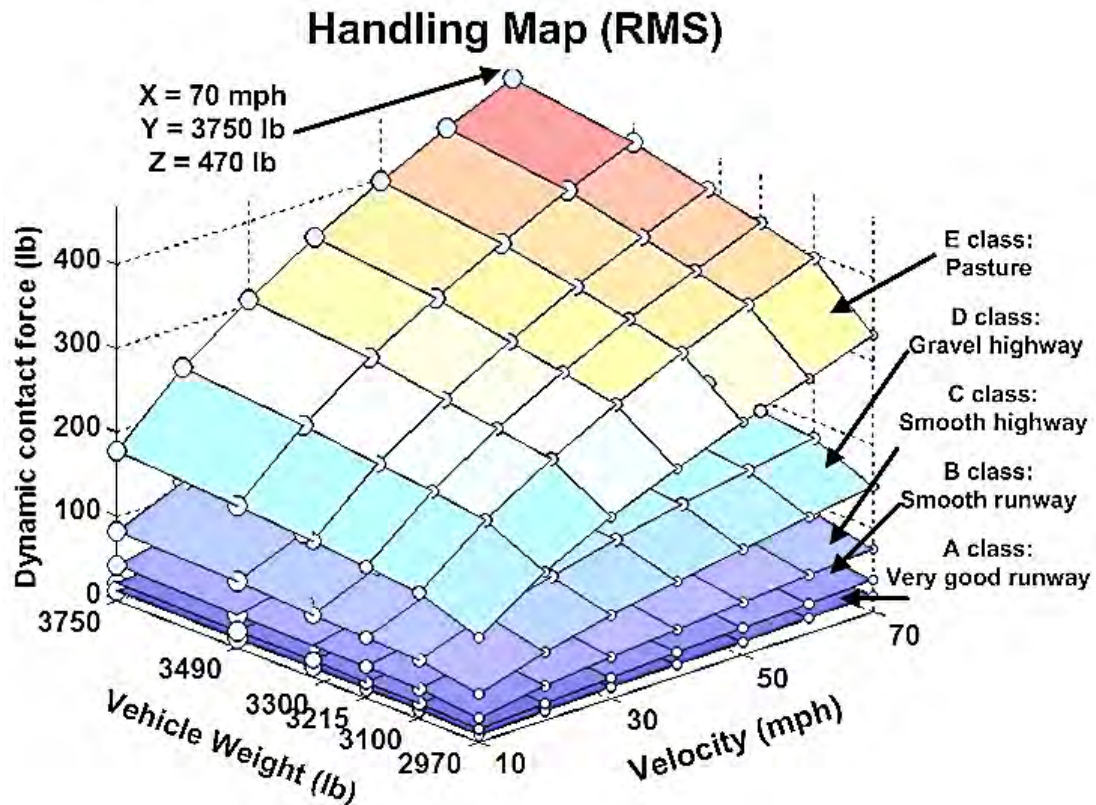


Figure 7-15: Handling performance map (dynamic contact force) with respect to six different vehicle weight and velocity in terms of five classes of road surfaces

Figure 7-15 shows the handling performance map (dynamic contact force(RMS)) as a function of the vehicle weight and velocity in terms of five classes of road surfaces which were presented by the International Organization for Standardization (ISO) and classified as ISO 8608:1995[Wong,2008]. The road surfaces are classified as follows: A class (very good runway), B class (smooth runway), C class (smooth highway), D class (gravel highway), and E class (pasture). As mentioned in Section 4.2.1.1, the dynamic contact force (RMS) in this figure is obtained from the integral of the power spectral density over the frequency band. Clearly, it is apparent that the handling performance of a vehicle worsens as the severity of the road and the vehicle weight increases.

According to [Murata,2011], an in-wheel motor can be used for suppressing the variations in the ground contact force using a different driving force of the front and rear wheels. The dynamic contact force as shown in Figure 7-15 will be decreased, so that the traction can be improved by applying the driving force or braking force at the time of bouncing of the vehicle body.

According to “World View of Research for Electric Vehicle Intelligent Corner” [Tesar,2011, August], the active suspension actuators would be used to balance the need for the undisturbed vehicle motion (i.e., ride comfort) and the need for maximizing the contact forces (i.e., drivability and safety). Furthermore, intelligent corner decision making (in milli-sec) can maintain balance between reduced contact force and increased contact force so that available traction force can increase in curves or rough roads by perhaps 50%.

7.1.8 Ride Comfort

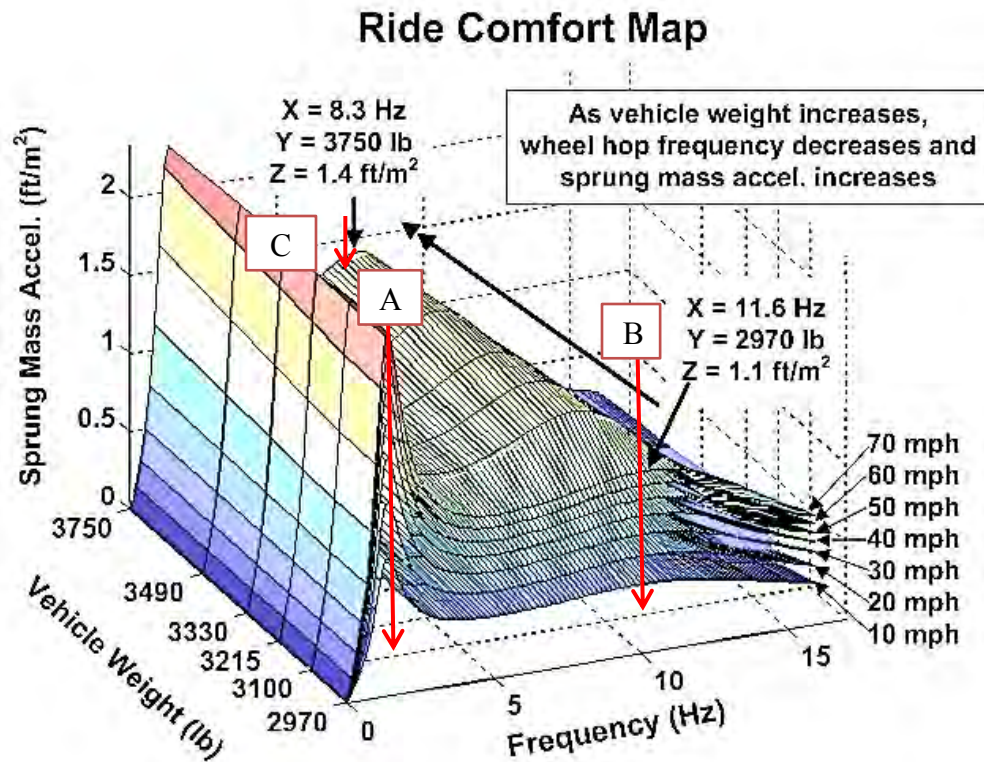


Figure 7-16: Sprung mass acceleration with six different vehicle weights under a random average (asphalt) road input, as speed increases from 10 mph to 70 mph

As mentioned in Section 4.2.1.3, the sprung mass acceleration is a measure of how comfortable a car ride feels. One measure of ride comfort can be quantified in terms of the vertical acceleration of a vehicle body. Figure 7-16 shows the performance map of the sprung mass acceleration output as a function of the vehicle weight and frequency with seven different speeds from 10 mph to 70 mph. As the vehicle weight increases, the second natural frequency which is the wheel hop frequency decreases and the sprung mass acceleration increases. The increased sprung mass acceleration leads to deteriorating ride comfort.

The performance values indicated by symbol ‘A’, ‘B’, and ‘C’ are listed in Table 7-5. The symbol ‘A’ is associated with sprung mass natural frequency given a standard car (2970 lb). The symbol ‘B’ and ‘C’ are associated with wheel hop frequency of vehicle weight of 2970 lb and 3750 lb, respectively.

	A (1.3 Hz)	B (11.6 Hz)	C (8.3 Hz)
70 mph	2.3	1.16	1.41
60 mph	2.1	1.07	1.30
50 mph	1.9	0.98	1.20
40 mph	1.7	0.87	1.07
30 mph	1.5	0.76	0.93
20 mph	1.2	0.62	0.76
10 mph	0.9	0.41	0.53

Table 7-5: Speed Related Vertical Body Acceleration Performance Values

Regarding the sprung mass natural frequency, sprung mass acceleration under 70 mph conditions is 2.5 times larger than that for 10 mph. In addition, as the vehicle weight increases, sprung mass acceleration increases at the wheel hop frequency as shown at ‘C’, deteriorating ride comfort.

Research[Katsuyama and CORPORATION,2011; Murata,2011] shows that an in-wheel motor can control the vertical motion of the sprung mass using an independently controlled driving force of the front and rear wheels. In their simulation, the sprung mass acceleration around sprung mass natural frequency (1.3 Hz) was significantly reduced. This indicates that in-wheel motor drives can provide some active ride control.

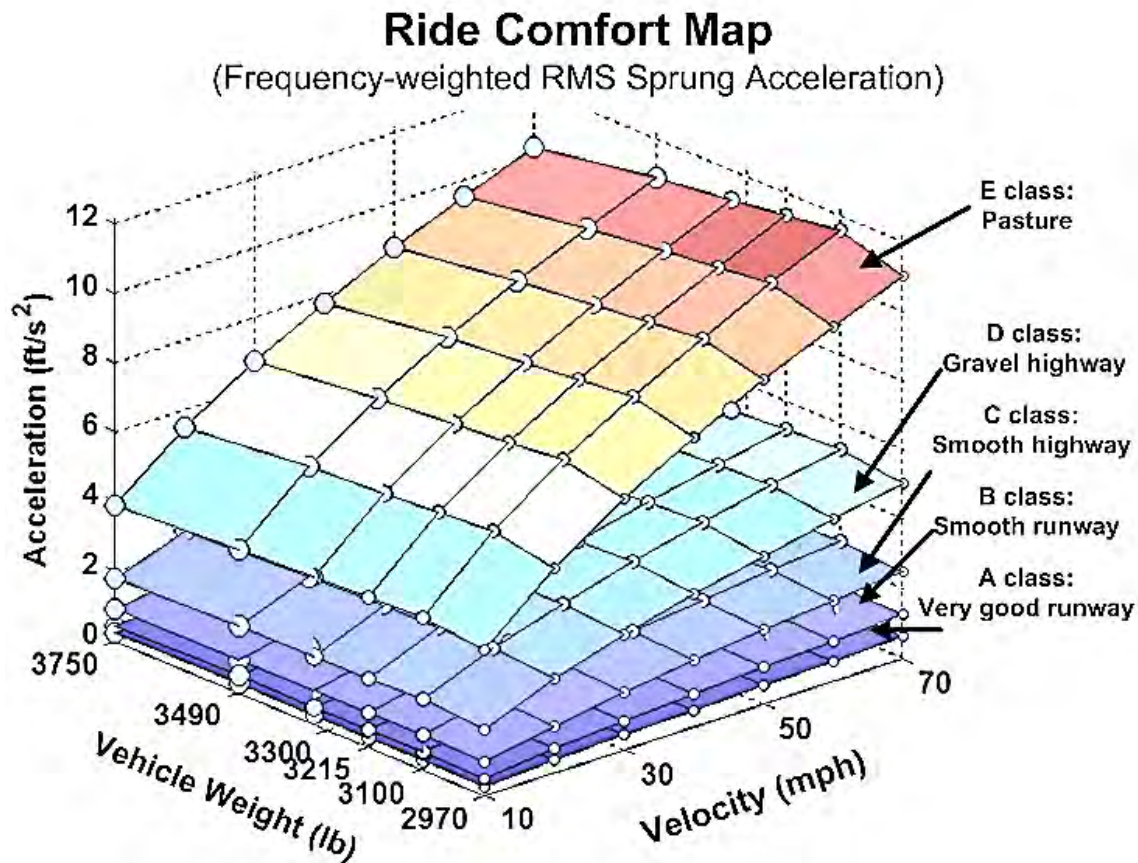


Figure 7-17: Ride comfort map (frequency weighted RMS sprung acceleration) with respect to six different vehicle weights and velocity in terms of five classes of road surfaces

Figure 7-17 shows the ride comfort performance map (frequency-weighted RMS sprung acceleration) as a function of the vehicle weight and velocity for five classes of road surfaces which were presented by the International Organization for Standardization (ISO) and classified into ISO 8608:1995[Wong,2008]. As mentioned in Section 4.2.1.3, it can be seen that the frequency-weighted RMS sprung acceleration increases rapidly, as the road surface deteriorates. However, as the vehicle weight varies from 3100 lb to 3750 lb, the frequency-weighted RMS sprung acceleration decreases slightly (as expected).

7.1.9 Efficiency

As mentioned in Section 6.1.7 and 6.3, we project that the MDW can have a high efficiency over its entire torque-speed profile by raising and flattening the efficiency sweet spot.

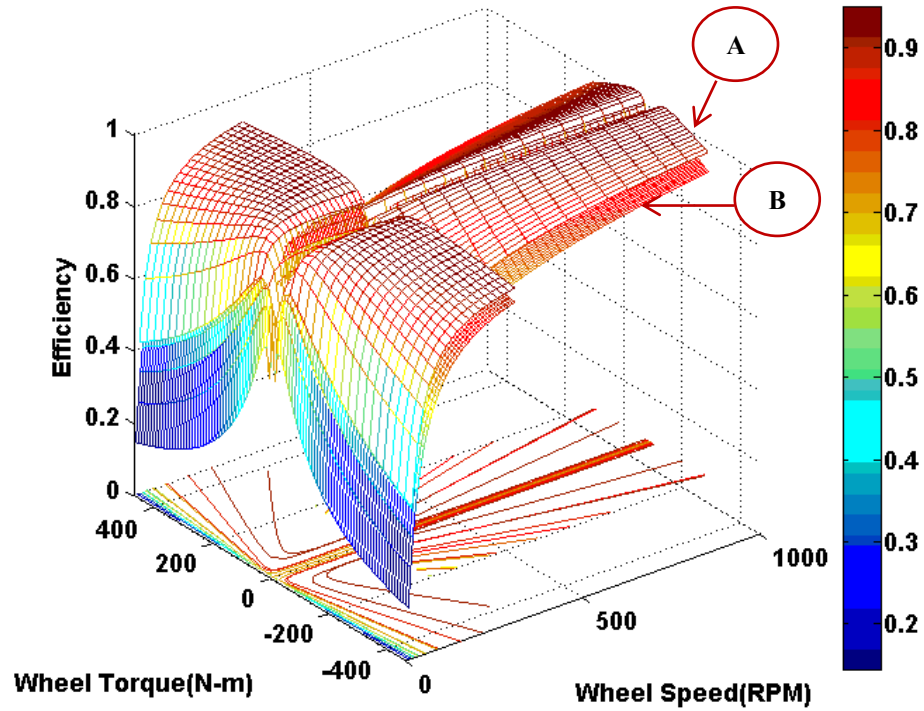


Figure 7-18: Efficiency maps of an MDW without & with a reconfigurable controller

Simulated efficiency maps of an MDW without & with a reconfigurable controller are shown in Figure 7-18. As seen at symbol 'A', this is the efficiency map of an MDW with a reconfigurable controller. Without a reconfigurable controller, the symbol 'B' indicates the efficiency map of an MDW. For the UDDS duty cycle, the efficiency of an MDW with and without a reconfigurable controller is calculated as

85.8 % and 88.2 %, respectively. It is suggested then that the MDW with a reconfigurable controller has a higher efficiency by a further 2.4 %.¹

7.1.10 Durability

As mentioned in Section 2.7, durability is related to the remaining useful life (condition-based maintenance) which is influenced by duty cycles. The equivalent dynamic load can be obtained from[Koran and Tesar,2008]:

$$P = \sqrt[3]{\sum_{i=1}^n P_i^3 \times \frac{V_i}{V_{mean}} \times \frac{t_i}{\Delta T}} \quad (7.1)$$

where P_i is the load for each data point, t_i is the time period of each sample, ΔT is the cycle period, and V_i / V_{mean} is the velocity duty cycle for each data point.

Bearings are expected to be the principal component in the MDW to fail first and can therefore be used as an indication of its durability. Bearing fatigue life (millions of revolutions) can be expressed as:

$$L_{10h} = \frac{10^6}{60n} \left(\frac{C}{P} \right)^3 \quad (7.2)$$

where n is RPM, L_{10h} is the bearing life in hours, C is the dynamic load rating of the bearing associated with a purely radial load that 90 % of a group of the same bearings reach a life of 10^6 cycles before they fail as a result of fatigue [Brandlein,1999]. The dynamic load rating (C) is selected as 10116 lb. If we choose a higher dynamic load rating in 40 hp MDW, the durability will be improved (see Section 2.7).

1. In contrast, the single speed Protean in-wheel drive offers a 73.8% efficiency for this whole duty cycle (see Section 6.3).

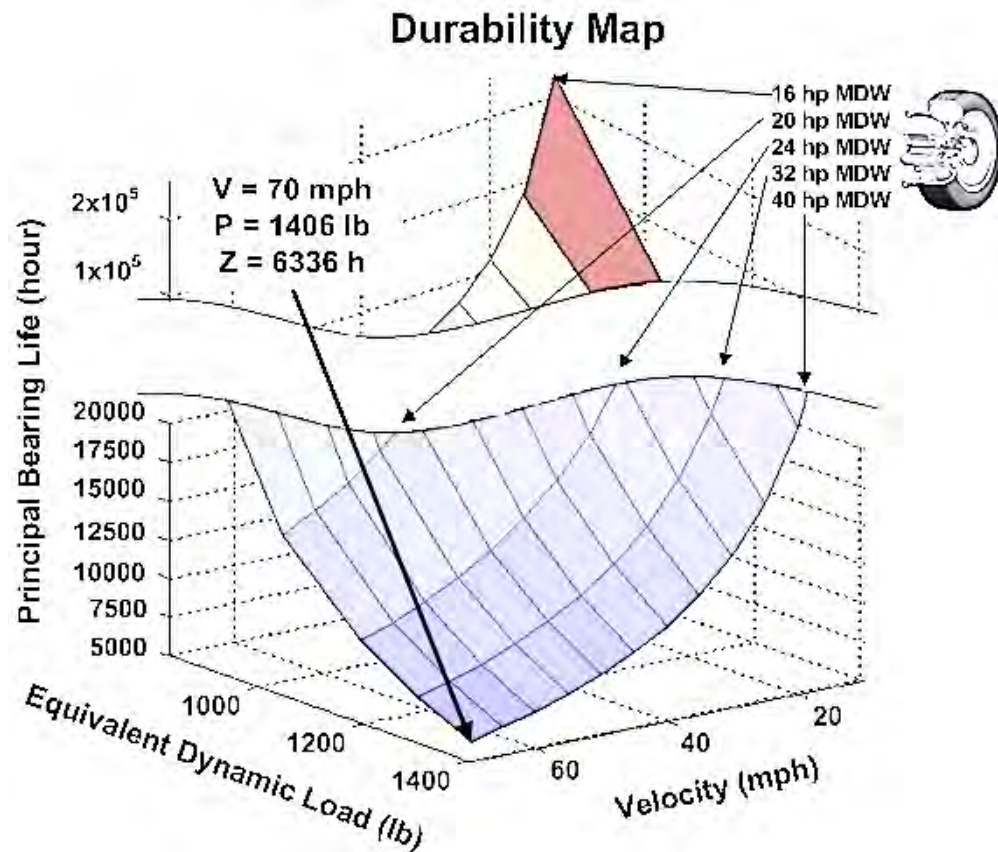


Figure 7-19: Durability map with respect to equivalent dynamic load and velocity

In terms of different sizes for the MDWs, a representative durability map as a function of equivalent dynamic load and velocity are shown in Figure 7-19. The velocity at each point is assumed to be steady-state condition.

As velocity and equivalent dynamic load increases, the principal bearing life decreases. This gives great insight how durability varies as a function of driving velocity. It can be seen that a hybrid vehicle equipped with four MDWs (40 hp) can operate at 70 mph for 6336 hours, given the equivalent dynamic load of 1406 lb.

7.2 OPERATION CRITERIA

7.2.1 Cornering Force Margin

From an operation standpoint, a driver can perceive situational awareness of all operational capability[Tesar,2011, August]. For instance, the force margin can be used to assist the driver to perceive situational awareness. Assuming there is adequate power from the MDW, the traction limit is influenced by various road conditions (i.e., friction coefficient between the tire and road). With these constraints, the needed performance maps will be generated based on the Simulink model of a 14 DOF full-vehicle model (see Section 4.5).

The force margin performance map during a cornering maneuver can be defined as how much traction force is available for control. As mentioned in Section 5.3.3 and 5.4.3, Figure 7-20 (a) – (d) show the force margin performance map of a rear-inside, front-inside, rear-outside, and front-outside wheel during a cornering maneuver in a single-lane change (i.e., single sinusoidal amplitude is 2 degree, and velocity is 60 mph). It should be noted that a zero value for the force margin indicates that the wheel's traction force is saturated, so that a vehicle starts skidding, and this leads to unstable vehicle motion.

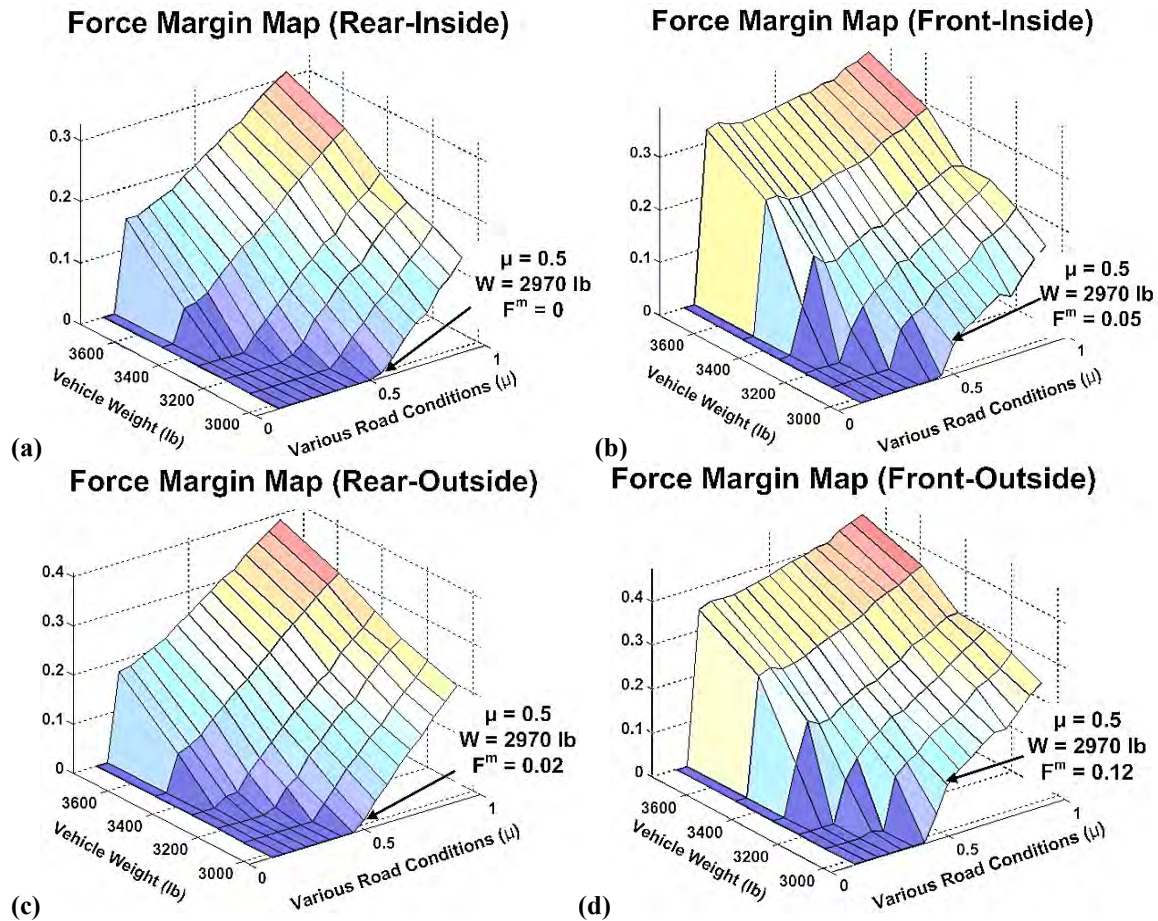


Figure 7-20: Force margin map with respect to vehicle weight and various road conditions for a single-lane change

Figure 7-20 (a) – (d) show the minimum force margin (F^m) performance map of rear-inside, front-inside, rear-outside, and front-outside wheels during a cornering maneuver in a single-lane change. When a vehicle runs on a wet road of $\mu = 0.5$, minimum force margin (F^m) of each wheel becomes 0% (rear-inside), 5% (front-inside), 2% (rear-outside), and 12% (front-outside) indicated by arrows.

It can be seen that the force margin of outside wheels is larger than that of inside wheels. This occurs because the normal force of outside wheels is larger than that of inside wheels (see Section 5.2.2.2). In addition, it is apparent that the force margin of

front wheels is larger than that of rear wheels. This is due to the fact that the lateral acceleration at the CG causes the rear slip angle to increase more than the front slip angle, resulting in larger lateral forces to counteract the lateral acceleration. This is called oversteer behavior (see Sections 4.3.1, 5.2.1.2, 5.2.2.2, and 5.2.3.2). The increased vehicle weight has little effect on the force margin of each wheel. We will discuss the effect of various road conditions on the front and rear slip angle.

7.2.2 Roll Angle

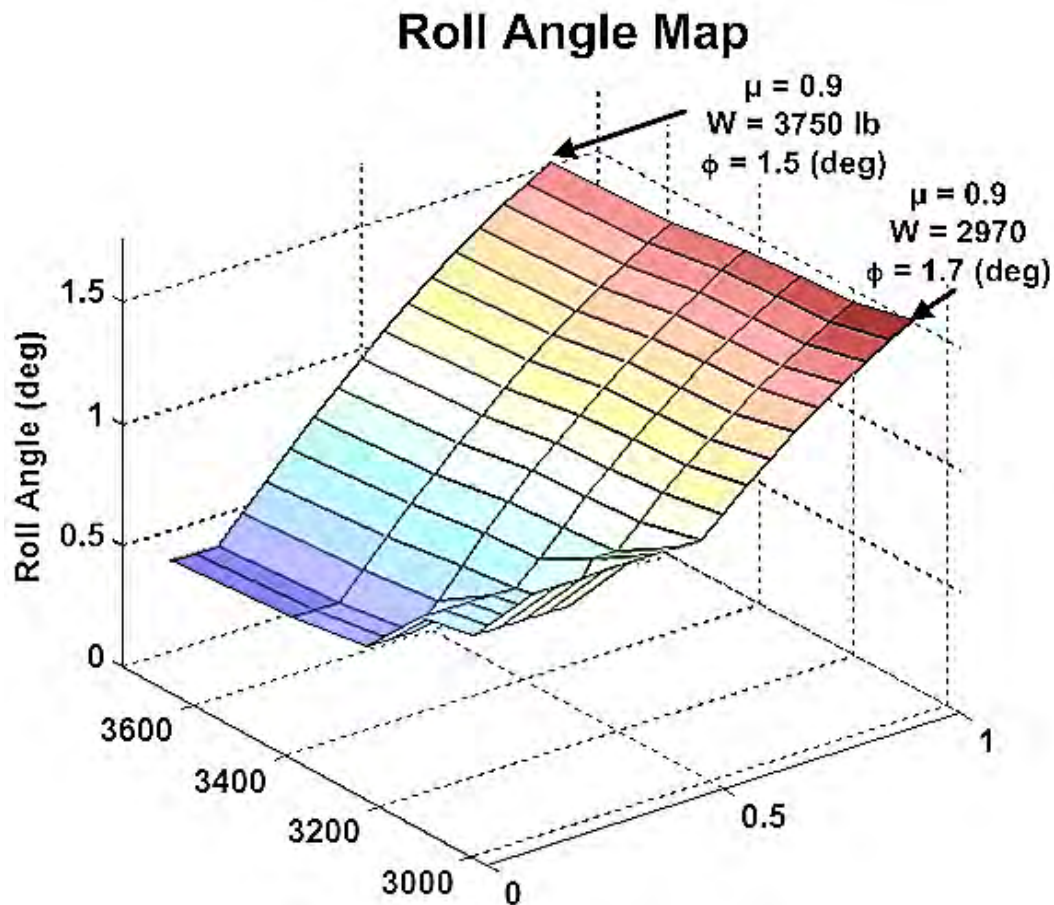


Figure 7-21: Roll angle map with respect to vehicle weight and various road conditons

Many studies have been evaluated for the roll angle (ϕ) response to step steer [Ghike and Shim,2006; Shim and Ghike,2007; Zhao, Chen et al.,2011]. As mentioned in Section 5.1.3, the roll angle can be used as a measure of the vehicle's handling performance. Figure 7-21 shows the roll angle map as a function of vehicle weight and various road conditions such as dry asphalt, wet asphalt, and snowy road. The values of the roll angle are maximum required values during a cornering maneuver in a single-lane change.

As the vehicle weight increases, the roll angle decreases from 1.7° to 1.5° as indicated by arrows. This is attributed to increased roll inertia of the sprung mass with respect to the vehicle roll center (see Section 4.3.2).

7.2.3 Sideslip Angle

As mentioned in Section 4.3.1 and 5.1.3, the side slip angle (β) is defined as the angle between the vehicle heading and the vehicle velocity direction due to the compliance of the pneumatic tire. Many studies have been evaluated for the sideslip angle response to a cornering maneuver [An, Yi et al.,2008; Baffet, Charara et al.,2009; Gao,2010; Hsu, Laws et al.,2010; Suzuki and Ikeda,2010].

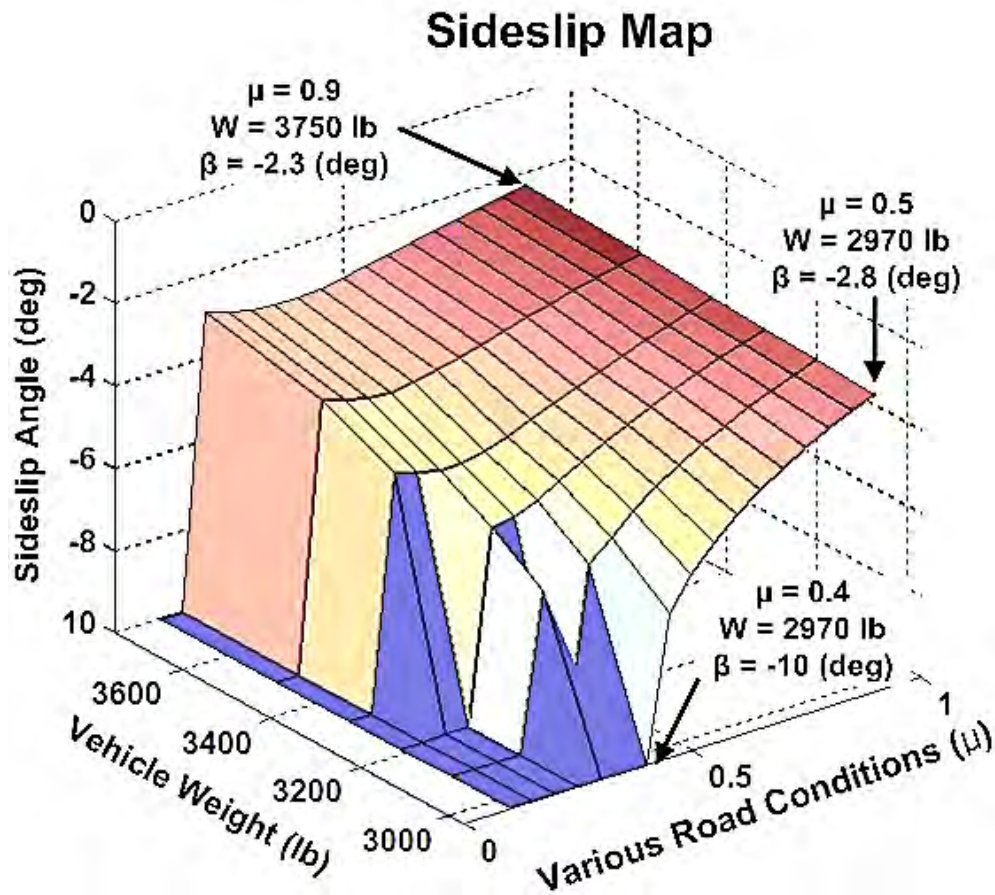


Figure 7-22: Sideslip angle map with respect to vehicle weight and various road conditons

As mentioned in Section 4.3.1, the side slip angle can be used for an important measure of vehicle performance. The side slip angle is strongly dependent on the lateral velocity and the longitudinal velocity. Figure 7-22 shows the sideslip angle map with respect to vehicle weight and various road conditions. The values of the sideslip angle are minimum values required for a cornering maneuver in a single-lane change.

As the vehicle weight increases from 2970 lb to 3750 lb, the absolute value of the sideslip angle decreases from 2.8 to 2.3 deg, given the dry asphalt road condition of $\mu = 0.9$. It can be seen that the sideslip angle suddenly drops at the road condition of $\mu = 0.4$.

This is due to unstable vehicle motion as a result of vehicle skidding caused by a zero value for the force margin (see Section 7.2.1).

7.2.4 Lateral Acceleration

As mentioned in Section 4.3.1, Section 4.3.2 and 5.1.3, the lateral acceleration occurs during cornering, resulting in contribution to the roll motion. That is, the lateral load is transferred from the inside wheels to the outside wheels. Some studies have been evaluated for the lateral acceleration response to step steer [Ghike and Shim,2006; Shim and Ghike,2007; Zhao, Chen et al.,2011].

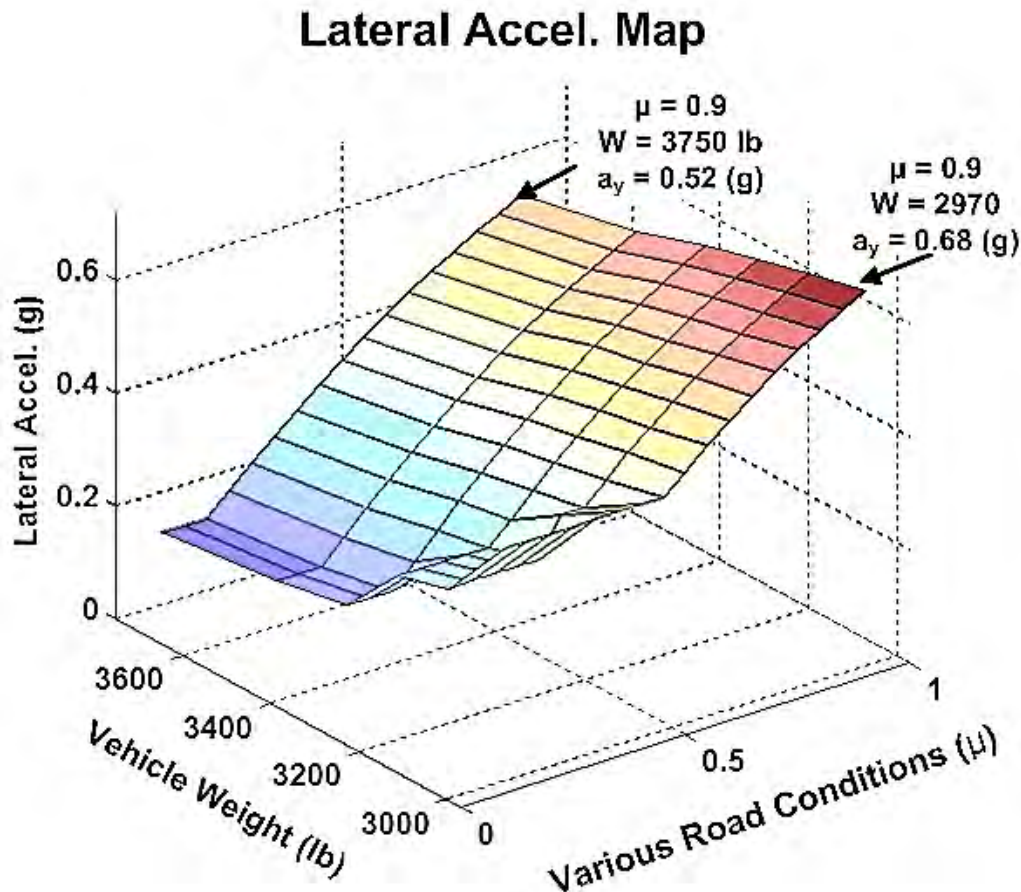


Figure 7-23: Lateral acceleration map with respect to vehicle weight and various road conditons

Figure 7-23 shows the normalized lateral acceleration map under various vehicle weights and various road conditions. The values of the lateral acceleration are maximum values during a cornering maneuver in a single-lane change.

The lateral acceleration (a_y) at the CG of the vehicle in the direction of the y axis consists of the motion along y axis (\dot{v}_y) and the centripetal acceleration ($v_x\dot{\psi}$) (see Section 4.3.2). Simulation results show that the increased vehicle weight decreases the lateral acceleration of a vehicle. In addition, since the traction limit is constrained by various road conditions (i.e., friction coefficient between the tire and road), the lateral acceleration decreases as the friction coefficient (μ) decreases.

7.2.5 Slip Angle

As mentioned in Section 4.3.1 and 5.1.3, the slip angles (α) can be defined as the angle between the heading direction of the tire and its travel direction which is the direction of the tire's velocity vector.

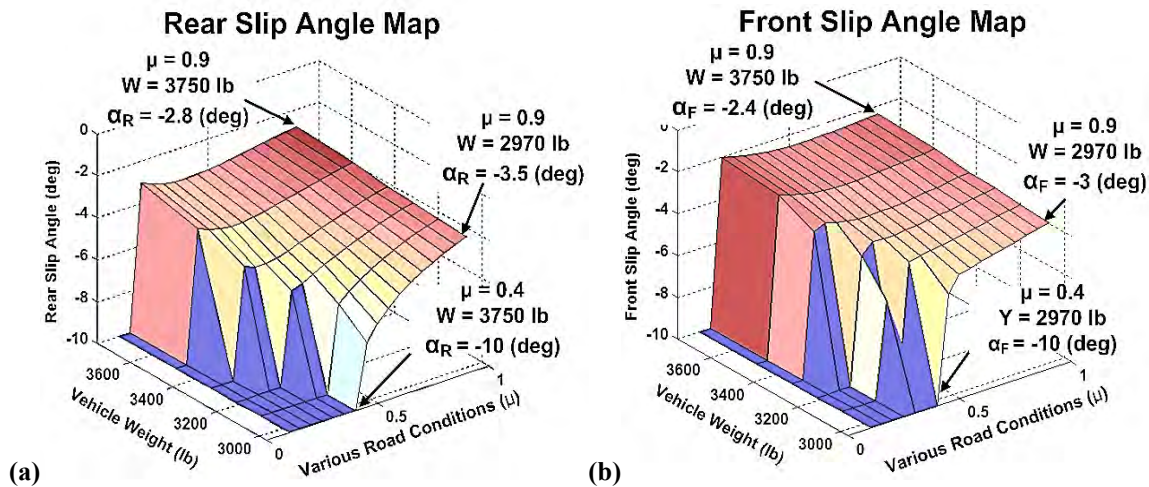


Figure 7-24: Slip angle map with respect to vehicle weight and various road conditons in terms of the front and rear wheels

Many studies have been evaluated for the slip angle response to step steer and single lane change [Setiawan, Safarudin et al.,2009; Guoying, Changfu et al.,2011; Li, Hong et al.,2012]. Figure 7-24 shows slip angle performance map as a function of vehicle weight and various road conditions. The values of the displayed slip angles are minimum required values during a cornering maneuver in a single-lane change. Clearly, it can be seen that the rear slip angle is larger than the front slip angle. As a result of that, the rear lateral force is larger than the front lateral force, resulting in the decreased force margin at the rear tires (see Section 7.2.1). This condition is termed oversteer.

For instance, given the vehicle weight of 3750 lb, the rear slip angle of 2.8° is larger than the front slip angle of 2.4° based on the absolute value. This leads to the decreased force margin of the rear wheels. In addition, as the vehicle weight increases from 2970 lb to 3750 lb, the front slip angle is varied from -3° to -2.4° due to increased vehicle weight.

7.2.6 Yaw Rate

As mentioned in Section 4.3.1 and 5.1.3, the yaw motion of the vehicle influences on vehicle lateral acceleration because the lateral acceleration (a_y) at the CG of the vehicle is the sum of the motion along y axis (\dot{v}_y) and the centripetal acceleration ($v_x \dot{\psi}$).

Many studies have shown the yaw rate feedback design to improve vehicle maneuverability, lateral stability, and prevent vehicle rollover [Chen and Lu,2009; Hac, Nichols et al.,2010; Kang and Heo,2012].

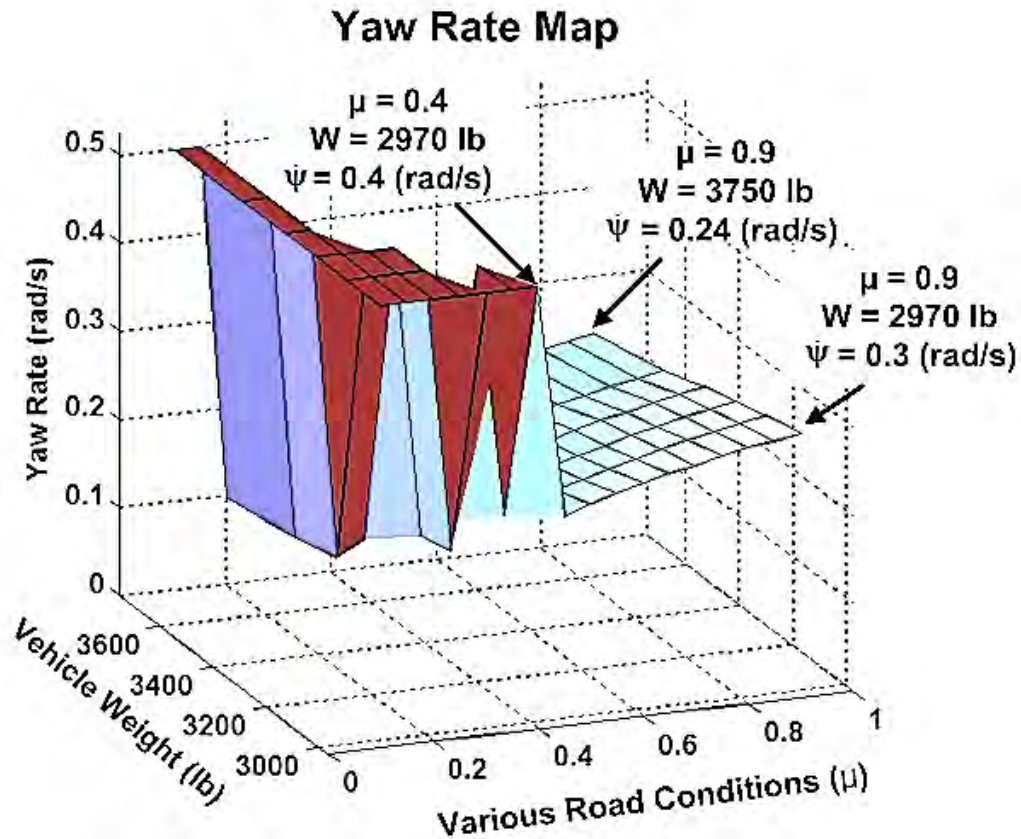


Figure 7-25: Yaw rate map with respect to vehicle weight and various road conditons

Figure 7-25 shows the yaw rate ($\dot{\psi}$) map as a function of vehicle weight and various road conditions. The values of the yaw rate are maximum required values during a cornering maneuver in a single-lane change.

As the vehicle weight increases from 2970 lb to 3750 lb, the yaw rate decreases slightly from 0.3 to 0.24 rad/s, given the dry asphalt road condition of $\mu = 0.9$. It can be seen that the yaw rate suddenly jumps up after the road condition of $\mu = 0.4$. This is due to unstable vehicle motion as a result of vehicle skidding caused by a zero value for the force margin (see Section 7.2.1).

7.2.7 Acceleration Force Margin

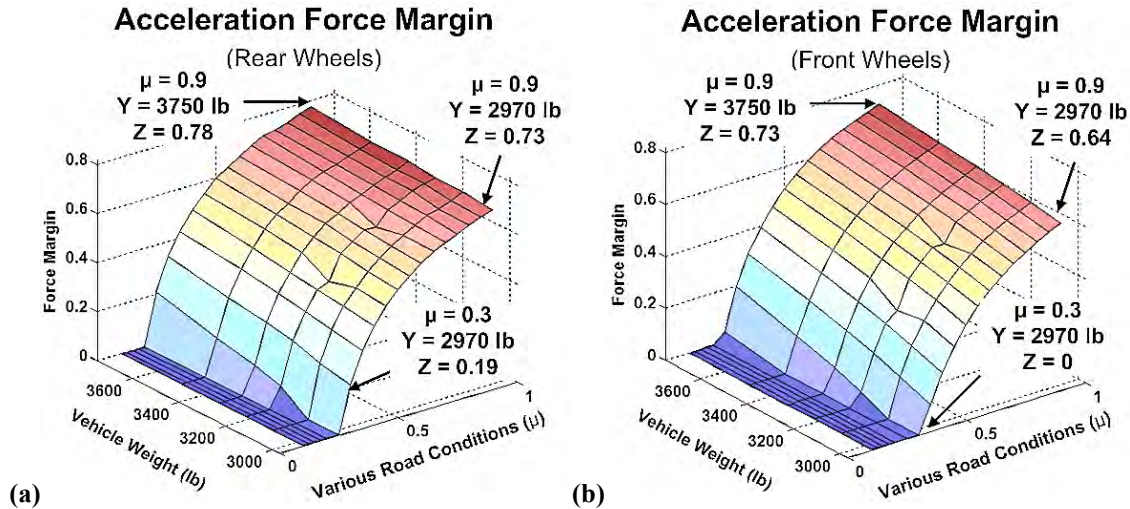


Figure 7-26: Acceleration force margin map with respect to vehicle weight and various road conditons given constant torque (290 N-m (214 ft-lb))

As mentioned in Section 5.2.1.1 (Dry Asphalt Road), Section 5.2.2.1 (Wet Asphalt Road), and Section 5.2.3.1 (Snowy Road), the acceleration force margin (F^m) decreases because it is constrained by the friction coefficient (μ).

Figure 7-26 shows the acceleration force margin performance map as a function of vehicle weight and various road conditions. Each point is simulated through the 14 DOF full-vehicle Simulink model, corresponding to two control parameters. The values of the acceleration force margin (F^m) are minimum required values during acceleration.

As the vehicle weight increases, the acceleration force margin of the rear and front wheels increases from 64% to 73% and from 73% to 78%, respectively, as shown in Figure 7-26 (a) and (b). At the friction coefficient value of $\mu = 0.3$, the acceleration force margin of front wheels becomes zero, while that of rear wheels is still 19% available. The reason that the force margin of the rear wheels is larger than that of the front wheels is

due to the larger normal forces on the rear wheels, as a result of the backward inertial force caused by acceleration (see Sections 5.2.1.1, 5.2.2.1, and 5.2.3.1).

7.2.8 Braking Force Margin

As mentioned in Section 5.2.1.1 (Dry Asphalt Road), Section 5.2.2.1 (Wet Asphalt Road), and Section 5.2.3.1 (Snowy Road), the braking force margin decreases because it is limited by the friction coefficient (μ).

Figure 7-27 shows the braking force margin performance map as a function of vehicle weight and various road conditions. The values of the braking force margin are minimum required values during braking. As the vehicle weight increases from 2970 lb to 3750 lb, the braking force margin of the rear and front wheels increases from 1% to 30 % and from 40% to 52%, as shown in Figure 7-27 (a) and (b), respectively.

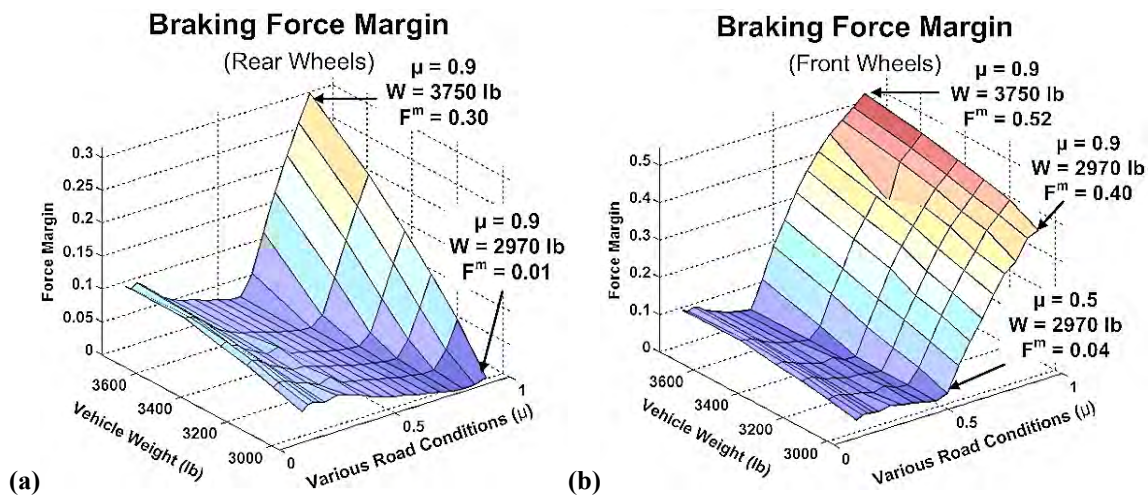


Figure 7-27: Braking force margin map with respect to vehicle weight and various road conditions given constant braking torque (570 N-m (420 ft-lb))

As can be seen, the braking force margin (F^m) is more available on the front wheels. This occurs because the normal force on the front wheels is larger than that on the rear wheels, as a result of the forward inertial force caused by braking.

7.2.9 Pitch Angle

As mentioned in Section 5.1.1 and 5.1.2, the pitch angle (θ) is influenced by acceleration and braking. At that time, the load transfer occurs from the front to the rear (or vice versa) because of the backward / forward inertia force acting on the vehicle, so that the normal force varies from the static values by the amount of load transfer.

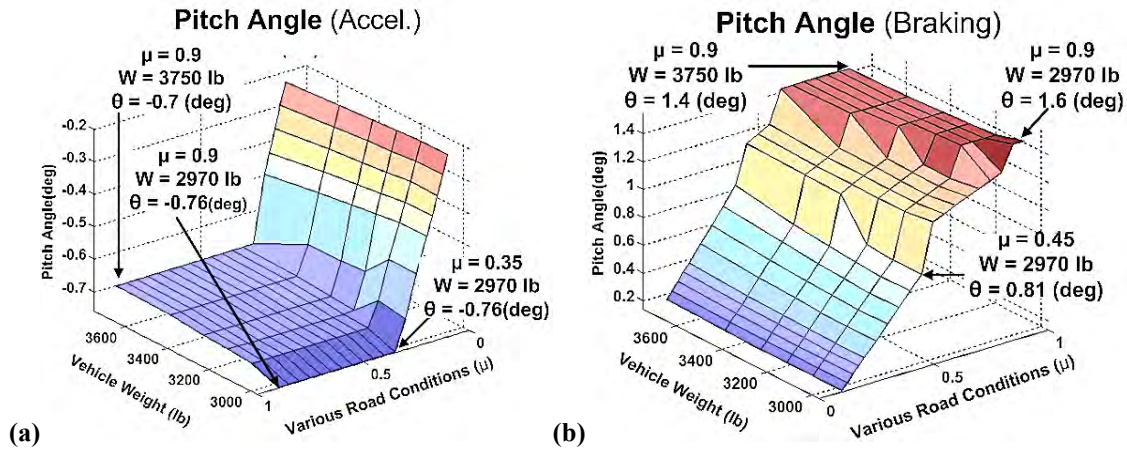


Figure 7-28: Pitch Angle map with respect to vehicle weight and various road conditions

Figure 7-28 shows the pitch angle (θ) map as a function of vehicle weight and various road conditions. The values of the pitch angle are steady-state value during acceleration and braking. As the vehicle weight increases from 2970 lb to 3750 lb given a dry asphalt of $\mu=0.9$, the pitch angle during acceleration decreases from -0.76° to -0.7° as shown in Figure 7-28 (a). This is attributed to different acceleration values where acceleration of a standard car (2970 lb) is 0.28 g, while acceleration of a vehicle (3750 lb) is 0.22 g.

Also, the pitch angle during braking decreases from 1.6° to 1.4°, as shown in Figure 7-28 (b). This occurs because deceleration of a vehicle weight of 2970 lb is 0.54 g, but deceleration of a vehicle weight of 3750 lb is 0.44 g.

7.2.10 Travel Range

In the real world driving, the travel range is influenced by many factors such as wind, climbing a hill, stop and go, variation in road surface, emergency braking, etc. [J.B. StaubeI,Dec. 2008]. In addition, the travel range in the electric vehicle will vary depending on auxiliary power (P_{aux}) which indicates the heating, cooling system, lights, component efficiency etc. The travel range (D_{tr}) in the steady-state condition can be expressed as [Besselink, van Oorschot et al.,2010]:

$$D_{tr} = \frac{\eta_{batt} C_{batt}}{\frac{1}{\eta_c \eta_m \eta_g} \left(\frac{1}{2} \rho_a A_f C_d v^2 + C_r m g \cos \theta \right) + \frac{P_{aux}}{v}} \quad (7.3)$$

where η_{batt} is the battery utilization factor, C_{batt} is the battery capacity, η_c is the controller efficiency, η_m is the motor efficiency, η_g is the gear train efficiency, P_{aux} is the auxiliary power. The aerodynamic and rolling resistances are explained in Section 4.1. The battery utilization factor is assumed to be 80%. For instance, 16 kWh AC electricity is required to charge a battery with a nominal capacity of 16 kWh, but only 12.8 kWh is charged to the battery. Assuming $\eta_c = 0.91$, $\eta_m = 0.9$ and $\eta_g = 0.98$, the electric power train (i.e., a controller + motor + gear train) has 80.3 % which is available at the wheels. Consequently, overall efficiency of the socket-to-wheel is 64%.

Mitsubishi i-Miev claimed that total efficiency of charging and battery is 82.8%, and efficiency of the electric power train is 80.2%. In their case, the overall efficiency of socket-to-wheel becomes 66.5% [I. Torii,June, 2009].

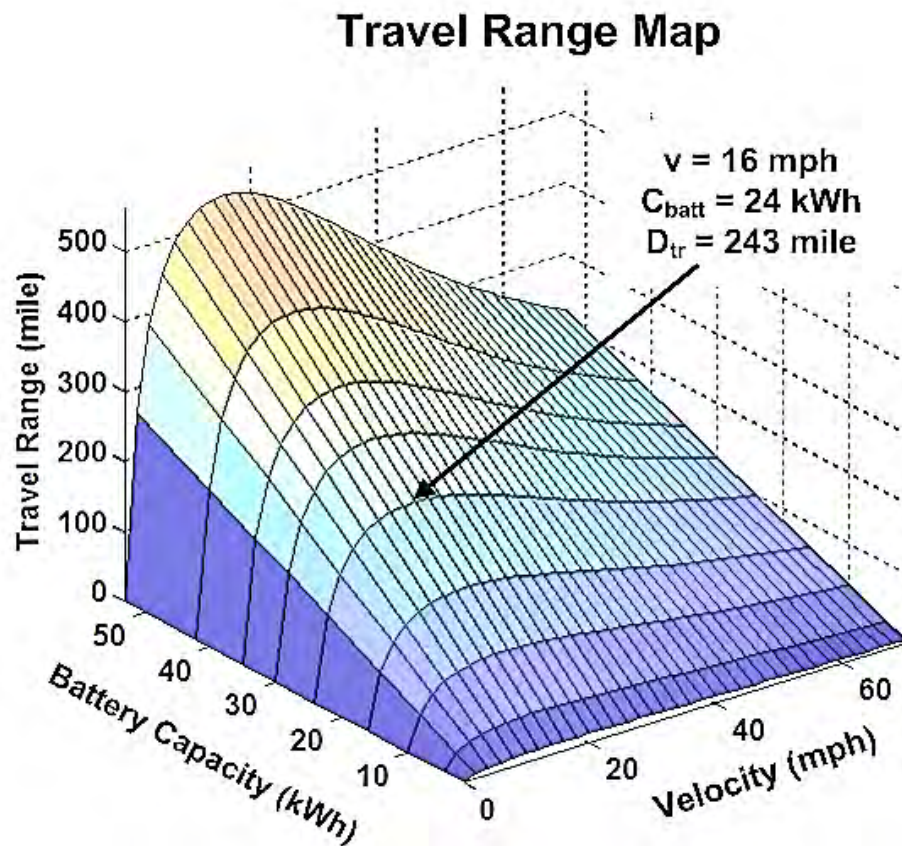


Figure 7-29: Travel range with respect to the battery capacity and velocity

Using Equation (7.3), the travel range (D_{tr}) as a function of the battery capacity (C_{batt}) and velocity (v) is shown in Figure 7-29. It is apparent that the travel range depends strongly on the vehicle velocity. This assumes that the component efficiencies are constant which certainly is not the case.

The battery capacity of Nissan Leaf is 24 kWh. The arrow indicates that the travel range of Nissan Leaf is around 243 miles given the velocity of 16 mph and the battery capacity of 24 kWh. It should be noted that the real world driving contains acceleration, braking, climbing a hill, emergency braking, etc. EPA has estimated that the travel range of the Nissan Leaf varies from 73 to 138 miles under various driving conditions such as

LA4, ideal driving conditions, highway driving with air-conditioner, stop-and-go winter and EPA five-cycle test [Hayes, de Oliveira et al.,2011].

Tesla Roadster has shown the energy loss distribution in terms of aerodynamic losses, tire losses, drivetrain losses, and auxiliary losses [J.B. Staubel,Dec. 2008]. The energy loss per distance travelled can be written as:

$$E_{loss}[Wh / mile] = \frac{1}{\eta_c \eta_m \eta_g} \left(\frac{1}{2} \rho_a A_f C_d v^2 + C_r mg \cos \theta \right) + \frac{P_{aux}}{v} \quad (7.4)$$

In an electric vehicle, the unit of energy consumption is expressed in terms of *Wh/mile*. It should be noted that the unit of *Wh/mile* is equal to $(3.6 \text{ Ws/m})/1.6$ or 2.24 N, which is actually a force.

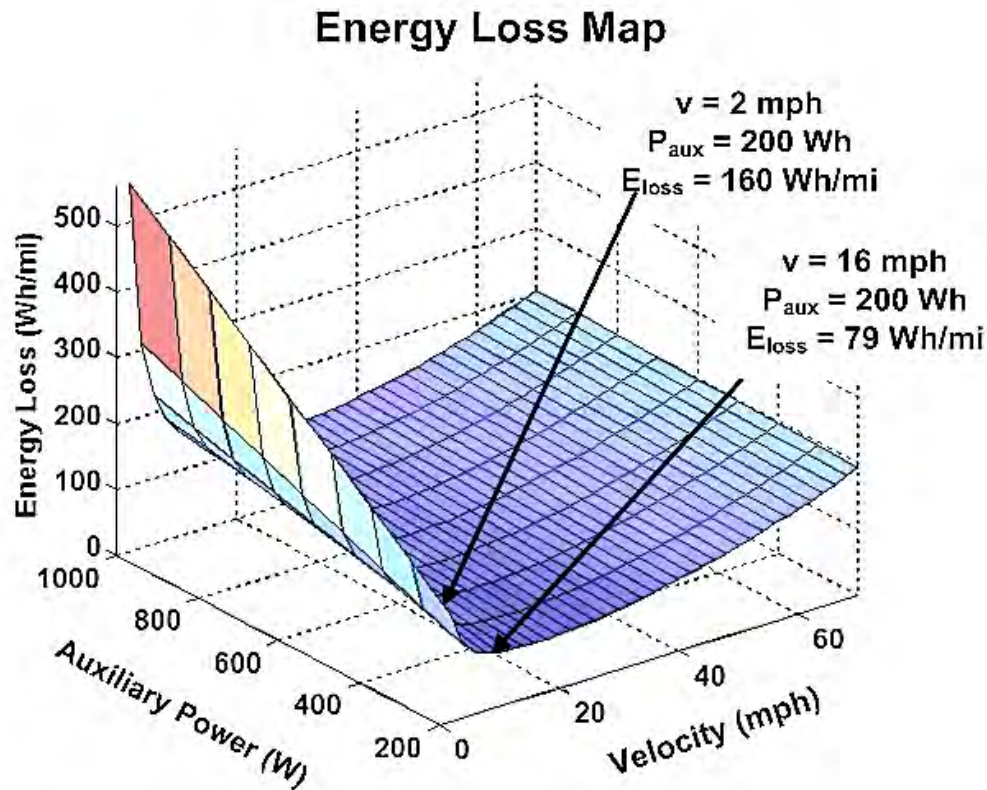


Figure 7-30: Energy loss map with respect to the auxiliary power and velocity

The energy loss per distance travelled as a function of the auxiliary power and velocity is shown in Figure 7-30. As the auxiliary power increases, the energy loss increases at the low speeds. Given the auxiliary power of 200 Wh, minimum energy loss becomes 80 Wh/mile at the velocity of 15 mph. Finally, the energy loss becomes 200 Wh/mile at the velocity of 70 mph.

7.3 MAINTENANCE CRITERIA

7.3.1 Efficiency

As the customers use electric vehicles equipped with four / two independent MDW, they are concerned about when to repair the MDW and how much time is left before failure. To address these problems, condition-based maintenance (CBM) is essential to help them obtain the right time to replace an old MDW with a new MDW. That is, conventional maintenance (i.e., scheduled maintenance and reactive maintenance) will be substituted by preemptive maintenance. This leads to increased MDW availability and dramatic cost savings due to a decrease in sudden failures[Hvass and Tesar,2004].

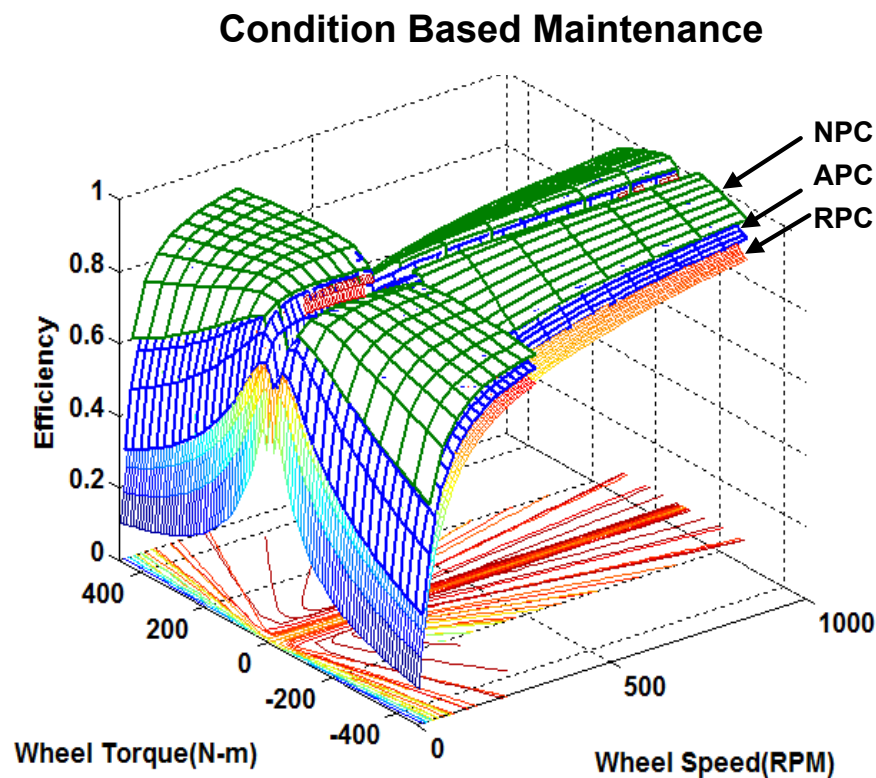


Figure 7-31: Condition-based maintenance using NPC, APC, and RPC

A general Decision Making (DM) method facilitating intelligent actuator condition-based maintenance (DM/CBM) was introduced by the Robotics Research Group [Hvass and Tesar,2004]. The health margin can be obtained from the ratio of the difference norm between assessed performance condition (APC, real time map) and required performance condition (RPC, minimum performance map) to the difference norm between nominal performance condition (NPC, certification birth map) and required performance condition (RPC) as follows [Hvass and Tesar,2004; Ashok and Tesar,2008]:

$$HM = \frac{NORM_DIF(APC - NPC)}{NORM_DIF(NPC - RPC)} \quad (7.5)$$

Norms are numerical values from the visual performance map. They can be provided for the operator as single-valued descriptions of the current actuator condition. Figure 7-31 shows the assumed efficiency map for condition-based maintenance using NPC, APC, and RPC. The remaining useful life can be estimated from the difference norm between APC and RPC. When the %Health Margin reaches zero, it is when the system doesn't meet task requirements.

As a result of aging and wear, the system condition will degrade from NPC to RPC. The vital variables are continuously monitored for signs of degradation. Consequently, the CBM will tell the customers in advance when their MDW will fail, when they should replace the failing component, and how much remaining useful life is left. All of this can be managed by intelligent (performance map based) decision-making software.

7.3.2 Power Level

Power level can be degraded after several thousand charge depleting cycles in terms of the battery. That is, a hybrid electric vehicle can be influenced by energy and power degradation which affect vehicle performance and efficiency [Wood, Alexander et al.,2011]. According to [Graham,2001], the Electric Power Research Institute (EPRI) presents the need for battery replacement by evaluating the distance required by battery warranties, state of charge (SOC), and how the battery management system (BMS) handles degradation over time.

In terms of switched reluctance motor, if a motor phase is disconnected, the rated power decreases with the number of disconnected motor phases, and the rotor is degraded by unbalanced forces [Gameiro and Cardoso,2011]. This power degradation of the MDW can be monitored by using sensors, so that CBM can identify incipient component degradation, and provide warnings regarding impending malfunctions.

7.3.3 Responsiveness

Regarding the star compound gear train, the input and output responsiveness is a measure of the acceleration at the input and output. The inertia of a gear train, reflected to the input is an important consideration in the selection of an optimum gear train combination [Vaculik,2008]. Simply, responsiveness is defined as the ratio of torque to inertia as follows[Bandar and Tesar,2011]:

$$Responsiveness(rad / s^2) = \frac{Rated Torque(ft - lb)}{Inertia(lbm - in^2)} \quad (7.6)$$

This equation tells us how the responsiveness of a system changes as the load inertia is varied. In addition, as the rated torque decreases, responsiveness decreases.

As mentioned in Section 7.3.2, , if a motor phase is disconnected, the rated power decreases with the number of disconnected motor phases, and the rotor is experienced by unbalanced forces. This leads to a poor electromagnetic torque capability. Eventually, responsiveness of an actuator decreases. With the CBM using a torque sensor attached to the MDW, the incipient component degradation will be identified.

7.3.4 Torque Margin

According to “Criteria Based Vehicle Motion Planning and Operation” [Tesar,Nov 1, 2011], the normalized torque margin can be expressed in:

$$\tau_i^m = \frac{T_i - t_i}{T_i} \quad (7.7)$$

where subscript i indicates each wheel, T_i is the available maximum torque at each wheel, t_i is the operational torque.

- 4) $\tau_i^m = + \rightarrow$ associated wheel is operated below its maximum capability
- 5) $\tau_i^m = 0 \rightarrow$ associated wheel is saturated
- 6) $\tau_i^m = - \rightarrow$ associated wheel is operated with inefficient (spinning) slip

As mentioned in Section 4.4.7, the normalized torque margin is equivalent to the normalized tire force margin. Equation (7.7) can be written as:

$$\tau_i^m = \left(\frac{r\mu F_{zjk} - r\sqrt{F_{xjk}^2 + F_{yjk}^2}}{r\mu F_{zjk}} \right) \times 100\% \quad (7.8)$$

The above equation becomes as follows:

$$F^m = \left(\frac{\mu F_{zjk} - \sqrt{F_{xjk}^2 + F_{yjk}^2}}{\mu F_{zjk}} \right) \times 100\% \quad (7.9)$$

As mentioned in Section 7.2.1, the cornering force margin can be the cornering torque margin as a function of vehicle weight and various road conditions as shown in Figure

7-32. The simulation of the vehicle's response subjected to a cornering maneuver has been carried out to show the torque margin performance map of a rear-inside, front-inside, rear-outside, and front-outside wheel in a single-lane change (i.e., single sinusoidal amplitude is 2 degree, and velocity is 60 mph).

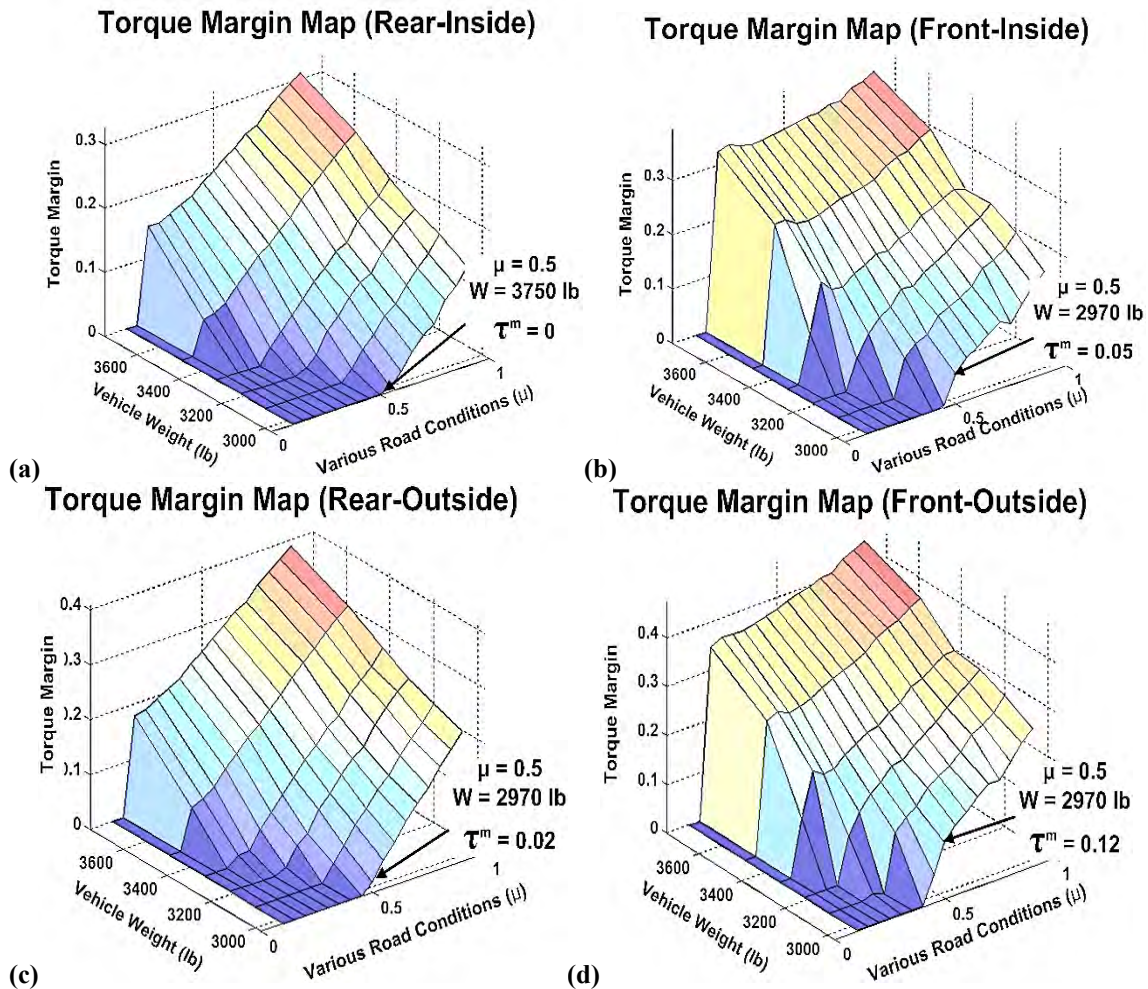


Figure 7-32: Torque margin map with respect to vehicle weight and various road conditions for a single-lane change

It should be noted that a zero value for the force margin indicates that the wheel's traction force is saturated, so that the vehicle starts skidding, and this leads to unstable vehicle motion.

7.3.5 Temperature Margin

As mentioned in Section 6.2, the heat energy lost results from inefficiencies during traction and braking. That is, the difference between traction at motor input power and motor output power generates heat caused by both copper loss and iron loss in the core of the SRM. In addition to that, the difference between braking at motor input power and motor output power generates heat energy.

The increased temperature in the motor not only degrades the motor efficiency but also leads to an overall degradation in the motor performance [Balamurugan and Sumathi,2004]. In spite of no danger of demagnetization of magnets at high temperature, the SRM could be affected by a high temperature because the winding insulation and the bearing lubrication are influenced by the high temperature. The increased resistance with the severe changes in temperature may be 20% for a 50 °C rise and 53% for a 135 °C rise in temperature in case of copper windings [Krishnamoorthy and Tesar,2010].

According to [Brancato,1992; Grinberg and Palmer,2005], the thermal life of insulation is halved for each increase of 10°C in maximum ambient temperature level. Regarding power circuit of a typical serial hybrid electric vehicles (HEV), the auxiliary energy system requires a high-specific power device (i.e., ultracapacitor) to release bursts of energy and obtain a higher efficiency [Moreno, Ortúzar et al.,2006]. Maxwell technologies has claimed that BCA P0010 cells (2600 F at 2.5V) and integrated modules (145 F at 42 V and 435 F at 14 V are in production. The specific power and specific energy the integrated modules are 2900 W/kg and 2.22 Wh/kg. Operating temperatures

range from -35 to 65 °C. Given standard conditions (25°C and 1 atm pressure), the temperature margin has to be sustained by the cooling system [Ehsani, Gao et al.,2009].

Industrial motors have continuous ratings under the conditions of thermal limitations of 40 °C to 60 °C temperature rise over ambient necessary to protect their insulation systems from degradation. In terms of the hybrid electric vehicles, the motor-generator will have a separate coolant supply from the vehicle's engine coolant (< 115°C) or transmission oil cooler (< 120°C). The power electronics coolant is operated based on a maximum inlet temperature of 65°C. This leads to temperature fluctuations (<40°C) at the semiconductor junctions, resulting in a reasonable durability (>6000 h life) [Miller,2008]

7.3.6 Noise Margin

There are a number of noise sources such as tire and road interaction, gear train, electric motor, ventilation system, etc [Wei and Rizzoni,2004]. When it comes to an actuator, there are two primary sources of noise such as the motor and gear train [Janardhan and Tesar,2008].

Regarding the switched reluctance motor (SRM), the torque ripple and acoustic noise is a disadvantage of SRM drives [Xue, Cheng et al.,2008]. However, due to absorbing energy in the tires, the torque ripple is not a potential problem that prohibits its use for a hybrid electric vehicle.

The acoustic noise is attributed to the varying magnetic forces between the stator and rotor poles. The varying magnetic forces (i.e., radial force) cause the deformation of the stator, resulting in radial vibration of the stator and acoustic noise[Xue, Cheng et al.,2008; Ehsani, Gao et al.,2009].

Sound variations lie in the range of 2×10^{-5} Pa and 100 Pa. In addition, sound intensity I is the power per unit area in W/m^2 . The decibel level can be expressed in [Wei and Rizzoni,2004; Janardhan and Tesar,2008]:

$$I(dB) = 10 \log_{10} \left(\frac{I}{I_0} \right) = 10 \log_{10} \left(\frac{P^2}{P_0^2} \right) \quad (7.10)$$

where I is the sound power per unit area in W/m^2 , I_0 is the standard threshold of hearing intensity of $10^{-12} W/m^2$, P_0 is the atmospheric sound pressure of $2 \times 10^{-5} Pa$. Human perception of loudness is the frequency-dependent.

With all windows and doors closed, the interior noise of a vehicle ranges from 38 to 51 dB at idle conditions. Under the same conditions, the interior noise of the vehicles at 70 mph is around 70 dB. The threshold of pain is 130 dB [Wei and Rizzoni,2004]. For instance, Hyundai Sonata (69.5 dB), 2011 Nissan Leaf (63.7 dB), and 2011 Hyundai Equus (60.5 dB) [Inside-Line].

7.3.7 Sensor Degradation

In term of the Electromechanical Actuator (EMA), a ten-sensor architecture (i.e., position, velocity, acceleration, torque, temperature, noise, vibration, current, voltage, magnetic field) was proposed to provide complete awareness of variations [Krishnamoorthy and Tesar,2005]

Decision Making / Condition-Based Maintenance (DM/CMB) was proposed by [Hvass and Tesar,2004] at the Robotics Research Group. The sensor inferred model continuously receives sensor signals from actuator inputs and outputs, and updates the estimate of the model parameters which reflects the actuator's current condition. The incipient faults cause gradual change in the sensor inferred model, generating a residual indicating degradation in the actuator health.

Recent dissertation [Krishnamoorthy and Tesar,2010] presents the development of a novel Sensor and Process Fault Detection and Isolation (SPFDI) algorithm. This framework uses a Bayesian network to model a system in terms of PWM duty cycle, PWM frequency, voltage, current, torque, speed, and noise based on extensive empirical data. This algorithm is capable of distinguishing between sensor and process faults. The SPFDI is used to treat single-point failures and reduce false alarms to improve the system's availability as complexity increases [Tesar,2011, August].

7.3.8 Bearing Degradation

Bearings are one of the foremost causes of breakdown in rotating machinery. Such bearing failures can be catastrophic in some situations, such as in helicopters and in manufacturing processes. In order to prevent these serious consequences, bearing condition diagnostics and monitoring techniques such as temperature monitoring, wear debris analysis, oil analysis, vibration analysis and acoustic emission analysis, have been developed to identify the existence of faults in a running bearing [Li, Billington et al.,1999].

Current available diagnostic methods primarily focus on determining any fault presence in a bearing as early as possible. A pitting defect can be detected, when it is smaller than 6.25 mm^2 (0.01 in^2), which is commonly considered to be a fatal failure size by industry standard. [Li, Billington et al.,1999]

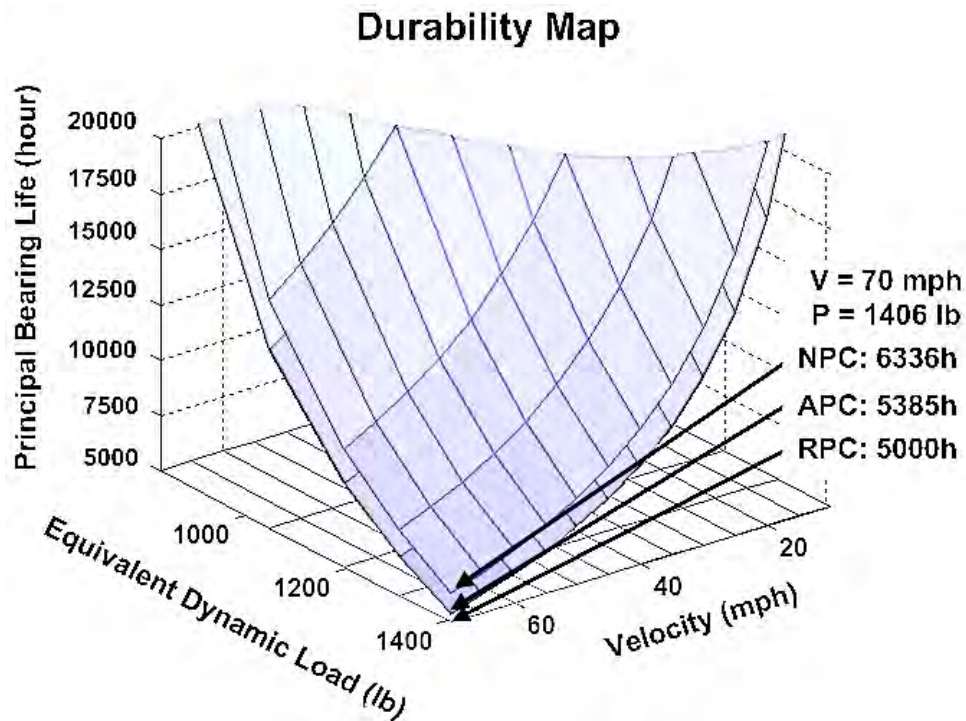


Figure 7-33: Durability map with respect to Equivalent dynamic load and velocity

The MDW consists of the front end bearings, back end bearings, and principal bearing. The crossed roller bearings, four-point bearings, and tapered roller bearings can be used for principal bearings because they can accommodate three different load types such as radial, axial, and moment loads [Lee and Tesar,2011]. In the MDW, the crossed roller bearing is used due to the increased bearing stiffness caused by the roller's line contact [Tesar,2007].

Figure 7-33 shows the assumed durability map as a function of equivalent dynamic load and velocity. As a result of aging and wear, the system condition will degrade from NPC to RPC (of 5000 hr. minimum). The APC will be continuously monitored for signs of degradation. Given the equivalent dynamic load of 1406 lb and velocity of 70 mph, the NPC and APC are 6336 h and 5385 h, respectively.

7.3.9 Wire Insulation Degradation

The integrity of the motor stator's insulation system is an important consideration for motor designer. Insulation's function separates electrical components from each other. This leads to preventing short circuits. In addition, the winding burnout and motor failure are avoided by the insulation system [Regal-Beloit,1999].

Wire insulation could be degraded by moisture, vibration, chemicals, abrasives, and temperature. The main factor to degrade the wire insulation is the temperature. The National Electrical Manufacturers Association (NEMA) sets specific temperature standards for motors based on thermal insulation classes: Class A (105°C), Class B (130°C), Class F (155°C), Class H (180°C). These temperatures indicate maximum operating temperatures for motors. Larger than 10 hp, Class F becomes common. A malfunction caused by insulation breakdown allows current flow to ground rather than through the intended circuit, which can become a sudden failure [Brancato,1992].

7.3.10 Clutch Degradation

As mentioned in Section 3.2, the clutch disk is located at the neutral position at the beginning of gear stage 1. When a vehicle moves, the clutch disk engages the first pinion by traveling 0.28 in. To the left (assuming that time of clutch operation is 0.1 sec), the acceleration of clutch disk demands 9.2 ft/s^2 and the inertial force will be 0.114 lb. At 20 mph, the clutch operation disengages the first pinion and engages the second pinion to the right. This leads to the clutch operation time of 0.2 sec, because of double travel distance of 0.56 in.

Recent research [Eo, Won et al.,2012] claims that the full parallel hybrid system of 2011 Hyundai Sonata Hybrid provides smooth and delicate drivability in any extreme

driving conditions. The engine clutch between engine and motor is the core component of this hybrid system.

Toyota Motor Company failed to develop the full parallel hybrid system 15 years ago because the time of engine clutch engagement takes more than 1 s. Thus, Toyota developed a series-parallel hybrid considering two motors: one as a drive motor and the other as a generator. The engine clutch developed by Hyundai Sonata Hybrid takes less than 0.6 s. In this case, a driver does not feel at that moment when the combination of motor and engine power delivery changes. This results in less cost and improves fuel efficiency [Seoul-Economy].

In the case of the MDW, the time of clutch engagement will be monitored by using sensors. Consequently, the CBM will tell the customers in advance when their MDW will fail, when they should replace it, and how much remaining useful life is left.

7.4 REFRESHMENT CRITERIA

7.4.1 Power Level

According to “All-Electric Modular Automobile” [Tesar,2009], a modular all-electric automobile in an open architecture could be assembled on demand based on the minimum set of highly certified, mass produced, and cost effective modules with a responsive supply chain, just as Dell computer does for personal computer. In addition, this will be efficient and open to permit refreshability or rapid repairs (plug-and-play).

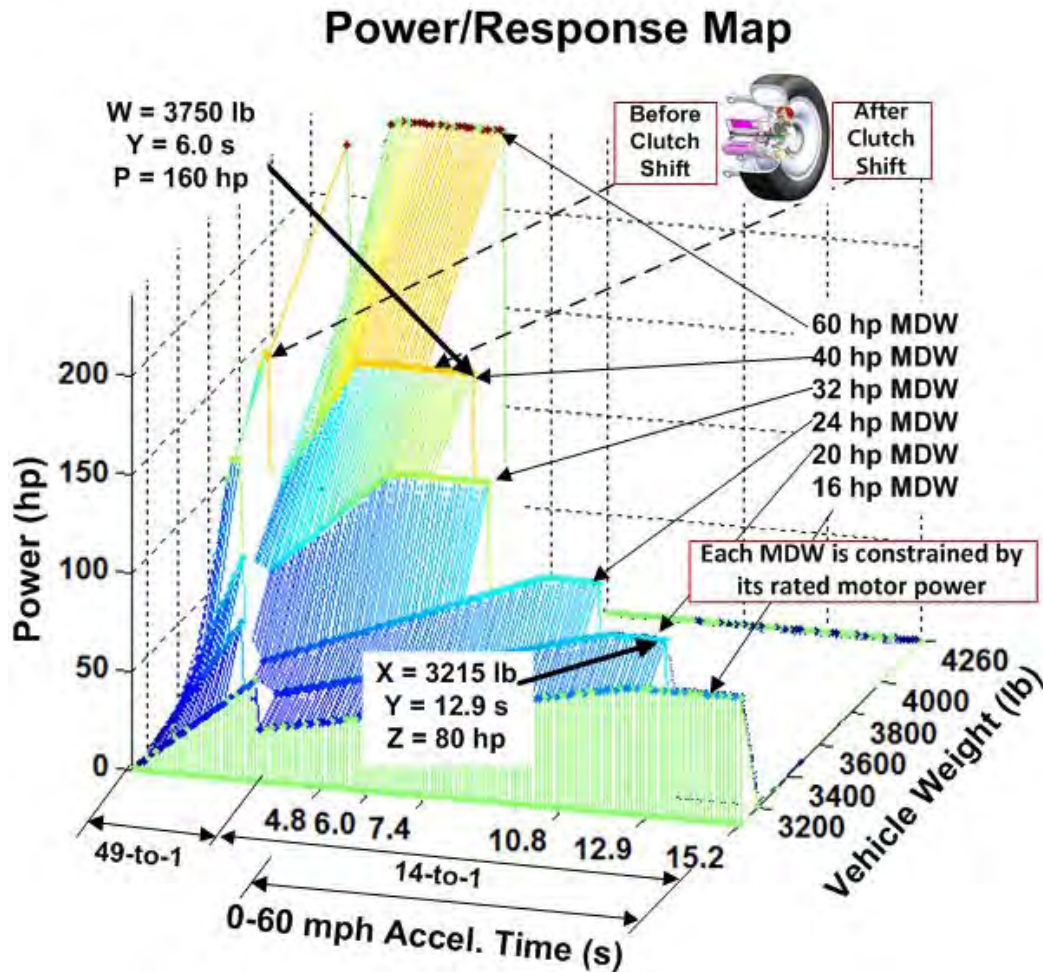


Figure 7-34: Updated Power/Response map with respect to 0-60 acceleration time and vehicle weight considering four independent drive wheels

Refreshment can be defined as updating the modules: engine, generator, batteries/super cap, skateboard chassis, car bodies, suspensions, drive wheel, and operational software. Regarding the MDW, if a customer updates the MDW from 20 hp to 40 hp, he / she can obtain the 0-60 mph acceleration time of 6.0 s, compared to the previous acceleration time of 12.9 s, as shown in Figure 7-34

7.4.2 Cost Benefit / Replacement Cost

The MDW is designed for expanding human choices to respond to the customer needs. This provides the OEM a larger potential market based on a responsive supply chain, just as M. Dell does for the personal computer. This leads to more income from the life cycle market (repairs and MDW update). All of this maximizes customer choice, made more frequently to give the OEM more sales (future repairs, upgrade, and reinvestment). Based on an aggressive/responsive supply chain (in-depth certification and constant upgrade in a minimum set as a standard for investment), the OEM get ahead of its competitors where continuous performance/cost ratio increases. Consequently, customers obtain the cost benefit associated with replacement cost, when they update the MDW which is provided by the OEM [Tesar and Ashok, May, 2011].

7.4.3 Efficiency Benefit

Mecrow claims that increasing the efficiency of the electrical drive and integrating design of the drive and the driven load to maximize system efficiency will become important until 2050 year and beyond [Mecrow and Jack, 2008]. This report strongly suggests that the relevant time frame is 2016 to 2020.

As mentioned in Section 6.3, the efficiency of an MDW with a reconfigurable controller is calculated as 88.2%. As technology related to the MDW improves in the future, the overall efficiency of an MDW with a reconfigurable controller must increase based on the enhanced switching devices (i.e., IGBT, MOSFET, etc.).

7.4.4 Torque Level

As mentioned in Section 7.4.1, if a customer updates the MDW from 20 hp to 60 hp, he / she can obtain the enhanced torque/response, as shown in Figure 7-35.

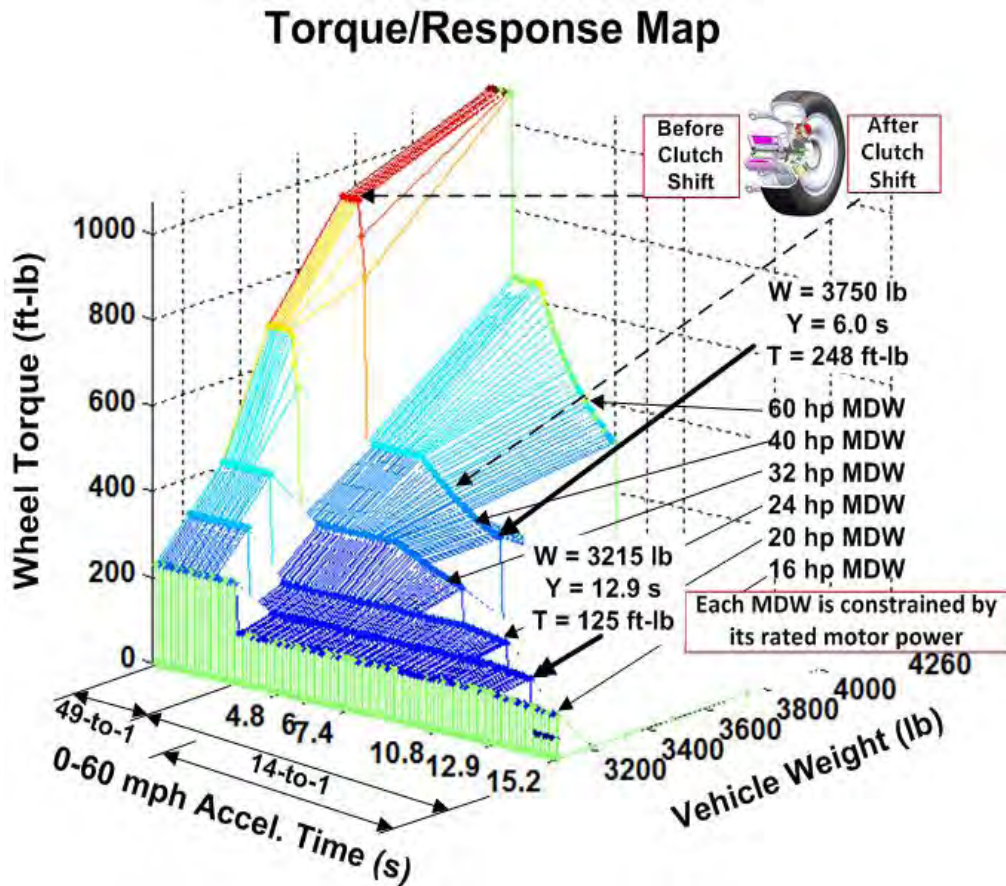


Figure 7-35: Updated torque/response map with respect to 0-60 acceleration time and vehicle weight considering four independent wheels

The arrow indicates a torque of 248 ft-lb, acceleration response of 6.0 s, for a vehicle weight of 3750 lb. Customers can choose the MDW depending on their performance preference such as aggressive driver and efficiency-priority driver.

7.4.5 Enhanced Handling and Ride Comfort

According to [Murata,2011], an in-wheel motor can be used for suppressing the variations in the ground contact force using a different driving force of the front and rear wheels. Therefore, the handling can be improved by applying the driving force or braking force at the time of bouncing of the vehicle body. Also, the ride comfort can be improved by the in-wheel motor.

According to “World View of Research for Electric Vehicle Intelligent Corner” [Tesar,2011, August], the active suspension actuators would be used to balance the need for the undisturbed vehicle motion (i.e., ride comfort) and the need for maximizing the contact forces (i.e., drivability and safety). Furthermore, intelligent corner decision making (in milli-sec) can maintain balance between reduced contact force and increased contact force so that available traction force can increase in curves or rough roads by perhaps 50%.

7.4.6 Enhanced Sensors

In terms of the Electromechanical Actuator (EMA), a ten-sensor architecture (i.e., position, velocity, acceleration, torque, temperature, noise, vibration, current, voltage, magnetic field) was proposed to provide complete awareness of nonlinear performance variations [Krishnamoorthy and Tesar,2005]

As technology associated with sensors improve in the future, the All-Electric Modular Automobile with the MDW generates precise real time data to quantify the actual condition of the MDW.

7.4.7 Enhanced Control Software

A modular electric vehicle can be upgraded after purchase. Old software can be replaced with new versions of the software. For instance, new versions of software contain an adaptive control system which is stored in memory some preset parameters. Adaptive control software enhances operation of adaptive electric motors to reduce noise, vibration, and harshness. Furthermore, this compensates for changes in motor operation due to aging and wear, and reduces torque ripple and other degraded motor characteristics. Consequently, all of the motor control may be implemented in software, and then the old control software can be modified by loading new or upgraded software, without replacing any hardware. If it is possible, this could be done over the internet through third party application [Durney,2009; Tesar and Ashok,May, 2011]

When it comes to an in-wheel drive system, independent motor control software is essential to control the in-wheel motor. Functions of four-wheel drive control can be done in software, so they can be maintained and upgraded at low cost [Durney,2009].

7.4.8 Enhanced Durability

The customer wants to choose durability (5,000 up to 20,000 hour) versus cost. As mentioned in 7.1.10, durability is related to the remaining useful life (condition-based maintenance) which is influenced by duty cycles. The equivalent dynamic load was evaluated based on cube-root mean cube norm for bearing life. The dynamic load rating (C) was selected as 2248 lb. If we choose a higher dynamic load rating in higher power of

the MDW, the durability will be enhanced. In addition, using a customer's demand cycle, the embedded software guides the operator in real time to maximize durability.

7.4.9 Enhanced Temperature Tolerance

The National Electrical Manufacturers Association (NEMA) sets specific temperature standards for motors based on thermal insulation classes: Class A (105°C), Class B (130°C), Class F (155°C), Class H (180°C). These temperature tolerances indicate maximum operating temperatures for motors. Larger than 10 hp, Class F becomes common. For instance, a motor might have class F insulation, but a class B temperature rise. This would give an extra thermal margin [LEESON; Brancato,1992].

7.4.10 Enhanced Safety

The MDW is designed to be a plug-in module in a hybrid-electric vehicle to provide precise power utilization to operate the vehicle. That is, the MDW would be independently controlled to meet the driver's needs for efficiency, drivability, and safety. An operational software called AMOS would be used to monitor all performance maps/envelopes to respond to driver commands and maintain overall goals for efficiency, drivability, and enhanced safety in emergency conditions. The MDW becomes the principal vehicle component for active response to the driver to enhance safety (i.e., active utilization) [Tesar and Ashok,May, 2011]

7.5 CHAPTER SUMMARY

In this chapter, we discussed the human choices in terms of purchase / operation / maintenance / refreshment standpoint. The following tables regarding them summarize the criteria, X and Y axes, and description in Table 7-6, Table 7-7, Table 7-8, and Table 7-9.

Purchase Standpoint				
#	Criteria	X and Y axes	Description	Source
1	Cost	Vehicle Configuration 0-60 mph Accel. Time	<ul style="list-style-type: none"> ● Cost/Performance Map - Rated power increases with vehicle configuration from '1' to '4' → Increased cost ● 40 hp MDW with a reconfigurable controller / intelligent corner ('4') - Cost: \$26,400, - Weight: 4290 lb - 0-60 acceleration time: 6 s 	Section 7.1.1
2	Weight	Vehicle Configuration 0-60 mph Accel. Time	<ul style="list-style-type: none"> ● Weight/Performance Map - Rated power increases with vehicle configuration from '1' to '4' → Increased weight ● 16 hp MDW with a reconfigurable controller / intelligent corner ('1') - Weight: 4290 lb, - Cost: \$13,000 - 0-60 acceleration time: 15.2 s 	Section 7.1.2
3	Power	Vehicle Weight 0-60 mph Accel. Time	<ul style="list-style-type: none"> ● Power/Response Map - High desired acceleration - Increased vehicle weight → Power level choice increases ● Each MDW is constrained by its rated motor power ● Given 0-60 mph accel. time of 6 s and vehicle weight of 3750 lb - Require the rated power of 160 hp 	Section 7.1.3
4	Acceleration	Vehicle Weight 0-60 mph Accel. Time	<ul style="list-style-type: none"> ● Torque/Response Map - High desired acceleration - Increased vehicle weight → Increased wheel torque ● Each MDW is constrained by its rated motor power ● Given 0-60 mph accel. time of 6 s and vehicle weight of 3750 lb - Wheel torque of 248 ft-lb at 60 mph 	Section 7.1.4
		Various Road conditions Vehicle Weight	<ul style="list-style-type: none"> ● 0-60 mph Acceleration Time Map - Given constant torque, low friction coeff. and increased vehicle weight → Increased 0-60 mph accel. time ● Given $\mu = 0.9$ and vehicle weight of 2970 lb to 3750 lb - Time: 10.1 s to 12.6 s 	
5	Gradeability	Vehicle Weight 0-60 mph Accel. Time	<ul style="list-style-type: none"> ● Gradeability Map - High desired acceleration - Increased vehicle weight → Increased gradeability 	Section 7.1.5

Purchase Standpoint				
#	Criteria	X and Y axes	Description	Source
6	Braking	Various Road conditions Vehicle Weight	<ul style="list-style-type: none"> 60-0mph Braking Time Map - Given braking torque, low friction coeff. and increased vehicle weight → Increased 0-60 mph braking time Given $\mu = 0.9$ and vehicle weight of 2970 lb to 3750 lb - Time: 5 s to 6.2 s 	Section 7.1.6
		Normalized Deceleration Velocity	<ul style="list-style-type: none"> Stopping Distance Map - Low normalized deceleration - High velocity → Increased stopping distance Given normalized deceleration of 1 g and velocity of 60 mph - Stopping distance: 120 ft 	
7	Handling	Frequency Vehicle Weight	<ul style="list-style-type: none"> Dynamic Contact Force Map - Increased vehicle weight → increased dynamic contact force → decreased wheel hop frequency (11.6 Hz → 8.3 Hz) 	Section 7.1.7
		Velocity Vehicle Weight	<ul style="list-style-type: none"> Dynamic Contact Force Map (RMS based on PSD) map - Increased velocity, vehicle weight, and road roughness → increased dynamic contact force 	
8	Ride Comfort	Frequency Vehicle Weight	<ul style="list-style-type: none"> Sprung Mass Acceleration Map - Increased vehicle weight → Increased sprung mass accel. 	Section 7.1.8
		Velocity Vehicle Weight	<ul style="list-style-type: none"> Sprung Mass Acceleration Map (Frequency-weighted RMS) - Increased velocity and road roughness → Increased sprung mass accel. - increased vehicle weight → Decreased sprung mass accel. 	
9	Efficiency	Wheel Speed Wheel Torque	<ul style="list-style-type: none"> Efficiency Map - Given the UDDS duty cycle → w/o a reconfig. Controller (85.8%) → w/ a reconfig. Controller (88.2%) 	Section 7.1.9
10	Durability	Velocity Equivalent Dynamic Load	<ul style="list-style-type: none"> Bearing Life Map - High load and velocity → decreased principal bearing life 	Section 7.1.10

Table 7-6: Summary of Purchase Criteria

Operation Standpoint				
#	Criteria	X and Y axes	Description	Source
1	Cornering Force Margin	Various Road conditions Vehicle Weight	<ul style="list-style-type: none"> • Force Margin Map - Low friction coefficient → Decreased FM • Given $\mu = 0.5$ and vehicle weight of 2970 lb - Rear-inside (0%), Front-inside (5%), Rear-outside(2%), Front-outside(12%) 	Section 7.2.1
2	Roll Angle	Various Road conditions Vehicle Weight	<ul style="list-style-type: none"> • Roll Angle Map - Low friction coefficient → Decreased roll angle - Increased vehicle weight(2970→3750) → Decreased roll angle ($1.7^\circ \rightarrow 1.5^\circ$) due to increased roll inertia of the sprung mass 	Section 7.2.2
3	Sideslip Angle	Various Road conditions Vehicle Weight	<ul style="list-style-type: none"> • Sideslip Angle Map - Low friction coefficient and increased vehicle weight (2970→3750) → Decreased sideslip angle($2.8 \rightarrow 2.3^\circ$) • Drop suddenly at the road condition of $\mu = 0.4$ - due to a zero for the force margin 	Section 7.2.3
4	Lateral Acceleration	Various Road conditions Vehicle Weight	<ul style="list-style-type: none"> • Lateral Acceleration Map - Low friction coefficient → Decreased lateral acceleration - Increased vehicle weight (2970→3750) → Decreased lateral acceleration ($0.68g \rightarrow 0.52g$) 	Section 7.2.4
5	Slip Angle	Various Road conditions Vehicle Weight	<ul style="list-style-type: none"> • Slip Angle Map - Low friction coefficient and increased vehicle weight → Decreased slip angle • Drop suddenly at the road condition of $\mu = 0.4$ - due to a zero for the force margin • Given $\mu = 0.9$ and vehicle weight of 2970 lb to 3750 lb - Rear: $-3.5^\circ \rightarrow -2.8^\circ$, Front: $-3^\circ \rightarrow -2.4^\circ$ • Rear slip angle is larger than the front slip angle → Higher rear lateral force → Decreased force margin (See 1.cornering force margin) → Oversteer condition 	Section 7.2.5

Operation Standpoint				
#	Criteria	X and Y axes	Description	Source
6	Yaw Rate	Various Road Conditions Vehicle Weight	<ul style="list-style-type: none"> ● Yaw Rate Map - Low friction coefficient and increased vehicle weight → Decreased yaw rate ● Jump up suddenly at the road condition of $\mu = 0.4$ - Due to a zero for the force margin ● Given $\mu = 0.9$ and 2970 → 3750 lb - Yaw rate: 0.3 → 0.24 rad/s 	Section 7.2.6
7	Acceleration Force Margin	Various Road Conditions Vehicle Weight	<ul style="list-style-type: none"> ● Acceleration Force Margin Map - Low friction coefficient → Decreased Acceleration FM - Increased vehicle weight → Increased Acceleration FM ● Given $\mu = 0.9$ and 2970 → 3750 lb - Rear: 73%→78%, Front: 64%→73% ● FM of the rear wheels is larger than that of the front wheels - Due to the larger normal forces on the rear wheels caused by the backward inertial force 	Section 7.2.7
8	Braking Force Margin	Various Road Conditions Vehicle Weight	<ul style="list-style-type: none"> ● Braking Force Margin Map - Low friction coefficient → Decreased Braking FM - Increased vehicle weight → Increased Braking FM ● Given $\mu = 0.9$ and 2970 → 3750 lb - Rear: 1%→30%, Front: 40%→52% ● FM of the front wheels is larger than that of the rear wheels - Due to the larger normal forces on the front wheels caused by the forward inertial force 	Section 7.2.8
9	Pitch Angle	Various Road Conditions Vehicle Weight	<ul style="list-style-type: none"> ● Pitch Angle Map (Acceleration) - Low friction coefficient - Increased vehicle weight(2970→3750) → Decreased pitch angle(0.76→0.7°) 	Section 7.2.9
		Various Road Conditions Vehicle Weight	<ul style="list-style-type: none"> ● Pitch Angle Map (Braking) - Low friction coefficient - Increased vehicle weight(2970→3750) → Decreased pitch angle(1.6→1.4°) 	
10	Travel Range	Velocity Battery Capacity	<ul style="list-style-type: none"> ● Travel Range Map - Higher battery capacity → Increased travel range - Depend strongly on the velocity 	Section 7.2.10
		Velocity Auxiliary Power	<ul style="list-style-type: none"> ● Energy Loss Map- Higher auxiliary power → Increased energy loss(low speed) 	

Table 7-7: Summary of Operation Criteria

Maintenance Standpoint				
#	Criteria	X and Y axes	Description	Source
1	Efficiency	Wheel Speed Wheel Torque	<ul style="list-style-type: none"> ● Condition-Based Maintenance Map - Nominal performance condition - Accessed performance condition - Required performance condition - Health Margin - Remaining useful life 	Section 7.3.1
2	Power Level		<ul style="list-style-type: none"> ● Degrade after several thousand charge depleting cycles in terms of the battery - Affect vehicle performance and efficiency 	Section 7.3.2
3	Responsiveness		<ul style="list-style-type: none"> ● Motor phase failure → Decreased electromagnetic torque capability → Decreased responsiveness 	Section 7.3.3
4	Torque Margin	Various Road Cond. Vehicle Weight	<ul style="list-style-type: none"> ● Torque Margin Map - Low friction coefficient → Decreased FM 	Section 7.3.4
5	Temperature Margin		<ul style="list-style-type: none"> ● Power electronics coolant is operated based on maximum inlet temperature of 65°C. → Result in temperature fluctuations (<40°C) at the semiconductor junctions 	Section 7.3.5
6	Noise Margin		<ul style="list-style-type: none"> ● Measure of the interior noise 	Section 7.3.6
7	Sensor Degradation		<ul style="list-style-type: none"> ● Sensor and process fault detection and isolation (SPFDI) 	Section 7.3.7
8	Bearing Degradation	Velocity Equivalent Dynamic Load	<ul style="list-style-type: none"> ● Condition-Based Maintenance Map - RPC of 5000 hr. minimum 	Section 7.3.8
9	Wire Insulation Degradation		<ul style="list-style-type: none"> ● Class F (155°C), larger than 10hp 	Section 7.3.9
10	Clutch Degradation		<ul style="list-style-type: none"> ● How fast does the clutch shift? 	Section 7.3.10

Table 7-8: Summary of Maintenance Criteria

Refreshment Standpoint				
#	Criteria	X and Y axes	Description	Source
1	Power Level	Vehicle Configuration 0-60 mph Accel. Time	<ul style="list-style-type: none"> ● Power/Response Map - Update 20 hp to 40 hp → Increased 0-60 mph acceleration time from 12.9 s to 6.0 s 	Section 7.4.1
2	Cost Benefit / Replacement Cost		<ul style="list-style-type: none"> ● Customers obtain the cost benefit associated with replacement cost - Based on an responsive supply chain (in-depth certification and a minimum set as a standard) 	Section 7.4.2
3	Efficiency Benefit		<ul style="list-style-type: none"> ● How much does efficiency improve? 	Section 7.4.3
4	Torque Level	Vehicle Weight 0-60 mph Accel. Time	<ul style="list-style-type: none"> ● Torque/Response Map - Update 20 hp to 40 hp → Increased torque level (at 60 mph) from 125 ft-lb to 248 ft-lb 	Section 7.4.4
5	Enhanced Handling / Ride Comfort		<ul style="list-style-type: none"> ● Handling and Ride Comfort - Improve by in-wheel motor and active suspension actuators 	Section 7.4.5
6	Enhanced Sensors		<ul style="list-style-type: none"> ● Precise real time data 	Section 7.4.6
7	Enhanced Control Software		<ul style="list-style-type: none"> ● Upgraded software can be done over the internet, through third party applications. 	Section 7.4.7
8	Enhanced Durability		<ul style="list-style-type: none"> ● How long do bearings last? 	Section 7.4.8
9	Enhanced Temperature Tolerance		<ul style="list-style-type: none"> ● How much does temperature tolerance improve? 	Section 7.4.9
10	Enhanced Safety		<ul style="list-style-type: none"> ● Enhanced safety in emergency conditions - Active response (MDW) to the driver to enhance safety 	Section 7.4.10

Table 7-9: Summary of Refreshment Criteria

From the purchase point of view, the cost and weight maps in terms of four different vehicle configurations are estimated, if a modular all-electric automobile in an open architecture could be assembled on demand based on the minimum set of highly certified, mass produced, and cost effective modules with a responsive supply chain, just as Dell computer does for personal computer. From the operation point of view, performance maps regarding operation criteria are generated based on the Simulink model of a 14 DOF full-vehicle model. These maps show the effects of vehicle weight and various road conditions. From the maintenance point of view, we demonstrated that the condition-based maintenance considering the NPC, APC, and RPC tell the customer in advance when their MDW will fail and how much time is left before failure in terms of efficiency and durability maps. Also, given four-independent wheels, if one wheel fails the other three wheels will operate, hence the vehicle will operate. However, for conventional transmissions, if the transmission fails, the whole vehicle fails.

Last, from the refreshment point of view, refreshment can be defined as updating the modules: engine, generator, batteries/super cap, skateboard chassis, car bodies, suspensions, drive wheel, and operational software. Assuming updates the MDW from 20 hp to 60 hp, we demonstrated how power level and torque respond to the customer's choice to meet customer needs.

Chapter 8. Summary and Conclusions

Equation Chapter 8 Section 1 This chapter will provide the research summary regarding research objective, literature review, key findings and results, and contribution in Chapter 1 to 7. Based on the research summary, recommended future work will be presented in Section 8.5.

8.1 RESEARCH OBJECTIVES

The overall objective of the research is to analytically develop a framework for maximizing human choice by means of visualizing human needs/requirements, so that customer demands can be met at the time of purchase of an open architecture HEV, which would be assembled on demand. In addition, based on the customer's individual duty/demand cycles, a vehicle will be tailored to meet the particular customer parameters such as an aggressive driver, an efficiency-priority driver, and a cost-priority driver, etc. This leads to the expanded human choice as a new set of marketing priorities.

Satisfying human needs implies responding directly to human commands / objectives at the time of purchase, in real time operation, and maintenance / tech mods over the life history of the vehicle. This framework demonstrates detailed human needs structured by performance maps to visually guide the customer in terms of purchase / operation / maintenance / refreshment decision.

To achieve the overall objective of the research, the specific goals are as follows:

- Investigate previous research on IWMs (in-wheel motors).
- Implement a nonlinear 14 DOF full-vehicle model consisting of the ride model, handling model, tire model, slip ratio, slip angle, and magic formula; this model is implemented in a MATLAB/SIMULINK environment.

- Evaluate simulation results for a nonlinear 14 DOF full-vehicle model in terms of the effect of the wheel subsystem unsprung mass on acceleration, braking, and cornering maneuvers under various road conditions (i.e., dry, wet, snow, ice)
- Evaluate simulations results for a quarter-vehicle model in terms of the effect of the unsprung mass on ride comfort and handling under different road profiles (i.e., concrete, asphalt, gravel).
- Implement algorithms to maximize the efficiency and maximize drivability depending on customer choices.
- Describe MDW design specifications such as different acceleration levels, gear ratio, continuous torque, peak torque, power rating, and clutch shift point for a MDW.
- Develop visual performance maps that would be of interest to the customers in terms of purchase / operation / maintenance / refreshment standpoints.
- Demonstrate the achievability of the framework for separate decision scenarios for the different customer types which might be aggressive driver, efficiency-priority driver, and cost-priority driver.

8.2 LITERATURE REVIEW

As mentioned in Section 2.4, literature review was presented in terms of the effect of the unsprung mass on drivability such as acceleration, braking, ride comfort and handling. In addition, electric vehicle configurations and comparison of a MDW and a single speed-in-wheel motor were made in Section 2.2 and 2.3. The literature review of efficiency was explained in Section 2.5. A nonlinear 14 DOF full-vehicle model consisting of ride model, handling model, and tire model including the tire magic formula was reviewed in Chapter 4. A literature review regarding duty / demand cycle is

presented in Chapter 6. The literature review in the Robotics Research Group is presented in Chapter 7. The key literature of this research is summarized in Table 8-1

Topics	Author	Description
Effect of the Unsprung Mass	(Rojas, Niederkofler, 2010)	<ul style="list-style-type: none"> • Suggested new suspension systems to assure vehicle ride comfort (body acceleration) and safety (contact force) when using in-wheel motors. For a given surface roughness, ride comfort and safety deteriorate due to the increased unsprung mass
	(Anderson, Harty, 2010)	<ul style="list-style-type: none"> • Presented subjective and objective measures of ride and handling, and provided numerical analysis based on a quarter-vehicle model
	(Vos, Besselink, 2010)	<ul style="list-style-type: none"> • Illustrated that the ride comfort and dynamic wheel load deteriorate as the roughness of the road is increased
	(Van Schalkwyk, 2006)	<ul style="list-style-type: none"> • Provided frequency analysis and simulation of the system based on a quarter-vehicle model
Vehicle Modeling	(Setiawan, Safarudin, 2009)	<ul style="list-style-type: none"> • Presented modeling, simulation, and validation of a 14 DOF full-vehicle model consisting of ride, handling, and tire model including the tire magic formula
	(Hudha, 2009)	<ul style="list-style-type: none"> • Provided modeling and validation of a 14 DOF full-vehicle model
Duty / Demand Cycles	(Greaves, Walker, 2011)	<ul style="list-style-type: none"> • Investigated operating requirement of electric vehicle motor drives based on duty cycles
	(Ren, 2009)	<ul style="list-style-type: none"> • Developed and predicted electric vehicle energy consumption with a variable and fixed ratio gearbox over a standard driving cycle to improve efficiency
Efficiency	(Mokhtari, Tara, 2008)	<ul style="list-style-type: none"> • Provided the efficiency map of switched reluctance motors (SRM) using a combination of the finite element method (FEM) and a mathematical model
Purchase / Operation / Maintenance / Refreshment Standpoints	(Tesar, 2011)	<ul style="list-style-type: none"> • Proposed the intelligent corner consisting of MDW, active camber/steering, active suspension, and TWIRE which is a reconfigurable surface contact system using a reconfigurable pneumatic tire
	(Tesar and Ashok, 2011)	<ul style="list-style-type: none"> • Developed the Multi-Speed Hub Drive Wheel for the ongoing revolution in more-electric cars
	(Tesar, 2009)	<ul style="list-style-type: none"> • Proposed the all-electric modular automobile, including intelligent MDW and active suspensions, and a modern decision making software to balance/interpret operator inputs, maximize efficiency, and to enhance maintainability, refreshability

Table 8-1: Summary of Literature Review

8.3 RESEARCH RESULTS AND DISCUSSIONS

8.3.1 Vehicle Modeling

8.3.1.1 Full-Vehicle (7 DOF) Ride Model

As mentioned in Section 4.2.3, the full-vehicle ride model consists of four unsprung masses connected to a sprung mass by a vertical spring-damper system. The sprung mass has three motions such as roll, pitch, and bounce motion. The four unsprung masses have four individual vertical motions. As a result, this leads to full-vehicle (7DOF) ride model as shown in Figure 8-1 [Setiawan, Safarudin et al.,2009].

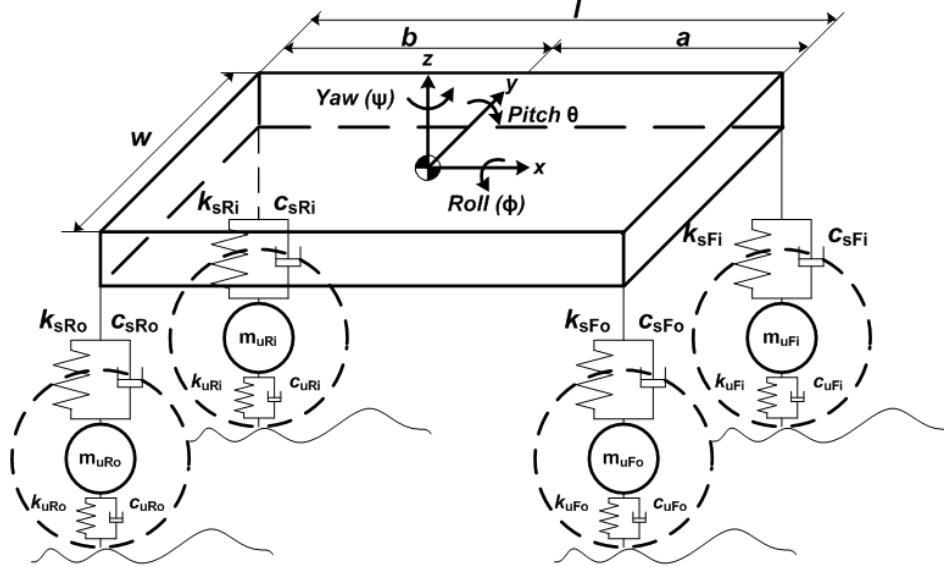


Figure 8-1: Full-vehicle (7 DOF) ride model

The bounce equation of motion is given by:

$$\begin{aligned}
 m_s \ddot{z}_s = & -2(k_{sF} + k_{sR})z_s - 2(c_{sF} + c_{sR})\dot{z}_s \\
 & + 2(ak_{sF} - bk_{sR})\theta + 2(ac_{sF} - bc_{sR})\dot{\theta} \\
 & + k_{sF}z_{uFi} + c_{sF}\dot{z}_{uFi} + k_{sF}z_{uFo} + c_{sF}\dot{z}_{uFo} \\
 & + k_{sR}z_{uRi} + c_{sR}\dot{z}_{uRi} + k_{sR}z_{uRo} + c_{sR}\dot{z}_{uRo}
 \end{aligned} \tag{8.1}$$

The rotational equation of motion for roll motion is given by:

$$\begin{aligned}
I_{xx}\ddot{\phi} = & -\frac{w^2}{2}(k_{sF} + k_{sR})\phi - \frac{w^2}{2}(c_{sF} + c_{sR})\dot{\phi} \\
& + \frac{w}{2}(k_{sF}z_{uFi} + c_{sF}\dot{z}_{uFi} - k_{sF}z_{uFo} - c_{sF}\dot{z}_{uFo}) \\
& + \frac{w}{2}(k_{sR}z_{uRi} + c_{sR}\dot{z}_{uRi} - k_{sR}z_{uRo} - c_{sR}\dot{z}_{uRo})
\end{aligned} \tag{8.2}$$

The rotational equation of motion for pitch motion is given by:

$$\begin{aligned}
I_{yy}\ddot{\theta} = & 2(ak_{sF} - bk_{sR})z_s + 2(ac_{sF} - bc_{sR})\dot{z}_s \\
& - 2(a^2k_{sF} + b^2k_{sR})\theta - 2(a^2c_{sF} + b^2c_{sR})\dot{\theta} \\
& - a(k_{sF}z_{uFi} + c_{sF}\dot{z}_{uFi} + k_{sF}z_{uFo} + c_{sF}\dot{z}_{uFo}) \\
& + b(k_{sR}z_{uRi} + c_{sR}\dot{z}_{uRi} + k_{sR}z_{uRo} + c_{sR}\dot{z}_{uRo})
\end{aligned} \tag{8.3}$$

The equation of motion associated with each wheel is given by:

$$\begin{aligned}
m_{uFi}\ddot{z}_{uFi} = & -a(k_{sF}\theta + c_{sF}\dot{\theta}) + \frac{w}{2}(k_{sF}\phi + c_{sF}\dot{\phi}) \\
& + k_{sF}z_s + c_{sF}\dot{z}_s - (k_{sF} + k_{uF})z_{uFi} - c_{sF}\dot{z}_{uFi} + k_{uF}z_{0Fi} \\
m_{uFo}\ddot{z}_{uFo} = & -a(k_{sF}\theta + c_{sF}\dot{\theta}) - \frac{w}{2}(k_{sF}\phi + c_{sF}\dot{\phi}) \\
& + k_{sF}z_s + c_{sF}\dot{z}_s - (k_{sF} + k_{uF})z_{uFo} - c_{sF}\dot{z}_{uFo} + k_{uF}z_{0Fo} \\
m_{uRi}\ddot{z}_{uRi} = & +a(k_{sR}\theta + c_{sR}\dot{\theta}) + \frac{w}{2}(k_{sR}\phi + c_{sR}\dot{\phi}) \\
& + k_{sR}z_s + c_{sR}\dot{z}_s - (k_{sR} + k_{uR})z_{uRi} - c_{sR}\dot{z}_{uRi} + k_{uR}z_{0Ri} \\
m_{uRo}\ddot{z}_{uRo} = & +a(k_{sR}\theta + c_{sR}\dot{\theta}) - \frac{w}{2}(k_{sR}\phi + c_{sR}\dot{\phi}) \\
& + k_{sR}z_s + c_{sR}\dot{z}_s - (k_{sR} + k_{uR})z_{uRo} - c_{sR}\dot{z}_{uRo} + k_{uR}z_{0Ro}
\end{aligned} \tag{8.4}$$

8.3.1.2 Horizontal Handling (3 DOF) Model

As mentioned in Section 4.3.2, the horizontal (3 DOF) handling model takes into account longitudinal, lateral, and yaw motions. Assuming that we consider the vehicle to be a rigid body, the global vehicle forces and moments act on the CG of the vehicle.

The self-aligning moments are generated by lateral force acting at a moment arm defined as the pneumatic trail (see Sec. 4.4.3).

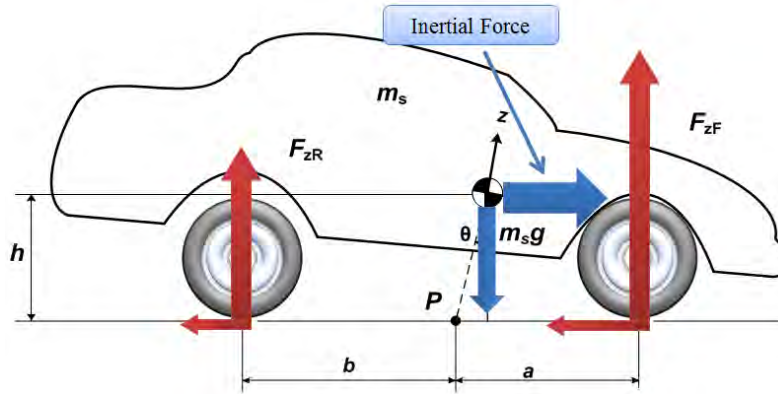


Figure 8-3: Pitch motion due to braking or traction

The longitudinal acceleration / deceleration lead to the pitch motion while the lateral acceleration contributes to the roll motion. Figure 8-3 shows longitudinal load transfer due to braking or traction, resulting in pitch motion. The equation of pitching motion with respect to pitch center (P) is given by [Setiawan, Safarudin et al.,2009]:

$$(I_{yy} + m_s h^2) \ddot{\theta} = m_s a_x h + m_s g h \theta - k_\theta \theta - c_\theta \dot{\theta} \quad (8.7)$$

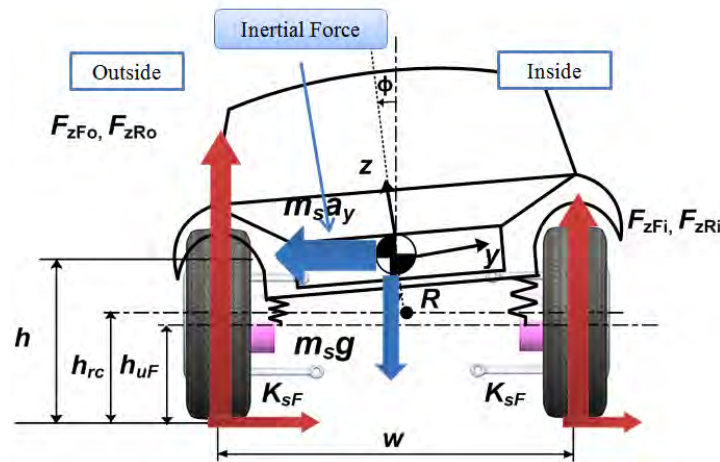


Figure 8-4: Roll motion due to a cornering maneuver

Figure 8-4 shows the lateral load transfer during a cornering maneuver. The equation of rolling motion with respect to roll center of the vehicle is as follows [Setiawan, Safarudin et al.,2009]:

$$\left(I_{xx} + m_s (h - h_{rc})^2\right) \ddot{\phi} = m_s a_y (h - h_{rc}) \cos \phi + m_s g (h - h_{rc}) \sin \phi - k_\phi \phi - c_\phi \dot{\phi} \quad (8.8)$$

It should be noted that above equation is written by considering moments acting on the vehicle roll center than the CG of sprung mass. The roll inertia of the sprung mass with respect to the vehicle roll center is considered in above equation.

8.3.1.3 Tire (4 DOF) Model

As described in Section 4.4, the mathematical model for the tire (4 DOF model) is obtained from one-wheel rotational dynamics.

1) Tire Model

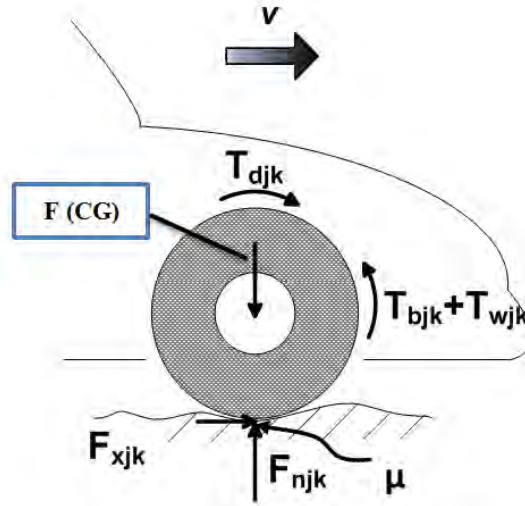


Figure 8-5: One-wheel rotational dynamics

As shown in Figure 8-5, assuming no wheel friction torque, the equation of motion for each wheel is given by [Setiawan, Safarudin et al.,2009]:

$$\begin{aligned}
J_{wFi} \dot{\omega}_{wFi} &= T_{dFi} - T_{bFi} - F_{xFi} r_w \\
J_{wFo} \dot{\omega}_{wFo} &= T_{dFo} - T_{bFo} - F_{xFo} r_w \\
J_{wRi} \dot{\omega}_{wRi} &= T_{dRi} - T_{bRi} - F_{xRi} r_w \\
J_{wRo} \dot{\omega}_{wRo} &= T_{dFo} - T_{bRo} - F_{xRo} r_w
\end{aligned} \tag{8.9}$$

The F_{xjk} represents traction force as follows:

$$\begin{aligned}
F_{xjk} &= \mu(\lambda) \cdot F_{njk}, \quad \text{acceleratoin (slip)} \quad s_F = \left(\frac{r\omega_F - v_{xF}}{r\omega_F} \right) \times 100\% \quad (r\omega_F > v_{xF}) \\
&\quad \text{braking (skid)} \quad s_F = \left(\frac{r\omega_F - v_{xF}}{v_{xF}} \right) \times 100\% \quad (r\omega_F < v_{xF})
\end{aligned} \tag{8.10}$$

The traction force is due to the friction force from the ground acting on the tires. It depends on the longitudinal slip/skid ratio, normal load on the tire, and the friction coefficient of the tire-road interface[Rajamani,2006].

2) Slip Angle

The slip angles (α) can be defined as the angle between the heading direction of the tire and its travel direction which is the direction of the hub velocity vector. The tire slip angle occurs due to the lateral elasticity of the tire [Wong,2008].

$$\begin{aligned}
\alpha_F &= \tan^{-1} \left(\beta + \frac{a\dot{\psi}}{v_x} \right) - \delta = \tan^{-1} \left(\frac{v_y + a\dot{\psi}}{v_x} \right) - \delta \\
\alpha_R &= \tan^{-1} \left(\frac{v_y - b\dot{\psi}}{v_x} \right)
\end{aligned} \tag{8.11}$$

3) Longitudinal Slip / Skid Ratio

Figure 8-6 shows the schematic diagram in terms of the longitudinal, lateral forces and velocity. The longitudinal force (F_{xF}) and lateral force (F_{yF}) at the front wheel are generated from longitudinal slip ($s_F = \frac{r\omega_F - v_{xF}}{r\omega_F}$) and slip angle (α_F) with normal force (F_{zF}), respectively.

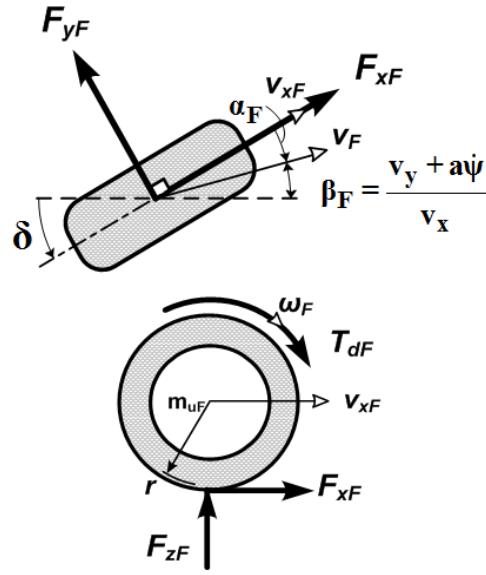


Figure 8-6: Longitudinal, later forces and velocity components

The longitudinal velocity of the front wheel can be defined by [Hudha, Kadir et al.,2009]:

$$v_{xF} = v_F \cos \alpha_F = \sqrt{(v_y + a\dot{\psi})^2 + v_x^2} \cos \alpha_F \quad (8.12)$$

$$v_{xR} = v_R \cos \alpha_R = \sqrt{(v_y - a\dot{\psi})^2 + v_x^2} \cos \alpha_R \quad (8.13)$$

If a vehicle moves in a straight line, the lateral velocity and yaw rate will not occur so that the longitudinal velocity of the rear / front wheels can be equal to the longitudinal velocity of the CG. Finally, assuming that the wheel's effective rolling radius is the same as the wheel radius, the longitudinal slip / skid at the front wheel are defined by:

$$\begin{aligned} \text{acceleratoin(slip)} \quad s_F &= \left(\frac{r\omega_F - v_{xF}}{r\omega_F} \right) \times 100\% \quad (r\omega_F > v_{xF}) \\ \text{braking(skid)} \quad s_F &= \left(\frac{r\omega_F - v_{xF}}{v_{xF}} \right) \times 100\% \quad (r\omega_F < v_{xF}) \end{aligned} \quad (8.14)$$

The longitudinal slip / skid at the rear wheel are similar to above equation. The longitudinal slip of the tire is 100%, indicates that tires are spinning while a vehicle doesn't move. For the skid, -100% represents a locked wheel while a vehicle moves.

4) **Magic Formula**

An empirical method to calculate steady-state tire force and moment as the Magic Formula has been used in vehicle dynamics (Section 4.4.5). When the local shear forces are below the limit of friction force (μF_z), the tire elements adhere to the road surface. The Magic Formula gives us the longitudinal ($F_x, driving$), and lateral ($F_y, cornering$) forces, and the self-aligning torque (M_z) based on slip angle and skid ratio. The Magic Formula provides the mathematical functions as follows [Pacejka,2006]:

$$\begin{aligned} F_{xjk} &= f(F_{zjk}, s_{jk}) \\ F_{yjk} &= f(F_{zjk}, \alpha_{jk}) \\ M_{yjk} &= f(F_{zjk}, \alpha_{jk}) \end{aligned} \quad (8.15)$$

The longitudinal force is a function of normal force and longitudinal slip. The lateral force and self-aligning moment is a function of normal force and slip angle.

8.3.1.4 Nonlinear 14 Degree-Of-Freedom Full-Vehicle Model

As mentioned in Section 4.5.5, the nonlinear 14 DOF full-vehicle model consists of the vehicle ride (7DOF), horizontal handling (3 DOF), and tire (4 DOF) with slip ratio, slip angle, and Magic Formula, as shown in Figure 8-7.

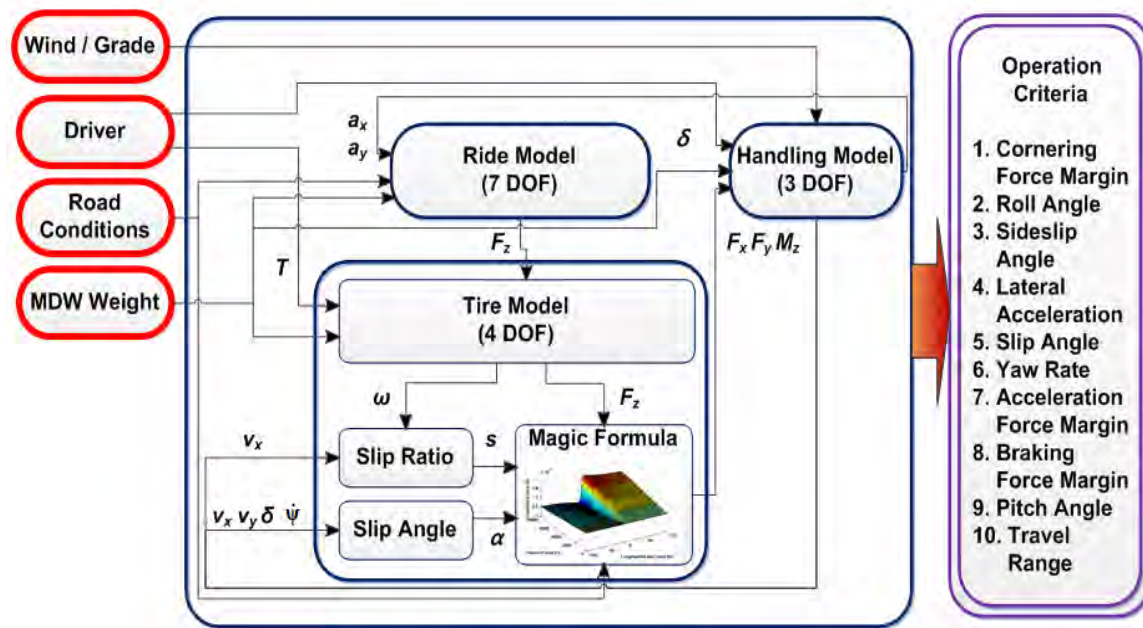


Figure 8-7: Schematic diagram of 14 DOF full-vehicle model consisting of block diagrams in MATLAB/SIMULINK

The control parameters are wind / grade, driver (i.e. torque, steering angle), road conditions, and MDW weight. The operation performance criteria such as cornering force margin, roll angle, sideslip angle, lateral acceleration, slip angle, yaw rate, acceleration force margin, braking force margin, pitch angle, and travel range can be adequately described by the nonlinear 14 DOF full-vehicle model, which is governed by the input control parameters.

8.3.2 Vehicle Simulation Results

8.3.2.1 Effects of Unsprung Mass on Performance Criteria

Acceleration and Braking

As mentioned in Section 5.1.1 and 5.1.2, the acceleration of an electric vehicle depends primarily on the torque generated by the motor. From the customer point of view, acceleration is judged by the time required to go from 0 to 60 mph. The braking performance can be a measure of stopping distance.

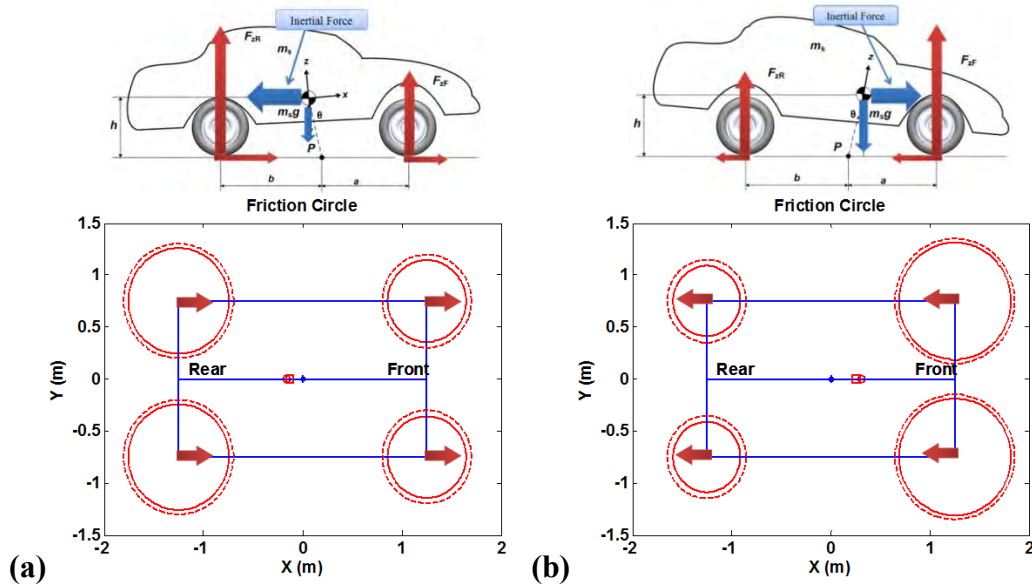


Figure 8-8: Friction circles of each wheel during acceleration and braking

Figure 8-8 (a) and (b) visualizes the friction circle of each wheel during acceleration and braking, respectively. During acceleration, the load transfer occurs from the front wheels to the rear wheels because of the forward inertial force acting on the vehicle. During braking, the reverse situation occurs.

% Unsprung Mass		0-60 mph acceleration	60-0 mph braking
		Dry asphalt	Dry asphalt
$m_u=22\%$	Time	11.9 s	6 s
	Accel.	0.23 g	0.45 g
	Distance	143 m(ft)	80(263) m(ft)
$m_u=10\%$	Time	10.8 s	5.5 s
	Accel.	0.25 g	0.5 g
	Distance	143 m(ft)	73(240) m(ft)

Table 8-2: Comparison of acceleration and braking

Given the wheel torque, the comparison of two distinct values of percent unsprung masses ($m_u = 22\%$ and $m_u = 10\%$) is made in terms of time, acceleration / deceleration, and distance during acceleration and braking, as shown in Table 8-2. The 0-60 mph acceleration time is $t = 11.9$ s and $t = 10.8$ s, and the corresponding acceleration level is 0.23 g and 0.25 g in terms of $m_u = 22\%$ and $m_u = 10\%$. Given the dry asphalt, the 60-0 mph braking stopping time is $t = 6$ s and $t = 5.5$ s, and the corresponding deceleration level is 0.45 g and 0.5 g, and the stopping distance is $SD = 263$ ft and $SD = 240$ ft in terms of $m_u = 22\%$ and $m_u = 10\%$.

As unsprung mass increases, the pitch angle of a vehicle with a $m_u = 10\%$ is larger than that of a vehicle with a $m_u = 22\%$. During acceleration and braking, the dynamic load is transferred from the front axle to the rear axle (vice versa). As the unsprung mass increases, the longitudinal load transfer decreases, given the same braking wheel torque (see Sections 5.1.1 and 5.1.2).

Cornering Maneuver

As mentioned in Section 5.1.3.2., many researchers use a standard single-lane change maneuver to examine a vehicle's dynamic responses

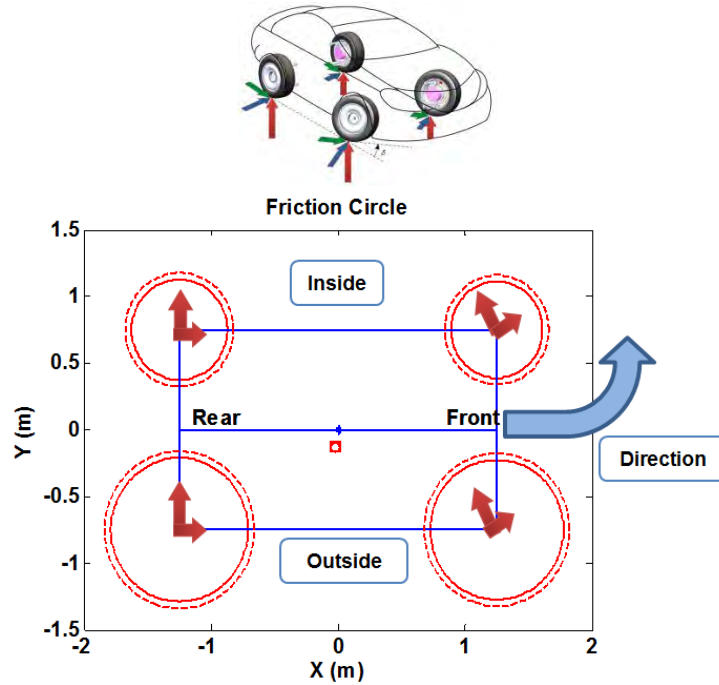


Figure 8-9: Friction circles of each wheel during cornering

Figure 8-9 visualizes the friction circles of each wheel for a single-lane change maneuver. Visually, it can be seen that friction circles of the outside wheels are larger than those of the inside wheels. The load transfer occurs from the inside to the outside (or vice versa) because of the inertia force acting on the vehicle, so that the normal force varies from the static values by the amount of load transfer.

As unsprung mass (m_u) increases, the sideslip angle, yaw rate, lateral acceleration, and roll motion decreases slightly given the wheel torque and steering angle command. (see Sections 5.1.3.1 and 5.1.3.1).

8.3.2.2 Effects of Increased Unsprung Mass under Various Road Conditions

Acceleration and Braking

As mentioned in Section 5.2.1.1, Section 5.2.2.1, and 5.2.3.1, simulations of the vehicle's response subjected to acceleration and braking have been carried out to evaluate the effects of increased unsprung mass under various road conditions: dry asphalt, wet asphalt, and snowy road.

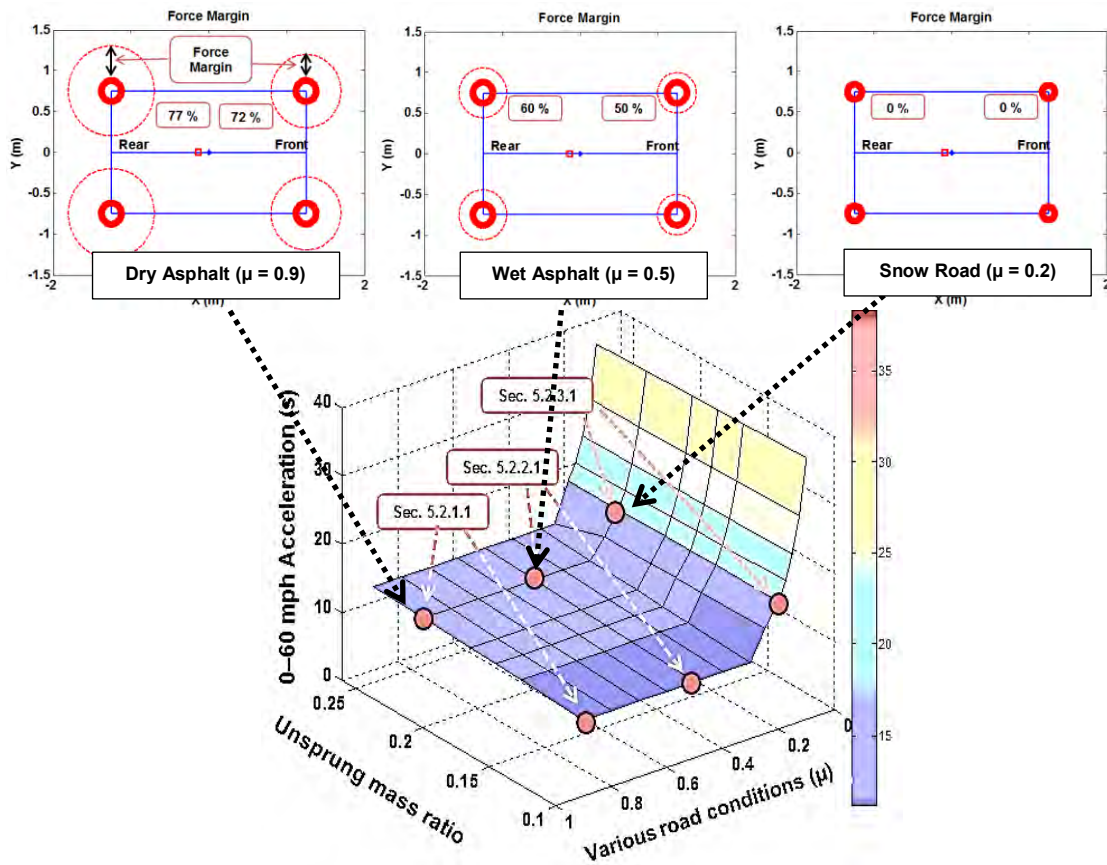


Figure 8-10: Acceleration map with the force margin of each wheel on dry asphalt, wet asphalt, and snowy road, given constant torque (290 N-m (214 ft-lb))

Figure 8-10 shows the variation of the force margins according to various road conditions during acceleration. The friction circles of each wheel become smaller because of the decreased friction force caused by a lower friction coefficient. In addition, the

increased unsprung mass increases slightly the force margin (i.e., $\mu=0.9$ (dry asphalt), $\mu=0.5$ (wet asphalt), $\mu=0.2$ (snowy road)) (see Sections 5.2.1.1, 5.2.2.1, and 5.2.3.1).

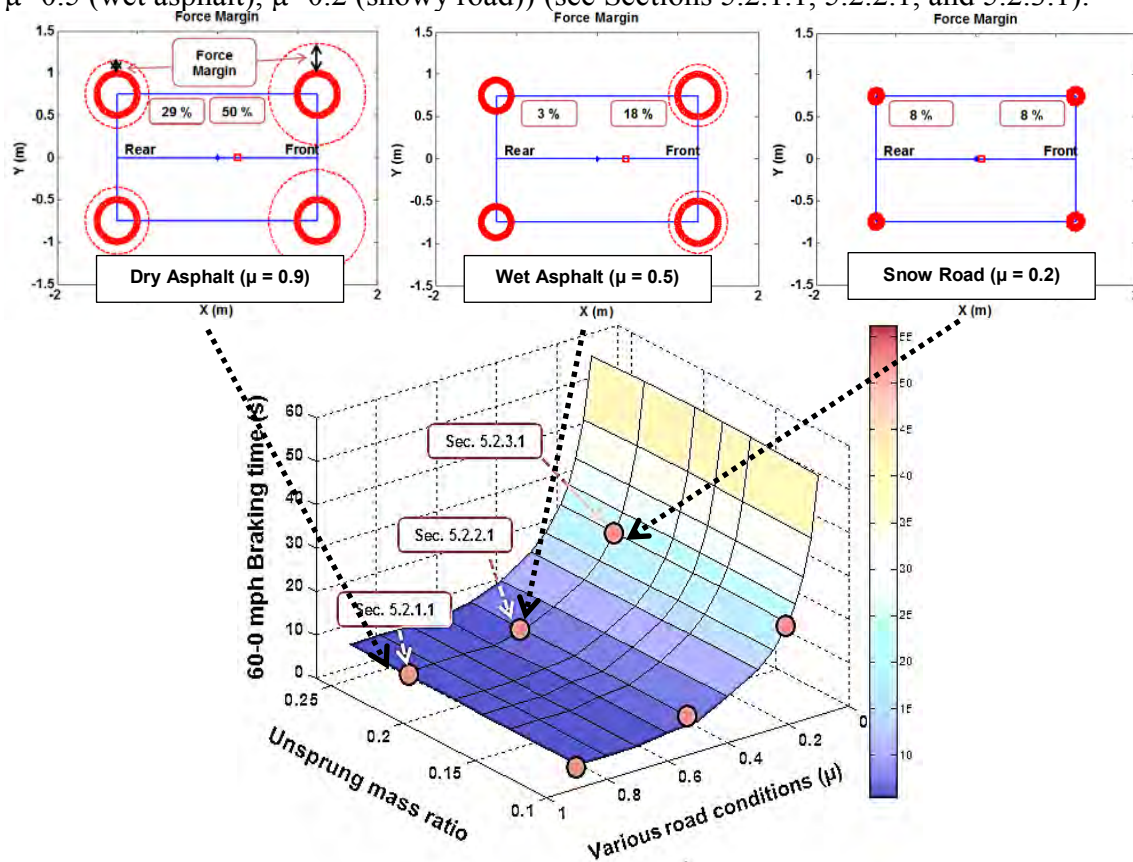


Figure 8-11: Acceleration map with force margin of each wheel on dry asphalt, wet asphalt, and snowy road, given constant braking torque (570 N-m(420 ft-lb))

Figure 8-11 shows the variation of the force margins according to various road conditions during braking. The friction circles of the front wheel are larger than those of the rear wheels due to the forward inertial force caused by braking. As the friction coefficient becomes smaller, the solid circle (i.e. simulated friction circle) becomes smaller. This implies that actual braking force becomes smaller, resulting in a larger 60-0 mph braking time. In addition, the increased unsprung mass increases slightly the force margin (see Sections 5.2.1.1, 5.2.2.1, and 5.2.3.1).

Cornering Maneuver

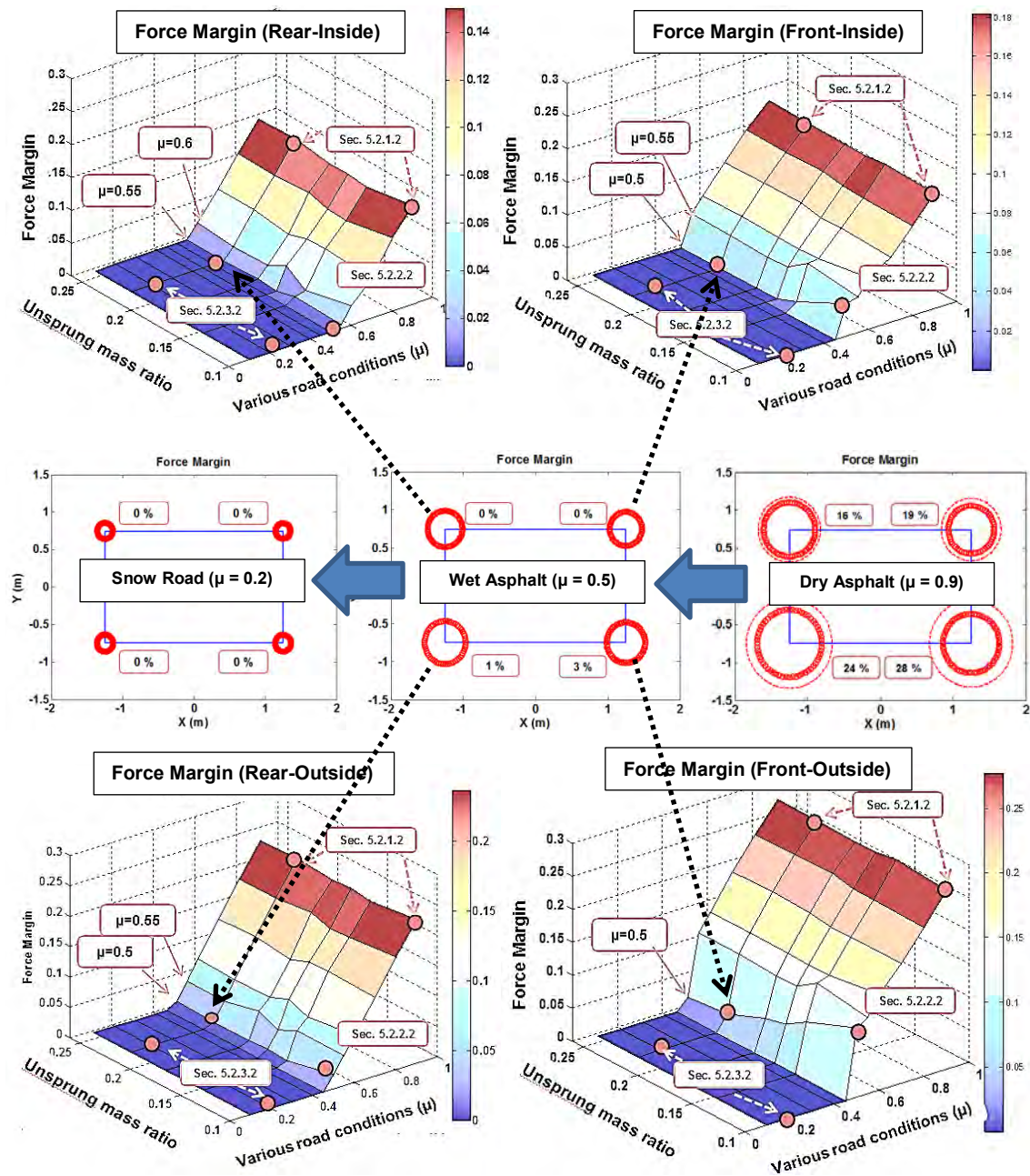


Figure 8-12: Force margin map during a cornering maneuver

In Section 5.2.1.2, Section 5.2.2.2, and 5.2.3.2, simulations of the vehicle's response subjected to a single lane change maneuver have been carried out to evaluate the effects of increased unsprung mass under various road conditions: dry asphalt ($\mu = 0.9$), wet asphalt ($\mu = 0.5$), and snowy road ($\mu = 0.2$). The force margins of each wheel are visualized by using friction circles for each wheel. As shown in Figure 8-12, given the wet asphalt of $\mu = 0.5$, each arrow indicates the corresponding force margin point of the rear-inside, front-inside, rear-outside, and front-outside wheel. The increased unsprung mass increases slightly the force margin (see Sections 5.2.1.2, 5.2.2.2, and 5.2.3.2).

The force margin of the outside wheels is larger than that of inside wheels. This occurs because the normal force of the outside wheels is larger than that of inside wheels (see Section 5.2.2.2). In addition, it is apparent that the force margin of front wheels is larger than that of rear wheels. This is due to the fact that the lateral acceleration at the CG causes the rear slip angle to increase more than the front slip angle, resulting in larger lateral forces to counteract the lateral acceleration. This is called oversteer behavior (see Sections 4.3.1, 5.2.1.2, 5.2.2.2, and 5.2.3.2).

8.3.3 Duty / Demand Cycles

As mentioned in Chapter 6, customer's demand cycle is critical for their desired drivability and efficiency. The questions that arise are: how to measure a customer?, how to classify a customer?, and how to satisfy a customer?

To address these questions, an automobile company will provide the customer with a representative vehicle to obtain the individual's demand cycles. The customer will drive for two weeks. Whenever he drives, numerous sensors equipped in the vehicle will keep storing information, so that all operational parameters can be recorded. After that, a third-party application would be used to analyze the specific duty cycle for that driver.

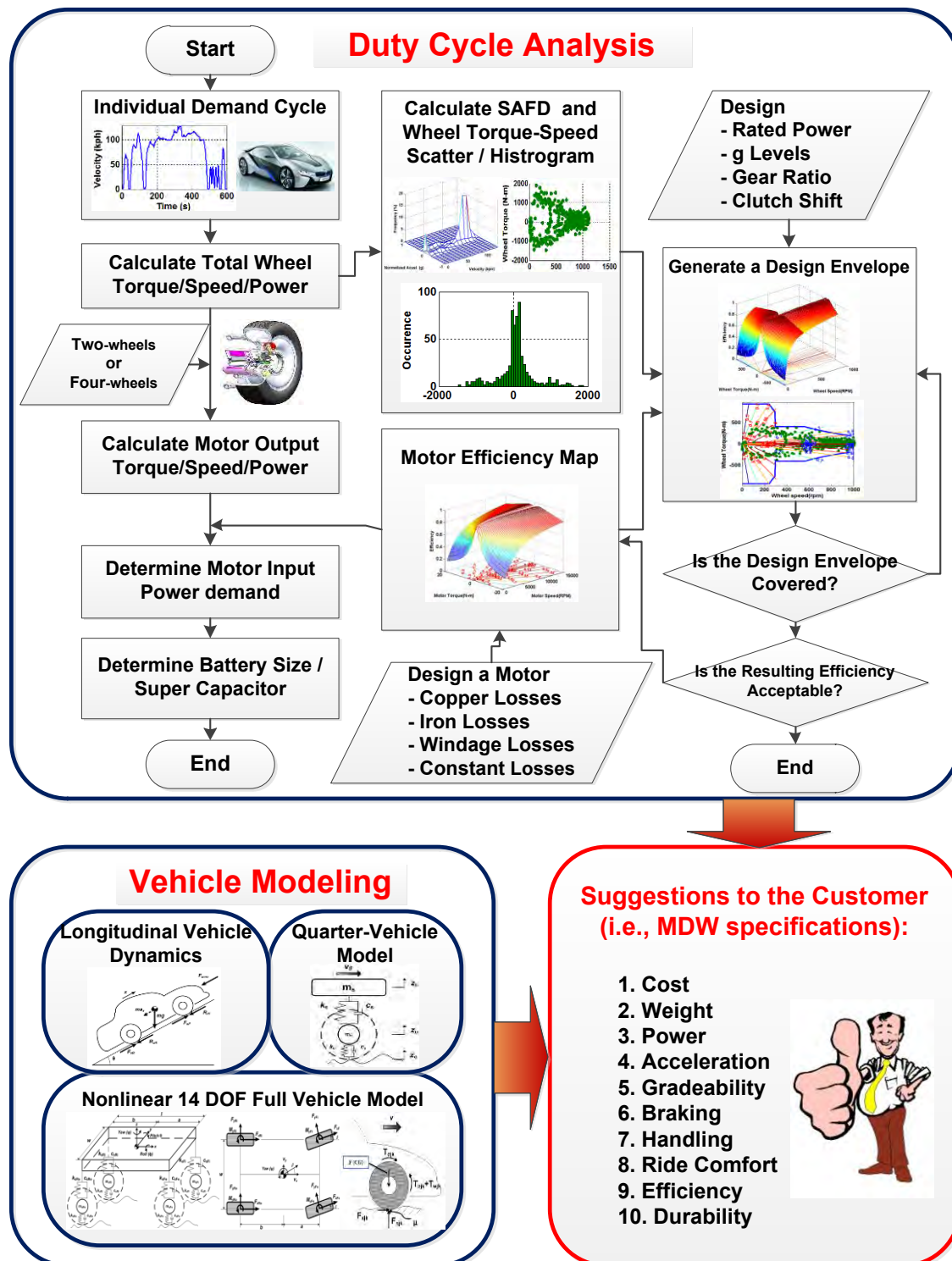


Figure 8-13: Flowchart illustrating the visual approach to duty cycle analysis

Then, we can use the customer's specific cycle to predict what the customer wants, and thus electric vehicles will be customized to suit the customer's demand style, so that the customer can be best satisfied with their purchase [Tesar and Ashok, May, 2011]. Figure 8-13 shows the flow chart illustrating the visual approach to duty cycle analysis. Given the individual demand cycles for the particular customer, total wheel torque / speed / power are calculated. Depending on the customer's choice of two-wheels or four-wheels, motor output torque / speed / power are calculated. Knowing the efficiency map of the SRM based on copper, iron, windage, constant losses, we are able to obtain the motor input power demand. This leads to determining the battery size / super capacitor, controller technology which is left here as future work.

Given the Speed-Acceleration Frequency Distribution (SAFD), wheel torque-speed scatter and histogram, we do the mapping of the wheel torque into motor torque with respect to the speed range of the first stage and the speed range of the second stage. In addition, the motor efficiency map is transformed into the needed speed range based on the rated power, different g levels, gear ratio, and clutch shift point (see Section 6.1.7).

The first decision question related to drivability is: 'is the design envelope covered?' The second decision question related to efficiency is: 'is the resulting efficiency acceptable?' If these two decision questions are satisfied, then we can make suggestions to the customer regarding the MDW specifications such as different g levels, gear ratio, rated power, continuous torque, peak torque, etc.

With this information and vehicle modeling (longitudinal vehicle dynamics, quarter vehicle model, nonlinear 14 DOF full vehicle model), 10 purchase criteria are presented to the customer in detail: cost, weight, power, acceleration, gradeability, braking, handling, ride comfort, efficiency, durability (see Section 7.1).

8.3.4 Comparison of Two Speed Regimes and One Speed Regime

As mentioned in Section 6.3.1, comparison of Protean's in-wheel motor and a MDW is made in terms of efficiency under both urban and highway duty cycle as shown in Figure 8-14.

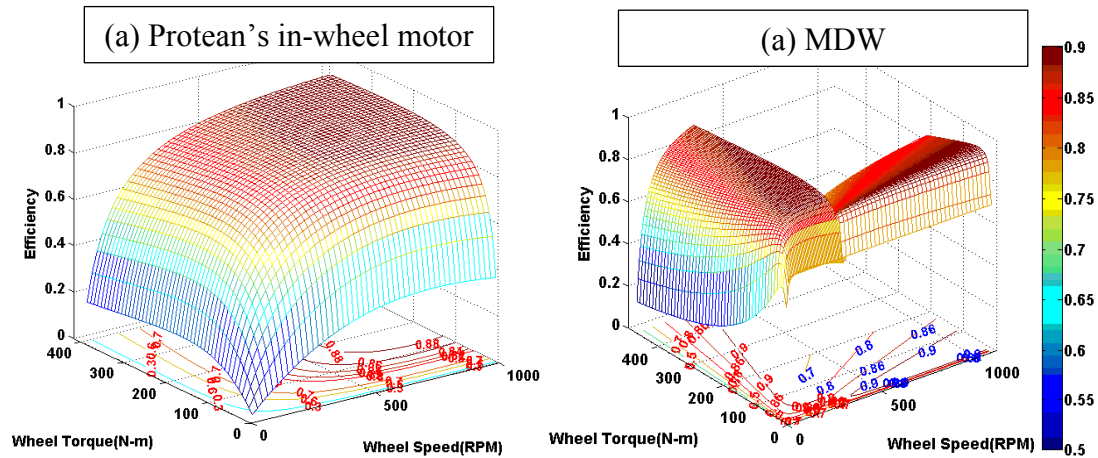


Figure 8-14: Comparison of efficiency maps

To visually understand the comparison of Protean's in-wheel motor and a MDW, 2-D contour maps are generated as shown in Figure 8-15, given a comparison of Protean's in-wheel motor and a MDW in terms of efficiency under a selected urban duty cycle (see Section 6.3.1.1).

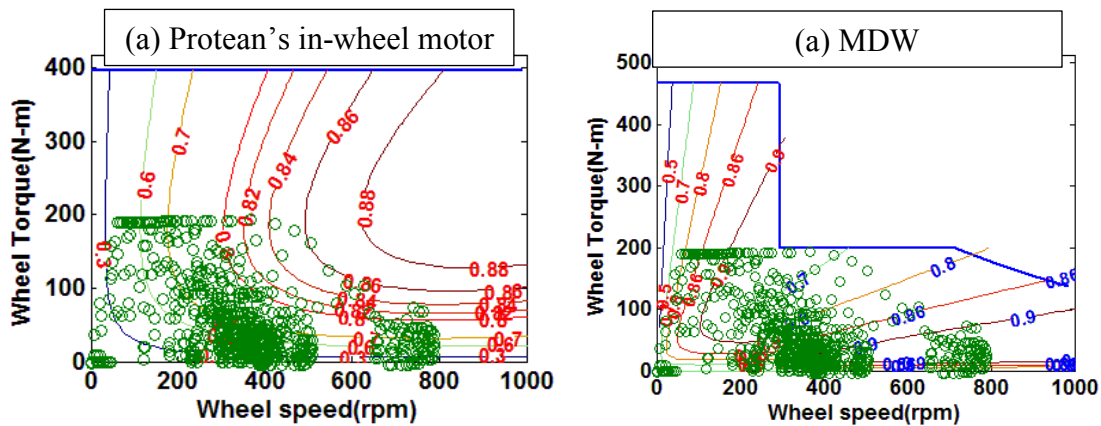


Figure 8-15: Comparison of efficiency maps under urban duty cycle

As can be seen, urban driving requires the capability to operate efficiently at low speed and low torque. The efficiency map of Protean's in-wheel motor shows the higher efficiency at high speed and moderate torque. However, the efficiency map of a MDW shows the higher efficiency at low speed and high torque as well as high speed and low torque. This leads to an improved efficiency under urban duty cycle. (see Table 8-3)

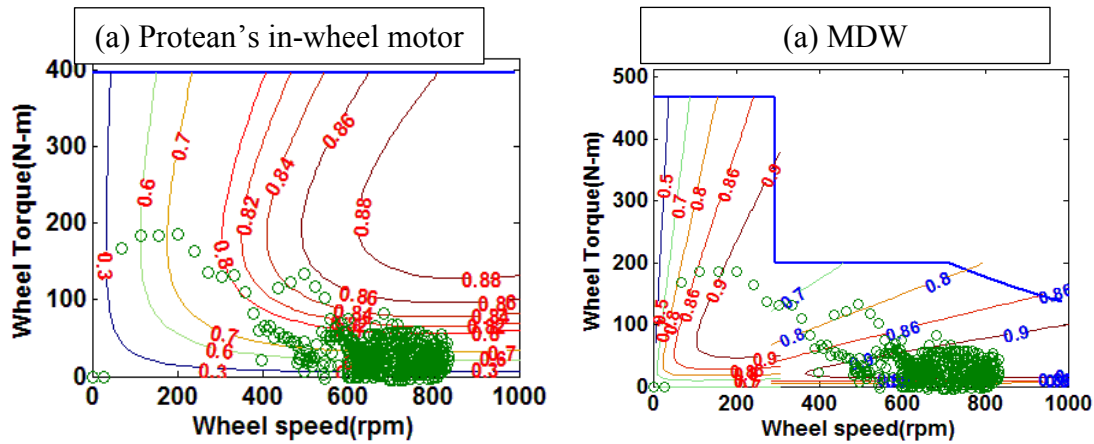


Figure 8-16: Comparison of efficiency maps under highway duty cycle

Section 6.3.1.2 compares Protean's in-wheel motor and a MDW in terms of efficiency under a selected highway duty cycle as shown in Figure 8-16. As can be seen, Highway driving requires the capability to operate in high speed and low torque. This leads to an improved efficiency under highway duty cycle for the MDW. (see Table 8-3)

	Protean's IWM (%)	MDW (%)	Difference (%)	Loss Improvement Ratio
Urban Driving (UDDS)	73.8	85.8	12.0	1.9
Highway Driving (HWFET)	81.5	89.6	8.1	1.8

Table 8-3: Simulation results

Efficiency comparisons between the in-wheel motor and the MDW are made in Table 8-3, in terms of an urban driving and a highway driving. Clearly, it is concluded that the MDW has the capability to have a higher efficiency not only for urban driving but also for highway driving, compared to Protean's single speed in-wheel motor. The loss improvement ratio indicates that the losses of a MDW are lower than that of Protean's IWM, by a factor of approximately two.

As a simulation result, we proved that efficiency of the MDW is significantly higher than that of Protean's in-wheel motor. The MDW has four speed regimes, just as a standard transmission has 5 or 6 speeds to increase efficiency [Tesar and Ashok, May, 2011]. Now we will discuss the comparison of a MDW using a reconfigurable controller.

8.3.5 Comparison of a MDW with a Reconfigurable Controller

With a reconfigurable power controller, we project that the MDW can have a higher efficiency over its entire torque-speed profile by raising and flattening the sweet spot. In other words, by choosing appropriate controller components, the overall efficiency can be further improved to meet the customer requirements for different purposes of the system in real time. The electric motor would be driven under two controller configurations, resulting in two additional "speed regimes". Hence, four distinct "speeds" are created in concert with mechanical clutch shift [Tesar and Ashok, May, 2011]

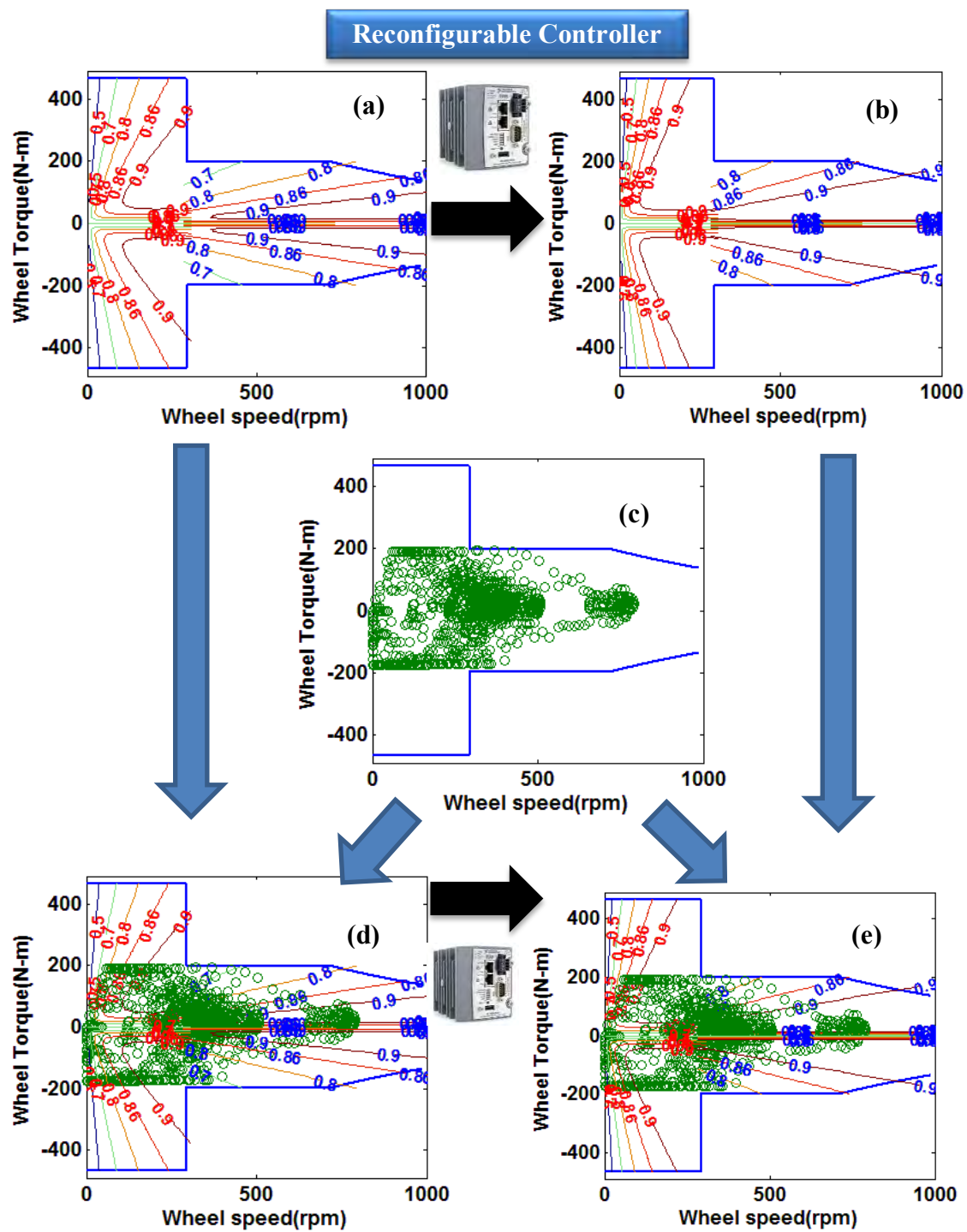


Figure 8-17: Efficiency maps of an MDW without & with a reconfigurable controller

Figure 8-17 (a) is simulation based on a clutch shift point at 20 mph considering motor mode and generator mode. This figure shows the efficiency map of a MDW without a reconfigurable controller. Figure 8-17 (b) shows the predicted efficiency map of a MDW with a reconfigurable controller which expands and raises the efficiency sweet spot. Figure 8-17 (c) shows the scatter points associated with UDDS duty cycle.

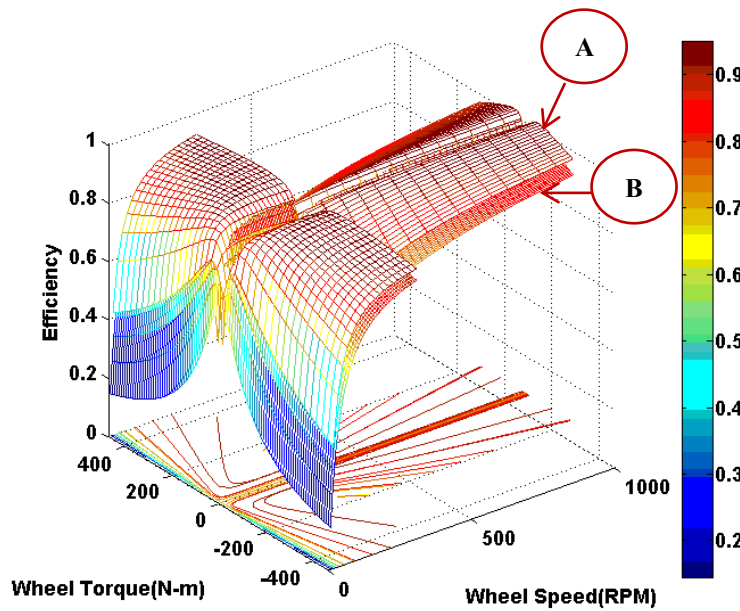


Figure 8-18: Efficiency maps of an MDW without & with a reconfigurable controller

Each point is an operating point. Figure 8-17 (d) and (e) show the combined maps (including efficiency map and scatter map), which is the basis for the efficiency of an MDW with and without a reconfigurable controller, respectively. The efficiency of an MDW with and without a reconfigurable controller is calculated as 85.8% and 88.2%, respectively. It is suggested then that the MDW with a reconfigurable controller has a higher efficiency by a further 2.4% (i.e., loss improvement = 1.2x) or an overall improvement loss ratio compared to the Protean of 2.2x for the UDDS.

Simulated efficiency maps of an MDW without & with a reconfigurable controller are shown in Figure 8-18. As seen at symbol ‘A’ shown in Figure 8-18, this is the improved efficiency map of an MDW with a reconfigurable controller. Without a reconfigurable controller, the symbol ‘B’ indicates the efficiency map of an MDW.

8.3.6 Purchase / Operation / Maintenance / Refreshment Standpoints

As mentioned in Chapter 7, we discussed the human choices and human needs in terms of purchase / operation / maintenance / refreshment standpoints. From the purchase point of view, the cost and weight maps in terms of four different vehicle configurations are estimated, if a modular all-electric automobile in an open architecture could be assembled on demand. The power/response (Section 7.1.3) and torque/response (Section 7.1.4) maps are shown in Figure 8-19.

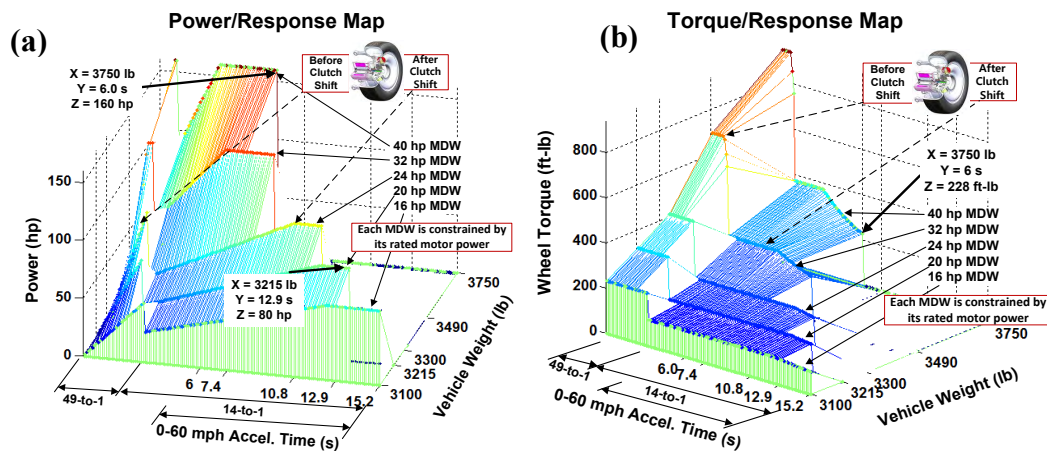


Figure 8-19: Power/Response and Torque/Response maps with respect to 0-60 acceleration time and vehicle weight considering four independent drive wheels

The suggested motor powers of the MDW are 16, 20, 24, 32, up to 40 hp. Total effective power utilization rating of the hybrid electric vehicles equipped with four-independent MDWs are 64, 80, 96, 128, up to 160 hp. From the power/response map as

shown in Figure 8-19 (a), it is clear that a very direct relationship exists between the power level choice and the customer desired acceleration (responsiveness). From the customer point of view, acceleration is judged by the time required to go from 0 to 60 mph. The wheel torque and 0-60 mph acceleration time can be simulated as shown in Figure 8-19 (b). Given four independent MDWs, the 0-60 mph acceleration times of the MDW (16 hp, 20 hp, and 24 hp) are 15.2 s, 12.9 s, and 10.8 s, respectively. The 0-60 mph acceleration times corresponding to the MDW (32hp) and MDW (40hp) are 7.3 s and 6.0 s. It should be noted that each MDW is constrained by its rated motor power.

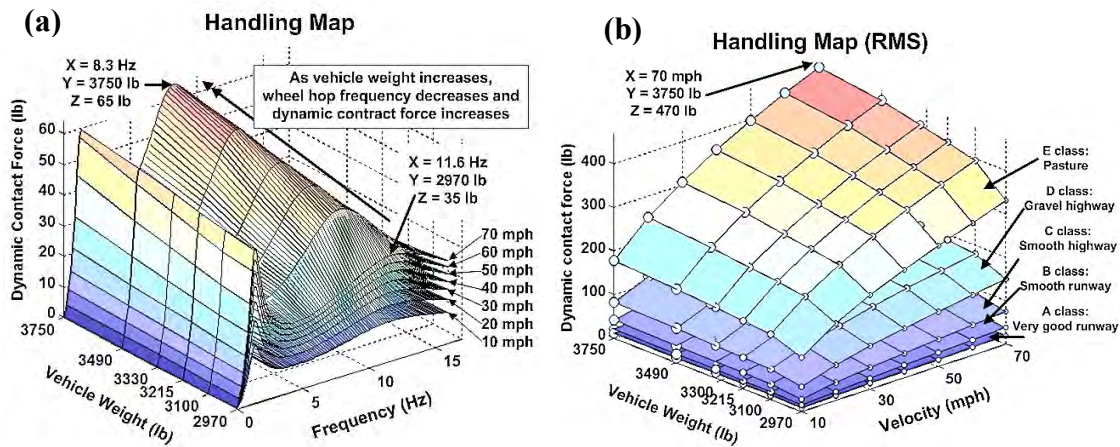


Figure 8-20: Handling maps

As mentioned in Section 7.1.7, dynamic contact force is a measure of a vehicle's handling capability. It conceptually can be obtained by multiplying tire stiffness with tire deflection, which is a useful measure of road holding and handling. Figure 8-20 (a) shows the frequency response of the dynamic contact force output as a function of vehicle weight and frequency for seven different speeds ranging from 10 mph to 70 mph. As the vehicle weight increases, the second natural frequency which is the wheel hop frequency decreases (i.e., 11.6 Hz \rightarrow 8.3 Hz) and the dynamic contact force increases (i.e., 35 lb \rightarrow

65 lb). The increased dynamic contact force leads to deteriorating traction required for acceleration, braking, or cornering.

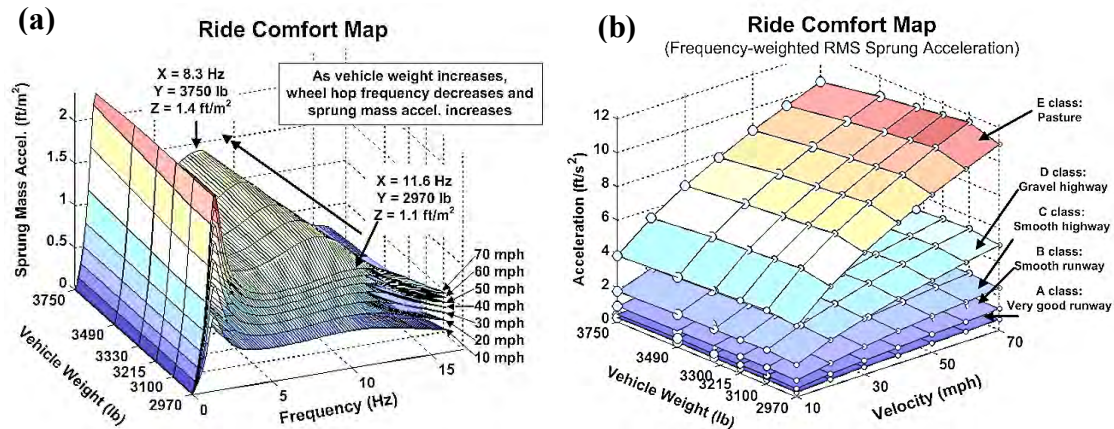


Figure 8-21: Ride comfort maps

As described in Section 7.1.8, the sprung mass acceleration is a measure of how comfortable a car ride feels. One measure of ride comfort can be quantified in terms of the vertical acceleration of a vehicle body. Figure 8-21 (a) shows the performance map of the sprung mass acceleration output as a function of the vehicle weight and frequency with seven different speeds from 10 mph to 70 mph. As the vehicle weight increases, the second natural frequency which is the wheel hop frequency decreases and the sprung mass acceleration increases. The increased sprung mass acceleration leads to deteriorating ride comfort. Figure 8-20 and Figure 8-21 (b) shows the handling and ride comfort maps using power spectral density. The following table summarizes purchase criteria studied in this report in terms of their usage, X and Y measures of interest to the customers, and description in Table 8-4.

Purchase Standpoint				
#	Criteria	X and Y axes	Significant Research Results	Source
1	Cost	Vehicle Configuration 0-60 mph Accel. Time	<ul style="list-style-type: none"> ● Cost/Performance Map - Rated power increases with vehicle configuration from '1' to '4' → Increased cost ● 40 hp MDW with a reconfigurable controller / intelligent corner ('4') - Cost: \$26,400, - Weight: 4290 lb - 0-60 acceleration time: 6 s 	Section 7.1.1
2	Weight	Vehicle Configuration 0-60 mph Accel. Time	<ul style="list-style-type: none"> ● Weight/Performance Map - Rated power increases with vehicle configuration from '1' to '4' → Increased weight ● 16 hp MDW with a reconfigurable controller / intelligent corner ('1') - Weight: 4290 lb, - Cost: \$13,000 - 0-60 acceleration time: 15.2 s 	Section 7.1.2
3	Power	Vehicle Weight 0-60 mph Accel. Time	<ul style="list-style-type: none"> ● Power/Response Map - High desired acceleration - Increased vehicle weight → Power level choice increases ● Each MDW is constrained by its rated motor power ● Given 0-60 mph accel. time of 6 s and vehicle weight of 3750 lb - Require the rated power of 160 hp 	Section 7.1.3
4	Acceleration	Vehicle Weight 0-60 mph Accel. Time	<ul style="list-style-type: none"> ● Torque/Response Map - High desired acceleration - Increased vehicle weight → Increased wheel torque ● Each MDW is constrained by its rated motor power ● Given 0-60 mph accel. time of 6 s and vehicle weight of 3750 lb - Wheel torque of 248 ft-lb at 60 mph 	Section 7.1.4
		Various Road conditions Vehicle Weight	<ul style="list-style-type: none"> ● 0-60 mph Acceleration Time Map - Given constant torque, low friction coeff. and increased vehicle weight → Increased 0-60 mph accel. time ● Given $\mu = 0.9$ and vehicle weight of 2970 lb to 3750 lb - Time: 10.1 s to 12.6 s 	
5	Gradeability	Vehicle Weight 0-60 mph Accel. Time	<ul style="list-style-type: none"> ● Gradeability Map - High desired acceleration - Increased vehicle weight → Increased gradeability 	Section 7.1.5

Purchase Standpoint				
#	Criteria	X and Y axes	Significant Research Results	Source
6	Braking	Various Road conditions Vehicle Weight	<ul style="list-style-type: none"> 60-0mph Braking Time Map - Given braking torque, low friction coeff. and increased vehicle weight → Increased 0-60 mph braking time Given $\mu = 0.9$ and vehicle weight of 2970 lb to 3750 lb - Time: 5 s to 6.2 s 	Section 7.1.6
		Normalized Deceleration Velocity	<ul style="list-style-type: none"> Stopping Distance Map - Low normalized deceleration - High velocity → Increased stopping distance Given normalized deceleration of 1 g and velocity of 60 mph - Stopping distance: 120 ft 	
7	Handling	Frequency Vehicle Weight	<ul style="list-style-type: none"> Dynamic Contact Force Map - Increased vehicle weight → increased dynamic contact force → decreased wheel hop frequency (11.6 Hz → 8.3 Hz) 	Section 7.1.7
		Velocity Vehicle Weight	<ul style="list-style-type: none"> Dynamic Contact Force Map (RMS based on PSD) map - Increased velocity, vehicle weight, and road roughness → increased dynamic contact force - Given 3750lb and 70 mph, 27 (A class) → 107 (C) → 470 lb (E) 	
8	Ride Comfort	Frequency Vehicle Weight	<ul style="list-style-type: none"> Sprung Mass Acceleration Map - Increased vehicle weight → Increased sprung mass accel. (1.16 → 1.41 ft/s² at wheel hop freq.) 	Section 7.1.8
		Velocity Vehicle Weight	<ul style="list-style-type: none"> Sprung Mass Acceleration Map (Frequency-weighted RMS) - Increased velocity and road roughness → Increased sprung mass accel. → Given 3750lb and 70 mph, 0.6 (A class) → 2.4 (C) → 10 ft/s²(E) - increased vehicle weight (2970 → 3750) → Decreased sprung mass accel. (2.5 → 2.3 ft/s² at C class) 	
9	Efficiency	Wheel Speed Wheel Torque	<ul style="list-style-type: none"> Efficiency Map - Given the UDDS duty cycle → w/o a reconfig. Controller (85.8%) → w/ a reconfig. Controller (88.2%) 	Section 7.1.9
10	Durability	Velocity Equivalent Dynamic Load	<ul style="list-style-type: none"> Bearing Life Map - High load (1047 → 1406 lb) → decreased principal bearing life (15330 h → 6336 h at 70 mph) - Increased velocity (30 → 70 mph) → 12670 h → 6336 h at 1406 lb 	Section 7.1.10

Table 8-4: Summary of Purchase Criteria

From the operation point of view, performance maps regarding operation criteria are generated based on the Simulink model of a 14 DOF full-vehicle model. These maps show the effects of vehicle weight and various road conditions.

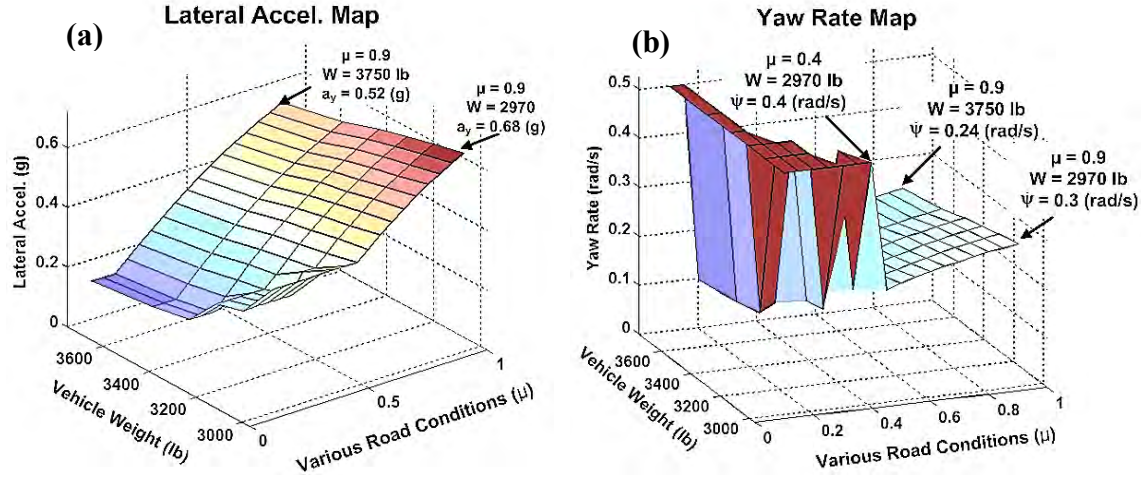


Figure 8-22: Lateral acceleration and yaw rate map with respect to vehicle weight and various road conditions

As discussed in Section 7.2.4, lateral acceleration occurs during cornering. Figure 8-22 shows the normalized lateral acceleration map under various vehicle weights and various road conditions. The values of the lateral acceleration are maximum values during a cornering maneuver in a single-lane change. The lateral acceleration (a_y) at the CG of the vehicle in the direction of the y axis consists of the motion along y axis (\dot{v}_y) and the centripetal acceleration ($v_x \dot{\psi}$) (see Section 4.3.2). Simulation results show that the increased vehicle weight increases the lateral acceleration of a vehicle. In addition, since the traction limit is constrained by various road conditions (i.e., friction coefficient between the tire and road), the resulting lateral acceleration decreases as the friction coefficient (μ) decreases.

As discussed in Section 7.2.6, Figure 8-22 (b) shows the yaw rate ($\dot{\psi}$) map as a function of vehicle weight and various road conditions. The values of the yaw rate are maximum required values during a cornering maneuver in a single-lane change. As the vehicle weight increases from 2970 lb to 3750 lb, the yaw rate decreases slightly from 0.3 to 0.24 rad/s, given the dry asphalt road condition of $\mu = 0.9$. It can be seen that the yaw rate suddenly jumps up after the road coefficient of friction goes below the value of $\mu=0.4$. This is due to unstable vehicle motion as a result of vehicle skidding caused by a zero value for the force margin (see Section 7.2.1).

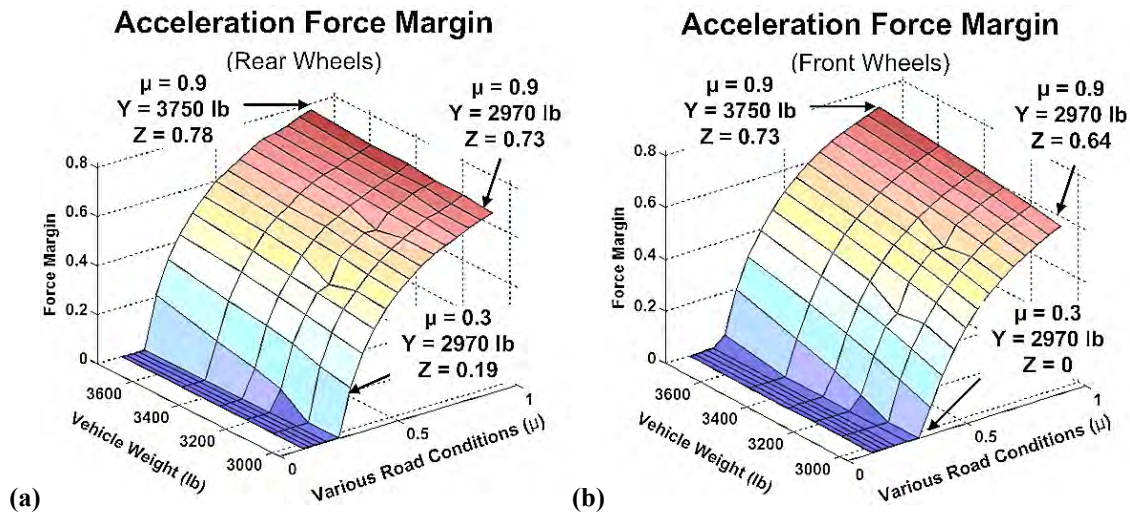


Figure 8-23: Acceleration force margin map with respect to vehicle weight and various road conditions given constant torque (290 N-m (214 ft-lb))

As discussed in 7.2.7, the acceleration force margin (F^m) decreases because it is constrained by the friction coefficient (μ). Figure 8-23 shows the acceleration force margin map as a function of vehicle weight and various road conditions. Each point is simulated through the 14 DOF full-vehicle Simulink model. The displayed values of the acceleration force margin (F^m) are the minimum required values during acceleration.

As the vehicle weight increases, the acceleration force margin of the rear and front wheels increases from 64% to 73% and from 73% to 78%, respectively, as shown in Figure 8-23 (a) and (b). At the friction coefficient value of $\mu = 0.3$, the acceleration force margin of front wheels becomes zero, while that of rear wheels is still 19% available. The reason that the force margin of the rear wheels is larger than that of the front wheels is due to the larger normal forces on the rear wheels, as a result of the backward inertial force caused by acceleration (see Sections 5.2.1.1, 5.2.2.1, and 5.2.3.1).

The following table summarizes operational criteria in terms of their usage, X and Y measures of interest to the customers, and description in Table 7-7.

Operation Standpoint				
#	Criteria	X and Y axes	Significant Research Results	Source
1	Cornering Force Margin	Various Road conditions Vehicle Weight	<ul style="list-style-type: none"> ● Force Margin Map - Low friction coefficient → Decreased FM ● Given $\mu = 0.5$ and vehicle weight of 2970 lb - Rear-inside (0%), Front-inside (5%), Rear-outside(2%), Front-outside(12%) 	Section 7.2.1
2	Roll Angle	Various Road conditions Vehicle Weight	<ul style="list-style-type: none"> ● Roll Angle Map - Low friction coefficient → Decreased roll angle - Increased vehicle weight(2970→3750) → Decreased roll angle ($1.7^\circ \rightarrow 1.5^\circ$) due to increased roll inertia of the sprung mass 	Section 7.2.2
3	Sideslip Angle	Various Road conditions Vehicle Weight	<ul style="list-style-type: none"> ● Sideslip Angle Map - Low friction coefficient and increased vehicle weight (2970→3750) → Decreased sideslip angle($2.8 \rightarrow 2.3^\circ$) ● Drop suddenly at the road condition of $\mu = 0.4$ - due to a zero for the force margin 	Section 7.2.3
4	Lateral Acceleration	Various Road conditions Vehicle Weight	<ul style="list-style-type: none"> ● Lateral Acceleration Map - Low friction coefficient → Decreased lateral acceleration - Increased vehicle weight (2970→3750) → Decreased lateral acceleration ($0.68 \text{ g} \rightarrow 0.52 \text{ g}$) 	Section 7.2.4
5	Slip Angle	Various Road conditions Vehicle Weight	<ul style="list-style-type: none"> ● Slip Angle Map - Low friction coefficient and increased vehicle weight → Decreased slip angle ● Drop suddenly at the road condition of $\mu = 0.4$ - due to a zero for the force margin ● Given $\mu = 0.9$ and vehicle weight of 2970 lb to 3750 lb - Rear: $-3.5^\circ \rightarrow -2.8^\circ$, Front: $-3^\circ \rightarrow -2.4^\circ$ ● Rear slip angle is larger than the front slip angle → Higher rear lateral force → Decreased force margin (See 1.cornering force margin) → Oversteer condition 	Section 7.2.5

Operation Standpoint				
#	Criteria	X and Y axes	Significant Research Results	Source
6	Yaw Rate	Various Road Conditions Vehicle Weight	<ul style="list-style-type: none"> ● Yaw Rate Map - Low friction coefficient and increased vehicle weight → Decreased yaw rate ● Jump up suddenly at the road condition of $\mu = 0.4$ - Due to a zero for the force margin ● Given $\mu = 0.9$ and 2970 → 3750 lb - Yaw rate: 0.3 → 0.24 rad/s 	Section 7.2.6
7	Acceleration Force Margin	Various Road Conditions Vehicle Weight	<ul style="list-style-type: none"> ● Acceleration Force Margin Map - Low friction coefficient → Decreased Acceleration FM - Increased vehicle weight → Increased Acceleration FM ● Given $\mu = 0.9$ and 2970 → 3750 lb - Rear: 73%→78%, Front: 64%→73% ● FM of the rear wheels is larger - Due to the larger normal forces on the rear wheels caused by the backward inertial force 	Section 7.2.7
8	Braking Force Margin	Various Road Conditions Vehicle Weight	<ul style="list-style-type: none"> ● Braking Force Margin Map - Low friction coefficient → Decreased Braking FM - Increased vehicle weight → Increased Braking FM ● Given $\mu = 0.9$ and 2970 → 3750 lb - Rear: 1%→30%, Front: 40%→52% ● FM of the front wheels is larger than that of the rear wheels - Due to the larger normal forces on the front wheels caused by the forward inertial force 	Section 7.2.8
9	Pitch Angle	Various Road Conditions Vehicle Weight	<ul style="list-style-type: none"> ● Pitch Angle Map (Acceleration) - Low friction coefficient - Increased vehicle weight(2970→3750) → Decreased pitch angle(0.76→0.7°) 	Section 7.2.9
		Various Road Conditions Vehicle Weight	<ul style="list-style-type: none"> ● Pitch Angle Map (Braking) - Low friction coefficient - Increased vehicle weight(2970→3750) → Decreased pitch angle(1.6→1.4°) 	
10	Travel Range	Velocity Battery Capacity	<ul style="list-style-type: none"> ● Travel Range Map - Higher battery capacity → Increased travel range - Depend strongly on the velocity 	Section 7.2.10
		Velocity Auxiliary Power	<ul style="list-style-type: none"> ● Energy Loss Map- Higher auxiliary power → Increased energy loss(low speed) 	

Table 8-5: Summary of Operation Criteria

From the maintenance point of view, we demonstrated that the condition-based maintenance considering the NPC, APC, and RPC tell the customer in advance when their MDW will fail and how much time is left before failure in terms of efficiency and durability maps.

Regarding the durability maps, the assumed durability map as a function of equivalent dynamic load and velocity are generated. (see Figure 7-33) As a result of aging and wear, the system condition will degrade from the Nominal Performance Conditions (NPC) to the Required Performance Conditions (RPC) of 5000 hr. minimum. The Assessed Performance Conditions (APC) will be continuously monitored for signs of degradation. Given the equivalent dynamic load of 1406 lb and velocity of 70 mph, the NPC and APC are 6336 h and 5385 h, respectively. These results are described in Table 8-6.

Also, given four-independent wheels, if one wheel fails the other three wheels will operate, hence the vehicle will operate at 75% of full capacity. However, for conventional transmissions, if the transmission fails, the whole vehicle fails. A principal goal for the use of a hybrid vehicle (motor, generator, battery) with 4 MDWs is to dramatically reduce the number of single point failures which is critical to continued operator under a particle failure for most automobile customers. This will be described in future work section.

The following table summarizes the maintenance criteria in terms of their usage, X and Y measures of interest to the customers, and description in Table 8-6.

Maintenance Standpoint				
#	Criteria	X and Y axes	Significant Research Results	Source
1	Efficiency	Wheel Speed Wheel Torque	<ul style="list-style-type: none"> ● Condition-Based Maintenance Map - Nominal performance condition - Accessed performance condition - Required performance condition - Health Margin - Remaining useful life 	Section 7.3.1
2	Power Level		<ul style="list-style-type: none"> ● Degrade after several thousand charge depleting cycles in terms of the battery - Affect vehicle performance and efficiency 	Section 7.3.2
3	Responsiveness		<ul style="list-style-type: none"> ● Motor phase failure → Decreased electromagnetic torque capability → Decreased responsiveness 	Section 7.3.3
4	Torque Margin	Various Road Cond. Vehicle Weight	<ul style="list-style-type: none"> ● Torque Margin Map - Low friction coefficient → Decreased FM 	Section 7.3.4
5	Temperature Margin		<ul style="list-style-type: none"> ● Power electronics coolant is operated based on maximum inlet temperature of 65°C. → Result in temperature fluctuations (<40°C) at the semiconductor junctions 	Section 7.3.5
6	Noise Margin		<ul style="list-style-type: none"> ● Measure of the interior noise 	Section 7.3.6
7	Sensor Degradation		<ul style="list-style-type: none"> ● Sensor and process fault detection and isolation (SPFDI) 	Section 7.3.7
8	Bearing Degradation	Velocity Equivalent Dynamic Load	<ul style="list-style-type: none"> ● Condition-Based Maintenance Map - Given 1406 lb and 70 mph - NPC = 6336 hr., APC = 5385 hr. - RPC of 5000 hr. minimum 	Section 7.3.8
9	Wire Insulation Degradation		<ul style="list-style-type: none"> ● Class F (155°C), larger than 10hp 	Section 7.3.9
10	Clutch Degradation		<ul style="list-style-type: none"> ● How fast does the clutch shift? 	Section 7.3.10

Table 8-6: Summary of Maintenance Criteria

Finally, from the refreshment point of view, refreshment can be defined as updating the modules: engine, generator, batteries/super cap, skateboard chassis, car bodies, suspensions, drive wheel, and operational software. Assuming that the customer updates the MDW from 20 hp to 40 hp, Table 8-7 describes how power level and torque respond to the customer's choice.

Customer's choice	0-60 mph accel.	Total power ratings	Torque at 60 mph
16 hp MDW	15.2 s	64 hp	99 ft-lb
20 hp MDW	12.9 s	80 hp	125 ft-lb
24 hp MDW	10.8 s	96 hp	150 ft-lb
32 hp MDW	7.4 s	128 hp	198 ft-lb
40 hp MDW	6.0 s	160 hp	248 ft-lb

Table 8-7: Acceleration, total power ratings, and torque responding to customer's choice

Given four-independent 20 hp MDW, the customer obtains 0-60 mph acceleration of 12.9 s, total power ratings of 80 hp, and torque of 125 ft-lb at 60 mph. If he / she updates from 20 hp MDW to 40 hp MDW to enhance drivability, he / she can obtain 0-60 mph acceleration of 6 s, total power ratings of 160 hp, and torque of 248 ft-lb at 60 mph, so that the customer can be best satisfied with their purchase.

The following table summarizes the refreshment criteria in terms of their usage, X and Y measures of interest to the customers, and description in Table 8-8.

Refreshment Standpoint				
#	Criteria	X and Y axes	Significant Research Results	Source
1	Power Level	Vehicle Configuration 0-60 mph Accel. Time	<ul style="list-style-type: none"> ● Power/Response Map - Update 20 hp to 40 hp → Increased 0-60 mph acceleration time from 12.9 s to 6.0 s 	Section 7.4.1
2	Cost Benefit / Replacement Cost		<ul style="list-style-type: none"> ● Customers obtain the cost benefit associated with replacement cost - Based on an responsive supply chain (in-depth certification and a minimum set as a standard) 	Section 7.4.2
3	Efficiency Benefit		<ul style="list-style-type: none"> ● How much does efficiency improve? 	Section 7.4.3
4	Torque Level	Vehicle Weight 0-60 mph Accel. Time	<ul style="list-style-type: none"> ● Torque/Response Map - Update 20 hp to 40 hp → Increased torque level (125 ft-lb → 248 ft-lb at 60 mph) 	Section 7.4.4
5	Enhanced Handling / Ride Comfort		<ul style="list-style-type: none"> ● Handling and Ride Comfort - Improve by in-wheel motor and active suspension actuators 	Section 7.4.5
6	Enhanced Sensors		<ul style="list-style-type: none"> ● Precise real time data 	Section 7.4.6
7	Enhanced Control Software		<ul style="list-style-type: none"> ● Upgraded software can be done over the internet, through third party applications. 	Section 7.4.7
8	Enhanced Durability		<ul style="list-style-type: none"> ● How long do bearings last? 	Section 7.4.8
9	Enhanced Temperature Tolerance		<ul style="list-style-type: none"> ● How much does temperature tolerance improve? 	Section 7.4.9
10	Enhanced Safety		<ul style="list-style-type: none"> ● Enhanced safety in emergency conditions - Active response (MDW) to the driver to enhance safety 	Section 7.4.10

Table 8-8: Summary of Refreshment Criteria

8.4 CONTRIBUTIONS

The significant contributions made by this research effort are shown in Table 8-9.

Contributions (Section References)
<ul style="list-style-type: none"> • The effect of the unsprung mass on the handling and ride comfort determined by two control parameters (i.e., velocity and unsprung masses) in terms of 5 classes of road profiles was evaluated based on a Quarter-Vehicle Model. (Section 4.2.1) <ul style="list-style-type: none"> ○ Handling (given smooth highway (C class) and velocity of 70 mph) <ul style="list-style-type: none"> → Increased dynamic contact force 79 lb ($m_u/m_s = 0.1$) → 104 lb ($m_u/m_s = 0.19$) → 119 lb ($m_u/m_s = 0.26$) ○ Ride Comfort (given smooth highway (C class) and velocity of 70 mph) <ul style="list-style-type: none"> → Increased sprung mass acceleration 2.30 ft/s² ($m_u/m_s = 0.1$) → 2.46 ft/s² ($m_u/m_s = 0.19$) → 2.50 ft/s² ($m_u/m_s = 0.26$) • The effect of the unsprung mass on acceleration, braking, and cornering maneuvers under various road conditions (i.e., dry asphalt, wet asphalt, snowy road) was evaluated and compared based on the implementation of a nonlinear 14 DOF full-vehicle model. (Sections 5.1, 5.2, 5.3, and 5.4) <ul style="list-style-type: none"> ○ Consist of the ride model, handling model, tire model, slip ratio, slip angle, and tire magic formula. (Sections 4.4 and 4.5) • The MDW design procedure of how to maximize efficiency and drivability was developed and demonstrated to respond to the customer such as an efficiency-priority driver and an aggressive driver. (Section 6.1.7.1 and 6.1.7.3) <ul style="list-style-type: none"> ○ Maximize efficiency (88.6% → 88.7%, clutch shift events of 40 → 7) <ul style="list-style-type: none"> ➤ Clutch shift point: 20 mph (280 RPM) → 35 mph (490 RPM) ➤ Four-independent 16 hp MDW ➤ Different g levels: $g_1 = 0.3$, $g_2 = 0.3$, $g_3 = 0.15$, $g_4 = 0.15$ ➤ 0-60 mph acceleration time = 15.2 s ➤ Weight of a MDW = 75 lb ○ Maximize drivability (four-independent 16 hp → 32 hp, US06) <ul style="list-style-type: none"> ➤ Clutch shift point: 20 mph (280 RPM) ➤ Different g levels: <ul style="list-style-type: none"> $g_1 = 0.3 \rightarrow 0.8$, $g_2 = 0.3 \rightarrow 0.8$, $g_3 = 0.15 \rightarrow 0.35$, $g_4 = 0.15 \rightarrow 0.35$

- 0-60 mph acceleration time = 7.4 s
- Weight of a MDW = 110 lb
- Customer-oriented duty cycle analysis based on customer's individual demand cycle was proposed to describe the MDW specifications in terms of ten purchase standpoint. (Section 6.1 and 6.4)
 - Cost, weight, power, acceleration, gradeability, braking, handling, ride comfort, efficiency, durability (Section 7.1)
 - ➔ Cost-priority driver: \$14,000 (cost), 3100 lb (weight), 64 hp (power), 15.2 s (acceleration), 6° (gradeability at 60 mph), 3.7 s (braking)
 - An electric vehicle can be tailored to meet the customer needs.
- Energy consumption analysis based on customer's individual demand cycle was presented to provide the energy consumption and heat energy lost due to inefficiencies during traction and braking. (Section 6.2)
- Comparison of two speed regimes (i.e., MDW) and one speed regime (i.e., Protean's in-wheel motor) is made and discussed. (Section 6.3)
 - Efficiency improvement in terms of loss reduction is 1.9x for urban and 1.8x for highway duty cycles
 - Another loss reduction of 1.2x is expected by using the reconfigurable power/electronic controllers
 - Overall improvement loss ratio compared to the Protean of 2.2x for the UDDS.
- Visual performance maps based on a nonlinear 14 DOF full-vehicle model are proposed in terms of ten operation standpoint to maximize the situational awareness of all operational capability. (Section 7.2)
 - Cornering force margin, roll angle, sideslip angle, lateral acceleration, slip angle, yaw rate, acceleration force margin, braking force margin, pitch angle, travel range. (Section 7.2)
- Maximizing human choice by means of visualizing human needs was performed in terms of purchase/operation/maintenance/refreshment standpoints (Chapter 7)

Table 8-9: Summary of Contribution

8.5 RECOMMENDATIONS AND FUTURE WORK

Next wave of technology requires computational intelligence associated with stratifying human needs. This new wave will consist of two major components: hardware component – actuators (analogous to computer chip – Intel Corp.) software component (analogous to Microsoft’s Windows). The MDW, which is an in-wheel actuator, will play a significant role in the automobile industry in the future. The software component enables the MDW to respond to the human command, and provide for maximum performance (norms and envelopes prioritized by the driver), condition based maintenance, and fault tolerance (on-line recovery from a fault to prevent loss of life) [Tesar, Oct, 2011].

One of the biggest advantages of the vehicle with the MDWs is that it has four wheels which are controlled independently. From the fault tolerance point of view, it gives a significant option when a partial failure occurs. We will discuss the effect of the total/partial failure on performance criteria and operational decision making based on the total/partial failure.

8.5.1 Effects of the Total/Partial Failure on Performance Criteria

Given four-independent wheels, if one wheel fails the other three wheels will operate, hence the vehicle will operate at 75% of full capacity (even at 100% for short periods). However, for conventional transmissions, if the transmission fails, the whole vehicle fails.

Assuming one wheel failure, the failure may be caused by numerous factors such as winding short circuit due to insulation damage caused by high temperature, gears and shaft of gear train due to aging, standard bearing failure due to a lubrication problem, MDW clutch with the motor overload, sensors due to dirt and foreign substances, etc.

Based on partial/total failure due to one wheel failure, the criteria in terms of operation and maintenance should be evaluated in future work. For example, given four-independent 16 hp MDW, the 0-60 mph acceleration time will be extended, so that time will be longer than 15.2 s. In addition, total power ratings will be degraded from 64 hp to perhaps 48 hp.

8.5.2 Operational Decision Making Based on the Total/Partial Failure

Assuming one wheel failure, operational decision making is necessary to compensate for that failure. This requires intelligence in terms of real time decision making. To manage the complexity, an Actuator Management Operating Software (AMOS) is being developed by the Robotics Research Group. Using the sensor data in real time, the AMOS analyzes this data to control the actuator's response to system demands based on the envelope decision surfaces, and updates decision surfaces to evaluate how these surfaces change in time, and creates measures of degradation for the purpose of indicating available capability versus that required. The difference between them can be regarded as residuals on which to make fundamental decisions relative to command responses. Criteria for action would be chosen by the system's operator [Tesar, July, 2009].

The operational intelligence would integrate a decision structure using criteria selected and ranked by direct commands from the driver (be efficient, move fast, watch out, go slow, be quiet, etc). If one wheel degrades due to a weakened motor phase, the rated power decreases with the number of disconnected motor phases, and the rotor experiences unbalanced forces. This leads to a poor electromagnetic torque output. Eventually, responsiveness of an actuator decreases. With the CBM using a torque sensor attached to the MDW, the incipient component degradation will be identified. The

operator has to make the decision whether the MDW needs to be replaced or not. Assuming total failure, the system would be reconfigurable to optimize the power distribution among the remaining drive wheels. The purchase, operation, and maintenance criteria would be reevaluated and updated in the embedded electronic controller to be selected by the operator. This can be considered as future work. The other future work is summarized in the Table 8-10.

#	Recommendations for future work	Section Reference
1	<ul style="list-style-type: none"> ● The overload torque and power should be understood in addition to the continuous torque and power. - The maximum torque is determined by the inverter current - The maximum power is limited by the battery 	Section 6.1.7.1
2	<ul style="list-style-type: none"> ● The efficiency map of a SRM should be confirmed based on the analytical method and Finite Element Method Magnetics. Finally, the efficiency map of a SRM should be obtained through numerous experiments. 	Section 6.1, 6.2, and 6.3
3	<ul style="list-style-type: none"> ● Intelligent corner, consisting of MDW, active camber / steering, active suspension, and TWIRE which is a reconfigurable surface contact system using a pneumatic tire, should be considered in terms of operation criteria - Evaluate cornering force margin during cornering maneuvers - Calculate acceleration / braking force margin - Analyze the effect of active camber/steering on performances - Analyze the effect of active suspension on performances 	Section 4.5 Section 5.3.3 Section 7.2.1, 7.2.7, and 7.2.8
4	<ul style="list-style-type: none"> ● Using Bayesian network, Structured Decision Making regarding the intelligent corner should be developed to maximize human choice - Manage decision-making in real-time based on structured performance map operation 	Section 4.1
5	<ul style="list-style-type: none"> ● The duty cycle of a fleet vehicle should be analyzed to describe the MDW specifications in terms of ten purchase criteria 	Section 7.1

6	<ul style="list-style-type: none"> ● As the MDW becomes a principal component, power utilization, which is how to use power to the road, becomes critical. - Evaluate the functional benefits for power utilization based on the 4 DOF intelligent vehicle corner - Analyze the capability to respond to drivers (i.e., acceleration / braking, climbing a hill, respond to emergencies under various road conditions - Evaluate power utilization capability in terms of ride comfort (i.e., vertical / roll / pitch performance) 	<p>Section 4.2.1</p> <p>Section 5.1</p> <p>Section 5.2</p> <p>Section 7.1.6</p>
7	<ul style="list-style-type: none"> ● Visual performance maps should be generated in terms of maintenance and refreshment criteria - Power level, responsiveness, temperature margin, noise margin, sensor degradation, wire insulation degradation, clutch degradation. - Cost benefit / replacement cost, efficiency benefit, enhanced handling and ride comfort, enhanced sensors, enhanced control software, enhanced durability, enhanced temperature tolerance, enhanced safety. ● Visual performance maps can be used to manage decision-making in real-time performance map operation of intelligent actuators. 	<p>Section 7.3</p> <p>Section 7.4</p>
8	<ul style="list-style-type: none"> ● Cost/Response and Weight/Response maps should be confirmed in the future 	Section 7.1
9	<ul style="list-style-type: none"> ● Battery Model should be added to duty cycle analysis in order to determine battery size and super capacitor 	Section 8.3.3
10	<ul style="list-style-type: none"> ● Durability analysis in duty cycle should be evaluated based on peak load and RMS load shock - Evaluate the normal force during acceleration and cornering - Evaluate the moment / lateral force during a cornering maneuver 	Section 7.3.8
11	<ul style="list-style-type: none"> ● Customer's individual demand cycle should be recorded based on the representative vehicle. - Use the specific duty cycle to predict the customer preference - Vehicle will be assembled on demand to meet customer needs 	Section 6.4

Table 8-10: Summary of future work

Appendix A. Road Roughness Classification

The road surface profiles are represented by the statistical features of road roughness and used as the base excitation. In other words, it is characterized by the Power Spectral Density (PSD) which is the profile amplitude in terms of spatial frequency to describe road irregularities as shown in Figure A-1

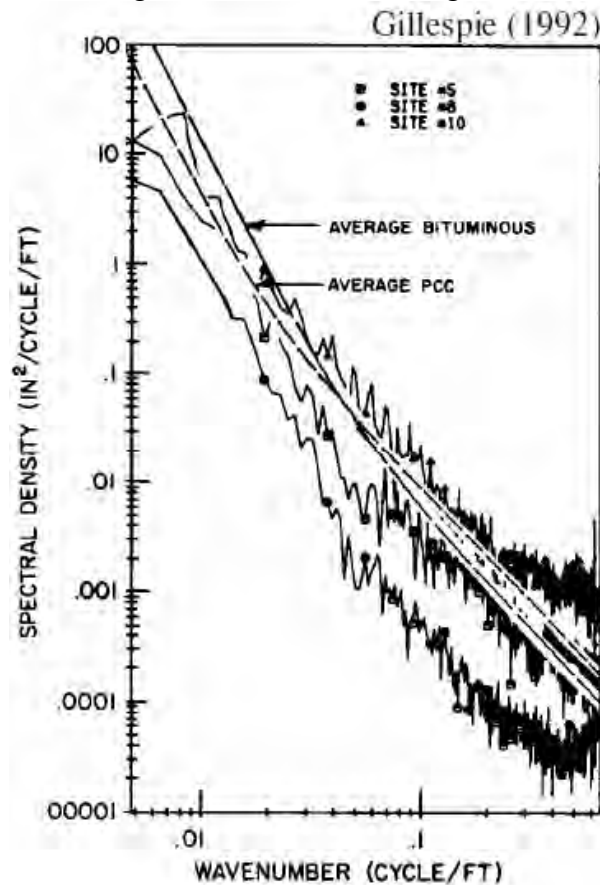
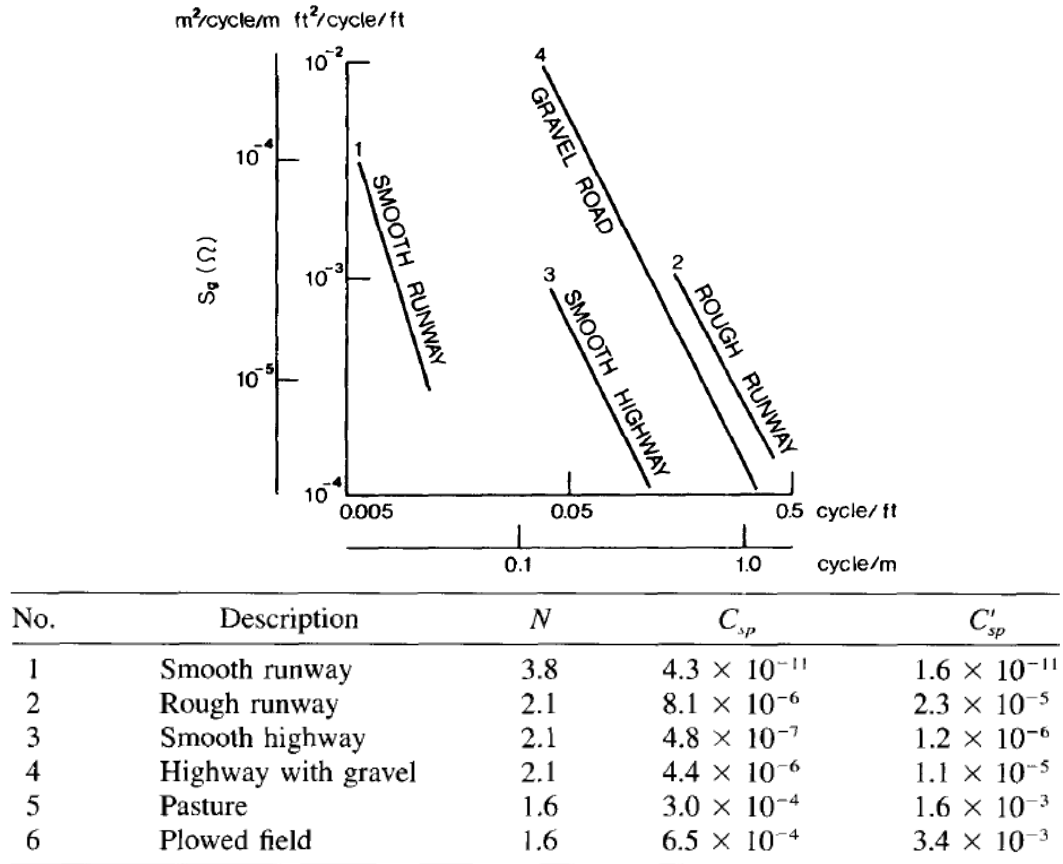


Figure A-1: Typical spectral densities of road elevation profiles [Gillespie,1992]

As spatial frequency (wavenumber) increases, the PSD decreases. That is, profile amplitude around hundreds of feet in wavelength may be inches, in contrast with fractions of an inch in amplitude under a few feet in wavelength. We recognize that the

higher amplitudes imply rougher roads.



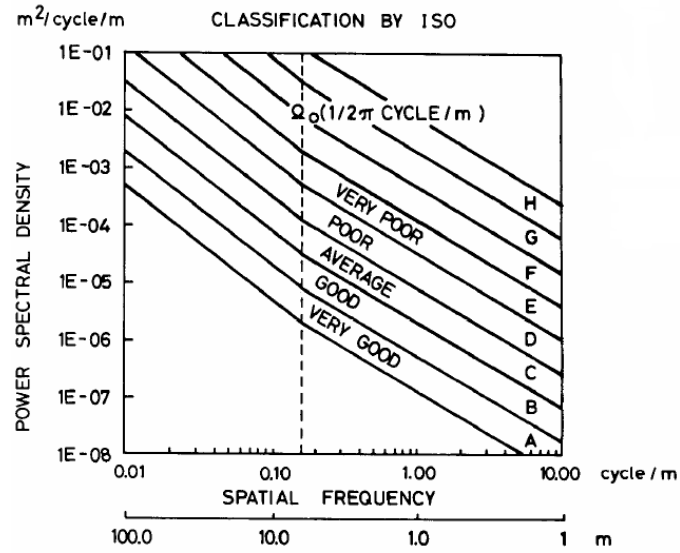
Source: References 7.10 and 7.11.

Note: C_{sp} is the value used for computing $S_g(\Omega)$ in $\text{m}^2/\text{cycles}/\text{m}$. C'_{sp} is the value used for computing $S_g(\Omega)$ in $\text{ft}^2/\text{cycles}/\text{ft}$. The numbers in the table refer to the curves shown in Figs. 7.25 and 7.26.

Figure A-2: PSD as a function of spatial frequency for various types of road and runway [Wong,2008]

The spatial frequency (Ω) is the inverse of the wavelength (l_w). The PSD for profile amplitude as shown in Figure A-2 can be expressed in the following:

$$S_g(\Omega) = C_{sp} \Omega^{-N} \quad (\text{A.1})$$



Road Class	Degree of Roughness	
	$S_g(\Omega_0), 10^{-6} \text{ m}^2/\text{cycles/m}$	
Road Class	Range	Geometric Mean
A (Very Good)	< 8	4
B (Good)	8–32	16
C (Average)	32–128	64
D (Poor)	128–512	256
E (Very Poor)	512–2048	1024
F	2048–8192	4096
G	8192–32,768	16384
H	> 32,768	

Figure A-3: Classification of road surface roughness proposed by ISO [Wong,2008]

As can be seen in Figure A-3, statistical investigation on road surface profiles are presented by the International Organization for Standardization (ISO) and classified into ISO 8608:1995. The formula is given by [Wong,2008]:

$$S_g(\Omega) = S_g(\Omega_c) \left(\frac{\Omega}{\Omega_c} \right)^{-N}$$

where $N=2$ if $\Omega \leq \Omega_c=1/2\pi$ (cycle/m)

$N=1.5$ if $\Omega > \Omega_c=1/2\pi$ (cycle/m)

(A.2)

As shown in Figure A-1, the road surface represents the random profile with length (l_w) which can be expressed in the form of Fourier series for a road class as shown in Figure A-3. The random profile is given by [Verros, Natsiavas et al.,2005]

$$z_r(t) = \sum_{n=1}^N \sqrt{2S_g(n\Omega_0) \cdot \Omega_0} \sin(nw_0 + \phi_n)$$

where $\Omega_0 = \frac{2\pi}{l_w}$, $w_0 = \frac{2\pi}{l_w}V$ (A.3)

ϕ_n a phase(n-th random harmonic wave)

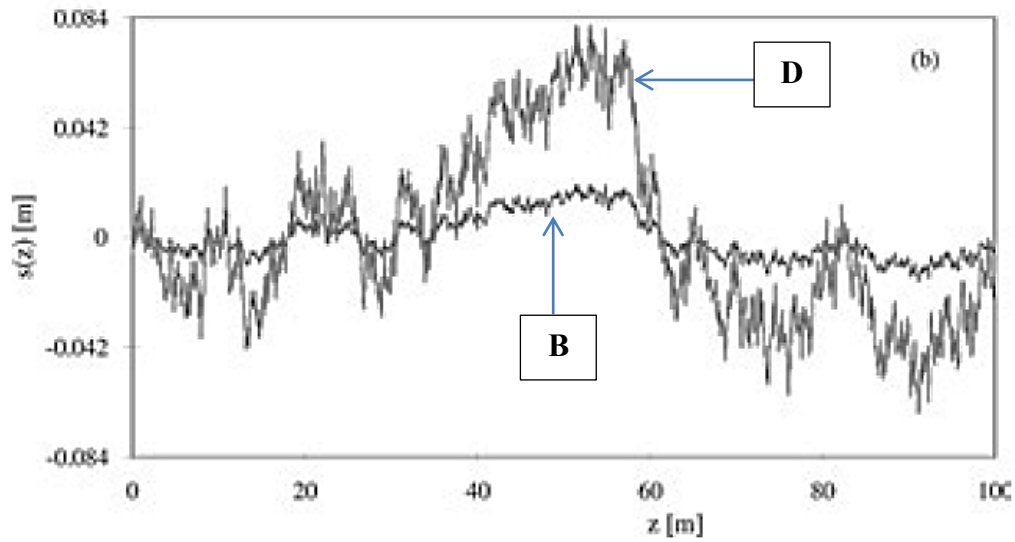


Figure A-4: Profile amplitude of B class and D class by ISO [Verros, Natsiavas et al.,2005]

Figure A-4 shows the road profile amplitude versus distance in terms of B class and D class proposed by ISO. It can be seen that D class indicates high road roughness.

Appendix B. Standard Driving Cycles

The standard driving cycles are used to assess vehicle fuel economy and emissions. Moreover, in order to develop the automotive power trains, they are used as a vehicle design evaluation tool. The U.S. Environmental Protection Agency (EPA) lists 17 types of road driving cycles from Figure B-1 to Figure B-17 [EPA].

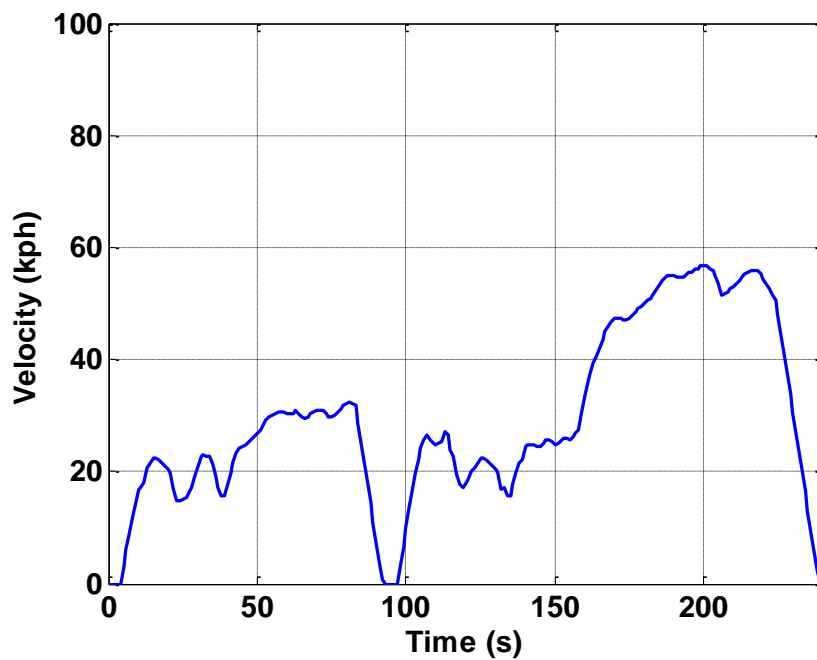


Figure B-1: IM240 Driving Cycle

The Inspection and Maintenance (IM240) is used for road-side vehicle testing.

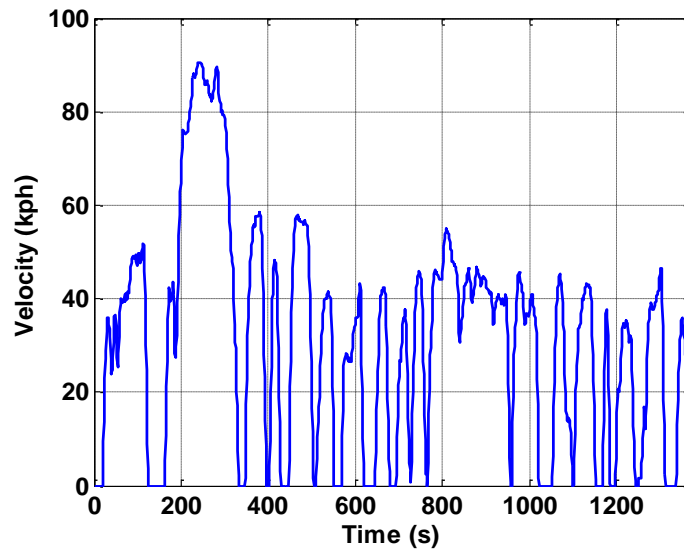


Figure B-2: UDDS Driving Cycle

The Urban Dynamometer Driving Schedule (UDDS) represents city driving condition.

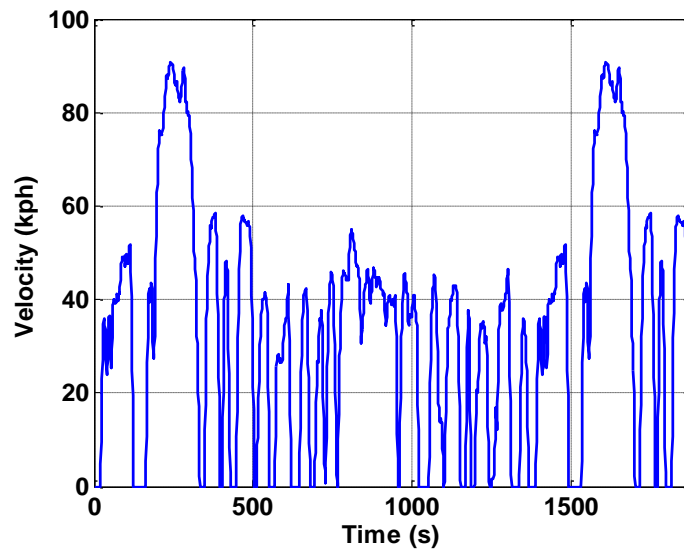


Figure B-3: FTP Driving Cycle

The Federal Test Procedure (FTP) is composed of the UDDS followed by the first 505 seconds of the UDDS. This is often called the EPA 75.

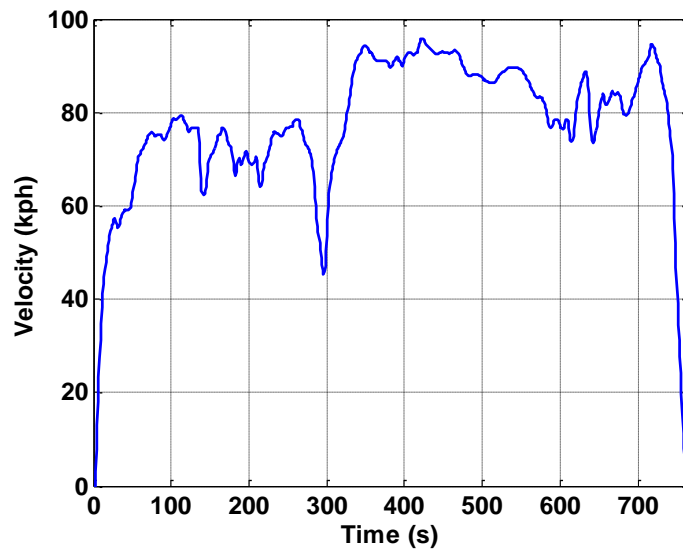


Figure B-4: HWFET Driving Cycle

The Highway Fuel Economy Driving Schedule (HWFET) indicates highway driving conditions under 60 mph.

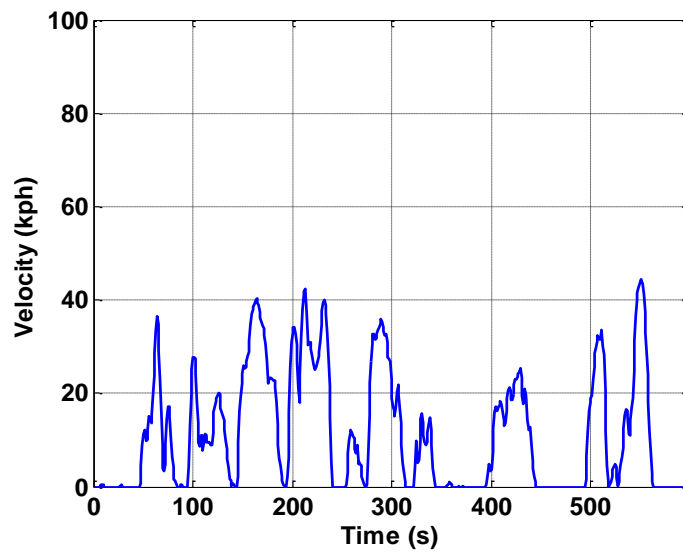


Figure B-5: NYCC Driving Cycle

The New York City Cycle (NYCC) represents low speed stop-and-go traffic conditions.

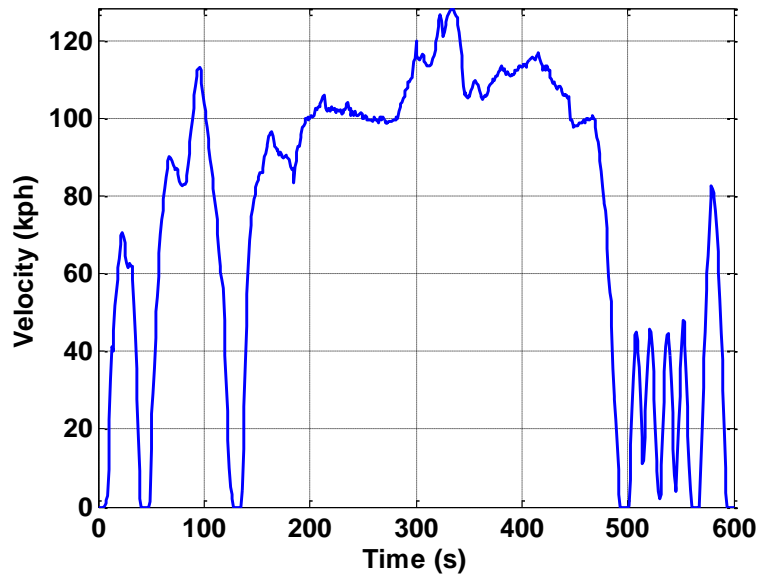


Figure B-6: US06 Driving Cycle

The US06 represents a high acceleration driving schedule (aggressive driver)

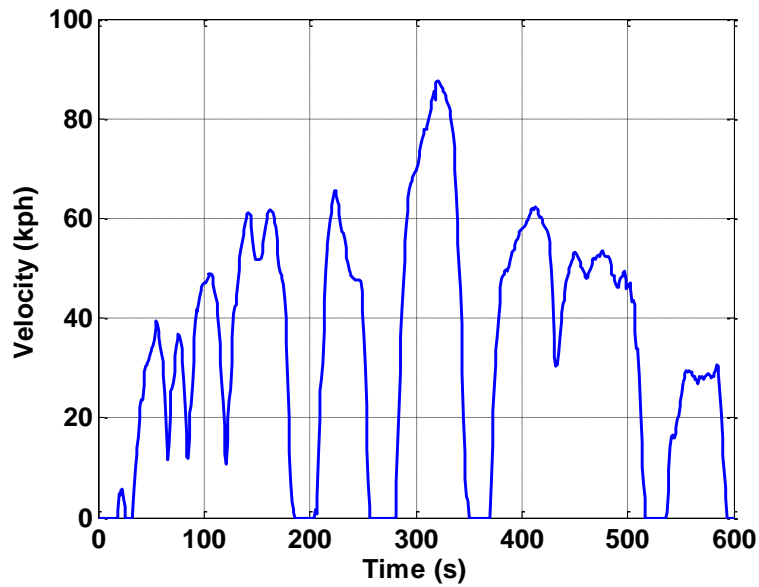


Figure B-7: SC03 Driving Cycle

The SC03 is the Air Conditioning “Supplemental FTP” driving schedule.

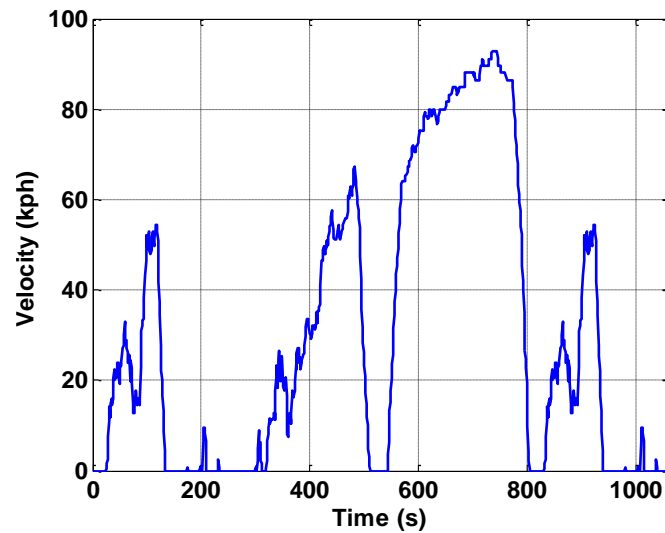


Figure B-8: HUDDS Driving Cycle

The Heavy Duty Urban Dynamometer Driving Schedule (HUDDS) is for heavy duty vehicle testing.

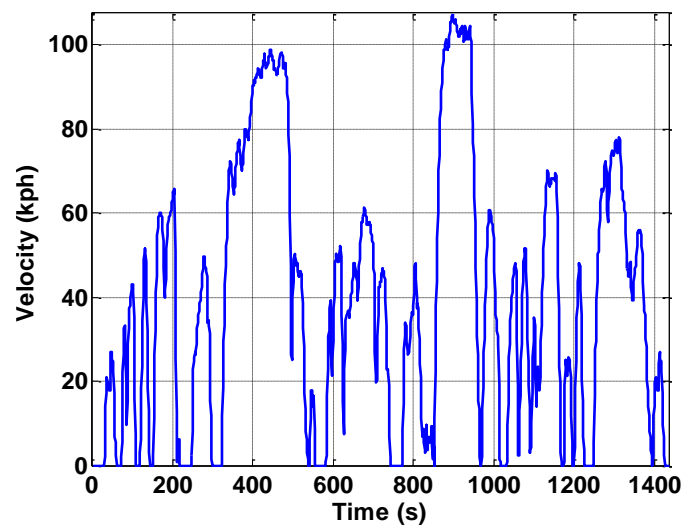


Figure B-9: LA92 Driving Cycle

The Air Resources Board LA92 Dynamometer Driving Schedule was developed as an emission inventory improvement tool.

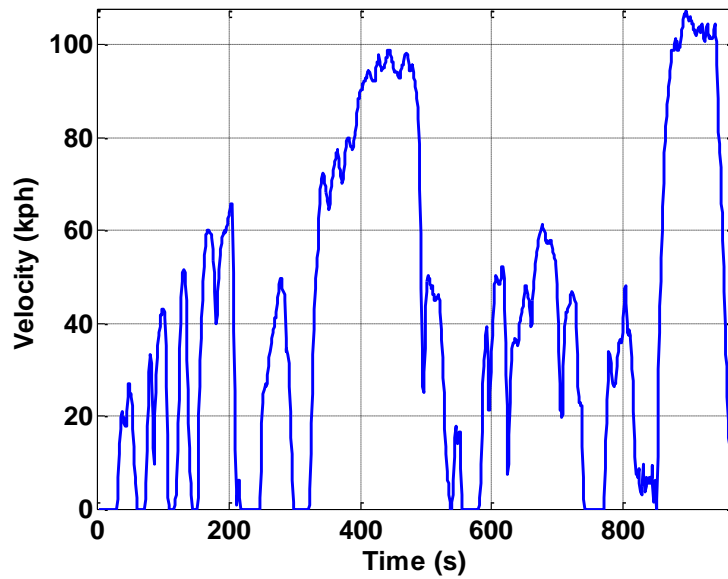


Figure B-10: LA92Short Driving Cycle

The LA92Short contains the first 969 seconds of the LA92 Driving Schedule

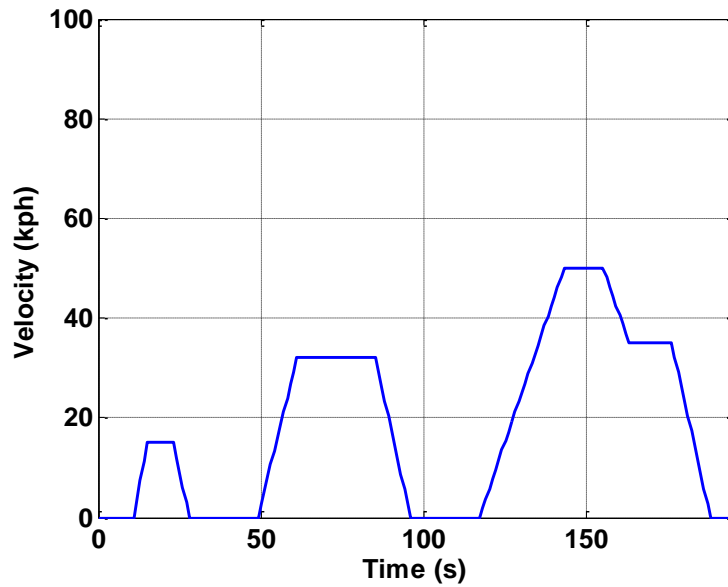


Figure B-11: ECE Driving Cycle

The UN/ECE Elementary Urban Cycle is Part 1 of the ECE Type 1 Test

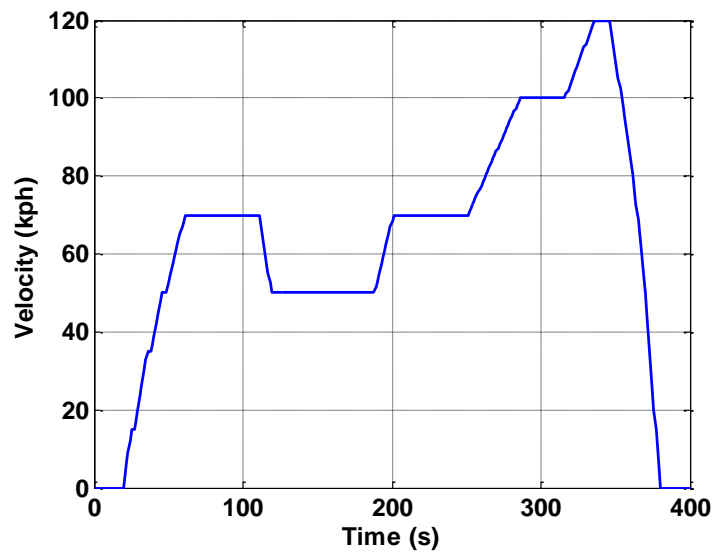


Figure B-12: EUDC Driving Cycle

The UN/ECE Extra-Urban Driving Cycle is Part 2 of the ECE Type 1 Test.

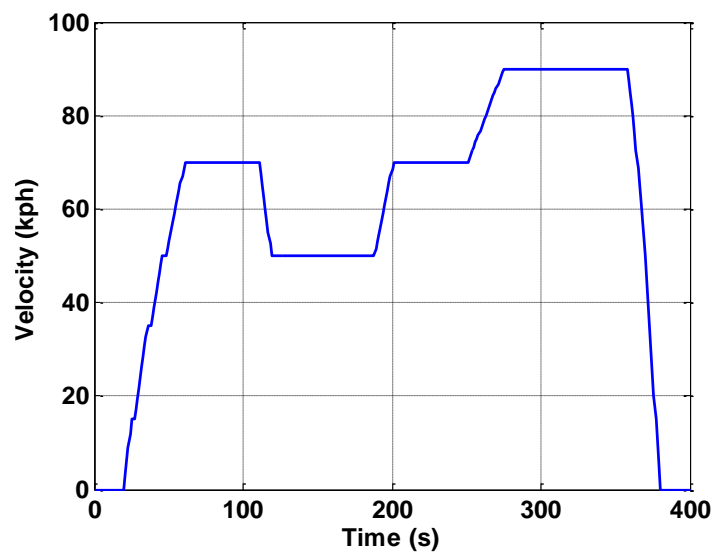


Figure B-13: EUDC_LP Driving Cycle

The UN/ECE Extra-Urban Driving Cycle (Low Powered Vehicles) is an alternative for Low-Powered Vehicles for Part 2 of the ECE Type 1 Test.

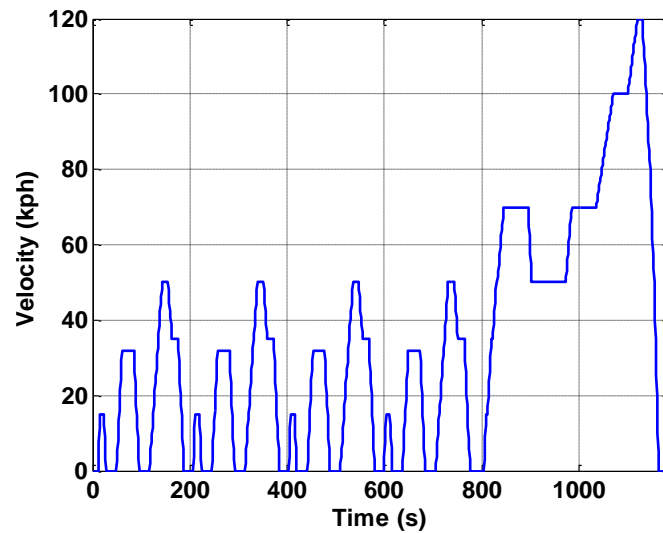


Figure B-14: NEDC Driving Cycle

The New European Driving Cycle (NEDC) consists of repeated ECE and EUDC. It represents the typical usage of a car in Europe.

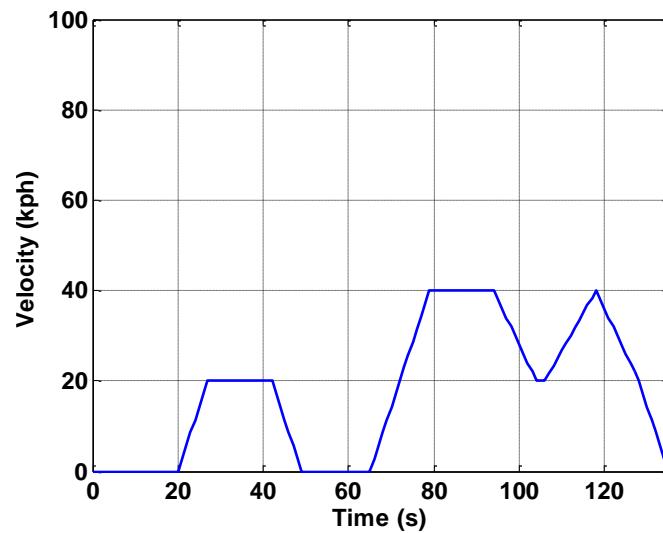


Figure B-15: J10 Driving Cycle

The Japanese 10 Mode Cycle is used as a component of the total driving schedule for the 10.15 Mode Exhaust Measurement and Fuel Economy Test Procedures.

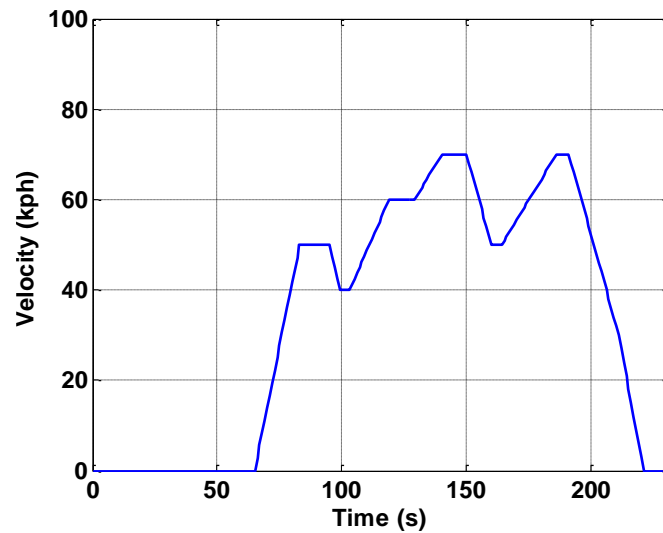


Figure B-16: J15 Driving Cycle

The Japanese 15 Mode Cycle is used as a component of the total driving schedule for the 10.15 Mode Exhaust Measurement and Fuel Economy Test Procedures.

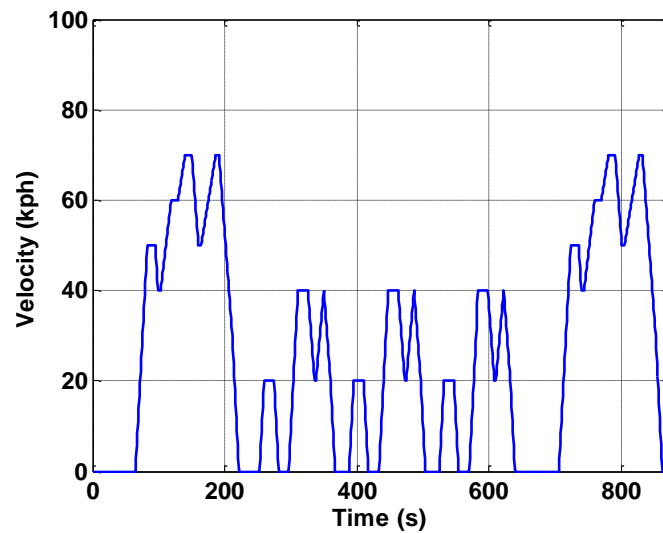


Figure B-17: J1015 Driving Cycle

The Japanese 10.15 Mode Driving Schedule for Exhaust Measurement and Fuel Economy Test Procedures are specified in Jisha Technical Standards (Jisha 899, 1983)

Appendix C. MDW Clutch Version 2

During high speed operation, the output gear of the front end gear train operates at 15,000 RPM, resulting in the front end input pinion operating over 50,000 RPM, which is undesirable. Therefore, to solve this issue, the amplifier gears of the front end star gears must freewheel by providing a synchro clutch in the output gear. Figure C-1 ~ C-7 shows the detailed drawing.

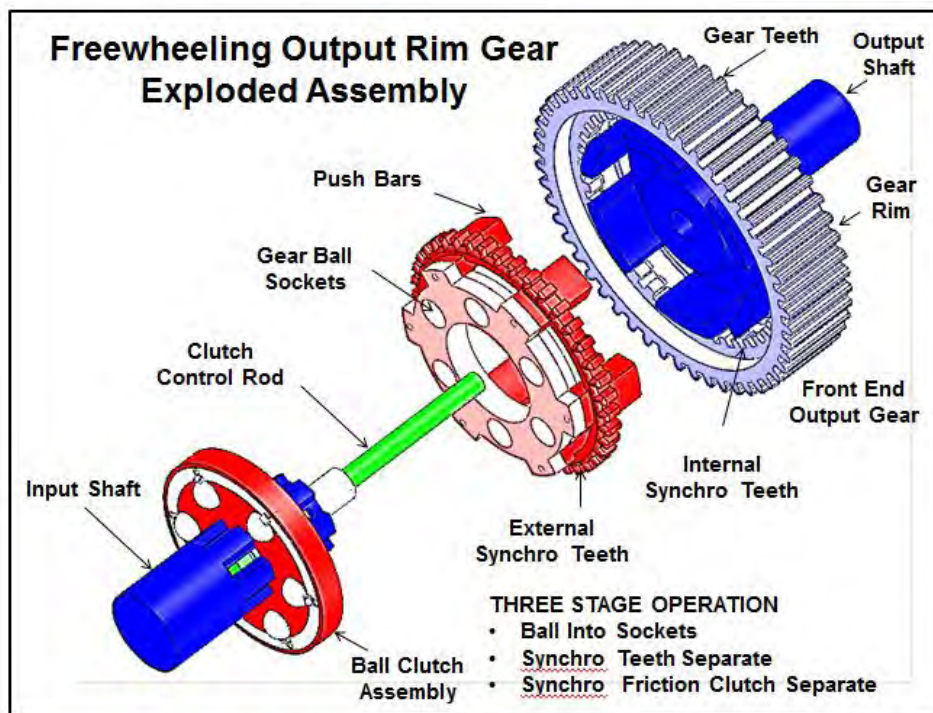


Figure C-1: Layout of Freewheeling Gear Rim

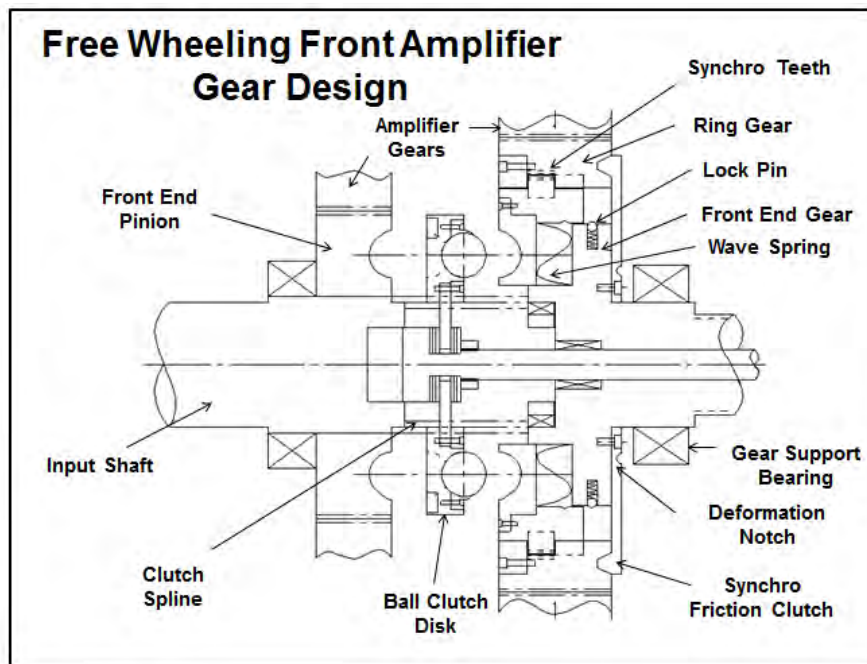


Figure C-2: Layout of Freewheeling Gear Rim

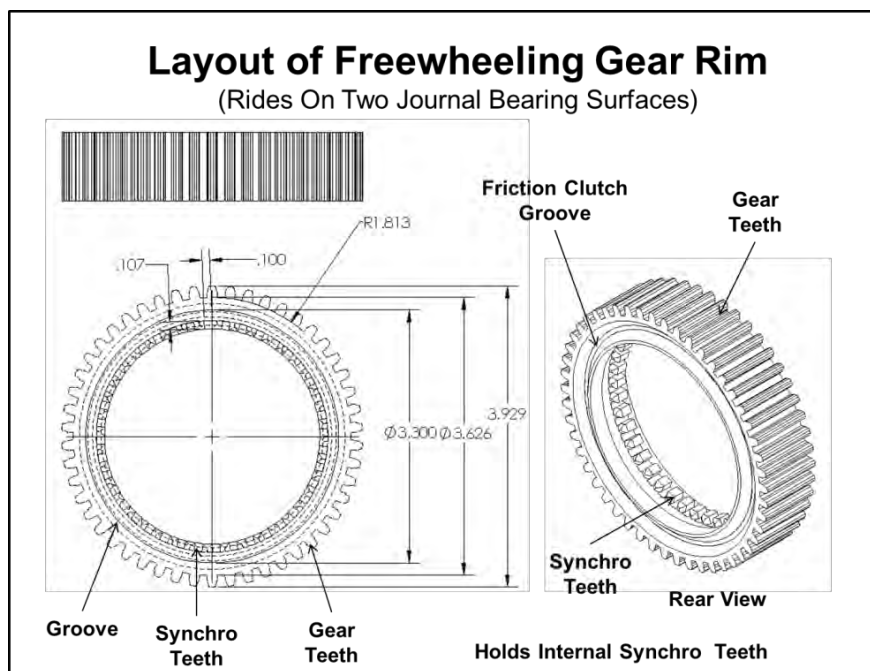
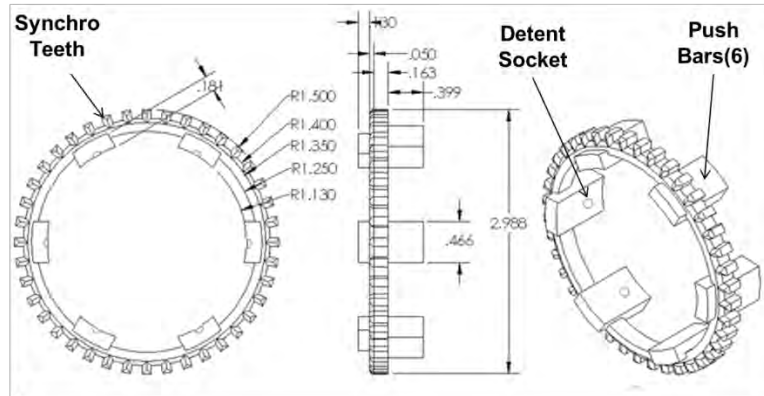


Figure C-3: Layout of Freewheeling Gear Rim

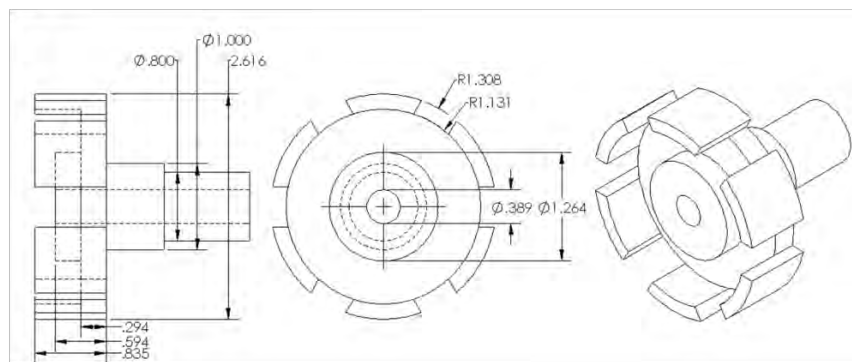
Layout of Push Bar Assembly (Holds External Synchro Teeth)



Push Bars Also Push Out
Synchro Friction Clutch

Figure C-4: Layout of Push Bar Assembly

Front End Output Gear Body Design (Slots Engage Push Bars To Drive Ring Gear)



Push Bars Hold External Synchro Teeth Ring to
Drive Internal Synchro Teeth Held By Ring Gear
Which Drives Front End Amplifier Gears

Figure C-5: Layout of Front End Output Gear Body Design

Gear Clutch Disk Holds Ball Sockets

(Disk at the key to Push Bar Assembly)

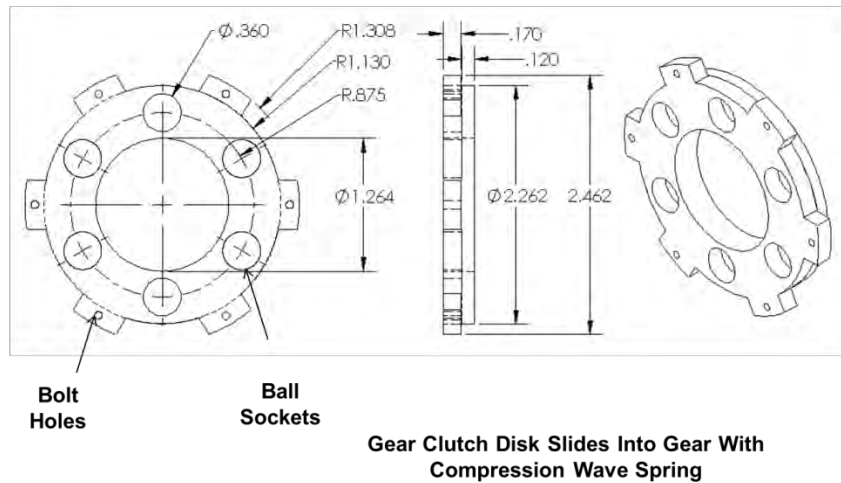


Figure C-6: Gear Clutch Disk Holds Ball Sockets

Synchro Friction Clutch Spider Disk

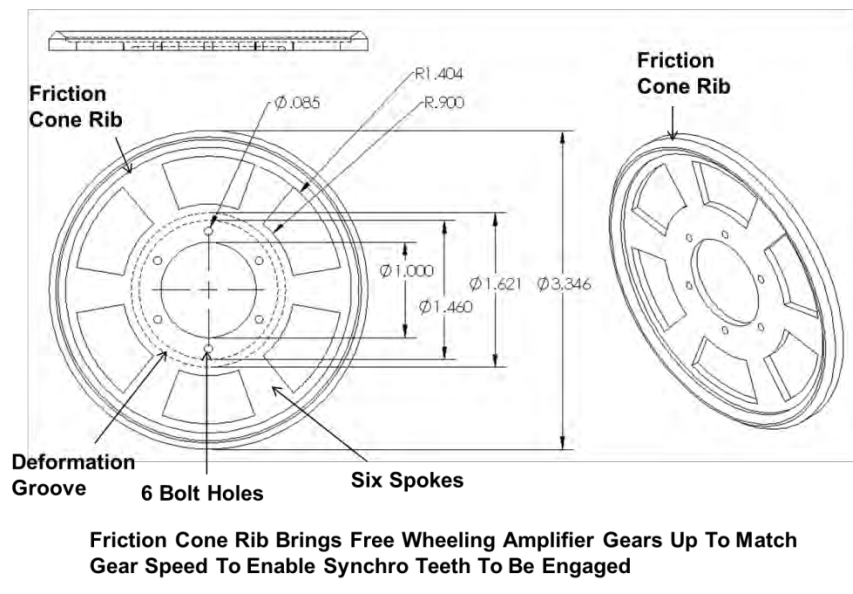


Figure C-7: Synchro Friction Clutch Spider Disk

References

- Ackermann, J. and T. Bunte (1998). Handling improvement of robust car steering, Citeseer.
- Ahmad, F., K. Hudha, et al. (2009). "Gain scheduling PID control with pitch moment rejection for reducing vehicle dive and squat." International Journal of Vehicle Safety **4**(1): 45-83.
- An, S. J., K. Yi, et al. (2008). "Desired yaw rate and steering control method during cornering for a six-wheeled vehicle." International Journal of Automotive Technology **9**(2): 173-181.
- Anderson, M. L. E. and D. D. L. Harty (2010). "Unsprung Mass with In-Wheel Motors - Myths and Realities." Advanced Vehicle Control (AVEC 10).
- Ashok, P. and D. Tesar (2002). "Design Synthesis Framework for Switched Reluctance Motors."
- Ashok, P. and D. Tesar (2007). "Math Framework for Decision Making in Intelligent Electromechanical Actuators." PhD. Dissertation, Robotics Research Group.
- Ashok, P. and D. Tesar (2008). "A visualization framework for real time decision making in a multi-input multi-output system." Systems Journal, IEEE **2**(1): 129-145.
- Ashok, P. and D. Tesar (2010). "The Need for a Performance Map Based Decision Theory." IEEE.
- Backmark, J., E. Karlsson, et al. (2009). "Using future path information for improving the stability of an over-actuated vehicle." International Journal of Vehicle Systems Modelling and Testing **4**(3): 218-231.
- Baffet, G., A. Charara, et al. (2009). "Estimation of vehicle sideslip, tire force and wheel cornering stiffness." Control Engineering Practice **17**(11): 1255-1264.
- Bakker, E., L. Nyborg, et al. (1987). Tyre modelling for use in vehicle dynamics studies, Chassis Engineering, Volvo Car Corp.
- Balamurugan, S. and P. Sumathi (2004). Analysis of temperature rise in switched reluctance motor due to the core and copper loss by coupled field finite element analysis, IEEE.
- Bandaru, N. and D. Tesar (2011). "Map Based Visual Design Process for Multi-Stage Gear Drives." Master Thesis, The University of Texas at Austin.
- Barak, P. and S. Tianbing (2003). "On Body Roll Angle During Transient Response Maneuver of a 3-D Model." SAE SP: 53-70.
- Berry, I. M. (2010). "The Effects of Driving Style and Vehicle Performance on the Real-World Fuel Consumption of U.S. Light-Duty Vehicles." Thesis, Massachusetts Institute of Technology.
- Besselink, I., P. van Oorschot, et al. (2010). "Design of an efficient, low weight battery electric vehicle based on a VW Lupo 3L."
- Blundell, M. and D. Harty (2004). "Multibody Systems Approach to Vehicle Dynamics." Elsevier.
- Blundell, M. and D. Harty (2004). Multibody systems approach to vehicle dynamics, Butterworth-Heinemann.

- Brancato, E. L. (1992). "Estimation of lifetime expectancies of motors." Electrical Insulation Magazine, IEEE **8**(3): 5-13.
- Brandlein, J. (1999). "Ball and roller bearings theory, design, and application, 3rd ed." John Wiley and Sons, New York.
- C. Alexandru, a. P. A. (2011). "Control Strategy for an Active Suspension System." World Academy of Science, Engineering and Technology **79**.
- Calderón-Meza, G. (2003). "A Simple Model of the Linear Speed of a Ground Vehicle Under Accelerating and Decelerating Forces" " in Embedded Systems Modeling Seminar. Modellierung Reaktiver Systeme: Ein Fallbeispiel . SFB 501-Report Nr. 08/2003, Germany.
- Cao, J., H. Liu, et al. (2008). "State of the art in vehicle active suspension adaptive control systems based on intelligent methodologies." Intelligent Transportation Systems, IEEE Transactions on **9**(3): 392-405.
- Cao, J. T., H. H. Liu, et al. (2007). "A study of electric vehicle suspension control system based on an improved half-vehicle model." International Journal of Automation and Computing **4**(3): 236-242.
- Cariou, C., R. Lenain, et al. (2008). Adaptive control of four-wheel-steering off-road mobile robots: Application to path tracking and heading control in presence of sliding, IEEE.
- Chan, C. (1993). "An overview of electric vehicle technology." Proceedings of the IEEE **81**(9): 1202-1213.
- Chan, C. (2002). "The state of the art of electric and hybrid vehicles." Proceedings of the IEEE **90**(2): 247-275.
- Chan, C. (2007). "The state of the art of electric, hybrid, and fuel cell vehicles." Proceedings of the IEEE **95**(4): 704-718.
- Chan, C. and K. Chau (2001). Modern electric vehicle technology, Oxford University Press, USA.
- Chan, C. and Y. Wong (2004). "Electric vehicles charge forward." Power and Energy Magazine, IEEE **2**(6): 24-33.
- Chen, H. and K. Guo (2001). An LMI approach to multiobjective RMS gain control for active suspensions, IEEE.
- Chen, H. and K. H. Guo (2005). "Constrained H_{∞} control of active suspensions: an LMI approach." Control Systems Technology, IEEE Transactions on **13**(3): 412-421.
- Chen, Y. and Z. Lu (2009). Simulation analysis of vertical and lateral dynamics of an electric vehicle driven by two rear hub-motors, IEEE.
- Cho, W., J. Yoon, et al. (2010). "Estimation of tire forces for application to vehicle stability control." Vehicular Technology, IEEE Transactions on **59**(2): 638-649.
- Consumer-Reports (2012). "Best Cars SUVs & Trucks."
- Cuenca, R., L. Gaines, et al. (2000). Evaluation of electric vehicle production and operating costs, Argonne National Lab., IL (US).
- Cunningham, J. D. and D. Tesar (2011). "Switched Reluctance Motor Drive Circuit Evaluation Criteria for Vehicle Efficiency and Responsiveness." Thesis, The University of Texas at Asutin.

- Darmstadt, T. M. T. U., S. R. T. U. Darmstadt, et al. (2011). "Electric Power Train Configurations with Appropriate Transmission Systems."
- Davis, S. C., S. W. Diegel, et al. (2011). Transportation Energy Data Book: Edition 30, Oak Ridge National Laboratory (ORNL).
- Dixon, J. C. (2009). "Suspension Geometry and Computation." Wiley.
- Durney, E. G. (2009). Re-inventing carmaking, Google Patents.
- Durney, E. G. (2009). Truly electric car, Google Patents.
- Ehsani, M., Y. Gao, et al. (2009). Modern electric, hybrid electric, and fuel cell vehicles: fundamentals, theory, and design, CRC.
- Ehsani, M., K. M. Rahman, et al. (1997). "Propulsion system design of electric and hybrid vehicles." Industrial Electronics, IEEE Transactions on **44**(1): 19-27.
- ElMadany, M. M. and Z. S. Abduljabbar (1999). "Linear quadratic Gaussian control of a quarter-car suspension." vehicle system dynamics **32**(6): 479-497.
- Eo, J. S., D. H. Won, et al. (2012). "Control Unit Development for Parallel Hybrid Electric Vehicle."
- EPA ""Testing and Measuring Emissions: Dynamometer Driver's Aid".
<http://www.epa.gov/nvfel/testing/dynamometer.htm#vehshift>.
- Gameiro, N. and A. Cardoso (2011). "A New Method for Power Converter Fault Diagnosis in SRM Drives." Industry Applications, IEEE Transactions on(99): 1-1.
- Gantt, L., Alley, R., Nelson, D. (2011). "Battery Sizing as a Function of Powertrain Component Efficiencies for Various Drive Cycles." DETC2011-47514. ASME IDETC/CIE. Washington, DC, USA.
- Gantt, L. R., D. E. Perkins, et al. (2011). Regenerative brake energy analysis for the VTREX plug-in hybrid electric vehicle, IEEE.
- Gao, X. (2010). "Nonlinear Estimation of Vehicle Sideslip Angle Based on Adaptive Extended Kalman Filter." Automotive Engineering.
- George, R. F. (1983). "Evaluating Bearings for Robots." Machine Design, v55, n7.
- Gerling, D., G. Dajaku, et al. (2007). "Electric Traction for Automobiles- Comparison of Different Wheel." Hub Drives, EVS 23. Anaheim California, December 2-5, 2007.
- Ghike, C. and T. Shim (2006). "14 Degree-of-Freedom Vehicle Model for Roll Dynamics Study."
- Ghoneim, Y. A. (2011). "Active roll control and integration with electronic stability control system: simulation study." International Journal of Vehicle Design **56**(1): 317-340.
- Gillespie, T. D. (1992). "Fundamentals of Vehicle Dynamics." SAE.
- Graham, R. (2001). "Comparing the benefits and impacts of hybrid electric vehicle options." Electric Power Research Institute **1000349**.
- Greaves, M., G. Walker, et al. (2011). Vehicle energy throughput analysis as a drivetrain motor design aid, Victoria University, Australia.
- Grinberg, R. and P. Palmer (2005). Advanced DC link capacitor technology application for a stiff voltage-source inverter, IEEE.

- Gruhler, G., J. Kranz, et al. (2011). "Electrical drive systems for road vehicles – concepts, examples, energy saving." UDC 621.313.04, Reutlingen University, Germany.
- Guoying, C., Z. Changfu, et al. (2011). The study of traction control system for Omni-directional electric vehicle, IEEE.
- Gusovius, E. (1992). "Thin Section Bearing Save Space and Weight." Machine Design, v64, n11, Jun 11.
- Guzzella, L. and A. Sciarretta (2005). "Vehicle Propulsion Systems: Introduction to Modeling and Optimization." Springer.
- Guzzella, L. and A. Sciarretta (2005). Vehicle propulsion systems: introduction to modeling and optimization, Springer Verlag.
- Hac, A., D. Nichols, et al. (2010). "Estimation of Vehicle Roll Angle and Side Slip for Crash Sensing." SAE Technical Paper: 01-0529.
- Hara, T. and I. Masuda (1995). Cross roller bearing, Google Patents.
- Hashemnia, N. and B. Asaei (2008). Comparative study of using different electric motors in the electric vehicles, IEEE.
- Hayes, J. G., R. P. R. de Oliveira, et al. (2011). Simplified electric vehicle power train models and range estimation, IEEE.
- Hibbeler, R. C. (2007). Engineering mechanics : Dynamics (8th Edition), Pearson Education.
- Hsu, Y. H. J., S. M. Laws, et al. (2010). "Estimation of Tire Slip Angle and Friction Limits Using Steering Torque." Control Systems Technology, IEEE Transactions on **18**(4): 896-907.
- Huang, K., F. Yu, et al. (2010). Model Predictive Controller Design for a Developed Electromagnetic Suspension Actuator Based on Experimental Data, IEEE.
- Hudha, K., F. Ahmad, et al. (2009). "Pid Controller with Roll Moment Rejection for Pneumatically Actuated Active Roll Control (Arc) Suspension System."
- Hudha, K., Z. A. Kadir, et al. (2009). "Modelling, validation and roll moment rejection control of pneumatically actuated active roll control for improving vehicle lateral dynamics performance." International Journal of Engineering Systems Modelling and Simulation **1**(2): 122-136.
- Huh, K., J. Kim, et al. (2000). "Handling and driving characteristics for six-wheeled vehicles." Proceedings of the Institution of Mechanical Engineers, Part D: Journal of Automobile Engineering **214**(2): 159-170.
- Hvass, P. B. and D. Tesar (2004). "Condition based maintenance for intelligent electromechanical actuators." The University of Texas, Austin, TX.
- I. Torii (June, 2009). "New generation electric vehicle i-Miev - a practical solution for sustainable mobility." ATC congress Helmond, .
- Ifedi, C., B. Mecrow, et al. (2011). Fault tolerant in-wheel motor topologies for high performance electric vehicles, IEEE.
- Inside-Line: <http://www.insideline.com/hyundai/sonata-hybrid/2011/2011-hyundai-sonata-hybrid-full-test.html>.

- ISO, I. S. (1997). "2631-1:1997, Mechanical Vibration and Shock - Evaluation of Human Exposure to Whole-body Vibration, Part 1: General Requirements, 2nd ed.,", International Organization for Standardization, .
- J.B. Staubel, C. (Dec. 2008). ""Roadster efficiency and range".
<http://www.teslamotors.com/blog/roadster-efficiency-and-range>, .
- Janardhan, J. and D. Tesar (2008). "Test Methodology for Electromechanical Actuators." Dissertation, The University of Texas at Austin.
- Jazar, R. N. (2008). Vehicle dynamics: theory and applications, Springer Verlag.
- Johnston, M. J. (2010). Development and Evaluation of Vehicle Suspension Tuning Metrics, University of Windsor.
- Jonasson, M. and J. Andreasson (2008). "Exploiting autonomous corner modules to resolve force constraints in the tyre contact patch." vehicle system dynamics **46**(7): 553-573.
- Jonasson, M., J. Andreasson, et al. (2010). "Global force potential of over-actuated vehicles." vehicle system dynamics **48**(9): 983-998.
- Jonasson, M., J. Andreasson, et al. (2011). "Utilization of Actuators to Improve Vehicle Stability at the Limit: From Hydraulic Brakes Toward Electric Propulsion." Journal of Dynamic Systems, Measurement, and Control **133**: 051003.
- Kadir, Z. A., K. Hudha, et al. (2011). Active roll control suspension system for improving dynamics performance of passenger vehicle, IEEE.
- Kajino, H., S. Buma, et al. (2008). "The Future Development and Analysis of an Electric Active Suspension System." SAE SP 2189: 13.
- Kang, J. and H. Heo (2012). "Control Allocation based Optimal Torque Vectoring for 4WD Electric Vehicle."
- Katsuyama, E. and T. M. CORPORATION (2011). "Decoupled 3-D moment control by an In-Wheel Motor vehicle."
- Kaydon-Bearing "Kaydon Bearing Manufacturer's Catalog, "CAT – 300 Thin Section Bearing".
- Kim, B. S., K. J. Joo, et al. (2011). "Ride Comfort Improvement of a Compact SUV Considering Driving Maneuver and Road Surface." SAE 2011 World Congress & Exhibition
- Kim, D. and H. Kim (2006). "Vehicle stability control with regenerative braking and electronic brake force distribution for a four-wheel drive hybrid electric vehicle." Proceedings of the Institution of Mechanical Engineers, Part D: Journal of Automobile Engineering **220**(6): 683-693.
- Kim, J. and H. Kim (2007). Electric vehicle yaw rate control using independent in-wheel motor, IEEE.
- Kim, S. H., D. H. Kim, et al. (2010). A study on motion control of 6WD/6WS vehicle using optimum tire force distribution method, IEEE.
- Kim, W., J. Kang, et al. (2011). "Drive control system design for stability and maneuverability of a 6WD/6WS vehicle." International Journal of Automotive Technology **12**(1): 67-74.

- Kim, W., K. Yi, et al. (2010). "Development of Driving Control System Based on Optimal Distribution for a 6WD/6WS Vehicle." SAE International Journal of Passenger Cars-Mechanical Systems **3**(1): 145-157.
- Koran, L. R. and D. Tesar (2008). "Duty cycle analysis to drive intelligent actuator development." Systems Journal, IEEE **2**(4): 453-463.
- Krishnamoorthy, G. and D. Tesar (2005). "A Multi-Sensor Architecture Development Framework for Intelligent Electromechanical Actuators." Thesis, The University of Texas at Austin.
- Krishnamoorthy, G. and D. Tesar (2010). "A Framework for Utilizing Data from Multiple Sensors in Intelligent Mechanical Systems." Dissertation, The University of Texas at Austin.
- Kwon, J., J. Kim, et al. (2008). "Impact of Drive Cycles on PHEV Component Requirements."
- Larminie, J. and J. Lowry (2003). "Electric Vehicle Technology Explained." John Wiley & Sons, Ltd.
- Lee, H. and D. Tesar (2011). "An Analytical Stiffness Analysis Between Actuator Structure and Principal Bearings Used For Robot Actuators." ASME 2011, DETC2011-48030.
- Lee, U., S. Lee, et al. (2008). "Active geometry control suspension system for the enhancement of vehicle stability." Proceedings of the Institution of Mechanical Engineers, Part D: Journal of Automobile Engineering **222**(6): 979-988.
- LEESON "Electric Corporation, www.leeson.com."
- Li, G., W. Hong, et al. (2012). "Four-Wheel Independently Driven In-Wheel Motors Electric Vehicle AFS and DYC Integrated Control."
- Li, Y., S. Billington, et al. (1999). "Dynamic prognostic prediction of defect propagation on rolling element bearings." Tribology transactions **42**(2): 385-392.
- Liaw, B. Y. and M. Dubarry (2007). "From driving cycle analysis to understanding battery performance in real-life electric hybrid vehicle operation." Journal of Power Sources **174**(1): 76-88.
- Macek, K., K. Thoma, et al. (2007). Dynamics modeling and parameter identification for autonomous vehicle navigation, IEEE.
- Marimuthu, R. P., N. S. Andres, et al. (2005). "A Study of Vehicle Parameters Sensitivity of Sports Utility Vehicle Rollover." The 13th International Pacific Conference on Automotive Engineering(TA04 : Vehicle Dynamics & Simulation I): p471-p476.
- Mecrow, B. and A. Jack (2008). "Efficiency trends in electric machines and drives." Energy Policy **36**(12): 4336-4341.
- Michelin-Active-Wheel "<http://www.gizmag.com/michelin-active-wheel-production-electric-car-by-2010/10489/>."
- Miller, J. M. (2004). Propulsion systems for hybrid vehicles, Peter Peregrinus Ltd.
- Miller, J. M. (2008). Propulsion systems for hybrid vehicles, 2nd Edition, Peter Peregrinus Ltd.
- Milliken, W. F. and D. L. Milliken (1995). Race car vehicle dynamics, SAE International.

- Mokhtari, H. and E. Tara (2008). Efficiency map of a Switched Reluctance Motor using Finite Element Method in vehicular applications, IEEE.
- Moreno, J., M. E. Ortúzar, et al. (2006). "Energy-management system for a hybrid electric vehicle, using ultracapacitors and neural networks." Industrial Electronics, IEEE Transactions on **53**(2): 614-623.
- Murata, S. (2011). "Vehicle Dynamics Innovation with In-Wheel Motor."
- Nagai, M., Y. Hirano, et al. (1997). "Integrated control of active rear wheel steering and direct yaw moment control." vehicle system dynamics **27**(5-6): 357-370.
- Norton, R. L. (2006). Machine design: an integrated approach, Pearson Education Inc., Upper Saddle River, NJ.
- Opila, D., X. Wang, et al. (2010). "An Energy Management Controller to Optimally Tradeoff Fuel Economy and Drivability for Hybrid Vehicles." Submitted to IEEE Transactions on Control Systems Technology.
- Pacejka, H. B. (2006). Tyre and vehicle dynamics.
- Paddan, G. and M. Griffin (2002). "Effect of seating on exposures to whole-body vibration in vehicles." Journal of Sound and Vibration **253**(1): 215-241.
- Paddan, G. and M. Griffin (2002). "Evaluation of whole-body vibration in vehicles." Journal of Sound and Vibration **253**(1): 195-213.
- Peng, H. and G. Ulsoy (2006). "Automotive Control Systems." Department of Mechanical Engineering, University of Michigan, Ann Arbor.
- Podra, P. and S. Andersson (1999). "Simulating sliding wear with finite element method." Tribology International **32**(2): 71-81.
- Protean-Electric "<http://www.proteanelectric.com/>."
- Protean Electric: <http://www.proteanelectric.com/>.
- Qian, H., G. Xu, et al. (2010). Energy management for four-wheel independent driving vehicle, IEEE.
- R.Q. Riley (2005). "Automobile Ride, Handling and Suspension Design with Implications for Low Mass Vehicles." Copyright 1999-2005, Robert Q. Riley Enterprises.
- Rahman, Z., K. L. Butler, et al. (2000). "Effect of extended-speed, constant-power operation of electric drives on the design and performance of EV-HEV propulsion system."
- Rahman, Z., M. Ehsani, et al. (2000). "An investigation of electric motor drive characteristics for EV and HEV propulsion systems." SAE transactions **109**(6): 2396-2403.
- Rajamani, R. (2006). Vehicle dynamics and control, Springer.
- Regal-Beloit (1999). "Basic Training Industrial-Duty & Commercial-Duty (Electric Motors Gearmotors)."
- Reinert, J., R. Inderka, et al. (2000). "Optimizing performance in switched-reluctance drives." Industry Applications Magazine, IEEE **6**(4): 63-70.
- Ren, Q., D. Crolla, et al. (2009). Effect of transmission design on Electric Vehicle (EV) performance, IEEE.

- Rinderknecht, S. and T. Meier (2010). Electric power train configurations and their transmission systems, IEEE.
- Riner, G. A. (2007). "A Comparison of Road Lengths Obtained by Odometer to Three Dimensional Calculation by GIS."
- Rojas, A. E., H. Niederkofler, et al. (2010). "Comfort and Safety Enhancement of Passenger Vehicles With In-Wheel Motors." SAE International **2010-01-1146**: Warrendale, Pennsylvania, USA.
- Rowntree, R. A. (1985). "The properties of thin-section, four-point-contact ball bearings in space." 1985: 141-166.
- Saini, G. (;Ashok, P.; Tesar, D., 2012, in progress, "Design Process for a Reconfigurable Power Controller"). "Design Process for a Reconfigurable Power Controller."
- Salem, M. and A. A. Aly (2009). "Fuzzy control of a quarter-car suspension system." World Academy of Science, Engineering and Technology **53**: 258-263.
- Schmidt, W. (1995). "Thin Section Bearings Excellent for Sophisticated Machines." Power Transmission Design, v37, n6, pp. 53-56.
- SchNorr, B. S. W.
["http://www.schnorr.com/?gclid=CPb_45DZra8CFWHDtgodTn9iqA."](http://www.schnorr.com/?gclid=CPb_45DZra8CFWHDtgodTn9iqA)
- Seoul-Economy
["http://economy.hankooki.com/lpage/industry/201108/e2011080218084370280.htm."](http://economy.hankooki.com/lpage/industry/201108/e2011080218084370280.htm)
- Setiawan, J. D., M. Safarudin, et al. (2009). Modeling, simulation and validation of 14 DOF full vehicle model, IEEE.
- Shahidinejad, S., E. Bibeau, et al. (2010). "Statistical Development of a Duty Cycle for Plug-in Vehicles in a North American Urban Setting Using Fleet Information." Vehicular Technology, IEEE Transactions on **59**(8): 3710-3719.
- Shigley, J. and C. R. Mischke Mechanical engineering design, 2001, McGraw-Hill, New York.
- Shim, T. and C. Ghike (2007). "Understanding the limitations of different vehicle models for roll dynamics studies." vehicle system dynamics **45**(3): 191-216.
- Siemens-VDO ["http://www.gizmag.com/go/5996/picture/25780/."](http://www.gizmag.com/go/5996/picture/25780/)
- Sim-Drive ["http://www.sim-drive.com/english/index.html."](http://www.sim-drive.com/english/index.html)
- SKF "Bearing Failures and Their Causes." Product Information 401.
- Soliman, A. M. A., S. Moustafa, et al. (2008). "Parameters Affecting Vehicle Ride Comfort using Half Vehicle Model." SAE SP **2184**: 89.
- Sun, L. (2003). "Simulation of pavement roughness and IRI based on power spectral density." Mathematics and computers in simulation **61**(2): 77-88.
- Sun, T., Y. Zhang, et al. (2002). Quarter vehicle ride model, SAE; 1999.
- Suzuki, R. and Y. Ikeda (2010). Driving/braking force distribution of four wheel vehicle by quadratic programming with constraints, IEEE.
- Talukdar, S. and S. Kulkarni (2011). "A Comparative Analysis of a Rigid Bicycle Model with an Elastic Bicycle Model for Small Trucks."

- Tate, E., M. O. Harpster, et al. (2008). The electrification of the automobile: From conventional hybrid, to plug-in hybrids, to extended-range electric vehicles, SAE International.
- Tesar, D. (2007). "Electro-Mechanical Actuator Architecture." White paper, 314 pages, University of Texas (UT)-Austin.
- Tesar, D. (2009). "All-Electric Modular Automobile (Its Design, Manufacture, and Operation)."
- Tesar, D. (2009). "Next Wave of Technology (Based On Machine Intelligence)." The University of Texas at Austin.
- Tesar, D. (2011, August). "World View of Research for Electric Vehicle Intelligent Corner."
- Tesar, D. (Dec 11, 2011). "Human Choice/Response to Human Command (Active Systems Driven by Intelligent Actuators)."
- Tesar, D. (Jan, 2012). "Freewheeling Amplifier Gear Synchro Assembly for High Speed MDW Operation."
- Tesar, D. (July, 2009). ""High Efficiency Multi-Speed Hub Wheel Drive Actuator"."
- Tesar, D. (Nov 1, 2011). "Criteria Based Vehicle Motion Planning and Operation."
- Tesar, D. (Oct, 2011). "It's Time for Computational Intelligence."
- Tesar, D. and P. Ashok (May, 2011). "Multi-speed Hub Drive Wheel Development Framework." MDW Project, Robotics Research Group, The University of Texas at Austin.
- Tesar, D., S. Vaculik, et al. (2005). "Actuator Intelligence Based on Performance Maps and Envelopes." White Paper, The University of Texas at Austin.
- THKBearing "THK General Catalog." CAT-200-1E, <http://www.thk.com/us/>, Cross-Roller Ring Series No: 382-3E.
- Timken-Company (1983). "Bearing Selection Handbook of Tapered Roller Bearings."
- Turkay, S. and H. Akcay (2005). "A study of random vibration characteristics of the quarter-car model." Journal of Sound and Vibration **282**(1-2): 111-124.
- Vaculik, S. A. (2008). "A Frame For Electromechanical Actuator Design." The University of Texas at Austin.
- Vagati, A., G. Pellegrino, et al. (2010). Comparison between SPM and IPM motor drives for EV application, IEEE.
- Van Schalkwyk, D. and M. Kamper (2006). Effect of hub motor mass on stability and comfort of electric vehicles, IEEE.
- Vandana, R. and B. Fernandes (2010). Optimal sizing of motor—Battery system for in wheel electric vehicles, IEEE.
- Verros, G., S. Natsiavas, et al. (2005). "Design Optimization of Quarter-car Models with Passive and Semi-active Suspensions under Random Road Excitation." Journal of Vibration & Control **11**(5): 581-606.
- Vos, R., I. Besselink, et al. (2010). "Influence of in-wheel motors on the ride comfort of electric vehicles." Advanced Vehicle Control (AVEC 10).

- Wang, R., Y. Chen, et al. (2011). "Development and performance characterization of an electric ground vehicle with independently actuated in-wheel motors." Journal of Power Sources **196**(8): 3962-3971.
- Watts, A., A. Vallance, et al. (2012). "Integrating In-Wheel Motors into Vehicles-Real-World Experiences."
- Watts, A., A. Vallance, et al. (2010). "The Technology and Economics of In-Wheel Motors." SAE International Journal of Passenger Cars-Electronic and Electrical Systems **3**(2): 37-55.
- Wei, X. and G. Rizzoni (2004). "Modeling and Control of A Hybrid Electric Drivetrain for Optimal Fuel Economy, Performance and Driveability." PhD thesis, The Ohio State University, Columbus.
- Wikipedia-1 "http://en.wikipedia.org/wiki/Wheel_hub_motor."
- Wikipedia "Tesla Roadster." http://en.wikipedia.org/wiki/Tesla_Roadster.
- Wikipedia "Unsprung Mass." http://en.wikipedia.org/wiki/Unsprung_mass.
- Wilcock, D. F. and E. R. Booser (1957). Bearing design and application, McGraw-Hill New York.
- Wilcoxon-Research "Bearing Failure: Causes and Cures."
- Williams, R. (1997). "Automotive active suspensions Part 1: basic principles." Proceedings of the Institution of Mechanical Engineers, Part D: Journal of Automobile Engineering **211**(6): 415-426.
- Wirje, A. and K. Carlsson (2011). "Modeling and Simulation of Peak Load Events Using Adams-Driving Over a Curb and Skid Against a Curb."
- Wong, J. Y. (2008). "Theory of Ground Vehicles." Wiley, John Wiley & Sons, INC.
- Wood, E., M. Alexander, et al. (2011). "Investigation of battery end-of-life conditions for plug-in hybrid electric vehicles." Journal of Power Sources.
- Xiong, L. and Z. Yu (2009). Control allocation of vehicle dynamics control for a 4 in-wheel-motored EV, IEEE.
- Xue, X., K. Cheng, et al. (2008). Selection of electric motor drives for electric vehicles, IEEE.
- Zeraoulia, M., M. E. H. Benbouzid, et al. (2006). "Electric motor drive selection issues for HEV propulsion systems: A comparative study." Vehicular Technology, IEEE Transactions on **55**(6): 1756-1764.
- Zhao, Y., S. Chen, et al. (2011). "Investigation of Trailer Yaw Motion Control Using Active Front Steer and Differential Brake." SAE International Journal of Materials & Manufacturing **4**(1): 1057.

Vita

Hoon Lee was born in Yeongam, South Korea on August 1, 1976, as the son of U-Bok Lee and Geum-Nan No. He received his Bachelor of Science in Mechanical Engineering at the Chosun University, Gwangju, in 1998. He worked in Hyundai-Kia Motors for six years before joining the University of Michigan at Ann Arbor. He then received his Master of Science in Mechanical Engineering in 2008. He continued his study in Doctor of Philosophy in Mechanical Engineering at The University of Texas at Austin.

Permanent Address: 310, Jeil-Park-Mansion, Wolsan 4-dong, Nam-Gu
Gwanju-si, 503-234, South Korea

This dissertation was typed by the author.